Properties of Glass-Forming Melts

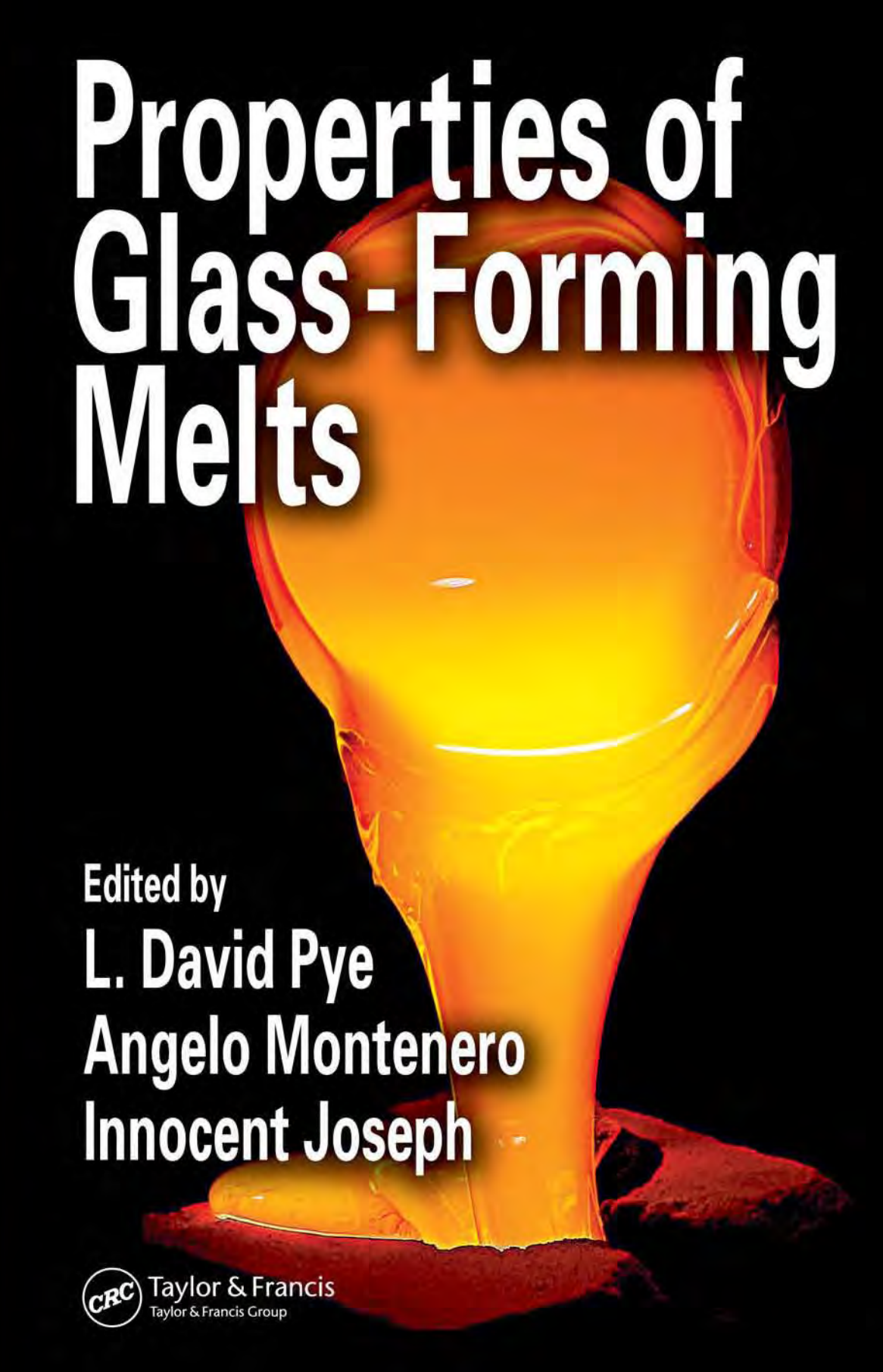

Edited by

L. David Pye
Angelo Montenero
Innocent Joseph

CRC Taylor & Francis
Taylor & Francis Group

Properties of Glass-Forming Melts

Properties of Glass-Forming Melts

Edited by
L. David Pye
Angelo Montenero
Innocent Joseph

Taylor & Francis
Taylor & Francis Group
Boca Raton London New York Singapore

A CRC title, part of the Taylor & Francis imprint, a member of the
Taylor & Francis Group, the academic division of T&F Informa plc.

Cover photo: Prof. Steven D. Edwards, Professor of Glass Art, the New York State College of Ceramics.

Published in 2005 by
CRC Press
Taylor & Francis Group
6000 Broken Sound Parkway NW, Suite 300
Boca Raton, FL 33487-2742

Printed in the United States of America on acid-free paper
10 9 8 7 6 5 4 3 2 1

International Standard Book Number-10: 1-57444-662-2 (Hardcover)
International Standard Book Number-13: 978-1-5744-4662-3 (Hardcover)
Library of Congress Card Number 2004061832

Library of Congress Cataloging-in-Publication Data

Pye, David L.
Properties of glass-forming melts / David L. Pye, Angelo Montenero, Innocent Joseph.
p. cm.
Includes bibliographical references and index.
ISBN 1-57444-662-2 (alk. paper)
1. Glass. 2. Electrochemistry. 3. Electrodes, Glass. I. Montenero, Angelo. II. Joseph, Innocent. III. Title.

QD575.G53P93 2005
666.1'04—dc22 2004061832

T&F informa
Taylor & Francis Group
is the Academic Division of T&F Informa plc.

Visit the Taylor & Francis Web site at
http://www.taylorandfrancis.com

and the CRC Press Web site at
http://www.crcpress.com

Dedication

The authors are pleased to dedicate the work embodied in this handbook to the students and researchers of glass science and engineering throughout the world, past, present, and future, who, by circumstance or choice, chose to study this remarkable substance we call glass, and in so doing helped to advance this field; and through their camaraderie, dedication and shared joy, promoted the causes of international peace, cultural understanding, and friendship in ways that only those involved can ever understand.

Foreword

The idea of compiling a handbook on the properties of glass melts had many origins. Among these were repeated statements by glass industrialists attesting to the need for this handbook, the incorporation of this task into the Mission Statement of the Industry Center for Glass Research at the New York State College of Ceramics at Alfred University, the creation of a new and continuing series of International Conferences on the Advances in the Fusion and Processing of Glass in 1987 and, in the mid-eighties, the establishment of a Technical Committee of the International Commission on Glass on this subject. All of these activities combined to suggest that a handbook on this topic would be of great value to glass scientists, engineers and researchers in their attempts to advance the broader fields of glass science and engineering.

Initial efforts in undertaking this task included carrying out literature surveys by scholars throughout the world and sharing the results with colleagues interested in this subject.

Being aware of the enormous impact on the glass industry of a more general text on the properties of glass (*Properties of Glass*, G.W. Morey, Reinhold Pub. Corp., 1938), it became readily apparent that transforming this database into concise summaries on select properties would be of equal value to the glass industry at this time, that is, to create a handbook that could serve as a reliable data source and provide insights by those with special knowledge and experiences in this field. This conclusion was buoyed by progress in the chemical, physical and computational modeling of glass melts that also occurred during the last couple of decades. In fact, the success of these new tools — made possible in part by the development of both advanced hardware and software in the computer industry — virtually demanded compilation of the best physical and chemical data on select properties to make possible even greater exploitation of these new engineering tools. Thus, the decision was made that the handbook should be the work of many authors to ensure the greatest possible relevance, thoroughness and scholarship of the individual chapters. By design, all chapters combine discussions of fundamental concepts with compilation of reliable data projected to be critical to the modeling of glass melting, fining, conditioning and forming.

It is hoped that users of this handbook will find it to be of considerable help in both the research and manufacturing of glass. In support of this goal, the handbook begins with a brief discussion of the liquid state followed by broader discussions of the thermodynamic, transport properties and redox effects. This approach naturally leads into more exact discussions of the several important properties of glass melts: viscosity, surface tension, density and heat capacity. This grouping of topics leads in turn to more generalized subjects of heat transfer and gas solubility. The chapter on electrical properties provides a solid foundation for understanding glass melting via direct Joule heating of the melt, and the discussion of the corrosive nature of

molten glasses will be of great interest to tank designers and operators. The handbook concludes with an overview of nuclear waste vitrification, a discipline that was a lead force in supporting and encouraging this effort.

L. David Pye
A. Montenero
I. Joseph
Alfred, New York
March 2005

Preface

The increasing amount of information on the properties and science of glass-forming melts, as well as a clear need for a concise compilation of this knowledge for use by glass scientists and engineers, requires efficient communication channels and platforms to exchange this information. At the close of the 20th century, several glass scientists took the initiative of establishing a new Technical Committee (TC) within the International Commission on Glass (ICG), which was designated as TC 18 on the Properties of Glass-forming Melts. The ICG, founded in 1932, is a worldwide organization for the glass community and brings together glass scientists (university, research groups), glass engineers (glass industry and their suppliers) and glass artists for the purposes of technology exchange, cultural understanding and advancement of the fields of glass science and engineering in general. In the fulfilment of these goals, the ICG creates platforms such as triennial congresses on glass, and annual meetings of the ICG and technical committees. The publication of this *Properties of Glass-forming Melts* is an extension of these aims.

TC 18 organizes technical meetings once or twice per year, conducts round-robin tests and engages in other transfer activities. The output of this TC is of high value for these scientists, who require reliable data on the behavior of viscous melts, which, upon fast cooling, show vitrification. Glass technologists applying mathematical models simulating the glass melting process and glass forming also need detailed information on the properties of the molten state. Only the availability of sufficient data on glass-melt density, thermal expansion, heat conductivity, radiation transfer, surface tension, chemical activities, chemical reactions and interaction with other phases makes mathematical models applicable in glass technology. Such models today offer an important tool for glass-melting furnace designs and forming machines, process control during melting and forming and for finding optimum process settings in melting, conditioning and forming of glass. Data of glass melt properties allow glass scientists to understand the behavior of these melts as related to their atomic scale structure, and the mechanisms involved in glass melting processes such as transport phenomena and thermodynamics.

On the proposal of the founding Chairman of TC 18, Dr. L. David Pye, Past President of the Commission and Dean Emeritus of the New York State College of Ceramics at Alfred University, members of TC 18 and others agreed to prepare a handbook on important glass melt properties that would gather existing knowledge on property data, mechanisms, measurement techniques and knowledge on the properties of glass-forming melts related to structure or other properties. Leading scientists in the field of properties of glass melt systems offered their contribution to this comprehensive work, as did authors from six different countries, and together they have created a very valuable source of information for glass scientists and engineers.

The publications of the ICG and especially the papers issued by the TCs are of great importance for the glass community, and this book, to be considered as the "state of the art" on information concerning glass melt properties, is an excellent example of the output of the work of the core members of the Technical Committee on Properties of Glass Forming Melts. The book will also help future-generation glass scientists and glass technologists as a starting point, as well as supporting students in accessing information on the fascinating material called glass.

Ruud Beerkens
TNO, The Netherlands
Chairman TC 18
1999–2004

Acknowledgments

The editors would like to thank the authors of each chapter for their enormous help, patience and dedication in making this handbook a reality. These authors have made a tremendous contribution to the field of glass science and industry, an effort sure to be appreciated and recognized throughout the world.

The financial and in-kind support of the following organizations is also gratefully acknowledged: the National Institute of Standards and Technology, the Center for Glass Research and the S.R. Scholes Library at the New York State College of Ceramics at Alfred University. The strong administrative help of Elizabeth Cartella and Maxine Kruger throughout this process is deeply appreciated.

Editors

L. David Pye, Ph.D. is Dean and Professor of Glass Science, Emeritus, the New York State College of Ceramics at Alfred University. His career in academe and industry involved teaching, scholarship, and research on the fabrication, characterization, and application of non-crystalline solids. He is the author of nearly 80 contributions to the literature and has served as editor of numerous conference proceedings. He was co-founder of the NSF Industry-University Center for Glass Research at Alfred, and, as Dean of the College, established several new academic programs in art and engineering. He was also a co-founder of multiple continuing conferences including Boron in Glass, Advances in the Fusion of Glass, Natural Glasses, and most recently, Photonic Glasses.

Dr. Pye's honors and awards include Glassman of the Year, 1996; the Labino Lecture Award, 1994; honorary membership in the German Society of Glass Technology, 1995; Alfred University Presidential Order of Merit Award, 2002; and Honorary Fellowship in the British Society of Glass Technology, 2004. From 1997–2000 he served as president of the International Commission on Glass. He has served on a number of national review panels for DOE, NSF, and the National Research Council. His biography appears in several standard references including *Who's Who in the World*, *Who's Who in America*, and *Who's Who in Engineering*. He was recently appointed Chair, The Globalization Task Force of the American Ceramic Society.

Angelo Montenero, Ph.D. was born in Rome and received his Ph.D. in Chemistry from Parma University. He joined the Faculty of Sciences of the University of Parma as an assistant professor of the Science of Metals. He later became associate professor of Science and Technology of Glasses, then full professor of General Chemistry in the Faculty of Sciences of the University of Parma. In 1976–77 he was elected president of the Council of Chemistry. In 1996, in the framework of the Science Faculty, he established in Parma a School of Packaging, the only one existing in Italy and one of the few in Europe. This school, sponsored by some of the biggest Italian and European packaging companies, was established with the aim of preparing technicians with a deep knowledge of the many-faceted world of packaging. He remains in charge of the school.

Because of the gap existing between the Italian Glass Companies and the research world, in 1985 Dr. Montenero co-founded the Associazione Tecnici Italiani del Vetro A.T.I.V (Italian Glass Association), and was its vice-president until 2000, when he became its president. In 1989, Prof. Montenero was the promoter and president of Consorzio Ricerca Innovazione Vetro (Consortium for Research and Innovation in Glass — CO.R.I.VE), a consortium with the aim of promoting research and continuing education in glass science and technology. Its members are Parma University,

Bormioli Rocco and Seves. In 1998, he received an honorary degree from the State University of New York.

Dr. Montenero is the author or co-author of more than 160 scientific papers published in international journals and has registered five international patents in the field of gas sensors, waste recycling, fashion glasses, and osteoinductive coatings. His research is mainly devoted to the study of glasses prepared by melting or sol-gel, and plastic films for food packaging with "intelligent features."

Dr. Montenero is a member of the International Advisory Board of the *Journal of Non-Crystalline Solids* and of TC 23 of the International Commission on Glasses. He has participated in many international congresses — in some serving as a session chairman. In 2003, he was chairman of the Xth International Conference on the Physics of Non-Crystalline Solids, held in Parma.

Innocent Joseph, Ph.D. is the Manager of Technology at Duratek, Inc., a leading provider of waste treatment, waste disposal, and decommissioning services to the United States government and commercial nuclear facilities. Before joining Duratek, he was Assistant Director for Technology at the Industry-University Center for Glass Research at the New York State College of Ceramics at Alfred University. He received his Ph. D. in Ceramic Science from the New York State College of Ceramics at Alfred University and his Bachelor of Technology degree in Ceramics from the Institute of Technology at Banaras Hindu University in India.

Dr. Joseph is actively involved in the development and implementation of Duratek's radioactive waste vitrification technology, which is used by the United States Department of Energy in the treatment and disposal of low- and high-level radioactive wastes. His current areas of interest include radioactive waste glass formulations, glass property–composition relationships, the effect of the redox state on waste glass processing and properties, and improvement of melter feed and glass compositions to optimize processing of waste feed in a joule-heated ceramic melter. He has several publications and presentations in the areas of nucleation and crystallization in glasses, glass structure, glass property–composition relationships, redox effects on glass properties, and effect of composition and redox state on glass crystallization.

Contributors

Rainer Backman
Energy Technology and Thermal Process Chemistry
Umeå University
Umeå, Sweden

M.K. Choudhary
Owens Corning Science & Technology Center
Granville, Ohio

Kaj H. Karlsson
Dept of Chemical Engineering
Åbo Akademi University
Turku, Finland

Fritz W. Krämer
Schott AG
Mainz, Germany

David Martlew
Pilkington Technology Management
Ormskirk, UK

Oleg V. Mazurin
Thermex Company
St. Petersburg, Russia

Rand A. Murnane
Corning Incorporated
Corning, New York

George A. Pecoraro
PPG Industries
Glass Technical Center
Harmas Township, Pennsylvania

R.M. Potter
Owens Corning Science & Technology Center
Granville, Ohio

Alexander I. Priven
Scite Ltd.
St. Petersburg, Russia

Oleg A. Prokhorenko
Laboratory of Glass Properties
St. Petersburg, Russia

David Pye
The New York State College of Ceramics at Alfred University
Alfred, New York

Christian Rüssel
Otto-Schott Institute
University of Jena
Jena, Germany

Robert R. Thomas
Corning Incorporated
Corning, New York

John D. Vienna
Pacific Northwest National Laboratory
Richland, Washington

Douglas A. Weirauch, Jr.
Alcoa Technical Center
Alcoa Center, Pennsylvania

Contents

1 Glass-Forming Melts

L. David Pye

CONTENTS

1.1 INTRODUCTION

This handbook was assembled with the intention of both documenting and accelerating the field of glass science and engineering in this new century. As is evident by the very title of this handbook and a glance at the table of contents, this daunting task is made much easier and far more efficient by involving authors who have studied these properties over the course of several years and even decades. With such expertise and attention comes both breadth and depth of understanding of the respective subject areas and, equally important, empowerment to write authoritatively.

1.2 PURPOSE OF THIS CHAPTER

This introductory chapter attempts to give a more precise technical description to the phrase “glass-forming melts,” and to comment briefly on the structure and penultimate property of many liquids — their ability to be readily quenched to the vitreous or glassy state. As realized in the last few decades, all melts will form glasses if quenched sufficiently rapidly, but in order to make the goals of this handbook realistic and manageable, only oxide melts are considered. It is hoped

that industrialists, academicians, students, scholars, artists, etc., will find this work helpful in not only making glass products, but also in understanding their intrinsic properties such as mechanical strength, transparency and chemical resistance. Chief beneficiaries will be manufacturers of many glasses we encounter in our everyday lives: windows, containers, tableware, optical fibers, television, eyeglasses, mirrors, insulating fibers, light fixtures, stained glass, etc. Those involved in nuclear waste vitrification programs throughout the world should also find this handbook useful. Additionally, it was our intention to provide broad support to modelers of (1) glassmaking processes, (2) atomic and microstructure structure of glass and (3) chemical and physical properties of glass at both melting and room temperatures.

1.3 HISTORICAL CONTEXT

Glassmakers in past centuries, of course, did not have our present-day database to call upon for problem solving; rather, they were guided by their observations, intuition, hearsay and maybe even a little superstition. Yet great works of glass art were created, instruments of science and engineering developed and great centers for glassmaking established. This legacy, which adds to the mystique of this substance we call glass, has inspired countless scientists, engineers and artists to contribute in their own small way to the total understanding of this remarkable material. The chapters in this handbook attempt to continue this tradition.

1.2 THERMODYNAMIC DESCRIPTION OF PHASES AND PHASE TRANSFORMATION

One of the great triumphs of glass science in the last century was to demonstrate that glassmaking via melt quenching could be described remarkably well as a subset of the broader fields of phase equilibria and phase transformation. To illustrate this concept, we begin by stating one of the great equations found in all of science, the Gibbs free energy equation:

$$G = H - TS \tag{1}$$

Here, G is the Gibbs free energy, H is enthalpy, and T and S have their usual meaning. Defining H as E + PV, and ignoring the PV term (generally a smaller part of the total energy) equation (1) can be rewritten as

$$F = E - TS \tag{2}$$

where F is now the Helmholtz free energy, P and V have their usual meaning, and E is internal energy. At absolute zero, the free energy is precisely equal to the internal energy, and E, in turn, is a function of structure and chemical bonding. With increasing temperature, electronic and lattice vibrational energies contribute to E as well. Changes in internal energies in solids or liquids caused by transformation are easily measured by employing standard methods of thermal analysis. These mea-

surements, in turn, are useful for determining not only the onset and conclusion of a phase transformation, but, equally important, the rate of the transformation itself.

1.3 CONDITIONS FOR PHASE STABILITY AND PHASE TRANSFORMATION

The beauty of equation (2) is that it can be applied directly to the phases of matter we routinely encounter: liquids, solids and gases. These phases can be single or multi-component; the equation still applies. When F is the same for each phase, a state of equilibrium exists. When F is greater for one phase relative to a second, a condition easily induced by changes in temperature or pressure, a driving force exists to transform to the phase with the lowest value of F, i.e., minimization of total system energy. These conditions for stability and transformation are easily calculated for many glass-forming systems over wide ranges of temperatures and pressures. Thus, we are able to define conditions where melts in these systems are stable, meta-stable, or even unstable with respect to crystalline or solid phases. The last term defines a situation where there is no intrinsic thermodynamic barrier for transformation other than diffusion.

From this approach, it is readily apparent that the most fundamental property of glass-forming melts is the thermodynamic delineation of temperature ranges that favor transformation to phases of lowest free energy and the transition (transformation) of a melt to the vitreous (glassy) state.*

1.4 CLASSIFICATION OF PHASE TRANSFORMATIONS

For reasons of completeness, we note that equations (1) and (2) not only provide a theoretical foundation of phase equilibria, but also serve to distinguish between what are commonly referred to as first-, 2nd- and 3rd-order transformations. First-order transformations are those where step-like discontinuities develop in properties defined by the first derivative of G or F with respect to temperature, i.e., enthalpy and entropy, whereas 2nd-order transformations are associated with similar discontinuities defined by the 2nd derivative of G or F, i.e., thermal expansion, compressibility, etc., and so forth for 3rd- and higher transformation orders. Examples of first-order transformation are melting and crystallization, whereas the glass transition takes on some characteristics of 2nd-order transformations.[1]

1.5 PHASE TRANSFORMATIONS IN GLASS-FORMING SYSTEMS

Insights into phase transformations in glass-forming systems are gained by preparing schematic diagrams of F vs. temperature as depicted in Figure 1.1. Figure 1.1(a) illustrates the condition for equilibrium for two solid phases in a one-component

* The preference here is to speak of the glass transition when a melt converts (transforms) to the vitreous or liquid state.

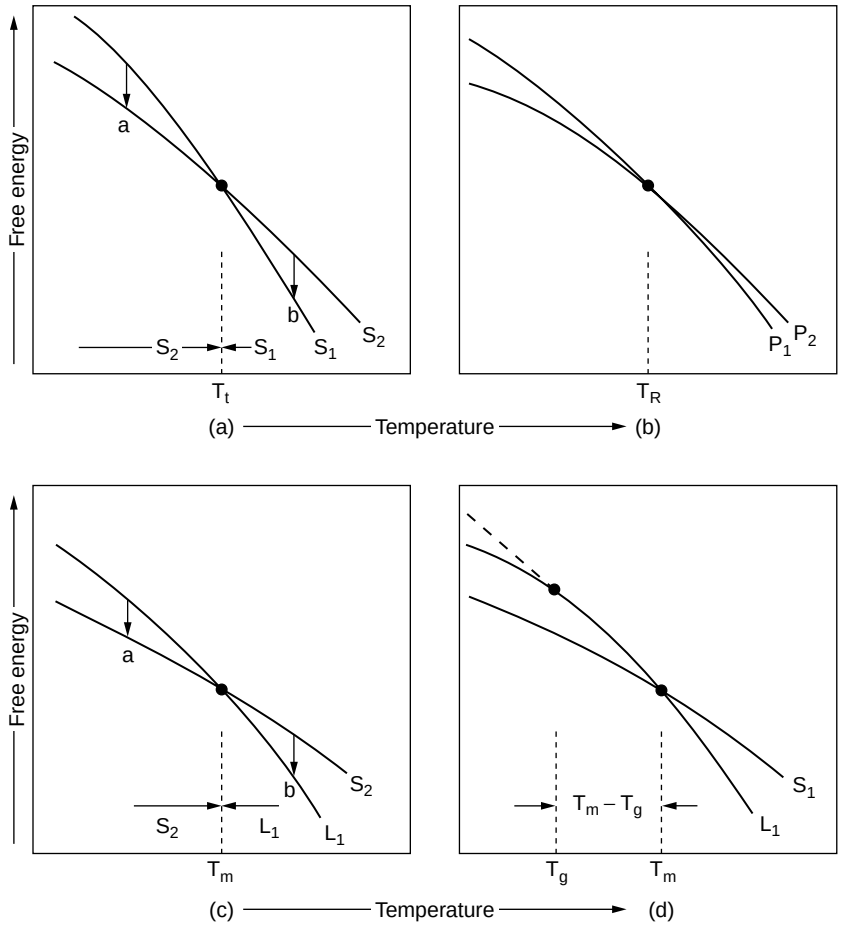

FIGURE 1.1 Schematic free energy-temperature relationships for (a) a solid–solid transformation; (b) 2nd-order transformation; (c) solid–liquid transformation; and (d) glass transformation.

system and conditions for transformation, i.e., a decrease in free energy at the transformation above or below the temperature at which both phases coexist. They are at equilibrium at T_1 because they have the same free energy. The liquid–solid or solid–liquid transformations shown in Figures 1.1(a) and 1.1(c) are classic first-order transformations. In Figure 1.1(c) they depict simple melting or crystallization. Second-order transformations, illustrated in Figure 1.1(b), are associated with phases that ostensibly coexist over wide ranges of temperatures. Figure 1.1(d) introduces the transformation to the vitreous state at the temperature defined as Tg. The interval between Tm, the thermodynamic melting temperature (liquidus), and Tg is of great importance in glass science and engineering. It is within this range that the viscosity changes by multiple orders of magnitude as the melt cools (solidifies) into a solid without crystallization. Moreover, this range depicts the liquid state of this system

as metastable with respect to the liquid state. Why metastable? The answer is that the melt must undergo a slight increase in free energy before the transformation will take place, i.e., there is an inherent thermodynamic barrier that must be surmounted before the transformation occurs. The process of overcoming this barrier is called nucleation. Its origin is found in the introduction of internal interfaces and concomitant diffusional processes that must also take place, and is described as either homogeneous (intrinsic) or heterogeneous (assisted). The overall transformation, nucleation and growth is, more simply, crystallization. Learning to control this process to make new materials with valuable properties, i.e., glass-ceramics, was one of the foremost achievements in glass science and engineering in the last century.

1.6 THE VITREOUS STATE

Further examination of Figure 1.1 demonstrates that the vitreous state is unstable with respect to the under-cooled liquid state, meaning the only barrier for the vitreous state to become in equilibrium with the liquid state below the glass transition temperature is thermally activated diffusion. That is, nucleation is not involved. Upon raising the temperature high enough, this transformation is virtually instantaneous. At lower temperatures, longer periods of time are required — perhaps even centuries. Two other points need to be made here. First, the vitreous state, like the liquid state, is also metastable to the solid phase of this system. Second, the structure of glass and its properties are dependent on the glass transition temperature itself. Faster quenching results in a higher transition temperature and a more open atomic structure, whereas slower quenching produces a more compact structure. It is for this reason that the properties of glass depend directly on its thermal history in the range of temperatures where glass transition occurs. This dependence also gives rise to the need to anneal or stabilize glass in the glass transition region in order to remove or prevent stresses induced by uneven quench rates within a given sample of glass. Application of this approach to $Si0_2$ can be reviewed in reference 2.

1.7 PHASE SEPARATION

When dealing with multicomponent systems, other transformations become possible such as decomposition of a single-phase homogenous liquid into two distinct liquid phases, a process often referred to as “phase separation.” This transformation is accompanied by the development of microstructure in the melt and cooled glass as revealed by a variety of experimental methods. It can be represented thermodynamically as shown in Figure 1.2, and is sometimes called stable or metastable liquid immiscibilty depending upon composition and temperature where this phenomenon occurs. Depending on composition, conditions exist where no thermodynamic barrier exists for this type of transformation other than diffusion. This process is sometimes referred to as spinodal decomposition.

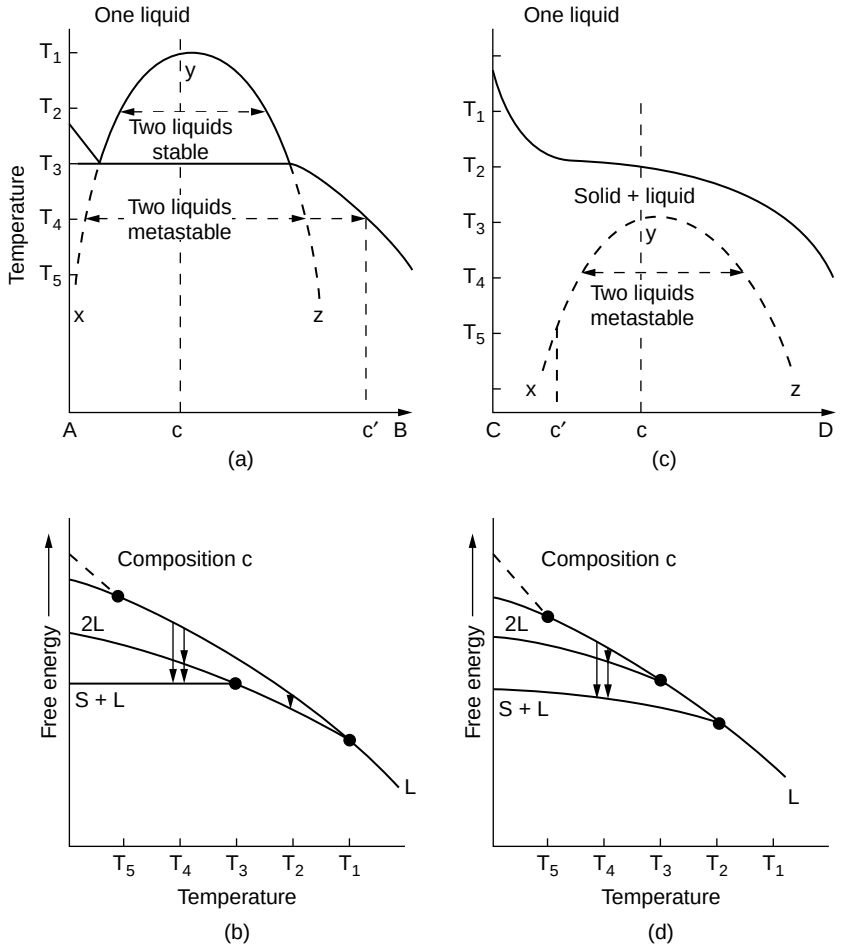

FIGURE 1.2 Stable and metastable liquid immiscibility in hypothetical binary systems. Free energy-temperature relationships of (b) correspond to (a), those in (d) correspond to (c), the Ostwald transformations at T_4, as shown here, yield a solid and new liquid; in many glass-ceramic systems, the end product is simply a new stable crystalline phase (or phases).

1.8 NUCLEATION THEORY

It should be noted that the theory of homogeneous nucleation in glass-forming melts is in need of attention. Several authors have noted that disagreement between theory and experimental results for some systems approaches many order magnitudes.[3] Paradoxically, we have a situation where disagreement between theory and experimental results hardly matters at all in the annual manufacture of millions of tons of glass throughout the world. It would seem this anomaly should be one of the foremost problems in glass science to be resolved in this century. In contrast, the theory of heterogeneous nucleation is well understood.[4]

1.9 THEORY OF GLASS FORMATION

The bypassing of crystallization, i.e., nucleation and subsequent growth of nuclei in glass-forming systems to achieve a more thermodynamically stable crystalline phase, is, of course, a phenomenon of great importance in glass science and engineering. There are important experimental conditions to be considered such as sample size, type of quench employed, quench rate and initial quench temperature. It has been recognized for some time that optimizing conditions for promoting glass formation via melt quenching was primarily a matter of maximizing the quench rate. That is, glass formation is favored by rapid transverse of the region Tm–Tg so as to minimize time available for nucleation and crystal growth of the thermodynamic stable crystalline phase. The formalization of this phenomenon as a subset of phase transformation was achieved by Uhlmann in a seminal paper on this subject.[5] In recognition of the underlying kinetics associated with nucleation and growth, the debate was changed from why do some melts form glasses to how fast must a melt be quenched to achieve the vitreous state? The ultimate property of these melts, therefore, is their ease to readily form a glass when quenched. It is this property that serves as a driving force for the search for new glass-forming compositions, and gives rise to the need to characterize these melts by measurement of their physical properties. Hence, the need for a handbook on this subject evolved quite naturally.

1.10 GLASS-FORMING MELTS

We can gain additional insight into the subject of this handbook by noting in Figures 1.1 and 1.2 that glass-forming melts can exist over a broad range of temperatures. Starting above the thermodynamic melting point, the liquid state is continuous well below the liquidus. The continuity of under-cooled melts over broad temperature ranges is significant in the melting, refining, homogenization and thermal conditioning processes necessary for forming these melts into useful glass articles. Two other factors need to be mentioned here. First, glass-forming melts are almost never in equilbrium with their vapor phase nor the crucibles commonly used to contain them at elevated temperatures. Therefore, one can expect volatilization, reaction with crucibles and a dependence of redox state of the melt on partial pressures of oxygen, nitrogen, water vapor and other gases found over the melts. That is, their thermodynamically driven tendencies to react with surrounding materials and ambient vapor phases are, in effect, important properties of glass melts. It was for this reason that chapters on refractory corrosion and redox behavior were included in this handbook. Second, glass melts are seldom in a truly chemical homogeneous state at the time they are first formed. That is, chemical and phase inhomogeneities are to be expected as a result of the melting process, and “time at temperature” is required to achieve a truly homogenous state. Coupling these facts with (1) a propensity of certain melts to transform to two liquids and (2) the existence of a driving force to crystallize, it is not surprising that numerous investigators have observed a dependence of properties on the thermal history of the melt.

1.11 THE STRUCTURE OF GLASS-FORMING MELTS

From the above, it is apparent that the existence of thermodynamic driving forces figures prominently in characterization of glass-forming melts in a structural sense. Allowing the possibility for more subtle driving forces for atomic clustering, we can speak of structural and chemical inhomogeneities in these melts and arrive at the arena of one of the longest and most fiercely argued subjects in the history of science, namely, the structure of glass derived from these melts through quenching. That this controversy existed over several decades and is still subject to passionate discourse speaks directly to the advancement of structural characterization methods beginning with x-ray diffraction and absorption, and continuing with electron microscopy through nuclear magnetic resonance, full spectrum spectroscopy, etc. The characterization of the parent melts by measurement of their physical and chemical properties must ultimately take into account this propensity for continuous change of structure with temperature and pressure. Notwithstanding this situation, such characterizations are extrordinarlly useful in manufacturing, advancing the theory of the glass-forming melts, and predicting the properties of glasses at room temperature.

1.12 THE PROPERTIES OF GLASS-FORMING MELTS

Having reviewed the thermodynamic description of glass-forming melts, it is relatively easy to place the measurements of the properties of these melts in proper perspective. Because of (1) favorable kinetics that prevent the achievement of full equilibrium with ambient vapor phases and refractories used as melting containers, and (2) the transformations of the metastable melt to lower free energy levels, i.e., crystallization or phase separation, we are able to measure properties of these melts over wide ranges of temperature. Therefore, the fact that these melts can be made chemically homogeneous and cooled to form glasses in the first place allows us to make these measurements in meaningful, reproducible ways. At this point, it remains only to choose those properties of greatest interest to both glassmakers and glass scientists. In this handbook, this selection includes more detailed examination of their thermodynamic, chemical and redox behavior, and standard properties such as transport, viscosity, heat capacity, surface tension, electrical conductivity, density and gas solubility. A stand-alone chapter dealing with the properties of melts concerned with nuclear waste vitrification was included because of (1) its uniqueness and importance and (2) the many contributions to our overall understanding of glass science and engineering many researchers have made in studying nuclear waste vitrification.

REFERENCES

1. G.W. Scheer, *Relaxation in Glass and Composites*, John Wiley and Sons, New York, 1986.

2. L. David Pye, Microstructure — Property Relationships in Some Non-Crystalline Solids, in *Treatise on Material Science and Technology*, Eds. R. MacCrone and H. Herman, pp. 151–197, Academic Press, 1977.
3. E.D. Zanutto and V.M. Fokin, Recent Studies of Internal and Surface Nucleation in Silicate Glasses, *Phil. Trans. R. Soc*., London, A(2003) 361, 591–613.
4. D.R. Stewart, Concepts of Glass Ceramics, in *Introduction to Glass Science*, Eds. L.D. Pye, H.J. Stevens, and W.C. LaCourse, pp. 257–265, Plenum Press, NY, 1970.
5. D.R. Uhlmann, Kinetic theory of glass formation, *J. Non-Cryst. Solids* 7(1972) pp. 337–358.

2 Thermodynamic Properties

Kaj H. Karlsson and Rainer Backman

CONTENTS

2.1 INTRODUCTION

Writing a chapter on thermodynamics of glass melts raises the question of how to relate it to other chapters in this book. If irreversible thermodynamics is included, this alone should be more than enough for one chapter. If the treatment were restricted to reversible thermodynamics, it would still include acid-base and redox properties, solubility of gases, transport phenomena, phase diagrams etc., to which, however, separate chapters are already devoted. Thus, what primarily remains is to try to compile an overview of thermodynamic constants like the heat of a reaction or enthalpy, H; the degree of disorder in the system; the available part of the enthalpy, i.e., the free enthalpy or Gibbs free energy, G; the temperature derivative of the enthalpy or heat capacity, C_P; and the deviation from ideality due to mixing or activity. As an alternative to activity, the corresponding mixing functions H_{mix}, S_{mix}, and G_{mix} could be treated. Again, H, S, G and C_P values for pure compounds can be found in thermodynamic tables. Thus, in general, deviations from ideality due to mixing remain to be considered. If the treatment is further restricted to areas of interest to the glass industry, only the effect of deviation from ideality on the liquidus temperature of multicomponent silicate glasses remains; binary and ternary phase

diagrams are easily accessible but of limited use. The subject as such is, however, still important enough to be discussed in a chapter of its own.

2.2 HEAT CAPACITY

The heat capacity, that is, the change in enthalpy for a given change in temperature, is of limited concern to the industry, but is used to transform accessible enthalpy data (usually given at NTP) to a temperature of interest. Some attention should be paid to how a published value is defined; the mean heat capacity, $\overline{C}_p$, is a linearization of the molar heat capacity, C_P, over a temperature range ΔT.

Almost 100 years ago, Winkelmann[1] observed that, for commercial glasses at around room temperature, the mean heat capacity

$$\overline{C}_p = (H_T - H_{T_0}) / (T - T_0) \tag{1}$$

is, to a few percent, an additive function of composition. Although this starting point has been found correct, subsequent extensions of Winkelmann's model, like the widely used one of Sharp and Ginther,[2] have been less successful. Writing

$$\overline{C}_p = \sum_i w_i \overline{C}_{p,i} \tag{2}$$

where *wi* is the weight fraction of oxide and $\overline{C}_{p,i}$ its contribution to mean heat capacity, Sharp and Ginther used the following equation for describing the temperature dependence of the $\overline{C}_{p,i}$'s between 0°C and any temperature ϑ

$$\overline{C}_{p,i} = (A_i \vartheta + C_i) / (0.00146\vartheta + 1) \tag{3}$$

where A_i and C_i are constants. The function provides a good representation of experimental data, but is not convenient for calculating either C_P at a given temperature, nor relative enthalpies and entropies between any two temperatures. Further, the change in C_P at glass transition temperature was neglected when deriving A_i and C_i. Because C_P increases 10–50% at T_g, equation (2) inevitably gives an erroneous result. In 1977 Bacon[3] took the temperature dependence into account, but the data were still too restricted to allow derivation of reliable partial molar heat capacities for all the major oxides. Fairly recently, Richet and Bottinga [4,5] as well as Stebbins, Carmichael and Weill[6] published models that both give good agreement above 400 K, despite relying on almost totally different sets of data; the results of Stebbins et al. were obtained by differential scanning calorimetry, Richet's and Bottinga's by dropping the sample into an ice calorimeter. The model, which both the groups used for fitting their data, was originally suggested by Haas and Fisher[7] and is of the form

$$C_{p,i} = a_i + / T^{1/2} \tag{4}$$

TABLE 2.1
A Selection of Coefficients for Equation (4)

	a_i	$10^3 b_i$	$10^{-5} c_i$	d_i	ΔT/K	Δx/mol%
SiO_2	127.200	–10.777	4.3127	–1463.9	270–1600	33–100
Na_2O	70.884	26.110	–3.5820	0	270–1700	0–33
K_2O	84.232	0.731	–8.2980	0	270–1190	0–17
CaO	39.159	18.650	–1.5230	0	270–1130	0–50
MgO	46.704	11.220	–13.280	0	270–1080	0–50
Al_2O_3	175.491	–5.839	–13.470	–1370	270–1190	0–33
B_2O_3	215.151	–3.435	15.836	–2920	270–510	100

Note: Partial molar heat capacities of oxides in silicate glasses are obtained in J $mol^{-1}K^{-1}$. The last two columns give validity ranges.

Source: Richet, P. (1987). Heat capacity of silicate glasses. *Chem. Geol.* 62.

Richet's and Bottinga's results have been updated and results from 1987 are given in Table 2.1.[5] Knowing C_P, the relative enthalpy between any two temperatures can be calculated

$$H_T - H_{T_0} = \sum_i x_i \int_{T_0}^{T} C_{pi} \mathrm{d}T \tag{5}$$

2.3 LIQUIDUS TEMPERATURE

By far more interesting to the glass industry is the liquidus temperature, the temperature above which a system is in the liquid state. No part of a furnace should be kept below the liquidus temperature. In an ideal system, the liquidus temperature depends only on the melting point and melting enthalpy of the pure compound and on the amount of impurity added. However, because of intermolecular interactions, in practice very few systems behave ideally. The deviation from ideality can be approached either by fitting a polynomial model through the experimental points or by modifying the ideal model to fit the data by introducing an excess function. In both cases, it is a question of curve fitting; the latter model, however, still has some resemblance to an ideal behavior.

Assuming ΔC_p between liquid and solid to be zero, then, in a binary phase equilibrium system, the liquidus temperature, *Tliq*, in the primary crystallization field of a congruently melting component, *i*, is given by

$$T_{liq} = \frac{T_{m,i} + \dfrac{G_i^E}{S_{m,i}}}{1 - \dfrac{R \ln x_i}{S_{m,i}}} \tag{6}$$

where T_{mi} is the melting point and S_{mi} is the melting entropy of pure *i*. G_i^E is the partial excess free energy for component *i* in the solution and x_i its mole fraction. The whole problem is concentrated on finding a proper value for G_i^E. For an incongruently melting compound, the problem is further complicated by the assessment of a fictive melting point.

The experimental binary and ternary phase diagrams in the system Na_2O – CaO – SiO_2 are well established, mainly due to the classical works by Morey and his coworkers.[8,9] It is common practice to use these diagrams even when extending the problem to a multicomponent system. The result is, however, usually no more than a good guess, and seldom predicts even the correct primary phase; the wollastonite and devitrite fields widen considerably even if the addition of new components are kept below a few percent. The problem with multicomponent systems can be approached in two different ways. The classical one is to develop phenomenological models for the dependence of liquidus temperature on composition.[10–13] A more recent method is to use thermodynamic modeling,[14–25] where experimental information, creativity and advanced optimization mathematics are all equally important.

2.3.1 Experimental Methods

Regardless of approach, however, both methods rely entirely on accurate experiments. Differential thermal analysis can be used to obtain a first approximation, but is not accurate enough to establish the actual liquidus temperature. Even in a gradient furnace, care must be taken that thermal currents do not cause misinterpretations. Variations of this method have been reported,[26,27] but the most reliable method seems to be to use small (about 1 g) samples of glass grains, each held in a cone of platinum foil.[28] In principle, a set of these is placed in the gradient furnace at intervals that makes the difference in temperature between two adjacent cones not more than 10°C. But even when extreme care is taken, the crystals need to be grown close to the liquidus, where the equilibrium volume fraction of crystal is small, because it is possible for the most rapidly growing phase found at temperatures not much lower to be not the true primary phase. Figure 2.1 illustrates this from an experiment done in the Saint Gobain laboratories, where the size of the largest crystals present has been divided by the heat treatment time to obtain an average growth rate.

2.3.2 Polynomial Modeling

First, let us have a brief look at phenomenological models. Using Morey's data,[8,9] the liquidus surface of each primary field in the ternary system Na_2O – CaO – SiO_2 can reasonably well be described by an equation of the form

$$T_{NCS} / °C = B_0 + B_1 \cdot p_{CaO} + B_2 \cdot p^2_{CaO} + B_3 \cdot p_{SiO_2} + B_4 \cdot p^2_{SiO_2} \qquad (7)$$

where T_{NCS} is the liquidus temperature in the ternary system, $B_0 \ldots B_4$ are coefficients and *pi* is weight percent oxide.[11,12] The values in Table 2.2 for the *B*-coefficients can be used.

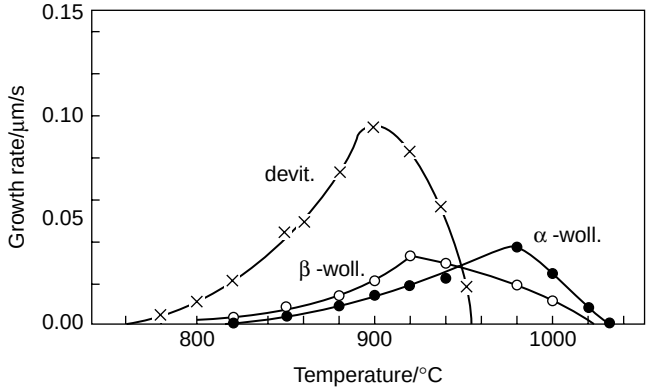

FIGURE 2.1 Growth rate of different crystals plotted versus temperature. The graph illustrates the difficulty in deciding the true primary phase.

The equation gives a satisfactory description, except for the low temperature part of the devitrite field, which is too narrow in the model compared with experimental facts. Minor additions of components to a system are expected to give a lowering of liquidus temperature. However, attempts to extend equation (7) to a multicomponent system fail if the correction factor is of the type

$$\Delta T_L = T_{\mathrm{NCS}} - T_{liq} \tag{8}$$

where ΔT_L is the difference between the liquidus temperature in the ternary system, T_{NCS}, and in the corresponding multicomponent system, T_{liq}. In the failed attempt, T_{liq} was modeled as a function of added minor components. The main reason for the failure is probably that the widening of the wollastonite and devitrite fields gives the NCS surface a slope of opposite sign when crossing a border between two phase fields.

TABLE 2.2
Coefficients for Equation (7)

Primary Phase	B_0	B_1	B_2	B_3	B_4
Devitrite	484.0	67.62	–1.975		
Wollastonite	–3.675	31.58	8.787		
Tridymite	–4601.0		1.545	73.20	
Disilicate	–6710.0		–3.003	226.9	–1.698
$NaO \cdot 3SiO_2$	1508.0	41.94	–1.266		–0.182

Note: Liquidus temperature is obtained in °C when oxides are given in weight percent.

Source: Data from Backman et al. (1990). Prediction of liquidus temperatures for multicomponent silica glasses. *Glastech. Ber.* 63K.

TABLE 2.3
Coefficients and Terms for Equation (9)

Coefficient	Value	Order	Oxides			
B_0	889.6	0				
B_1	30.657	1	CaO			
B_2	–1.829	2	Na_2O	Na_2O		
B_3	2.694	2	Al_2O_3	Na_2O		
B_4	–1.442	2	SrO	CaO		
B_5	0.283	3	MgO	Na_2O	CaO	
B_6	–0.885	4	K_2O	MgO	Al_2O_3	B_2O_3
B_7	0.018	4	SrO	SrO	Na_2O	Na_2O
B_8	–0.053	4	MgO	MgO	CaO	CaO
B_9	0.0021	4	Na_2O	Na_2O	Na_2	Na_2O
B_{10}	0.349	4	K_2O	K_2O	MgO 2	BaO
B_{11}	–0.278	4	K_2O	K_2O	BaO	Al_2O_3
B_{12}	–0.129	4	K_2O	K_2O	K_2O	BaO
B_{13}	0.563	4	K_2O	K_2O	Al_2O_3	B_2O_3

Note: Liquidus temperature is obtained in °C when oxides are given in weight percent.

Source: Data from Backman et al. (1997). Model for liquidus temperatures for multicomponent silicate glasses. *Phys. Chem. Glasses* 38.

2.3.2.1 EURAM Model

In a project within the European Research of Advanced Materials scheme (EURAM) the liquidus temperature in the system Na_2O–K_2O–MgO–CaO–SrO–BaO–PbO–Al_2O_3–B_2O_3–SiO_2 was estimated by a phenomenological equation of the general type[11]

$$T_{liq} / °C = B_0 + B_1 \cdot (term_1) + B_2 \cdot (term_2) + \ldots + B_{13} \cdot (term_{13}) \tag{9}$$

when in weight percent Na_2O: 8.5 – 30.0, K_2O: 0.5 – 7.0, MgO: 0.5 – 5.0, CaO: 2.5 – 15.0, SrO: 0.5 – 5.0, BaO: 0.5 – 5.0, PbO: 0.0 – 5.0, Al_2O_3: 0.5 – 3.0, B_2O_3: 0.5 – 3.0, SiO_2: 50.0 – 68.0. In equation (9) $term_i \ldots term_{13}$ are first-, second-, third- or fourth-order combinations of oxide contents given in weight percent. Thus, for instance,

$$term_5 = p_{MgO} \cdot p_{Na_2O} \cdot p_{CaO} \tag{10}$$

where p_i is the content in weight percent. The data used in modeling can be found in reference 13. The model is summarized in Table 2.3. For the model, the regression

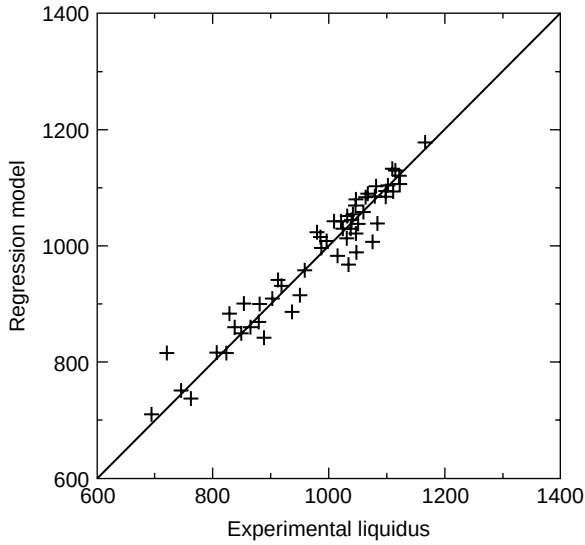

FIGURE 2.2 Diagram showing correlation between experimental liquidus temperatures and those estimated by using equation (9). The diagonal represents perfect agreement. (Data from Backman et al. (1990). Liquidus temperatures in multicomponent silicates. EURAM project MA1E/0009/C.)

coefficient r^2 = 93.1%, residual standard deviation = 35.1 K, degrees of freedom = 36 and F-test = 37.5.

No correlation between liquidus temperature and the lead oxide content was found in the experimental range investigated. A correlation diagram is given in Figure 2.2. The differences are generally larger in the low temperature range. The worst estimate is 86°C above the experimental temperature of 724°C. In general, the model covers a larger number of oxides, a wider oxide range and gives a better description than the model developed by Lakatos.[10]

3.2.2 Extended Babcock Model

Recently, the primary phase fields determined by Backman et al.[11] were modeled as function of composition.[29] The approach is an extension to multicomponent systems of a method originally published in 1977 by Babcock.[30] It involves one polynomial for estimating the primary phase and another describing the liquidus temperature within the obtained primary phase.

The experiments were the same as those used in developing equation (9).[11,13] The primary phases were denoted by an integer, 1 for wollastonite, 2 for devitrite and 3 for the solid solution $(Na_2O \cdot 2\,CaO \cdot 3\,SiO_2)_{ss}$. Only these three phases were represented by enough experiments to make a regression analysis possible. However, data kindly supplied by Philips Glass[31] allowed a description of the cristobalite field. The field was denoted by the integer 4.

The best model to describe the experimentally obtained primary phase field[11] is

$$\begin{aligned} P_{\text{phase}} = {} & 20.2156315 + 0.29252243 \cdot p_{K_2O} + 0.210441694 \cdot p_{MgO} + \\ & 0.275951952 \cdot p_{BaO} + 0.721820772 \cdot p_{B_2O_3} + 0.59449172 \cdot p_{SrO} + \\ & 0.493156791 \cdot p_{Na_2O} + 0.119287364 \cdot p_{CaO} - 1.12851012 \cdot p_{SiO_2} \\ & - 0.203847259 \cdot p^2_{B_2O_3} - 0.0607549697 \cdot p^2_{SrO} + 0.0514076352 \cdot p^2_{PbO} \\ & - 0.00691996608 \cdot p^2_{Na_2O} + 0.0106422286 \cdot p^2_{SiO_2} \end{aligned} \tag{11}$$

where *pi* denotes weight percent oxide. For equation (11) the regression coefficient r^2 = 71.51%, the residual variance = 0.242, while the F-test gave F_{tot} = 6.95 for a significance level of 95%. When $P_{\text{phase}} \leq 1.5$, the result was interpreted as describing the wollastonite field, for $1.5 < P_{\text{phase}} < 2.5$ devitrite and for $2.5 \leq P_{\text{phase}} \leq 3.5$, the solid solution $(Na_2O \cdot 2\,CaO \cdot 3\,SiO_2)_{ss}$.

Within the wollastonite field, i.e., for $P_{\text{phase}} \leq 1.5$, the liquidus temperature in °C can be estimated by

$$\begin{aligned} \vartheta_{liq} = {} & 703.909 + 11.2471 \cdot p_{K_2O} + 13.3897 \cdot p_{MgO} + 10.1381 \cdot p_{BaO} + \\ & 34.7753 \cdot p_{Al_2O_3} + 19.0823 \cdot p_{B_2O_3} \\ & + 11.8052 \cdot p_{SrO} - 112.450 \cdot p_{Na_2O} + 12.3114 \cdot p_{SiO_2} + \\ & 4.16628 \cdot p^2_{Na_2O} + 1.19451 \cdot p^2_{CaO} \end{aligned} \tag{12}$$

for which r^2 = 99.80 $r^2 = 99.80,$ residual variance = 12.44K and F_{tot} = 99.0.

Within the devitrite field, i.e., for $1.5 < P_{\text{phase}} < 2.5$, the liquidus temperature can be estimated by

$$\begin{aligned} \vartheta_{liq} = {} & -1176.37 + 24.8254 \cdot p_{K_2O} + 42.6270 \cdot p_{MgO} + 24.1788 \cdot p_{BaO} + \\ & 36.0791 \cdot p_{Al_2O_3} + 28.0282 \cdot p_{SrO} + 33.7561 \cdot p_{PbO} + 45.2996 \cdot p_{CaO} + \\ & 20.0059 \cdot p_{SiO_2} + 0.446271 \cdot p^2_{Na_2O} \end{aligned} \tag{13}$$

for which r^2 = 88.17%, residual variance = 1401K and F_{tot} = 25.7.

Finally, for the $(Na_2O \cdot 2\,CaO \cdot 3\,SiO_2)_{ss}$ field, i.e., for $2.5 \leq P_{\text{phase}} \leq 3.5$,

$$\begin{aligned} \vartheta_{liq} = {} & 1847.46 + 10.4334 \cdot p_{MgO} + 19.8177 \cdot p_{Al_2O_3} - 151.592 \cdot p_{Na_2O} + \\ & 75.7960 \cdot p_{CaO} + 4.26746 \cdot p^2_{Na_2O} - 3.07671 \cdot p^2_{CaO} \end{aligned} \tag{14}$$

with r^2 = 92.25 residual variance=837.1K and F_{tot} = 19.8.

The data supplied by Philips Glass[31] were determined by a different experimental method. Thus, the compatibility of the models is a bit doubtful. Anyway, with this reservation, the liquidus temperature in the cristobalite field can be estimated by

$$\vartheta_{liq} = 1794.21 + 76.5815 \cdot p_{B_2O_3} - 34.6304 \cdot p_{Al_2O_3} - 41.0916 \cdot p_{Na_2O} - 71.5795 \cdot p_{K_2O} - 32.2649 \cdot p_{MgO} - 5.03770 \cdot p_{CaO} \quad (15)$$

The validity range of the above models is limited to a silica content below about 69 … 70 wt%. Philips' data allowed modeling the acidic glasses with 70 ≤ SiO_2 ≤ 77 wt%. In this range the liquidus temperature can be estimated as[31]

$$\vartheta_{liq} = 4785.48 - 29.8314 \cdot p_{SiO_2} - 60.4794 \cdot p_{P_2O_5} - 82.2195 \cdot p_{Na_2O} - 118.279 \cdot p_{K_2O} - 43.5043 \cdot p_{MgO} - 35.0431 \cdot p_{CaO} \quad (16)$$

The coefficients for alumina and boric oxide were insignificant. The regression coefficient r^2 = 95.4% and standard deviation 24K. In general, the extended Babcock approach looks quite promising. Refining the method by using a larger set of experiments seems to be an important future task.

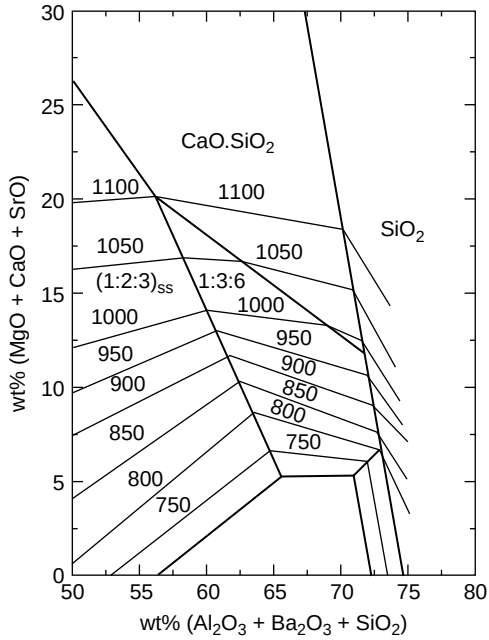

FIGURE 2.3 Phase diagram based on experimental points.

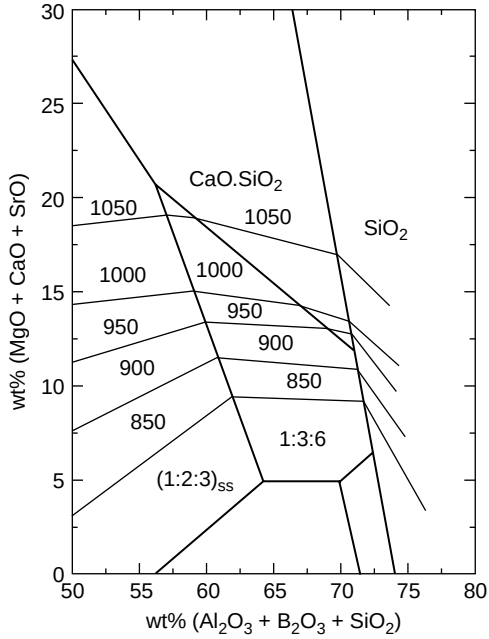

FIGURE 2.4 Phase diagram calculated from equations (11) to (15).

2.3.3 Thermodynamic Modeling

Thermodynamic modeling of phase diagrams has made enormous progress in recent years. The purpose is to derive a mathematical model, which can be used to calculate properties of the chemical system considered. This can be made at different levels of generality, depending on the use of the model.

One general method for modeling phase equilibria is the Calphad method.[14,15] The modeling process is a stepwise iterative process principally using two kinds of information, experimental phase diagrams (temperature-composition data) and experimental thermochemical data (activity, heat of reaction, C_P-data). However, available activity data for silicate systems are still far from coherent, as pointed out by Rego et al.[35] When proper data are collected, the next step is to decide which model should be used as a first suggestion in the assessment. The choice of model can be based on structural information about the phases in the system, or the model can be regarded as a purely empirical one.

The gallery of models available is very large, ranging from the classical Margules and van Laar models to sophisticated models with many adjustable parameters. Once the model is chosen, the experimental information is evaluated. It is usually necessary to give different weights to various experimental data to achieve a consistent set of experimental points. One of the most general models is the ionic sublattice model developed by Hillert et al.,[16] which can handle both charged and neutral molecular species. Also, vacancies can be introduced on the sublattices. This model has been

applied successfully on binary metallic systems[17,18] and also on higher-order systems and systems containing molecular species like oxides.[19,20,21]

When the adjustable parameters in the model have been optimized, the result is analyzed and compared to experimental data, and a check is done to see whether extrapolations into regions beyond experimental points are possible. The Calphad method is laborious because of the requirements of generality and consistency, but its great advantage is that a description of the whole system is produced. The consistency requirement makes extensions to higher-order systems possible and allows coupling of several systems without too much repetition of the fundamental work already done. Despite the model's fairly close contact to a physical reality, sometimes quite dubious molecular species have to be introduced in order to obtain an acceptable fit.

However, from a practical point of view, a more limited quasichemical modeling often gives enough information to be used for a particular problem.[22–26] The quasichemical model was originally introduced by Guggenheim but has been modified for silicate systems by Pelton and his co-workers. Recently, this model has been successfully applied to multicomponent silicate systems. Its great advantage is that very few interaction parameters are needed, and the extension to higher systems is rather straightforward with the use of binary parameters.

Below, a brief presentation of the model is given. It is exemplified by the systems Na_2O – SiO_2 and CaO – SiO_2.

2.3.3.1 Quasichemical Binary System

In a binary system A_nO – SiO_2 (A = Na, Ca, etc.) consider the formation of two A-Si second-nearest-neighbor pairs from A – A and Si – Si pair

$$(A - A) + (Si - Si) = 2(A - Si) \tag{17}$$

If we denote with *w* and *n* the molar enthalpy and non-configurational entropy respectively, the molar "free energy of pair-formation" will be $(\omega - \eta T)$, where *T* is the temperature. The maximum order in such a liquid system is obtained at the composition where only A-Si pairs are present. In systems MO – SiO_2 (M = divalent cation) this occurs at $X_{SiO_2} = 1/3$. In the Na_2O – SiO_2 system maximum ordering occurs at the orthosilicate composition, where $X_{SiO_2} = 0.2$.

"Equivalent fractions" Y_A and Y_{Si} are introduced by parameters b_A and b_{Si} for each component to fix the point of maximum order at desired composition. If the mole fractions for the different pairs in the liquid are denoted X_{AA}, X_{SiSi} and X_{ASi} the "quasichemical equilibrium constant" will be

$$Q = X_{ASi} \cdot X_{ASi} / X_{AA} \cdot X_{SiSi.} \tag{18}$$

The value of *Q* can be calculated by minimization of the Gibbs free energy of the system,

$$Q = 4 \cdot \exp(-2(\omega - \eta T) / zRT) \tag{19}$$

where z is the coordination number. The mass balances can be written

$$\begin{aligned} 2\,Y_{\mathrm{A}} &= 2\,X_{\mathrm{AA}} + X_{\mathrm{ASi}} \\ 2\,Y_{\mathrm{Si}} &= 2\,X_{\mathrm{SiSi}} + X_{\mathrm{ASi}} \end{aligned} \tag{20}$$

Equations (18)–(20) can be solved if $(\omega - \eta T)$, z, T and the total composition of the system are known.

Further, w and n can be expressed as polynomial functions in Y_{Si}

$$\begin{aligned} \omega &= \omega_0 + \omega_1 \cdot Y_{\mathrm{Si}} + \omega_2 \cdot Y_{\mathrm{Si}}^2 \cdots \\ \eta &= n_0 + \eta_1 \cdot Y_{\mathrm{Si}} + \eta_2 \cdot Y_{\mathrm{Si}}^2 \cdots \end{aligned} \tag{21}$$

The parameters ω_i and η_i are the parameters to be fitted on the basis of experimental data to get the best representation of the whole system. In this work some kind of nontrivial optimization routine must be used, where data for all phases in the system can be taken into account.

2.3.3.2 Extension to Ternary Systems

In a ternary system, say $\mathrm{Na_2O - CaO - SiO_2}$, we consider three pair-bond equilibria:

$$\begin{aligned} &(\mathrm{Na - Na}) + (\mathrm{Si - Si}) = 2\,(\mathrm{Na - Si}) \\ &(\mathrm{Si - Si}) + (\mathrm{Ca - Ca}) = 2\,(\mathrm{Si - C}) \\ &(\mathrm{Ca - Ca}) + (\mathrm{Na - Na}) = 2\,(\mathrm{Ca - Na}). \end{aligned} \tag{22}$$

The energy and entropy changes for these reactions(ω_{NaSi}, ω_{SiCa}, ω_{CaNa}; η_{NaSi}, η_{SiCa} and η_{CaNa}) are obtained from the three binary subsystems. For silicate melts an "asymmetric approximation" is convenient to use when values for w_{ij} and η_{ij} are calculated at ternary compositions. This approximation considers $\mathrm{SiO_2}$ as a main component and the value of a parameter is supposed to be independent of the presence of the third component. It is also possible to introduce ternary parameters in the model. When higher systems are studied, the presence of, e.g., ternary compounds must of course be considered.

Good examples of the success of quasichemical modeling were published by Pelton and his co-workers.[24] Their FACT database, available in the program FactSage 5.2,[33] is very extensive and contains data for most oxides of interest in glass making. More recently, the quasi-chemical model has been further developed to simultaneously treat first- and second-nearest-neighbor short-range ordering in solutions with two sublattices.[34] Furthermore, a model has been developed[35] for the "charge compensation effect" in $\mathrm{Na_2O - K_2O - Al_2O_3 - SiO_2}$ melts between tetravalent $\mathrm{Si^{4+}}$ and trivalent $\mathrm{Al^{3+}}$.

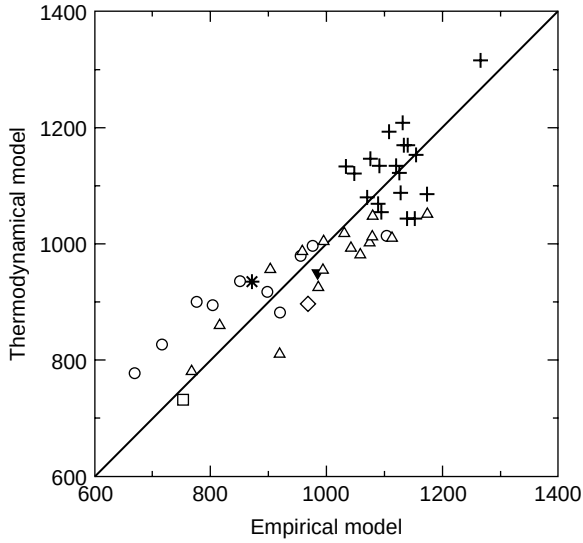

FIGURE 2.5 Diagram showing correlation between thermodynamically calculated and empirically modeled liquidus temperature. Primary phases denoted as: + = wollastonite ○ = $Na_2O \cdot 3CaO \cdot 6SiO_2$, △ = $Na_2O \cdot 2CaO \cdot 3SiO_2$, ∗ = SiO_2, ◇ = $2Na_2O \cdot CaO \cdot 3SiO_2$, ▽ = $Na_2O \cdot CaO \cdot 5SiO_2$.

Using this database, the liquidus temperature and the primary phase have been calculated for 50 glasses.[30] The database is, in principle, the same as that used for polynomial modeling, but unfortunately data for boric, strontium and barium oxides have not yet been released. In Figure 2.5, the experimental data for the ten-component system is compared with the thermodynamically calculated data for the seven-component system. The fit is reasonable for data in the wollastonite and $(Na_2O \cdot 2CaO \cdot 3SiO_2)_{ss}$ phase fields. In the devitrite region, the scatter is larger, even >100°C. The corresponding phase diagram is shown in Figure 2.6. It is, however, interesting to note that the thermodynamic model gives slightly higher values in the primary phase region of devitrite and slightly lower values in the $(Na_2O \cdot 2CaO \cdot 3SiO_2)_{ss}$ region than the experimental diagram shown in Figure 2.3.

An example more suited to illustrate the power of thermodynamic calculations is the solid solution along the quasi-binary $CaSiO_3 - Na_2SiO_3$ shown in Figure 2.7. The solution between the solid components $Na_2O \cdot 2CaO \cdot 3siO_2$ and $2Na_2O \cdot CaO \cdot 3siO_2$ was first found by Prof. Pelton,[24] when modeling the three-component phase diagram $Na_2O - CaO - SiO_2$. This calculation explains the problems accounted in identifying some x-ray diffraction patterns in the ten-component system described in section 2.3.2.[11,12]

2.4 FUTURE DEVELOPMENT

The next progress in thermodynamic modeling of phase diagrams is probably based on calculations in which the features of both the quasichemical and the ionic two-

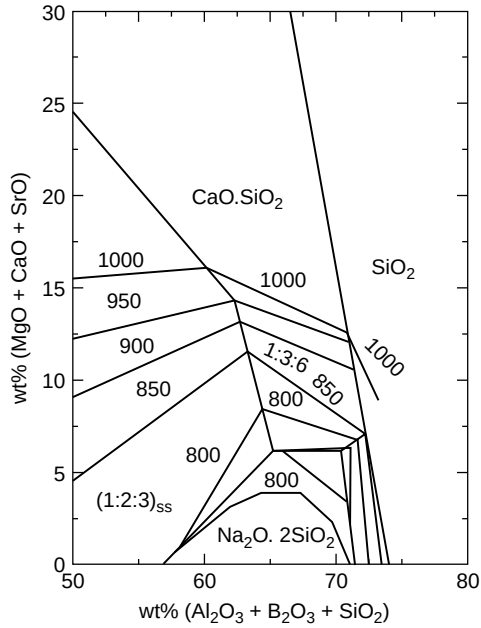

FIGURE 2.6 Phase diagram calculated by the quasichemical model.

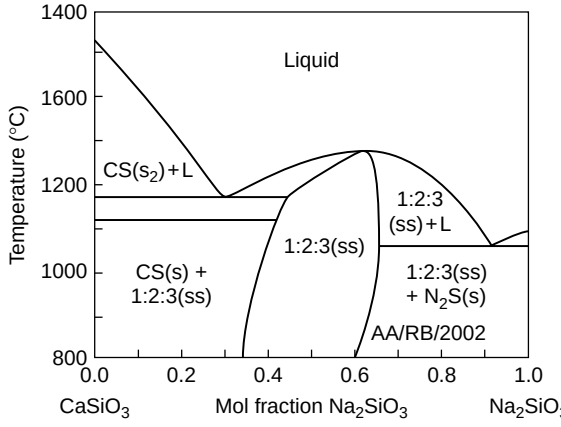

FIGURE 2.7 The quasibinary Na_2SiO_3–$CaSiO_3$ regions with solid solution. Calculated by FactSage 5.0.

sublattice models are considered.[36] It should also be noted that once the thermodynamic calculation is performed, the thermodynamic constants *H*, *S*, *G* and C_p are also known. It should, however, be observed that the calculated (true) primary phase, in practice, is often obscured by faster growing secondary or ternary crystals.

Progress can also be expected in accuracy when estimating solidus temperatures. Also, extended consideration of the influence of solid solutions on liquidus can be

foreseen. However, these calculations are quite laborious and still of limited value for glass industry.

For glasses in commercial use, empirical models remain the quickest way of obtaining a first approximation of liquidus temperature and heat capacity. In the future, however, such models will not be based on data obtained in laborious experiments, but by thermodynamic calculations made by experts.

REFERENCES

1. Winkelmann, A. (1892). Ueber die spezifischen Wärmen verschieden zusammengesetzter Gläser. *Ann. Phys. Chem.* 49:401–420.
2. Sharp, D.E., Ginther, L.B. (1951). Effect of composition and temperature on the specific heat of glass. *J. Am. Ceram. Soc.* 34:260–271.
3. Bacon, C.R. (1977). High-temperature heat content and heat capacity of silicate glasses. *Am. J. Sci.*, 277:109–135.
4. Richet, P., Bottinga, Y. (1982). Modeles de calcul des capacites calorifiques des verres et liquides silicates. *C.R. Acad.Sci.*, Paris, 295:1121–1124.
5. Richet, P. (1987). Heat capacity of silicate glasses. *Chem. Geol.* 62:111–124.
6. Stebbins, J.E., Carmichael, I.S.E., Weill, D.F. (1983). The high temperature liquid and glass heat contents and the heats of fusion of diopside, albite, sanidine and nepheline. *Am. Mineral.* 68:717–730.
7. Haas, J.L., Fisher, J.R. (1976). Simultaneous evaluation and correlation of thermodynamic data. *Am. J. Sci.* 276:525–545.
8. Morey, G.W. (1930). The devitrification of soda-lime-silica glasses. *J. Am. Ceram. Soc.* 13:683–713.
9. Morey, G.W., Bowen, N.L. (1925). The ternary system sodium metasilicate-calcium metasilicate-silica. *J. Soc. Glass Technol.* 9:226–264.
10. Lakatos, T., Johansson, L.-G. (1976). SiO_2–Al_2O_3–Na_2O–K_2O–CaO–MgO-systemets likvidustemperatur och hydrolytiska resistens. *Glastekn. Tidskr.* 31:31–35.
11. Backman, R., Cable, M., Karlsson, K. and Pennington, N. (1990). Liquidus temperatures in multicomponent silicates. EURAM project MA1E/0009/C.
12. Backman, R., Karlsson, K.H., Cable, M. and Pennington, N. (1990). Prediction of liquidus temperatures for multicomponent silica glasses. *Glastech. Ber.* 63K:460–469.
13. Backman, R., Karlsson, K.H., Cable, M., Pennington, N. (1997). Model for liquidus temperatures for multicomponent silicate glasses. *Phys. Chem. Glasses* 38:103–109.
14. Kaufman, L., Bernstein, H. (1970). *Computer Calculation of Phase Diagrams.* New York: Academic Press.
15. Sundman, B., Jansson, B., Andersson, J.-E. (1985). The Thermo-Calc databank system, *Calphad* 9:150–193.
16. Hillert, M., Jansson, B., Sundman, B., Gren, J. (1985) A two-sublattice model for molten solutions with different tendency for ionization. *Metallurgical Trans.* 16A:261–266.
17. Andersson, J-0. (1988). A thermodynamic evaluation of the Fe-Cr-C system, *Metallurgical Trans.* 19A:627–636.
18. Kajihara, M., Hillert, M. (1990). Thermodynamic evaluation of the Cr-Ni-C system, *Metallurgical Trans.* 21A:2777–2787.
19. Hillert, M., Sundman, B., Wang, X. (1987). An assessment of the CaO – SiO_2 system. *TRITA-MAC 355*, Royal Institute of Technology, Stockholm.

20. Hillert, M., Wang, X. (1989). A study of the thermodynamic properties of MgO – SiO_2 system. *Calphad* 13:253–266.
21. Hillert, M., Selleby, M. and Sundman, B.(1990). An assessment of the Ca-Fe-O system. *Metallurgical Trans.* 21A:2759–2776.
22. Pelton, A.D., Blander, M.(1986). Thermodynamic analysis of ordered liquid solutions by a modified quasichemical approach: Application to silicate slags, *Metallurgical Trans.* 17B:805–815.
23. Blander, M., Pelton, A.D. (1987). Thermodynamic analysis of binary liquid silicates and predictions of ternary solution properties by modified quasichemical equations. *Geochim. et Cosmochim. Acta* 51:85–95.
24. Pelton, A.D., Wu, P. (1999) Thermodynamic modeling in glass-forming melts. *J. Non-Cryst. Solids*. 253:178–191.
25. Greenberg, J.P., Weare, J.H., Harvie, C.E. (1985). An equilibrium computation algorithm for complex highly nonideal systems: Application to silicate phase equilibria. *High Temp. Sci.* 20:141–162.
26. Zchimmer, E., Dietzel, A. (1926). Die Temperatur-Zeit-Kurven der sichtbaren Entglasung bei Spiegelglas. *Z. Tech. Phys.* 7:278–282.
27. Jones, S.P. (1961). Structural interpretation of liquidus temperature measurements in the soda-lime-silica system, *Phys. Chem. Glasses* 2:55–67.
28. Barton, J., Personal communication, 1987.
29. Karlsson, K.H., Backman, R., Hupa, L. (2002). Models for liquidus temperatures. *Glass Odyssey, 6th ESG Conference*. Montpellier, France, Session A2.
30. Babcock, C.L. (1977). *Silicate Glass Technology Methods.* New York:Wiley 1977, pp 18–64 and 225–235.
31. Karlsson, K.H., Backman, R., Cable, M., Peelen, J., Hermans, J. (2001). Estimation of liquidus temperatures in silicate glasses. *Glastech. Ber. Glass Sci. Technol.* 74:187–191.
32. Bale, C.W, Pelton, A.D., Thompson, W.T, Eriksson, G., Hack, K., Chartrand, P., Degterov, S., Melancon, J., Petersen, S. (2003). FactSage User Manual. www.factsage.com.
33. Pelton, A. D., Chartrand, P., Eriksson, G. (2001). The Modified Quasi- chemical Model: Part IV. Two-Sublattice Quadruplet Approximation, *Met. Mat. Trans.*, 32A:1409–1416.
34. Chartrand, P., Pelton, A.D. (1999) Modeling the charge compensation effect in silica-rich Na_2O–K_2O–Al_2O_3–SiO_2 melts. *Calphad* 23:219–230.
35. Rego, D.N., Sigworth, G.K., Philbrook, W.O. (1988). Thermodynamic activity of Na_2O in Na_2O–CaO–SiO_2, Na_2O–MgO–SiO_2, and Na_2O–CaO–SiO_2–Al_2O_3 melts at 1400°C. *Metallurg. Trans.* 19B:655–661.
36. Pelton, M., Personal communication, (1998).

3 Redox Behavior and Electrochemical Behavior of Glass Melts

Christian Rüssel

CONTENTS

3.1 INTRODUCTION

Most glasses contain more or less high quantities of polyvalent elements. This results from the impurities, such as iron, in the raw materials, or polyvalent elements that

are added, e.g., as oxides to the glass batch. Typical for the latter type are fining or coloring agents. In this chapter, all those elements will be considered to be polyvalent, which may occur in a glass melt in at least two different oxidation states, even if extreme oxidizing or reducing conditions are necessary. Besides the refining behavior, many other properties of glass melts and solid glasses depend on the type, concentration and redox ratio of polyvalent elements present. Among these, the color, i.e., the transmittivity of light in a certain wavelength, is the most important for both solid glass and the glass melt [1–3]. The first determines the product quality to a great extent and the latter the melting behavior, especially the temperature distribution within the glass tank.

Other properties of melts influenced by polyvalent elements are the viscosity [4], the surface tension [5], the tendency to liquid–liquid phase separation [6] and to devitrification [7]. For the production of glass ceramics, the nucleation and crystallization kinetics and hence also the microstructure are strongly influenced. In the case of iron, it has even been reported that the quantity and redox ratio may determine the type of crystalline phases formed [7]. Among the properties of solid glasses that depend on polyvalent elements, the solarization behavior [8] and the nonlinear optical behavior should also be mentioned. While, in most technical glasses, the types and quantities of polyvalent elements depend solely on the glass batch used, in high purity glasses e.g., for special optical and optoelectronical applications, the whole melting technology, including the interaction with the refractory material and the gas atmosphere, must be taken into account [9]. The redox ratio in industrially melted glasses is mainly determined by the batch composition, i.e., by the type and quantity of oxidizing and reducing components [10]. These components may quantitatively remain in the glass (e.g., Fe_2O_3), be partially (e.g., SO_4^{2-}) or fully (e.g., NO_3^-) evaporated during the glass melting process. The glass melting process itself also affects the redox ratio; e.g., notable differences in this ratio have been reported when air or oxygen has been used for bubbling or when oxyfuel melters have been used [11,12].

In the past decade, great efforts have been achieved in controlling oxygen activity and also the quantity of polyvalent elements during glass melting. For these purposes, oxygen activity sensors [13,14] and voltammetric sensors (e.g., [15]) were constructed and applied to industrial glass tanks also [16–19]. These are mainly long-time sensors that remain in the feeder of a glass furnace over some months and monitor the oxygen activity or e.g., the iron or sulfur concentration continuously.

If only one type of polyvalent element occurs in a glass melt, the oxygen activity can be strictly correlated to the redox ratio in the solid glass. If, however, more than one type of polyvalent element is present, the situation is more complicated, because redox reactions during cooling may occur. In general, the redox ratio of a polyvalent element does not depend on the oxygen activity solely, but also on the glass melt composition [2,20–24]. Here, the incorporation into the melt seems to play a very important part that, until now, has not been fully understood. In this chapter, a general overview on the behavior of polyvalent elements in glass melts is given, especially with respect to electrochemical measurements carried out in the past decade.

3.2 THEORY

3.2.1 Model: Ions in a Dielectric Continuum

In most studies, the glass melt containing polyvalent elements is assumed to act as a polar solvent in which the oxides are dissolved. In the melt, they occur as ionic species that are coordinated by other ionic species of the melt. These may be e.g., O^{2-}, bridging or non-bridging oxygen or F-. For the validity of the formal treatment, the type of species, the coordination number and the type of chemical bond, i.e., the degree of covalency, are not of importance. Since, according to this model, the polyvalent elements are coordinated solely by other species, a structural interaction between them does not occur. This means that within that model a possible structural interaction e.g., Fe-O-Fe or Fe-O-Ce [25], is not included. Therefore, the thermodynamics do not depend on the concentration and on the occurrence of other polyvalent elements in the same melt.

It should be noted that at high concentrations and if clusters are formed, this model can be used only as a first approximation.

3.2.2 Thermodynamic

It is generally accepted that at high temperatures, polyvalent elements are in equilibrium with the physically dissolved oxygen in the glass melt. This equilibrium can be described by defining an equilibrium constant K:

$$Me^{x+z} + z/2O^{2-} \leftrightarrow Me^{x} + z/4O_2 \tag{1}$$

$$K = K'[O^{2-}]^{z/2} = \frac{[Me^{x+}]a_{O_2}^{z/4}}{[Me^{x+2}]} \tag{2}$$

where K is a function of the temperature, the glass melt composition and the type of polyvalent element. If the polyvalent element occurs in more than two different oxidation states (e.g., in the case of vanadium, which may occur as V^{5+}, V^{4+} and V^{3+}), more than one equilibrium exists and more than one equilbrium constant is to be defined. That does not mean that the melt is in equilibrium with the surrounding atmosphere, because this can be achieved only by diffusion of oxygen in or out of the melt, which is a very slow process.

The equilibrium constant K can be related to the standard free enthalpy, ΔG^0, of the redox reaction according to equation (1):

$$\Delta G^0 = -RT \ln K \tag{3}$$

If the temperature dependence of K is known, the standard enthalpy, ΔH^0, and the standard entropy, ΔS^0, can be calculated.

$$\Delta G^0 = \Delta H^0 - T\Delta S^0 \tag{4}$$

The same information can also be obtained if the electrochemical standard potential, E_O, is measured.

$$\Delta G^0 = -zFE_0 \tag{5}$$

with: z = number of electron transferred, F = Faraday constant.

If a melt is cooled down, its oxygen activity decreases. This is caused by a shift of the redox equilibrium to the left side, according to equation (1).

$$e^{\Delta S^0/R} \cdot e^{-\Delta H^0/RT} = (a_{O_2})^{z/4} \frac{[Me^x]}{[Me^{x+2}]} \tag{6}$$

If oxygen diffusion in or out of the melt does not play any part and the concentration of the polyvalent element is large in comparison to that of physically dissolved oxygen, the following equation can be derived:

$$z/4 \ln(a^I_{O_2} / a^{II}_{O_2}) = \frac{\Delta S^{0I} - \Delta S^{0II}}{R} - \frac{\Delta H^{0I}}{RT_I} + \frac{\Delta H^{0II}}{RT_{II}} \tag{7}$$

The indices I and II mean at the temperatures T_I and T_{II}. Also, in a larger temperature range, ΔS^0 and ΔH^0 can be assumed to be independent from temperature and hence equation (8) can be written (see e.g., [25]):

$$z/4 \ln(a^I_{O_2} / a^{II}_{O_2}) = -\frac{\Delta H^0}{R} \left(\frac{1}{T_I} - \frac{1}{T_{II}} \right) \tag{8}$$

Therefore, if the oxygen activity of the melt is measured at two different temperatures, ΔH^0 of the redox reaction can be calculated.

If more than one polyvalent element occurs in the glass melt, for each redox pair an equilibrium, according to equation (1), can be established. For the case of two polyvalent elements, A and B, the following redox equilibria occur:

$$4/z\, A^{m+z} + 2O^{2-} \xleftrightarrow{K_A} 4/z\, A^m + O_2 \tag{9}$$

$$4/z'\, B^{n+z'} + 2O^{2-} \xleftrightarrow{K_B} 4/z'\, B^n + O_2 \tag{10}$$

$$K_A = \frac{[A^m]^{4/z}}{[A^{m+z}]^{4/z}} p_{O_2} \tag{11}$$

$$K_B = \frac{[B^n]^{4/z'}}{[B^{n+z'}]^{4/z'}} p_{O_2} \tag{12}$$

By subtracting equation (10) from equation (9), it follows:

$$4 / z\, A^{m+z} + 4 / z'\, B^n \xleftrightarrow{K_{AB}} 4 / z\, A^m + 4 / z'\, B^{n+z'} \tag{13}$$

$$K_{AB} = K_A / K_B = \frac{[A^m]^{4/z}[B^{n+z'}]^{4/z'}}{[A^{m+z}]^{4/z}[B^n]^{4/z'}} = \exp(\Delta S^0_{AB} / R) \cdot \exp(-\Delta H^0_{AB} / RT) \tag{14}$$

If at a certain temperature, a melt containing the polyvalent element A in a concentration of, e.g., 0.5 mol%, is equilibrated with the same gas atmosphere as another melt containing the polyvalent elements A and B simultaneously, the redox ratio $[A^m]/[A^{m+z}]$ will be the same, because in both melts, the equilibrium according to equation (9) is established. If these melts are now cooled quickly, the melt containing A alone will show the same redox ratio as at high temperature, because this ratio can be changed only if oxygen diffuses into the melt; however, this is not possible during quenching of conventional silicate melts. Also in this melt, K_A is a function of temperature and hence the oxygen activity decreases, as already pointed out. When the melt containing both the polyvalent elements A and B is quenched, the equilibrium constants K_A and K_B will both change with temperature. Since, in this case, oxygen diffusion into the melt is negligible, and the equilibria according to equations (9) and (10) are both shifted to the left, the oxygen activity of the melt also decreases here. Since the temperature dependences of K_A and K_B are usually not the same, K_{AB} will also depend on temperature [26, 27]. Therefore, the equilibrium according to equation (13) will be shifted during cooling, due to the differences in the standard enthalpies of equations (9) and (10) [26–29]. Otherwise, that means if two glass melts are mixed, one of them containing only the polyvalent element A and the other only B, but both equilibrated with the same gas atmosphere at the same temperature, the redox ratios $[A^{m+z}]/[A^m]$ and $[B^{n+z}]/[B^n]$ remain the same.

Sometimes, the behavior of melts containing two redox pairs is compared with a redox titration. This comparison, however, is very doubtful, because during redox titrations, one totally oxidized solution (which is attributed to very high oxygen activity) and a totally reduced solution (which is attributed to very low oxygen activity) react with each other. Hence, the reason that a redox titration works is that the oxygen activities of the two solutions used are very different. But also in this case, the redox reaction stops if $\Delta G^0 = 0$ and hence the reaction is in equilibrium. Because, according to the model introduced at the beginning, both polyvalent elements are homogeneously dissolved in the melt, the diffusion paths will be very short and in the nanometer range. This enables the establishment of a new equilibrium in the melt. By contrast, oxygen diffusion into the melt requires diffusion paths in the millimeter range during quenching. Since the time required for diffusion is proportional to the square of the diffusion path, it differs by the factor 10^{12} for the nanometer and the millimeter range. Hence, diffusion processes required for a

homogeneous redox reaction according to equation (13) are much faster than those necessary for an equilibration with a certain gas atmosphere.

3.2.3 Kinetics of Redox Reactions

Since diffusion is necessary for all homogeneous redox reactions and the diffusion coefficients depend on temperature, it can be assumed that redox reactions are frozen in below a certain temperature. Then the redox ratios of the polyvalent elements are no longer in agreement with the attributed equilibrium constants.

The kinetics of redox reactions during cooling can easily be described, if it is assumed that they are controlled by diffusion [26]. For $z = z'$, it follows:

$$A^{m+z} + B^{n} \underset{k_{-2}}{\overset{k_2}{\longleftrightarrow}} A^{m} + B^{n+z} \tag{15}$$

$$\frac{dx}{dt} = k_2(T)([A_O^{m+z}] - x)([B_O^{n}] - x) - \frac{k_2(T)}{K_{AB}(T)}([A_O^{m}] + x)([B_O^{n+z}] + x) \tag{16}$$

with k_2 = rate constant, and $K_{AB} > 1$, ($[A_O^{m+z}]$, $[A_O^{m}]$, $[B_O^{n}]$, $[B_O^{n+z}]$ are the concentrations at the beginning ($x = 0$)).

For a diffusion controlled reaction, the rate constant k_2 can be calculated by the Smoluchowsky equation:

$$k_2 = C(D_A + D_B)(a_A + a_B) \tag{17}$$

where D_A and D_B are the diffusion coefficients and a_A and a_B the radii of the species A and B, respectively.

After inserting equation (17) in equation (16), the latter can be solved numerically for experimentally determined diffusion coefficients. In Ref. [26], this has been done for a redox reaction in a soda-lime-silica glass melt doped with both iron and manganese. The rate-determining step was assumed to be the diffusion of iron. From that calculation it was concluded that a high quenching rate of 10^3 K/s should result in a redox freezing temperature around 50 K above T_g, whereas a quenching rate of 10^{-4} K/s is attributed to a freezing-in temperature of around 150 K below T_g. From this calculation it can be assumed that homogeneous redox reactions are usually not frozen-in above T_g. This assumption has also been supported by high-temperature EPR-studies [27] as well as by high-temperature UV-vis-NIR spectroscopy [28–30].

3.2.4 Diffusivity of Polyvalent Elements in Glass Melts

Self diffusion coefficients of polyvalent elements in glass melts are important for modeling of the fining process, including bubble evolution and for understanding the kinetics of redox processes, as already described above. Self diffusion coefficients of polyvalent elements follow the Arrhenius law in a wide temperature range:

$$D = D_O \cdot \exp(-E_D / RT) \tag{18}$$

Measured at the same temperature and in the same glass melt composition, the self diffusion coefficients of different polyvalent elements differ by some orders of magnitude. Therefore, the diffusion coefficient in a glass melt cannot be correlated with the ionic radius according to Stokes-Einstein equation, but depends on the incorporation of the polyvalent element into the glass melt, e.g., whether it acts as a network modifier or as a network former (see e.g. [31]).

3.3 NOMENCLATURE, DEFINITIONS, UNITS

As polyvalents, all those elements are defined that may occur in at least two different oxidation states in a glass melt. The redox ratio is defined as the ratio of the concentration of the reduced and oxidized form of the polyvalent element. The oxygen activity of a melt is given in bar and corresponds to that oxygen fugacity with which the melt is in equilibrium. All energies and enthalpies are given in kJ mol^{-1}, whereas the entropies are in JK^{-1} mol^{-1}. The standard potentials are given in mV and referenced to a zirconia/air electrode. All concentrations mentioned are in mol%.

With the aid of voltammetric methods, redox ratios cannot be measured, however, if the oxygen activity of the melt is known, they can be calculated from the standard potentials.

3.4 METHODS OF MEASUREMENTS

3.4.1 Thermodynamic Measurements

Various types of measurements can be carried out to determine the thermodynamics of polyvalent elements in glass melts. The first method used was the equilibration method [13, 32–39]. Here a glass melt is equilibrated with a gas atmosphere of a well defined oxygen fugacity. Then the glass melt is quenched and the solid glass is analyzed physically or chemically. The first problem is the equilibration procedure. Since the diffusion of oxygen into or out of the melt is a time-consuming step, the equilibration takes a long time and it is advantageous to enhance it by convection. This can be done, e.g., by stirring or by tilting and rotating the crucible. Nevertheless, even applying convection, the equilibration of some grams of a silicate melt takes up to 20 h, depending on temperature. If the temperature is too low, e.g., for a float glass composition at 800°C, the melt is too viscous and the equilibration cannot be carried out within justifiable time [13]. To prove that the glass melt is really in an equilibrium, it is necessary to analyze the glass as a function of the equilibration time. If the times applied were long enough, the redox ratio will no longer depend on the equilibration time. An even better way is to carry out this procedure with two different glass melts, one extremely oxidized and one extremely reduced. If, after some hours, both glass melts possess the same redox ratios, the equilibrium is reached.

Depending on the polyvalent element present, various methods to analyze the solid glass have been applied. The physical methods are mainly focused on spectroscopy, although, in some cases, other methods, e.g., magnetic measurements, can also be applied. The methods most frequently carried out are UV-vis-NIR spectroscopy [40–44], electron paramagnetic resonance (EPR) spectroscopy [45–47], x-ray photoelectron spectroscopy (XPS) [48, 49] and, in the case of iron and tin, Mössbauer spectroscopy [50–52]. The latter three methods enable the quantitative determination of redox states without any calibration, whereas, using UV-vis-NIR-spectroscopy, extinction coefficients have to be known. Since they depend on the glass composition, it is necessary to calibrate the UV-vis-NIR-measurements with spectroscopically or chemically determined redox ratios.

For a chemical determination of the redox ratio, the glass has to be dissolved, in most cases in fluoric acid. Then a redox titration is carried out, or a certain redox state is photometrically determined, e.g., in the case of iron as orthophenanthroline complex. During the whole procedure, the redox state must not change. Most importantly, oxidation by atmospheric oxygen must be avoided.

To determine the thermodynamics in a glass melt, just one type of polyvalent element may be present. If more than one occurs, then redox reactions during cooling usually take place, and hence, the redox ratio in the glass melt and in the solid glass will not be the same. It should be noted that conventional fining agents are polyvalent elements and thus also have to be excluded. Using physical methods, the redox ratios determined in a glass containing more than one type of polyvalent element are attributed to the solid glass solely. By contrast, if such a glass is dissolved in acid and subsequently analyzed chemically, the redox ratios determined are not even attributed to the solid glass, because during dissolution, new equilibria are formed and hence another redox reaction occurs. This is also the case if the glass additionally contains fining agents.

Another possible method of determining thermodynamic properties of polyvalent elements in a glass melt is to use electrochemical methods [15, 53–94]. Today, the most frequently applied methods are voltammetric, especially the square-wave voltammetry [57–94]. In this method, current-potential curves are recorded that exhibit distinct maxima or minima. From the peak potentials, the standard potentials of the redox pair present can be calculated. To carry out voltammetric measurements, a certain ionic conductivity of the glass melt is necessary and hence it is not possible, e.g., in pure silica.

Today, for voltammetric measurements, three electrodes are inserted in the glass melt (see, e.g., [15]). As working electrode, usually a platinum wire and as counter electrode, a platinum plate is used. The third electrode is the reference electrode, which has to possess a thermodynamically well defined and, with respect to time, constant potential. Usually, for that purpose, a zirconia sensor, flushed with air or oxygen as reference gas is used (see also Figure 3.1). The same type of electrode has previously been used as reference to determine the oxygen activity of a glass melt [13,14]. The electrodes are connected to a potentiostat, which controls the potentials between all electrodes so that the potential between working and reference electrodes is always equal to the required value. In the case of the square-wave voltammetry, the potential-time dependence is a staircase ramp superimposed by a

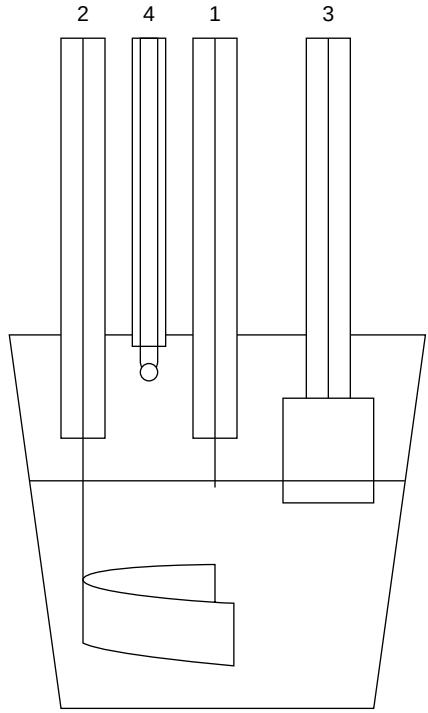

FIGURE 3.1 Schematic drawing of the electrochemical cell used for voltammetric measurements in glass melts; 1: working electrode, 2: counter electrode, 3: reference electrode, 4: thermocouple.

rectangular wave of comparably high frequency (5 to 500 s^{-1}) and amplitude (50–200 mV) (See Figure 3.2; for a description of the fundamentals of the method see Refs. [95–98].) The glass melts need not be equilibrated, because the signal obtained is solely attributed to a small layer around the working electrode. The potential applied before the measurement is carried out (usually 0 V vs. the reference electrode) leads to an equilibration of that small layer so that the redox ratios accord to this potential. The measurements usually are carried out in a fairly broad temperature range of 900–1500°C. This range, however, depends on the ionic conductivity and hence the glass melt composition. At lower alkali concentrations, higher temperatures are required. In principle, different types of polyvalent elements can be present if their standard potentials are different enough. However, in this case, the current-potential curve has to be deconvoluted numerically.

Figure 3.3 (curve 1) shows a square-wave voltammogram recorded at 1200°C in a glass melt with the basic mol% composition of 74 SiO_2, 16 Na_2O and 10 CaO doped with 0.25 mol% Fe_2O_3. The peak observed is caused by the reduction of Fe^{3+} to Fe^{2+}. The current-potential curve is also affected by background effects caused by the electrochemical decomposition of the glass matrix. At far cathodic potentials, elemental Si or platinum silicide, and at potentials higher than 0 mV, gaseous oxygen is formed [15, 57]. This is also shown in Figure 3.3 (curve 2),

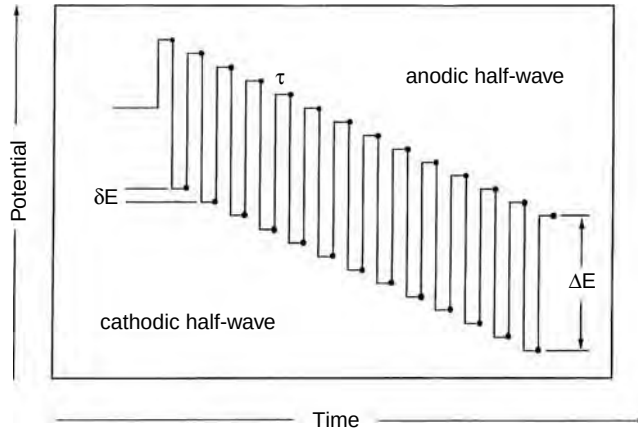

FIGURE 3.2 Potential-time dependence supplied to the working electrode during square-wave voltammetry.

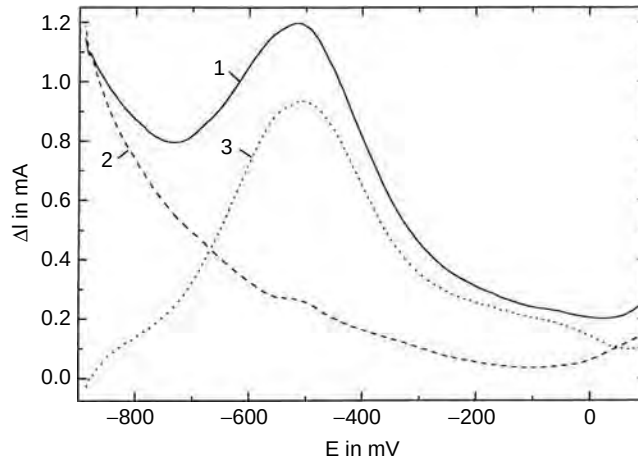

FIGURE 3.3 Square-wave voltammogram recorded in a soda-lime-silica glass melt with the basic mol% composition of 74 SiO_2, 16 Na_2O, 10 CaO. Curve 1: doped with 0.25 mol% Fe_2O_3; curve 2: undoped; curve 3: curve 1 – curve 2.

recorded in a glass melt with the same basic composition, however, not doped with polyvalent elements. If curve 2 has been subtracted from curve 1, the resulting current-potential curve 3 is solely attributed to electrochemical effects caused by iron. A more accurate determination of the standard potentials is possible if only small concentrations are present.

From the obtained standard potentials, ΔG^0 and the equilibrium constant, K can be calculated using equations (5) and (3), respectively. If the temperature dependence has also been measured, ΔH^0 and ΔS^0 can be calculated. The same experimental equipment can, in principle, also be used for the determination of the oxygen activity

in the melt. Here, the potential, E, between the reference and a large platinum electrode is measured. If air is used as reference gas, the oxygen activity, a_{O_2}, of the melt can be calculated by equation (19):

$$E = \frac{RT}{4F} \cdot \ln(a_{O_2} / 0.21 \text{ bar}) \tag{19}$$

According to equation (8), the measurement of a_{O_2} while varying the temperature also enables the calculation of ΔH^0.

3.4.2 Measurement of Self Diffusion Coefficients

While the peak potentials of voltammetric measurements enable the determination of standard potentials of the attributed redox pair, from the peak currents, I_p, the diffusion coefficients can be calculated.

$$I_p = D^{1/2} \cdot \Delta E \cdot \tau^{1/2} z^2 C_0 \cdot \text{const.} \tag{20}$$

with: D = self diffusion coefficient, ΔE = pulse amplitude, τ: step time, z = numbers of electrons transferred, C_0 = total bulk concentration of the polyvalent element, const. = 0.31 F^2/RT.

Since the peak currents are more notably influenced by the background currents than the peak potentials, a deconvolution of the current potential curves measured should always be carried out. Since voltammograms can be recorded only if the glass melt possesses a fairly high ionic conductivity, standard potentials as well as self diffusion coefficients can be measured only at high temperature.

Especially at temperatures around and below T_g, tracer experiments are the only way to determine self diffusion coefficients of polyvalent elements. Here, diffusion profiles of tracer doped glasses are usually recorded (see e.g., [99–101]).

3.4.3 Kinetic Measurements

Kinetic measurements of redox reactions in glassy materials have been carried out by high-temperature spectroscopy. The first report describes measurements by high-temperature EPR-spectroscopy of the redox systems $Fe^{2+}/Fe^{3+}/Mn^{2+}/Mn^{3+}$ and $Fe^{2+}/Fe^{3+}/As^{3+}/As^{5+}$ [27]. The signal intensities of the paramagnetic Fe^{3+} was normalized to room temperature. It remains constant during heating up to a temperature of around 500°C and then changes. In the case of the iron/manganese-system, the Fe^{3+} signal increases at temperatures > 500°C. Recently, high-temperature UV-vis-NIR spectroscopic measurements have been performed [28–30] using a microscope heating stage. The light from a lamp passes a chopper, and the sample is then focused by a parabolic mirror on the entrance slit of a monochromator, which gives the signal to a log-in amplifier synchronized to the chopper frequency [28].

3.5 KNOWN RESULTS

3.5.1 Effect of Experimental Parameters on the Redox Ratio

3.5.1.1 Effect of the Oxygen Activity

The effect of the oxygen activity on the redox ratio $[Me^{x+}]/[Me^{x+z}]$ is given theoretically by equation (2). Usually, this dependence is illustrated by a plot of log $([Me^{x+}]/[Me^{x+z}])$ versus log a_{O_2}. According to equation (2), a straight line with the slope z/4 should be obtained. The experiment that has to be carried out to verify the validity of this relationship is as follows: glass melts of the same basic composition doped with the same polyvalent element are equilibrated at the same temperature with gas atmospheres of different oxygen fugacities. The melts are subsequently quenched and analyzed using methods already described in section 4.1. As far as I know, all studies reported up to now in the literature (see, e.g., [21, 32, 35, 102–105]) came to the same conclusion: within the limits of error, equation (2) is valid and allows us to quantitatively describe the effect of the oxygen activity on the redox ratio.

3.5.1.2 Effect of Temperature

As pointed out in section 2.2, redox equilibria depend on temperature. In the case of equilibration experiments, glass melts of the same basic composition doped by the polyvalent element are equilibrated with the same atmosphere at different temperatures. This experiment is usually illustrated by a plot of log $([Me^{x+}]/[Me^{x+z}])$ vs. the reciprocal temperature. In the case of a constant standard enthalpy, this drawing should result in a straight line. In the case of voltammetric measurements, the temperature dependence is usually illustrated by a plot of the standard potential against the temperature. According to equations (4) and (5), this also should result in a straight line. Up to now, all results reported in the literature obtained from both equilibration and electrochemical experiments (see also Figure 3.4) confirmed the validity of the theoretically predicted temperature dependence. If within the temperature range studied, phase separation or crystallization occurs, deviations from linearity are observed. With the exception of the Ag^+/Ag^0-redox pair [106], higher temperatures always shift the equilibrium according to equation (1) to the left, i.e., to the reduced state. The attributed standard enthalpies and standard entropies depend on the type of polyvalent element and the glass melt composition and are usually constant over the temperature range studied (see, e.g., [21, 35, 37, 58, 63, 64, 72, 103, 105]).

3.5.2 Occurrence of Redox Species and the Electrochemical Series in a Soda-Lime-Silica Glass Melt

The oxidation numbers of species occurring in glass melts, in many cases, are clearly known, as they can be determined using spectroscopic methods in the solid glass. With the aid of electrochemical methods and using the shape of the current-potential curve, the number of the redox steps occurring within the potential window and the

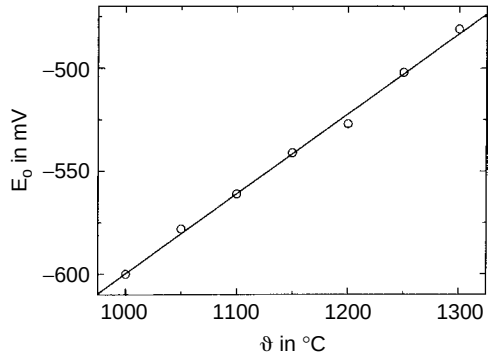

FIGURE 3.4 Voltammetrically determined standard potential of the Fe^{3+}/Fe^{2+}-redox pair, determined in a glass melt with the basic mol% composition of 74 SiO_2, 16 Na_2O, 10 CaO as a function of the temperature.

attributed number of electrons transferred (from the peak width) are obtained. Therefore, in the most cases, the attribution of the observed peaks to a certain redox pair is clear. In some cases, such as that of sulfur, there is still confusion, because from spectroscopic studies it is concluded that sulfur solely occurs as SO_3 and S^{2-}, while in electrochemical studies more redox steps are observed. Also from species, such as Bi^{5+} or Pb^{4+}, which might be present in melts only under extremely oxidizing conditions, it is not clear whether they really occur. The oxidation numbers of the species that may occur in a glass melt do not depend on the glass melt composition, but the redox ratios do.

The first electrochemical series of elements was given by Weyl [107]. He melted glasses containing two different types of polyvalent elements, quenched the melt and analyzed the glass. The shift in the redox ratio observed in comparison with a glass containing only one type of polyvalent element was interpreted, e.g., as "Cr^{6+} oxidizes Mn^{2+}." This was related to the melt properties and not to processes during cooling. Since, however, the redox shift can occur only during cooling, as pointed out in sections 3.3.2 and 3.2.3, this "electrochemical series" is not related to ΔG^0 or E_0 of the redox pairs, but to ΔH_{AB} of equation (14).

Table 3.1 presents an electrochemical series of elements that was measured with the aid of square-wave voltammetry at 1100°C in a soda-lime-silica glass melt with the basic mol% composition of 74 SiO_2, 16 Na_2O and 10 CaO [58, 60, 61]. The series is in good agreement with the empirical "knowledge" of glass technologists. In Figure 3.5 and Figure 3.6, the standard potentials of various redox pairs are drawn against the temperature (illustrated by the regression lines) and it is seen that the electrochemical series depends upon the temperature. For example, the standard potential of the Fe^{3+}/Fe^{2+}-redox pair is more negative than that of the Ni^{2+}/Ni^0-redox pair at temperatures above 1200°C. It also should be mentioned that these data cannot be simply correlated to other electrochemical series, that is, measured in aqueous solutions or to thermodynamic data, e.g., of the pure oxides. Similar electrochemical series of elements were reported from $Na_2O \cdot 2SiO_2$ [91], $15Na_2O \cdot 85SiO_2$ [89] and a waste glass composition [92].

TABLE 3.1
Electrochemical Series of Elements: Standard Potentials Measured Voltammetrically at 1100°C in a Glass Melt with Basic mol% Composition of 74 SiO_2, 16 Na_2O, 10 Na_2O

Redox Pair	E_O/V (vs. ZrO_2/P_{O_2} = 0.21 bar)
Ce^{4+}/Ce^{3+}	+ 0.08
Sb^{5+}/Sb^{3+}	+ 0.05
Cr^{6+}/Cr^{3+}	+ 0.03
Sn^{4+}/Sn^{2+}	–0.11
As^{5+}/As^{3+}	–0.17
Te^{4+}/Te^{0}	–0.18
Se^{4+}/Se^{0}	–0.21
Sn^{2+}/Sn^{0}	–0.24
Sb^{3+}/Sb^{0}	–0.33
Bi^{3+}/Bi^{0}	–0.35
Ag^{+}/Ag^{0}	–0.37
S^{4+}/S^{0}	–0.38
As^{3+}/As^{0}	–0.41
$U^{6+}/U^{5+}/U^{4+}$	–0.45
Cu^{+}/Cu^{0}	–0.46
Fe^{3+}/Fe^{2+}	–0.56
Ni^{2+}/Ni^{0}	–0.59
Co^{2+}/Co^{0}	–0.60
Mo^{6+}/Mo^{3+}	–0.65
Zn^{2+}/Zn^{0}	–0.73
Pb^{2+}/Pb^{0}	–0.74
Cd^{2+}/Cd^{0}	–0.78
V^{4+}/V^{3+}	–0.80
Cr^{3+}/Cr^{2+}	–0.86
Mo^{3+}/Mo^{0}	–0.91

3.5.3 Effect of the Glass Composition on the Redox Ratio

The electrochemical series given in Table 3.1 was measured in a soda-lime-silica glass melt of the basic composition $74SiO_2 \cdot 16Na_2O \cdot 10CaO$. The results cannot be quantitatively transferred to other glass melt compositions. At present, general rules that enable this transfer are not known. Hence, for every glass system, the thermodynamics of the redox pairs have to be measured.

In the past few years, numerous systematic studies on the effect of the glass composition on the redox ratio have been reported [2, 20, 21, 32, 37, 108–111]. Reliable data from single-component systems are not available, mainly due to experimental problems. Electrochemical measurements cannot be carried out in pure silica glass melts because the ionic conductivity is very poor. Equilibration experiments are also extremely difficult to carry out because of the high temperatures required to achieve an equilibrium with the gas atmosphere.

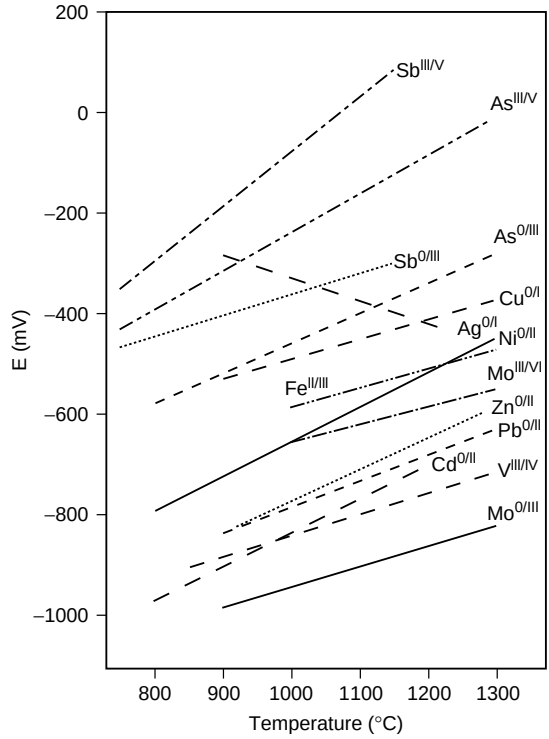

FIGURE 3.5 Voltammetrically determined standard potentials of various polyvalent elements recorded in a glass melt with the basic mol% composition of 74 SiO_2, 16 Na_2O, 10 CaO as a function of the temperature (illustrated by means of the regression lines).

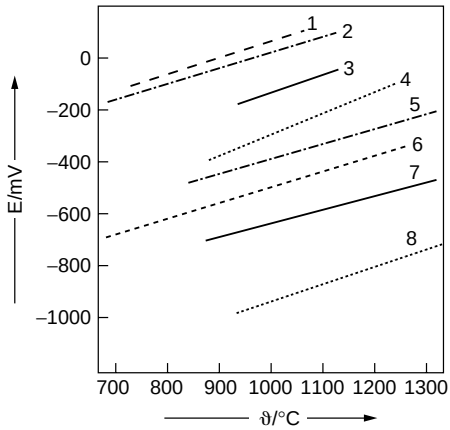

FIGURE 3.6 Voltammetrically determined standard potentials of various polyvalent elements recorded in a glass melt with the basic mol% composition of 74 SiO_2, 16 Na_2O, 10 CaO as a function of the temperature (illustrated by means of the regression lines). 1: Ce^{3+}/Ce^{4+}; 2: Cr^{3+}/Cr^{6+}; 3: Sn^{2+}/Sn^{4+}; 4: Sn^0/Sn^{2+}; 5: Bi^0/Bi^{3+}; 6: $U^{4+}/U^{5+}/U^{6+}$; 7: Co^0/Co^{2+}; 8: Cr^{2+}/Cr^{3+}.

In the literature, two types of redox reactions according to equation (1) are distinguished: the O- and the R-type [114]. While the O-type redox reaction is shifted to the right with increasing basicity of the melt, the R-type redox reaction shows the opposite behavior. As far as is known up to now, O-type redox reactions solely occur in the case of the Cu^{2+}/Cu^{+}-equilibrium, while all other polyvalent elements are attributed to the R-type. Sometimes this observation is described as "redox equilibrium paradox" because, according to equation (1), increasing O^{2-} activity should shift the equilibrium to the right. The basicity usually is calculated by empirical formulae derived to describe the shift in the UV-absorption as a function of the glass composition. As pointed out by R. Araujo, the basicity does not directly enter into the equilibrium constant and hence the redox equilibrium paradox does not exist [115].

3.5.3.1 Two-Component Systems

In the literature, the most carefully described two-component systems are binary alkali silicate glasses. Here, the type and quantity of alkali were varied and the redox equilibria were predominantly determined using equilibration experiments. Within a series of experiments, a strict correlation with the basicity of the melt has often been reported [2, 108, 112, 116, 117]. In principle, while increasing the alkali concentration, the equilibrium according to equation (1) is shifted to the left (with the exeption of the Cu^{2-}/Cu^{+}-redox pair).

The effect of the type and concentration of alkali is described for the redox pairs As^{3+}/As^{5+} [38, 111] Ce^{3+}/Ce^{4+} [38, 109, 113], Fe^{2+}/Fe^{3+} [20, 38, 113], Sn^{2+}/Sn^{4+} [110], Cu^{+}/Cu^{2+} [113, 114], Cr^{3+}/Cr^{6+} [108, 113], Mn^{2+}/Mn^{3+} [113] and U^{5+}/U^{6+} [113] using equilibration methods. In the most cases [20, 21, 38, 109–117], a linear dependence of a redox ratio upon the optical basicity is described. As already mentioned, in all cases except that of copper [113, 114], increasing alkali concentrations shift the redox ratio to the more oxidized state. Within one series of experiments, this relationship seems to be fairly clear (see, e.g., Figure 3.7). However, if the results reported in different studies are compared with each other, the deviations are fairly large. This is pointed out in Table 3.2 for the example of the Fe^{2+}/Fe^{3+}-equilibrium. Here, the results from both equilibration and voltammetric studies are included and illustrated by means of the calculated or measured standard potentials, E_0, respec-

TABLE 3.2
Standard Potentials of the Fe^{2+}/Fe^{3+} Equilibrium in Na_2O/SiO_2 Melts at 1300°C

$[Na_2O]$ in mol %	E_0 in mV	Method	Reference
20	–506	voltammetry	[23]
26	–512	voltammetry	[119]
30	–260	equilibration	[21]
33	–390	equilibration	[32]
33	–450	voltammetry	[53]

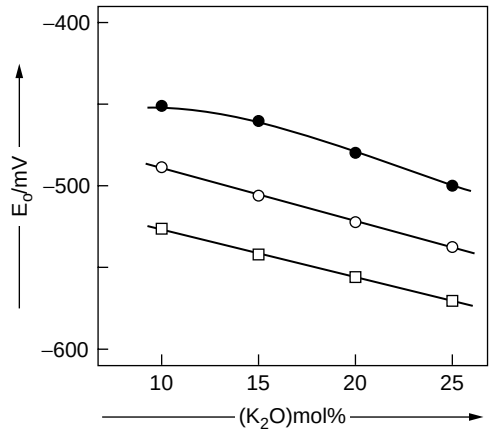

FIGURE 3.7 Standard potentials of the Fe^{2+}/Fe^{3+}-redox pair recorded in a glass melt with the basic composition of (90-x) SiO_2, x K_2O and 10 CaO as a function of the [K_2O]-content at ●: 1300°C, ○: 1200°C and □: 1100°C.

tively. Although the melt compositions are fairly similar, the results reported are not in good agreement. The deviations within the voltammetric measurements are not as large as those of equilibration experiments.

Besides voltammetric studies of the Cu^+/Cu^{2+}- [118], the Pb^0/Pb^{2+}- [119], the Sb^{3+}/Sb^{5+}- [120], the Ni^0/Ni^{2+}- [53, 121], the Zn^0/Zn^{2+}- [53], and the Ag^0/Ag^+-redox pair [106] have been carried out in binary soda-silicate glasses. Other voltammetric studies are focused on the Sb^{3+}/Sb^{5+}- [120], the Ce^{3+}/Ce^{4+}- [122] and the Fe^{2+}/Fe^{3+}-redox pair [54] in sodium borate glasses. In binary phosphate glasses (alkaline earth), until now, only the Fe^{2+}/Fe^{3+}-equilibrium has been studied [123] with the aid of equilibration methods.

3.5.3.2 Multicomponent Systems

In the literature, iron-containing alkali-lime alumino silicate and alkali magnesia alumino silicate systems have most often been described. The electrochemical series of elements and the temperature dependences measured using square-wave voltammetry have already been described in Table 3.1 and Figures 3.5 and 3.6 for a glass melt with the basic mol% composition of 74 SiO_2, 16 Na_2O, 10 CaO. The effect of the alkali concentration in glasses with the basic composition of (90-x) SiO_2, x M_2O, 10 CaO for x = 10 to 25 and M_2O = Na_2O and K_2O have been described in Ref. [23] for the case of Fe^{3+}/Fe^{2+}-redox couple. Figure 3.7 presents the standard potentials measured for a K_2O-CaO-SiO_2 glass melt as a function of K_2O-concentration (from Ref. [23]) at different temperatures. In analogy to binary alkali silicate glasses, a decrease in the standard potentials was also observed here while increasing the alkali concentration. In the case of soda-lime silicate glasses, however, the thermodynamic behavior cannot be fully described in terms of basicity, as, e.g., pointed out in Ref. [74]. Here, iron-doped glasses with the basic composition of 74 SiO_2, x Na_2O, (26-x) CaO with x = 10 to 26 were studied. Although the replacement of

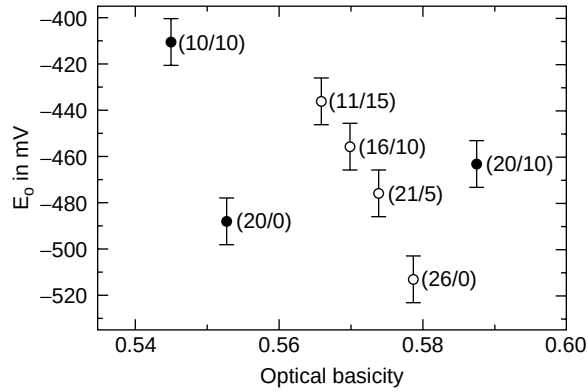

FIGURE 3.8 Standard potentials of the Fe^{2+}/Fe^{3+}-redox pair recorded in soda-lime-silica glass melts with different compositions as a function of the optical basicity; parameters in brackets: (soda concentration/lime concentration) in mol%.

Na_2O against CaO does not affect the basicity to a great extent, a large variation of the standard potentials were observed. As shown in Figure 3.8, a replacement of Na_2O against CaO resulted in drastically increasing standard potentials.

$$E_O(1300°C) = -400\ \text{mV} - [Na_2O]/\text{mol\%} \cdot 4.5\ \text{mV} + [CaO]/\text{mol\%} \cdot 2\ \text{mV} \quad (21)$$

In the past few years numerous studies on aluminosilicate systems have been reported. Here, the systems $Na_2O/CaO/Al_2O_3/SiO_2$ [75, 77, 80] and $Na_2O/MgO/Al_2O_3/SiO_2$ [83, 84] were considered. Additionally, the mixed alkaline earth system [85] was studied. The effect of glass composition on the Fe^{2+}/Fe^{3+}-equilibrium can be summarized as follows:

- Increasing the Na_2O-concentration results in more negative standard potentials, i.e., the equilibrium is shifted to Fe^{3+}.
- Introducing alumina and increasing its concentration up to $[Al_2O_3] = [Na_2O]$ results in less negative standard potentials, i.e., the equilibrium is shifted to Fe^{2+}.
- A further increase in the Al_2O_3-concentration ($[Al_2O_3] > [Na_2O]$) or ($[Al_2O_3] > [Na_2O] + [CaO]/2$) results again in more negative standard potentials (see Figure 3.9).
- The maximum in the standard potentials while varying the Al_2O_3-concentrations in $Na_2O/Al_2O_3/SiO_2$ and $Na_2O/MgO/Al_2O_3/SiO_2$ melts occurs at $[Al_2O_3] = [Na_2O]$, while it is observed at $[Al_2O_3] = [Na_2O] + [CaO]/2$ in $Na_2O/CaO/Al_2O_3/SiO_2$ melts.
- Introducing MgO in a $Na_2O/Al_2O_3/SiO_2$ melt and increasing the MgO-concentration results in more negative standard potentials, i.e., the equilibrium is shifted toward Fe^{3+} (see Figure 3.10).

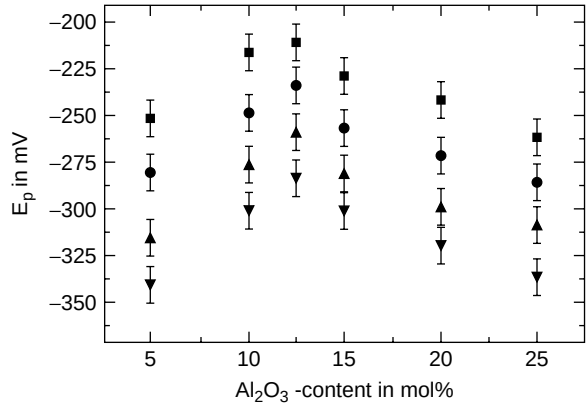

FIGURE 3.9 Standard potentials as a function of the Al_2O_3 concentration in $5Na_2O \cdot 15CaO \cdot xAl_2O_3 \cdot (80 - x)SiO_2$ melts. ■: 1600°C, ●: 1500°C, ▲: 1400°C and ▼: 1300˚C.

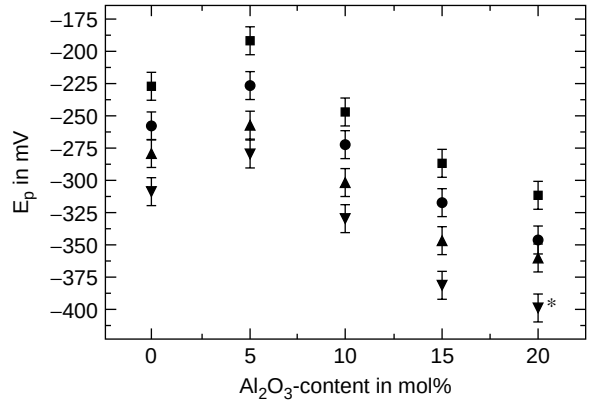

FIGURE 3.10 Standard potentials as a function of the Al_2O_3 concentration in $5Na_2O \cdot 15MgO \cdot xAl_2O_3 \cdot (80 - x)SiO_2$ melts. ■: 1600°C, ●: 1500°C, ▲: 1400°C and ▼: 1300˚C.

The effect of the melt composition on the Fe^{2+}/Fe^{3+}-redox equilibrium was described by the empirical equation:

$$E_p(1300°C) = a + b[Na_2O]_{NBO} + c[Na_2O]_{AL} + d[MgO] + e[CaO] + f[Al_2O_3]_T + g[Al_2O_3]_O + h[SiO_2] \quad (22)$$

with a = 20 mV, b = -8.76 mV/mol%, c = -3.42 mV/mol%, d = -7.84 mV/mol%, e = -11.19 mV/mol%, f = 2.7 mV/mol%, g = -7.34 mV/mol% and h = -2.72 mV/mol%.

The concentration $[Na_2O]_{NBO}$ stands for that Na_2O-concentration, which is coordinated with non-bridging oxygen, i.e., that molar Na_2O-concentration which exceeds the alumina concentration, while $[Na_2O]_{Al}$ is attributed to that Na_2O-concentration necessary to compensate the charge of AlO_4^--tetrahedra. $[Al_2O_3]_T$ is that

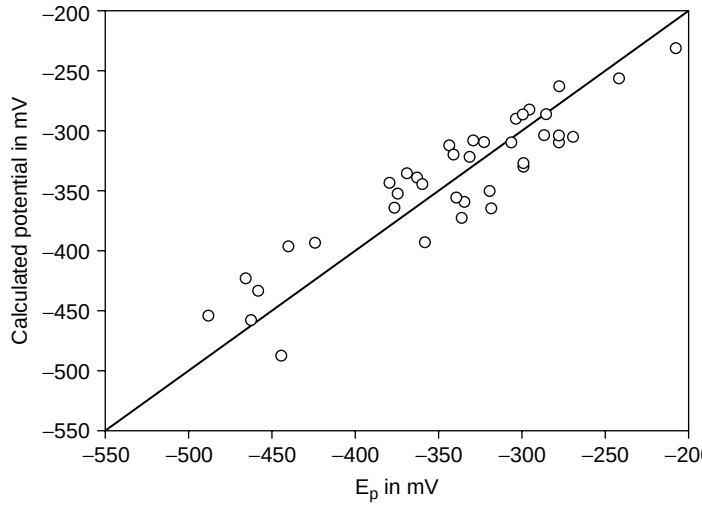

FIGURE 3.11 Standard potentials, calculated by Eq. 21 as a function of experimentally determined standard potentials at 1300°C.

alumina concentration that occurs in tetrahedral coordination. $[Al_2O_3]_O$ stands for that Al_2O_3-concentration that exceeds $[Na_2O]+[CaO]/2$. Figure 3.11 shows the standard potentials calculated using equation (21) as a function of the measured standard potentials. The agreement is fairly good.

The effect of glass composition on the Fe^{2+}/Fe^{3+}-equilibrium was explained by a structural model: iron as Fe^{3+} is predominantly incorporated as FeO_4^--tetrahedra, which needs alkali for charge compensation. If the alkali concentration is increased, the FeO_4^--tetrahedra are better stabilized and the equilibrium is shifted toward Fe^{3+}. If alumina is introduced into an alkali silicate melt, it is also incorporated in fourfold coordination, i.e., as AlO_4^- tetrahedra, which also need alkali for charge compensation. Hence, the quantity of alkali available to stabilize the FeO_4^--tetrahedra decreases. This results in a shift of the redox equilibrium toward Fe^{2+} with increasing alumina concentrations. If $[Al_2O_3] > [Na_2O]$, additional alumina is no longer incorporated as AlO_4^- tetrahedra but in octahedral coordination or as triclusters [126]. This also contributes to the stabilization of FeO_4^--tetrahedra and the equilibrium is shifted toward Fe^{3+}. If CaO is introduced additionally, the maximum in the peak potentials occurs at $[Al_2O_3] = [Na_2O] + [CaO]/2$. Hence, Ca^{2+} stabilizes only one tetrahedra (and not two). In contrast to Ca^{2+}, Mg^{2+} does not stabilize AlO_4^- and FeO_4^--tetrahedra; in the $Na_2O/MgO/Al_2O_3/SiO_2$ system, the maximum is observed at $[Al_2O_3] = [Na_2O]$. The observed shift in the redox equilibrium toward Fe^{3+} is supposedly due to the similarities of Mg^{2+} and Fe^{2+} with respect to their ionic radii and metal-oxygen bond lengths. Increasing MgO-concentrations hence leads to the incorporation of Fe^{2+} in energetically less advantageous sites, which favors the Fe^{3+}-redox species.

It should be known that the structural explanation given above is also in agreement with the effect of the melt composition on iron diffusivity [81, 86]. Additionally,

it is in agreement with the effect of composition on viscosity with respect to the main components: Na_2O, MgO, CaO, Al_2O_3 and SiO_2 [127].

Table 3.3 summarizes thermodynamic datas of the Fe^{3+}/Fe^{2+}-redox couple measured in alkali-lime-silica glasses of various compositions, all measured with the aid of square-wave voltammetry.

Other redox couples have, by far, not been investigated so intensively as Fe^{2+}/Fe^{3+}. Here, the effect of glass composition on redox equilibria is scarcely described. In the past few years, some studies on the Sn^{2+}/Sn^{4+}-equilibrium [52, 93] have been performed and describe the effect of Na_2O-, CaO- and Al_2O_3-concentration. It should be noted that an increase in the Al_2O_3 concentration has the largest effect on the Sn^{2+}/Sn^{4+}-equilibrium.

Other three-component glass melts studied were in the Na_2O-B_2O_3-SiO_2 system. An effect of phase separation on the thermodynamics was also observed here [67]. The results, as well as those obtained in a melt of the Na_2O-SrO-P_2O_5-system [71], are summarized in Table 3.4. While data obtained in the borosilicate glass melt are fairly similar to those of silicate melts, those obtained from the phosphate melts deviate drastically. For example, according to the data of Table 3.4, As_2O_5 in phosphate glasses should act as a fining agent at lower temperatures than Sb_2O_5.

3.5.3.3 Waste Glasses

Waste glasses with the basic mol% composition of 57 SiO_2/12.2 B_2O_3/16.8 Na_2O/11.1 Li_2O/2.9 MgO/0.2 ZrO_2 and 0.1 La_2O_3 doped with various polyvalent elements were studied with the aid of square-wave-voltammetry [64, 66, 68], whereas glasses of nearly the same composition but additionally containing 0.5 mol% TiO_2, were investigated by H.D. Schreiber et al. [103, 124, 125] using equilibration methods. The results of the voltammetric studies are summarized in Table 3.5. Figure 3.12 presents a plot of the voltammetric standard potentials against standard potentials calculated from the results of equilibration experiments, both attributed to a temperature of 1100°C. At comparably low [Ox]/[Red]-values, a good correlation can be observed, whereas at higher [Ox]/[Red] values, notable deviations are seen. For example, in the case of a glass melt containing 1 mol% NiO, after equilibration with air, a Ni^0-concentration as low as 10^{-5} mol% should occur. This is low enough to allow minor contaminations, e.g., of sulfate from the raw materials, to interact with the Ni^0/Ni^{2+}-redox pair during cooling and therefore shift the redox ratio during equilibration experiments. In my opinion, in such cases, electrochemical measurements are more reliable. The electrochemical series of elements in Table 3.5 is nearly the same as that of Table 3.1, attributed to a soda-lime-silicate glass melt with the basic mol% composition of 74 SiO_2, 16 Na_2O and 10 CaO. This is pointed out in Figure 3.13. The deviations of the full line attributed to the total agreement is not large, although the glass melt compositions are very different.

3.5.4 Redox Kinetics

First measurements on redox kinetics were carried out using high-temperature EPR spectroscopy of the paramagnetic Fe^{3+}-species. With increasing temperature, the

TABLE 3.3
Measured Standard Potentials at 1300°C, Standard Enthalpies, and standard Entropies of the Fe^{2+}/Fe^{3+} Equilibrium in the Melt Compositions Studied

$[Na_2O]$ in mol %	[CaO] in mol %	[MgO] in mol %	$[Al_2O_3]$ in mol %	ΔH^0 in kJ·mol^{-1}	ΔS^0 in kJ·mol^{-1}	E_0 (exp.) (at 1300°C) in mV
5	15	0	5	84	29	–340
5	15	0	10	78	28	–300
5	15	0	15	71	24	–300
5	15	0	20	77	26	–320
5	15	0	25	76	25	–337
5	10	5	0	91	33	–359
5	10	5	5	84	31	–363
5	10	5	10	74	26	–344
5	10	5	15	78	27	–370
5	5	10	5	79	30	–332
5	5	10	7.5	77	29	–323
5	5	10	10	73	25	–341
5	5	10	15	79	27	–380
5	0	10	10	78	29	–279
5	0	15	0	75	26	–335
5	0	15	5	72	26	–270
5	0	15	10	83	29	–300
5	0	15	15	87	29	–375
10	10	0	0	104	36	–440
10	10	0	5	105	41	–360
10	10	0	10	75	26	–304
10	10	0	15	68	23	–278
10	10	0	20	64	20	–286
10	10	0	25	54	12	–307
10	0	10	0	95	35	–377
10	0	10	5	79	30	–278
10	0	10	10	77	31	–242
10	0	10	15	82	31	–287
10	0	10	20	83	30	–319
10	0	5	10	71	29	–208
10	0	15	10	80	29	–296
10	0	20	10	81	28	–330
16	10	0	0	102	33	–460
20	10	0	0	98	30	–463
25	10	0	0	115	42	–445
15	0	10	10	86	33	–300
15	0	10	0	95	31	–425
20	0	10	0	102	33	–466
25	0	10	0	101	31	–489

TABLE 3.4
Standard Potentials Measured Voltammetrically in Three Component Melts

Redox Pair	Melt Composition	E_O at 1000°C in mV	ΔH^0 in kJ/mol	ΔS^0 in J/K · mol	Reference
Fe^{2+}/Fe^{3+}	$12.5Na_2O \cdot 62.5B_2O_5 \cdot 25SiO_2$	–510	74	19.3	[67]
Fe^{2+}/Fe^{3}	$6.5Na_2O \cdot 33.5B_2O_3 \cdot 60SiO_2$	–510	77	22.1	[67]
Fe^{2+}/Fe^{3}	$15Na_2O \cdot 42.5B_2O_3 \cdot 42.5SiO_2$	–520	81	24.1	[67]
Fe^{2+}/Fe^{3}	$33.3NaPO_3 \cdot 66.7Sr(PO_3)_2$	–170	119	78	[71]
As^{3+}/As^{5+}	$33.3NaPO_3 \cdot 66.7Sr(PO_3)_2$	–100	104	60	[71]
Sb^{3+}/Sb^{5+}	$33.3NaPO_3 \cdot 66.7Sr(PO_3)_2$	–200	159	93	[71]
Cu^{+}/Cu^{2+}	$33.NaPO_3 \cdot 66.7Sr(PO_3)_2$	–280	138	85	[71]
As^{0}/As^{3+}	$33.NaPO_3 \cdot 66.7Sr(PO_3)_2$	–440	337	153	[71]
Sb^{0}/Sb^{3+}	$33.3NaPO_3 \cdot 66.7Sr(PO_3)_2$	–630	471	229	[71]

TABLE 3.5
Standard Potentials, Standard Enthalpies, ΔH^0, and Standard Entropies, ΔS^0 Measured in a Borosilicat Waste Glass Melt

Redox Pair	E_O at 1100 °C in mV	ΔH° in kJ · mol	ΔS° in J·K · mol
Ce^{3+}/Ce^{4+}	+105	82	64
Sb^{5+}/Sb^{3+}	+15	207	147
Cr^{6+}/Cr^{3+}	+10	107	71
Cu^{2+}/Cu^{0}	–5	59	39
Sn^{4+}/Sn^{2+}	–165	194	112
As^{5+}/As^{3+}	–180	155	81
Te^{4+}/Te^{0}	–255	335	158
Sb^{3+}/Sb^{0}	–355	291	127
Sn^{2+}/Sn^{0}	–370	239	116
Bi^{3+}/Bi^{0}	–390	281	113
As^{3+}/As^{0}	–440	311	124
V^{5+}/V^{4+}	–480	100	36
Nr^{2+}/Nr^{0}	–510	274	122
Cu^{+}/Cu^{0}	–525	120	47
Fe^{2+}/Fe^{2+}	–590	126	47
Cd^{2+}/Cd^{0}	–650	259	91
Pb^{2+}/Pb^{0}	–680	222	60
Co^{2+}/Co^{0}	–700	393	181
Cr^{3+}/Cr^{2+}	–785	150	51
Zn^{2+}/Zn^{0}	–790	479	232
V^{4+}/V^{3+}	–800	112	23
Mn^{2+}/Mn^{0}	–880	251	52

Note: For composition, see text.

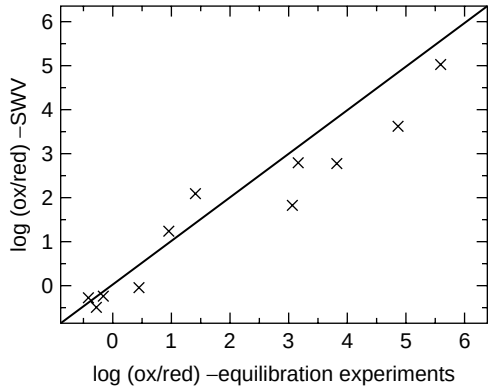

FIGURE 3.12 Redox ratios for an equilibrium with air of various redox pairs at 1100°C, calculated from voltammetric datas (measured by O. Claussen and C. Rüssel [64, 66, 68]) and determined using equilibration methods (measured by H.D. Schreiber [103, 124, 125]).

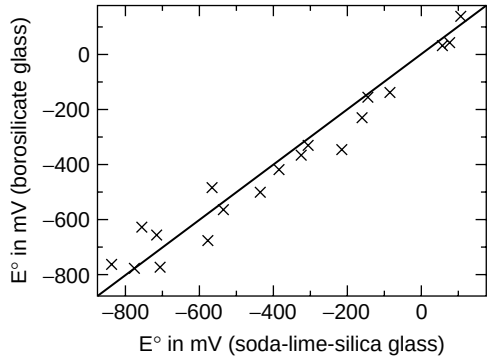

FIGURE 3.13 Voltammetric standard potentials measured in a borosilicate waste glass melt and a soda-lime-silicate glass melt with the basic composition of 74 SiO_2, 16 Na_2O and 10 CaO at 1100°C (full line: total agreement).

EPR signals normalized to room temperature remained constant up to a temperature of around 500°C and then changed with temperature, e.g., in the system $Fe^{2+}/Fe^{3+}/Mn^{2+}/Mn^{3+}$, the Fe^{3+} signal intensity (and hence the Fe^{3+}-concentration) increased with increasing temperature. Theoretical considerations and numerical calculations based on equation (16) showed that redox equilibria in glass melts should be in equilibrium at higher temperatures and frozen in at room temperature. Assuming that, in the systems studied, the diffusivity of iron is the rate-determining step (iron is most mobile redox species), rate constants (see equation (17)) based on experimentally determined diffusion coefficients can be calculated, and using thermodynamic data of the Fe^{2+}/Fe^{3+}-redox equilibrium, equation (16) can be solved numerically. As shown in Ref. [26], these calculations give evidence that the redox reaction is in equilibrium at temperatures > 600°C and is frozen in at < 500°C, supplying cooling rates usually applied in laboratory experiments and glass tech-

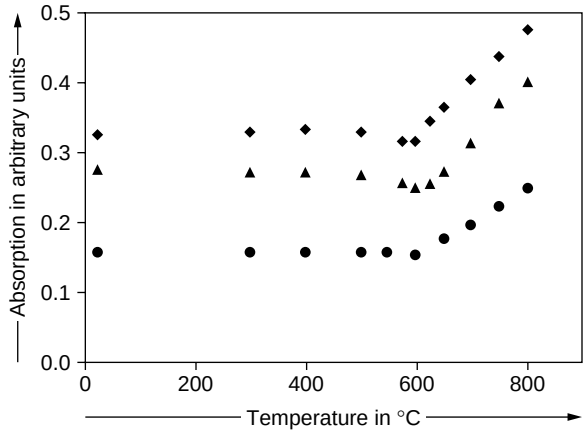

FIGURE 3.14 Absorption at the maximum of the band at around 13,000 cm^{-1} as a function of the temperature for samples ●: doped with 0.3 mol % CuO + 0.15 mol % Sb_2O_5, ▲: 0.6 mol % CuO + 0.3 mol % Sb_2O_5 and ◆: 0.6 mol % CuO + 0.15 mol % Sb_2O_5.

nology. Recently, UV-vis-NIR spectroscopy was applied to study glasses in the system $Fe^{2+}/Fe^{3+}/As^{3+}/As^{5+}$ [28], $Cu^{+}/Cu^{2+}/Sb^{3+}/Sb^{5+}$ [29], $Cu^{+}/Cu^{2+}/Sn^{2+}/Sn^{4+}$ [29] and $Mn^{2+}/Mn^{3+}/Cr^{3+}/Cr^{6+}$ [30]. In all these systems, the redox reactions are frozen in below 500°C and are in equilibrium above 600°C.

In melts solely doped with CuO, the absorption decreases slightly (< 10%) in the temperature range from 25–800°C. The same behavior is observed in melts doped with both copper and tin. By contrast, in melts doped with both copper and antimony, a different behavior is seen. This is illustrated in Figure 3.14 for glasses doped with 0.3 mol% CuO + 0.15 mol% Sb_2O_5, 0.6 mol% CuO + 0.3 mol% Sb_2O_5 and 0.6 mol% CuO + 0.15 mol% Sb_2O_5. First, from 25–600°C, a slight decrease in the absorptivity is observed, while at further increasing temperatures, a notable regain is observed.

In the case of glasses doped with both copper and tin, the Cu^{2+} concentration remains constant within the whole temperature range studied, while the Cu^{2+} concentration increases above 600°C in the glass doped with both CuO and Sb_2O_5. As shown in equation (14), the equilibrium constant $K_{AB}(T)$ depends on temperature, if $z \cdot \Delta H_B^0 \neq y\Delta H_A^0$. Then, the respective redox ratios $[A^n]/[A^{(n-z)+}]$ and $[B^m]/[B^{(m-y)+}]$ will also change if the temperature changes. For copper-containing melts, the following reactions are to be taken into account [29]:

$$2Cu^{2+} + Sb^{3+} \leftrightarrow 2Cu^{+} + Sb^{5+} \tag{23}$$

$$2Cu^{2+} + Sn^{2+} \leftrightarrow 2Cu^{+} + Sn^{4+} \tag{24}$$

Thermodynamic data of the redox equilibria of each redox pair are available from voltammetric measurements ($\Delta H^0(Cu^{+}/Cu^{2+})$ = 92 kJ · mol^{-1}, $\Delta S^0(Cu^{+}/Cu^{2+})$ = 32 J·mol^{-1} · K^{-1} [31], $\Delta H^0(Sn^{2+}/Sn^{4+})$ = 192 kJ · mol^{-1}, $\Delta S^0(Sn^{2+}/Sn^{4+})$ = 118 J·mol^{-1} · K^{-1}

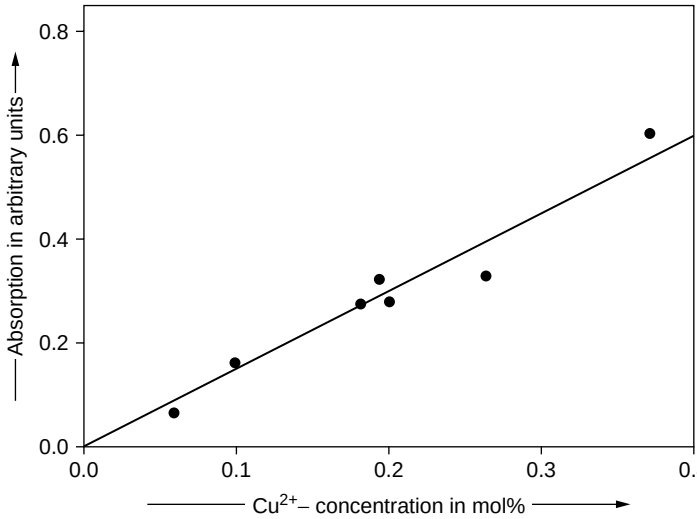

FIGURE 3.15 Maximum absorptions at room temperature and Cu^{2+} concentrations calculated from thermodynamic data (for 550°C).

[58], $\Delta H^0(Sb^{3+}/Sb^{5+}) = 286\ kJ \cdot mol^{-1}$, $\Delta S^0(Sb^{3+}/Sb^{5+}) = 206\ J \cdot mol^{-1} \cdot K^{-1}$ [31]. The temperature dependent term in Eq. 14 $(z\Delta H_B^0 - y\Delta H_A^0) = \Delta H_{AB}$ is then 102 $kJ \cdot mol^{-1}$ for melts doped with both copper and antimony and only 8 $kJ \cdot mol^{-1}$ for melts doped with both copper and tin. In the following, the melts were assumed to be in equilibrium with air at 1600°C, the temperature at which they were melted. According to the thermodynamic data above, this results in a $[Cu^{2+}]/[Cu^{+}]$-ratio of 1.8. In the melts solely doped with copper, this ratio remains the same during cooling. In the melts additionally doped with antimony, the Cu^{2+} concentration decreases during cooling. At initial CuO and Sb_2O_5 concentration of 0.3 and 0.15 mol %, the Cu^{2+} concentration is 0.193 mol% at 1600°C ($[Cu^{2+}]/[Cu^{+}] = 1.8$). During cooling, a Cu^{2+} concentration of 0.1 mol% is reached at 550°C. At a copper concentration of 0.6 and an Sb_2O_5 concentration of 0.3 mol%, the Cu^{2+} concentration decreases from 0.386 mol% to 0.262 mol% during cooling. In Figure 3.15, a plot of the maximum absorptions obtained from room temperature spectra and the Cu^{2+} concentrations calculated from the thermodynamic data for 550°C is shown. A linear correlation between the measured and calculated data is seen. The shift in the Cu^{2+} concentration during cooling is readily seen in the absorption spectra. Whereas, in the case of antimony-doped melts, the redox equilibrium is significantly shifted with temperature due to the large $\Delta H^0_{Cu/Sb} = 102\ kJ \cdot mol^{-1}$, the shift is small in the case of melts doped with copper and tin $(\Delta H^0_{Cu/Sn} = 8\ kJ \cdot mol^{-1})$.

REFERENCES

1. C.R. Bamford in: *Glass Science and Technology,* Elsevier, Amsterdam, Oxford, New York (1979) 88.

2. A. Paul: *Chemistry of Glasses*, Chapman and Hall, New York (1990).
3. W. Vogel: *Glass Chemistry*, Springer, Heidelberg, New York (1993).
4. H. Hessenkemper and R. Brückner, *Glastech. Ber.* 63 (1990) 244.
5. A.E. Badger, C.W. Parmelee, A.W. Williams, *J. Am. Ceram. Soc.* 20 (1937) 325.
6. D. Ehrt, H. Reiß and W. Vogel, *Silikattechnik* 27 (1976) 304.
7. C. Kasten, G. Carl and C. Rüssel, *Ber. Bunsenges. Phys. Chem.* 100 (1996) 1462.
8. W. Vogel: *Glass Chemistry*, Springer, Heidelberg, New York (1993) 403.
9. U. Kolberg in: *The Properties of Optical Glass*, Eds. H. Bach, N. Neuroth, Springer, Berlin, Heidelberg, New York (1995) p. 362.
10. W.H. Manring and R.W. Hopkins, *Glass Ind.* 39 (1958) 139.
11. R. Beerkens, *Glastech. Ber.* 68 (1995) 369.
12. R. Beerkens, A.J. Faber and O. Verheyen, 70. *Glastechnische Tagung*, Deutsche Glastechnische Gesellschaft, Cottbus, Germany (1996) p. 123.
13. A. Lenhart and H.A. Schaeffer, *Glastech. Ber.* 58 (1985) 139.
14. P. Ruz, A. Lenhart and H.A. Schaeffer, *Fortschrittsber. Dtsch. Keram. Ges*. 1 (1985) 138.
15. E. Freude and C. Rüssel, *Glastech. Ber.* 60 (1987) 202.
16. H. Müller-Simon, K. W. Mergler, *Glastech. Ber.* 6 (1988) 243.
17. M. Zink, C. Rüssel, H. Müller-Simon, K. W. Mergler, *Glastech. Ber.* 65 (1992) 25.
18. H. Müller-Simon, K. Mergler, *Glastech. Ber. Glass Sci. Technol*. 68 (1993) 273.
19. J. Bauer, H. Müller-Simon, *Glastech. Ber. Glass Sci. Technol*. 73 C2 (2000) 204.
20. A. Paul, R.W. Douglas, *Phys. Chem. Glasses* 6 (1965) 207.
21. A. Paul, J. *Non-Cryst. Solids* 71 (1985) 269.
22. C. Rüssel, *Glastech. Ber.* 66 (1993) 68.
23. C. Rüssel, *Glastech. Ber.* 66 (1993) 93
24. R.O. Sack, I.S.E. Carmichael, M. Rivers, M.S. Ghiorso, *Contrib. Mineral. Petrol* 75 (1980) 369.
25. S. Xu, W. Taug, W. Huang, *J. Non-Cryst. Solids* 112 (1989) 186.
26. C. Rüssel, *Glastech. Ber.* 62 (1989) 199.
27. G. Gravanis, C. Rüssel, *Glastech. Ber.* 62 (1989) 345.
28. H. Schirmer, Ma. Müller, C. Rüssel, *Glass Sci. Technol*. 76 (2202) 49.
29. L. Kido, Ma. Müller, C. Rüssel, *Phys. Chem. Glasses* 45 (2004) 21.
30. L. Kido, Ma. Müller, C. Rüssel, *Glass Sci. Technol*. 77C (2004) 397.
31. E. Freude, C. Rüssel, *J. Non-Cryst. Solids* 119 (1990) 303.
32. W.D. Johnston, *J. Am. Ceram. Soc*. 47 (1964) 198.
33. H.V. Lauer, *Phys. Chem. Glasses* 18 (1977) 49.
34. H.D. Schreiber, T. Tanyarasin, L.L. Lach, R.A. Legerc, *Phys. Chem. Glasses* 19 (1978) 126.
35. H.D. Schreiber, *J. Non-Cryst. Solids* 84 (1986) 129.
36. B. Stahlberg, B.M. Mosel, W. Müller-Warmuth, F.G.K. Baucke, *Glastech. Ber.* 61 (1988) 335.
37. R. Majumdar and D. Lahiri, *J. Am. Ceram. Soc*. 58 (1975) 99.
38. G. Jeddeloh, *Phys. Chem. Glasses* 25 (1984) 163.
39. Z.D. Xiang, M. Cable, *Phys. Chem. Glasses* 38 (1997) 167.
40. J.P. Traverse, T. Toganidis, C. Ades, *Glastech. Ber.* 65 (1992) 201.
41. C. Ades, T. Toganides, J.P. Traverse, *J. Non-Cryst. Solids* 125 (1990) 272.
42. E. Ebendorff-Heidepriem, D. Ehrt, *Opt. Mater.* 15 (2000) 7.
43. E. Ehrt, M. Leister, A. Matthai, *Phys. Chem. Glasses* 45 (2001) 231.
44. M. Leister, D. Ehrt, *Glastech. Ber. Glass Sci. Technol*. 73 C2 (2000) 194.
45. R. H. Sands, *Phys. Rev.* 99 (1955) 1222.

46. D. L. Griscom in: *Glass Science and Technology, Vol. 4B: Advances in Structural Analysis*, Eds. D.R. Uhlmann, N.J. Kreidl. Academic Press, New York (1990) 151.
47. D. Loveridge and S. Parke, *Phys. Chem. Glasses* 12 (1971) 19.
48. R.K. Brow, C.M. Arens, X. Yu and E. Day, *Phys. Chem. Glasses* 35 (1994) 132.
49. M. Schneider, W. Richter, R. Keding, C. Rüssel, *J. Non-Cryst. Solids* 226 (1998) 273.
50. C.R. Kurkjian and E.A. Sigety, *Phys. Chem. Glasses* 9 (1969) 73.
51. G. Tomandl in: *Glass Science and Technology, Vol. 4B: Advances in Structural Analysis*, Eds. D.R. Uhlmann, N.J. Kreidl. Academic Press, New York (1990) 273.
52. D. Benne, C. Rüssel, M. Menzel, K.D. Becker, *J. Non-Cryst. Solids* 337 (2004) 232.
53. K. Takahashi and Y. Miura, *J. Non-Cryst. Solids* 80 (1986) 11.
54. K. Takahashi and Y. Miura, *J. Non-Cryst. Solids* 38 & 39 (1980) 527.
55. A. Sasahira and T. Yokokawa, *Electrochimica Acta* 30 (1985) 441.
56. M. Maric, M.P. Brungs and M. Skylias-Kazacos, *Phys. Chem. Glasses* 30 (1989) 5.
57. C. Montel, C. Rüssel, E. Freude, *Glastech. Ber.* 61 (1988) 59.
58. C. Rüssel and E. Freude, *Phys. Chem. Glasses* 30 (1989) 62.
59. E. Freude and C. Rüssel, *Glastech. Ber.* 63 (1990) 193.
60. O. Claußen, C. Rüssel, *Ber. Bunsenges. Phys. Chem*. 100 (1996) 1475.
61. C. Rüssel, *Phys. Chem. Glasses* 32 (1990) 138.
62. O. Claußen and C. Rüssel, *Glastech. Ber. Glass. Sci. Technol*. 61 (1996) 95.
63. C. Rüssel, *Glastech. Ber.* 66 (1993) 93.
64. O. Claußen and C. Rüssel, *Ber. Bunsenges. Phys. Chem*. 100 (1996) 1475.
65. C. Rüssel, Glastech. *Ber. Glass Sci. Technol*. 70 (1997) 17.
66. O. Claußen and C. Rüssel, *Phys. Chem. Glasses* 39 (1998) 200.
67. R. Pascova and C. Rüssel, *J. Non-Cryst. Solids* 208 (1997) 237.
68. O. Claußen and C. Rüssel, *J. Non-Cryst. Solids* 209 (1997) 292.
69. C. Rüssel, *J. Non-Cryst. Solids* 134 (1991) 169.
70. O. Claußen and C. Rüssel, *J. Non-Cryst. Solids* 215 (1997) 68.
71. A. Matthai, O. Claußen, D. Ehrt and C. Rüssel, *Glastech. Ber. Glass Sci. Technol*. 71 (1998) 29.
72. C. Rüssel and G. Sprachmann, *J. Non-Cryst. Solids* 127 (1991) 197.
73. J.-Y. Tilquin, E. Herman, J. Gilbert and P. Claes, *Electrochim. Acta* 40 (1995) 1933.
74. O. Claußen, C. Rüssel, *Phys. Chem. Glasses* 39 (1998) 205.
75. J. de Strycker, S. Gerlach, G. von der Gönna, C. Rüssel, J. Non-Cryst. Solids 272 (2000) 131.
76. S. Gerlach, O. Claußen, C. Rüssel, *J. Non-Cryst. Solids* 226 (1998) 11.
77. S. Gerlach, O. Claußen, C. Rüssel, *J. Non-Cryst. Solids* 240 (1998) 110.
78. S. Gerlach, O. Claußen, C. Rüssel, *J. Non-Cryst. Solids* 238 (1998) 75.
79. S. Gerlach, O. Claußen, C. Rüssel, *J. Non-Cryst. Solids* 248 (1999) 92.
80. A. Wiedenroth, C. Rüssel, *J. Non-Cryst. Solids* 290 (2001) 41.
81. A. Wiedenroth, C. Rüssel, *Phys. Chem. Glasses* 43 (2002) 7.
82. A. Wiedenroth, C. Rüssel, *J. Non-Cryst. Solids* 292 (2002) 173.
83. A. Wiedenroth, C. Rüssel, *J. Non-Cryst. Solids* 318 (2003) 79.
84. A. Wiedenroth, C. Rüssel, *J. Non-Cryst. Solids* 320 (2003) 238.
85. A. Wiedenroth, C. Rüssel, *J. Non-Cryst. Solids* 330 (2003) 90.
86. G. von der Gönna, C. Rüssel, *J. Non-Cryst. Solids* 306 (2002) 263.
87. G. von der Gönna, C. Rüssel, *J. Non-Cryst. Solids* 288 (2001) 175.
88. G. von der Gönna, C. Rüssel, *J. Non-Cryst. Solids* 272 (2000) 139.
89. G. von der Gönna, C. Rüssel, *J. Non-Cryst. Solids* 262 (2000) 236.
90. G. von der Gönna, C. Rüssel, *J. Non-Cryst. Solids* 261 (2000) 204.
91. G. von der Gönna, C. Rüssel, *J. Non-Cryst. Solids* 260 (1999) 147.

92. O. Claußen, C. Rüssel, *J. Non-Cryst. Solids* 209 (1997) 292.
93. D. Benne, C. Rüssel, *Glass Sci. Technol.* 75 C2 (2002) 374.
94. H. Schirmer, R. Keding, C. Rüssel, *J. Non-Cryst. Solids* 336 (2004) 32.
95. G.C. Barker, *Anal. Chim. Acta* 18 (1958) 118.
96. J.G. Osteryoung, R.A. Osteryoung, *Anal. Chem*. 57 (1985) 101 A.
97. J.G. Osteryoung, J.J. O'Dea in: A.J. Bard (Ed.): *Electroanalytical Chemistry, Vol. 14*, Dekker, New York, Basel, (1986) 209.
98. J.J. O'Dea, J.A. Osteryoung, R.A. Osteryoung, *Anal. Chem*. 53 (1981) 695.
99. W. Köhler and G.H. Frischat, *Phys. Chem. Glasses* 19 (1978) 103.
100. T. Das, A.S. Sanyal, J. Mukerji, *Phys. Chem. Glasses* 35 (1994) 198.
101. T. Das, A.S. Sanyal, J. Mukerji, *Phys. Chem. Glasses* 36 (1995) 191.
102. H.D. Schreiber, T. Tanyarasin, L.L. Lach, R.A. Legerc, *Phys. Chem. Glasses* 1 (1978) 126.
103. H.D. Schreiber, L.M. Minnix, G.B. Balazs, B.E. Carpenter, *Phys. Chem. Glasses* 25 (1984) 1.
104. H.D. Schreiber, S.J. Kozak, R.C. Merkel, G.B. Balazs, P.W. Jones, *J. Non-Cryst. Solids* 84 (1986) 186.
105. X.Y. Shi and M.P. Brungs, *Phys. Chem. Glasses* 36 (1995) 275.
106. O. Claußen, C. Rüssel, *J. Mol. Liquids* 83 (1999) 295.
107. W.A. Weyl, *J. Phys. Coll. Chem*. 55 (1951) 507.
108. P. Nath, R.W. Douglas, *Phys. Chem. Glasses* 6 (1965) 197.
109. A. Paul, R.W. Douglas, *Phys. Chem. Glasses* 6 (1965) 212.
110. R. Pyare, P. Nath, *J. Am. Ceram. Soc*. 65 (1982) 549.
111. R. Pyarc, S. P. Singh, A. Singh, P. Nath, *Phys. Chem. Glasses* 23 (1982) 158.
112. J.A. Duffy, *J. Non-Cryst. Solids* 196 (1996) 45.
113. H.D. Schreiber, B.K. Kochanowski, C.W. Schreiber, A.B. Morgan, M.T. Coolbaugh, T.G. Dunlap, *J. Non-Cryst. Solids* 177 (1994) 340.
114. H. Hirashima, T. Yoshida, R. Brückner, *Glastech. Ber.* 61 (1988) 283.
115. R. Araujo, *Phys. Chem. Glasses* 36 (1995) 131.
116. F.G.K. Baucke, J.A. Duffy, *Phys. Chem. Glasses* 34 (1993) 158.
117. F.G.K. Baucke, J.A. Duffy, *Phys. Chem. Glasses* 32 (1991) 211.
118. B. Strzelbicka, A. Bogacz, *Electrochimica Acta* 30 (1985) 731.
119. B. Strzelbicka, A. Bogacz, E*lectrochimica Acta* 30 (1985) 865.
120. P. Claes, Z. Bacananwo, J.Y. Tilquin, J. Gilbert in: XV. Int. Congress on Glass, Leningrad (USSR), Nautika, Vol. 1b (1989) 215.
121. P. Claes, J. Tilquin, J. Gilbert, *Bull. Soc. Chim. Belg*. 97 (1988) 1101.
122. A. Sasahira, T. Yokokawa, *Electrochimica Acta* 29 (1984) 533.
123. H. Hirashima, H. Toyada, T. Yoshida, *Yogyo-Kyokai-Shi* 81 (1973) 281.
124. H.D. Schreiber, *Glass Res*. 3 (1993) 6.
125. H.D. Schreiber, A.L. Hockman, *J. Am. Ceram. Soc*. 70 (1987) 591.
126. G. Engelhardt, M. Nofz, K. Forkel, F. G. Wiksmann, M. Magi, A. Samoson, E. Lippmann, *Phys. Chem. Glasses* 26 (1985) 157.
127. M.J. Toplis, D.B. Dingwell, T. Lenci, *Geochim. Cosmochim. Acta* 61 (1997) 1605.

4 Transport Phenomena in Molten Glass: A Continuum Approach

Rand A. Murnane and Robert R. Thomas

CONTENTS

4.1 INTRODUCTION

The successful study of momentum (viscous flow), energy (heat conduction, convection, radiation), and mass transport (diffusion, chemical kinetics) in molten glass processes is dependent upon the accuracy of the scientific assumptions and physical properties used to describe these phenomena. All three areas have a long history of development in the chemical industry and the associated mathematical equations are well posed. The difficulty comes when these equations are applied to molten glass where the critical physical and chemical properties are unknown. This problem arises

due to the difficulty of measuring these properties in a high-temperature environment. The range of uncertainty in the properties forces the process analysis to consider ranges of operating conditions and parametric studies. In some cases, property information is so deficient that educated guesses have been used that later are shown to be completely incorrect.

The purpose of this chapter is to describe where the important physical and chemical properties occur when studying transport phenomena in molten glass. A continuum approach is used and there is no consideration from the molecular point of view. Some understanding of the mathematics of transport phenomena is assumed, but we have tried to keep the mathematics to a minimum. The initial section reviews the general governing equations for a variety of phenomena and relates them to glass applications. The latter section is a short summary describing the important transport phenomena occurring in the melter, the refiner, the forehearth, and the bowl sectors of the glass process. The aim is to provide a starting point from which one can become familiar with the methodology of this field and the critical importance of numerous glass properties.

4.2 THE NATURE OF GLASS VISCOSITY

For this discussion we will limit ourselves to glass viscosities above the softening point. At the softening point, a glass will elongate under its own weight. The resistance of glass to flow is described as its viscosity, μ, and can be defined using Newton's law of viscosity as

$$\tau_{ij} = -\mu \frac{dv_i}{dj} \tag{1}$$

where the shear stress, τ_{ij} (dyne/cm^2), is imposed in the *i*-direction on a glass surface of constant *j* distance and with a velocity in the *i*-direction.

Most simple fluids follow this relationship. This leads to the interpretation of momentum transfer as the viscous flux of *i*-momentum in the *j*-direction. The negative sign reflects that the flux is in the direction of decreasing velocity.

Molten glass has a broad range of viscosities. Figure 4.1 shows the viscosity vs. temperature relationship of some commercial glasses. As a reference of comparison, air is approximately 0.0002 poise, water 0.01 poise, and glycerol 11 poise. Even on a semi-log scale, the viscosity curves show a strong curvature with temperature; in some temperature ranges the viscosity can change by two to four orders of magnitude.

In the majority of applications glass can be considered a Newtonian fluid. Numerous models in the literature can handle non-Newtonian situations where the glass viscosity is a function of shear rate. The investigator must ensure that the correct viscosity relationship is used since it will directly affect the analysis for momentum transport. For the purposes here, the equations will use the Newtonian assumption.

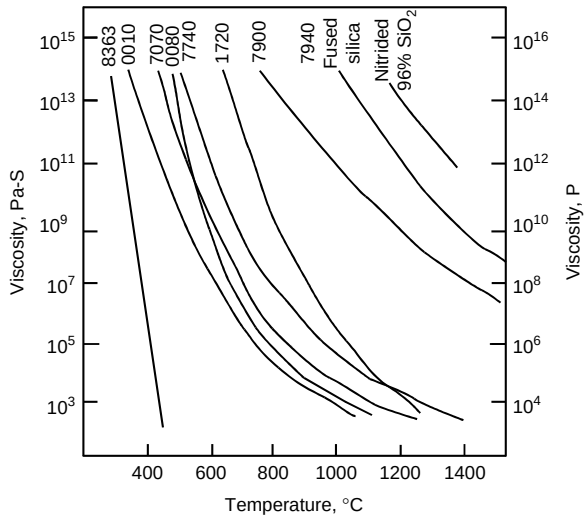

FIGURE 4.1 Viscosity vs. temperature for some commercial glasses. (Courtesy of Corning Incorporated.)

4.3 CONSERVATION OF MASS

A mass balance on a volume of glass accounts for the net accumulation of material within that space over time, *t*. The rate of change of density, ρ, resulting from the convection of material into the volume element can be written as the equation of continuity

$$\frac{D\rho}{Dt} = -\rho(D - \bar{v}) \tag{2}$$

where $(D \cdot \bar{v})$ is the divergence of the velocity vector

$$(\nabla \cdot \bar{v}) = \frac{\partial v_x}{\partial x} + \frac{\partial v_y}{\partial y} + \frac{\partial v_z}{\partial z} \tag{3}$$

The operator $\frac{D\rho}{Dt}$ is referred to as the substantial time derivative and is related in Cartesian coordinates to the partial time derivative

$$\frac{D\rho}{Dt} = \frac{\partial \rho}{\partial t} + \frac{\partial \rho}{\partial x}\frac{\partial x}{\partial t} + \frac{\partial \rho}{\partial y}\frac{\partial y}{\partial t} + \frac{\partial \rho}{\partial z}\frac{\partial z}{\partial t} \tag{4}$$

Often the continuity equation can be simplified for glass processes where the density is relatively constant. For these incompressible fluids, $\frac{D\rho}{Dt} = 0$.

4.4 CONSERVATION OF MOMENTUM

Consideration of a momentum balance around the same glass volume element introduces the concept of a stress tensor. Where a velocity vector has three components for direction and magnitude, the stress tensor contains nine elements representing three *normal* stresses and six *tangential* stresses. Momentum flows into and out of the glass by the nature of the bulk fluid flow and by the existence of velocity gradients. The equation of motion derived for this system is

$$\frac{\partial \rho \bar{v}}{\partial t} = -(\nabla \cdot \rho \bar{v}\bar{v}) - \nabla p - (\nabla \cdot \bar{\tau}) + \rho \bar{g} \tag{5}$$

This is equivalent to Newton's second law of motion. The expression associates the rate of increase of momentum ($\rho\bar{v}$) to the rate gained by the bulk transfer of glass into and out of the element ($\rho\bar{v}\bar{v}$), the rate gained by a pressure force (p), the rate gained by viscous transfer ($\bar{\tau}$), and the rate gained by gravitational force ($\bar{g}$). This equation is used to study the effects of weirs, throats, bubblers, geometry, stirrers, etc. on glass movement.

For a Newtonian glass, the equation of motion in one coordinate is

$$\begin{aligned} \rho \frac{Dv_x}{Dt} = &-\frac{\partial p}{\partial x} + \frac{\partial}{\partial x}\left[2\mu \frac{\partial v_x}{\partial x} - \frac{2}{3}\mu(\nabla \cdot \bar{v})\right] \\ &+ \frac{\partial}{\partial y}\left[\mu\left(\frac{\partial v_x}{\partial y} + \frac{\partial v_y}{\partial x}\right)\right] \\ &+ \frac{\partial}{\partial z}\left[\mu\left(\frac{\partial v_z}{\partial x} + \frac{\partial v_x}{\partial z}\right)\right] + \rho g_x \end{aligned} \tag{6}$$

which determines the pressure, density, and velocity components in flowing isothermal glass system.

The equation of motion is coupled to the energy equation by the relationship of viscosity with temperature and the change in density with temperature. The Boussinesq approximation for density variation, $\rho\,(1\text{-}\beta\Delta T)$, is used while assuming the only significant effect from glass density occurs in the gravitational or buoyancy term. This buoyancy is the main driving force for free convection in a glass process and has substantial effect on the glass motion, particularly in the melter and refiner. The volumetric expansion coefficient, β, must be known with a good deal of accuracy

to ensure that the buoyancy forces are in the correct scale to the other momentum forces in the system.

There are several important boundary conditions used to solve the equation of motion. The glass–refractory interfaces are assumed to have a "no-slip'' condition where the glass velocity is zero. The "slip'' boundary condition where the velocity gradient is zero is used at glass–gas interfaces. In situations like stirring, where a constant motion is imposed, a fixed velocity condition is used at the glass–stirrer boundary.

4.5 EQUATION OF MECHANICAL ENERGY

By considering the glass process as a "macroscopic'' flow system with one inlet and one outlet rather than using the previous "microscopic'' volume element view, a series of macroscopic balances for mass, momentum, and mechanical energy can be created. These equations are widely used in the analysis of pressure drop, flow obstructions, and drainage times for glass channels and orifices.

The mechanical energy equation, which accounts for the rate of increase in kinetic energy due to bulk flow, pressure, reversible conversion to internal energy, viscous forces, irreversible conversion to internal energy, and gravity can be integrated over the system to give the steady-state macroscopic mechanical energy balance

$$\Delta \frac{1}{2} \frac{\left\langle \bar{v}^3 \right\rangle}{\left\langle \bar{v} \right\rangle} + \Delta \overline{\Phi} + \int_{p_1}^{p_2} \frac{1}{\rho} dp + \hat{W} + \hat{E}_v = 0 \tag{7}$$

where the terms are respectively kinetic energy, potential energy, pressure drop, mechanical work on surroundings, and irreversible conversion of mechanical energy to thermal energy.

4.6 ENERGY TRANSPORT AND EFFECTIVE THERMAL CONDUCTIVITY

Energy transfer within molten glass is by conduction, convection, and radiation. The first two situations can be described using the standard mathematical definitions for thermal conductivity and fluid flow. The latter is complicated by the fact that the glass participates in the overall transfer process by absorbing, emitting, and scattering the radiation. Since the effect of these phenomena can vary with wavelength, the solution of the problem requires knowledge of the temperature and physical properties of the glass at every point within the process.

The quantity κ_λ, optical thickness, is a measure of the ability of a given glass path length to absorb and scatter radiation at a wavelength, λ. The optical thickness is defined as

$$\kappa_\lambda(L) = \int_0^L K_\lambda(l) dl \tag{8}$$

where K_λ is the extinction coefficient and L is the path length. Optical thickness can be thought of as the number of mean penetration distances before absorption or scattering. The concept of optical thickness is useful in studying the two radiation regimes at the extremum of the range; when $\kappa_\lambda << 1$, the optically thin limit, and when $\kappa_\lambda >> 1$, the optically thick limit.

The optically thin limit is more likely reached with very clear glasses or processes with small dimensions. The radiation flux includes absorption of energy originating at the boundaries of the process and energy emitted by the glass volume. There is no energy exchange between different volume elements of glass. This leads to a differential equation for radiative heat flux, q_R, of

$$-\frac{dq_R}{dy} = 2\sigma[\kappa_P(T_{\text{surf},1})T_{\text{surf},1}^4 + \kappa_P(T_{\text{surf},2})T_{\text{surf},2}^4 - 2\kappa_P(T)T^4(y)] \tag{9}$$

where κ_P is the Planck mean absorption coefficient and σ is the Stefan-Boltzmann constant.

When the process dimensions are large or if the glass is colored, the optically thick limit is usually applicable. Every glass element is similar to molecular conduction only by its neighbors. The radiation transfer becomes a diffusion process, which can be described by

$$q_R = -\frac{16}{3}\frac{n^2\sigma}{K_R}T^3\frac{dT}{dy} \tag{10}$$

where n is the glass refractive index and K_R is the Rosseland mean absorption coefficient defined as

$$\frac{1}{K_R} = \sum_{i=1}^{N}\frac{1}{K_{Ri}} \tag{11}$$

with

$$\frac{1}{K_{Ri}} = \int_{\Delta\lambda_i}\frac{de_{b\lambda}}{de}d\lambda \tag{12}$$

where $e_{b\lambda}$ is the spectral black-body emissive power. In this form, the radiation flux can be written in terms of an effective thermal conductivity, k_{eff},

$$q_R = -k_{\text{eff}}\frac{dT}{dy} \tag{13}$$

The reason for showing these radiation equations is to underscore the point that the optical properties of the molten glass are very important in determining the rate of energy transfer within the process. These properties are affected by temperature and are dependent on the wavelength. An accurate accounting of radiant exchange must integrate over the appropriate ranges. For the rest of the discussion in this transfer, the glass process will be assumed to be at the optically thick limit.

4.7 EQUATION OF ENERGY

The energy balance on a glass volume element accounts for the convection, conduction, and source/sink processes affecting heat transfer. As discussed previously, free convection is coupled to the momentum equation by the Boussinesq approximation for the buoyancy term. The radiation transfer is considered to be at the optically thick limit where the effective thermal conductivity approximation can be used. The source/sink terms refer to energy absorbing or dissipating phenomena such as joule heating, heat pipes, etc. Neglecting the viscous dissipation for a glass process at constant pressure, the energy equation becomes

$$\rho C_p \frac{DT}{Dt} = -(\nabla \cdot \bar{q}) + S_i \tag{14}$$

where C_p is the glass heat capacity, $\bar{q}$ is the conductive energy flux described by the molecular and effective thermal conductivities, and S_i is the energy source term.

The boundary conditions used to solve this equation vary from the melter to the orifice. The batch-to-glass interface requires an understanding of the heat of fusion requirements as well as the thermal transport properties of loosely packed material. The glass free surface can radiate to the crown, gas flames, or cooling air. The glass-refractory interfaces can have conductive cooling to a specified heat flux, temperature, or reference temperature.

When joule heating is used in the molten glass process, the energy dissipated is dependent on the fluid's electrical resistance to the passage of current. This resistance is characterized by the geometry of the process and the glass electrical conductivity. Similar to viscosity and thermal conductivity, the electrical conductivity is a strong function of temperature and can be a critical factor determining the stability of the system.

4.8 DIMENSIONAL ANALYSIS

Converting the previously mentioned equations into their dimensionless forms can be very beneficial when making engineering approximations or deciding on the best approach to solving the problem. The dimensionless equations have those variables that describe the size, speed, and properties of the systems consolidated into dimensionless groupings. Since the form of these equations is the same from one glass system to another, the only difference is in the values of these dimensionless numbers. When these dimensionless groups have the same values, the systems are

TABLE 4.1
Dimensionless Groups from Momentum and Energy Equations

Froude (Fr)	$\frac{gL}{v_R^2}$	$\frac{\text{inertial force}}{\text{gravitational force}}$
Galileo (Ga)	$\frac{g\rho^2 L^3}{\mu^2}$	$\frac{\text{gravitational force}}{\text{viscous force}}$
Grashof (Gr)	$\frac{\rho^2 g\beta\Delta T_R L^3}{\mu^2}$	$\frac{\text{buoyancy force}}{\text{viscous force}}$
Nusselt (Nu)	$\frac{hL}{k}$	$\frac{\text{convective heat transfer}}{\text{conduction}}$
Peclet (Pe)	$\frac{\rho C_p v_R L}{k}$	$\frac{\text{forced heat transfer}}{\text{conduction}}$
Power (Po)	$\frac{W}{\rho C_p v_R \Delta T_R L^2}$	$\frac{\text{electrical energy input}}{\text{convection}}$
Prandtl (Pr)	$\frac{\nu}{\alpha}$	$\frac{\text{momentum diffusivity}}{\text{thermal diffusivity}}$
Reynolds (Re)	$\frac{\rho L v_R}{\mu}$	$\frac{\text{inertial force}}{\text{viscous force}}$

said to be similar to each other; that is, the same equations can be used to analyze either problem.

Table 4.1 shows the set of dimensionless groups obtained from the equations and their physical interpretation. By comparing the order of magnitude of these groups for the chosen glass process under analysis, one can decide which phenomena are the most important forces on the system and study only them.

4.9 BOUNDARY-LAYER CONCERNS

A brief mention of momentum vs. thermal boundary layers should be made in regard to the study of transition flow regimes such as those that occur from melter to distributor and from distributor to forehearth. A boundary layer can be thought of as that region near a solid boundary where more than 90% of the changes in velocity or temperature are occurring. The momentum boundary layer is proportional to $Re^{-1/2}$ and the thermal boundary layer is proportional to $Pr^{-1/2}$. Since glass Reynolds numbers are < 1 and Prandtl numbers > 50, the thermal boundary layer is much larger than the momentum boundary layer. This creates situations in the transition

regions where the flow profiles develop very quickly, while the temperature profiles lag behind. This can lead to higher than expected heat fluxes in the transition zones if these effects are not considered.

4.10 MASS TRANSPORT EQUATIONS OF CHANGE

Glass-refractory, glass-gas, and glass-batch chemistry are some examples where it is important to describe the change of various chemical species over time. The mass transport is complicated because we must deal with mixtures. The mixtures are handled by writing an equation of continuity for each chemical species as well as for each mixture. The form of these equations is

$$\frac{\partial \rho_i}{\partial t} + (\nabla \cdot \rho_i \bar{v}) = (\nabla \cdot \rho D_i \nabla w_i) + r_i \tag{15}$$

where for species i, D_i is the diffusivity, w_i is the mass fraction, and r_i is the rate of production. This points to the need to develop an extensive knowledge about the chemical kinetics and equilibria associated to specific reactions.

4.11 GLASS PROCESS APPLICATIONS

The melting process can be thought of as a set of discrete "unit operations," each dependent on the output of the one preceding it but each different in function. This section will briefly review each of these parts of the melting process and describe the important physical and chemical transport phenomena in each section that can be related to the transport equations discussed previously.

4.11.1 MELTER

The primary function of the melter is to convert mixed batch materials to the molten state and complete the evolution of gases from the raw materials. The melter is thus a chemical reactor. The output from this reactor depends on the residence time and temperature history of all of the elements of glass while they are inside the melter.

Batch materials are normally pushed or dropped onto the surface of the molten glass bath. They float on the surface because the raw materials are of lower density than the molten glass. Heat is transferred to the batch from above by radiation from gas fires and superstructure and from below by conduction, convection and radiation from the glass melt. The batch particles are slowly pulled into the melt from the floating batch piles, and, through a time–temperature profile, are dissolved into the melt. Since the melting of a glass follows kinetic reaction rates, which are functions of temperature, each unmelted particle must be subjected to a time and temperature profile that will ensure that it is fully melted. Batch-related solid inclusions occur when some of the batch particles pass through the melter with insufficient time to completely melt at the temperatures in the melter. The determination of these

time–temperature profiles is limited by the knowledge about heat-of-fusion and chemical reaction rate data for batch melting.

Increasing temperatures in the melter is the recommended solution to a solid inclusion problem resulting from unmelted batch. However, higher temperatures accelerate the dissolution of the melter refractory walls and bottom and may create solid inclusions of refractory origin. Higher temperatures near the batch area also may cause the undesirable agglomeration of small batch particles into larger particles that are harder to melt at the given time and temperature.

Most melter designs gain residence time by containing a large glass volume compared with the bulk throughput of glass. Free convection is the dominant mechanism causing the distribution of velocities, and thus residence times, in the melter. Free convection velocities result from density differences in the melt that are the result of temperature differences established in the melter by cooling at some locations and heating at other locations within the melter. Typically, the design becomes a matter of compromise between the optimum times from Re (inertial) flows and the minimum and maximum times from Gr (buoyancy) flows.

High-temperature glass properties are critical to describing the free convection in the melter mathematically. Most critical of these are density, viscosity, and effective thermal conductivity. For a given temperature field in the melter, the resulting density differences will drive free convection roll patterns. Density differences as little as.01–.05 grams/cc resulting from normal temperature variations in the melter are sufficient to cause the convection rolls. As density differences increase, convection velocity will increase. Higher velocities in the roll will usually result in more stability of the convection pattern but usually less residence time. Higher viscosity will generally slow the convection velocity, while a more colored glass will increase it.

The melter convective flows usually arise from temperature differences, but they may also be caused by glass chemistry changes such as those at a glass change. If a lighter glass is to be used to flush out a heavier glass, the temperature field must be adjusted to expedite the process. If the density difference due to composition is larger than about .01 grams per cc, it is likely that it will be very difficult to achieve the required temperature difference and the light glass will not be able to flush out the heavy glass. In this event, a series of flush glasses with gradually changing density may be required.

Heat is transferred in the melt by other modes in addition to convective flow. Heat transfer is a strong function of the effective thermal conductivity of the glass. The effective thermal conductivity of molten glass has conduction and radiation components. Most glasses have approximately the same inherent molecular thermal conductivity. However, radiation usually makes up the largest portion of the effective thermal conductivity. The radiation component is often one to two orders of magnitude greater than the conduction component. The radiation conductivity can be estimated from the glass transmission properties at high temperature.

Temperatures at the boundaries of the melter (bottom, walls, crown) are imposed by physical design and operating conditions, but temperatures within the melt are the result of the heat transfer within the glass. Glasses with high transmission tend to have small temperature differences within the melt with high temperatures in the normally colder regions of the melter such as the bottom and corners. The magnitude

of these temperature differences within the melt will have a substantial effect on convection flows and stagnation points within the melter. For low transmission glasses, shallower melters or boosted melters may be necessary to avoid unacceptably low temperatures that would reduce glass quality.

The use of joule heating by locating electrodes in the melter results in locally high temperatures near the electrodes. Current density is highest near the electrode surface but decreases as the current paths spread out away from the electrode into the glass. A majority of the power from the electrodes is dissipated within 0 to 100 mm from the electrode. The glass in this area will become hot and the resistivity of the glass will decrease, causing more current and more energy dissipation for a constant voltage. The glass outside of this area will be colder, with higher resistivity and less energy dissipation. Equilibrium is attained by transferring the energy from the vicinity of the electrode to the rest of the melt by conduction, convection, and radiation. Boosting is thus best for high transmission glasses and becomes less effective as the transmission decreases, since the heat will be less efficiently transferred away from the electrodes.

Design for electric melting requires an understanding of the glass electrical resistivity. The resistance of a path between electrodes in glass is a function of geometry (distance between the electrodes and conduction path width) and the resistivity of the glass. Glass resistivity, like viscosity, decreases with increasing temperature. Thus, at low temperatures, the conduction path will have high resistance and the power system will be voltage-limited. As temperature increases, the system may become current-limited. A system designed for a low resistivity glass may be voltage-limited if a change is made to a high resistivity glass. Likewise, a system designed for a high resistivity glass may be current limited when a low resistivity glass is melted. Thus, a melter that relies on electric boosting for a substantial amount of the heat input may not be applicable to a wide range of glasses.

Obstructions in the melter are primarily intended to isolate the part of the melter containing unmelted batch materials from the part that is completing the melting of already partly dissolved particles. Thus, melters may be made up of a number of zones divided by walls. Glass passes from one zone to the other and from the melter to the refiner via throats or weirs.

The throat velocity associated directly with the throughput of glass is usually small compared with the free convection. There is frequently both a forward flow and a rearward flow through a throat caused by the convection forces. The throat opening will increase with time as the glass corrodes the refractory. As this happens, rearward convective flows will increase, causing a recycle stream in the melter. The recycle of the flow may have a beneficial effect on glass quality. In fact, the recycle stream may flow at a greater flow rate than the forward flow after much enlargement of the throat.

Weirs, in which the glass passes through an opening near the top of the wall, and submerged throats, where the opening is below the grade of the tank bottom, are unlikely to have return flow. Lack of a return or recycle flow means that corrosion rate of the throat will be less (often considerably less) than for a standard throat (near the bottom of a wall at grade with the tank bottom). Since throat life is frequently the limit for melting process life, a submerged throat or weir may improve

overall process life. A weir would be chosen only if there were no concern about unmelted batch materials being carried over the wall.

4.11.2 Refiner and Distributor

Glass should be completely melted, with no unmelted batch materials remaining as solid inclusions when it leaves the melter and enters the refiner. The purposes of the refiner are to allow sufficient time for gaseous inclusions to be eliminated from the melt and to begin the cooling of the glass toward its forming temperature. Refiners often act as distributors where the glass is circulated from the refiner directly to one or more forehearths or channels.

The refiner operates under the same principles as the melter. Free convection flow patterns are generated by temperature differences among the crown, walls and hot glass entering from the melting zone. Since the refiner is intended to facilitate fining, it is desirable for the glass to spend some time near the surface. However, glasses with large percentages of volatile components may be sensitive to too much volatilization, which may alter final properties or result in silica stones or cord (striae).

Fining will take place either by rise of the bubbles through the melt to the surface ("Stokes Fining"), or by chemical reabsorption of the gases into the glass matrix. Stokes fining is accelerated by higher temperatures and low viscosity, while chemical reabsorption is initiated by lowering temperatures. Thus, the refiner design must take into account which fining mechanism is preferred for the particular glass.

Frequently, refiners get relatively little direct energy input and depend on indirect heat from the melter and heat losses to the walls, bottom, and crown to produce the density differences that will drive convection currents. Sometimes, relatively little residence time is needed in the refiner. In this case, a throat that allows return flow to the melter will cause fast currents that shorten surface and bulk residence time. Longer residence times can be obtained by using throats that do not allow return currents.

Refiners are often semicircular in shape, or have other geometries that may contribute to areas that have relatively little movement of glass. These areas of stagnant glass may need augmentation of the normal superstructure heat to avoid formation of scum or other defects. This augmentation may be from additional spot burners in the corners or by electrodes located at the corners or near the throat. The intent of these additional sources of energy is to create temperature differences that will move the glass in normally stagnant areas. Defects such as scum or knots originating in the refiner are difficult to eliminate in the forehearth.

4.11.3 Forehearth

Forehearths or channels, sometimes also called "delivery systems," are intended to cool and condition completely melted and refined glass to the delivery temperature for the forming process (pressing, tube draw, sheet draw, fiber forming, blowing, etc.). Some forehearths include stirring, which is intended to improve thermal and chemical homogeneity of the delivered glass.

Since all melting and fining should already have been completed before the glass enters the forehearth, additional chemical phenomena in the forehearth are often undesirable. Volatilization in the forehearth may cause knots or cord. Forehearth design must specifically address the chemical nature of the glass to be delivered. Borosilicate glasses and others with high levels of volatile components may require all-electric forehearths with submerged covers to limit the effects of volatility. High resistivity glasses may need fuel-fired channels in order to input enough heat. Muffled superstructures, in which heat is supplied indirectly to the glass surface either by fuel fires or by electric heating elements, may be necessary for high resistivity glasses that are also volatile.

Complex volatilization reactions between some glasses and refractory can cause refractory material to volatilize and then recondense very near the glassline. For this reason (and also for forming stability), control of glass level in forehearths is critical. Variable glass level can wash these stones off the refractory wall and entrain them in the flowing glass. Glass temperatures in forehearths are seldom sufficient to redissolve such defects.

Flow in forehearths is primarily governed by forced convection. Flow is laminar with a generally parabolic velocity profile. However, the velocity profile is substantially affected by viscosity variation and buoyancy of the glass. In fuel-fired forehearths, the hottest glass is near the surface and the coldest glass is near the walls and bottom. The maximum velocity is near the surface where the hottest glass is. Even in enclosed forehearths, buoyancy causes the maximum velocity to be near the top of the channel.

This natural asymmetry means that unless some homogenization is done, the forehearth will deliver glass to the feeder, which will not be uniform even if temperature is tightly controlled. Channel or bowl stirring can homogenize glass that would naturally tend to be asymmetric.

Stirring is most often done in a forehearth or channel either at the rear, where the glass is hottest, or at the bowl, where it is closest to the delivery point. Effective stirring must accomplish two tasks in glass. First, sufficient shear must be applied to the incoming streams to attenuate inhomogeneous areas of glass. Second, the attenuated streams must be cut into many short segments that can be dispersed in the body of the glass.

Shear is created by applying a large velocity gradient in a short distance, such as between fast-moving blades and a wall. This can be done either for flow normal to or parallel to the blades. Cutting and dispersing is done when the streams are moving normal to the blades. For this reason, channel stirring must also include some degree of pumping in order to move the glass normal to the blades. Glass is already moving normal to the blades in bowl stirring. However, more energy is required to do bowl stirring because the viscosity is usually higher than in the rear of the forehearth. Bowl stirring may also not be feasible if it is inconsistent with product forming, such as with tube or sheet drawing.

The length and width of a forehearth are primarily determined by how much heat must be transferred from the glass to cool the glass from the refiner (or distributor) exit temperature to the delivery (feeder) temperature. This amount of heat is the product of the glass flow rate, the glass heat capacity and the difference

between forehearth inlet and outlet temperatures. Glass heat capacity is a function of glass chemistry and can be estimated if the glass chemistry is known. Heat-loss rates can be estimated for any forehearth configuration, either based on experience or by using estimated and measured refractory thermal conductivities. The length of the forehearth then is essentially the total desired heat loss divided by the design cooling rate of the forehearth. In some cases, forehearth length may be determined by logistical considerations (forming machinery space requirements, factory obstructions) but usually is determined by cooling requirements.

Heat transfer in a forehearth is by similar conduction, convection and radiation mechanisms as in the melter and refiner. However, because the governing distance for radiation in a forehearth is usually much shorter for a forehearth than for a large volume component such as a melter, the radiation component of the effective thermal conductivity in a forehearth is less than in the melter or refiner. Thus, overall heat transfer rates are lower in a forehearth.

Temperature uniformity at the delivery end is the prime function of forehearth cooling. Forehearth cooling profiles are designed to have relatively high cooling in the entry section of the forehearth and little cooling at the delivery end. This allows radiation and convection to equalize temperatures in the last third or so of the forehearth, so that glass entering the bowl will be uniform in temperature. This is important because flow and heat transfer in the bowl may be asymmetric, either with or without stirring.

Electric power in forehearths is designed in the same way as electric power in melters and refiners. Since forehearths run at colder temperatures, glass resistivity is generally high in the forehearth and suitable provision must be made for electrode position to keep reasonable glass path resistance. High glass path resistance will mean that the forehearth may need to operate at high voltages. High voltages in the forehearth may lead to high common mode voltage on other conducting parts in the forehearth such as thermocouples, tube draw bell shafts, stirrers and level probes. High voltages on these parts can result in personnel danger and the possibility of local chemical reactions. It is most desirable to locate the electrodes as close together as possible to forestall the effects of high voltage.

4.11.4 Bowls and Orifices

At the delivery end of the forehearth are the bowl, bowl well, and orifice. This assembly of equipment is sometimes called a feeder. The purpose of the feeder is to collect the conditioned glass from the forehearth and deliver it in the correct form and at the correct rate to the forming process. This usually takes the form of turning horizontal flow into vertical flow in the bowl, measuring the flow, and delivering it in the correct form (gob, sheet, tube, etc.).

Chemical phenomena are usually limited in a feeder to unwanted effects such as formation of blisters. These may be formed by air inspiration or by negative pressure associated with the bowl stirrer. Air inspiration has been discovered in some installations by flooding an inert gas, such as argon, into the joint area between the bowl well and orifice ring. Formation of gaseous inclusions is known to occur on portions of stirrer blades and gobbing hummocks, which operate at a negative

pressure. This must be removed from the stirrer by reversing it or removing and replacing it.

Flow patterns in a feeder area are often highly complex as the glass changes direction from horizontal to vertical (downward). If there is a central forming device such as a bell shaft or gobbing stirrer, flow will proceed around both sides of the device until it meets on the nose side of the bowl. This meeting of the two streams will form a stagnation point, or "nose cord." Unless the nose cord is eliminated by stirring, it will show up in the formed ware as a visible cord or streak.

Nose cord is dealt with in gobbing systems with a rotating gobbing stirrer, or a rotating sleeve in the case of a nonrotating gobbing needle. These have the effect of pulling all of the glass flow around one side of the rotating part and forcing the stagnation point away from the nose of the bowl. The glass flowing down the well and into the orifice is much more uniform when this stirring takes place although there may be a trace of the nose cord remaining. An additional measure is to use an overflow in the bowl, located approximately where the stagnation line is, to skim the cord off the surface. This works well in conjunction with stirring if it is properly placed; it is mandatory for tube draws.

The possibility exists in a bowl well for relatively high local heat losses. For this reason, bowl wells and orifices are frequently heated with electrical windings. Some all-electric forehearths also have electrodes in the bowl, although bowls are most often heated with burners. Electrically heated bowl wells and orifices are often necessary to prevent local devitrification or premature opalization, which could seriously affect the forming process.

4.12 FUTURE APPLICATIONS

The progress of the process engineer to understand the phenomena in the molten glass system will always be limited by how accurately his models simulate the true physics of the situation. It is unreasonable to expect great advances in our process understanding, when the models used to test our hypotheses are based on physical and chemical property data that are inadequate. The need for rigorous property data will increase in the near future. Studies in the fields of glass science concerning batch melting, bubble nucleation and refining, volatilization, corrosion kinetics, combustion, power dissipation, electrochemistry, internal radiation, process stability and control, process sensors, and homogenization are just some of the areas where more detailed transport models will be developed. With the availability of desktop high-speed computing, these models will be readily tested. The fundamental property data must be available to ensure the viability of this glass process design.

GLOSSARY

$\alpha = k/\rho\, C_p$	thermal diffusivity
β	volumetric expansion coefficient
κ	optical thickness
λ	wavelength

μ	glass viscosity
$\nu = \mu/\rho$	kinematic viscosity
Φ	potential energy
ρ	glass density
σ	Stefan-Boltzmann constant
τ	shear stress or shear rate tensor
C_p	specific heat
D	diffusivity
e_b	black-body emissive power
$\hat{E}_v$	mechanical energy to thermal energy
g	gravitational acceleration vector
k_{eff}	glass effective thermal conductivity
K	extinction coefficient
L	characteristic length
n	refractive index
p	pressure
q_R	radiation energy flux
q	conductive energy flux
r	rate of production
t	time
T	temperature
ΔT	temperature difference
v, v_R	velocity and reference velocity
$\langle \bar{v}^n \rangle$	$= \int_0^X \int_0^Y \bar{v}^n \, dx \, dy \Big/ \int_0^X \int_0^Y dx \, dy$
v	velocity vector
w	mass fraction
$\hat{W}$	mechanical work

OPERATORS

$$\nabla = \left(\frac{\partial}{\partial x}, \frac{\partial}{\partial y}, \frac{\partial}{\partial z} \right)$$

$$\frac{Dc}{Dt} = \frac{\partial c}{\partial t} + \frac{\partial c}{\partial x}\frac{\partial x}{\partial t} + \frac{\partial c}{\partial y}\frac{\partial y}{\partial t} + \frac{\partial c}{\partial z}\frac{\partial z}{\partial t}$$

$$(\nabla \cdot \bar{v}) = \frac{\partial v_x}{\partial x} + \frac{\partial v_y}{\partial y} + \frac{\partial v_z}{\partial z}$$

REFERENCES

The following list is not meant to be comprehensive, but only a notation of a few books and articles that the authors have found useful. The reader should use these references as a guide for understanding basic principles of transport phenomena. Most have extensive bibliographies and citations from which one can pursue a chosen topic in more depth.

B. Bansal, Physical Modeling of All-Electric Furnaces, *Coll. Pap. Annu. Conf. Glass Probl., 37th*, 137–153 (1976).

R.B. Bird, W.E. Stewart, and E.N. Lightfoot, *Transport Phenomena*, John Wiley & Sons, New York, 1960.

J.C. Carling, A reappraisal of the mathematical modelling of flow and heat transfer in glass tank forehearths, *Glass Technol.*, 23 (5): 201–222 (1982).

G.K. Chui and R. Gardon, Interaction of radiation and conduction in glass, *J. Amer. Cer. Soc.*, 52 (10): 548–553 (1969).

E. Conze and G. Woelk, Experimental investigations concerning the use of stirrers in feeder channels, *Glastechn. Ber.*, 54(4): 83–88 (1981).

R.L. Curran, Mathematical model of an electric glass furnace: effects of glass color and resistivity, *IEEE Trans. on Ind. Appl.*, IA-9: 348–356 (1973).

R.L. Curran, Use of mathematical modeling in determining the effects of electrode configuration on convection currents in an electric glass melter, *IEEE Trans. of Ind. and Gen. Appl.*, IGA-7: 116–129 (1971).

J. Happel and H. Brenner, *Low Reynolds Number Hydrodynamics*, Prentice-Hall, Englewood Cliffs, New Jersey, 1965.

J.O. Hirschfelder, C.F. Curtiss, and R.B. Bird, *Molecular Theory of Liquids and Gases*, John Wiley & Sons, Inc., New York, 1954.

B.S. Kellett, The steady flow of heat through hot glass, *J.Optical Soc. Am.*, 42 (5): 339–343 (1952).

J.G. Knudsen and D.L. Katz, *Fluid Dynamics and Heat Transfer*, McGraw-Hill, New York, 1958.

H. Lamb, *Hydrodynamics*, Dover, New York, 1945.

H.L. Langhaar, *Dimensional Analysis and Theory of Models*, John Wiley, New York, 1951.

O. Levenspiel, *Chemical Reaction Engineering*, John Wiley & Sons, Inc., New York, 1972.

H. Mase and K. Oda, Mathematical model of glass tank furnace with batch melting process, *J. Non-Crystalline Solids*, 38-39: 807–812 (1980).

R.C. Reid, J.M. Prausnitz, and T.K. Sherwood, *The Properties of Gases and Liquids*, McGraw-Hill, New York, 1977.

A. Schild, Studies on the heat current in tanks by means of models, *Glastech. Ber.*, 11: 305–314 (1933).

H. Schlichting, *Boundary Layer Theory*, McGraw-Hill, New York, 1955.

R. Siegel and J.R. Howell, *Thermal Radiation Heat Transfer*, McGraw-Hill, New York, 1972.

E.M. Sparrow and R.D. Cess, *Radiation Heat Transfer*, McGraw-Hill, New York, 1978.

J. Stanek, *Electric Melting of Glass*, Elsevier, Amsterdam, The Netherlands, 1977.

5 Viscosity of Molten Glasses

David Martlew

CONTENTS

5.1 THEORETICAL CONSIDERATIONS AND DEFINITIONS

5.1.1 Introduction

Molten glasses (or liquids that have the propensity on cooling to solidify in an amorphous rather than a crystalline form) are usually thought of as being "viscous." Comparisons are made with liquids of common experience such as syrup or honey

to express the unusual difficulty persuading them to flow. This viscous nature was exploited by early glassmakers, who found that the melt could be sampled and manipulated by means of an iron tube. Glass blowing was readily possible because the high viscosity of the molten mass allowed it to be gathered and retained on the blow pipe for long enough to be shaped as desired in a temperature range where crystallization did not prejudice the integrity of the eventual product. We can argue that if it were not for the highly viscous nature of silicate glasses, neither the elegant stemware of Venice nor the sumptuous stained glass of Chartres could have been manufactured.

Resistance to flow in the macroscopic world is a byproduct of reluctance to move at a molecular scale. Familiar glass-forming substances when molten have some degree of polymeric molecular structure, which limits the freedom of molecular diffusion. Cooling the melt reduces the energy associated with molecular motion, bringing about a rapid increase in viscosity and inhibiting the molecular juggling necessary for nucleation and growth of crystals. Crystallization becomes slow compared with practically achievable rates of cooling, which means that by suitable handling the liquid can be solidified before crystallization has had time to happen. Rawson [1] pointed out that it is this behavior that defines what we mean by a molten glass.

The importance of viscosity as a property of molten glasses has long been recognized. It has direct bearing on the ease or difficulty with which gaseous or solid inclusions can be removed from the melt and it markedly affects the process of rendering a finite volume of glass sufficiently homogeneous to satisfy the user's requirements. The medieval glassmaker found himself grappling with the way in which viscosity varied with temperature as he sought to work his gather into the desired article, and the variability of viscosity with glass composition no doubt plagued him as he coped with the vagaries of highly variable raw materials. A vocabulary of descriptive terms evolved to express the characteristics of the glass; "short," for example, spoke of a glass with a comparatively steep change of viscosity with temperature in the forming range, because the glass worker had only a short time for manipulation as the gather cooled. A "long" glass on the other hand changed its viscosity much more slowly as the glass cooled, allowing greater time before it became necessary to reheat the gather. Verbal description was all that was possible until there grew up a clearer understanding of liquids and how they behaved, together with a satisfactory theoretical picture of what was involved in their movement. Two men whose names are indelibly associated with the early studies of viscous flow phenomena are Newton and Poiseuille.

5.1.2 Definitions and Nomenclature

Sir Isaac Newton (1642–1727) laid the foundations for the study of fluid mechanics, inventing the necessary mathematical structures and formulating the laws governing fluid motion [2]. He noted that the resistance to flow of a fluid in a conduit "…arising from the want of lubricity in the parts of a fluid is, other things being equal, proportional to the velocity with which the parts of a fluid are separated from one

another," (quoted by Stuart Winston Churchill [3], page 18), an insight that is now expressed as:

$$\tau_{xy} = -\eta(dv_x/dy)$$

where τ_{xy} is the shear force per unit area exerted in the *x* direction on a fluid surface of constant *y* by the fluid in the region of lesser *y*, v_x is the component of fluid velocity in the *x* direction, *x, y* are orthogonal cartesian axes, and η is the viscosity of the fluid (Bird, Stewart and Lightfoot [4], page 5).

This equation is now known as *Newton's law of viscosity* and it defines for us the concept of viscosity as a fluid property; fluids for which that property is independent of shear are known as *Newtonian*. Generally in the field of rheology the viscosity of a Newtonian fluid is denoted by the symbol μ and the symbol η is reserved to express non-Newtonian behavior. Even though molten glass generally behaves as a simple Newtonian liquid, it is an eccentricity of the glass community to use η for glass viscosity, so that notation is used here.

Jean-Louis-Marie Poiseuille (1799–1869) was a French physician who studied flow in capillary tubes with a view to modeling the circulation of the blood. The text of his lecture to the Academie Royale des Sciences de l'Institut de France was published in 1846 [5] and later translated into English by Herschel (see [3] page 16). His analysis of capillary flow formed the basis for methods of measuring viscosity, for example, the Ostwald viscometer for laboratory use and the more robust Redwood, Saybolt or Engler devices commonly used in industrial settings (see general texts such as that by Massey [6]). It seems appropriate therefore that Poiseuille's achievements are commemorated in the use of part of his name (poise, denoted by P) to describe the unit of viscosity most widely used in the study of molten glass behavior. The advent of the SI system of units encouraged scientific workers to adopt the larger pascal-second (Pa s) unit, but the glass community retained its allegiance to Poiseuille and continued to use the poise. Latterly, this stance has been legitimized by regarding the poise as equivalent to the deci-pascal-second (dPa s). For the purposes of this chapter, viscosity values are taken to be expressed in poise unless otherwise stated.

5.1.3 The Objectives of This Chapter

In his recent review of classical glass technology, Cable underlines the importance of dynamic viscosity in determining how glasses can be prepared and used [7]. Not surprisingly, there is a voluminous literature containing viscosity data of interest to the glass community. Measurements are available covering the composition ranges from single oxide melts to complex commercial glasses, giving viscosity values spanning over 15 orders of magnitude, measured by a variety of techniques for a variety of purposes. Presentation of the results varies widely according to each author's interests and expectations; there are graphs with and without data points, lists of smoothed data with and without details of how smoothing was done, parameter sets for a variety of smoothing equations, and (all too infrequently) unadorned lists of measured temperatures and viscosity values. To search the literature for

specific information of interest and having found it to assess its reliability can be a very time-consuming business.

Tribute should be paid to those who have made compilations of viscosity data for glassforming melts. Without their labors the task would be unmanageable. Among them are:

- O.V. Mazurin, M.V. Streltsina, T.P. Shvaiko-Shvaikovskaya, *Handbook of Glass Data,* (1983, 1987) Elsevier
- M.P. Ryan, J.Y.K. Blevins, *Viscosity of Synthetic and Natural Silicate Melts and Glasses,* (1987) U.S. Geological Survey Bulletin 1764
- N.P. Bansal, R.H. Doremus, *Handbook of Glass Properties,* (1986) Academic Press
- H. Cole, C.L. Babcock, *Viscosity — Temperature Relations in Glass,* (1970) bibliography published by the International Commission on Glass

In the interests of precision, these compilations have presented the viscosity data in substantially the same form as that in which it was originally published. This offers the serious enquirer direct access to specific data, but makes it difficult to survey a compositional field of interest or to make comparisons among the works of different authors. This chapter has followed a different philosophy. The tables have been constructed by fitting the Vogel-Fulcher-Tamman equation to each set of viscosity and temperature data as given; the resulting constants are presented in the first part of each table, and in the second part, these constants are used to calculate the temperatures corresponding to an appropriate set of viscosity values. This approach sacrifices precision but makes the data available in a compact form that facilitates comparisons and appreciation of compositional trends. So this chapter aims to complement rather than supplant the existing compilations.

5.1.4 Viscosity and Temperature

Most traditional glass-melting and -forming operations are carried out under conditions of low stress. Under these conditions it is a permissible approximation to regard glass melts as Newtonian fluids. For practical purposes, a number of important stages in the variation of viscosity with temperature have been named, though not always consistently; these names serve to label the temperatures at which particular glass-making operations can be carried out. Table 5.1.1 gives typical viscosity values for some of the common named temperature reference points.

These points have provided a valuable vocabulary that has passed into the language of glass technology, but they are merely labels on a continuous curve of viscosity vs. temperature. Unlike, for example, the melting point of a crystalline solid, they have no absolute significance. Cable's presentation of viscosity ranges for typical glassmaking operations is more helpful to the understanding but too cumbersome for day-to-day usage [7]; some of these are given in Table 5.1.2.

TABLE 5.1.1
Some Typical Named Viscosity Values

Melting point	2.0
Working point	4.0
Flow point	5.0
Littleton's softening point	7.65
Deformation point	11.50
Annealing point	13.0
Strain point	14.5

Note: values are given as $\log_{10}$ (viscosity in poise).

Source: Data from: M. Cable in *Glasses and Amorphous Materials,* J. Zarzycki (Ed.),Volume 9 of the series *"Materials Science and Technology"* (1994), VCH; *Introduction to Glass Science,* L.D. Pye, H.J. Stevens, W.C. LaCourse, (Eds.) (1972) Plenum Press; C.L. Babcock, *Silicate Glass Technology Methods,* (1977) John Wiley & Sons.

TABLE 5.1.2
Viscosity Ranges for Some Glassmaking Operations

Glass melting	1.5 to 2.5
Sealing glasses to other glasses or to metals	3.5 to 3.8
Producing gobs for container forming	3.6 to 4.2
Drawing sheet glass (Fourcault process)	4.0 to 4.4
Glass pressing	4.0 to 6.3
Surface of a bottle during blowing	5.7 to 10.0
Sinter glass powder to a solid body	6.0
Sinter glass powder to form a porous body	8.0 to 8.8
Dilatometric softening point	11.3 to 1.7
Annealing range	12.0 to 4.0
Stress release occurs in a few seconds	12.8
Temperature for matching expansion curves for seals	14.0 to 4.5
Stress release too slow to be useful	above 14.6

Note: values are given as $\log_{10}$ (viscosity in poise)

5.1.5 The Form of the Viscosity vs. Temperature Relation

In the last two decades of the 19th century, S. Arrhenius was interested in chemical reactions that go faster when the temperature increases. He explained this by proposing that molecules needed to aquire kinetic energy above a particular threshold value before reaction was possible; this they did by chance collisions with other molecules in their vicinity. He noted (see, for example, [10] page 1090) that the

TABLE 5.1.3
Some Empirical Equations Used to Describe the Variation of Viscosity with Temperature

$$\log \eta = A - (B/T) + (C/T^2)$$
$$\log \eta = -A + B\,T + (C/T^2)$$
$$\log \eta = -A + B \log T + (C/T^2)$$
$$\log \eta = -A + B/(T - T_o)^2$$
$$\log \eta = -a + b/(T + 273)^{2.33}$$
$$\log \eta = -A + (B \times 10^3)/(T - T_o)$$

Note: temperatures are usually given in Celsius, and the logarithms are to base ten

Source: After G.S. Fulcher *J.Am.Ceram. Soc.* (1925).

probability of a molecule attaining such excess energy in a low-viscosity fluid system was exponentially related to the thermodynamic or absolute temperature, and this led to the classic equation that now bears his name:

$$k = A \exp(-E/RT_A)$$

Although this equation has since been widely used in studies of thermally activated processes, the concept properly relates to simple bi-molecular reactions in the gas phase. It was rapidly found that in systems where the reactions are more complex, for example those involving several steps in sequence, the observed temperature dependence of rate deviated markedly from this simple relationship.

Thirty years or so later, the shape of the temperature vs. viscosity graph for molten glasses was the subject of much interest and some perplexity. Gordon Fulcher [11] pointed out that the viscosity of silicate glasses did not vary strictly logarithmically as the reciprocal of absolute temperature, and attempts to fit an Arrhenius form of equation to good experimental measurements resulted in large systematic deviations from the curve. He listed a selection of empirical equations that had been tried (see Table 5.1.3), but came to the conclusion that the best was a three-parameter equation that modified the Arrhenius form by in effect displacing the start of the temperature scale upward from the thermodynamic absolute zero to some temperature he denoted by T_o.

The last entry in Table 5.1.3 is the form of equation as given by Fulcher, apparently derived independently of the contemporaneous work by Vogel [12] and Tammann [13]. The Vogel-Fulcher-Tammann (VFT) equation provides a very good fit for data relating to silicate glasses, but for other compositions (borate glasses for example), the residuals are much larger. In most cases, the residual errors appear systematic rather than random, which leads most workers to doubt the physical significance of the equation. As an empirical curve-fitting tool, the VFT equation has the advantages of simplicity and quite wide applicability, so it has been the most universally employed for the study of glass melts and seems the most appropriate equation for use in this chapter.

The tables at the end of this chapter make extensive use of the VFT equation with the following form and conventions:

$$\log \eta = A + B/(T - T_o)$$

where η is the viscosity expressed in poise (or dPa.s); T, T_o are temperatures in degrees Celsius; A, B are parameters with appropriate units; and logarithms are to base 10.

It is worth noting that when the equation is expressed in this way the coefficient A is usually a negative number.

Some attempts have been made to provide a theoretical basis based on structural arguments for the observed viscosity–temperature relation. For example, Plumat [14] proposed that structural transitions within the glass melt occurred at three or four temperatures, splitting the viscosity–temperature curve into distinct regions. Activation energy for viscous flow in each region was seen as constant, so plots of log (viscosity) vs. reciprocal absolute temperature could be constructed using a series of straight lines intersecting at the critical temperatures. To test this suggestion, Fontana and Plummer [15] carried out some very careful and complete studies of eight silicate glass compositions, finding no support for such critical temperatures. Activation energies changed continuously over the temperature ranges covered, but these authors found some indications of a more subtle transition at which the temperature coefficient of activation energy changed. From the empirical point of view, it is interesting to note that the VFT equation emerged from their studies as certainly no worse than the other equation forms they used to interpret their data.

Some authors have sought to provide a physical interpretation for the VFT equation. Angell and Moynihan [16] gave a particularly clear exposition of the idea that T_o is the thermodynamic equivalent of the kinetically determined glass transition temperature. In the highly structured melts associated with glass formation, transport processes involve collaborative movement of quite large molecular groupings (which contrasts sharply with the much simpler translations of thermally activated molecules envisaged in an Arrhenius process). As temperature falls, the number of alternative molecular structures available in a given region of melt diminishes, until finally a temperature is reached at which only one structure is possible. Change of configuration by collaborative molecular relaxation is now no longer achievable, so the melt becomes, to all intents and purposes, solid and will have become a glass. In principle, this cooling process could proceed infinitely slowly, so here is an equilibrium glass transition that is independent of kinetics. Arguments based on the loss of entropy of fusion suggest that this transition temperature would be considerably above absolute zero, while data from molten salt systems would place it not far below the glass transition temperature determined by ordinary means.

T_o in the viscosity–temperature equation is identified as the configurational zero point for the kinds of cooperative molecular change involved in momentum transport. As temperatures rise higher than T_o the number of possible configurational states would increase exponentially, therefore so would the fluidity of the melt. T_o is to configurational processes what absolute zero is to vibrational and simple translational processes. By this argument, there is a strong correspondence between the Arrhenius

equation for gaslike transport processes at high fluidity and the VFT equation for molten glasses immediately above their glass transitions.

Angell and Moynihan identify a region between T_o and $2T_o$ (expressed in kelvins) where the VFT equation would be expected to hold. At higher temperatures than this, molecular structures in the melt would be expected to break down, transport processes would become more gas-like and there would be a transition to the Arrhenius type of temperature dependence. In the light of this fundamental complexity of behavior it is unlikely that a simple three-parameter equation would be capable of describing effectively the variation of viscosity with temperature over the full range accessible to measurement. The VFT form, however, does remarkably well for many glass melts of commercial interest. For a typical window glass composition, for example, the glass transition temperature is in the region of 550°C, so T_o might be around 700 K; the VFT equation would then be expected to hold usefully well up to 1400 K or 1125°C. In practice, the equation is commonly used to smooth data up to 1500°C without generating residuals larger than might be expected from experimental errors, though it must be said that there is a discernible tendency for the residuals to be systematically rather than randomly distributed and for the T_o values to be in the range 240°C to 280°C. For other compositions, for example, commercial glasses with significant amounts of boron present, the best fit to the data yields significant residuals that clearly are arranged systematically. Nevertheless, if a single simple equation is to be used for summarizing viscosity and temperature information for glass-forming melts, then the VFT equation is probably the most useful.

5.1.6 Fitting the VFT Equation to Experimental Data

Fulcher [11] used a graphical technique to explore goodness of fit of his equation to viscosity data on soda-silica melts obtained by English [17] and by Washburn and co-workers [18]. Having obtained an estimate of T_o algebraically from three representative points he plotted $\{\log \eta\}$ against $\{1/(T - T_o)\}$ and fitted a straight line to the data. His results for the six data sets available led him to conclude that the three constants A, B and T_o vary smoothly with composition in the soda-silica system, a finding that he clearly exploited in his exploration of the changes in viscosity brought about by adding lime, magnesia, alumina and boric oxide to the composition. These findings paved the way for the careful and systematic compositional studies of Lakatos and his colleagues during the 1970s [19].

In the early 50s, R.W. Douglas suggested an alternative curve-fitting approach in which the VFT equation is rearranged thus:

$$T\log \eta = T_o \log \eta + AT + (B - AT_o)$$

Application of the standard multiple linear regression procedure to this equation allowed estimates of A, B and T_o to be obtained [20]. This method was convenient for hand calculation, but because of coupling between the regression variables it did not give the best possible parameter estimates — the method used by Fulcher is sounder. Lakatos and colleagues [19] encountered this problem during their work

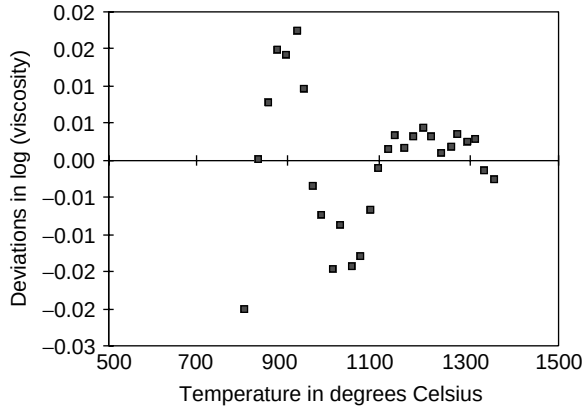

FIGURE 5.1 Data on a soda-lime-silica composition [15], showing deviations from the fitted VFT equation as log η residuals.

on the compositional sensitivity of viscosity in commercially important glass compositions, and they elected to follow Fulcher's calculation scheme.

The advent of affordable computing equipment transformed the practice of curve-fitting, allowing Fulcher's method to be applied with greater precision and objectivity. Now a good spreadsheet program running on a PC allows easy and rapid exploration of the data, encouraging the use of graphical techniques as well as numerical indices in the assessment of "goodness of fit."

Given the levels of precision achievable with ordinary experimental care, very little can usually be gleaned from a temperature-based plot of observed viscosities and those calculated from a fitted curve. The graph of deviations from the calculated curve can, however, be very revealing. Figure 5.1 is one such plot for data measured by Fontana and Plummer [15] on a soda-lime-silica melt, showing deviations in log η from a VFT curve fitted to the data on a least-squares basis. It is apparent that the deviations are not randomly distributed but lie on a sinuous curve about the temperature axis, indicating that the viscosity varies with temperature in a more complex fashion than is implied by the simple equation. Also, it is apparent that the values of the deviations are greater at the lower temperatures (higher viscosities) than at the opposite end of the data range.

In practical use, glass viscosity information is often employed to provide temperature settings for glassmaking operations; it is natural therefore to think of errors in terms of the change in temperature that is implied by any deviation. Figure 5.2 presents the same information as Figure 5.1, but plotted in terms of the deviation of observed temperature from that calculated using the fitted equation.

Using temperature residuals in this way presents the practical glassmaker with a less biased picture of the adequacy of the VFT equation as a means of summarizing the data. In the tables at the end of this chapter, the standard deviation of temperature residuals is given as an indicator of the adequacy of the fitted curve. It should be borne in mind, however, that the residuals in almost all cases were systematically

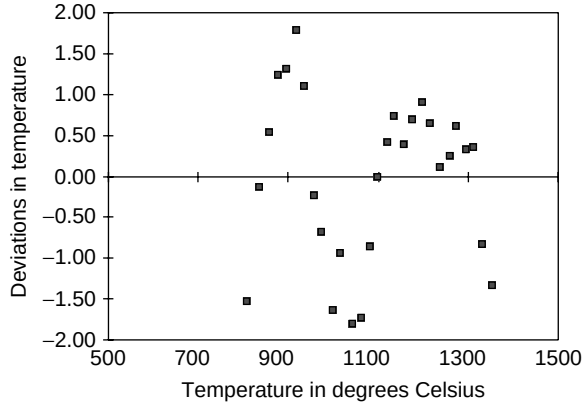

FIGURE 5.2 Data on a soda-lime-silica composition, showing deviations from the fitted VFT equation as temperature residuals. (Data from E.H. Fontana, W.A. Plummer, *J. Amer. Ceram. Soc.*, (1979) 62.)

distributed so Figure 5.2 should not be interpreted as an assessment of the experimental errors involved in the original measurements.

5.1.7 Non-Newtonian Behavior

At the upper limit of the measurable viscosity range it has long been recognized that flow behavior can become non-Newtonian. When the viscosity of a typical soda-lime-silica melt is around 10^{13} poise, imposed stresses take several minutes to dissipate; it is therefore experimentally easy to observe such melts behaving like a brittle solid by employing high deformation rates. If very slow deformation rates are used (as for example in the fiber-elongation methods for viscosity measurement), then Newtonian flow may be observed. Between the two extremes, both viscous and elastic responses are seen, giving an apparent viscosity that varies in response to the rate of shear involved.

Non-Newtonian behavior is discussed in a recent paper by Brückner and Yue [21] in which they also demonstrate the possibility of shear-thinning behavior in some glasses due to the alignment of molecular flow units under the influence of applied stresses. Reference to visco-elastic behavior of some silicate glasses will also be found in the excellent reference work by Mazurin and his colleagues [22]. This chapter concerns itself with the equilibrium viscosity of molten glasses, so non-Newtonian behavior has not been included in the data compiled here.

5.1.8 Estimation of Viscosity Characteristics from Composition

It would be very convenient to be able to calculate viscosity and its variation with temperature from the composition of a glass melt. Such a capability would speed up the process of developing a new complex glass composition that has a desired viscosity characteristic. As early as 1925, English [23] was engaged in studies of

four component glasses of the soda-lime-silica family to establish the sensitivity of viscosity to compositional changes. Lakatos and his colleagues more recently published the results of an extensive and systematic study that covered borosilicate [108] and lead crystal systems [109–111] as well as soda-lime-silica glasses. A number of workers have been active in this area and a very good overview was given in 1977 by Scholze [24]. Continuing relevance is demonstrated by the recently published extension of the work on soda-lime-silica-type glasses by Öksoy et al. using current statistical and computational techniques [25]. Disposal of radioactive waste is an emotive issue and the quest for a stable, highly durable glass to act as a retaining matrix for active materials is provoking work over an ever-widening compositional field; viscosity estimation forms a part of such work [26].

The way in which log (viscosity) varies with composition must in general be curved, and possibly exhibits discontinuities in the first or second derivatives. For wide ranges of composition, attempts have been made to take account of the molecular structures of the melts, using thermodynamic data and structural arguments to express the shape of the viscosity hypersurface and deriving only a few curve-fitting parameters from the viscosity database [26]. Purely empirical derivations of composition–viscosity relationships are simple enough to be useful only if the compositional range is rather restricted. If experimental studies are well designed and the range is small enough, linear dependence of log (viscosity) on oxide concentration is a viable approximation. Most studies have selected a basic composition of interest and made small range excursions from it, but Babcock (see [9] pages 228–229) chose to divide the soda-lime-alumina-silica compositional field on the basis of the primary devitrification phase as a means of accounting for molecular structures in the melt. However the correlation study has been constructed, it is important for the user of the coefficients to be aware of the compositional range covered by the original measurements, since extrapolation beyond that range can give misleading results.

English [23] chose to calculate viscosity values at selected fixed temperatures but Lakatos and colleagues [19] adopted the rather more useful method of calculating the temperatures corresponding to selected fixed viscosity points. This empirical approach made no assumptions about the form of the viscosity–temperature relationship — an advantage for some practically important glass systems where rather large systematic deviations from the VFT equation are observed. For the soda-lime-silica glass family however, they found it possible to derive the VFT coefficients directly from composition with useful precision. Their careful viscosity measurements were made on arrays of glass compositions selected according to sound statistical experimental designs (as far as practicable). This was cited as a major factor in avoiding the complex compositional terms found necessary by some other workers (see, for example, [27]).

Composition can be expressed in a number of ways and errors may obviously arise if coefficients are used with a nonconsistent set of composition data. Mole fractions or moles percent may seem a natural choice, but as Lyon [27] points out, such measures are based on neither weight nor volume, and are therefore less suitable for this purpose than the commonly used weight percent. Lakatos and colleagues had used moles percent in an early paper [19], but returned to some form of weight-based expression in later publications. In the silicate glass systems it proved conve-

nient to ratio the concentration of each component to that of silica, which neatly dealt with the problem of nontotaling analyses. Even then, differences in expression occur; percent of component per percent of silica has been used [28], parts by weight per ten parts by weight of silica [27] and parts by weight per 100 parts of silica [29].

Some compositional correlations are summarized in section 5.3.5. below. The calculation has the general form:

$$\{\text{parameter}\} = \Sigma\ \{\text{coefficient}\} \times \{\text{concentration}\}$$

where the {parameter} may be one of the VFT coefficients or else the temperature at which log(viscosity) has a particular value and the summation is usually over all the components in the melt, in some cases with an additional constant term. In each case the method of expressing concentration is specified in the introduction to the table.

5.2 METHODS OF MEASUREMENT

5.2.1 Introduction

Poiseuille's work on the flow of blood paved the way for a class of viscometers based on measuring flow within a capillary tube and the pressure difference that drives that flow. Low flow rates are employed and experimentally it is found that the major resistance to flow stems from viscous forces and only a minor correction is needed to account for the kinetic energy effects at the inlet to and outlet from the capillary tube. These instruments are commonly used at room temperature, but there are difficulties in applying them to molten glasses (see [30], page 219) — not the least the problems of fabricating capillary tubes for use at high temperatures, which are capable of maintaining precise dimensions in the face of repeated heating and cooling cycles. This is particularly important because the tube radius appears in the flow equations raised to the fourth power. Corrosion of the inside surface of the capillary by a glass melt is not easy to avoid and would also seriously affect the accuracy of the measurement. Vitreous silica tubes have, however, been successfully used in measuring the viscosity of low melting molten metals by this method [31].

Falling sphere viscometry is convenient for moderately viscous fluids (such as lubricating oils) at room temperature, where the time of descent at terminal velocity can be sufficiently accurately determined by observation through the transparent walls of glass apparatus. Ryan and Blevins [32] give a thorough account of how this technique may be applied at high temperature by using radiographic techniques or inductive sensing to locate the ball in a crucible of molten material. The need to maintain good temperature uniformity over the measurement volume favors the use of a relatively narrow cylindrical crucible, which means that the proximity of the container wall must be taken into account. Shartsis and his colleagues [33] measured viscosities of a range of optical glasses using a variation of this method in which the sphere was suspended by a fine wire from the beam of a chemical balance. This suited their purpose because the same apparatus could be used to obtain melt densities. They established the superiority of the Faxen scheme of allowing for the

confined nature of the experiment and demonstrated good agreement with rotating cylinder measurements on some of their glasses. Good experimental details can be found in their paper, but in spite of the elegance of their work, the restrained sphere method has not become popular with other workers.

Details of the methods most commonly found effective in measuring the viscosity of molten glasses are set out in the International Standard specification ISO 7884 [34]. They include rotational methods covering the viscosity range from 10 to 10^8 poise, fiber elongation methods covering the range from 10^8 to 10^{13} poise, and beam bending methods covering the range from 10^9 to 10^{15} poise. Parallel documents have been issued by the various national standards organizations to provide similar guidance.

5.2.2 Experimental Issues

Whatever method is used, there are some experimental issues that require attention just because the measurement is made at elevated temperatures. Clearly, the materials used in the construction of the apparatus must be capable of withstanding the required temperatures without undue deformation under the mechanical or thermal stresses involved, and without being corroded significantly by the atmosphere or by the melt. Often in work on molten glasses this implies extensive use of refractory metal alloys such as platinum-rhodium alloys, or else pure ceramics such as recrystallized alumina.

Because the viscosity of most glass melts is highly sensitive to temperature, it is essential to provide a furnace chamber with the minimum possible temperature variation throughout the volume occupied by the sample. Constancy to within 1°C should be the aim. Equally clearly, the measurement of temperature should be carefully done, with thermocouples so placed as to give the best estimate of the sample's average temperature. Thermocouple wires should enter the furnace cavity along a route designed to minimize differential thermal gradients and electrical noise pickup, and the wires should be sufficiently long to allow proper connection to the measuring device. Since thermocouples suffer aging in service to some extent, it is necessary to calibrate them at intervals against a subsidiary standard thermocouple reserved for that purpose.

Sample preparation and handling also needs care. Selection to avoid clearly visible inhomogeneities or contamination is an obvious precaution, as is the avoidance of conditions likely to cause crystal formation. Excessive heating can cause change of composition due to volatilization or reaction with the surrounding atmosphere; if possible, the viscosity measurement temperature should be regarded as the maximum to be used in sample preparation. Grinding a sample to powder while exposed to the usual laboratory atmosphere could encourage water absorption with consequent composition change, and is best avoided.

5.2.3 Rotational Viscometers

Rotational viscometers are used to measure viscosities in the range 10 to 10^8 poise. They typically comprise a crucible to contain the molten glass and an immersed

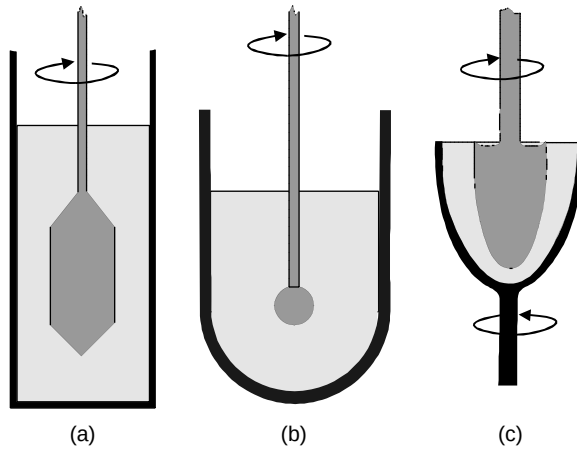

FIGURE 5.3 Typical designs for rotational viscometer crucibles.

coaxial plunger, both of which have rotational symmetry about their common vertical axis (see [34] part 2). In use, either the crucible or the plunger is rotated and the relationship between the measured torque and the rotational speed gives a measure of the viscous drag exerted by the liquid. Some typical geometries are illustrated in Figure 5.3.

The assembly of crucible and plunger is mounted in a furnace designed to provide a working volume throughout which the temperature is constant to better than, say, ±1°C and controllable over the desired working range. In some cases, the crucible is in the form of a directly heated platinum alloy bushing, which achieves good spatial temperature distribution by exploiting external fins to modify the distribution of dissipated electrical power. Such units require the plunger to be the driven element and usually the apparatus incorporates a constant speed drive coupled via some form of torsion-measuring device. If the crucible is independent of the furnace heating system, the possibility exists of holding the plunger stationary while the crucible is rotated. Continuous monitoring of torque is rather easier for this arrangement, which was an option favored in early work with glasses. Whichever drive option is selected, it is important to design the apparatus so that torque attributable to sources other than the viscosity of the glass melt does not constitute a significant error.

Since this geometry is intended for use at the lower end of the viscosity scale (10 to 10^8 poise) corrosion of the equipment with consequent contamination of the glass sample is a real possibiliy that must be considered when determining the material from which crucible and plunger are fabricated. In the inter-laboratory study carried out by the Physical Properties Committee of the Society of Glass Technology under the chairmanship of H. Cole [35], clear evidence emerged that the use of apparatus made from ceramic refractories gave consistently higher viscosity values. Platinum-rhodium alloys are commonly used for silicate glasses, but may not be suitable for other compositions.

The temperature of the melt can be sensed by an immersed thermocouple in the vicinity of the plunger, but the advantage of continuous measurement may be outweighed by the disturbance created in the flow field. Often, it is possible to insert a thermocouple down the axis of the plunger to obtain an improved measure of the temperature within the adjacent melt; however, connections to the temperature-measuring device would introduce error into the torque measurement, so simultaneous measurement of torque and temperature are not feasible.

The basic equation linking viscosity and the measured torque and rotational speed is

$$\eta = k\ (T/n)$$

where η is the viscosity, T is the measured torque (corrected for any extraneous frictional errors), n is the rotational speed, and k is a coefficient dependent on the instrument.

The coefficient in this equation is determined by the geometric shape of the instrument flow field and may be determined analytically in some special cases — for example, when crucible and plunger form two confocal surfaces of revolution (Figure 5.3(c)). More generally, it is necessary to calibrate the equipment using a liquid of known viscosity, preferably a standardized glass so that the working temperature range can be covered. Factors affecting the geometry of the flow field will alter the value of the coefficient k, so precise control is necessary to avoid errors. These factors include the depth of liquid in the crucible, the immersion depth of the plunger and its positioning on the axis, and the avoidance of any adhering bubbles on the surfaces in contact with the melt.

5.2.4 Fiber Elongation Viscometers

These methods are applicable in the viscosity range 10^8 to 10^{13} poise and are based on measuring the rate of extension of a glass fiber suspended vertically in a suitable furnace, as, for example, that shown in Figure 5.4 and described in [34] part 3.

Fibers are drawn with diameters between 0.6 and 0.8mm to yield test samples between 50 and 100mm in length. Each end of the sample is fused to a bead about 2mm in diameter to allow the sample to be suspended in the furnace and coupled to a loading device. Any surface layer resulting from the drawing process is removed by etching, and samples with visible imperfections (scratches, inclusions, obviously non-constant diameter, et cetera) are discarded. The sample is mounted as indicated in Figure 5.4 linked by a wire or ceramic coupling to a thin vitreous silica rod which extends outside the furnace to accept the weights used for loading. Some means of measuring precisely the extension of the sample is required – this may take the form of a cathetometer focused on an index mark on the silica rod.

Fiber extension determines the dynamic viscosity of the glass by measuring the elongation of the sample under uniaxial stress, implicitly assuming that the flow behavior is Newtonian. The method is absolute in that the viscosity is calculated directly from knowledge of the sample geometry, the loading and the measured extension rate. Provided that the dead weight of the fiber and the effects of surface

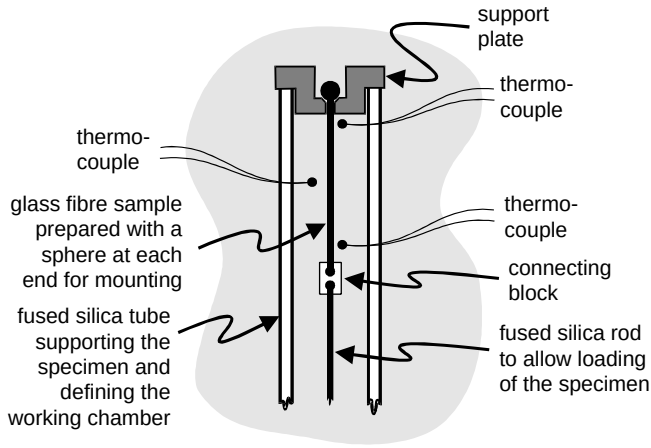

FIGURE 5.4 Typical arrangement for a fiber elongation viscometer.

tension of the glass may be neglected, the rate of extension of the loaded fiber is given by

$$\frac{dl}{dt} = \frac{mgl^2}{3\eta V}$$

which leads to an expression for viscosity

$$\eta = \frac{mg\Delta t}{3V} \frac{l_2 l}{(l_2 - l_1)}$$

where η is the dynamic viscosity, m is the mass of the system that loads the fiber, g is the acceleration due to gravity, l_1 is the length of the fiber at the start of a measurement, l_2 is the length of the fiber at the end of the measurement, Δt is the time interval over which the measurement is taken, and V is the volume of the fiber specimen (excluding the balls at the ends).

Before making a measurement, the fiber volume must be determined, usually by measuring the length (excluding the balls at each end used for suspension) and then by averaging diameter measurements made at several places along the length. Fiber temperature is monitored by several thermocouples distributed along the length of that portion of the furnace chamber occupied by the sample.

Measurements may be made with the furnace temperature rising steadily (although this invites a difference between the sample temperature and that measured) or at constant temperature. The extension rate required for calculating viscosity is that obtained when the fiber has come to equilibrium with the furnace, the load being adjusted to produce an acceptable rate at the temperature involved. When the viscosity of the sample is greater than 10^{11} poise it is necessary for sufficient

time to be allowed after load application so that delayed elasticity in the glass does not introduce errors. To limit the danger of the fiber's necking and producing anomalous results, the total extension of one particular sample should not exceed 10% over the series of readings. Each viscosity determination should be based on a measured extension large enough not to be prejudiced by errors in the length measurement, but should not exceed 2% of the fiber length. At higher temperatures, the required loading may be quite low, in which case, account must be taken of the load imposed by the dead weight of the fiber itself and of the restraining influence of glass surface tension.

Mention should be made of the Littleton softening point, which is a variation on the fiber extension method. Here, a glass fiber of specified dimensions is subjected to a defined constantly rising temperature environment and allowed to extend under its own weight. The measurement depends on establishing the temperature at which the fiber tip moves downward at a rate of 1mm/minute. Originally intended as a quality-control method to check the compositional consistency of commercial glasses, this method provides a simple, rapid and robust way of detecting changes of melt composition with time [36]. Since then, however, the correspondence between the measured softening point and a particular viscosity value has been the subject of some debate. Glass density and surface tension affect the measurement and may be allowed for (see, for example, [34] page 1), but experience shows that the resulting data can deviate markedly from the viscosity curve derived from the other methods. It is best therefore to avoid using Littleton softening point data as viscosity estimates.

5.2.5 Bending Beam Viscometers

This measurement technique is suitable for viscosities in the range 10^9 to 10^{15} poise and uses a specimen in the shape of a rod or beam supported near its ends and loaded midway between the supports. The arrangement is shown schematically in Figure 5.5; at the top is the initial (no-load) condition with the horizontal sample supported on knife edges, below which is the situation after considerable viscous deflection under load has occurred.

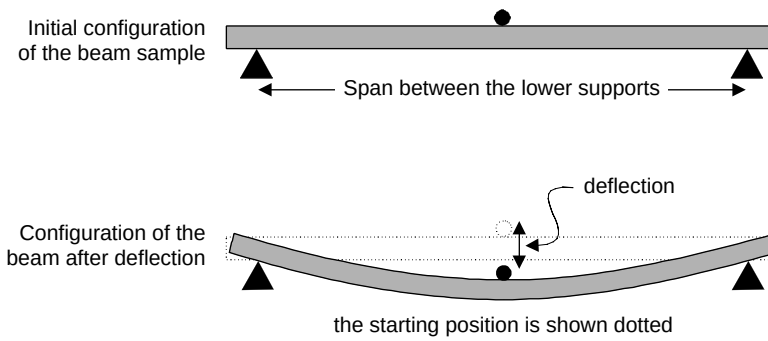

FIGURE 5.5 Schematic showing the arrangement used for beam-bending viscometry.

When a load is applied the initial response of the sample is a rapid elastic deflection, followed by a slower deflection as flow occurs. Provided the sample is behaving in a Newtonian fashion and the sag is sufficiently small, the midpoint deflection rate is described by

$$\frac{df}{dt} = \frac{F l^3}{144 \eta I_c}$$

where F is the downward force exerted on the beam, l is the length of sample between the lower supports, η is the dynamic viscosity of the glass, and I_c is the cross-sectional moment of inertia of the beam.

For beams having a rectangular cross section the cross sectional moment of inertia is given by

$$I_c = h^3 b/12$$

where h is the height of the cross section and b is the breadth of the cross section.

When the cross section is circular, the expression becomes

$$I_c = \pi d^4/64$$

where d is the diameter of the cross section.

During a determination of viscosity, the knife edge that applies the loading to the beam descends a measured distance Δf in a measured time interval Δt, and the viscosity can be calculated using the simplified equation

$$\eta = 681 \frac{l^3 \Delta t m}{I_c \Delta f}$$

where m is the mass of the load, including that of the glass sample itself (in grams); l is the length of sample (in mm) between the lower supports; η is the dynamic viscosity of the glass (in poise); I_c is the beam's cross-sectional moment of inertia (in mm^4); Δf is the sag of the beam (in mm); and Δt is the time (in seconds) over which sag is measured.

Typically for measurements in the middle of the viscosity range covered by this technique, the beams are about 3mm in diameter and the distance between the supports is about 40mm. The dead weight of the sample should be taken into account, since it will contribute around 1g to a loading in the range 10 to 100g.

This equation is appropriate when the diameter of the beam is not less than about 10% of the span between the lower supports and when the total mid-point deflection has not exceeded about 5% of that span. It is desirable to design the equipment so that the measurement time is typically in the range 200 to 2000 seconds, which involves some adaptation of the sample geometry to suit the intended viscosity range. To measure the lower viscosities (10^9 to 10^{11} poise) accessible with

this method it is usual to use samples with high cross-sectional moments of inertia, small external loading and a relatively small value of the ratio (known as the *support ratio*) between the inter-support span and the height of the beam cross section. Clearly, the dead weight of the sample is particularly important at this end of the range. For the higher viscosities, it is usual to design the measurement to exploit relatively large loadings, higher values of support ratio and small cross-sectional moments of inertia. In these cases, the dead weight of the specimen can usually be neglected, but the high loadings and thin samples involved demand careful experimental technique.

The simplified equations hold only for very thin beams and very small deflections. If the experimental conditions do not comply strictly with these requirements, it may be desirable to calibrate the specific geometrical arrangement by making measurements on standardized samples of known viscosity and using the results to derive a suitable correction factor.

5.3 TABLES OF VISCOSITY DATA

5.3.1 Single-Component Systems

TABLE 5.3.1.1A
VFT Parameters for B_2O_3 Melts

	Material Source and Preparation	A	B	T_o	$\sigma(\Delta T)$	n	T_{min}	T_{max}
(39)		–0.9623	2826.5	–41.0	30.19	12	452	1201
(40)	carefully dried	0.1280	1503.8	171.0	11.77	60	318	1404
(41)	carefully dried	0.1374	1505.1	163.0	10.88	26	373	1279
(42)		–0.8686	3543.8	–273.0	0.00	9	800	1200

Note: $\sigma(\Delta T)$ is the standard deviation of temperature residuals, n is the number of data points used in fitting the VFT equation, T_{min} and T_{max} show the range of temperature in °C covered by the data.

TABLE 5.3.1.1B
Temperatures at Specified Viscosity Values (Poise) for B_2O_3 Melts

		Temperature (°C) at Which Log(Viscosity) is								
	Material Source and Preparation	1.5	2.0	3.0	4.0	5.0	6.0	7.0	8.0	10.0
[39]		1107	913	672	529					
[40]	carefully dried	1267	974	695	559	480	427	390	362	323
[41]	carefully dried	1268	971	689	553	473	420	382		
[42]		1223	962							

Note: calculated using the VFT equation with the parameters given in the previous table.

TABLE 5.3.1.2A
VFT Parameters for GeO_2 Melts

	Material Source and Preparation	A	B	T_o	σ(ΔT)	n	T_{min}	T_{max}
[43]	graphically smoothed	2.6962	367.2	1150.0	5.73	6	1300	1550
[44]	low temperature values	–5.1841	15263.8	–273.0		3	550	1000
[44]	high temp values only	–5.7232	15971.8	–273.0	4.79	11	1000	1500
[44]	carefully dried	–5.3867	15457.6	–273.0	7.75	13	550	1500

Note: σ(ΔT) is the standard deviation of temperature residuals, n is the number of data points used in fitting the VFT equation, T_{min} and T_{max} show the range of temperature in °C covered by the data.

TABLE 5.3.1.2B
Temperatures at Specified Viscosity Values (Poise) for GeO_2 Melts

	Material Source and Preparation	Temperature (°C) at Which Log(Viscosity) is								
		3.5	4.0	5.0	6.0	7.6	10.0	11.0	12.0	13.0
[43]	graphically smoothed		1432	1309						
[44]	low temperature values					921	732	670	615	566
[44]	high temp values only	1459	1370	1216	1089					
[44]	carefully dried	1466	1374	1215	1085	917	732	670	616	568

Note: Calculated using the VFT equation with the parameters given in the previous table.

TABLE 5.3.1.3A
VFT Parameters for SiO_2 Melts

	Material Source and Preparation	A	B	T_o	σ(ΔT)	n	T_{min}	T_{max}
[45]	melted in gas fired furnace	–5.6688	25172.2	–273.0	5.69	10	1100	2000
[45]	from SiCl4 — vapor phase	–7.9445	30669.1	–273.0	10.79	10	1100	2000
[45]	from rock crystals in hydrogen atm.	–9.4388	33579.5	–273.0	10.87	8	1300	2000
[46]	from SiCl4 — vapor phase	–4.7036	23295.8	–239.0	3.09	10	1100	2000
[46]	Synthetic silica (gas fired furnace)	–6.9580	28816.8	–273.0	4.83	10	1100	2000
[46]	Gangue granular quartz (N2 plasma)	–7.5589	30151.0	–273.0	3.92	10	1100	2000
[46]	Synthetic silica (N2 plasma)	–8.3336	30976.8	–273.0	2.98	10	1100	2000
[46]	Gangue granular quartz (rod furnace)	–5.0005	23863.9	–273.0	21.42	10	1100	2000
[46]	Gangue milk-white quartz	–6.2412	27398.9	–254.0	2.95	10	1100	2000

TABLE 5.3.1.3A (Continued)
VFT Parameters for SiO_2 Melts

	Material Source and Preparation	A	B	T_o	σ(ΔT)	n	T_{min}	T_{max}
[46]	Synthetic silica (cristobalite)	–7.7000	30064.1	–273.0	5.52	10	1100	2000
[46]	Artificial rock crystals	–6.8088	28445.0	–273.0	2.49	10	1100	2000
[46]	Brazilian rock crystals	–7.2567	29294.2	–273.0	4.42	10	1100	2000
[47]	Amersil silica glass	–6.1722	27567.0	–273.0	2.40	20	1236	1335
[48]	Homosil and Osram silica glasses	0.3792	7208.2	739.0	5.96	42	1686	2006
[49], [50]	Amersil silica — measured in argon	2.2888	2316.3	1289.0	46.39	12	1935	2322

Note: σ(ΔT) is the standard deviation of temperature residuals, n is the number of data points used in fitting the VFT equation, T_{min} and T_{max} show the range of temperature in °C covered by the data.

TABLE 5.3.1.3B
Temperatures at Specified Viscosity Values (Poise) for SiO_2 Melts

	Material Source and Preparation	Temperature (°C) at Which Log(Viscosity) is								
		5.0	5.5	6.0	7.0	7.6	10.0	12.0	13.0	14.0
[45]	melted in gas fired furnace		1981	1884	1714	1624	1334	1152		
[45]	from SiCl4 – vapor phase			1926	1779	1700	1436	1265	1191	1125
[45]	from rock crystals in hydrogen atm.		1975	1902	1770	1698	1454			
[46]	from SiCl4 – vapor phase			1937	1751	1654	1345	1156		
[46]	Synthetic silica (gas fired furnace)			1951	1792	1706	1426	1247	1171	1102
[46]	Gangue granular quartz (N2 plasma)			1951	1798	1716	1444	1269	1194	1126
[46]	Synthetic silica (N2 plasma)		1966	1888	1747	1671	1417	1250	1179	1114
[46]	Gangue granular quartz (rod furnace)		2000	1896	1716	1621	1318	1131		
[46]	Gangue milk-white quartz			1984	1815	1726	1433	1248	1170	
[46]	Synthetic silica (cristobalite)			1921	1772	1692	1426	1253	1179	1112
[46]	Artificial rock crystals			1948	1787	1701	1419	1239	1163	
[46]	Brazilian rock crystals			1937	1782	1699	1425	1248	1173	1105
[47]	Amersil silica glass							1244		
[48]	Homosil and Osram silica glasses			2021	1828	1737				
[49], [50]	Amersil silica – measured in argon	2143	2010							

Note: calculated using the VFT equation with the parameters given in the previous table.

5.3.2 Two-Component Melts

TABLE 5.3.2.1A
VFT Parameters for Al_2O_3:SiO_2 Melts

	Al_2O_3	SiO_2	A	B	To	σ(ΔT)	n	T_{min}	T_{max}
[51]	6.2	93.8	–7.5091	23909.3	–273.0	0.90	8	1653	2003
[51]	20.2	79.8	–5.1755	14188.3	–145.0	0.54	8	1653	2003
[52]	37.1	62.9	–0.2436	272.4	1580.0	4.26	6	1850	2100
[52]	46.9	53.1	–0.2791	158.9	1653.0	6.05	6	1850	2100
[51]	50.0	50.0	–4.3703	10469.6	–273.0	0.93	8	1853	2050
[51]	70.0	30.0	–3.3806	7004.1	–112.0	1.43	8	1853	2204
[52]	70.2	29.8	–2.8191	6176.3	–273.0	8.99	4	1950	2100

Note: Melt compositions are given in moles percent, σ(ΔT) is the standard deviation of temperature residuals, n is the number of data points used in fitting the VFT equation, T_{min} and T_{max} show the range of temperature in °C covered by the data.

TABLE 5.3.2.1B
Temperatures at Specified Viscosity Values (Poise) for Al_2O_3:SiO_2 Melts

			Temperature (°C) at Which Log (Viscosity) is:								
	Al_2O_3	SiO_2	–0.20	0.0	0.2	0.4	0.6	1.5	2.5	3.0	4.5
[51]	6.2	93.8								2002	1718
[51]	20.2	79.8						1980	1704		
[52]	37.1	62.9				2003	1903				
[52]	46.9	53.1			1985	1887					
[51]	50.0	50.0			2018	1922	1833				
[51]	70.0	30.0	2090	1960	1844						
[52]	70.2	29.8	2085	1918							

Note: Calculated using the VFT equation with the parameters given in the previous table, melt compositions are given in moles percent.

TABLE 5.3.2.2A
VFT Parameters for BaO:B_2O_3 Melts

	BaO	B_2O_3	A	B	To	σ(ΔT)	n	T_{min}	T_{max}
[53]	32.1	67.9	–2.5718	1635.3	523.0		3	846	947
[53]	27.3	72.7	–0.5703	633.8	643.0		3	846	949
[53]	23.8	76.2	–5.2236	5122.9	194.0	3.40	4	854	1004
[53]	20.2	79.8	–3.5734	3068.9	351.0	1.21	4	854	1007
[53]	17.8	82.2	–2.3019	1855.7	454.0	3.70	7	804	1007

TABLE 5.3.2.2A (Continued)
VFT Parameters for $BaO:B_2O_3$ Melts

	BaO	B_2O_3	A	B	To	σ(ΔT)	n	T_{min}	T_{max}
[54]	0.0	100.0	–0.9623	2826.5	–41.0	30.19	12	452	1201

Note: Melt compositions are given in moles percent, σ(ΔT) is the standard deviation of temperature residuals, n is the number of data points used in fitting the VFT equation, T_{min} and T_{max} show the range of temperature in °C covered by the data.

TABLE 5.3.2.2B
Temperatures at Specified Viscosity Values (Poise) for $BaO:B_2O_3$ Melts

			Temperature (°C) at Which Log(Viscosity) Is:								
	BaO	B_2O_3	1.25	1.50	1.75	2.00	2.25	2.50	2.75	3.00	3.25
[53]	32.1	67.9		925	901	881	862				
[53]	27.3	72.7			916	890	868	849			
[53]	23.8	76.2	985	956	929	903	879	857			
[53]	20.2	79.8	987	956	927	902	878	856			
[53]	17.8	82.2	976	942	912	885	862	840	821	804	
[54]	0.0	100.0		1107	1001	913	839	775	720	672	630

Note: Calculated using the VFT equation with the parameters given in the previous table, melt compositions are given in moles percent.

TABLE 5.3.2.3A
VFT Parameters for $BaO:SiO_2$ Melts

	BaO	SiO_2	A	B	T_o	σ(ΔT)	n	T_{min}	T_{max}
[51]	3.7	96.3	–3.2178	8481.9	75.0	2.41	8	1632	2082
[55]	15.4	84.6	0.4265	1014.7	1155.0	0.76	4	1650	1800
[56]	20.0	80.0	–3.9227	11158.4	–183.0		3	1600	2500
[55]	25.1	74.9	–0.8563	1793.2	881.0	1.36	7	1500	1800
[55]	30.7	69.3	–1.7816	3127.1	551.0	2.84	7	1500	1800
[55]	33.6	66.4	–1.6122	2701.3	609.0	2.63	7	1500	1800
[55]	40.2	59.8	–0.2142	552.8	1119.0	3.72	7	1500	1800
[55]	42.1	57.9	–1.1924	1408.9	876.0	1.20	6	1550	1800
[55]	49.8	50.2	–0.1303	129.7	1376.0	1.97	5	1600	1800
[51]	50.0	50.0	–3.8189	7734.1	–207.0	2.15	9	1602	2063
[56]	50.0	50.0	–3.6879	7233.2	–142.0		3	1600	2500

Note: Melt compositions are given in moles percent, σ(ΔT) is the standard deviation of temperature residuals, n is the number of data points used in fitting the VFT equation, T_{min} and T_{max} show the range of temperature in °C covered by the data.

TABLE 5.3.2.3B
Temperatures at Specified Viscosity Values (Poise) for $BaO:SiO_2$ Melts

			Temperature (°C) at which log(viscosity) is:								
	BaO	SiO_2	–0.80	–0.4	0	0.4	0.8	1.2	1.6	2.0	2.2
[51]	3.7	96.3						1995	1836	1701	1641
[55]	15.4	84.6								1800	1727
[56]	20.0	80.0				2398	2180	1995	1837	1701	1639
[55]	25.1	74.9						1753	1611	1509	
[55]	30.7	69.3					1762	1600			
[55]	33.6	66.4					1729	1570			
[55]	40.2	59.8					1664	1510			
[55]	42.1	57.9				1761	1583				
[55]	49.8	50.2				1621					
[51]	50.0	50.0		2055	1818	1626					
[56]	50.0	50.0	2363	2058	1819	1627					

Note: Calculated using the VFT equation with the parameters given in the previous table, melt compositions are given in moles percent.

TABLE 5.3.2.4A
VFT Parameters for $CaO:SiO_2$ Melts

	CaO	SiO_2	A	B	To	σ(ΔT)	n	T_{min}	T_{max}
[56]	30.0	70.0	–3.8634	9561.3	–170.0		3	1600	2500
[57]	30.5	69.5	0.3109	249.2	1397.0		3	1700	1800
[52]	31.5	68.5	0.1410	312.6	1371.0	1.17	5	1700	1900
[51]	32.0	68.0	–4.1223	10602.0	–273.0	2.13	6	1717	1972
[57]	34.5	65.5	–3.7577	9162.6	–273.0	7.29	4	1650	1800
[51]	37.6	62.4	–4.0150	9562.9	–273.0	2.14	8	1552	1903
[56]	37.6	62.4	–3.7471	8512.4	–159.0		3	1600	2500
[57]	38.8	61.2	–1.8015	2589.3	622.0	2.65	7	1450	1750
[57]	38.8	61.2	–1.9177	2808.1	583.0	3.64	8	1450	1800
[57]	38.8	61.2	–2.8028	4840.5	278.0	2.70	7	1450	1750
[57]	41.6	58.4	–1.4252	1677.5	800.0	2.12	7	1500	1800
[52]	41.7	58.3	–1.1952	1313.7	895.0	4.18	11	1500	2000
[57]	43.6	56.4	–1.9549	2583.4	591.0	5.82	7	1500	1800
[58]	46.0	54.0	–6.2109	5911.4	462.0	1.92	6	769	879
[57]	48.7	51.3	–2.2209	2965.3	462.0	1.55	7	1500	1800
[57]	49.7	50.3	–2.0970	2519.2	565.0	1.43	6	1550	1800
[51]	50.0	50.0	–3.3228	5913.4	–26.0	6.36	10	1585	2096
[56]	50.0	50.0	–3.5066	6619.4	–132.0		3	1600	2500
[57]	50.7	49.3	–1.5942	1433.0	843.0	0.98	6	1550	1800
[52]	51.7	48.3	–1.0000	636.1	1091.0	5.98	6	1550	1800
[52]	51.7	48.3	–0.3544	120.3	1392.0	36.58	8	1550	2000
[57]	51.7	48.3	–1.6024	1437.4	827.0	0.56	6	1550	1800

TABLE 5.3.2.4A (Continued)
VFT Parameters for $CaO:SiO_2$ Melts

	CaO	SiO_2	A	B	To	σ(ΔT)	n	T_{min}	T_{max}
[57]	52.7	47.3	–1.3785	1085.6	918.0	3.80	7	1500	1800
[57]	53.7	46.3	–1.6142	1385.9	833.0	1.69	7	1500	1800
[57]	54.7	45.3	–1.0901	686.3	1043.0	2.99	6	1500	1800
[57]	56.2	43.8	–1.8380	1739.4	715.0	7.85	8	1450	1800
[57]	57.7	42.3	–1.1550	664.9	1050.0	1.58	5	1600	1800
[51]	60.0	40.0	–3.4833	6480.8	–273.0	11.22	9	1811	2120
[56]	60.0	40.0	–3.2828	5590.5	–111.0		3	1600	2500

Note: Melt compositions are given in moles percent, σ(ΔT) is the standard deviation of temperature residuals, n is the number of data points used in fitting the VFT equation, T_{min} and T_{max} show the range of temperature in °C covered by the data.

TABLE 5.3.2.4B
Temperatures at Specified Viscosity Values (Poise) for $CaO:SiO_2$ Melts

			Temperature (°C) at which log(viscosity) is:								
	CaO	SiO2	–1.00	–0.5	0	0.5	1.0	8.0	10.0	12.0	13.0
[56]	30.0	70.0			2305	2021	1796				
[57]	30.5	69.5					1759				
[52]	31.5	68.5					1735				
[51]	32.0	68.0					1797				
[57]	34.5	65.5					1653				
[51]	37.6	62.4				1845	1634				
[56]	37.6	62.4		2463	2113	1845	1634				
[57]	38.8	61.2				1747	1546				
[57]	38.8	61.2				1744	1545				
[57]	38.8	61.2				1744	1551				
[57]	41.6	58.4				1671	1492				
[52]	41.7	58.3			1994	1670	1493				
[57]	43.6	56.4				1643					
[58]	46.0	54.0						878	827	787	770
[57]	48.7	51.3			1797	1552					
[57]	49.7	50.3			1766	1535					
[51]	50.0	50.0		2069	1754						
[56]	50.0	50.0	2509	2070	1756						
[57]	50.7	49.3			1742	1527					
[52]	51.7	48.3			1727						
[52]	51.7	48.3			1732	1533					
[57]	51.7	48.3			1724						
[57]	52.7	47.3			1705	1496					
[57]	53.7	46.3			1692	1489					
[57]	54.7	45.3			1673	1475					

TABLE 5.3.2.4B (Continued)
Temperatures at Specified Viscosity Values (Poise) for $CaO:SiO_2$ Melts

			Temperature (°C) at which log(viscosity) is:								
	CaO	SiO2	–1.00	–0.5	0	0.5	1.0	8.0	10.0	12.0	13.0
[57]	56.2	43.8			1661	1459					
[57]	57.7	42.3			1626						
[51]	60.0	40.0		1899							
[56]	60.0	40.0	2338	1898	1592						

Note: Calculated using the VFT equation with the parameters given in the previous table, melt compositions are given in moles percent.

TABLE 5.3.2.5A
VFT Parameters for $FeO:SiO_2$ Melts

	FeO	SiO_2	A	B	To	σ(ΔT)	n	T_{min}	T_{max}
[59]	55.5	44.5	–0.0848	51.2	1138.0	23.42	6	1200	1450
[59]	56.9	43.1	–12.7684	19795.8	–273.0	28.79	4	1200	1350
[51]	60.0	40.0	–2.6428	4054.3	–273.0	2.06	10	1350	1440
[59]	60.8	39.2	0.0481	17.0	1176.0	17.06	4	1200	1350
[59]	61.0	39.0	–0.9141	1518.5	–273.0	33.45	5	1250	1450
[59]	62.0	38.0	–1.7115	2787.3	–273.0	10.66	6	1200	1450
[59]	63.0	37.0	–1.9910	2802.1	–273.0	32.74	6	1200	1450
[51]	65.0	35.0	–0.1571	302.9	823.0	2.64	8	1170	1430
[59]	65.5	34.5	–1.7397	2495.2	–273.0	21.85	6	1200	1450
[51]	66.7	33.3	–1.6321	1577.2	221.0	3.31	15	1166	1412
[59]	66.8	33.2	0.1142	26.8	1161.0	11.51	4	1200	1350
[59]	68.5	31.5	–1.1586	1715.4	–273.0	37.98	5	1250	1450
[51]	70.0	30.0	–1.9606	2148.3	–138.0	7.22	12	1205	1415
[59]	71.5	28.5	–3.3171	4864.2	–273.0	16.51	6	1200	1450
[59]	71.5	28.5	–4.2352	6372.7	–273.0	30.34	4	1200	1350
[59]	79.5	20.5	–3.4171	4784.1	–273.0	42.05	5	1250	1450
[59]	91.0	9.0	–1.8814	337.6	1076.0	41.60	6	1200	1450

Note: Melt compositions are given in moles percent, σ(ΔT) is the standard deviation of temperature residuals, n is the number of data points used in fitting the VFT equation, T_{min} and T_{max} show the range of temperature in °C covered by the data.

TABLE 5.3.2.5B
Temperatures at Specified Viscosity Values (Poise) for FeO:SiO_2 Melts*)*

			Temperature (°C) at which log(viscosity) is:								
	FeO	SiO2	–0.80	–0.6	–0.4	–0.2	0.0	0.2	0.4	0.6	0.8
[59]	55.5	44.5						1318	1244	1213	
[59]	56.9	43.1		1354	1328	1302	1277	1253	1230	1208	
[51]	60.0	40.0				1387					
[59]	60.8	39.2						1288	1224	1207	1199
[59]	61.0	39.0					1388				
[59]	62.0	38.0					1356	1185			
[59]	63.0	37.0			1488	1292					
[51]	65.0	35.0							1367	1223	
[59]	65.5	34.5				1348	1161				
[51]	66.7	33.3				1322	1187				
[59]	66.8	33.2							1255	1216	1200
[59]	68.5	31.5				1517	1208				
[51]	70.0	30.0		1441	1239						
[59]	71.5	28.5			1395	1288	1193				
[59]	71.5	28.5				1306	1232				
[59]	79.5	20.5		1425	1313						
[59]	91.0	9.0	1388	1339	1304	1277	1255	1238	1224	1212	1202

Note: Calculated using the VFT equation with the parameters given in the previous table, melt compositions are given in moles percent.

TABLE 5.3.2.6A
VFT Parameters for K_2O:B_2O_3 Melts

	K_2O	B_2O_3	A	B	To	σ(ΔT)	n	T_{min}	T_{max}
[54]	31.5	68.5	–3.2291	1997.7	317.0		3	600	802
[54]	27.9	72.1	–2.6021	1647.7	382.0		3	704	899
[54]	23.5	76.5	–2.9019	2392.2	283.0	1.94	4	597	899
[54]	11.6	88.4	–1.2723	1422.2	308.0		3	696	899
[54]	8.4	91.6	–2.0697	2241.7	179.0	10.63	7	473	996
[54]	3.9	96.1	–0.8837	1554.0	198.0	8.81	6	503	997
[54]	2.1	97.9	–0.2630	1264.6	212.0	3.91	6	495	997
[54]	1.1	98.9	–0.3065	1593.6	146.0	3.89	6	503	995
[54]	0.0	100.0	–0.9623	2826.5	–41.0	30.19	12	452	1201

Note: Melt compositions are given in moles percent, σ(ΔT) is the standard deviation of temperature residuals, n is the number of data points used in fitting the VFT equation, T_{min} and T_{max} show the range of temperature in °C covered by the data.

TABLE 5.3.2.6B
Temperatures (°C) at Specified Viscosity Values (Poise) for K_2O:B_2O_3 Melts

	K_2O	B_2O_3	0.75	1.0	1.5	2.0	2.5	3.0	3.5	4.0	5.0
[54]	31.5	68.5		789	739	699	666	638	614		
[54]	27.9	72.1	874	839	784	740	705				
[54]	23.5	76.5		896	826	771	726	688	657	630	
[54]	11.6	88.4			821	743					
[54]	8.4	91.6	974	909	807	730	670	621	581	548	496
[54]	3.9	96.1			850	737	657	598	552	516	
[54]	2.1	97.9			929	771	670	600	548	509	
[54]	1.1	98.9				837	714	628	565	516	
[54]	0.0	100.0			1107	913	775	672	592	529	

Note: Calculated using the VFT equation with the parameters given in the previous table; melt compositions are given in moles percent.

TABLE 5.3.2.7A
VFT Parameters for K_2O:SiO_2 Melts

	K_2O	SiO_2	A	B	To	σ(ΔT)	n	T_{min}	T_{max}
[55]	2.5	97.5	1.7747	663.1	1250.0	0.97	4	1600	1750
[62]	5.0	95.0	–7.2491	15142.4	–155.0	0.77	11	592	838
[55]	6.3	93.7	1.6500	505.6	1232.0	1.75	5	1500	1700
[60], [61]	8.0	92.0	–13.6170	22039.0	–273.0		3	570	697
[60], [61]	10.6	89.4	–15.4600	22562.0	–273.0		3	505	612
[55]	10.8	89.2	–3.3711	10779.5	–273.0	2.23	6	1350	1600
[62]	13.0	87.0	–4.3807	7946.8	61.0	1.36	11	517	702
[64]	15.6	84.4	–1.8162	6173.2	36.0	1.05	5	1000	1350
[63]	16.7	83.3	–1.5122	5165.2	139.0	1.66	6	909	1393
[55]	16.9	83.1	–3.3053	9851.8	–273.0	15.37	7	1100	1400
[66]	17.1	82.9	9.6535	237.8	390.0	11.30	7	450	494
[65]	17.5	82.5	–18.7881	24844.1	–273.0	5.22	5	517	584
[64]	17.5	82.5	–2.1056	6636.5	–8.0	0.76	5	1000	1350
[60], [61]	18.0	82.0	–16.1630	22427.0	–273.0		3	502	612
[60], [61]	18.5	81.5	–16.3020	22602.0	–273.0		3	497	583
[63]	18.9	81.1	–2.1478	6189.2	52.0	3.68	6	906	1397
[64]	18.9	81.1	–2.2056	6636.5	–8.0	0.76	5	1000	1350
[64]	19.6	80.4	–0.8378	3960.0	224.0	3.67	4	1000	1300
[67]	20.0	80.0	–24.8916	29404.2	–273.0	0.63	5	480	513
[62]	20.0	80.0	–9.0722	12894.8	–93.0	0.70	11	491	662
[64]	20.4	79.6	–1.9572	6047.1	41.0	1.00	5	1000	1350
[64]	21.1	78.9	–1.9824	5980.9	51.0	0.93	5	1000	1350
[64]	21.3	78.7	–1.9724	5980.9	51.0	0.93	5	1000	1350

TABLE 5.3.2.7A (Continued)
VFT Parameters for K_2O:SiO_2 Melts

	K_2O	SiO_2	A	B	To	σ(ΔT)	n	T_{min}	T_{max}
[63]	21.4	78.6	–2.2915	6284.3	34.0	5.46	6	904	1428
[65]	21.5	78.5	–9.8850	17234.9	–273.0	9.58	6	459	556
[64]	21.5	78.5	–1.1291	4402.2	191.0	1.08	5	1000	1350
[64]	21.9	78.1	–1.7428	5609.5	60.0	2.67	5	1000	1350
[55]	22.3	77.7	–2.9594	8193.2	–141.0	1.06	7	1100	1400
[64]	22.7	77.3	–2.1885	6071.1	58.0	1.55	6	950	1350
[63]	23.8	76.2	–3.1053	7771.0	–72.0	5.78	6	908	1403
[64]	23.9	76.1	–2.2816	6375.9	17.0	0.91	6	950	1350
[66]	24.1	75.9	–18.0277	22585.2	–266.0	0.59	8	441	494
[60], [61]	24.5	75.5	–16.3930	22052.0	–273.0		3	485	612
[64]	24.7	75.3	–1.5202	4659.1	177.0	1.19	6	950	1350
[65]	25.6	74.4	0.2559	3241.2	232.0	2.01	6	500	560
[55]	25.6	74.4	–3.2721	8235.0	–145.0	1.18	6	1100	1400
[63]	26.9	73.1	–3.2637	7826.0	–71.0	2.34	6	904	1399
[64]	27.1	72.9	–2.0353	5304.2	137.0	1.16	6	950	1350
[64]	27.7	72.3	–2.0248	5505.1	86.0	0.78	5	1000	1350
[64]	28.6	71.4	–2.6520	7074.8	–72.0	1.39	5	1000	1350
[63]	28.7	71.3	–4.4277	10603.3	–269.0	6.65	6	908	1400
[60], [61]	29.2	70.8	–18.6790	23061.0	–273.0		3	473	582
[62]	30.0	70.0	–12.1834	11042.2	10.0	0.70	11	448	558
[64]	30.2	69.8	–2.8450	6920.4	–19.0	1.77	5	1000	1350
[66]	30.9	69.1	–20.5289	23993.5	–273.0	0.92	6	429	494
[64]	31.2	68.8	–2.6827	6121.3	81.0	0.71	5	1000	1350
[64]	32.0	68.0	–3.2951	7437.0	–32.0	1.69	6	950	1350
[64]	32.2	67.8	–2.1868	5038.3	171.0	1.07	6	950	1350
[64]	32.8	67.2	–2.8085	6195.0	69.0	0.81	6	950	1350
[63]	33.0	67.0	–4.1934	9913.2	–273.0	12.68	6	892	1406
[64]	33.3	66.7	–2.4977	5515.0	114.0	1.78	5	1000	1350
[55]	33.4	66.6	–3.2923	7269.4	–37.0	4.85	7	1100	1400
[64]	33.8	66.2	–3.3657	7086.5	5.0	1.31	6	950	1350
[61]	34.1	66.0	–29.0420	30303.0	–273.0		3	457	502
[64]	34.4	65.6	–3.1956	7164.7	–44.0	1.68	6	950	1350
[64]	35.1	64.9	–2.8224	5920.5	89.0	1.09	6	950	1350
[64]	37.2	62.8	–2.6003	5111.3	159.0	0.49	4	950	1200
[64]	38.2	61.8	–2.4384	4748.1	180.0	0.70	5	950	1300
[64]	41.4	58.6	–5.5931	10078.3	–213.0	0.89	4	950	1200

Note: Melt compositions are given in moles percent, σ(ΔT) is the standard deviation of temperature residuals, n is the number of data points used in fitting the VFT equation, T_{min} and T_{max} show the range of temperature in °C covered by the data.

TABLE 5.3.2.7B
Temperatures at Specified Viscosity Values (Poise) for K_2O:SiO_2 Melts

			Temperature (°C) at which log (viscosity) is:								
	K_2O	SiO_2	2.0	3.0	4.0	5.0	10.0	11.0	12.0	13.0	14.0
[55]	2.5	97.5		1791	1548						
[62]	5.0	95.0					723	675	632	593	
[55]	6.3	93.7		1606							
[60], [61]	8.0	92.0					660	622	587		
[60], [61]	10.6	89.4						580	549	520	
[55]	10.8	89.2		1419							
[62]	13.0	87.0					614	578	546	518	
[64]	15.6	84.4		1318	1097						
[63]	16.7	83.3		1284	1076	932					
[55]	16.9	83.1		1289							
[66]	17.1	82.9							491	461	
[65]	17.5	82.5						561	534		
[64]	17.5	82.5		1292	1079						
[60], [61]	18.0	82.0					584	553	523		
[60], [61]	18.5	81.5						555	526	498	
[63]	18.9	81.1		1254	1059	918					
[64]	18.9	81.1		1267	1061						
[64]	19.6	80.4		1256	1043						
[67]	20.0	80.0								503	483
[62]	20.0	80.0					583	549	519	491	
[64]	20.4	79.6		1261	1056						
[64]	21.1	78.9		1251	1051						
[64]	21.3	78.7		1254	1052						
[63]	21.4	78.6		1222	1033						
[65]	21.5	78.5						552	515	480	
[64]	21.5	78.5		1257	1049						
[64]	21.9	78.1		1243	1037						
[55]	22.3	77.7		1234							
[64]	22.7	77.3		1228	1039						
[63]	23.8	76.2		1201	1022						
[64]	23.9	76.1		1224	1032						
[66]	24.1	75.9							486	462	
[60], [61]	24.5	75.5					563	532	504		
[64]	24.7	75.3		1208	1021						
[65]	25.6	74.4						534	508		
[55]	25.6	74.4		1168							
[63]	26.9	73.1		1178	1006						
[64]	27.1	72.9		1190	1016						
[64]	27.7	72.3		1182							
[64]	28.6	71.4		1180							

TABLE 5.3.2.7B (Continued)
Temperatures at Specified Viscosity Values (Poise) for K_2O:SiO_2 Melts

			Temperature (°C) at which log (viscosity) is:								
	K_2O	SiO_2	2.0	3.0	4.0	5.0	10.0	11.0	12.0	13.0	14.0
[63]	28.7	71.3	1381	1159	989						
[60], [61]	29.2	70.8					531	504	479		
[62]	30.0	70.0					508	486	467	448	
[64]	30.2	69.8		1165							
[66]	30.9	69.1						488	465	443	
[64]	31.2	68.8		1158							
[64]	32.0	68.0		1149	987						
[64]	32.2	67.8		1142	985						
[64]	32.8	67.2		1136	979						
[63]	33.0	67.0	1328	1105	937						
[64]	33.3	66.7	1340	1117							
[55]	33.4	66.6	1337	1118							
[64]	33.8	66.2	1326	1118	967						
[61]	34.1	66.0						484	465		
[64]	34.4	65.6	1335	1112	952						
[64]	35.1	64.9	1317	1106	957						
[64]	37.2	62.8		1072							
[64]	38.2	61.8	1250	1053							
[64]	41.4	58.6	1114	960							

Note: Calculated using the VFT equation with the parameters given in the previous table, melt compositions are given in moles percent.

TABLE 5.3.2.8A
VFT Parameters for Li_2O:B_2O_3 Melts

	LiO_2	B_2O_3	A	B	To	σ(ΔT)	n	T_{min}	T_{max}
[54]	0.0	100.0	–0.9623	2826.5	–41.0	30.19	12	452	1201
[54]	2.5	97.5	–1.0223	1851.9	160.0	4.55	6	503	1007
[54]	6.3	93.7	–1.6491	1920.9	214.0	1.10	5	600	990
[54]	9.9	90.1	–2.4766	2334.7	217.0	5.47	6	494	998
[54]	13.9	86.1	–2.2558	1909.4	306.0	1.05	4	605	897
[54]	16.8	83.2	–2.6270	1993.0	337.0	9.10	4	699	1000
[54]	25.6	74.4	–7.4588	9632.4	–273.0		3	801	901

Note: Melt compositions are given in moles percent, σ(ΔT) is the standard deviation of temperature residuals, n is the number of data points used in fitting the VFT equation, T_{min} and T_{max} show the range of temperature in °C covered by the data.

TABLE 5.3.2.8B
Temperatures at Specified Viscosity Values (Poise) for Li_2O:B_2O_3 Melts

			Temperature (°C) at which log(viscosity) is:								
	LiO_2	B_2O_3	0.50	1.0	1.5	2.0	2.5	3.0	3.5	4.0	4.5
[54]	0.0	100.0			1107	913	775	672	592	529	476
[54]	2.5	97.5			894	773	686	620	570	529	
[54]	6.3	93.7		939	824	740	677	627			
[54]	9.9	90.1		889	804	739	686	643	608	577	552
[54]	13.9	86.1		892	814	755	707	669	638	611	
[54]	16.8	83.2	974	886	820	768	726				
[54]	25.6	74.4		866	802						

Note: Calculated using the VFT equation with the parameters given in the previous table, melt compositions are given in moles percent.

TABLE 5.3.2.9A
VFT Parameters for Li_2O:SiO_2 Melts

	Li_2O	SiO_2	A	B	T_o	σ(ΔT)	n	T_{min}	T_{max}
[62]	20.0	80.0	–7.8556	9144.1	–12.0	0.82	11	426	565
[55]	20.0	80.0	–3.2500	9261.6	–273.0	5.68	7	1400	1700
[55]	25.0	75.0	–3.1294	8383.9	–273.0	11.51	7	1300	1600
[63]	28.6	71.4	–3.4393	8425.5	–273.0	6.07	4	1099	1400
[62]	30.0	70.0	–1.3766	3602.1	189.0	1.98	11	438	575
[55]	30.0	70.0	–2.9072	7113.6	–232.0	1.00	7	1200	1500
[63]	30.3	69.7	–3.3932	8079.6	–273.0	9.58	8	1000	1391
[63]	32.6	67.4	–2.5362	5465.7	–22.0	3.78	4	1102	1402
[55]	33.0	67.0	–2.7199	6157.2	–130.0	1.06	7	1150	1450
[68]	33.3	66.7	–4.2137	4707.3	181.0	0.35	10	448	502
[63]	33.4	66.6	–3.2118	7536.2	–273.0	12.39	4	1109	1390
[55]	35.0	65.0	–2.8698	6489.7	–223.0	1.23	8	1150	1500
[63]	35.9	64.1	–3.4887	7616.6	–273.0	10.63	4	1110	1401
[63]	38.7	61.3	–3.2565	7030.8	–273.0	55.24	4	1099	1386
[55]	40.0	60.0	–1.9771	4601.5	–153.0	2.59	8	1150	1500
[63]	41.3	58.7	–1.9432	3366.4	161.0	1.54	4	1095	1393
[55]	45.0	55.0	–2.8660	5620.2	–273.0	2.01	7	1200	1500
[55]	50.0	50.0	–2.3316	3362.1	46.0	1.68	6	1250	1500
[55]	55.0	45.0	–2.5447	3568.0	–173.0	1.38	5	1250	1450

Note: Melt compositions are given in moles percent, σ(ΔT) is the standard deviation of temperature residuals, n is the number of data points used in fitting the VFT equation, T_{min} and T_{max} show the range of temperature in °C covered by the data.

TABLE 5.3.2.9B
Temperatures at Specified Viscosity Values (Poise) for Li_2O:SiO_2 Melts

			Temperature (°C) at which log (viscosity) is:								
	Li_2O	SiO_2	–0.25	0.0	0.5	1.0	1.5	2.0	10.0	12.0	13.0
[62]	20.0	80.0							500	449	426
[55]	20.0	80.0					1677	1491			
[55]	25.0	75.0					1538	1361			
[63]	28.6	71.4						1276			
[62]	30.0	70.0							506	458	440
[55]	30.0	70.0					1382	1218			
[63]	30.3	69.7					1378	1225			
[63]	32.6	67.4					1332	1183			
[55]	33.0	67.0					1329	1175			
[68]	33.3	66.7								471	454
[63]	33.4	66.6					1326	1173			
[55]	35.0	65.0				1454	1262				
[63]	35.9	64.1					1254	1115			
[63]	38.7	61.3				1379	1205				
[55]	40.0	60.0				1393	1170				
[63]	41.3	58.7				1305	1139				
[55]	45.0	55.0			1397						
[55]	50.0	50.0		1488							
[55]	55.0	45.0	1382								

Note: Calculated using the VFT equation with the parameters given in the previous table, melt compositions are given in moles percent.

TABLE 5.3.2.10A
VFT Parameters for MgO:SiO_2 Melts

	MgO	SiO_2	A	B	T_o	σ(ΔT)	n	T_{min}	T_{max}
[51]	41.4	58.6	–0.1714	156.8	1560.0	6.22	7	1774	1947
[56]	41.4	58.6	–3.4703	7707.7	–149.0		3	1600	2500
[55]	44.3	55.7	–2.9430	5720.5	115.0	0.37	4	1650	1800
[55]	45.1	54.9	–3.9892	8948.0	–273.0	6.32	6	1550	1800
[55]	45.8	54.2	–1.0493	1052.0	987.0	8.15	6	1550	1800
[55]	50.0	50.0	–1.8763	2158.4	693.0	6.64	5	1600	1800
[51]	50.0	50.0	–2.3598	3137.1	545.0	4.69	11	1714	1995
[56]	50.0	50.0	–3.7170	7535.1	–146.0		3	1600	2500
[55]	51.3	48.7	–0.6938	426.4	1210.0	2.28	4	1650	1800
[51]	65.1	34.9	–2.6346	4789.2	–273.0	33.97	10	2020	2188
[56]	66.7	33.3	–2.4361	3931.7	–59.0		3	1600	2500

Note: Melt compositions are given in moles percent, σ(ΔT) is the standard deviation of temperature residuals, n is the number of data points used in fitting the VFT equation, T_{min} and T_{max} show the range of temperature in °C covered by the data.

TABLE 5.3.2.2.10B
Temperatures at Specified Viscosity Values (Poise) for$MgO:SiO_2$ Melts

			Temperature (°C) at which log (viscosity) is:								
	MgO	SiO_2	–0.80	–0.6	–0.4	–0.2	0.0	0.2	0.4	0.6	0.8
[51]	41.4	58.6							1834		
[56]	41.4	58.6			2361	2208	2072	1951	1842	1745	1656
[55]	44.3	55.7								1730	
[55]	45.1	54.9							1766	1677	1595
[55]	45.8	54.2							1713	1625	1556
[55]	50.0	50.0						1733	1641		
[51]	50.0	50.0					1874	1771			
[56]	50.0	50.0	2437	2271	2126	1996	1881	1778	1684		
[55]	51.3	48.7						1687			
[51]	65.1	34.9		2081							
[56]	66.7	33.3	2344	2082	1872	1699					

Note: Calculated using the VFT equation with the parameters given in the previous table, melt compositions are given in moles percent.

TABLE 5.3.2.11A
VFT Parameters for $Na_2O:B_2O_3$ Melts

	Na_2O	B_2O_3	A	B	To	σ(ΔT)	n	T_{min}	T_{max}
[42]	0.0	100.0	–0.8686	3543.8	–273.0		3	800	1200
[54]	0.0	100.0	–0.9623	2826.5	–41.0	30.19	12	452	1201
[54]	1.0	99.0	–0.6710	1851.2	123.0	9.19	7	493	1003
[54]	3.0	97.0	–1.0438	1849.5	157.0	6.47	6	495	994
[42]	5.5	94.6	–2.4069	3795.2	–124.0	0.02	9	800	1200
[54]	6.2	93.8	–1.1770	1609.4	228.0	5.70	6	499	1002
[54]	10.0	90.0	–4.2151	5128.6	–77.0	14.09	5	498	899
[42]	10.2	89.8	–2.2717	2587.1	148.0	0.31	9	800	1200
[54]	15.7	84.3	–2.2996	2108.2	282.0	0.72	4	603	895
[42]	17.2	82.8	–1.9457	1538.2	414.0	1.84	9	800	1200
[54]	19.6	80.4	–2.8125	2334.2	304.0		3	697	900
[42]	21.9	78.1	–2.1203	1510.3	432.0	2.08	9	800	1200
[42]	27.1	72.9	–1.9558	1201.4	470.0	2.73	9	800	1200
[54]	28.7	71.3	–5.8131	5255.0	86.0		3	694	903
[42]	33.3	66.7	–1.5458	705.6	548.0	5.03	9	800	1200
[54]	33.3	66.7	–3.0497	1840.9	355.0		3	599	798

Note: Melt compositions are given in moles percent, σ(ΔT) is the standard deviation of temperature residuals, n is the number of data points used in fitting the VFT equation, T_{min} and T_{max} show the range of temperature in °C covered by the data.

TABLE 5.3.2.11B
Temperatures at Specified Viscosity Values (Poise) for Na_2O:B_2O_3 Melts

			Temperature (°C) at which log(viscosity) is:								
	Na_2O	B_2O_3	0.75	1.0	1.5	2.0	2.5	3.0	3.5	4.0	4.5
[42]	0.0	100.0			1223	962	779				
[54]	0.0	100.0			1107	913	775	672	592	529	476
[54]	1.0	99.0			976	816	707	627	567	519	
[54]	3.0	97.0			884	765	679	614	564	524	491
[42]	5.5	94.6	1078	990	847						
[54]	6.2	93.8		967	829	735	666	613	572	539	512
[54]	10.0	90.0		906	820	748	687	634	588	547	511
[42]	10.2	89.8	1004	939	834						
[54]	15.7	84.3			837	772	721	680	646	617	
[42]	17.2	82.8	985	936	860	804					
[54]	19.6	80.4			845	789	743	706			
[42]	21.9	78.1	958	916	849	799					
[42]	27.1	72.9	914	876	818						
[54]	28.7	71.3	887	857	805	759	718				
[42]	33.3	66.7	855	825							
[54]	33.3	66.7			760	720	687	659	636	616	599

Note: Calculated using the VFT equation with the parameters given in the previous table, melt compositions are given in moles percent.

TABLE 5.3.2.12A
VFT Parameters for Na_2O:GeO_2 Melts

	Na_2O	GeO_2	A	B	To	σ(ΔT)	n	T_{min}	T_{max}
[44]	0.000	100.00	–5.3867	15457.6	–273.0	7.75	13	550	1500
[44]	0.045	99.955	–4.0526	13045.8	–273.0	6.29	11	1000	1500
[44]	0.3	99.7	–2.7413	10046.2	–273.0	4.32	11	1000	1500
[44]	1.2	98.8	–2.4279	7660.8	–273.0	4.89	11	1000	1500
[44]	7.5	92.5	–2.3301	4048.3	14.0	12.78	11	1000	1500
[44]	10.9	89.2	–2.7040	5156.7	–273.0	5.21	11	1000	1500
[44]	16.4	83.6	–2.7802	4756.4	–273.0	16.59	11	1000	1500

Note: Melt compositions are given in moles percent, σ(ΔT) is the standard deviation of temperature residuals, n is the number of data points used in fitting the VFT equation, T_{min} and T_{max} show the range of temperature in °C covered by the data.

TABLE 5.3.2.12B
Temperatures at Specified Viscosity Values (Poise) for Na_2O:GeO_2 Melts

			Temperature (°C) at which log (viscosity) is								
	Na_2O	GeO_2	0.00	0.5	1.0	1.5	2.0	3.0	4.0	5.0	6.0
[44]	0.000	100.00							1374	1215	1085
[44]	0.045	99.955							1347	1168	1025
[44]	0.3	99.7						1477	1217	1025	
[44]	1.2	98.8					1457	1138			
[44]	7.5	92.5		1444	1230	1071					
[44]	10.9	89.2		1336	1119						
[44]	16.4	83.6	1438	1177							

Note: Calculated using the VFT equation with the parameters given in the previous table, melt compositions are given in moles percent.

TABLE 5.3.2.13A
VFT Parameters for Na_2O:P_2O_5 Melts

	Na_2O	P_2O_5	A	B	To	σ(ΔT)	n	T_{min}	T_{max}
[69]	35.0	65.0	–0.9277	1492.9	133.0	16.21	18	362.7	810.4
[69]	40.0	60.0	–41.4286	23350.5	–158.0	0.81	6	274.9	305.0
[69]	40.0	60.0	–1.4743	1828.1	97.0	6.76	15	461.8	926.0
[69]	45.0	55.0	–0.8048	1104.3	247.0	6.63	12	460.1	801.1
[69]	50.0	50.0	–30.7724	22998.1	–273.0	1.36	6	258.9	305.0
[69]	50.0	50.0	–2.9020	3459.9	–125.0	3.68	7	619.9	846.8
[69]	55.0	45.0	–31.7896	17404.0	–111.0	0.85	6	282.6	315.2
[69]	55.0	45.0	–1.7457	1600.7	69.0	9.39	7	612.7	840.6

Note: Melt compositions are given in moles percent, σ(ΔT) is the standard deviation of temperature residuals, n is the number of data points used in fitting the VFT equation, T_{min} and T_{max} show the range of temperature in °C covered by the data.

TABLE 5.3.2.13B
Temperatures at Specified Viscosity Values (Poise) for Na_2O: P_2O_5 Melts

			Temperature (°C) at which log (viscosity) is:								
	Na_2O	P_2O_5	0.75	1.25	2.0	3.0	4.0	5.0	9.0	11.0	12.5
[69]	35.0	65.0		819	643	513	436	385			
[69]	40.0	60.0							305	287	275
[69]	40.0	60.0	919	768	623	506					
[69]	45.0	55.0		784	641	537	477				
[69]	50.0	50.0							305	278	258
[69]	50.0	50.0	822	708							

TABLE 5.3.2.13B (Continued)
Temperatures at Specified Viscosity Values (Poise) for Na_2O: P_2O_5 Melts

			Temperature (°C) at which log (viscosity) is:								
	Na_2O	P_2O_5	0.75	1.25	2.0	3.0	4.0	5.0	9.0	11.0	12.5
[69]	55.0	45.0							316	296	282
[69]	55.0	45.0	710	603							

Note: Calculated using the VFT equation with the parameters given in the previous table, melt compositions are given in moles percent.

TABLE 5.3.2.14A
VFT Parameters for Na_2O:SiO_2 Melts

	Na_2O	SiO_2	A	B	To	σ(ΔT)	n	T_{min}	T_{max}
[62]	5.0	95.0	–8.3624	19900.2	–273.0	3.93	8	653	838
[55]	10.0	90.0	–4.5114	13028.8	–273.0	2.32	5	1550	1750
[70]	11.7	88.3	0.3569	1766.5	740.0		3	1400	1500
[62]	13.0	87.0	–16.2411	24875.7	–273.0	0.68	9	578	712
[61]	14.7	85.3	–9.9190	17806.0	–273.0		3	495	645
[71]	14.8	85.2	0.8425	861.5	916.0	2.59	5	1300	1500
[72]	15.0	85.0	–3.8066	10392.8	–209.0	10.53	5	1100	1500
[55]	15.0	85.0	–3.6310	10365.4	–273.0	5.41	6	1350	1600
[70]	15.7	84.3	–2.7697	8407.0	–150.0	1.49	6	1250	1500
[71]	16.4	83.6	0.1828	1753.0	650.0		3	1200	1400
[73]	16.7	83.3	–5.9308	14896.6	–273.0	2.88	7	434	482
[71]	17.2	82.8	–2.9010	8974.9	–273.0		3	1200	1400
[71]	18.3	81.7	–2.5704	8252.2	–273.0		3	1200	1400
[74]	19.0	81.0	–2.5045	5499.3	148.0	4.43	9	505	1410
[63]	19.5	80.5	–1.5847	4890.3	120.0	7.40	9	898	1408
[70]	19.6	80.4	–2.3033	6462.3	–15.0	0.67	10	1050	1500
[75]	19.6	80.4	1.8624	2470.0	253.0	0.54	7	442	471
[72]	20.0	80.0	–2.3884	6544.0	–36.0	6.25	7	900	1500
[62]	20.0	80.0	–12.8844	19286.0	–273.0	1.33	11	473	652
[73]	20.0	80.0	–7.2647	15562.2	–273.0	4.37	6	425	473
[55]	20.0	80.0	–3.5168	9236.9	–273.0	1.83	6	1250	1500
[61]	20.1	79.9	–15.6190	21432.0	–273.0		3	490	590
[71]	20.4	79.6	–0.3256	2534.2	404.0	2.27	10	1000	1450
[71]	21.2	78.8	–1.0528	3771.3	222.0	2.52	4	1100	1400
[76]	21.4	78.6	–1.7694	5038.0	102.0	1.36	6	900	1400
[77]	21.7	78.3	–2.2185	6379.8	–83.0	2.17	6	900	1400
[71]	22.0	78.0	0.0962	1781.9	523.0	4.57	4	1100	1400
[78]	22.0	78.0	–0.7991	3204.8	308.0	3.15	10	1000	1420
[73]	22.2	77.8	–10.9482	18154.3	–273.0	4.50	6	427	472
[77]	22.2	77.8	–1.9705	5607.2	–15.0	1.50	6	900	1400
[77]	22.4	77.6	–1.3813	4613.6	42.0	3.67	7	800	1400

TABLE 5.3.2.14A (Continued)
VFT Parameters for Na_2O:SiO_2 Melts

	Na_2O	SiO_2	A	B	To	σ(ΔT)	n	T_{min}	T_{max}
[77]	22.6	77.4	–1.9519	5685.0	–34.0	3.94	6	900	1400
[75]	23.1	76.9	–8.9861	8793.7	61.0	0.64	7	442	472
[77]	23.4	76.6	–1.4348	4358.7	85.0	1.35	7	800	1400
[78]	23.5	76.5	–1.2754	3978.5	216.0	3.00	12	960	1420
[77]	23.8	76.2	–1.4427	4276.8	96.0	2.66	6	900	1400
[76]	24.3	75.7	–1.8435	4964.0	91.0	0.81	6	900	1400
[70]	24.4	75.6	–2.1090	5615.7	29.0	2.21	11	1000	1500
[61]	24.8	75.2	–17.8480	22759.0	–273.0		3	455	635
[15]	25.0	75.0	–1.6465	4495.2	139.0	1.14	32	698	1351
[72]	25.0	75.0	–2.8255	7057.8	–96.0	5.73	7	900	1500
[71]	25.0	75.0	–0.2654	2347.4	379.0	2.74	13	850	1450
[55]	25.0	75.0	–3.2005	8498.3	–273.0	1.89	8	1150	1500
[77]	25.0	75.0	–1.5045	4655.2	26.0	3.94	7	800	1400
[76]	25.2	74.8	–1.7786	4792.2	101.0	0.51	6	900	1400
[71]	25.6	74.4	–0.8625	3046.3	277.0	3.52	6	900	1400
[76]	26.0	74.0	–1.7377	4646.8	116.0	0.84	6	900	1400
[74]	26.1	73.9	–2.7141	5262.8	144.0	9.67	17	485	1310
[78]	26.1	73.9	–1.9664	5296.1	36.0	3.32	13	900	1420
[76]	26.2	73.8	–1.7068	4574.1	122.0	1.70	6	900	1400
[77]	26.3	73.7	–1.7698	5118.5	–22.0	1.38	7	800	1400
[78]	26.5	73.5	–1.6992	4567.4	107.0	2.45	14	860	1420
[55]	27.0	73.0	–2.7897	7403.1	–214.0	1.68	8	1150	1500
[71]	27.2	72.8	–0.8153	2941.1	296.0	1.26	6	900	1400
[77]	27.5	72.5	–1.2196	3955.3	118.0	3.86	6	900	1400
[75]	27.6	72.4	–8.8870	7981.7	91.0	0.50	8	428	471
[77]	27.7	72.3	–3.1252	8004.0	–273.0	3.65	7	800	1400
[76]	27.8	72.2	–2.2784	5703.6	0.0	3.04	6	900	1400
[71]	28.4	71.6	–0.0736	1875.7	437.0	6.68	6	900	1400
[76]	29.1	70.9	–2.0507	5047.9	62.0	1.62	6	900	1400
[77]	29.3	70.7	–1.3222	3941.0	116.0	1.98	6	900	1400
[70]	29.5	70.6	–2.3130	5559.2	27.0	1.18	11	1000	1500
[78]	29.5	70.5	–1.6289	4240.5	146.0	4.24	13	860	1400
[71]	29.9	70.1	–0.0146	1790.5	441.0	8.59	13	850	1450
[72]	30.0	70.0	–2.5352	6052.0	–40.0	5.18	7	900	1500
[55]	30.0	70.0	–3.3940	8385.0	–273.0	0.90	8	1100	1450
[63]	30.1	69.9	–0.8677	2744.7	323.0	11.00	6	894	1403
[71]	30.6	69.4	–0.2068	1835.9	447.0	7.50	6	900	1400
[77]	30.8	69.2	–2.0453	5267.5	–50.0	2.42	7	800	1400
[77]	31.0	69.0	–1.3963	4122.5	76.0	5.65	7	800	1400
[76]	31.1	68.9	–2.2254	5263.1	32.0	1.00	6	900	1400
[78]	31.5	68.5	–1.3492	3656.9	204.0	13.54	12	860	1360
[77]	31.6	68.4	–1.3680	3765.3	132.0	3.91	7	800	1400
[77]	31.7	68.3	–1.2689	3610.9	136.0	1.64	7	800	1400
[71]	31.8	68.2	–0.5968	2192.2	395.0	9.52	6	900	1400

TABLE 5.3.2.14A (Continued)
VFT Parameters for Na_2O:SiO_2 Melts

	Na_2O	SiO_2	A	B	To	σ(ΔT)	n	T_{min}	T_{max}
[71]	31.9	68.1	–0.6395	2175.1	392.0	2.83	6	900	1400
[76]	32.2	67.8	–2.3827	5552.5	–4.0	1.29	6	900	1400
[71]	32.5	67.5	–1.9004	3983.8	170.0	1.68	6	900	1400
[76]	32.5	67.5	–2.4197	5612.0	–12.0	2.67	6	900	1400
[77]	32.6	67.4	–2.3276	4978.5	6.0	1.82	6	800	1300
[75]	32.8	67.2	–34.7024	34269.1	–273.0	0.54	6	428	471
[77]	32.8	67.2	–1.8381	3895.5	132.0	4.04	6	800	1300
[63]	32.9	67.1	–3.6277	8549.3	–273.0	4.66	6	899	1404
[55]	33.0	67.0	–3.4795	8140.2	–250.0	1.70	8	1100	1450
[71]	33.1	66.9	–2.6487	5489.7	–1.0	2.38	6	900	1400
[76]	33.1	66.9	–2.3066	5282.0	21.0	2.35	6	900	1400
[77]	33.1	66.9	–1.3033	2843.1	253.0	1.24	5	800	1200
[15]	33.3	66.7	–1.7457	4163.8	142.0	1.90	32	669	1251
[73]	33.3	66.7	–8.1007	16043.6	–273.0	7.78	6	416	463
[78]	33.3	66.7	–2.0399	4880.0	46.0	2.13	15	760	1400
[71]	33.6	66.4	–1.9411	4151.2	128.0	3.09	6	900	1400
[76]	33.6	66.4	–2.0844	4808.6	69.0	1.80	6	900	1400
[77]	33.7	66.3	–1.6409	3495.6	192.0	9.24	6	800	1300
[77]	33.8	66.2	–1.2277	3176.0	206.0	11.15	7	800	1400
[79]	34.0	66.0	–1.2353	3456.8	191.0	5.92	17	396	1300
[77]	34.0	66.0	–1.9753	4626.8	41.0	1.26	7	800	1400
[76]	34.2	65.8	–2.2073	5052.8	38.0	2.22	6	900	1400
[70]	34.3	65.7	–2.6394	5906.4	–19.0	2.38	11	1000	1500
[77]	34.4	65.6	–1.5993	3859.1	138.0	1.52	7	800	1400
[71]	34.5	65.5	–0.9206	2751.2	288.0	6.26	13	850	1450
[78]	34.5	65.5	–2.3661	5377.5	4.0	2.55	15	760	1400
[61]	34.5	65.5	–20.6040	23980.0	–273.0		3	425	575
[72]	35.0	65.0	–1.3614	3195.7	260.0	11.51	7	900	1500
[71]	35.0	65.0	–0.9243	2536.4	331.0	1.43	6	900	1400
[55]	35.0	65.0	–3.4912	8113.6	–273.0	1.55	9	1100	1500
[78]	35.6	64.4	–2.2067	4979.6	40.0	3.74	16	760	1420
[15]	35.7	64.3	–1.9215	4286.6	122.0	1.97	29	651	1251
[77]	35.8	64.2	–1.8927	4593.1	60.0	4.29	7	800	1400
[71]	35.9	64.1	–1.0065	2634.7	312.0	4.42	6	900	1400
[76]	36.0	64.0	–2.3228	5073.2	38.0	1.88	6	900	1400
[63]	36.2	63.8	–2.0999	4698.6	62.0	8.07	6	900	1400
[77]	36.3	63.7	–1.4629	3810.7	118.0	0.99	7	800	1400
[71]	36.4	63.6	–1.3513	3286.6	211.0	5.40	6	900	1400
[71]	37.4	62.6	–2.3046	4893.8	42.0	3.45	6	900	1400
[77]	37.4	62.6	–1.5604	3653.4	140.0	2.68	6	800	1300
[70]	38.7	61.3	–3.7728	8103.3	–243.0	1.70	11	1000	1500
[77]	38.9	61.1	–2.3163	4820.0	26.0	2.04	6	800	1300
[76]	39.0	61.0	–2.8730	5939.6	–57.0	2.42	6	900	1400
[61]	39.5	60.5	–21.7800	23675.0	–273.0	5.41	0	415	545

TABLE 5.3.2.14A (Continued)
VFT Parameters for Na_2O:SiO_2 Melts

	Na_2O	SiO_2	A	B	To	σ(ΔT)	n	T_{min}	T_{max}
[72]	40.0	60.0	–1.9891	3004.7	262.0	11.02	5	1000	1400
[72]	40.0	60.0	–1.8137	3596.6	190.0	7.66	6	900	1400
[71]	40.2	59.8	–2.4300	4775.0	57.0	2.44	13	850	1450
[78]	41.0	59.0	–3.2844	6766.4	–140.0	3.81	15	800	1420
[71]	41.9	58.1	–3.1427	5717.2	–22.0	8.58	5	1000	1400
[77]	41.9	58.1	–1.8182	3467.4	155.0	1.01	5	800	1200
[78]	42.8	57.2	–2.8335	5376.9	–14.0	6.53	9	960	1300
[77]	44.0	56.0	–1.5450	2799.8	260.0	3.14	5	800	1200
[71]	44.4	55.6	–3.2185	5404.7	–18.0	5.85	10	1000	1450
[70]	44.8	55.2	–3.7186	6786.3	–130.0	4.30	11	1000	1500
[71]	46.6	53.4	–3.0428	4348.1	106.0	2.72	5	1000	1400
[78]	47.0	53.0	–3.8952	7536.5	–273.0	4.45	7	1000	1300
[70]	48.2	51.8	–2.9758	4446.9	33.0	3.42	6	1000	1250
[71]	49.3	50.7	–2.4671	2546.4	361.0	11.15	7	1100	1400
[70]	49.4	50.6	–2.9879	4348.5	32.0	2.14	5	1050	1250
[72]	50.0	50.0	–2.5391	3004.7	262.0	11.02	5	1000	1400
[70]	50.0	50.0	–2.4741	3351.5	133.0	1.94	10	1050	1500
[78]	50.0	50.0	–1.2410	1430.8	455.0	5.09	6	1000	1260
[70]	51.2	48.8	–1.5438	1576.0	422.0	1.77	6	1000	1250
[70]	54.6	45.4	–2.0294	2137.4	249.0	3.83	11	1000	1500
[70]	60.1	39.9	–1.7141	1018.1	499.0	2.67	9	1100	1500

Note: Melt compositions are given in moles percent, σ(ΔT) is the standard deviation of temperature residuals, n is the number of data points used in fitting the VFT equation, T_{min} and T_{max} show the range of temperature in °C covered by the data.

TABLE 5.3.2.14B
Temperatures at Specified Viscosity Values (Poise) for Na_2O:SiO_2 Melts

			Temperature (°C) at which log (viscosity) is								
	Na_2O	SiO_2	0.0	1.0	2.0	3.0	4.0	7.6	12.0	13.0	14.0
[62]	5.0	95.0							704	659	
[55]	10.0	90.0			1728						
[70]	11.7	88.3				1408					
[62]	13.0	87.0							608	578	
[61]	14.7	85.3							539	504	
[71]	14.8	85.2				1315					
[72]	15.0	85.0				1318	1122				
[55]	15.0	85.0			1568						
[70]	15.7	84.3				1307					
[71]	16.4	83.6				1272					
[73]	16.7	83.3									474

TABLE 5.3.2.14B (Continued)
Temperatures at Specified Viscosity Values (Poise) for Na_2O:SiO_2 Melts

			Temperature (°C) at which log (viscosity) is								
	Na_2O	SiO_2	0.0	1.0	2.0	3.0	4.0	7.6	12.0	13.0	14.0
[71]	17.2	82.8				1248					
[71]	18.3	81.7				1208					
[74]	19.0	81.0			1369	1147	993	692	527		
[63]	19.5	80.5				1187	996				
[70]	19.6	80.4			1487	1204					
[75]	19.6	80.4									457
[72]	20.0	80.0			1455	1178	988				
[62]	20.0	80.0							502	472	
[73]	20.0	80.0									459
[55]	20.0	80.0			1401						
[61]	20.1	79.9							503		
[71]	20.4	79.6			1494	1166	990				
[71]	21.2	78.8				1153					
[76]	21.4	78.6				1158	975				
[77]	21.7	78.3			1429	1140	943				
[71]	22.0	78.0				1137					
[78]	22.0	78.0			1453	1152					
[73]	22.2	77.8									455
[77]	22.2	77.8			1397	1113	924				
[77]	22.4	77.6			1406	1095	899				
[77]	22.6	77.4			1405	1114	921				
[75]	23.1	76.9								461	444
[77]	23.4	76.6			1354	1068	887				
[78]	23.5	76.5			1431	1147	970				
[77]	23.8	76.2			1338	1059					
[76]	24.3	75.7			1383	1116	940				
[70]	24.4	75.6			1396	1128					
[61]	24.8	75.2						621	489	465	
[15]	25.0	75.0			1372	1106	935				
[72]	25.0	75.0			1367	1116	938				
[71]	25.0	75.0			1415	1098	929				
[55]	25.0	75.0			1361						
[77]	25.0	75.0			1354	1059	872				
[76]	25.2	74.8			1369	1104	930				
[71]	25.6	74.4			1341	1066	903				
[76]	26.0	74.0			1359	1097	926				
[74]	26.1	73.9			1260	1065	928	654	502		
[78]	26.1	73.9			1371	1102	924				
[76]	26.2	73.8			1356	1094	924				
[77]	26.3	73.7			1336	1051	865				
[78]	26.5	73.5			1342	1079	908				
[55]	27.0	73.0			1332						
[71]	27.2	72.8			1341	1067	907				
[77]	27.5	72.5			1347	1055					

TABLE 5.3.2.14B (Continued)
Temperatures at Specified Viscosity Values (Poise) for Na_2O:SiO_2 Melts

			Temperature (°C) at which log (viscosity) is								
	Na_2O	SiO_2	0.0	1.0	2.0	3.0	4.0	7.6	12.0	13.0	14.0
[75]	27.6	72.4								456	440
[77]	27.7	72.3			1289	1034	850				
[76]	27.8	72.2			1333	1081	908				
[71]	28.4	71.6			1342	1047	897				
[76]	29.1	70.9			1308	1061	896				
[77]	29.3	70.7			1302	1028					
[70]	29.5	70.6			1316	1073					
[78]	29.5	70.5			1315	1062	899				
[71]	29.9	70.1			1330	1035	887				
[72]	30.0	70.0			1294	1053	886				
[55]	30.0	70.0			1282						
[63]	30.1	69.9			1280	1033	887				
[71]	30.6	69.4			1279	1019					
[77]	30.8	69.2			1252	994	821				
[77]	31.0	69.0			1290	1014	840				
[76]	31.1	68.9			1278	1039					
[78]	31.5	68.5			1296	1045	888				
[77]	31.6	68.4			1250	994	833				
[77]	31.7	68.3			1241	982	821				
[71]	31.8	68.2			1239	1004					
[71]	31.9	68.1			1216	990					
[76]	32.2	67.8			1263	1028					
[71]	32.5	67.5			1191	983					
[76]	32.5	67.5			1258	1023					
[77]	32.6	67.4			1156	940	793				
[75]	32.8	67.2							461	445	431
[77]	32.8	67.2			1147	937	799				
[63]	32.9	67.1			1246	1017					
[55]	33.0	67.0			1236						
[71]	33.1	66.9			1180	971					
[76]	33.1	66.9			1247	1016					
[77]	33.1	66.9			1114	914					
[15]	33.3	66.7			1254	1019	867				
[73]	33.3	66.7									453
[78]	33.3	66.7			1254	1014	854				
[71]	33.6	66.4			1181	968					
[76]	33.6	66.4			1246	1015					
[77]	33.7	66.3			1152	945	812				
[77]	33.8	66.2			1190	957	814				
[79]	34.0	66.0			1259	1007	851	582	452	434	418
[77]	34.0	66.0			1205	971	815				
[76]	34.2	65.8			1239	1008					
[70]	34.3	65.7			1254	1028					
[77]	34.4	65.6			1210	977	827				

TABLE 5.3.2.14B (Continued)
Temperatures at Specified Viscosity Values (Poise) for Na_2O:SiO_2 Melts

			Temperature (°C) at which log (viscosity) is								
	Na_2O	SiO_2	0.0	1.0	2.0	3.0	4.0	7.6	12.0	13.0	14.0
[71]	34.5	65.5			1230	990	847				
[78]	34.5	65.5			1236	1006	849				
[61]	34.5	65.5						577	462	441	
[72]	35.0	65.0			1211	993					
[71]	35.0	65.0			1198	977					
[55]	35.0	65.0		1534	1205						
[78]	35.6	64.4			1224	996	842				
[15]	35.7	64.3			1215	993	846				
[77]	35.8	64.2			1240	999	839				
[71]	35.9	64.1			1188	970					
[76]	36.0	64.0			1212	991					
[63]	36.2	63.8			1208	983					
[77]	36.3	63.7			1218	972	816				
[71]	36.4	63.6			1192	966					
[71]	37.4	62.6			1179	965					
[77]	37.4	62.6			1166	941	797				
[70]	38.7	61.3		1455	1161						
[77]	38.9	61.1			1143	933	789				
[76]	39.0	61.0			1162	954					
[61]	39.5	60.5						533	428		
[72]	40.0	60.0		1267	1015						
[72]	40.0	60.0			1133	937					
[71]	40.2	59.8		1449	1135	936					
[78]	41.0	59.0		1439	1140	937	789				
[71]	41.9	58.1		1358	1090						
[77]	41.9	58.1			1063	875					
[78]	42.8	57.2			1098						
[77]	44.0	56.0			1050	876					
[71]	44.4	55.6		1263	1018						
[70]	44.8	55.2		1308	1057						
[71]	46.6	53.4		1182							
[78]	47.0	53.0		1267	1005						
[70]	48.2	51.8		1151							
[71]	49.3	50.7	1393	1095							
[70]	49.4	50.6		1122							
[72]	50.0	50.0		1111							
[70]	50.0	50.0	1488	1098							
[78]	50.0	50.0		1093							
[70]	51.2	48.8		1042							
[70]	54.6	45.4	1302								
[70]	60.1	39.9	1093								

Note: Calculated using the VFT equation with the parameters given in the previous table, melt compositions are given in moles percent.

TABLE 5.3.2.15A
VFT Parameters for PbO:SiO_2 Melts

	PbO	SiO_2	A	B	To	σ(ΔT)	n	T_{min}	T_{max}
[80]	20.0	80.0	–1.9077	5748.5	151.0	4.22	6	535	733
[80]	30.0	70.0	–7.0918	9078.3	41.0	4.01	8	492	737
[80]	33.3	66.7	–3.4563	5115.2	168.0	3.33	10	476	856
[80]	35.0	65.0	–2.0564	3964.9	214.0	3.99	10	473	870
[81],[82]	35.0	65.0	–1.4272	2921.9	281.0	9.10	32	840	1460
[81],[82]	40.0	60.0	–1.4001	2574.3	249.0	4.65	31	740	1340
[80]	40.1	59.9	–3.4555	4492.3	186.0	6.11	10	455	794
[83]	40.2	59.8	–20.1639	20278.8	–160.0	0.48	5	444	536
[84]	40.3	59.7	–1.5870	2857.4	258.0	12.54	31	447	1384
[84]	42.1	57.9	–1.6188	2667.7	264.0	15.10	31	438	1319
[80]	42.1	57.9	–2.3442	3418.7	211.0	6.16	10	430	754
[84]	44.6	55.4	–1.8593	2569.0	266.0	11.40	31	431	1190
[80]	45.0	55.0	0.1446	2423.2	238.0	4.05	7	424	593
[81],[82]	46.0	54.0	–0.8432	1518.8	354.0	11.20	35	700	1380
[84]	47.3	52.8	–1.9208	2450.6	262.0	8.50	31	420	1118
[80]	48.0	52.0	–17.5946	15151.9	–93.0	1.21	7	402	524
[84]	48.7	51.3	–1.8339	2169.9	272.0	13.04	31	412	1070
[80]	49.4	50.6	–12.9348	9945.9	24.0	1.41	7	407	524
[84]	49.5	50.5	–2.0133	2318.9	259.0	10.58	31	408	1051
[80]	49.6	50.4	–1.8843	2509.0	235.0	2.78	7	402	519
[79]	50.0	50.0	–1.9303	2294.2	240.0	22.08	16	373	1400
[67]	50.0	50.0	–3.9438	3684.4	192.0	0.52	8	395	460
[80]	50.0	50.0	–4.1884	3577.5	194.0	2.66	7	400	515
[81],[82]	50.0	50.0	–1.1362	1389.4	343.0	8.20	33	580	1220
[84]	50.2	49.8	–1.8946	2180.9	264.0	15.12	31	402	1051
[84]	51.2	48.8	–1.7953	2012.5	272.0	17.63	31	400	1030
[84]	52.3	47.8	–2.1228	2152.7	259.0	11.66	31	396	980
[80]	55.0	45.0	–30.3824	28050.9	–273.0	1.00	6	373	457
[81],[82]	55.0	45.0	–2.4083	2785.6	48.0	6.65	27	680	1200
[84]	55.0	45.0	–2.7987	2337.5	241.0	6.95	31	385	878
[84]	57.5	42.5	–2.7580	2179.3	236.0	6.96	31	370	837
[80]	60.0	40.0	–33.8259	30001.0	–273.0	0.75	6	367	444
[81],[82]	60.0	40.0	–1.9484	1602.3	196.0	8.64	22	660	1080
[83]	60.1	39.9	–22.6513	13547.6	–18.0	0.13	4	373	410
[84]	60.2	39.8	–2.4182	1783.6	253.0	6.90	32	364	832
[84]	62.3	37.7	–2.8100	1761.1	251.0	13.07	32	357	783
[80]	63.0	37.0	–38.7490	32719.4	–273.0	0.34	6	359	427
[81],[82]	64.0	36.0	–2.5664	2123.8	68.0	15.29	21	680	1080
[80]	66.0	34.0	–4.6834	2876.8	183.0	0.98	6	345	410
[80]	66.6	33.4	–2.7068	2116.4	212.0	1.02	6	346	410
[81],[82]	66.7	33.3	–3.2449	3620.9	–273.0	8.12	16	740	1040
[80]	68.0	32.0	–13.1519	7074.2	84.0	1.02	6	354	419
[80]	70.0	30.0	–24.5757	14848.5	–41.0	0.49	6	354	415
[81],[82]	70.0	30.0	–4.7025	5003.1	–273.0	17.04	16	700	1000

TABLE 5.3.2.15A (Continued)
VFT Parameters for PbO:SiO_2 Melts

	PbO	SiO_2	A	B	To	σ(ΔT)	n	T_{min}	T_{max}
[85]	70.1	29.9	–0.6556	1894.2	364.0		3	764	972
[80]	73.0	27.0	–44.5523	34914.3	–273.0	0.80	5	333	379
[85]	80.0	20.0	–1.3810	1460.0	338.0	13.60	5	610	889

Note: Melt compositions are given in moles percent, σ(ΔT) is the standard deviation of temperature residuals, n is the number of data points used in fitting the VFT equation, T_{min} and T_{max} show the range of temperature in °C covered by the data.

TABLE 5.3.2.15B
Temperatures at Specified Viscosity Values (Poise) for PbO:SiO_2 Melts

			Temperature (°C) at which log (viscosity) is:								
	PbO	SiO_2	0.0	0.5	1.0	1.5	2.0	4.0	10.0	12.0	13.0
[80]	20.0	80.0							634	564	537
[80]	30.0	70.0							572	517	493
[80]	33.3	66.7						854	548	499	479
[81],[82]	35.0	65.0						869	543	496	477
[81],[82]	35.0	65.0			1485	1279	1134				
[80]	40.0	60.0			1322	1137	1006				
[83]	40.1	59.9						789	520	477	459
[84]	40.2	59.8							512	470	451
[84]	40.3	59.7			1363	1184	1055	769	505	468	454
[80]	42.1	57.9			1283	1119	1001	739	494	460	446
[84]	42.1	57.9						750	488	449	434
[80]	44.6	55.4			1164	1031	932	704	483	451	439
[81],[82]	45.0	55.0							484	442	426
[84]	46.0	54.0			1178	1002	888				
[80]	47.3	52.8			1101	978	887	676	468	438	426
[84]	48.0	52.0							456	419	402
[80]	48.7	51.3			1038	923	838	644	455	429	418
[84]	49.4	50.6							458	423	407
[80]	49.5	50.5			1029	919	837	645	452	424	413
[79]	49.6	50.4							446	416	404
[67]	50.0	50.0	1429	1184	1023	909	824	627	432	405	394
[80]	50.0	50.0							456	423	409
[81],[82]	50.0	50.0							446	415	402
[84]	50.0	50.0		1192	993	870	786	614			
[84]	50.2	49.8			1017	906	824	634	447	421	410
[84]	51.2	48.8			992	883	802	619	443	418	408
[80]	52.3	47.8			948	853	781	611	437	411	401
[81],[82]	55.0	45.0							422	389	374
[84]	55.0	45.0	1205	1006	865	761	680				

TABLE 5.3.2.15B (Continued)
Temperatures at Specified Viscosity Values (Poise) for $PbO:SiO_2$ Melts

			Temperature (°C) at which log (viscosity) is:								
	PbO	SiO_2	0.0	0.5	1.0	1.5	2.0	4.0	10.0	12.0	13.0
[84]	55.0	45.0			856	785	728	585	424	399	389
[80]	57.5	42.5			816	748	694	558	407	384	374
[81], [82]	60.0	40.0							412	382	368
[83]	60.0	40.0	1018	850	739	661					
[84]	60.1	39.9							397	373	
[84]	60.2	39.8			775	708	657	531	397	377	369
[80]	62.3	37.7		783	713	660	617	510	388	370	362
[81], [82]	63.0	37.0							398	372	359
[80]	64.0	36.0	896	761	664						
[80]	66.0	34.0							379	355	346
[81],[82]	66.6	33.4							379	356	347
[80]	66.7	33.3	843								
[80]	68.0	32.0							390	365	355
[81], [82]	70.0	30.0							388	365	354
[85]	70.0	30.0	791	689							
[80]	70.1	29.9						771			
[85]	73.0	27.0							367	344	334
	80.0	20.0				845	770	609			

Note: Calculated using the VFT equation with the parameters given in the previous table, melt compositions are given in moles percent.

TABLE 5.3.2.16A
VFT Parameters for $SrO:SiO_2$ Melts

	SrO	SiO_2	A	B	To	σ[ΔT]	n	T_{min}	T_{max}
[55]	20.1	79.9	–1.9371	5068.1	381.0		3	1700	1800
[55]	25.5	74.5	–0.4097	1262.3	1027.0	6.68	5	1600	1800
[55]	29.7	70.3	–3.8060	9069.9	–184.0	2.63	6	1550	1800
[55]	40.5	59.5	–1.9559	3137.0	508.0	3.09	6	1550	1800
[55]	44.5	55.5	–1.9756	2794.1	546.0	6.17	6	1550	1800
[56]	50.0	50.0	–3.5624	7036.1	–139.0		3	1600	2500
[51]	50.0	50.0	–2.8556	4627.3	211.0	4.46	12	1464	2101
[55]	50.3	49.7	–1.7451	2142.7	647.0	0.91	5	1600	1800

Note: Melt compositions are given in moles percent, σ[ΔT] is the standard deviation of temperature residuals, n is the number of data points used in fitting the VFT equation, T_{min} and T_{max} show the range of temperature in °C covered by the data.

TABLE 5.3.2.16B
Temperatures at Specified Viscosity Values (Poise) for $SrO:SiO_2$ Melts

			Temperature (°C) at which log (viscosity) is:								
	SrO	SiO_2	–0.60	–0.3	0.0	0.3	0.6	0.9	1.2	1.5	1.8
[55]	20.1	79.9									1737
[55]	25.5	74.5							1811	1688	1598
[55]	29.7	70.3						1743	1628	1525	
[55]	40.5	59.5					1735	1606			
[55]	44.5	55.5				1774	1631	1518			
[56]	50.0	50.0	2236	2018	1836	1683					
[51]	50.0	50.0		2022	1831	1677	1550	1443			
[55]	50.3	49.7				1695	1561				

Note: Calculated using the VFT equation with the parameters given in the previous table, melt compositions are given in moles percent.

5.3.3 Three-Component Melts

TABLE 5.3.3.1A
VFT Parameters for $K_2O:PbO:SiO_2$ Melts

	K_2O	PbO	SiO_2	A	B	T_o	$\sigma[\Delta T]$	n	T_{min}	T_{max}
[86]	20.0	10.0	70.0	–0.5403	3006.6	225.0	2.75	8	449	683
[33]	6.6	25.2	68.2	–1.6253	3858.4	201.0	5.18	14	740	1308
[33]	5.3	28.0	66.8	–1.7166	3915.2	180.0	7.44	17	734	1305
[33]	3.8	31.6	64.6	–1.8726	3788.2	188.0	11.26	14	698	1311
[33]	2.9	35.1	62.0	–1.7650	3303.9	214.0	4.39	14	690	1305
[86]	20.0	20.0	60.0	–0.7790	2772.4	207.0	0.51	6	408	523

Note: Melt compositions are given in moles percent, $\sigma[\Delta T]$ is the standard deviation of temperature residuals, n is the number of data points used in fitting the VFT equation, T_{min} and T_{max} show the range of temperature in °C covered by the data.

TABLE 5.3.3.1B
Temperatures (°C) at Specified Viscosity Values (Poise) for $K_2O:PbO:SiO_2$ Melts

				Temperature (°C) at which log (viscosity) is:								
	K_2O	PbO	SiO_2	2.0	3.0	4.0	5.0	7.6	8.0	10.0	12.0	13.0
[86]	20.0	10.0	70.0					594	577	510	465	447
[33]	6.6	25.2	68.2	1265	1035	887	783					

TABLE 5.3.3.1B (Continued)
Temperatures (°C) at Specified Viscosity Values (Poise) for K_2O:PbO:SiO_2 Melts

				Temperature (°C) at which log (viscosity) is:								
	K_2O	PbO	SiO_2	2.0	3.0	4.0	5.0	7.6	8.0	10.0	12.0	13.0
[33]	5.3	28.0	66.8	1233	1010	865	763					
[33]	3.8	31.6	64.6	1166	965	833	739					
[33]	2.9	35.1	62.0	1092	907	787	702					
[86]	20.0	20.0	60.0						523	464	424	408

Note: Calculated using the VFT equation with the parameters given in the previous table, melt compositions are given in moles percent.

TABLE 5.3.3.2A
VFT Parameters for Na_2O:Al_2O_3:SiO_2 Melts

	Na_2O	Al_2O_3	SiO_2	A	B	To	σ[ΔT]	n	T_{min}	T_{max}
[87]	12.3	12.5	75.2	–6.0900	18641.0	–273.0		3	1570	1680
[87]	9.5	15.4	75.1	–6.5000	18870.0	–273.0		3	1570	1680
[88]	25.0	0.0	75.0	–20.3370	24461.0	–273.0		3	455	533
[89]	25.0	0.0	75.0	–17.5494	22028.8	–273.0	3.19	5	463	569
[88]	21.9	3.1	75.0	–16.0610	24470.0	–273.0		3	562	666
[88]	18.8	6.3	75.0	–17.5000	24185.0	–273.0		3	514	606
[88]	15.6	9.4	75.0	–15.8370	24487.0	–273.0		3	569	675
[88]	13.8	11.3	75.0	–12.4150	24018.0	–273.0		3	663	799
[88]	12.5	12.5	75.0	–13.7080	29107.0	–273.0		3	807	955
[90]	12.5	12.5	75.0	–7.3187	21029.7	–273.0	1.22	6	1300	1425
[88]	11.3	13.8	75.0	–13.9810	29730.0	–273.0		3	819	967
[88]	10.0	15.0	75.0	–14.0110	29734.0	–273.0		3	818	965
[88]	8.8	16.3	75.0	–14.4790	30292.0	–273.0		3	819	964
[87]	11.1	14.0	74.9	–6.0500	18434.0	–273.0		3	1580	1690
[87]	19.9	5.4	74.7	–2.5700	8655.0	–273.0		3	1390	1590
[61]	22.4	3.1	74.6	–18.4094	23958.8	–273.0		3	478	601
[87]	16.1	9.6	74.3	–3.0900	10836.0	–273.0		3	1540	1680
[61]	20.1	6.1	73.9	–17.7776	24480.4	–273.0		3	510	641
[88]	23.3	3.3	73.3	–21.1810	25819.0	–273.0		3	477	555
[61]	24.5	3.3	72.1	–18.7333	24059.3	–273.0		3	473	595
[88]	21.4	7.1	71.4	–17.5030	24389.0	–273.0		3	520	614
[89]	25.0	3.8	71.2	–0.1044	2947.4	250.0	3.10	5	482	593
[91]	20.0	10.0	70.0	–0.9115	4496.3	242.0	1.82	8	627	800
[88]	19.7	10.6	69.7	–17.8690	26048.0	–273.0		3	564	662
[61]	25.4	6.3	68.3	–20.1979	25891.2	–273.0		3	495	614
[88]	17.7	14.5	67.7	–12.7000	24084.0	–273.0		3	655	788
[89]	25.0	7.5	67.5	–2.2813	5100.5	158.0	4.29	5	504	620
[87]	18.9	13.8	67.3	–3.9700	12576.0	–273.0		3	1460	1640

TABLE 5.3.3.2A (Continued)
VFT Parameters for Na_2O:Al_2O_3:SiO_2 Melts

	Na_2O	Al_2O_3	SiO_2	A	B	To	σ[ΔT]	n	T_{min}	T_{max}
[87]	27.9	4.9	67.2	–3.0700	8527.0	–273.0		3	1300	1460
[87]	15.0	17.9	67.1	–6.5000	18334.0	–273.0		3	1560	1680
[87]	15.0	17.9	67.1	–6.5000	18334.0	–273.0		3	1560	1680
[87]	11.0	21.9	67.1	–6.6000	17611.0	–273.0		3	1580	1670
[87]	22.9	10.3	66.8	–3.2800	9909.0	–273.0		3	1250	1500
[87]	13.8	19.4	66.8	–6.3300	17689.0	–273.0		3	1540	1690
[88]	16.7	16.7	66.7	–14.0540	28480.0	–273.0		3	770	911
[87]	16.3	17.2	66.5	–6.8300	18925.0	–273.0		3	1500	1660
[88]	16.1	17.8	66.1	–15.4850	31057.0	–273.0		3	808	946
[88]	15.5	19.0	65.5	–17.2500	32986.0	–273.0		3	809	937
[88]	14.3	21.4	64.3	–18.2180	33793.0	–273.0		3	801	925
[92]	10.0	26.3	63.8	3.3275	51.2	1409.0	6.47	7	1480	1600
[88]	13.0	24.1	63.0	–19.8050	35423.0	–273.0		3	799	915
[92]	9.5	28.8	61.7	2.7417	124.6	1451.0	5.21	6	1540	1640
[87]	18.5	21.3	60.2	–6.1800	16927.0	–273.0		3	1530	1650
[87]	33.9	6.0	60.1	–3.6800	9043.0	–273.0		3	1210	1470
[87]	17.0	22.9	60.1	–5.9800	16365.0	–273.0		3	1550	1660
[87]	28.1	11.9	60.0	–3.7000	10158.0	–273.0		3	1300	1510
[87]	20.1	19.9	60.0	–6.4900	17638.0	–273.0		3	1520	1640
[87]	24.1	16.3	59.6	–3.9300	11788.0	–273.0		3	1400	1600
[87]	22.1	22.1	55.8	–6.4200	17040.0	–273.0		3	1480	1630
[87]	29.8	19.8	50.4	–4.6600	12610.0	–273.0		3	1500	1620
[87]	24.7	25.2	50.1	–6.3200	16217.0	–273.0		3	1560	1670
[87]	35.1	14.9	50.0	–4.1900	10646.0	–273.0		3	1310	1500
[93]	25.0	25.0	50.0	1.5528	375.1	1374.0	5.39	4	1594	1728
[87]	23.0	27.6	49.4	–6.6500	16876.0	–273.0		3	1540	1650

Note: Melt compositions are given in moles percent, σ[ΔT] is the standard deviation of temperature residuals, n is the number of data points used in fitting the VFT equation, T_{min} and T_{max} show the range of temperature in °C covered by the data.

TABLE 5.3.3.2B
Temperatures at Specified Viscosity Values (Poise) for Na_2O:Al_2O_3:SiO_2 Melts

				Temperature (°C) at which log (viscosity) is:								
	Na_2O	Al_2O_3	SiO_2	2.0	2.5	3.0	3.5	5.0	9.0	10.0	11.0	12.0
[87]	12.3	12.5	75.2				1671					
[87]	9.5	15.4	75.1				1614					
[88]	25.0	0.0	75.0							533	508	483
[89]	25.0	0.0	75.0						557	527	499	472
[88]	21.9	3.1	75.0							666	631	599
[88]	18.8	6.3	75.0							606	576	547

TABLE 5.3.3.2B (Continued)
Temperatures at Specified Viscosity Values (Poise) for Na_2O:Al_2O_3:SiO_2 Melts

				Temperature (°C) at which log (viscosity) is:								
	Na_2O	Al_2O_3	SiO_2	2.0	2.5	3.0	3.5	5.0	9.0	10.0	11.0	12.0
[88]	15.6	9.4	75.0							675	639	607
[88]	13.8	11.3	75.0							799	753	711
[88]	12.5	12.5	75.0							955	905	859
[90]	12.5	12.5	75.0					1434				
[88]	11.3	13.8	75.0							967	917	871
[88]	10.0	15.0	75.0							965	916	870
[88]	8.8	16.3	75.0							964	916	871
[87]	11.1	14.0	74.9				1657					
[87]	19.9	5.4	74.7	1621	1434							
[61]	22.4	3.1	74.6						601	570	542	515
[87]	16.1	9.6	74.3		1665							
[61]	20.1	6.1	73.9						641	608	578	549
[88]	23.3	3.3	73.3							555	529	505
[61]	24.5	3.3	72.1						595	564	536	510
[88]	21.4	7.1	71.4							614	583	554
[89]	25.0	3.8	71.2						574	542	515	493
[91]	20.0	10.0	70.0						696	654		
[88]	19.7	10.6	69.7							662	629	599
[61]	25.4	6.3	68.3						614	584	557	531
[88]	17.7	14.5	67.7							788	743	702
[89]	25.0	7.5	67.5						610	573	542	515
[87]	18.9	13.8	67.3			1531						
[87]	27.9	4.9	67.2	1409								
[87]	15.0	17.9	67.1			1657	1560					
[87]	15.0	17.9	67.1			1657	1560					
[87]	11.0	21.9	67.1		1662	1561						
[87]	22.9	10.3	66.8		1441	1305						
[87]	13.8	19.4	66.8			1623	1526					
[88]	16.7	16.7	66.7							911	864	820
[87]	16.3	17.2	66.5			1652	1559					
[88]	16.1	17.8	66.1							946	900	857
[88]	15.5	19.0	65.5							937	895	855
[88]	14.3	21.4	64.3							925	884	845
[92]	10.0	26.3	63.8				1706					
[88]	13.0	24.1	63.0							915	877	841
[92]	9.5	28.8	61.7				1615					
[87]	18.5	21.3	60.2			1571						
[87]	33.9	6.0	60.1	1319	1190							
[87]	17.0	22.9	60.1		1657	1549						
[87]	28.1	11.9	60.0	1509	1365							
[87]	20.1	19.9	60.0			1586						
[87]	24.1	16.3	59.6		1560	1428						
[87]	22.1	22.1	55.8		1637	1536						
[87]	29.8	19.8	50.4	1620	1488							

TABLE 5.3.3.2B (Continued)
Temperatures at Specified Viscosity Values (Poise) for Na_2O:Al_2O_3:SiO_2 Melts

				Temperature (°C) at which log (viscosity) is:								
	Na_2O	Al_2O_3	SiO_2	2.0	2.5	3.0	3.5	5.0	9.0	10.0	11.0	12.0
[87]	24.7	25.2	50.1	1676	1566							
[87]	35.1	14.9	50.0	1447	1318							
[93]	25.0	25.0	50.0			1633						
[87]	23.0	27.6	49.4		1571							

Note: Calculated using the VFT equation with the parameters given in the previous table, melt compositions are given in moles percent.

TABLE 5.3.3.3A
VFT Parameters for Na_2O:B_2O_3:SiO_2 Melts

	Na_2O	B_2O_3	SiO_2	A	B	To	σ[ΔT]	n	T_{min}	T_{max}
[94]	25.0	0.0	75.0	–16.3451	21902.1	–273.0		3	591	665
[89]	25.0	0.0	75.0	–17.5494	22028.8	–273.0	3.19	5	463	569
[95]	20.0	5.0	75.0	–26.0223	30422.4	–273.0	1.23	4	506	571
[95]	8.0	17.0	75.0	–17.5743	27340.4	–273.0	2.75	4	620	717
[95]	4.0	21.0	75.0	–10.7295	21546.9	–273.0	2.96	4	635	765
[89]	25.0	3.8	71.3	–14.3530	19894.0	–273.0	12.99	5	496	585
[96]	6.8	22.7	70.5	–1.1572	3506.3	320.0	2.97	20	758	1301
[95]	20.0	10.0	70.0	–28.6306	34425.4	–273.0	0.47	4	554	618
[95]	15.0	15.0	70.0	–7.9008	7338.1	238.0	0.38	4	589	648
[95]	10.0	20.0	70.0	–13.8488	21858.9	–273.0	2.71	4	540	642
[95]	9.0	21.0	70.0	–25.0893	30267.7	–273.0	1.31	4	521	589
[95]	8.0	22.0	70.0	–23.3987	32893.2	–273.0	1.56	4	630	711
[95]	7.0	23.0	70.0	–15.1294	25273.3	–273.0	1.23	4	625	732
[95]	6.0	24.0	70.0	–20.6812	30382.7	–273.0	2.34	4	628	716
[95]	4.0	26.0	70.0	–11.4505	20732.4	–273.0	2.52	4	574	692
[95]	2.0	28.0	70.0	–8.8330	17129.7	–273.0	4.18	4	510	634
[94]	33.0	0.0	67.0	–2.4246	3930.1	205.0		3	549	622
[97]	15.0	20.0	65.0	–0.6203	2000.7	472.0	4.10	7	774	1024
[95]	8.0	27.0	65.0	–17.3069	27728.2	–273.0	2.39	4	641	741
[95]	4.0	31.0	65.0	–4.9599	14037.6	–273.0	6.97	4	506	661
[89]	25.0	11.3	63.8	–10.9099	9771.4	109.0	0.90	5	535	610
[97]	23.4	15.0	61.6	–1.3401	2329.1	395.0	1.17	7	713	932
[94]	30.0	10.0	60.0	–5.0000	4368.0	265.0		3	577	629
[95]	25.0	15.0	60.0	–29.5410	34172.0	–273.0	0.53	4	530	591
[95]	22.0	18.0	60.0	–25.3044	31163.0	–273.0	1.26	4	540	609
[95]	20.0	20.0	60.0	–25.1569	24958.4	–87.0	0.43	4	567	623
[95]	17.0	23.0	60.0	–24.6140	31262.8	–273.0	0.33	4	558	630
[95]	15.0	25.0	60.0	–23.6284	29881.6	–273.0	1.64	4	542	615
[95]	13.0	27.0	60.0	–25.9434	31246.8	–273.0	0.72	4	529	596
[95]	12.0	28.0	60.0	–18.9104	24978.9	–273.0	1.79	4	509	590

TABLE 5.3.3.3A (Continued)
VFT Parameters for Na_2O:B_2O_3:SiO_2 Melts

	Na_2O	B_2O_3	SiO_2	A	B	To	σ[ΔT]	n	T_{min}	T_{max}
[95]	10.0	30.0	60.0	–6.6188	15004.3	–273.0	4.65	4	490	627
[95]	9.0	31.0	60.0	–3.8899	13144.4	–273.0	13.85	4	500	665
[95]	8.0	32.0	60.0	–14.5526	23878.9	–273.0	4.36	4	592	699
[95]	7.0	33.0	60.0	–10.0133	19395.9	–273.0	5.06	4	568	693
[95]	6.0	34.0	60.0	–10.0620	19015.1	–273.0	3.38	4	550	673
[95]	4.0	36.0	60.0	2.3130	3149.3	198.0	4.24	4	494	607
[95]	2.0	38.0	60.0	–10.4416	16862.3	–273.0	3.23	4	445	550
[95]	1.0	39.0	60.0	–4.5620	11469.2	–273.0	5.71	4	378	511
[97]	31.7	10.0	58.3	0.2211	1254.5	459.0	1.69	7	675	911
[89]	25.0	18.8	56.3	–13.6640	10920.7	113.0	2.06	5	510	611
[97]	40.0	5.0	55.0	–0.2790	1804.2	334.0	3.10	7	621	885
[97]	20.0	25.0	55.0	–1.3368	2283.4	424.0	1.37	7	734	951
[95]	10.0	35.0	55.0	–7.6797	16252.5	–273.0	5.26	4	511	643
[95]	8.0	37.0	55.0	–30.2799	38410.0	–273.0	1.06	4	614	680
[95]	4.0	41.0	55.0	–7.4018	14776.8	–273.0	3.49	4	450	574
[95]	3.0	42.0	55.0	–7.5289	14279.6	–273.0	4.26	4	421	539
[94]	27.0	20.0	53.0	–31.4433	34984.3	–273.0		3	592	637
[97]	28.5	20.0	51.5	–0.1938	1373.6	460.0	3.70	6	683	891
[95]	5.0	45.0	50.0	–11.0588	18267.3	–273.0	2.78	4	485	593
[89]	25.0	26.3	48.7	–4.0495	3694.8	309.0	1.09	5	533	611
[97]	36.7	15.0	48.3	–0.6129	1439.1	472.0	1.39	7	689	870
[94]	23.0	30.0	47.0	–37.6165	40616.1	–273.0		3	598	637
[94]	45.0	10.0	45.0	–4.2131	4518.9	291.0		3	633	694
[94]	45.0	10.0	45.0	–10.0000	5814.0	150.0		3	456	492
[97]	25.0	30.0	45.0	–1.2272	1807.3	447.0	1.21	7	696	875
[97]	30.0	27.0	43.0	–1.6164	1930.3	429.0	1.42	7	682	848
[97]	33.3	25.0	41.7	–1.6943	2056.1	413.0	1.31	7	681	851
[89]	25.0	33.8	41.2	–14.6741	10385.9	139.0	1.79	5	521	587
[94]	40.0	20.0	40.0	–2.3549	1646.5	344.0		3	489	520
[94]	20.0	40.0	40.0	–35.4883	38806.9	–273.0		3	599	640
[94]	35.0	30.0	35.0	–41.2442	40057.4	–273.0		3	524	557
[97]	30.0	35.0	35.0	–1.0189	1334.8	443.0	1.75	7	635	775
[89]	25.0	41.2	33.8	–43.4392	46651.7	–327.0	1.52	5	496	570
[94]	17.0	50.0	33.0	–16.0000	13800.0	4.0		3	556	604
[94]	17.0	50.0	33.0	–26.9148	29847.5	–273.0		3	558	607
[94]	25.0	50.0	25.0	–37.3011	38991.6	–273.0		3	569	607
[94]	25.0	50.0	25.0	–41.1243	42431.7	–273.0		3	573	608
[94]	20.0	60.0	20.0	–34.3340	34983.2	–273.0		3	534	573
[95]	15.0	65.0	20.0	–30.6091	30149.9	–273.0	0.81	4	418	469
[95]	10.0	70.0	20.0	6.3129	307.5	341.0	2.72	4	388	424
[95]	5.0	75.0	20.0	–56.3883	42486.5	–273.0	0.93	4	339	367

Note: Melt compositions are given in moles percent, σ[ΔT] is the standard deviation of temperature residuals, n is the number of data points used in fitting the VFT equation, T_{min} and T_{max} show the range of temperature in °C covered by the data.

TABLE 5.3.3.3B
Temperatures at Specified Viscosity Values (Poise) for Na_2O:B_2O_3:SiO_2 Melts

				Temperature (°C) at which log (viscosity) is								
	Na_2O	B_2O_3	SiO_2	3.0	4.5	6.0	7.0	9.0	10.0	11.0	12.0	13.0
[94]	25.0	0.0	75.0				665	591				
[89]	25.0	0.0	75.0					557	527	499	472	
[95]	20.0	5.0	75.0						572	549	527	507
[95]	8.0	17.0	75.0						719	684	651	621
[95]	4.0	21.0	75.0						766	719	675	635
[89]	25.0	3.8	71.3					579	544	512		
[96]	6.8	22.7	70.5	1163	940	810						
[95]	20.0	10.0	70.0						618	596	574	554
[95]	15.0	15.0	70.0						648	626	607	589
[95]	10.0	20.0	70.0						644	607	573	541
[95]	9.0	21.0	70.0						590	566	543	522
[95]	8.0	22.0	70.0						712	683	656	631
[95]	7.0	23.0	70.0						733	694	659	625
[95]	6.0	24.0	70.0						717	686	657	629
[95]	4.0	26.0	70.0						694	650	611	575
[95]	2.0	28.0	70.0						637	591	549	512
[94]	33.0	0.0	67.0				622	549				
[97]	15.0	20.0	65.0	1025	863	774						
[95]	8.0	27.0	65.0						742	707	673	642
[95]	4.0	31.0	65.0						665	607	555	509
[89]	25.0	11.3	63.8					600	576	555	536	
[97]	23.4	15.0	61.6	932	794	712						
[94]	30.0	10.0	60.0				629	577				
[95]	25.0	15.0	60.0						591	570	550	530
[95]	22.0	18.0	60.0						610	585	562	541
[95]	20.0	20.0	60.0						623	603	585	567
[95]	17.0	23.0	60.0						630	605	581	558
[95]	15.0	25.0	60.0						616	590	566	543
[95]	13.0	27.0	60.0						596	573	551	529
[95]	12.0	28.0	60.0						591	562	535	510
[95]	10.0	30.0	60.0						630	579	533	492
[95]	9.0	31.0	60.0							610	554	505
[95]	8.0	32.0	60.0						700	662	626	594
[95]	7.0	33.0	60.0						696	650	608	570
[95]	6.0	34.0	60.0						675	630	589	552
[95]	4.0	36.0	60.0						608	561	523	493
[95]	2.0	38.0	60.0						552	513	478	446
[95]	1.0	39.0	60.0						515	464	419	380
[97]	31.7	10.0	58.3	910	752	676						
[89]	25.0	18.8	56.3					595	574	556	539	523
[97]	40.0	5.0	55.0	884	712	621						
[97]	20.0	25.0	55.0	951	815	735						

TABLE 5.3.3.3B (Continued)
Temperatures at Specified Viscosity Values (Poise) for Na_2O:B_2O_3:SiO_2 Melts

				Temperature (°C) at which log (viscosity) is								
	Na_2O	B_2O_3	SiO_2	3.0	4.5	6.0	7.0	9.0	10.0	11.0	12.0	13.0
[95]	10.0	35.0	55.0						646	597	553	513
[95]	8.0	37.0	55.0						681	657	635	614
[95]	4.0	41.0	55.0						576	530	489	451
[95]	3.0	42.0	55.0						542	498	458	423
[94]	27.0	20.0	53.0				637	592				
[97]	28.5	20.0	51.5	890	753	682						
[95]	5.0	45.0	50.0						594	555	519	486
[89]	25.0	26.3	48.7					592	572	555	539	
[97]	36.7	15.0	48.3	870	753	690						
[94]	23.0	30.0	47.0				637	598				
[94]	45.0	10.0	45.0				694	633				
[94]	45.0	10.0	45.0				492	456				
[97]	25.0	30.0	45.0	875	763	697						
[97]	30.0	27.0	43.0	847	745	682						
[97]	33.3	25.0	41.7	851	745	680						
[89]	25.0	33.8	41.2					578	560	544	528	
[94]	40.0	20.0	40.0				520	489				
[94]	20.0	40.0	40.0				640	599				
[94]	35.0	30.0	35.0				557	524				
[97]	30.0	35.0	35.0	775	685	633						
[89]	25.0	41.2	33.8					563	546	530	514	500
[94]	17.0	50.0	33.0				604	556				
[94]	17.0	50.0	33.0				607	558				
[94]	25.0	50.0	25.0				607	569				
[94]	25.0	50.0	25.0				609	574				
[94]	20.0	60.0	20.0				573	534				
[95]	15.0	65.0	20.0						469	452	435	418
[95]	10.0	70.0	20.0						424	407	395	
[95]	5.0	75.0	20.0						367	357	348	339

Note: Calculated using the VFT equation with the parameters given in the previous table, melt compositions are given in moles percent.

TABLE 5.3.3.4A
VFT Parameters for Na_2O:CaO:SiO_2 Melts

	Na_2O	CaO	SiO_2	A	B	To	σ[ΔT]	n	T_{min}	T_{max}
[72], [98]	15.0	5.0	80.0	–2.1182	5543.1	134.0		3	1040	1480
[72], [98]	4.6	18.4	77.0	–13.2968	15920.8	53.0	2.53	6	657	802
[61]	19.9	4.1	76.0	–19.7380	25304.0	–273.0		3	488	607
[61]	14.5	9.6	75.9	–26.4620	32525.0	–273.0		3	540	644.
[61]	9.3	15.0	75.7	–24.4340	32665.0	–273.0		3	588	703.
[61]	24.8	0.0	75.2	–17.8480	22759.0	–273.0		3	453	574.
[99], [100]	14.8	10.0	75.2	–1.5385	3981.3	274.0	0.72	7	707	1399
[72], [98]	20.0	5.0	75.0	–1.4928	4126.3	215.0	2.14	12	498	1395
[72], [98]	15.0	10.0	75.0	–1.5574	4123.0	262.0	1.69	12	543	1420
[15]	12.5	12.5	75.0	–1.3248	3781.4	313.0	1.04	28	805	1352
[72], [98]	10.0	15.0	75.0	–2.0017	4654.4	277.0	1.94	8	585	1440
[72], [98]	5.0	20.0	75.0	–7.9415	12148.6	78.0	1.05	6	658	840
[99], [100]	13.3	12.2	74.5	–1.4415	3902.5	298.0	0.94	7	728	1432
[101]	20.2	6.8	73.1	–1.7632	4203.5	222.0	8.22	20	469	1346
[101]	18.7	8.9	72.4	–1.8180	4234.8	235.0	8.54	20	482	1352
[102]	18.1	9.7	72.2	–1.5881	4347.4	222.0	6.41	11	600	1400
[103]	23.4	5.6	71.0	–3.7351	9182.0	–273.0	2.71	9	1000	1400
[61]	24.1	5.2	70.7	–19.6640	24781.0	–273.0		3	474	592
[101]	20.3	9.1	70.6	–1.8076	4124.5	237.0	7.65	20	479	1325
[72], [98]	25.0	5.0	70.0	–1.4271	3648.3	227.0	1.73	12	479	1290
[104]	20.4	9.6	70.0	–1.5400	3751.4	263.0	3.89	17	500	1300
[86]	20.0	10.0	70.0	–1.1553	3332.8	291.0	2.19	10	526	1346
[72], [98]	20.0	10.0	70.0	–1.5422	3723.9	259.0	3.57	12	515	1310
[72], [98]	15.0	15.0	70.0	–1.4967	3546.0	313.0	2.89	12	556	1325
[72], [98]	10.0	20.0	70.0	–2.0252	4088.0	334.0	3.11	7	606	1350
[61]	20.7	9.5	69.8	–26.3370	31055.0	–273.0		3	506.6	606
[61]	23.4	10.3	66.3	–26.2690	30523.0	–273.0		3	494.5	592
[61]	19.9	15.0	65.2	–29.3840	34262.0	–273.0		3	525.9	620
[72], [98]	30.0	5.0	65.0	–1.3611	3441.2	226.0	2.39	12	464	1250
[72], [98]	25.0	10.0	65.0	–1.4047	3478.6	252.0	4.91	12	492	1275
[72], [98]	20.0	15.0	65.0	–1.3239	3332.9	296.0	3.80	9	525	1300
[72], [98]	15.0	20.0	65.0	–1.2785	3191.3	349.0	13.16	7	570	1325
[61]	23.4	15.2	61.4	–30.5000	34115.0	–273.0		3	502.3	591
[61]	19.1	19.7	61.3	–31.1390	36080.0	–273.0		3	535.3	626
[72], [98]	35.0	5.0	60.0	–2.0036	3811.5	186.0	4.49	9	437	1140
[86]	30.0	10.0	60.0	–0.9813	2618.3	291.0	7.69	9	479	1165
[72], [98]	30.0	10.0	60.0	–2.0433	3825.2	212.0	5.13	8	465	1160
[86]	20.0	20.0	60.0	–1.5917	3132.9	327.0	3.69	8	543	1198
[72], [98]	25.0	25.0	50.0	–2.1855	4007.8	229.0	11.81	7	488	1190

Note: Melt compositions are given in moles percent, σ[ΔT] is the standard deviation of temperature residuals, n is the number of data points used in fitting the VFT equation, T_{min} and T_{max} show the range of temperature in °C covered by the data.

TABLE 5.3.3.4B
Temperatures at Specified Viscosity Values (Poise) for Na_2O:CaO:SiO_2 Melts

				Temperature (°C) at which log (viscosity) is:								
	Na_2O	CaO	SiO_2	2.0	3.0	4.0	5.0	6.0	7.6	10.0	12.0	13.0
[72], [98]	15.0	5.0	80.0	1480	1217	1040						
[72], [98]	4.6	18.4	77.0							736	682	658
[61]	19.9	4.1	76.0							578	524	500
[61]	14.5	9.6	75.9							619	573	551
[61]	9.3	15.0	75.7							676	624	600
[61]	24.8	0.0	75.2							544	489	465
[99], [100]	14.8	10.0	75.2	1399	1151	993	883	802	710			
[72], [98]	20.0	5.0	75.0	1396	1133	966	851	766	669	574	521	500
[72], [98]	15.0	10.0	75.0	1421	1167	1004	891	808	712	619	566	545
[15]	12.5	12.5	75.0		1187	1023	911	829				
[72], [98]	10.0	15.0	75.0	1440	1208	1053	942	859	762	665	609	587
[72], [98]	5.0	20.0	75.0							755	687	658
[99], [100]	13.3	12.2	74.5	1432	1177	1015	904	822	730			
[101]	20.2	6.8	73.1	1339	1105	951	844	763	671	579	527	507
[101]	18.7	8.9	72.4	1344	1114	963	856	777	685	593	541	521
[102]	18.1	9.7	72.2		1170	1000	882	795	695	597		
[103]	23.4	5.6	71.0	1328	1090							
[61]	24.1	5.2	70.7							562	510	486
[101]	20.3	9.1	70.6	1320	1095	947	843	765	675	586	536	516
[72], [98]	25.0	5.0	70.0	1292	1051	899	795	718	631	546	499	480
[104]	20.4	9.6	70.0	1323	1089	940	837	761	673	588	540	521
[86]	20.0	10.0	70.0	1347	1093	937	832	757	672	590	544	526
[72], [98]	20.0	10.0	70.0	1310	1079	931	828	753	666	582	534	515
[72], [98]	15.0	15.0	70.0	1327	1102	958	859	786	703	621	576	558
[72], [98]	10.0	20.0	70.0	1350	1148	1012	916	843	759	674	625	606
[61]	20.7	9.5	69.8							582	537	516
[61]	23.4	10.3	66.3							569	525	504
[61]	19.9	15.0	65.2							597	555	535
[72], [98]	30.0	5.0	65.0	1250	1015	868	767	693	610	529	484	466
[72], [98]	25.0	10.0	65.0	1274	1042	896	795	722	638	557	512	493
[72], [98]	20.0	15.0	65.0	1299	1067	922	823	751	669	590	546	529
[72], [98]	15.0	20.0	65.0	1322	1095	954	857	787	708	632	589	573
[61]	23.4	15.2	61.4							569	530	511
[61]	19.1	19.7	61.3							604	563	544
[72], [98]	35.0	5.0	60.0	1138	948	821	730	662	583	504	458	440
[86]	30.0	10.0	60.0	1169	949	817	729	666	596	529	493	478
[72], [98]	30.0	10.0	60.0	1158	970	845	755	688	609	530	484	466
[86]	20.0	20.0	60.0	1199	1009	887	802	740	668	597	558	542
[72], [98]	25.0	25.0	50.0	1187	1002	877	787	719	639	558	512	493

5.3.4 Complex and Commercial Glass Systems

TABLE 5.3.4.1A
Compositions of Glass Melts in Moles Percent

	SiO_2	Na_2O	K_2O	Li_2O	CaO	MgO	BaO	ZnO	PbO	Al_2O_3	Fe_2O_3	B_2O_3	GeO_2	TiO_2	ZrO_2
Aluminosilicate (EZ-1)–[105]	64.00	1.30	0.70	0.00	8.90	10.20	0.00	0.00	0.00	10.400	0.000	4.50	0.00	0.00	0.00
Borosilicate for cookware (KG-33)–[105]	81.00	4.00	0.00	0.00	0.00	0.00	0.00	0.00	0.00	2.000	0.000	13.00	0.00	0.00	0.00
Soda-lime window glass (R-6)–[105]	72.60	15.20	0.00	0.00	4.60	3.60	0.00	0.00	0.00	1.700	0.000	0.80	0.00	0.00	0.00
Alkali lead lamp glass (KG-1)–[105]	77.00	9.00	5.00	0.00	1.00	0.00	0.00	0.00	8.00	0.000	0.000	0.00	0.00	0.00	0.00
Corning crown #8361–[15]	67.50	8.06	9.23	0.00	8.55	0.00	0.00	3.35	0.00	2.240	0.000	0.00	0.00	0.46	0.00
Borosilicate–[20]	80.04	4.12	0.24	0.00	0.00	0.00	0.00	0.00	0.00	2.070	0.061	13.20	0.00	0.04	0.00
Sheet (all results)–[20]	72.76	12.86	0.67	0.00	8.11	3.81	0.00	0.00	0.00	1.360	0.069	0.00	0.00	0.05	0.00

TABLE 5.3.4.1B
VFT Parameters and Temperatures at Specified Viscosity Values

								Temperature (°C) at which log (viscosity) is:													
	A	B	To	σ(ΔT)	n	T_{min}	T_{max}	2	2.5	3	4	5	6	7.6	8	9	10	11	12	13	13.5	14
Aluminosilicate (EZ-1)–[105]	–2.5015	5347.7	381.0	8.81	10	695	1400			1353	1204	1094	1010	910	890	846	809	777	750	726	715	705
Borosilicate for cookware (KG-33)–[105]	–1.0836	5433.1	179.0	9.12	9	531	1400				1248	1072	946	805	777	718	669	629	594	565	552	539
Soda-lime window glass (R-6)–[105]	–1.6085	4159.3	242.0	4.18	11	505	1400	1395	1254	1145	984	871	789	694	675	634	600	572	548	527	517	508
Alkali lead lamp glass (KG-1)–[105]	–1.7188	5056.5	94.0	10.78	11	408	1400		1293	1166	978	847	749	637	614	566	525	492	463	438	426	416
Corning crown #8361–[15]	–1.6954	4518.1	243.0	0.81	30	800	1349		1320	1205	1036	918	830									
Borosilicate–[20]	–1.4607	5641.0	180.0	12.09	36	516	1447			1445	1213	1053	936	803	776	719	672	633	599	570	557	545
Sheet (all results)–[20]	–1.9072	4838.5	225.0	6.99	86	514	1449		1323	1211	1044	926	837	734	713	669	631	600	573	550	539	529

5.3.5 CALCULATION OF VISCOSITY FROM COMPOSITION

Some compositional correlations are given in the tables that follow. The calculation has the general form:

$$\{\text{parameter}\} = \Sigma\ \{\text{coefficient}\} \times \{\text{concentration}\}$$

where the {parameter} may be one of the VFT coefficients or the temperature at which log (viscosity) has a particular value and the summation is over all the components in the melt. In each case the method of expressing concentration is described — for present purposes, simple weight ratios are preferred and in some cases coefficients have been adapted from those given in the original publication. The range of concentration covered in the original viscosity measurements has also been given for each component in the tables, specified in weight percent. Use of the equations outside the ranges covered by measurement is likely to give uncertain results.

The VFT equation is used here with the following form and conventions:

$$\log \eta = A + B/(T - T_o)$$

where η is the viscosity expressed in poise (or dPa.s); T, T_o are temperatures in degrees Celsius; A, B are parameters having appropriate units; and logarithms are to base 10.

It is worth noting that when the equation is expressed in this way the coefficient A is usually a negative number.

TABLE 5.3.5.1
Soda-Lime-Silica Family of Glasses — Oksoy and Colleagues [25]

Component	From (wt %)	To (wt %)	A	B	To
SiO_2	59.55	77.53	–1.572	5914	182.7
Na_2O	10.41	15.27	1.617	–6078	–11.5
K_2O	0.02	8.7	–0.419	–1020	–201.4
MgO	0.0	3.92	–7.724	8697	–511.9
CaO	7.52	13.32	–1.314	–4900	651.4
Al_2O_3	0.0	8.26	1.003	1242	184.1
Fe_2O_3	0.0	0.88	–26.76	40180	–3074.0
TiO_2	0.0	0.04	–781.2	1502000	–265700.0
SO_3	0.0	0.23	194.4	–334800	24020.0

Note: These factors are used to calculate the parameters of the VFT equation. For calculation, concentrations are expressed as weight per weight of SiO_2. The original measurements were in the viscosity range 10^2 to 10^7 poise.

TABLE 5.3.5.2
Soda-Lime-Silica Family of Glasses — Lakatos and Colleagues [106]

Component	From (wt %)	To (wt %)	A	B	To
SiO_2	59.52	77.02	–1.713	6237.013	149.4
Li_2O	0.0	3.0	3.180	–11518	–1329
Na_2O	10.41	17.0	1.620	–6601	50
K_2O	0.0	8.7	–0.660	–541	–236
MgO	0.0	6.0	–5.890	5621	–212
CaO	4.48	13.0	–0.640	–6063	771
ZnO	0.0	9.38	–1.60	–376	96
BaO	0.0	16.54	–0.260	–2103	109
PbO	0.0	12.22	0.500	–2544	82
Al_2O_3	0.0	8.26	0.870	1521	140
B_2O_3	0.0	14.37	4.650	–15511	1203
$[B_2O_3]^2$	–	–	–16.27	40999	–2765

Note: These factors are used to calculate the parameters of the VFT equation. For calculation, concentrations are expressed as weight per weight of SiO_2. Note that there are both first and second order terms for B_2O_3. The original measurements were in the viscosity range 10^2 to 10^7 poise.

TABLE 5.3.5.3
Soda- Lime-Silica Family of Glasses — Lakatos and Colleagues [107]

Component	From (wt %)	To (wt %)	$\eta = 10^{2.0}$	$\eta = 10^{4.0}$	$\eta = 10^{6.0}$
SiO_2	59.52	77.02	+1847.8	+1249.7	+962.9
Li_2O	0.0	3.0	–3554	–3004	–2645
Na_2O	10.41	17.0	–1265	–919	–706
K_2O	0.0	8.7	–593	–417	–353
MgO	0.0	6.0	–587	–12	+91
CaO	4.48	13.0	–1127	–399	–74
ZnO	0.0	9.38	–537	–188	–71
BaO	0.0	16.54	–567	–304	–188
PbO	0.0	12.22	–485	–317	–224
Al_2O_3	0.0	8.26	+832	+523	+401
B_2O_3	0.0	14.37	–2162	–1197	–642
$[B_2O_3]^2$	–	–	+5122	+3182	+1900
Std devn.	–	–	*4.6°C*	*3.3°C*	*3.1°C*

Note: These factors are used to calculate temperatures (°C) for the specified viscosities. For calculation, concentrations are expressed as weight per weight of SiO_2. Note that there are both first and second order terms for B_2O_3. The original measurements were in the viscosity range 10^2 to 10^7 poise.

TABLE 5.3.5.4
Soda-Lime-Silica Family of Glasses — Braginskii [24]

Component	From (wt %)	To (wt %)	$\eta = 10^{3.0}$	$\eta = 10^{5.0}$	$\eta = 10^{7.0}$	$\eta = 10^{9.0}$	$\eta = 10^{11.0}$	$\eta = 10^{13.0}$
			+1659.2	+1178.4	+900.6	+757.5	+682.2	+606.0
Na_2O	12	16	–22.70	–14.79	–10.67	–8.88	–7.89	–6.31
MgO	0	5	–7.13	–1.33	+1.55	+2.15	+1.14	–0.83
CaO	5	12	–15.68	–6.47	–0.89	+1.98	+3.06	+3.27
Al_2O_3	0	5	+6.46	+5.26	+4.33	+3.72	+3.49	+3.72

Note: These factors are used to calculate temperatures (°C) for the specified viscosities. For calculation, concentrations are expressed as weight percent. SiO_2 content is not specified in the calculation, the first coefficient in each column being a constant term. The original measurements were in the viscosity range 10^3 to 10^{13} poise.

TABLE 5.3.5.5
Soda-Lime-Silica Family of Glasses — Rodriguez Cuartas [24]

Component	From (wt %)	to (wt %)	$\eta = 10^{2.0}$	$\eta = 10^{3.0}$	$\eta = 10^{4.0}$	$\eta = 10^{7.6}$	$\eta = 10^{13.0}$
SiO_2	62.7	72.8	+1715.52	+1472.79	+1254.20	+822.37	+569.91
Na_2O	5.7	15.4	–794.97	–1065.63	–931.13	–514.08	–369.05
K_2O	0.0	4.4	+123.42	–240.40	–357.53	–200.07	–45.10
MgO	0.0	5.0	–373.46	–202.70	–83.26	–35.40	+168.93
CaO	4.8	12.2	–857.51	–595.98	–430.87	+2.03	–289.34
BaO	0.0	2.8	+171.78	–112.01	–220.02	+344.80	–222.01
Al_2O_3	0.1	5.5	+485.25	+365.58	+408.58	+117.37	+121.58
B_2O_3	0.0	8.7	–1796.89	–1218.56	–926.75	–459.96	+150.79
Fe_2O_3	0.0	1.6	–610.70	–90.16	–125.42	–680.17	–128.38

Note: These factors are used to calculate temperatures (°C) for the specified viscosities. For calculation, concentrations are expressed as weight percent. The original measurements were in the viscosity range 10^2 to 10^{13} poise.

TABLE 5.3.5.6
Soda-Lime-Silica Family of Glasses — Ledererova and Colleagues [24]

Component	From (wt %)	To (wt %)	$\eta = 10^{2.0}$	$\eta = 10^{4.0}$	$\eta = 10^{7.6}$	$\eta = 10^{13.1}$
			+2066.54	+1338.91	+842.86	+628.80
Na_2O	10.3	16.5	–24.4210	–15.3762	–9.1468	–8.1180
K_2O	0.0	4.8	–15.5020	–9.8774	–7.0140	–9.3102
MgO	0.0	4.7	–12.0313	–3.7000	+1.3107	–1.0150
CaO	4.5	11.4	–20.5830	–7.4880	+0.7546	+2.1924
BaO	0.0	4.5	–42.5734	–12.2447	–2.1822	–0.5139
Al_2O_3	0.0	6.1	+10.5717	+7.0814	+4.0423	+4.7720
Fe_2O_3	0.0	0.9	–29.6283	–6.3061	+2.2512	–6.4359
SO_3	0.0	0.44	–14.3538	+10.5308	+5.5364	+11.7038

Note: These factors are used to calculate temperatures (°C) for the specified viscosities. For calculation, concentrations are expressed as weight percent. SiO_2 content is not specified in the calculation, the first coefficient in each column being a constant term. The original measurements were in the viscosity range 10^2 to 10^{13} poise.

TABLE 5.3.5.7
Borosilicate Glasses for Fiberizing — Lakatos and Colleagues [108]

Component	From (wt %)	To (wt %)	$\eta = 10^{2.0}$	$\eta = 10^{4.0}$	$\eta = 10^{6.0}$
SiO_2	40.3	56.1	+1858.5	1253.5	984.4
Li_2O	0.0	0.5	–2063.26	–2308.76	–1958.36
Na_2O	0.23	5.6	–307.95	–558.06	–668.57
MgO	0.0	5.8	–1591.85	–629.81	–114.27
CaO	17.6	36.0	–1397.66	–528.02	–151.68
Al_2O_3	10.0	19.3	+176.62	+241.63	+233.19
B_2O_3	2.3	9.7	–497.57	–399.17	–408.15
$[CaO]^2$	–	–	+771.57	+241.39	+36.13
[CaO]×[MgO]	–	–	+1696.61	+586.24	+1.54
std devn.	–	–	*14.7°C*	*9.5°C*	*14.1°C*

Note: These factors are used to calculate temperatures (°C) for the specified viscosities. For calculation, concentrations are expressed as weight per weight of SiO_2. Note that there are both first and second order terms for CaO and a term expressing interaction between CaO and MgO. The original measurements were in the viscosity range 10^2 to 10^7 poise.

TABLE 5.3.5.8
Lead Crystal Family of Glasses–Lakatos and Colleagues [109], [110]

Component	From (wt %)	To (wt %)	$\eta = 10^{2.5}$	$\eta = 10^{3.5}$	$\eta = 10^{4.5}$
SiO_2	52.0	62.2	1661.2	1346.6	1133.5
Li_2O	0.0	0.73	–3227.74	–2909.46	–2713.10
Na_2O	1.1	4.6	–1925.60	–1691.69	–1462.40
K_2O	10.0	16.3	–803.36	–601.78	–473.21
MgO	0.0	3.2	+833.59	+967.82	+984.43
CaO	0.0	8.58	–511.20	–206.40	+10.20
ZnO	0.0	5.2	+287.74	+388.44	+437.57
BaO	0.0	4.7	–247.99	–175.43	–128.63
SrO	0.0	4.31	–539.00	–324.44	–159.45
PbO	23.1	31.1	–299.31	–224.51	–175.10
B_2O_3	0.0	3.37	–1436.99	–785.15	–251.57
Std devn.	–	–	*7.9°C*	*6.0°C*	*5.0°C*

Note: These factors are used to calculate temperatures (°C) for the specified viscosities. For calculation, concentrations are expressed as weight per weight of SiO_2. The original measurements were in the viscosity range 10^2 to 10^6 poise.

TABLE 5.3.5.9
Crystal Family of Glasses — Lakatos and Colleagues [111]

Component	From (wt %)	To (wt %)	$\eta = 10^{2.0}$	$\eta = 10^{4.0}$	$\eta = 10^{6.0}$
SiO_2	59.3	73.7	1775.15	1231.7	964.1
Li_2O	0.0	1.09	–2786.22	–2771.90	–2573.42
Na_2O	1.4	14.19	–1437.82	–1150.01	–948.72
K_2O	0.0	18.2	–693.79	–531.35	–446.25
CaO	0.0	12.24	–544.93	–55.60	+179.85
ZnO	0.0	9.39	–199.70	+9.57	+62.97
BaO	0.0	16.54	–364.65	–187.14	–103.33
PbO	0.0	12.22	–291.75	–209.73	–123.19
Al_2O_3	0.0	5.36	+1132.87	+756.43	+577.49
B_2O_3	0.0	5.92	–1610.46	–898.11	–470.45
std devn.	–	–	*5.8°C*	*5.1°C*	*4.6°C*

Note: These factors are used to calculate temperatures (°C) for the specified viscosities. For calculation, concentrations are expressed as weight per weight of SiO_2. The original measurements were in the viscosity range 10^2 to 10^7 poise.

ACKNOWLEDGMENTS

The author wishes to thank Dr. A. Ledwith, Director of Research, and Dr. P. Sewell, Head of Advanced Glass Technology at the Pilkington Technology Centre, Lathom, for making possible the writing of this chapter, and also to acknowledge help given by colleagues at the same center.

REFERENCES

1. H. Rawson, *Inorganic Glassforming Systems* (1970) Academic Press.
2. Isaac Newton, *Principia* (1686) published by S. Pepys of London.
3. Stuart Winston Churchill, *Viscous Flows: the Practical use of Theory* (1988) Butterworth.
4. Bird, Stewart and Lightfoot, *Transport Phenomena,* (1966) Wiley.
5. J. Poiseuille, *Sci., Math. Phys.,* (1846) **9** 433.
6. B.S. Massey, *Mechanics of Fluids,* (1989) Van Nostrand Reinhold.
7. M. Cable, *Classical Glass Technology,* chapter 1 in *Glasses and Amorphous Materials,* J. Zarzycki (Ed.), Volume 9 of the series *Materials Science and Technology* (1994) published by VCH.
8. L.D. Pye, H.J. Stevens, W.C. LaCourse (Eds.), *Introduction to Glass Science,* (1972) Plenum Press.
9. C.L. Babcock, *Silicate Glass Technology Methods,* (1977) John Wiley & Sons.
10. S. Glasstone, *Textbook of Physical Chemistry* MacMillan & Co., London, (1962).
11. G.S. Fulcher *J. Am. Ceram. Soc.* (1925) **8** (6) 339–355.
12. H. Vogel, *Phys.Z.,* (1921) **22** 645.
13. G. Tamman, W. Hesse, *Z. Anor. Allgem. Chem.,* (1926) **156** 245.
14. E. Plumat *Proceedings IVth International Congress on Glass* (1956) 299–309, Commission International du Verre, Paris.
15. E.H. Fontana, W.A. Plummer, *J. Amer. Ceram. Soc.,* (1979) **62** (7–8) 367–369.
16. C.A. Angell, C.T. Moynihan, Transport Processes in Low-Melting Molten Salt Systems in *Molten Salts: Analysis and Characterisation* (1969), G. Mamantov (Ed.) published by Marcel Dekker.
17. S. English, *J. Soc. Glass Tech.,* (1923) **7** (1) 25, (1924) **8** (4) 205–248.
18. E.W. Washburn, G.R. Shelton, E.E. Libman, *Univ. Illinois Eng. Exp. Station Bull,* (1924) **140** 74.
19. T. Lakatos, L. -G. Johansson, B. Simmingsköld, *Glass Technol.,* (1972) **13** 88–95.
20. Society of Glass Technology Physical Properties Committee, *J. Soc. Glass Tech.,* (1956) **40** 83P–104P, see p. 87P.
21. R. Brückner, Y. Yue, *J. Non-Cryst. Solids,* (1994) **175** 118–128.
22. O.V. Mazurin, M.V. Streltsina, T.P. Shvaiko-Shvaikovskaya, *Handbook of Glass Data,* (1983, 1987) Elsevier.
23. S. English, *J. Soc. Glass Tech.,* (1925) **9** 83–98.
24. H. Scholze, *Glass–Nature, Structure and Properties* (1977) Springer-Verlag.
25. D. Öksoy, L.D. Pye, E.N. Boulos, *Glastn. Ber.* (1994) **67** (7) 189–195.
26. X. Feng, E. Saad, I.L. Pegg, *Ceramic Trans. — Nuclear Waste Management* (1990) **9** 457–468.
27. K. C. Lyon, *J. Res. Nat. Bur. Standards* (1974) **78A** (4) 497–504.
28. T. Lakatos, L. -G. Johansson, B. Simmingsköld, *Glastekn. Tidskr.* (1972) **27** (2) 25–28.
29. T. Lakatos, L. -G. Johansson, B. Simmingsköld, *Glastekn. Tidskr.* (1975) **30** (1) 7–8.

30. W.D. Kingery, *Property Measurements at High Temperatures*, (1962) John Wiley & Sons Inc.
31. C.T. Ewing, J.A. Grand, R.R. Miller, *J. Amer. Chem. Soc.*, (1951) **73** 1168.
32. M.P. Ryan, J.Y.K. Blevins, Viscosity of synthetic and natural silicate melts and glasses, (1987) *U.S. Geological Survey Bulletin 1764*.
33. L. Shartsis, S. Spinner, *J. Res. Nat. Bur. Stand*. (1951) **46** (3) 176–194.
34. International Organization for Standardization *Glass–Viscosity and Viscometric Fixed Points*, ISO 7884 (1987) parts 1 to 8.
35. Society of Glass Technology Physical Properties Committee, *J. Soc. Glass Tech.* (1956) **40** 83P–104P, see pp. 102P–104P.
36. J.T. Littleton, *J. Soc. Glass Tech.* (1940) **24** 176–185.
37. N.P. Bansal, R.H. Doremus, *Handbook of Glass Properties*, (1986) Academic Press.
38. H. Cole, C.L. Babcock *Viscosity–Temperature Relations in Glass*, (1970) bibliography published by the International Commission on Glass.
39. L. Shartsis, S. Spinner, W. Capps, *J. Am. Ceram. Soc*. (1953) **36** (10) 319–326.
40. A. Napolitano, P.B. Macedo, E.G. Hawkins, *J. Am. Ceram. Soc*. (1965) **48** (12) 613–616.
41. R.A. Eppler, *J. Am. Ceram. Soc*. (1966) **49** (12) 679–680.
42. G.H. Kaiura, J.M. Toguri, *Phys. Chem. Glasses* (1976) **17** (3) 62–69 (data given as polynomial coefficients).
43. J.D. Mackenzie, *J. Chem. Physics* (1958) **29** (3) 605–607.
44. C.R. Kurkjian, R.W. Douglas, *Phys. Chem. Glasses* (1960) **1** (1) 19–25.
45. S.G. Loryan, K.A. Kostyanyan, R.S. Saringyulyan, V.M. Kafyrov, E.Kh. Bagdasaryan, *Elektron. Tekh., Ser. 6: Mater.*,(1976) **2** 53–59.
46. V.K. Leko, E.V. Meshcheryakova, N.K. Gusakova, R.B. Lebedeva, *Opt. Mekh. Prom.*, (1974) **12** 42–45.
47. E.H. Fontana, W.A. Plummer, *Phys. Chem. Glasses* (1966) **7** (4) 139–146.
48. R. Bruckner, *Glastech. Ber.* (1964) **37** (9) 413–425.
49. J.F. Bacon, A.A. Hasapis, *J. Appl. Phys*. (1959) **30** (9) 1470–1471.
50. J.F. Bacon, A.A. Hasapis, J.W. Whooley, *Phys. Chem. Glasses* (1960) **1** (3) 90–98.
51. G. Urbain, Y. Bottinga, P. Richet, *Geochim. Cosmochim. Acta*, (1982) **46** 1061.
52. P. Kozakevitch, *Rev. Metall., Paris*, (1960) **57** (2) 149–160.
53. L. Shartsis, H.F. Shermer, *J. Am. Ceram. Soc*. (1954) **37** (11) 544–551.
54. L. Shartsis, S. Spinner, W. Capps, *J. Am. Ceram. Soc*. (1953) **36** (10) 319–326.
55. J. O'M. Bockris, J.D. Mackenzie, J.A. Kitchener *Trans. Faraday Soc*. (1955) **51** (12) 1734–1748.
56. G. Urbain, *Rev. Int. Hautes Temp. Refract*., (1974) **11** (2) 133–145 (data given as equation parameters).
57. J. O'M. Bockris, D.C. Lowe, *Proc. R. Soc. London, Ser. A*, (1954) **226** (1167) 423–435.
58. B.G. Varshal, V.Yu. Goikhman, L.L. Mirskikh, L.K. Shitts, Yu. A. Shitts, *Fiz. Khim. Stekla*, (1980) **6** (6) 734–736.
59. P. Roentgen, H. Winterhager, R. Kammel, *Zeit. Erzb. Metall*. (1956) **9** 207–214.
60. J.P. Poole, *J. Am. Ceram. Soc*. (1949) **32** (7) 230–233 (data given as Arrhenius coefficients).
61. J.P. Poole, M. Gensamer, *J. Am. Ceram. Soc*. (1949) **32** (7) 220–229 (data given as Arrhenius coefficients).
62. S.V. Nemilov, *Zh. Prikl. Khim*. (1969) **42** (1) 55–62.
63. L. Shartsis, S. Spinner, W. Capps, *J. Am. Ceram. Soc*. (1952) **35** (6) 155–160.
64. E. Eipeltauer, A. More, *Radex-Rundsch*. (1960) (4) 230–238.

65. M.M. Ammar, Kh. El-Badry, S. Gharib, *Egypt. J. Phys*. (1977) **8** (1) 1–8.
66. N.W. Taylor, R.F. Doran, *J. Am. Ceram. Soc*. (1941) **24** (3) 103–109.
67. Yu. K. Startsev, V.P. Klyuev, M.S. Vostrikova, *Fiz. Khim. Stekla*, (1978) **4** (3) 278–288.
68. V.M. Fokin, A.M. Kalinina, V.N. Filipovich, *J. Cryst. Growth* (1981) **52** (1) 115–121.
69. P.E. Gray, L.C. Klein, *Phys. Chem. Glasses* (1986) **27** (6) 241–244.
70. G. Heidtkamp, K. Endell, *Glastech. Ber.* (1936) **14** (3) 89–103.
71. E. Preston, *J. Soc. Glass Technol*. (1938) **22** (9) 45–81.
72. T.P. Shvaiko-Shvaikovskaya, Gusakova, O.V. Mazurin, *Neorg. Mater.* (1971) **7** (4) 713; *VINITI* 483–71.
73. T. Moriya, *J. Soc. Chem. Ind. Japan* (1939) **42** (10) 746–750.
74. S. English, *J. Soc. Glass Tech.* (1924) **8** (4) 205–248.
75. N.W. Taylor, P.S. Dear, *J. Am. Ceram. Soc*. (1937) **20** (9) 296–304.
76. H.R. Lillie, *J. Am. Ceram. Soc*. (1939) **22** (11) 367–374.
77. E. Eipeltauer, G. Jangg, *Kolloid-Z.* (1955) **142** (2/3) 77–84.
78. M.M. Skornyakov, A. Ya. Kuznetsov, K.S. Evstropiev, *Zh. Fiz. Khim*. (1941) **15** (1) 116–124.
79. B.A. Pospelov, K.S. Evstropiev, *Zh. Fiz. Khim*. (1941) **15** (1) 125–133.
80. S.V. Nemilov, *Izv. Akad. Nauk SSSR, Neorg. Mater.* (1968) **4** (6) 952–956.
81. A.A. Konovalov, K.S. Evstropiev, *Zh. Fiz. Khim*. (1941) **15** (1) 109–115.
82. M.M. Skornyakov, in *Physico-Chemical Properties of the Ternary Na2O-PbO-SiO2 System*, Moscow-Leningrad (1949) pp 39–69.
83. J. Gallup, A.G.F. Dingwall, *Am. Ceram. Soc. Bull*, (1957) **36** (2) 47–51.
84. S.V. Nemilov, A.I. Ignat'ev, *Fizika i Khimiya Stekla* (1990) **16** (1) 85–93.
85. F. Imoto, K. Hirao, *J. Ceram. Assoc. Jpn*. (1959) **67** (11) 381–385.
86. O.G. Ivanov, N.I. Tretyakova, O.V. Mazurin, *Steklo Keram*. (1969) **7** 42–45.
87. E.F. Riebling, *J. Chem. Phys*. (1966) **44** (8) 2857–2865.
88. T.D. Taylor, G.E. Rindone, *J. Am. Ceram. Soc.* (1970) **53** (12) 629–695 (data given as Arrhenius coefficients).
89. L.C. Hoffman, T.A. Kupinski, R.L. Thakur, W.A. Weyl, *J. Soc. Glass Technol.* (1952) **36** 196–216.
90. K. Kani, *Proc. Imper. Acad. Tokyo* (1935) **11** (8) 334–336.
91. S. Sakka, K. Kamiya, N. Kato, *Rws. Rep. Fac. Eng. Mie Univ.* (1981) **6** 81–92.
92. E.V. Ermolaeva, *Ogneupory* (1951) **4** 162-171.
93. I. N'Dala, F. Cambier, M.R. Anseau, G. Urbain, *Brit. Ceram. Soc. Trans*. (1984) **83** 105–107.
94. Y. Shiraishi, L. Gra'na'sy, Y. Waseda, E. Matsubara, *J. Non-Cryst. Solids* (1987) **95&96** (2) 1031–1038.
95. O.V. Mazurin, M.V. Streltsina, *J. Non-Cryst. Solids*, (1972) **11** (3) 199–212.
96. J.H. Simmons, A. Napolitano, P.B. Macedo, *J. Chem. Phys*. (1970) **53** (3) 1165–1170.
97. Ya. I. Belyi, V.I. Goleus, *Ukr. Khim. Zh*. (1979) **45** (12) 1163–1167.
98. T.P. Shvaiko-Shvaikovskaya, *Steklo* (1968) **3** 93–95.
99. Owens Illinois, *J. Am. Ceram. Soc*. (1944) **27** (8) 221–225.
100. Owens Illinois, *J. Am. Ceram. Soc*. (1948) **31** (1) 1–8.
101. H.R. Lillie, *J. Am. Ceram. Soc.* (1931) **14** (7) 502–511.
102. L. Sasek, H. Meissnerova, *J. Prochazka, Sb. Vys. Sk. Chem. Technol. Praze, Chem. Technol. Silik.*, (1975) **L6** 95–129.
103. J.D. Mackenzie, *Trans. Faraday Soc*. (1957) **58** 1488–1493.
104. R.S. Saringyulyan, K.A. Kostanyan, *VINITI* (1969) 902–969.
105. R.H. Doremus, *Glass Science* (1973) John Wiley & Sons.
106. T. Lakatos, L. -G. Johansson, B. Simmingsköld, *Glastekn. Tidskr.* (1976) **31** 31–35.

107. T. Lakatos, L. -G. Johansson, B. Simmingsköld, *Glastekn. Tidskr.* (1976) **31** 51–54.
108. T. Lakatos, L. -G. Johansson, B. Simmingsköld, *Glastekn. Tidskr.* (1973) **28** 75–79.
109. T. Lakatos, L. -G. Johansson, B. Simmingsköld, *Glastekn. Tidskr.* (1977) **32** (2) 31–35.
110. T. Lakatos, L. -G. Johansson, B. Simmingsköld, *Glastekn. Tidskr.* (1978) **33** (3) 55–59.
111. T. Lakatos, L. -G. Johansson, B. Simmingsköld, *Glastekn. Tidskr.* (1979) **34** 61–65.
112. N. P. Bansal, R. H. Doremus, *Handbook of Glass Properties*, (1986) Academic Press.
113. M.P. Ryan, J.Y.K. Blevins, The viscosity of synthetic and natural silicate melts and glasses *U. S. Geological Survey Bulletin 1764*, (1987).

6 The Surface Tension of Glass-Forming Melts

Douglas A. Weirauch, Jr.

CONTENTS

6.1 INTRODUCTION

6.1.1 The Technological Significance of Glass Melt Surface Tension

Within the glass industry, liquid surface tension has widespread technological significance ranging from glass melting and refining through forming to product performance. Glass batch components that reduce glass surface tension (chlorides, fluorides, iodides, sulphates) are concentrated at the surface of batch particles, thereby promoting their fusion (1). These same substances also support refining or the removal of gas bubbles from the glass melt (1–3), and the elimination of the elongated compositional homogeneities known as cords (4–6). Heat transfer from the melter to the glass bath in gas-fired furnaces is affected by the presence of foam, whose stability depends on surface tension (7, 8). Surface tension gradients can lead to convection, which aids in homogenization (8) or aggravates the flux-line corrosion of refractories (8–10). Refractory corrosion is accelerated by penetration into pores (11) that is driven by surface tension (12, 13). Those oxide components of the glassmelt that have a low surface tension (B_2O_3, K_2O, PbO) also volatilize readily (8). Finally, in glass forming, surface tension causes sharp edges to round and enables the production of smooth, planar surfaces (8). Its importance in forming glass sheet (14), and drawing fibers has been recognized (8,15). Even glass-forming ability and tendency to crystallize can be influenced by surface tension (16). The importance of surface tension phenomena to glass-manufacturing processes has led to its inclusion in databases being developed for computer modeling of production processes (338).

In derivative technologies where glass may be a subordinate or transient phase, glass surface tension also exerts its influence. Examples include the liquid phase sintering of ceramics (17–21), the formation of glass–metal seals (22–26), metallization of ceramics for ceramic–metal seals (26–28) or electronic circuitry (29). In the enameling of metals (30) and glazing of ceramics (31), the flow and adhesion of the coating are affected by glass surface tension (32).

Although not driven by technological objectives, studies of natural systems likewise find interest in the surface tension of glass melts. The surface tension of natural silicate melts is closely related to the rates of bubble nucleation and growth and therefore affects the eruptive behavior of volcanic rocks (33, 34).

6.1.2 The Concept of Liquid Surface Tension

The historical development of understanding of the surface tension of liquids has been outlined by Padday (35). The earliest recorded discussion of its manifestation is attributed to Leonardo da Vinci, who explored the rise of a liquid in tubes whose bore was "fine as a hair;" hence the terms capillary and capillarity derived from the Latin word for hair, *capillus*. Hawksbee in 1709 demonstrated that capillary behavior was related to surface atoms since thick-walled tubes yielded identical results to thin-walled tube of the same internal diameter (36). The existence of a tension within the liquid at the vapor–liquid interface is an easily envisioned concept. An atom within the bulk liquid is subjected to the forces of its neighbors from all sides, while a surface atom is only partly surrounded. This results in an internal pressure that is

counterbalanced by a tension acting tangentially to the surface. The early descriptions of capillary phenomena were based on mechanical equilibrium in curved surfaces. The imbalanced cohesive forces that exist across a nonspherical curved surface lead to a pressure difference, ΔP, described by the Laplace equation:

$$\Delta P = \gamma (1/ r_1 + 1/r_2) \quad (1)$$

where r_1 and r_2 are the two principle radii of curvature and γ is the liquid surface tension. This equation governs the shape of macroscopic menisci and forms the basis for all liquid surface tension measurements. Derivations of equation 1 are found in Padday (35) and Adamson (37). A free liquid drop will tend toward a spherical shape in order to minimize its surface area and thereby its surface energy.

The Young-Dupré equation describes the three-phase mechanical equilibrium of forces acting on a stationary liquid drop that is at rest on a smooth, horizontal, solid surface (sessile drop):

$$\gamma_{SV} = \gamma_{SL} + \gamma_{LV} \cos \theta \quad (2)$$

In this equation γ_{SV} is the solid–vapor interfacial energy, γ_{SL} is the solid–liquid interfacial energy, γ_{LV} is the liquid–vapor interfacial energy, and θ is the contact angle of the liquid on the solid at the SLV triple point. Here, a compromise is reached between the areas of the three interfaces that will minimize the surface energy of the system. Gauss provided rigorous derivations of both equations 1 and 2 in 1830 (38).

The equivalency of surface tension with the interfacial free energy of a liquid as proven by Guggenheim (39) is outlined by Kingery (40). Surface or interfacial tension is defined as the irreversible work required to increase the surface of a liquid by unit area. Surface energy is defined as the increase in free energy accompanying the formation of a new surface. The liquid–vapor interfacial free energy is therefore a thermodynamic quantity that necessitates chemical equilibrium (41). A description of the conditions for chemical equilibrium of a sessile drop is provided by Aksay et al. (42). A perturbation in the Gibbs free energy of a system, dG, attending the creation of a new phase is described by:

$$dG = -S\, dT + V\, dP + \gamma\, dA + \Sigma\, \mu_i\, dn_i \quad (3)$$

where: S is the entropy of the system, T is temperature, V is volume, γ is the interfacial free energy, A is the interfacial area, μ_i is the chemical potential of component i, and n_i is the number of moles of component i. The interfacial free energy is therefore related to the Gibbs free energy of the system by:

$$\gamma = (\partial G/\partial A)_{P, T, ni} \quad (4)$$

Since liquids do not support shear stresses, either extension of an existing surface or the creation of a new surface (equation 4) produces the surface tension. Therefore, surface tension and surface energy are equal and often used interchangeably (40).

TABLE 6.1
Equivalent Units of Surface Tension

1	N/m
1	J/m^2
10^3	dyn/cm
10^3	erg/cm^2
0.102	kg/m

This is not the case in solids where surface energy depends on factors such as orientation and lattice imperfections and therefore usually doesn't coincide with surface stress (43). The units of surface tension expressed as either force/distance or energy/area are outlined in Table 6.1.

6.1.3 Bonding and Surface Tension — A Comparison of Liquids

The relationship of surface energy to bonding and atomic structure is considered in detail elsewhere (44, 45). Only the broad features that are relevant to understanding the effect of glass-melt composition on surface tension will be presented here.

The solid–vapor surface energy can be closely approximated by the energy associated with the unsatisfied bonds that result from the transfer of an atom from the solid interior to the surface. This is borne out by the good agreement between γ_{sv} measurements and those calculated from sublimation energies (45). The transition from the solid phase to a liquid is marked by a loss of atomic coordination and the breaking of bonds. Therefore, the liquid–vapor surface energy (surface tension) is expected to be lower than the solid–vapor surface energy. The surface tension of liquid metals is approximately 0.75–0.96 that of the solid surface energy (45). This broken bond argument works well with materials whose bonding is dominated by short-range forces of a metallic or covalent nature. In materials where the bonding is predominantly ionic, the longer-range coulombic forces might still influence an atom that has been moved to the surface. The limitation in this case is a detailed knowledge of the potential-distance functions.

There is a general increase in surface tension with increasing bond strength (46). Bondi showed that divers liquids such as organic molecules, metals, inorganic salts and oxides fall on a continuum when the energy of vaporization is plotted against the molar surface free energy (44). Table 6.2 groups the surface tension of selected liquids by their predominant bonding type. Liquids possess two components of surface tension that relate to physical dispersion forces that operate between molecules and those that result from all other types of chemical interaction. In molecular liquids the contribution of the dispersion forces can be significant. It is the primary component of hydrocarbons such as n-decane: $CH_3\ (CH_2)_8\ CH_3$, but subordinate to hydrogen bonding in water. The reader is directed to Fowkes (50) for further discussion on the surface tension of low-temperature liquids, and Yaws (51) for a useful compilation of data. When two solid ionic substances, such as NaCl and NaF, share

TABLE 6.2
The Surface Tension of Selected Liquids

Predominant Bonding Type	Liquid	Surface Tension (mN/m)	dg/dT (mN/m/°C)	Temp. (°C)	Reference
Molecular	n-decane	23.9	–0.10	20	35
	nitrobenzene	43.4		20	35
	H_2O	72	–0.17	25	35
Ionic	KI	78	–0.11	681	44
	KCl	97	–0.07	780	44
	NaCl	114	–0.07	801	44
	LiCl	140	–0.07	608	44
	NaF	186	–0.08	993	47
Covalent	SiO_2	307	+0.03	1800	48
	Cu_2S	410		1130	46
	Si	865	–0.13	1410	49
Metallic	Al	914	–0.35	660	49
	Ni	1778	–0.38	1454	49
	W	2500	–0.29	3377	49
Mixed	B_2O_3	83	+0.055	1000	48
	Al_2O_3	690		2050	48
	P_2O_5	60	–0.021	100	48

a common cation that with the smaller cation:anion radius ratio will possess the higher ionic bond strength (52). This is reflected in the higher surface tension for the substance with the smaller anion (radius of Cl^- = 0.18 nm and radius F^- = 0.14 nm). This general rule of decreasing surface tension with increasing cationic radius of the melt components has been noted for both simple salts and oxide melts (44). In covalent substances, complex electronic interactions determine the strength and number of bonds. Representative covalent substances are listed in Table 6.2. Bonding in oxide melts can be either ionic or covalent in nature, resulting in a wide range of surface tension. Nevertheless, similar trends related to the size of the cation have been observed for simple silicate (46, 53) and borate (54, 55) melts. Dietzel (56) and King (53) used the field strength of the cation, z/r^2, instead of the ionic potential, z/r, to explain the increase in surface tension with increasing cation size (where z is the valence of the cation and r is its radius). The use of z/r^2 results in a smooth transition between melts with monovalent and those with divalent cations (56). The relationship between bond strength and surface tension in glass melts will be discussed further in Section 6.1.5. The good correlation between melting point, bond strength and surface tension in metals explains the dramatic increase observed from Al to Ni to W.

The focus of this data review is on traditional glass-forming systems (silicate, oxide, borate, and phosphate melts). The emerging importance of chalcogenide (8) (based on the Group VI elements S, Se, or Te) and fluoride glasses as optical fibers (57) necessitates some consideration of the surface tension of halides (F, Cl, molten salts) as well as a review of the literature on mattes (Metal-S). In some glass systems,

the data on surface tension is sparse or nonexistent, and much insight can be gained from a consideration of measurements on related slag systems. With the possible exception of the mattes, this review will therefore consider all nonmetallic high-temperature liquids.

6.1.4 The Effect of Temperature on Glass Surface Tension

The decrease in the free surface energy of most materials is nearly linear from very low temperatures to within a few degrees of the critical temperature. The surface tension of pure liquids is zero at the critical temperature at which differences in cohesion between the liquid and vapor phases disappear. Numerous empirical relationships to describe the change in surface tension with temperature based on this critical point behavior have been proposed, but are approximations at best (35, 40). The physical dimensions of the temperature coefficient of surface tension, $d\gamma/dT$, are those of surface entropy. The change in surface tension with temperature of a pure component is therefore the change in entropy associated with the formation of the surface. In multicomponent systems, changes in relative surface concentrations must also be taken into account.

Liquids with a positive temperature coefficient of surface tension have been called abnormal liquids, while those with a negative coefficient have been called normal liquids (53). Liquid metals do possess negative temperature coefficients of surface tension, $d\gamma/dT$ (refer to Brandes and Brook (49) and Table 6.1); those cases where positive coefficients have been reported can be attributed to the effect of impurities (40). Positive temperature coefficients of surface tension in pure oxides (B_2O_3, GeO_2, SiO_2) are linked to structural changes in the melt (48). Similar behavior in more complex oxide and silicate melts (2, 53, 58–62) has likewise been ascribed to the dissociation of structural units with increasing temperature (46, 53, 61, 62). The dissociation leads to more unsatisfied silicate bonds available for coordination with cations and leads to an increase in surface tension (53). This seems to be the most widely accepted explanation, although two alternatives are worth mentioning. Weyl maintained that a molecular group that reduces the surface tension becomes more symmetrical with increasing thermal agitation thereby resulting in an increase in surface tension.(63) Worley argued that the surface-active species of partly miscible liquids migrated inward with increasing temperature (64).

The temperature coefficient of surface tension for most complex (commercial) glass melts is negative (23). That for molten binary metasilicates ranges from strongly negative to strongly positive with increasing ionic potential (46, 61). Furthermore, King observed that $d\gamma/dT$ became more positive as the silica content increased (53). The transition from a negative to a positive temperature coefficient shifts to higher silica contents as the cation–oxygen attraction increases (61). The temperature coefficient of binary lead silicates is more complex. It is positive in melts with a high silica content, decreases as silica decreases, becomes negative with further decrease in silica, reaches a minimum, and finally increases and becomes positive again (65). This behavior was correlated to similar “V-shaped” compositional behavior of the coefficient of thermal expansion (65) as had been suggested earlier by Freundlich for other liquids, and will be discussed further in the next section (66).

The magnitudes of the reported temperature coefficients for the surface tension of glass melts are low, ranging from approximately –0.20 to +0.20 dyn/(cm°C). This results in wide discrepancies in temperature coefficients reported for a given glass system (see the work of Gunji and Dan (67) on calcium silicate melts as an example). If the error of surface tension measurement were only 2%, over a 200°C interval this would translate to a possible disparity in temperature coefficient of 0.035 dyn/(cm°C) for a glass with a surface tension of 350 dyn/cm. Thus, very precise surface tension measurements are required to determine temperature coefficients.

6.1.5 The Effect of Glass Composition on Surface Tension

The earliest attempts to determine the effect of glass melt composition on surface tension were empirical in nature.

Badger et al. measured the effect of small equimolar additions of 20 different cations on the surface tension of a 17.4% Na_2O-10.1% CaO-72.5% SiO_2 base glass at 1200 and 1350°C (59). ZrO_2 and CaO increased the surface tension by 5%, while PbO and V_2O_5 reduced the surface tension by 10 and 23 %, respectively.

Tillotson treated surface tension as an additive function of glass composition:

$$\gamma = \Sigma\, x_i\, \gamma_i \tag{5}$$

where x_i is the composition (%) of a given component of the glass and γ_i is an additive factor for the component (68). Babcock systematically studied the effect of glass composition in the Al_2O_3-CaO-MgO-Na_2O-SiO_2 system (69). He presented his results in the form of an oxide substitution table. The largest observed effect was for a 0.1 mol fraction substitution of Al_2O_3 for Na_2O, which resulted in an approximate 20% increase in surface tension. Dietzel developed compositional factors for glass surface tension at 900°C (70). Lyon extended the work of Dietzel by determining factors at 1200 and 1400°C using a base Na_2O-CaO-SiO_2 glass in which the SiO_2: Na_2O on a weight basis exceeded 4 (71).

Petzold criticized Lyon's approach, maintaining that the surface tension of many glasses had much more complex compositional dependencies (72). Furthermore, the calculations broke down in the presence of strongly surface-active components such as halides, As_2O_3, Cr_2O_3, MoO_3, SO_3, V_2O_5, and WO_3. The concentration of these species near the liquid–vapor surface in an ideal solution follows the Gibbs adsorption isotherm:

$$\Gamma_i = -(1/RT)\, d\gamma/d \ln c_i \tag{6}$$

where Γ_i is the surface concentration of the active substance, i, γ is the surface tension, R is the molar gas constant, T is the absolute temperature, and c_i is the bulk concentration of component i. Sulfur (73), Na_2S (74), and CaF_2 (75) have also been shown to be surface-active species. Cooper and Kitcher avoided the assumption of ideal solution behavior implicit in equation 6 since the activity of silica in binary calcium silicate melts was known (7). They determined that, for compositions above 60 mol % silica, the surface is expected to be almost entirely SiO_2.

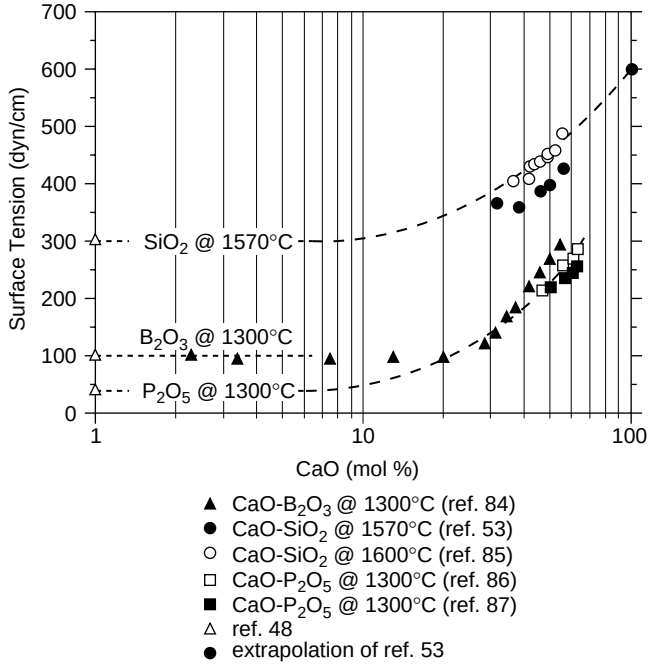

FIGURE 6.1 The surface tension of selected binary glass melts.

Plotting surface tension against the logarithm of concentration, as suggested by Equation 6, reveals the nature of simple solutions. A measure of the surface activity of a given component is the range of composition over which a linear slope, $-RT\,\Gamma_i$, exists. Glass surface tension generally decreases with increasing concentration of acidic oxides, indicating that the anionic groups are surface-active (76). This can be seen in the effect of composition on the surface tension of binary calcium silicates, borates, and phosphates (Figure 6.1). The value shown for the surface tension of liquid CaO at 1570°C is based on the extrapolation cited by Livey and Murray (77) of the surface tension of calcium-silicate melts measured by King (53). The end-point values for silicon dioxide, boric oxide, and phosphorus pentoxide are based on the experimental results of Kingery (48). Weyl explained the large reduction of surface tension attending the addition of boric oxide to silicate glasses as due to the formation of planar BO_3 triangles at the glass surface; the central boron ion exerts strong forces in the direction of the plane, but weak forces perpendicular to it (63).

The simple picture of a smooth increase in surface tension with increasing bond strength, as approximated by ionic field strength z/r^2, was developed in Section 6.1.3. Dietzel showed that if one neglects the highly polarizable or poorly soluble surface-active elements, there is an inversion in this behavior at a field strength of approximately 0.5 (56). The compositional factors of Rubenstein 1964 were used to demonstrate this behavior (Figure 6.2) (78). The network modifiers fall on the left side of the "inverted V," where surface tension increases with field strength, while the network formers lie on the right side, where surface tension decreases with increasing

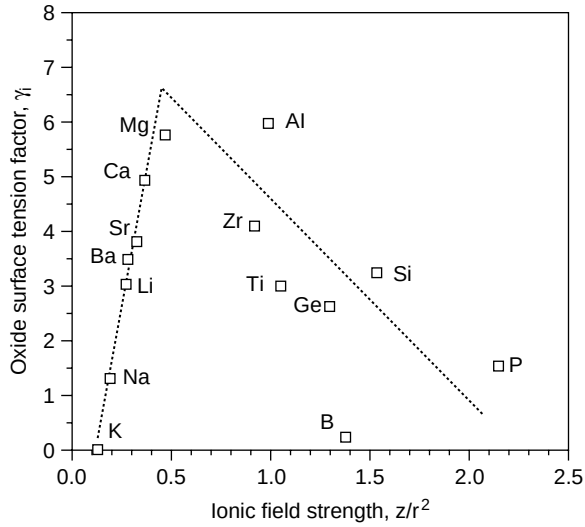

FIGURE 6.2 The V-phenomenon of surface tension using the additive factors of Rubenstein 1964.

field strength. This behavior is the inverse of thermal expansion, as observed in an earlier section. Similar "V phenomena" are also observed for viscosity, modulus of elasticity, heats of formation, and certain electrical properties of molten oxides, glasses and salts (79). The scatter in the data for field strengths greater than 0.5 is probably related to complex structural interactions in the glass melt. Aluminum is an example of such behavior since it is only a network former in the presence of silica (61). Thus, while a general decrease is observed for species on the right side of the "V," the relative position of the network formers can be shifted depending on the data used to construct the plot. Mg and Al have both been reported to form anionic species in silicate melts since they have a lower effect on the surface tension than their ionic field strength would predict (61, 74).

Boni and Derge argued that the approach of Dietzel and Lyon led to some unreasonable compositional factors since, in some cases, minor constituents of the glass were used (46). They compiled factors based on single-component and binary oxide melts. Rubenstein expanded the nine oxide additive factors of Lyon to 30 by applying a relationship between surface tension and microhardness (78). Good reviews of composition factors are found in Volf (79) and Scholze (80). Sanditov has revisited the correlation between surface tension and microhardness in silicate glasses (81). Winer and Pilgrim presented an empirical, main-effects-plus-interactions model of the surface tension CaO-MgO-Al_2O_3-SiO_2 melts that fit measurements very well using only terms for Al_2O_3 and SiO_2 (82). The most recent work on compositional factors is found in Nakajima (90) and Goleus et al. (91), Villa et al.(92), who present surface tension coefficients for multicomponent glazes at temperatures between 1000 and 1250°C, and Kucuk et al. (93), who report parameters for calculating the surface tension of silicate glasses at 1400°C.

Despite the limitations imposed by complex compositional dependency and surface active components, the error is less than 1% when using the additive expressions for calculating surface tension of silicate melts over limited ranges of glass composition (1). This may be better understood by considering the surface tension of more complex ternary silicate melts. Barrett and Thomas described the compositional dependency of surface tension in terms of the proportions of associated and dissociated molecules (62). The effect of CaO additions to $CaO\text{-}Al_2O_3\text{-}SiO_2$ melts is to gradually break down the short-range order of the liquid into simple SiO_4^- groups that increase the surface tension. They observed monotonic changes in surface tension with composition, without any discontinuities that would indicate the presence of associated species or compounds in the melt. This is consistent with the picture developed by King to explain the reduction in surface tension of binary silicates with increasing silica content (53). Orthosilicates, with the lowest silica content, are composed of isolated silicate tetrahedra with all four oxygen atoms available for coordination and have the highest surface tension. Metasilicates, of intermediate silica content have a chain structure with two oxygen atoms available and an intermediate surface tension. Ring structures and complete three-dimensional networks are also possible as the silica content increases further. Silica, with a three-dimensional network, has the lowest surface tension. Toropov and Bryantsev also observed a continuous decrease in surface tension as the silica content of melts in the $FeO\text{-}MgO\text{-}SiO_2$ system was increased (83). This trend was related to a shift from predominantly $[SiO_4]^{-4}$ tetrahedra to $[Si_2O_6]^{-4}$ chains (2).

The influence of the silica content on the surface tension of ternary silicate melts is illustrated in Figure 6.3. The surface tension of $CaO\text{-}Al_2O_3\text{-}SiO_2$ melts is weakly affected by the Ca:Al ratio and deviates little from a straight line between 0 and 100% silica. The superposition of the data for binary calcium silicate melts on these data strengthens the conclusion that there is little effect on surface tension when calcium oxide is substituted for alumina. This behavior is in agreement with the location of these species on the V-curve for ionic field strength (Figure 6.2).

Appen developed a semi-empirical approach modified by considerations of bond strength, structure, and thermodynamics (94, 95). His approach begins with partial molar quantities that have been derived from a large number of measurements. The basic calculation is similar to the summation described above, but corrections follow that account for structural complexities introduced by B_2O_3, CdO, PbO, SiO_2, and TiO_2. A detailed description of the method of Appen is found in Volf (1).

Tremendous progress has been made in recent years toward the development of thermodynamic databases that can be used to calculate phase equilibria in alloy, salt, and oxide systems using the CALPHAD or computer calculation of phase diagrams approach (96–98). With further development, these databases can also be used to calculate the surface tension of molten alloys, salts, and oxide mixtures (99, 339, 342, 348). With few exceptions, the majority of the work to date has involved binary systems, but the aim is to develop databases to the extent that physical property calculations can be coupled with the computation of phase equilibria. The modeling of the surface tension of $CaO\text{-}Al_2O_3\text{-}SiO_2$ glasses is an example of a ternary system that has been evaluated by this approach (346).

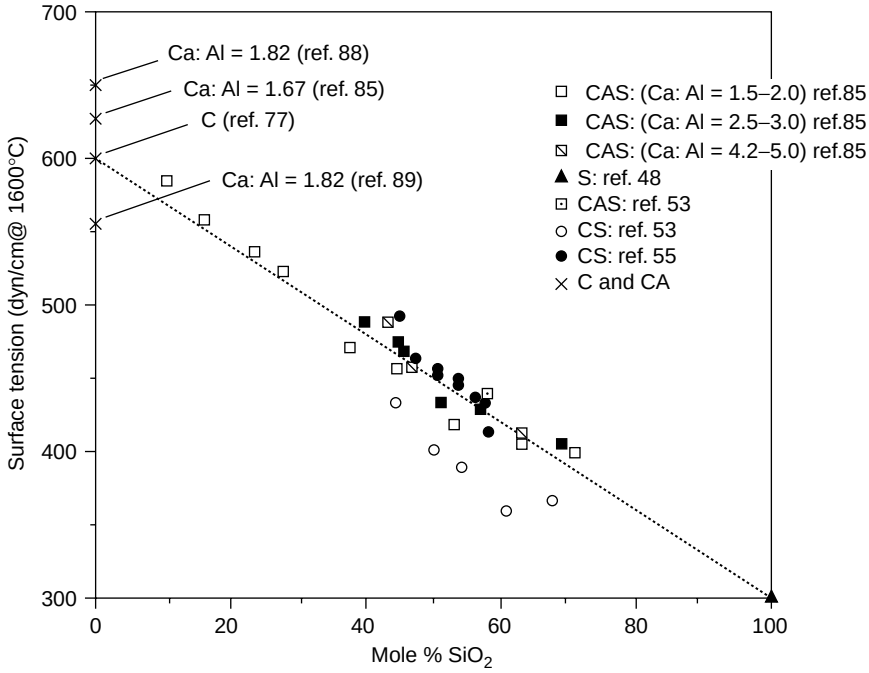

FIGURE 6.3 The surface tension of binary and ternary melts in the CaO-Al_2O_3-SiO_2 system.

6.1.6 The Effect of Atmosphere on Surface Tension

Within the bulk of a liquid the forces acting on a given element are screened and compensated by surrounding species. At the gas–liquid surface, however, there is a net inward attraction that leads to surface contraction and therefore a surface tension. Gases containing molecules with dipoles can attach to the liquid surface and compensate this inward attraction. The magnitude of this surface tension reduction will depend on the strength of the dipole (100).

Vickers cited the effect of atmosphere on the attack of furnace refractories by slags as well as the effect of dissolved gas content on the flow of lavas as reasons to improve the understanding of the effect of atmospheres on the surface tension of high-temperature liquids (101). He determined the surface tension of a soda-lime-silicate glass in a wide variety of atmospheres (air, carbon dioxide, ammonia, steam, sulfur dioxide, and hydrogen) using both a dipping-cylinder and maximum bubble pressure technique. He found very different effects when using the two techniques. The SO_2 atmosphere generally reduced the melt surface tension, but complicated the evaluation since it also induced crystallization of the melt. Boni and Derge observed a pronounced reduction of surface tension in alkaline earth silicates when sulfur was added to the melt (73). By contrast, Dietzel (56) and Jebsen-Marwedel and Dinger (102) observed increases in glass melt surface tension in SO_2-SO_3 gas mixtures. Parikh used a fiber-elongation method to evaluate gas atmosphere effects near the softening point of soda-lime-silica glass (450–700°C) (103). Polar gases

(SO_2, H_2O, NH_3, and HCl) tended to reduce the surface tension while nonpolar or linear gas molecules (dry air, H_2, N_2) had a negligible effect. They observed a similar effect in wet SO_2 and H_2O atmospheres and speculated that water content was the more important factor. Ellefson and Taylor concluded that the surface tension of a sodium silicate melt was similar in vacuum, nitrogen, and oxygen atmospheres (104). Popel and Esin reported a decrease in the surface tension of iron silicate melts with decreasing Fe^{2+}/Fe^{3+} ratio (i.e., increasing oxygen activity) (105). Similar results were reported by Toropov and Bryantsev for melts in the FeO-Fe_2O_3-MgO-SiO_2 system (83). Akhtar and Cable obtained the best results for soda-lime-silica glass when the bubbling gas was the same as that passed over the melt (106). They found that carbon dioxide reduced the melt surface tension; a result was not expected from the simple dipole model of Parikh (103). In addition, sulfur dioxide had a complex effect on surface tension that could not be explained. Sharma and Philbrook observed calcium silicate surface tensions in N_2-9%H_2 that were 10% higher than those in argon and attributed the effect to the low levels of oxygen and water (107). Mukai and Ishikawa obtained similar results using the pendant drop technique for CAS glass melts in argon and O_2 (85). Plodinec reported surface tension reductions of approximately 4.3% for borosilicate glass bubbled with oxygen compared with that bubbled with carbon dioxide (108). A similar reduction of 3.6% was noted for a soda-lime-silicate melt bubbled with 5 vol.% water in argon when compared with dry argon (109). Recent work on the effect of atmospheric moisture on surface tension has extended the field to include additional glass systems (335, 344, 350). The effect of compositional changes linked to vaporization is a critical consideration related to vapor phase chemistry that was considered in a recent study (334).

6.2 THE MEASUREMENT OF SURFACE TENSION

Many of the experimental difficulties associated with the measurement of the surface tension of glass melts, slags, mattes, or molten salts are also common to liquid metals and alloys. Therefore, this section on measurement techniques will draw from the literature that is available for all of these high-temperature liquids.

Helpful comparisons of the attributes of techniques used to measure the surface tension of high-temperature liquids are found in Mitchell et al. (23), Padday (35), Kingery (40), Boni and Derge (46), Kozakevitch (110), and White (111). This section will begin with a general description of the most widely used techniques. Advances that have been made in the last 25 years will then be emphasized. Finally, a comparison of the techniques will be presented.

Techniques used for the determination of the surface tension of high-temperature liquids fall into one of the following categories:

1. Capillary Rise (Capillary Flow)
2. Drop Weight (Crucible Drop Weight)
3. Fiber Elongation
4. Dipping Cylinder (Ring Method, Wilhelmy Plate, Hollow Cylinder)
5. Maximum Bubble Pressure

6. Drop Shape
   a. Pendant Drop
   b. Sessile Drop

The general nature of these techniques is illustrated in Figure 6.4. The principles governing each of these approaches will now be briefly discussed.

6.2.1 The Capillary Rise Method (Figure 6.4a)

As was mentioned in Section 6.1.2, the capillary rise technique is the oldest method used to measure the surface tension of liquids. When a capillary tube is immersed in a liquid, the liquid rises (or falls) until the pressure difference across the curved meniscus is balanced against the hydrostatic pressure. Surface tension, γ, is then described by the following equation:

$$2 \cos \theta \gamma / r = g \Delta\rho h \tag{7}$$

or

$$\gamma = r g \Delta\rho h/2 \cos \theta \tag{8}$$

where θ is the contact angle formed by the liquid on the capillary tube material, g is the gravitational constant, h is the capillary rise, $\Delta\rho$ is the density difference between the liquid and the gas phase, and r is the radius of the capillary. At high temperatures, the difficulty of determining r, h, and θ are sizable and the technique is not recommended (40). Secrist used a derivative technique that measured the distance of penetration of several silicate glasses into a specially constructed capillary joint (112). Eaton successfully measured the surface tension of boric oxide and complex silicate glasses with this technique (113).

6.2.2 The Drop Weight Method (Figure 6.4b)

The general relationship between the weight of a drop that falls from a tube and the surface tension of the liquid was described by Tate in 1864 (114). The same condition holds for a drop that falls from a rod. His expression was later corrected for drop:rod dimensional effects by Quincke:

$$W = a d + b d^2 \tag{9}$$

where W is the weight of the drop (mg), d is the diameter of the rod, a is a number related to surface tension and b is a constant that depends on the cohesion of the liquid (approximately 15 for molten glass when cgs units are used) (115). Tillotson (68) applied this technique to glass but obtained values that are much lower than those determined by other techniques (23). Lecrenier modified the technique to determine the surface tension of glass drops that issued from a circular orifice at the bottom of a crucible (crucible drop weight method):

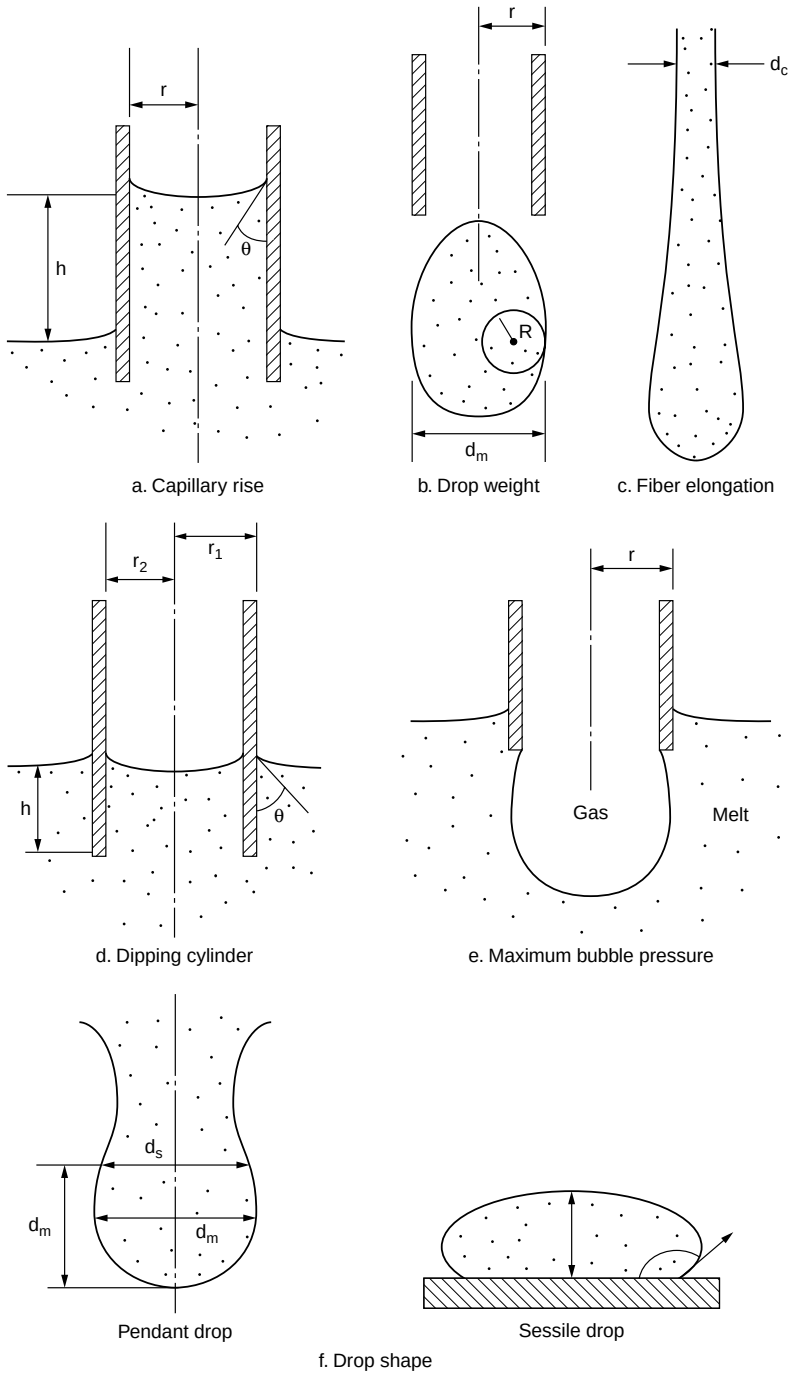

FIGURE 6.4 Measurement techniques used to determine the surface tension of glassmelts.

$$\gamma = (1 + r/R)\,(W/2\pi r) \tag{10}$$

where r is the orifice radius and R is the radius of curvature at the widest point of the drop (116). His results appear to be too high, raising serious doubts about the accuracy of this technique. Clearly, the strength of this method lies in its simplicity, and it should be used only to generate relative surface tensions (23, 117). Studies of oxide melts that are representative of this technique are found in the literature (30, 58, 68, 120–124). Appen improved upon the method for viscous liquids by photographing the growth of the drops over a several-hour period (58). Additional discussion on refinements of this technique, largely for low-temperature liquids, can be found in Padday (35) and Adamson (37). McNally et al. used this technique to overcome difficulties associated with the measurement of the surface tension of refractory materials (temperatures greater than 2000°C) using drop shape techniques (125).

6.2.3 The Fiber Elongation Method (Figure 6.4c)

The origin of this method is attributed to Berggren (126). Tammann and Rabe suspended a glass fiber in a furnace and observed the progressive changes due to thermal expansion, contraction due to surface tension, and final lengthening when gravitational forces overcame surface tension (127). Just prior to the final lengthening stage the fiber diameter is a maximum and the forces of surface tension and gravity are equal so that:

$$\gamma = W/\pi d_c \tag{11}$$

where in this case W is the weight of the fiber below the heated zone, and d_c is the critical, maximum fiber diameter. Like the drop weight method, this technique is simple but not very accurate (23, 46, 117).

The temperature limits of the method for glasses depend on measurable flow in a reasonable time at low temperature and devitrification at high temperature (103). Studies of oxide melts that are representative of this technique are found in the literature (103, 127–130).

6.2.4 The Dipping Cylinder Method (Figure 6.4d)

The forces acting on a partially submerged solid plate were first described by Wilhelmy (131). The downward force exerted by the surface tension of the liquid is complemented by the weight of the sample and that of the liquid in the meniscus, and countered by buoyancy. Du Nouy described a technique whereby a ring (instead of a plate) is dipped into the liquid (132). The ring method is more applicable to low-viscosity liquids such as molten salts (133), and further discussion of this can be found elsewhere (34, 35, 134, 135). Washburn and Libman (136) and Washburn and Shelton (137) developed a method for molten glasses that used a platinum cylinder. The forces acting on a thin-walled cylinder are:

$$\gamma\, 2\pi\,(r_1 + r_2) = \Delta F + h\,\Delta\rho\, g\, 2\pi\,(r_1^2 - r_2^2) \tag{12}$$

where r_1 and r_2 are the outer and inner radius of the tube, h is the cylinder immersion depth, $\Delta\rho$ is the liquid density, and g is the gravitational constant. Babcock derived the surface tension of glasses from the maximum force required to extract the cylinder from the liquid surface, ΔF_m:

$$\gamma = f\,\Delta F_m/4\pi r \tag{13}$$

where r is the average radius of the tube, and f is a correction factor that depends on the size and shape of the ring (69). This is one of the more widely used techniques for the accurate determination of the surface tension of high-temperature liquids or melts. Babcock found excellent agreement with the maximum bubble pressure technique when the maximum force method was used (69). The maximum force method as described by Shartsis and Smock (2) works best for high-viscosity glass melts, while an alternate method that requires measurement of the contact angle (138) is recommended for lower-viscosity oxide melts or molten salts (110). Precautions to be taken include assuring that: (a) the cylinder is vertical, (b) loading is done slowly, (c) the contact angle is below 30°, and (d) the proper correction factor is used (40).

Kidd and Gaskell used a variation of this approach, the Padday's cone technique, to measure the surface tension of Fe-saturated calcium ferrite melts (139). The advantage of this technique is that the meniscus is not ruptured as it is in the dipping cylinder or maximum bubble pressure techniques. They concluded that the error resulting from a failure to account for the volume of melt raised above the general liquid level in the dipping cylinder technique was minimal.

Studies of oxide and silicate melts that employed this technique are found in the literature (2, 5, 53–55, 69, 87, 101, 134–165, 337, 340, 353, 354).

6.2.5 Maximum Bubble Pressure Technique (Figure 6.4e)

In 1917, Jaeger first applied this technique to the study of high-temperature liquids (166). It has been modified for glass melts (129, 167, 168), molten salts (169, 170), and molten metals (111, 171, 172). The gas pressure, P_{max}, required for a small hemispherical bubble to break away from the tip of a platinum capillary tube immersed in the melt a known depth is the sum of the hydrostatic pressure and the capillary pressure:

$$P_{max} = P_h + P\gamma = g\,h\,\Delta\rho + 2\gamma/r \tag{14}$$

where g is the gravitational constant, h is the depth of immersion, $\Delta\rho$ is the density difference between the liquid and the gas phase, and r is the radius of the capillary (173). Dorsey (174) describes correction factors for hydrostatic flattening of large bubbles (see discussion in Kingery (40)).

The main experimental difficulty associated with this technique is the accurate positioning of the capillary to a known depth (40). In addition, if the bubbles are not formed slowly enough, an overestimate of the surface tension is obtained (46). Some melts may corrode the capillary tube, but control of the tip diameter can be achieved by careful measurement and periodic calibration with a standard liquid

(110). Kingery states that the contact angle formed between the liquid and the tube material should be less than 30 degrees (40). The effective tube radius to be used in equation 14 depends on how the liquid wets the tube material (46). Ellefson and Taylor limited the maximum bubble pressure technique to liquids with viscosities below 50 to 70 poises (175).

Many studies that have employed this technique can be found in the literature (7, 53, 60, 62, 67, 73, 83, 86, 88, 89, 101, 105, 106, 108, 129, 156, 167–169, 176–215, 349, 336, 340, 343).

Closely related to the maximum bubble pressure technique is the bulb method devised by Pietenpol (118). In this method, the gas pressure required to retain the dimensions of a hollow glass bulb is equated to the capillary pressure. It is important to ensure that an equilibrium size is reached since the readings are viscosity-dependent when the bulb is increasing or decreasing in size. Consequently, this method has not been widely used.

6.2.6 Drop Shape Methods (Figure 6.4f)

There are two variants of drop shape techniques in use depending on whether the liquid rests on a horizontal solid surface (sessile drop) or is hanging from a tube or rod (pendant drop).

Surface tension tends to force a liquid into a spherical shape, while gravity tends to flatten the sessile drop or elongate the pendant drop. The shape of these drops is completely described given the liquid mass, density, and surface tension, but the second-order differential equation that describes this balance cannot be integrated (23, 37). Many approximations have been devised to circumvent this problem (23), but the assumptions have often led to erroneous results (40). Two widely used approaches, the Bashforth and Adams method and the Dorsey method, are based on numerical solutions of the differential equation that describes the balance of capillary and hydrostatic forces. Bashforth and Adams (216) presented a numerical solution to the problem in table form (compiled by Padday (35)). Their solution is described by Mitchell et al. (23) and Adamson (37). Prokop et al. (217) and Glazov et al. (218) provide recent reassessments of the drop shape analysis problem.

6.2.6.1 The Sessile Drop Technique (Figures 6.4f and 6.5)

The relevant dimensions of a sessile drop are shown in Figure 6.5a. Measurement of the maximum diameter of the drop, 2x, the distance from the maximum diameter to the drop apex, z, the diameter of the drop at its base, 2x′, and the height of the drop, z′, allow determination of contact angle, surface tension, and drop volume. Interpolation between values listed in the Bashforth and Adams tables allows determination of the shape factor, β, and a scale factor, b. The density of the liquid, $\Delta\rho$, is a critical part of the surface tension calculation and is usually determined by an independent method. Insertion of the appropriate values into the following equation yields the surface tension:

$$\gamma = (g\ \Delta\rho\ b^2)/\ \beta \qquad (15)$$

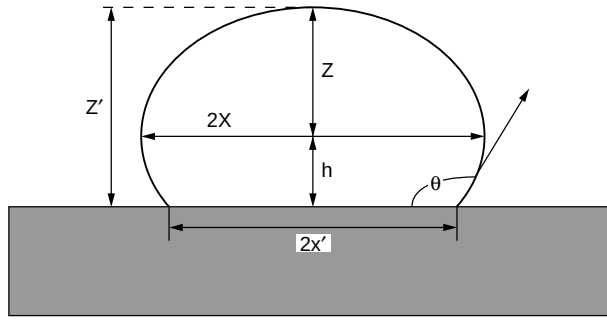

The Bashforth and Adams method

(a)

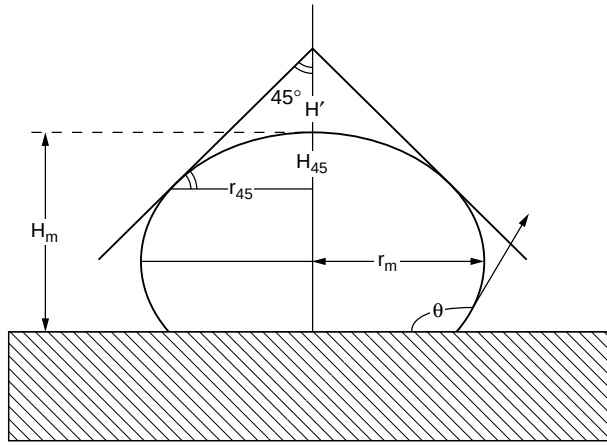

The Dorsey method

(b)

FIGURE 6.5 Dimensions of a sessile drop used in the determination of surface tension.

where g is the acceleration of gravity. Given the mass of the drop, the liquid density can be determined by using the volume calculated with the following expression:

$$V = \pi b^2 (x')^2 / \beta \left[(2/b) - (2 \sin \theta / x') + (\beta z' / b^2) \right] \quad (16)$$

Kingery and Humenick (219) made accurate measurements of the surface tension of metals using the alternative calculation method of Dorsey (220), which is based on the Bashforth and Adams tables. In this method, the distance, H′ (Figure 6.5b), from the apex of the drop to a 45-degree tangent is determined. This value is combined with the maximum radius of the drop, r_m, to calculate a factor, f, which is defined as:

$$f = (H'/r_m) - 0.4142 \quad (17)$$

The surface tension is calculated with the following expression:

$$\gamma = g \Delta\rho r_m^2 [(0.052/f) - 0.12268 + 0.0481 f] \quad (18)$$

Angles other than 45° can be used, and it has been suggested that they yield more reliable values of the shape factor, β, and the size factor, b (110, 221).

The size of the sessile drop does affect the error associated with the determination of surface tension when the Bashforth and Adams approach is used, largely due to its effect on the drop shape factor, β. Errors in the magnification factor affect only the radius of curvature, b (221). Sangorgi et al. provide a nomogram that allows the investigator to select a drop of sufficient size to obtain a β of 2 or greater, thereby enabling the attainment of a 2% accuracy for the surface-tension evaluation (221). Kingery and Humenick hold that the Bashforth and Adams and Dorsey methods should yield deviations of ± 2–3% and ± 5%, respectively for metals and ionic materials having drop diameters of about 0.8 cm (219).

The sessile drop technique has not been as widely used for the measurement of the surface tension of high-temperature liquids as some of those discussed earlier. With attention to experimental details, however, it is a relatively simple technique that yields accurate results. At low temperatures, the surface of sessile drops is not easily renewed, and atmospheric contaminants pose a challenge (222). This problem is largely overcome at high temperatures; furthermore, the minimal contact with container walls as well as the ready attainment of equilibrium, for low-viscosity liquids, present attractive advantages over other techniques.

Quincke was the first to use this technique at high temperatures for the measurement of the surface tension of boric oxide (115). Ellefson and Taylor allowed 1–2 hrs for the attainment of the equilibrium shape although runs up to 82 hrs were conducted with a sodium silicate melt to assure that the final equilibrium contact angle was reached (175). They also cautioned about distortion of the drop profile due to gas evolution from the substrate. They outgassed their sample assembly in vacuum at a temperature below the melting point of the liquid under study in order to avoid this problem. While theory renders the sessile drop technique independent of contact angle, some analytical techniques require large obtuse angles to reduce experimental error to an acceptable level (110, 221, 223). Finding a nonreactive, nonwetted solid substrate for molten silicates is not always easy, and dense graphite or vitreous carbon (74, 175, 224–229), silica (34), refractory metals (230), or noble metals (60, 104, 229) have been used. Additional discussion of errors common to imaging samples at high temperature can be found in Kozakevitch (110), White (111), Sangiorgi et al. (221), Dan et al. (231), and Chung and Iseki (232).

Studies of molten glasses, slags, and salts that have employed the sessile drop technique include references 34, 48, 60, 74, 104, 105, 109, 115, 128, 175, 177, 188, 220, 224–230, 233–248, 333, 334, 344, 345, 348, 350, 351, 352).

6.2.6.2 The Pendant Drop Technique (Figure 6.4f)

When a nonwetted substrate cannot be identified for the sessile drop technique, the pendant drop technique can be used. Here,

$$\gamma = g \Delta\rho d_m^2 \quad (20)$$

where J is the drop shape factor, g is the gravitational constant, $\Delta\rho$ is the liquid density, and d_m is the maximum diameter (Figure 6.4f). Values of J can be found in tables as a function of the ratio $d_{s:}\, d_m$ (249). Pendant drop images can be obtained at temperature or after cooling (250). The effect of drop volume (251) and tilt (252) on the accuracy of this technique has been recently evaluated using low-temperature liquids.

Studies of molten glasses, slags, and salts that have employed the pendant drop technique include references 48, 85, 250, 253–255, 334, 335, 343, 344, 345, 350.

6.2.6.3 Image Analysis for Drop Shape Techniques

There has been a recent revival of interest in these shape evaluation methods due to the accessibility, speed, reduced cost, and ease of application of modern computers. Computerized methods have the advantage over the previously discussed methods of deriving the best fit to the drop profile over the entire meridional section instead of depending on the precise determination of drop dimensions at a few points (221, 256). Maze and Burnet developed a numerical procedure for generating a best fit to a drop profile (257). Rotenburg et al. (256) improved on their method and generalized it to both pendant and sessile drops. This approach has been applied for glass melts (225, 228, 239, 241), molten metals (239, 241, 258–261) and molten salts (261). The speed afforded by the drop shape analysis packages expedites the analysis of experimental drop profiles. Drop symmetry, contact angles, and local shape variations can be readily determined, thereby permitting the detection of experimental errors. This methodology has been extended to include high-resolution video imaging of low-temperature (251, 252, 263–266, 267) as well as high-temperature liquids (229, 231, 232, 239, 243,246, 248, 259, 261, 268, 334, 335, 344, 347, 349, 350). The advantage of this enhancement is in the simplification of data analysis and incorporation of statistical evaluation.

6.2.7 A Comparison of Surface Tension Measurement Techniques

The most important techniques used to determine the surface tension of molten metals and alloys are the sessile drop method, the pendant drop method and the maximum bubble pressure method (268). Murr gives preference to the sessile drop, pendant drop, and drop weight methods, since they cover the broadest range of temperature for liquid metals and alloys (269). Errors as low as 1.5–2 % can be expected with the proper execution of the drop-shape techniques (221). White provided a thorough review of the measurement techniques and their sources of error (111, 270). By far the most widely used technique for molten salts is the maximum bubble pressure technique (271). The other methods in descending order of use are the Wilhelmy plate, capillary rise, dipping cylinder, pin, pendant drop, ring, and sessile drop methods. This ranking was based on experimental difficulties that are characteristic of molten salts such as the inconvenience of visual observation of the melt, the corrosive nature of molten salts, and the vaporization and condensation on the measurement apparatus. Boni and Derge ranked the various methods for deter-

mining the surface tension of slags based on the accuracy of results, rapidity of measurement, simplicity of apparatus, and ease of analysis of the experimental data (46). The maximum bubble pressure technique was the most suitable followed by the dipping cylinder, crucible drop weight and sessile drop methods. These methods yield values of surface tension that are within 4–10 % of each other for sodium silicate glasses. Mitchell et al. stated that the maximum bubble pressure, dipping cylinder, and pendant drop methods agree to within 1% for soda-lime-silicate glasses (23). It is likely that the recent improvements to the sessile drop technique that were discussed in the previous section would improve its standing, although no recent comparative study has been made. The fiber elongation method (129) originally yielded surface tension values for soda-lime-silicate glass that were approximately half of those determined by the maximum bubble pressure method. Parikh demonstrated that the fiber elongation can be used for glasses if proper precautions are taken (103). The capillary rise technique should probably be restricted to special cases where other techniques cannot be used due to the difficulty of determining the capillary radius, capillary rise and contact angle at elevated temperatures.

Aerodynamic levitation techniques have been used to completely eliminate sample-crucible interactions in simple oxide melt systems (347). Whatever technique is used, it should be made clear that proper attention must be paid to sources of chemical contamination (atmosphere, materials of construction, sample preparation, liquid contact material) as well as the physical requirements discussed above.

6.3 DATA FOR SELECTED SYSTEMS

6.3.1 Data Compilations

The focus of this review has been on the surface tension of high-temperature, nonmetallic melts (glasses, slags, molten salts, chalcogenides) and mattes. Surface-tension measurements are very sensitive to seemingly minor differences in trace impurities, experimental technique, and furnace atmospheres. These differences contribute to the wide scatter in the reported data within a given chemical system and are still the subject of discussion in even the most basic systems. It is therefore incumbent on the user to review the data as thoroughly as possible before use. The intent of this section is to review previous data compilations and provide an updated outline of references on sources of data in a fashion that can be readily accessed. No attempt has been made to judge the quality of the data since many of the required experimental details are not reported.

Previous compilations of data for glasses and slags include: Washburn and Libman (136), Washburn and Shelton (137), Appen, Shishov, and Kayalova (120, 124), Mitchell et al. (23), Morey (272), Duga (273), Turkdogan (76, 274). The more recent data compilations of Bansal and Doremus (275) and Mazurin et al. (276-280) are very useful. Data on the surface tension of molten salts can be found in Janz (281), Janz and Dijkhuis (170), Janz, Allen, Bansal, Murphy, and Tomkins (282), Mills and Keene (283), Brandes and Brook (284), and Thonstad et al. (356).

Suzuki described the database, named INTERGLAD, that was constructed by the New Glass Forum in Japan (286). It includes many glass properties that are

organized according to the chemical composition of amorphous materials including oxides, halide, chalcogenides, as well as glass ceramics. The system is based on a CD ROM accessible by a personal computer. Unfortunately, the original references are not always cited. Several types of search strategies are available to retrieve the data. 1170 compositional entries were found in this data file for surface tension. The data compilation of Mazurin et al. (276–280) accounted for 44% of the entries, while 39% were from Bansal and Doremus (275). The increasing use of computer modeling of glass-manufacturing processes has led to the development of databases for commercial glass compositions (338).

6.3.2 Outline of Sources of High-Temperature Surface Tension Data for Non-Metallic Liquids

An alphabetical listing according to chemistry of the melt is provided in this section as a guide to the literature on surface tension. The first section (Table 6.3) contains oxide melts (including simple oxides, silicates, borates, etc.) classified by the number of components:

1. Unary
2. Binary
3. Ternary
4. Quaternary
5. Quinary
6. Oxide melts having more than five components

The component in section case is an oxide species. The second section (Table 6.4) contains chalcogenides, halides, and mixed oxide/halide systems. Again, the references are classified according to the number of components. The review of the literature in this section is not as comprehensive as the previous one, and only representative studies are listed.

ACKNOWLEDGMENTS

The skillful retrieval of many of the citations and copies of manuscripts cited in this work was orchestrated by N. Kotow, E. Mounts, and M. Xidis.

TABLE 6.3
Index to Studies of the Surface Tension of Oxide Melts

	Unary Oxides
Al_2O_3	24, 44, 48, 125, 199, 207, 230, 253, 255, 287–290, 347
B_2O_3	44, 48, 54, 60, 65, 113, 115, 129, 135, 143, 156, 179, 200, 288, 290
BeO	288, 289
CaO	288
FeO	44, 140, 142, 288, 290
GeO_2	48
La_2O_3	44, 286
MgO	290
MnO	288
Nb_2O_5	207
P_2O_5	48
PbO	44, 288
SiO_2	48, 103, 188, 290
Sm_2O_3	230
Ti_2O_3	207
UO_2	230
V_2O_5	207
ZrO_2	255
	Binary Oxides
Al_2O_3-CaO	53, 85, 89, 177, 180–183, 185, 195, 196, 198, 293, 294
Al_2O_3-FeO	140
Al_2O_3-Cr_2O_3	199, 255
Al_2O_3-MgO	195, 230, 255
Al_2O_3-SiO_2	85, 199, 295
Al_2O_3-TiO_2	255
Al_2O_3-Y_2O_3	209
Al_2O_3-ZrO_2	255
B_2O_3-BaO	55, 145, 296, 297
B_2O_3-CaO	55, 145, 241
B_2O_3-CdO	55
B_2O_3-CeO_2	179
B_2O_3-Cs_2O	179
B_2O_3-K_2O	54
B_2O_3-La_2O_3	179
B_2O_3-Li_2O	54, 55, 166, 175, 327
B_2O_3-MgO	55
B_2O_3-Na_2O	54, 166, 200, 292, 298, 343
B_2O_3-PbO	54, 65, 153, 354
B_2O_3-Rb_2O	179
B_2O_3-SiO_2	65, 343
B_2O_3-Sm_2O_3	179
B_2O_3-SrO	55, 145
B_2O_3-TeO_2	206
B_2O_3-Y_2O_3	179

TABLE 6.3 (Continued)
Index to Studies of the Surface Tension of Oxide Melts

B_2O_3-ZnO	54, 55, 143
BaO-SiO_2	149
BaO-TiO_2	208
Bi_2O_3-Ga_2O_3	212
Bi_2O_3-GeO_2	237
B_2O_3-$L2_2O_3$	212
Bi_2O_3-MoO_3	281, 326
Bi_2O_3-SiO_2	237
CO_2-Na_2O	61
CaO-Cu_xO	349
CaO-FeO	140, 142, 247, 330
CaO-Fe_2O_3	53, 159, 247, 330
CaO-P_2O_5	86, 87
CaO-SiO_2	7, 53, 61, 67, 75, 85, 105, 177, 187, 188, 192, 224, 233, 299
Cr_2O_3-FeO	140
Cr_2O_3-Na_2O	159
Cs_2O-SiO_2	121
Cu_xO-SiO_2	348
FeO-Fe_2O_3	105, 163
FeO-MnO	142
FeO-Na_2O	142
FeO-P_2O_5	142
FeO-SiO_2	53, 61, 139, 142, 188, 242, 246
FeO-TiO_2	142
K_2O-MoO_3	154, 281
K_2O-Nb_2O_5	160
K_2O-P_2O_5	87, 281
K_2O-SiO_2	61, 120, 121, 123, 124, 141, 229, 333
K_2O-WO_3	281
Li_2O-MoO_3	154
Li_2O-P_2O_5	86
Li_2O-SiO_2	61, 120, 121, 123, 124, 141, 166
MgO-SiO_2	53, 61, 233
MgO-P_2O_5	186
MnO-SiO_2	53, 61, 188, 300
MoO_3-Na_2O	154, 281
MoO_3-PbO	281, 326
Na_2O-P_2O_5	86, 87, 129, 166, 281, 301, 302
Na_2O-SiO_2	44, 53, 61, 68, 101, 106, 109, 119–121, 123, 124, 136, 137, 141, 153, 167, 175, 176, 225, 238, 243, 292, 298
Na_2O-TiO_2	208
Na_2O-WO_3	281
P_2O_5-ZnO	86, 190
PbO-SiO_2	65, 76, 103, 119, 146, 150, 157, 164, 354
Rb_2O-SiO_2	121, 158
SnO_2-SiO_2	303

TABLE 6.3 (Continued)
Index to Studies of the Surface Tension of Oxide Melts

Ternary Oxides	
Al_2O_3-B_2O_3-BaO	55
Al_2O_3-B_2O_3-ZnO	55
Al_2O_3-BaO-SiO_2	73, 120, 124, 149
Al_2O_3-CaO-Fe_2O_3	198
Al_2O_3-CaO-MgO	144, 182, 185, 198
Al_2O_3-CaO-SiO_2	53, 60, 62, 67, 73, 82, 85, 105, 144, 177, 180, 182, 185, 189, 194, 213, 218, 224, 228, 235, 245, 290, 293, 294, 304, 305
Al_2O_3-CaO-TiO_2	185
Al_2O_3-CaO-ZrO_2	185
Al_2O_3-FeO-SiO_2	134
Al_2O_3-MgO-SiO_2	73, 144
Al_2O_3-MnO-SiO_2	53
Al_2O_3-Na_2O-SiO_2	74, 120, 124
Al_2O_3-PbO-SiO_2	148
Al_2O_3-SiO_2-TiO_2	135
Al_2O_3-SnO-SiO_2	303
As_2O_3-Na_2O-SiO_2	303
B_2O_3-BaO-Cs_2O	55
B_2O_3-BaO-K_2O	55
B_2O_3-BaO-Li_2O	55
B_2O_3-BaO-Na_2O	55
B_2O_3-BaO-SiO_2	149, 296
B_2O_3-BaO-ZnO	55
B_2O_3-CaO-Cs_2O	55
B_2O_3-CaO-K_2O	55
B_2O_3-CaO-Li_2O	55, 145
B_2O_3-CaO-Na_2O	55, 145
B_2O_3-CaO-ZnO	55
B_2O_3-CdO-K_2O	55
B_2O_3-CdO-La_2O_3	306
B_2O_3-CdO-ZnO	55
B_2O_3-K_2O-MgO	55
B_2O_3-K_2O-SiO_2	120, 122–124
B_2O_3-K_2O-SrO	55
B_2O_3-K_2O-ZnO	55
B_2O_3-Li_2O-CaO	55
B_2O_3-Li_2O-SiO_2	120, 122–124
B_2O_3-Li_2O-SrO	55
B_2O_3-Li_2O-ZnO	55
B_2O_3-Na_2O-SiO_2	120, 122–124, 153, 193, 203, 239, 240
B_2O_3-Na_2O-SrO	55, 145
B_2O_3-Na_2O-V_2O_5	327
B_2O_3-Na_2O-ZnO	55
B_2O_3-PbO-SiO_2	148, 157, 307, 329, 354

TABLE 6.3 (Continued)
Index to Studies of the Surface Tension of Oxide Melts

B_2O_3-PbO-TeO_2	206
B_2O_3-PbO-ZnO	55
B_2O_3-SrO-ZnO	55
BaO-BeO-SiO_2	149
BaO-CaO-SiO_2	149
BaO-CdO-SiO_2	149
BaO-Fe_2O_3-SiO_2	149
BaO-K_2O-SiO_2	120, 124, 149
BaO-Li_2O-SiO_2	120, 122, 124, 149
BaO-MgO-SiO_2	149
BaO-Na_2O-SiO_2	120, 122, 124, 149
BaO-P_2O_5-ZnO	353
BaO-PbO-SiO_2	147–149
BaO-SiO_2-SrO	149
BaO-SiO_2-TiO_2	149
BaO-SiO_2-ZnO	149
BaO-SiO_2-ZrO_2	149
BeO-K_2O-SiO_2	120, 124
BeO-Li_2O-SiO_2	120, 122, 124
BeO-Na_2O-SiO_2	120, 124
Bi_2O_3-MoO_4-PbO	326
Bi_2O_3-Na_2O-SiO_2	120, 124
Bi_2O_3-PbO-SiO_2	122
CaO-K_2O-SiO_2	308, 309
CaO-FeO-Fe_2O_3	139, 247, 337
CaO-FeO-SiO_2	105, 122, 134, 140, 142, 204, 309, 336, 337
CaO-Li_2O-SiO_2	120, 122, 124
CaO-MgO-SiO_2	53, 105, 144, 177, 233
CaO-Na_2O-SiO_2	5, 59, 68, 69, 74, 101, 106, 109, 116, 118, 120, 124, 129, 136, 137, 168, 176, 178, 229, 243, 308–312, 335, 336, 343, 345, 351
CaO-P_2O_5-SiO_2	7
CaO-PbO-SiO_2	147, 148
CaO-SiO_2-SnO	303
CdO-K_2O-SiO_2	120, 124
CdO-Li_2O-SiO_2	120, 124
CdO-Na_2O-SiO_2	120, 124
CdO-PbO-SiO_2	147, 148
Ce_2O_3-Na_2O-SiO_2	58
CoO-Na_2O-SiO_2	120, 124, 331
Cr_2O_3-K_2O-SiO_2	122
Cr_2O_3-Li_2O-SiO_2	122
Cr_2O_3-Na_2O-SiO_2	58, 122
Cs_2O-PbO-SiO_2	147, 148
FeO-Fe_2O_3-SiO_2	105, 134, 139
FeO-MgO-SiO_2	83, 134, 204

TABLE 6.3 (Continued)
Index to Studies of the Surface Tension of Oxide Melts

$FeO-MnO-SiO_2$	105, 142, 177
$FeO-Na_2O-SiO_2$	120, 124
$FeO-SiO_2-SnO$	303
$FeO-SiO_2-ZnO$	134
$Fe_2O_3-Na_2O-SiO_2$	58, 120, 124, 243
$Fe_2O_3-PbO-SiO_2$	148
$K_2O-MgO-SiO_2$	120, 124
$K_2O-MoO_3-SiO_2$	122
$K_2O-Na_2O-SiO_2$	120, 124
$K_2O-P_2O_5-ZnO$	184, 191
$K_2O-PbO-SiO_2$	2, 120, 122, 124, 147, 148, 151
$K_2O-Sb_2O_3-SiO_2$	122
K_2O-SiO_2-SrO	120, 124
$K_2O-SiO_2-TiO_2$	120, 122, 124
$K_2O-SiO_2-V_2O_5$	122
$K_2O-SiO_2-WO_3$	122
K_2O-SiO_2-ZnO	120, 124
$La_2O_3-Na_2O-SiO_2$	225
$Li_2O-MgO-SiO_2$	120, 124
$Li_2O-MoO_3-SiO_2$	122
$Li_2O-Na_2O-SiO_2$	120, 124, 176
$Li_2O-PbO-SiO_2$	120, 122, 124, 147, 148, 152
$Li_2O-Sb_2O_3-SiO_2$	122
Li_2O-SiO_2-SrO	120, 122, 124
$Li_2O-SiO_2-TiO_2$	120, 122, 124
$Li_2O-SiO_2-V_2O_5$	122
$Li_2O-SiO_2-WO_3$	122
Li_2O-SiO_2-ZnO	120, 122, 124
$MgO-Na_2O-SiO_2$	74, 120, 124, 308
$MgO-PbO-SiO_2$	147, 148
$MnO-Na_2O-SiO_2$	58, 74, 120, 124
$Mn_2O_3-Na_2O-SiO_2$	58
$MoO_3-Na_2O-SiO_2$	58, 122, 193
$Na_2O-NiO-SiO_2$	120, 124
$Na_2O-P_2O_5-SiO_2$	58, 122
$Na_2O-P_2O_5-ZnO$	184, 191
$Na_2O-PbO-SiO_2$	58, 119, 120, 124, 147, 148, 150
$Na_2O-Rb_2O-SiO_2$	158
$Na_2O-Sb_2O_3-SiO_2$	58, 122
Na_2O-SiO_2-SrO	120, 124
$Na_2O-SiO_2-TiO_2$	120, 122, 124
$Na_2O-SiO_2-UO_3$	58, 122
$Na_2O-SiO_2-V_2O_5$	122
$Na_2O-SiO_2-WO_3$	58, 122
Na_2O-SiO_2-ZnO	120, 124
$PbO-Rb_2O-SiO_2$	147, 148

TABLE 6.3 (Continued)
Index to Studies of the Surface Tension of Oxide Melts

PbO-SiO_2-TiO_2	147, 148
PbO-SiO_2-ZnO	147, 148
PbO-SiO_2-ZrO_2	147, 148
Quaternary	
Al_2O_3-BaO-Na_2O-SiO_2	120, 124
Al_2O_3-BeO-Na_2O-SiO_2	120, 124
Al_2O_3-CaO-FeO-Fe_2O_3	215
Al_2O_3-CaO-FeO-SiO_2	214
Al_2O_3-CaO-K_2O-SiO_2	305
Al_2O_3-CaO-MgO-SiO_2	177, 197
Al_2O_3-CaO-Na_2O-SiO_2	305
Al_2O_3-CaO-SiO_2-TiO_2	236
Al_2O_3-CdO-Na_2O-SiO_2	120, 124
Al_2O_3-CoO-Na_2O-SiO_2	120, 124
Al_2O_3-FeO-Fe_2O_3-SiO_2	134
Al_2O_3-FeO-Na_2O-SiO_2	120, 124
Al_2O_3-MgO-Na_2O-SiO_2	120, 124
Al_2O_3-MnO-Na_2O-SiO_2	120, 124
Al_2O_3-Na_2O-PbO-SiO_2	120, 124
Al_2O_3-Na_2O-SiO_2-SrO	120, 124
Al_2O_3-Na_2O-SiO_2-ZnO	120, 124
As_2O_3-CaO-Na_2O-SiO_2	311
As_2O_3-K_2O-PbO-SiO_2	2
B_2O_3-BaO-Na_2O-SiO_2	120, 124
B_2O_3-BeO-Na_2O-SiO_2	120, 124
B_2O_3-CaO-Na_2O-SiO_2	59, 120, 124
B_2O_3-CdO-Na_2O-SiO_2	120, 124
B_2O_3-MgO-Na_2O-SiO_2	120, 124
B_2O_3-MoO_3-Na_2O-SiO_2	193
B_2O_3-Na_2O-PbO-SiO_2	120, 124
B_2O_3-Na_2O-SiO_2-ZnO	120, 124
B_2O_3-SrO-Na_2O-SiO_2	120, 124
BaO-CO_2-K_2O-Li_2O	210
BaO-CaO-Na_2O-SiO_2	59, 120, 124
BaO-Na_2O-SiO_2-SnO_2	120, 124
BaO-Na_2O-SiO_2-TiO_2	120, 124
BaO-Na_2O-SiO_2-ZrO_2	120, 124
BeO-CaO-Na_2O-SiO_2	120, 124
BeO-Na_2O-SiO_2-TiO_2	120, 124
CO_2-CaO-K_2O-Li_2O	210
CO_2-K_2O-Li_2O-SrO	210
CaO-CeO_2-Na_2O-SiO_2	59
CaO-CdO-Na_2O-SiO_2	120, 124
CaO-CoO-Na_2O-SiO_2	59, 310
CaO-Cu_2O-FeO-Fe_2O_3	247
CaO-FeO-Fe_2O_3-ZnO	211

TABLE 6.3 (Continued)
Index to Studies of the Surface Tension of Oxide Melts

$CaO\text{-}FeO\text{-}Fe_2O_3\text{-}SiO_2$	134, 215, 340
$CaO\text{-}Fe_2O_3\text{-}Na_2O\text{-}SiO_2$	59, 229, 344
$CaO\text{-}K_2O\text{-}Na_2O\text{-}SiO_2$	34, 59, 112, 250
$CaO\text{-}Li_2O\text{-}Na_2O\text{-}SiO_2$	59, 176
$CaO\text{-}MgO\text{-}Na_2O\text{-}SiO_2$	2, 3, 59, 60, 120, 124, 229
$CaO\text{-}Mn_2O_3\text{-}Na_2O\text{-}SiO_2$	59, 311
$CaO\text{-}MoO_3\text{-}Na_2O\text{-}SiO_2$	311
$CaO\text{-}Na_2O\text{-}NiO\text{-}SiO_2$	59
$CaO\text{-}Na_2O\text{-}P_2O_5\text{-}SiO_2$	311
$CaO\text{-}Na_2O\text{-}PbO\text{-}SiO_2$	59, 120, 124
$CaO\text{-}Na_2O\text{-}Sb_2O_3\text{-}SiO_2$	311
$CaO\text{-}Na_2O\text{-}SiO_2\text{-}SnO_2$	120, 124
$CaO\text{-}Na_2O\text{-}SiO_2\text{-}SrO$	120, 124
$CaO\text{-}Na_2O\text{-}SiO_2\text{-}TiO_2$	59, 120, 124
$CaO\text{-}Na_2O\text{-}SiO_2\text{-}UO_2$	311
$CaO\text{-}Na_2O\text{-}SiO_2\text{-}V_2O_5$	311
$CaO\text{-}Na_2O\text{-}SiO_2\text{-}WO_3$	311
$CaO\text{-}Na_2O\text{-}SiO_2\text{-}ZnO$	59, 120, 124
$CaO\text{-}Na_2O\text{-}SiO_2\text{-}ZrO_2$	59, 120, 124
$CdO\text{-}Na_2O\text{-}SiO_2\text{-}TiO_2$	120, 124
$FeO\text{-}Fe_2O_3\text{-}MgO\text{-}SiO_2$	83 (in presence of Fe)
$MgO\text{-}Na_2O\text{-}SiO_2\text{-}TiO_2$	120, 124
$Na_2O\text{-}PbO\text{-}SiO_2\text{-}TiO_2$	120, 124
$Na_2O\text{-}SiO_2\text{-}SrO\text{-}TiO_2$	120, 124
$Na_2O\text{-}SiO_2\text{-}TiO_2\text{-}ZnO$	120, 124
Quinary Oxides	
$Al_2O_3\text{-}B_2O_3\text{-}CaO\text{-}Na_2O\text{-}SiO_2$	129
$Al_2O_3\text{-}B_2O_3\text{-}K_2O\text{-}Na_2O\text{-}SiO_2$	343
$Al_2O_3\text{-}CaO\text{-}FeO\text{-}MgO\text{-}SiO_2$	172
$Al_2O_3\text{-}CaO\text{-}K_2O\text{-}MgO\text{-}SiO_2$	305
$Al_2O_3\text{-}CaO\text{-}MgO\text{-}Na_2O\text{-}SiO_2$	59, 69, 103, 155, 168, 227, 250
$Al_2O_3\text{-}MgO\text{-}NO_x\text{-}SiO_2\text{-}Y_2O_3$	244
$As_2O_3\text{-}B_2O_3\text{-}K_2O\text{-}Na_2O\text{-}SiO_2$	2
$As_2O_3\text{-}K_2O\text{-}Na_2O\text{-}PbO\text{-}SiO_2$	2
$B_2O_3\text{-}CaO\text{-}Na_2O\text{-}R_2O_3\text{-}SiO_2$	129
$B_2O_3\text{-}K_2O\text{-}Li_2O\text{-}Na_2O\text{-}SiO_2$	108
$BaO\text{-}K_2O\text{-}Na_2O\text{-}PbO\text{-}SiO_2$	2, 59, 60
$CaO\text{-}Cu_2O\text{-}FeO\text{-}Fe_2O_3\text{-}SiO_2$	247
$CaO\text{-}FeO\text{-}Fe_2O_3\text{-}MgO\text{-}SiO_2$	134
$K_2O\text{-}Na_2O\text{-}PbO\text{-}R_2O_3\text{-}SiO_2$	112, 113
Complex Oxide Melts with More Than Five Components	
$Al_2O_3\text{-}As_2O_3\text{-}B_2O_3\text{-}BaO\text{-}CaO\text{-}PbO\text{-}Sb_2O_3\text{-}SiO_2$	2
$Al_2O_3\text{-}As_2O_3\text{-}B_2O_3\text{-}BaO\text{-}K_2O\text{-}Na_2O\text{-}PbO\text{-}Sb_2O_3\text{-}SiO_2\text{-}ZnO$	2

TABLE 6.3 (Continued)
Index to Studies of the Surface Tension of Oxide Melts

Al_2O_3-As_2O_3-B_2O_3-BaO-K_2O-Na_2O-Sb_2O_3-SiO_2-ZnO	2
Al_2O_3-B_2O_3-BaO-CaO-CeO_2-Cr_2O_3-Cs_2O-Fe_2O_3-K_2O-La_2O_3-Li_2O-MgO-MnO_2-MoO_3-Na_2O-Nd_2O_3-NiO-P_2O_5-SO_3-SiO_2-SrO-TiO_2-Y_2O_3-ZnO-ZrO_2	113
Al_2O_3-B_2O_3-BaO-CaO-Fe_2O_3-K_2O-Na_2O-SiO_2-ZnO-ZrO_2	175
Al_2O_3-B_2O_3-BaO-CaO-K_2O-Na_2O-SiO_2-SO_3	5
Al_2O_3-B_2O_3-CaF_2-CoO-K_2O-Li_2O-MnO_2-Na_2O-NiO-SiO_2	176
Al_2O_3-B_2O_3-CaF_2-CoO-K_2O-MnO_2-Na_2O-NiO-SiO_2	176
Al_2O_3-B_2O_3-CaO-K_2O-Li_2O-MgO-NaF-Na_2O-Sb_2O_3-SiO_2-TiO_2-ZnO	176
Al_2O_3-B_2O_3-CaO-K_2O-Li_2O-Na_2O-PbO-SiO_2-ZnO	176
Al_2O_3-B_2O_3-CaO-K_2O-MgO-NaF-Na_2O-Sb_2O_3-SiO_2-TiO_2-ZnO	176
Al_2O_3-B_2O_3-CaO-F-K_2O-MgO-Na_2O-SiO_2	155
Al_2O_3-B_2O_3-CaO-Fe_2O_3-K_2O-MgO-Na_2O-SiO_2	335
Al_2O_3-B_2O_3-CaO-Fe_2O_3-MgO-Na_2O-SiO_2-TiO_2	335
Al_2O_3-B_2O_3-CaO-K_2O-MgO-Na_2O-SiO_2	350
Al_2O_3-B_2O_3-CaO-Li_2O-Na_2O-SiO_2	176
Al_2O_3-B_2O_3-CaO-MgO-Na_2O-SiO_2-SrO	342, 343
Al_2O_3-B_2O_3-CaO-K_2O-Na_2O-PbO-SiO_2-ZnO	176
Al_2O_3-BaO-CeO_2-K_2O-Na_2O-Sb_2O_3-SiO_2-SrO-TiO_2-ZnO-ZrO_2	165, 335
Al_2O_3-CaO-FeO-Fe_2O_3-K_2O-MgO-MnO-Na_2O-P_2O_5-SiO_2-TiO_2	34
Al_2O_3-CaO-Fe_2O_3-K_2O-MgO-Na_2O-SiO_2-SO_3-TiO_2	336
Al_2O_3-CaO-K_2O-Li_2O-MgO-Na_2O-SiO_2	162
Al_2O_3-CaO-K_2O-MgO-Na_2O-SiO_2	162, 250, 343
As_2O_3-B_2O_3-BaO-BeO-CaO-Sb_2O_3-SiO_2-SrO	2
As_2O_3-B_2O_3-BaO-K_2O-Na_2O-PbO-SiO_2-ZrO_2	2
As_2O_3-B_2O_3-BaO-K_2O-Na_2O-SiO_2-ZnO	2
As_2O_3-B_2O_3-BeO-K_2O-Li_2O-SiO_2-SrO	2
As_2O_3-B_2O_3-K_2O-Na_2O-SiO_2-ZnO	2
As_2O_3-BaO-K_2O-Na_2O-PbO-Sb_2O_3-SiO_2	2
As_2O_3-BaO-K_2O-Na_2O-PbO-Sb_2O_3-SiO_2-ZnO	2
As_2O_3-BaO-K_2O-Na_2O-PbO-SiO_2	2
As_2O_3-BaO-K_2O-Na_2O-PbO-SiO_2-ZnO	2
As_2O_3-BaO-K_2O-PbO-SiO_2-ZnO	2
B_2O_3-BaO-CoO-Fe_2O_3-Na_2O-SnO_2	161
B_2O_3-CaO-K_2O-Na_2O-Sb_2O_3-SiO_2	2

TABLE 6.4
Index to Studies of the Surface Tension of Chalcogenide, Halide, and Mixed Oxide/Halide Melts

Unary Salts

Halide	
AgCl	281, 313
AgBr	281, 313
$AlCl_3$	282
$BaBr_2$	281, 314
$BaCl_2$	281, 315
BaI_2	281
$BiBr_3$	44, 281, 314
$BiCl_3$	44, 281
$CaBr_2$	281, 314
$CaCl_2$	281, 282
CaI_2	281, 314
$CdCl_2$	44
CsBr	281, 316
CsCl	281, 316
CsF	281, 285, 316
CsI	281, 316
$GaCl_2$	281, 318
KBr	281, 319
KCl	281, 282, 316
KF	281, 282, 285, 316
KI	44, 281, 282, 317
LiBr	282
LiCl	44, 281, 282
LiF	281, 282, 285, 316
LiI	282
$MgCl_2$	281, 282
Na_3AlF_6	47
NaBr	281, 320
NaCl	170, 281, 282, 285, 290, 316, 317
NaF	47, 175, 281, 282, 316
NaI	316, 317, 281
$PbCl_2$	281
RbBr	281, 316
RbCl	281, 316
RbF	281, 285, 316
RbI	281, 316
$SnCl_2$	44, 281
$SrBr_2$	281, 314
$SrCl_2$	281, 314
SrI_2	281, 314

TABLE 6.4 (Continued)
Index to Studies of the Surface Tension of Chalcogenide, Halide, and Mixed Oxide/Halide Melts

Carbonates	
K_2CO_3	281, 282, 321
Li_2CO_3	281, 282, 321
Na_2CO_3	281, 282, 321
Chalcogenide Melts Containing Group VI Elements	
S	282
Cu_2S	281, 288, 322
FeS	287, 288, 323
Na_2S_4, Na_2S_5	282
Ni_3S_2	322
Nitrates	
$AgNO_3$	281, 317
$Ba(NO_3)_2$	281, 291
$Ca(NO_3)_2$	281, 291
$CsNO_3$	44, 281, 291
KNO_3	281, 282, 317
$LiNO_3$	44, 281, 282, 291
$NaNO_3$	281, 282, 317
$Sr(NO_3)_2$	281, 291
$RbNO_3$	281, 324
Sulphates	
$BaSO_4$	281
Cs_2SO_4	44, 281
K_2SO_4	282
Li_2SO_4	44, 281, 282
Na_2SO_4	44, 281, 282
Rb_2SO_4	281
Binary Carbonates	
K_2CO_3-Li_2CO_3	282
K_2CO_3-Na_2CO_3	282
Li_2CO_3-Na_2CO_3	282
Binary Halides	
AlF_3-CsF	285
AlF_3-KF	356
AlF_3-LiF	285
AlF_3-Na_3AlF_6	169
AlF_3-NaF	47, 332, 355, 356
AlF_3--RbF	285
$CaCl_2$-NaCl	282
KCl-LiCl	282

TABLE 6.4 (Continued)
Index to Studies of the Surface Tension of Chalcogenide, Halide, and Mixed Oxide/Halide Melts

KCl-NaCl	282
KF-NaF	282
LiCl-LiF	282
Na_3AlF_6-NaF	169
Binary Nitrates	
$AgNO_3$-KNO_3	325
$AgNO_3$-$NaNO_3$	325
KNO_3-$NaNO_3$	282
Mixed Binary Systems	
Al_2O_3-CaF_2	283
B_2O_3-CaF_2	283
BaO-CaF_2	205, 283
CaF_2-CaO	205, 283
CaF_2-Cr_2O_3	283
CaF_2-MgO	196, 205, 283
CaF_2-Nb_2O_5	283
CaF_2-SiO_2	283
CaF_2-TiO_2	283
CaF_2-V_2O_5	283
Li_2SO_4-NaCl	283
CaF_2-ZrO_2	283
Ternary Salts	
AlF_3-CaF_2-NaF	355, 356
AlF_3-KF-NaF	355, 356
AlF_3-LiF-NaF	355, 356
AlF_3-MgF_2-NaF	355
AlF_3-NaCl-NaF	355
BaF_2-LaF_3-ZrF_4	254
K_2CO_3-Li_2CO_3-Na_2CO_3	282
KCl-NaCl-$PbCl_2$	202, 238
Ternary Mixed	
AlF_3-Al_2O_3-NaF	47, 332, 169, 354–356
Al_2O_3-B_2O_3-CaF_2	283
Al_2O_3-CaF_2-CaO	89, 185, 198, 226, 283
Al_2O_3-CaF_2-TiO_2	283
Al_2O_3-CaO-NaF	185, 198
Al_2O_3-CaF_2-V_2O_5	283
BaF_2-CaO-SiO_2	75
CaF_2-CaO-Cr_2O_3	283
CaF_2-CaO-SiO_2	283
CaF_2-Na_2O-SiO_2	120, 124
CaO-KF-SiO_2	75

TABLE 6.4 (Continued)
Index to Studies of the Surface Tension of Chalcogenide, Halide, and Mixed Oxide/Halide Melts

CaO-LiF-SiO_2	75
CaO-MgF_2-SiO_2	75
CaO-NaF-SiO_2	75
Na_2O-Na_2S-SiO_2	74
Ternary Mattes or Chalcogenides	
Cu Ni-S	242
Fe-Ni-S	242
Mixed Systems with Four or More Components	
AlF_3-Al_2O_3-CaF_2-NaF	355, 356
AlF_3-Al_2O_3-CaF_2-KF-LiF-NaF	356
AlF_3-Al_2O_3-CaO-NaF	182
Al_2N_2-Al_2O_3-MgO-$SiN_{4/3}$-SiO_2	244
Al_2N_2-Al_2O_3-SiO_2-Y_2O_3	244
Al_2N_2-MgO-$SiN_{4/3}$-SiO_2-Y_2O_3	244
Al_2O_3-CaF_2-CaO-MgO-SiO_2	196
Al_2O_3-CaF_2-CaO-SiO_2	235, 304
Al_2O_3-BaO-S-SiO_2	73
Al_2O_3-CaO-MgO-S-SiO_2	197
Al_2O_3-CaO-S-SiO_2	73
Al_2O_3-MgO-S-SiO_2	73
Al_2O_3-CaF_2-MgO-Na_2O-SiO_2	333
CaF_2-MgO-Na_2O-SiO_2	120, 124

REFERENCES

1. M. B. Volf, *Mathematical Approach to Glass*, Elsevier Scientific Publishing Company, Amsterdam, 1988, p. 313.
2. L. Shartsis and A. W. Smock, Surface tensions of some optical glasses, *J. Res. Nat. Bur. Stds.* 38:241 (1947), and *J. Amer. Ceram. Soc.* 30:130 (1947).
3. L. Sasek, Viscosity, surface tension, and fining of silicate glass, *Sb.Vys. Sk. Chem.-Technol. Praze, Chem. Technol. Silik.* L9:111 (1982).
4. H. Jebsen-Marwedel, Influence of surface tension in glassmelting processes, *J. Soc. Glass Tech.* 21:436 (1937).
5. W. B. Silverman, Surface tension of glass and its effect on cords, *J. Amer. Ceram. Soc.* 25:168 (1942).
6. M. A. Knight, Surface tension and the persistence of cords in glass, *J. Amer. Ceram. Soc.* 27:143 (1944).
7. C. F. Cooper and J. A. Kitchener, Foaming of silicate melts, *J. Iron Steel Inst.*, London 193:48 (1959).
8. J. Hlaváč, *The Technology of Glass and Ceramics, An Introduction*, Elsevier Scientific Publishing Company, Amsterdam, 1983, p. 78.

9. H. J. Tress, Some distinctive contours worn on alumina-silica refractory faces by different molten glasses: surface tension and mechanism of refractory attack, *Trans. Soc. Glass Tech.* 38:89 (1954).
10. R. Bruckner, Die zu Erosionen an Modellsubstanzen und feüerfesten Stoffen fuhrenden Grundmechanismen der Grennzflächenkonvektion, *Glastech. Be*r. 40:451 (1967).
11. T.-I. Oh, L. N. Shen, R. W. Ure, Jr., and I. B. Cutler, Slag penetration into oxide refractories, *Ceram. Bull*. 56:649 (1977).
12. J. E. Comeforo and R. K. Hursh, Wetting of Al_2O_3-SiO_2 refractories by molten glass: II, effect of wetting on penetration of glass into refractory, *J. Amer. Ceram. Soc.* 35:142 (1952).
13. J. Antal-Boza, Slag infiltration into the refractory lining of furnaces, *Proc. 8th Conf. Silicate Ind.*,1965, pp. 743-749.
14. C. K. Edge, *Float Glass, Commercial Glasses, Advances in Ceramics Vol. 18* (D. C. Boyd and J. F. MacDowell, Eds.), The American Ceramic Society, Columbus, Ohio, 1986, p. 43.
15. P. K. Gupta, Fiber forming from low viscosity melts, *Advances in the Fusion and Processing of Glass, Ceramic Trans. Vol. 29*, (A. K. Varshneya, D. F. Bickford, and P. P. Bihuniak, Eds.), The American Ceramic Society, Westerville, Ohio, 1993, p. 35.
16. E. Ruckenstein and S. K. Ihm, Kinetics of glass formation, *J. Chem. Soc. Far, Trans.* 3:764 (1976).
17. W. D. Kingery, Densification during sintering in the presence of a liquid phase. I. Theory, *J. Appl. Phys*. 30:301 (1959).
18. S. Petjovnik, D. Kolar, W. J. Huppmann and G. Petzow, Sintering of alumina in presence of liquid phase, *Mat. Sci. Monogr.* 4 (Sintering-New Dev.) 285 (1979).
19. R. M. German, *Liquid Phase Sintering*, Plenum Press, New York, 1985, p. 65.
20. T. M. Shaw, Liquid redistribution during liquid-phase sintering, *J. Amer. Ceram. Soc.* 69:27 (1986).
21. O-H. Kwon and G. L. Messing, Kinetic analysis of solution-precipitation during liquid-phase sintering of alumina, *J. Amer. Ceram. Soc.*73:275 (1990).
22. J. H. Partridge, *Glass-to-Metal Seals*, The Society of Glass Technology, Sheffield, 1949.
23. D. W. Mitchell, S. P. Mitoff, V. F. Zackay, and J. A. Pask, Measurement of surface tension of glasses, Part I. *The Glass Industry* 33:453 (1952) and Part II. *The Glass Industry* 33:515 (1952).
24. W. D. Kingery, The role of surface energy and wetting in metal-ceramic sealing, *Bull. Am. Ceram. Soc.* 35:108 (1956).
25. E. B. Shand, *Glass Engineering Handbook*, McGraw-Hill Book Company, Inc., NY, 1958, p. 120.
26. J. A. Pask, From technology to the science of glass/metal and ceramic/metal sealing, *Ceram. Bull*. 66:1587 (1987).
27. M. E. Twentyman, High-temperature metallizing, part 1. the mechanism of glass migration in the production of metal-ceramic seals, *J. Mat. Sci*. 10:765 (1975).
28. J. T. Klomp, Interfacial reactions between metals and oxides during sealing, *Ceram. Bull.* 59:794 (1980).
29. T. R. Gattuso, Liquid phase sintering of tungsten, *Ceram. Trans. Sintering of Advanced Ceram*. 7, American Ceramic Society, Westerville, Ohio, 1990, p. 452.
30. C. R. Amberg, Effect of molybdenum and other oxides on surface tension of silicate melts and on properties of refractories and abrasives, *J. Amer. Ceram. Soc*. 29: 87 (1946).

31. C. W. Parmelee, *Ceramic Glazes*, Industrial Publications, Inc., Chicago, 1948, p. 107.
32. R. A. Eppler, Glazes and enamels, *Commercial Glasses, Advances in Ceramics Vol. 18* (D. C. Boyd and J. F. MacDowell, Eds.), The American Ceramic Society, Columbus, Ohio, 1986, p. 65.
33. A. R. McBirney and T. Murase, Factors governing the formation of pyroclastic rocks, *Bull. Volcanol*. 34:372 (1970).
34. T. Murase and A. R. McBirney, Properties of some common igneous rocks and their melts at high temperatures, *G.S.A. Bull*. 84:3563 (1973).
35. J. F. Padday, Surface tension. Part I. The theory of surface tension, *Surface and Colloid Science, Vol. 1*, (E. Matijevic, Ed.), Wiley-Interscience, New York, 1969, p. 39.
36. F. Hawksbee, *Physico-Mechanical Experiments*, London, 1709, p. 139.
37. A. W. Adamson, *Physical Chemistry of Surfaces*, John Wiley and Sons, New York, 1982, p. 6.
38. K. F. Gauss, *Principae Generalia Theoreticae Figurae Fluidorum in Statu Aequilibrii*, Göttingen, 1830.
39. E. A. Guggenheim, *Thermodynamics, 4th ed*., North Holland, Amsterdam, 1959, p. 195.
40. W. D. Kingery, *Property Measurements at High Temperatures*, John Wiley and Sons, New York, 1959, p. 362.
41. J. Willard Gibbs, in: *Scientific Papers of J.W. Gibbs Vol. 1*, Dover Publications, New York, 1961, p. 314.
42. I. A. Aksay, C. E. Hoge, and J. A. Pask, Wetting under chemical equilibrium and nonequilibrium conditions, *J. Phys. Chem.* 78: 1178 (1974).
43. E. D. Hondros, *Surface Energy Measurements, Techniques of Metals Research Vol. IV* (R. A. Rapp, Ed.), J. Wiley & Sons, Inc., NY, 1970, p. 293-348.
44. A. Bondi, The spreading of liquid metals on solid surfaces, surface chemistry of high-energy surfaces, *Chem. Rev.* 52:417 (1953).
45. J. H. Brophy, R. M. Rose, and J. Wulff, *The Structure and Properties of Materials. Vol. II Thermodynamics and Structure*, J. Wiley & Sons, Inc., NY, 1964, p. 46-61.
46. R. E. Boni and G. Derge, Surface tension of silicates, *J. Metals* 206:53 (1956).
47. H. Bloom and B. W. Burrows, Surface properties of molten mixtures of sodium fluoride, aluminum fluoride, and alumina, *Proc. First Australian Conf. Electrochem*., Sydney, Hobart, Australia, Pergamon Press, 1963 (pub. 1965), p. 882.
48. W. D. Kingery, Surface tension of some liquid oxides and their temperature coefficients, *J. Amer. Ceram. Soc.* 42:6 (1959).
49. E. A. Brandes and G. B. Brook (Eds.), *Smithells Metal Reference Book*, Butterworth-Heinemann, Ltd., London, 1992, p. 14-6.
50. F. M. Fowkes, Attractive forces at interfaces, *Ind. Eng. Chem*.56:40 (1964).
51. C. L. Yaws, *Physical Properties: A Guide to the Physical, Thermodynamic, and Transport Properties of Industrially Important Chemical Compounds*, McGraw-Hill Pub. Co., New York, 1971, p. 218.
52. R. C. Evans, *An Introduction to Crystal Chemistry*, Cambridge University Press, Cambridge, 1966, p. 38.
53. T. B. King, The surface tension and structure of silicate slags, *J. Soc. Glass Tech*. 35:241 (1951).
54. L. Shartsis and W. Capps, Surface tension of molten alkali borates, *J. Amer. Ceram. Soc*. 35:169 (1952).
55. L. Shartsis, H. F. Shermer, and A. B. Bestul, Immiscibility and surface tension of some simple borates, *J. Amer. Ceram. Soc*. 41:507 (1958).
56. A. Dietzel, Relations between surface tension and structure of glass melts, *Kolloid Zeitschrift* 100:368 (1942).

57. M. G. Drexhage, Heavy-metal fluoride glasses, *Treatise on Materials Science and Technology Vol. 26* (M. Tomozawa and R. H. Doremus, Eds.), 1985, p. 151.
58. A. A. Appen, The role of surface tension in the clarifying process during the fusion of glass, *Optiko-Mekh. Prom*. 5: 5 (1936).
59. A. E. Badger, C. W. Parmelee, and A. E. Williams, Surface tension of various molten glasses, *J. Amer. Ceram. Soc*. 20: 325 (1937).
60. C. A. Bradley, Jr., Measurement of surface tension of viscous liquids, *J. Amer. Ceram. Soc.* 21: 339 (1938).
61. T. B. King, Anomalies in Surface Tension of Silicates, *The Physical Chemistry of Melts*, a symposium, Inst. Min. Metall., London, 1953, p. 35.
62. L. R. Barrett and A. G. Thomas, Surface tension and density measurements on molten glasses in the CaO-Al_2O_3-SiO_2 system, *J. Soc. Glass Tech*.43:179T (1959).
63. W. A. Weyl, Boric oxide — Its chemistry and role in glass technology, Part III, *Glass Ind*. 25:264 (1948).
64. R. P. Worley, Surface tension of mixtures, *J. Chem. Soc*. 105:260 (1914).
65. L. Shartsis, S. Spinner, and A. W. Smock, Surface tension of compositions in the systems B_2O_3-PbO and PbO-SiO_2, *J. Res. Nat. Bur. Stds*. 40:61 (1948), and *J. Amer. Ceram. Soc*. 31:23 (1948).
66. H. Freundlich, *Colloid and Capillary Chemistry*, E. P. Dutton, NY, 1922, p. 52.
67. K. Gunji and T. Dan, Surface tension of the molten CaO-SiO_2 binary and ternary CaO-Al_2O_3-SiO_2 systems, *Trans. ISIJ* 14:162 (1974).
68. E. W. Tillotson, Surface tensions of molten glasses, *J. Ind. Eng. Chem*. 3:631 (1911), 4:651 (1912).
69. C. L. Babcock, Surface tension measurements on molten glass by a modified dipping cylinder method, *J. Amer. Ceram. Soc*. 23:12 (1940).
70. A. Dietzel, Practical importance and calculation of surface tension in glasses, glazes, and enamels, *Sprechsaal* 75:82 (1942).
71. K. C. Lyon, Calculation of the surface tension of glasses, *J. Amer. Ceram. Soc*. 27:6 (1944).
72. A. Petzold, Classification of glass components according to their effects on the surface tension of silicate melts, *Silikat Tech*. 5:11 (1954).
73. R. E. Boni and G. Derge, Surface structure of nonoxidizing slags containing sulphur, *J. Metals* 206:59 (1956).
74. A. Adachi, K. Ogino, and H. Toritani, On the surface tension of molten silicates, *Tech. Rep. Osaka Univ.* 10:149 (1960).
75. A. Ejima and M. Shimoji, Effect of alkali and alkaline earth fluorides on surface tension of molten calcium silicates, *Trans. Faraday Soc*. 66:99 (1970).
76. E. T. Turkdogan, *Physicochemical Properties of Molten Slags and Glasses*, The Metals Society, London, 1983, p. 163.
77. D. T. Livey and P. Murray, The wetting properties of solid oxides and carbides by liquid metals, *Proc. 2nd Plansee-Seminar, Reutte/Tyrol*, 1955, pp. 375-404.
78. C. Rubenstein, Factors for the calculation of the surface tension of glasses at 1200˚C, *Glass Tech*. 5:36 (1964).
79. M. B. Volf, *Chemical Approach to Glass*, Elsevier Scientific Publishing Company, Amsterdam, 1984, p. 91.
80. H. Scholze, *Glas: Natur. Struktur und Eigenschaften*, Friedr. Vieweg & Sohn, Braunschweig, 1965, p. 212-221.
81. D. S. Sanditov, Surface tension and microhardness of silicate glasses, *Fiz. Khim. Stekla* 6:558 (1980).

82. A. A. Winer and R. F. Pilgrim, Density and surface tension as parameters in the processing of mineral insulation, *J. Can. Ceram. Soc*. 49:22 (1980).
83. N. A. Toropov and B. A. Bryantsev, Physicochemical properties and crystallization of melts in the system magnesium oxide-ferrous oxide-silica, in: *Structural Transformations in Glasses at High Temperatures,* (N. A. Toropov and E. A. Porai-Koshits, Eds.), Consultants Bureau, New York, 1965, p. 178.
84. L. Shartsis and H. F. Shermer, Surface tension, density, viscosity, and electrical resistivity of molten binary alkaline-earth borates, *J. Amer. Ceram. Soc*. 37:544 (1954).
85. K. Mukai and T. Ishikawa, Surface tension measurements on liquid slags in CaO-SiO_2, CaO-Al_2O_3 and CaO-Al_2O_3-SiO_2 systems by a pendant drop method, *J. Japan Inst. Metals* 45:147 (1981).
86. A. J. G. Boyer, D. J. Fray, and T. R. Meadowcroft, The surface tensions and molar volumes of the binary phosphates of sodium, lithium, calcium, and zinc, *J. Phys. Chem.* 71: 1442 (1967).
87. B. T. Bradbury and W. R. Maddocks, Studies of phosphate melts and glasses: II, Surface tension measurements on binary phosphates, *J. Soc. Glass Technol.* 43:325 (1959).
88. G. S. Ershov and E. A. Popova, Kinetics of solution of silica in molten oxides, *Zh. Neorg. Khim*. 9:654 (1964).
89. B. Sikora and M. Zielinski, Density, surface tension, viscosity, and electric conductivity of fused calcium oxide-alumina-calcium fluoride systems, *Hutnik* 41: 433 (1974).
90. K. Nakajima, Estimation of surface tension for multicomponent silicate melts, J. *Iron and Steel Inst. Jpn.* 80(8):599 (1994).
91. V. I. Goleus, A. Ya. Belyi, M. Sardak, and E. Ya. I. Belyi, Calculation of the surface tension of molten borosilicate glasses, *Glasses and Ceram*. 53(7-8):226(1996).
92. C. E. Villa, D. R. Dinger, and J. E. Funk, A spreadsheet program to predict glaze compositions, I, *Interceram* 46(5):303 (1997).
93. A. Kucuk, A. G. Clare and L. Jones, An estimation of the surface tension for silicate glass melts at 1400°C using statistical analysis, *Glass Technol*. 40(5):149 (1999).
94. A. A. Appen, Attempt to classify components according ti their effect on the surface tension of silicate melts, *Zhur. Fiz. Khim*. 26:1399(1952).
95. A. A. Appen, The Chemistry of Glass(in Russian), *Izd. Chimica*, Leningrad, 1970.
96. C. W. Bale and A. D. Pelton, Optimization of binary thermodynamic and phase diagram data, *Met. Trans. B* 14B(3):77(1983).
97. C. W. Bale and G. Eriksson, Metallurgical thermochemical databases: A review, *Can. Metall. Quart*. 29:105(1990).
98. E. Konigsberger and G. Eriksson, A new optimization routine for ChemSage, *CALPHAD* 19:207(1995).
99. T. Tanaka, K. Hack, T. Iida and S. Hara, Application of thermodynamic databases to the evaluation of surface tensions of molten alloys, salt mixtures and oxide mixtures, *Z. Metallkd*. 87(5):380 (1996).
100. W. Vogel, *Chemistry of Glass*, Amer. Ceram. Soc., Columbus, OH, 1985, p.296.
101. A.E.J. Vickers, The effect of atmosphere on the viscosity and surface tension of a simple glass, *J. Appl.Chem*.57:14(1938).
102. H. Jebsen-Marwedel and K. Dinger, Modification of the surface tension under the influence of the furnace atmosphere and the consequences, *Verre et Réfractaires* 2:81 (1948).
103. N. M. Parikh, Effect of atmosphere on surface tension of glass, *J. Amer. Ceram. Soc*. 41:18 (1958).

104. B. S. Ellefson and N. W. Taylor, Surface properties of fused salts and glasses: II. contact angle and work of adhesion on gold and platinum in various atmospheres, *J. Amer. Ceram. Soc.* 21: 205 (1938).
105. S. I. Popel and O. A. Esin, Surface tension and densities of simplest oxide systems, Fiz.-Khim. Osn. Proizvod. Stali, Akad. Nauk SSSR, Inst. Met. im. A.A.Baikova Tr. 3-ei Konf., 1955, p. 497, (1957); *J. Phys. Chem*.30:1193 (1956).
106. S. Akhtar and M. Cable, Some effects of atmosphere and minor constituents on the surface tension of glass melts, *Glass Technol*. 9:145 (1968).
107. S. K. Sharma and W. O. Philbrook, The influence of atmosphere on the surface tension of calcium- and manganese-silicate melts, *Proc. ICSTIS, Suppl. Trans. ISIJ* 11:569 (1971).
108. M. J. Plodinec, Effect of glass composition on surface tension, viscosity, and redox equilibria of initial defense waste processing facility glass, D.O.E. rep. no. DPST-86-740, Savannah River Laboratory, Aiken, SC,1986.
109. A. Kucuk, A. G. Clare and L. E. Jones, Differences between the surface and bulk of glass melts. Part 2. Influence of the redox ratio on the surface properties of silicate melts, *Phys. Chem. Glasses* 41(2):75(2000).
110. P. Kozakevitch, Surface tension, in: P*hysicochemical Measurements at High Temperatures* (J. O'M. Bockris, J. L. White, and J. D. Mackenzie, Eds.), Butterworth Scientific Publications, London, 1959, p. 208.
111. D. W. G. White, Theory and experiment in methods for the precision measurement of surface tension, *ASM Trans*. 55:757 (1962).
112. D. R. Secrist, Measurement of surface tension of glasses by a capillary flow technique, *Ceram. Bull*. 48:563 (1969).
113. W. C. Eaton, Properties of simulated glass forming nuclear waste melts, M.S. thesis, Alfred University, NY, 1992, p. 16.
114. T. Tate, On the magnitude of a drop of liquid formed under different circumstances, *Phil. Mag*. 27:48 (1864).
115. G. Quincke, Regarding the capillary constants of molten bodies, *Ann. Phys. Chemie* 135:621 (1868).
116. A. Lecrenier, Measurement of the surface tension of glass, *Bull. Soc. Chem. Belg*. 33:119 (1924).
117. L. Holland, *The Properties of Glass Surfaces*, J. Wiley and Sons, Inc., NY, 1964, p. 403.
118. W. B. Pietenpol, Surface tension of molten glass, *Physics* 7:26 (1936).
119. A. A. Appen, Surface tension of fused soda and lead glasses, Optiko-Mekh. Prom. 6:7 (1936); *Chemisches Zentralblatt* I:2428 (1937).
120. A. A. Appen, K. A. Shishov, and S. S. Kayalova, Surface tension of silicate melts, *Zhur. Fiz. Khim*. 26:1131 (1952).
121. A. A. Appen and S. S. Kayalova, Surface tension of alkali-silica melts, *Dokl. Akad. Nauk. SSSR* 145:592 (1962).
122. A. A. Appen and S. S. Kayalova, Experimental basis for the classification of oxides according to their influence on the surface tension of silicate melts, in: *Advances in Glass Technology*, Plenum Press, NY, p. 61, (1963).
123. A. A. Appen and S. S. Kayalova, in: *Khimiya i Prakticheskoe Primenenie Silikatov*, Leningrad, 1960, p. 57.
124. A. A. Appen, K. A. Schischow, and S. S. Kajalova, Die Oberflächenspannung von Silikatschemelzen, *Silikat Tech.* 4:104 (1953).
125. R. N. McNally, H. C. Yeh, and N. Balasubramanian, Surface tension measurements of refractory liquids using the modified drop weight method, *J. Mat. Sci*. 3:136 (1968).

126. B. Berggren, A method for the determination of the surface tension of amorphous substances, *Annalen der Physik* 44:61 (1914).
127. G. Tammann and H. Rabe, Dependence of the surface tension of highly viscous liquids on temperature, Ztsch. für Anorg. *Allgem. Chemie* 152:17 (1927).
128. A. A. Griffith, Phenomena of flow and rupture in solids, *Phil. Trans. Roy. Soc*. [London] 221A:163 (1920).
129. G. Keppeler, Surface tension of glass, *J. Soc. Glass Tech*. 21:53 (1937).
130. H. R. Lillie, A method for measuring the flow point of glass, *J. Amer. Ceram. Soc*. 35:149 (1952).
131. L. Wilhelmy, Uber die Abhängigkeit der Capillaritäts-constanten des Alkohols von Substanz und Gestalt des benetzten festen Körpers, *Ann. Physik* 119:177 (1863).
132. P. L. Du Nouy, A new apparatus for measuring surface tension, *J. Gen. Physiol*.1:521 (1919).
133. G. J. Janz and M. R. Lorenz, Precise measurement of density and surface tension at temperatures up to 1000˚C in one apparatus, *Rev. Sci. Instrum*. 31:18 (1960).
134. L. Bodnar, S. Cempa, K. Tomasek, and L. Bobok, Survey of physical properties of slag systems in copper metallurgy, in: *Advances in Extractive Metallurgy*, Imperial College of London, April 18-20, Inst. Min. Metall., London, 1977, p. 35.
135. M. Sugai and S. Somiya, Measurement of density, viscosity and surface tension of the melt of the system SiO_2-TiO_2-Al_2O_3 at 1600°C, *Yogyo-Kyokai-Shi* 90:56 (1982).
136. E. W. Washburn and E. E. Libman, I. Viscosities and surface tensions of soda-lime-silica glasses at high temperatures, *Univ. Illinois Eng. Expt. Station Bull*. 140:53 (1924).
137. E. W. Washburn and G. R. Shelton, II. Surface tensions of glasses at high temperatures, Univ. *Illinois Eng. Expt. Station Bull*. 140:53 (1924).
138. W. N. Harrison and D. G. Moore, Surface tension of vitreous enamel frits at and near firing temperatures, *J. Res. Nat. Bur. Stand*. 18:13 (1938).
139. M. Kidd and D. R. Gaskell, Measurement of the surface tensions of Fe-saturated iron silicate and Fe-saturated calcium ferrite melts by Padday's Cone Technique, *Met. Trans. B* 17B:771(1986).
140. P. Kozakevitch and Kononenko, Surface tension in binary and ternary mixtures of oxides, *J. Phys. Chem*.(U.S.S.R.) 14:1118 (1940).
141. L. Shartsis and S. Spinner, Surface tension of molten alkali silicates, *J. Res. Nat. Bur. Stds*. 46:385 (1951).
142. P. Kozakevitch, Surface tension and viscosity of synthetic slags, *Rev. Metall*. (Paris) 46:505, 572 (1949).
143. L. Shartsis and R. Canga, Surface tension of molten zinc borates, *J. Res. Nat. Bur. Stds*. 43:221 (1949).
144. E. V. Ermolaeva, Relationship between surface tension, viscosity, and density of some ternary melts of refractory oxides, *Ogneupory* 20:221 (1955).
145. L. Shartsis, H. F. Shermer, and A. B. Bestul, Surface tension of alkaline-earth borates containing 3 mole % potassium oxide, *J. Amer. Ceram. Soc*. 42:242 (1959).
146. H. Ito, T. Yanagase, and Y. Suginohara, Surface tension of molten lead silicate, *J. Min. Metall. Inst. Jpn*. 77:895 (1961).
147. Y. Suginohara, *Technol. Rep. Kyushu Univ.* 34:229 (1961).
148. Y. Suginohara, T. Yanagase, and H. Ito, *Trans. Jpn. Inst. Metals* 3:227 (1962).
149. K. Ikeda, Y. Suginohara, and T. Yanagase, Effects of oxide additions on the density and surface tension of barium silicate melts, *Nippon Kinzuko Gakkaishi*. (J. Jpn. Inst. Metals)31:547 (1967).
150. M. Hino, T. Ejima, and M. Kameda, Surface tension and density of liquid lead silicate, *Nippon Kinzuko Gakkaishi*. (J. Jpn. Inst. Metals) 31:113 (1967).

151. M. Hino, T. Ejima, and M. Kameda, Surface tension, density, and viscosity of PbO-K_2O-SiO_2 ternary melts, *Nippon Kinzuko Gakkaishi*. (J. Jpn. Inst. Metals) 33:617 (1969).
152. A. Ejima, M. Hino, and M. Kameda, Surface tension, density, and viscosity of PbO-SiO_2-Li_2O ternary melts, *Nippon Kinzoku Gakkaishi* (J. Jpn. Inst. Metals) 34:546 (1970).
153. M. Imaoka, H. Hasegawa, Y. Hamaguchi, and Y. Kurotaki, Chemical composition and tensile strength of glasses in the B_2O_3-PbO and B_2O_3-SiO_2-Na_2O system, *J. Ceram. Soc. Jpn.* 79:164 (1971).
154. R. G. Gossink and J. M. Stevels, Density and surface tension of molten alkali molybdates and tungstates in connection with structure and glass formation, *J. Non-Cryst. Solids* 5:217 (1971).
155. R. L. Tiede, Modification of the dipping cylinder method of measuring surface tension, *Ceram. Bull*. 51:539 (1972).
156. E. E. Shpil'rain, K. A. Yakimovich, and A. F. Tsitsarkin, Surface tension of liquid boric oxide at up to 2100°C, *High Temp*. (Engl. Trans.) 12:68 (1974).
157. A. Prabhu, G. L. Fuller, R. L. Reed, and R. W. Vest, Viscosity and surface tension of a molten lead borosilicate glass, *J. Amer. Ceram. Soc*. 58:144 (1975).
158. G. Frischat and W. Beier, Surface tension of Na_2O-Rb_2O-SiO_2 melts, *Glastechn. Ber.* 52:116 (1979).
159. Sh. Sumita, K. Morinaga, and T. Yanagase, The physical properties of sodium oxide-iron(III) oxide and calcium oxide-iron(III) oxide melts, *Nippon Kagaku Kaishi* 6:983 (1982).
160. X. Hong, K. Lu, Y. Zhao, and X. Wu, Density and surface tension properties of molten potassium niobate system, *J. Cryst. Growth* 147:104 (1995).
161. R. Solé, X. Ruiz, R. Cabré, M. Aguiló and F. Díaz High-temperature solutions of the $(0.4Na_2O$-$0.6B_2O_3)$-BaO-$((6\text{-}x)Fe_2O_3 + xCoSnO_3)$ system. Physical properties, *Mat. Res. Bull.* 30(6):779(1995).
162. Y. Tang and G. H. Frischat, Influence of small additions of Li_2O raw materials on glass melting, *Glastech. Ber. Glass Sci. Technol*. 68(7):213 (1995).
163. P. K. Bhattacharyya and D. R. Gaskell, The influence of oxygen pressure and P_2O_5 on the surface tension of liquid iron oxide at 1435°C, *Met. Mat. Trans B* 27B(1):139(1996).
164. G. Gorchenin, A. A. Zhukov, and S. I. Popel, Determination of interface tension by means of vertical cylinder immersion method, *Rasplavy* 2 (2):12(1999).
165. J.-H. Hwang, J.-H. Park, K.-D. Kim and S.-S. Choi, Influence of mixed alkali oxides on some melt properties of TV screen glass, *Glastech. Ber. Glass Sci. Technol.* 73(1):8 (2000).
166. F. M. Jaeger, Temperature coefficient of free molecular surface energy of liquids between 80˚C and 1650˚C, *Z. anorg. allgem. Chem*. 101:1 (1917).
167. C. W. Parmelee and K. C. Lyon, The maximum bubble-pressure (Jaeger) method for measurement of the surface tension of molten glass, *J. Soc. Glass Tech*. 21:44 (1937).
168. C. W. Parmelee and C. G. Harman, The effect of alumina on the surface tension of molten glass, *J. Amer. Ceram. Soc*. 20:224 (1937).
169. E. Elchardus, Surface tension of molten mixtures containing cryolite, *Compte Rendu* 206:1460 (1938).
170. G. J. Janz, G. M. Dijkhuis, G. R. Lakshminarayanan, R. P. T. Tomkins, and J. Wong, *Molten Salts, vol. 2*, U.S. Dept. Commerce, N.B.S., 1969.
171. L. L. Bircumshaw, Surface tension of liquid metals, *Phil. Mag*. 2:341 (1926).
172. F. Sauerwald, B. Schmidt and F. Pelka, Die Oberflächenspannung geschmolzener Metalle und Legierungen, *Zeit. Anorg. Allg. Chem*. 223:84 (1935).

173. M. Cantor, Concerning capillary constants, *Wied. Annalen* 47:399 (1892).
174. N. E. Dorsey, Measurement of surface tension, Nat. Bur. Stds. Sci. Papers 21:563 (1927).
175. B. S. Ellefson and N. W. Taylor, Surface properties of fused salts and glasses: I. sessile drop method for determining surface tension and density of viscous liquids at high temperatures, *J. Amer. Ceram. Soc*. 21: 193 (1938).
176. R. M. Williams and H. E. Simpson, A note on the effect of lithium oxide upon the surface tension of several silicate melts, *J. Amer. Ceram. Soc*. 34:74 (1951).
177. S. I. Popel and O. A. Esin, Surface tension of fused silicates, *Zh. Nrorg. Khim*. 2:632 (1957).
178. L. Merker, Determination of the densities of glass melts at high temperatures, *Glastech. Ber.* 32:501 (1959).
179. Pei-Ching Li, A. C. Ghose, and Gouq-Jen Su, Surface tension of molten boron oxide and binary borates containing rubidium, cesium, lanthanum, yttrium, samarium, and cerium oxides, *Phys. Chem. Glasses* 1:198 (1960).
180. O. S. Bobkova and V. S. Petukhov, The role of the surface effects during mixing of steel with synthetic slags, *Izdatelstvo Akad. Nauk. USSR*, Kiev, 212 (1963).
181. A. A. Deryabin and S. I. Popel, Effect of fluorite on density and surface tension of the melt CaO-Al_2O_3 and its adhesion to steel, *Izv. VUZov. Chern. Met*. 7:5 (1964).
182. V. D. Smolyarenko, A. M. Yakushev, and F. P. Edneral, Density and surface tension of lime-alumina slags with additions of SiO_2, MgO, and Na_3AlF_6, *Izv. VUZov. Chern. Met.* 8:55 (1965).
183. S. B. Yabobashivili, T. G. Mudzhiri, and A. V. Sklyarov, The surface tension of CaO + Al_2O_3-system slags, *Avtomaticheskaya Svarka* 8:44 (1965).
184. E. L. Krivovyazov, N. K. Voskresenskaya, and I. D. Sokolova, in: Poverkhnostnye yavleniya v rasplavakh i voznikayushchikh iz nikh tverdykh fazakh, *Nalchik*, 1965, p. 479.
185. P. P. Evseev and A. F. Filippov, Physical and chemical properties of slags of the CaO-Al_2O_3-M_xA_y system. II. Surface tension and density of the slags, *Izv. VUZov. Chern. Met.* 10:55 (1967).
186. I. D. Sokolov, E. L. Krivovyazov, and V. A. Kosteltsev, Surface tension of magnesium metaphosphate, *Zh. Fiz. Khim*. 43:1616 (1969).
187. K. Ono, K. Gunji, and T. Araki, Surface tension of molten sinary CaO-SiO_2 slag, *J. Jap. Inst. Metals* 33:299 (1969).
188. S. I. Popel, V. I. Sokolov, and O. A. Esin., Surface tensions of MO-SiO_2 melts, Russian *J. Physical Chemistry* 43:1782 (1969).
189. L. N. Sokolov, V. V. Baidov, and L. L. Kunin, Velocity of ultrasound sensitivity, and surface tension as information on the structure of calcium oxide-alumina-silica system, *Fiz. Khim. Elecktrokhim. Rasplav. Solei Shlakov* 1: 299 (1969).
190. E. L. Krivovyazov, and N. K. Voskresenskaya, Surface tension of $Zn(PO_3)_2$-ZnO system melts, *Izv. Akad. Nauk. SSSR*, Neorg. Mater. 5:1734 (1969).
191. E. L. Krivovyazov, and N. K. Voskresenskaya, Surface and volume properties of diagonal cross sections of (Na, Zn)PO_3-O and (Na, Zn)PO_3-O reciprocal systems, *Zh. Neorg. Khim*. 15:246 (1970).
192. S. K. Sharma and W. O. Philbrook, Improved values of surface tension of calcium silicate melts, *Scr. Metall*. 4:107 (1970).
193. A. A. Perminov, T. V. Mirova, and S. I. Popel, Effect of molybdenum trioxide on surface properties of molten silicates, *J. Appl. Chem. USSR* (Engl. Transl.) 44:1041 (1971).

194. L. N. Sokolov, V. V. Baidov, L. L. Kunin, and V. V. Dymov, Surface and volume characteristics of melted slags of the calcium oxide-alumina-silica system, *Sb. Tr. Tsent. Nauch.-Issled. Inst. Chern. Met*. 74:53 (1971).
195. V. P. Elyutin, B. S. Mitin, and Yu. S. Anisimov, Surface tension and density of alumina-magnesia and alumina-calcia melts, I*zv. VUZov. Chern. Met*. 4:42 (1974).
196. A. S. Zubrev, V. V. Shakhnovich, and M. F. Sidorenko, Refining capability of injected fluxes in regard to nonmetallic inclusions in steel, *Izv. Akad. Nauk SSSR Metal*. 2:22 (1976).
197. R. Benesch, R. Knihnicki, and J. Janowski, Density and surface tension of blast-furnace type slags, *Arch. Hutn*. 21:591 (1976).
198. M. Zielinski and B. Sikora, Surface tension of the calcium oxide-alumina system with additions of silica, iron(III) oxide, calcium fluoride, sodium fluoride, and magnesia, *Pr. Inst. Metal Zelaza* 29:157 (1977).
199. Yu. S. Anisimov, E. F. Grits, and B. S. Mitin, Surface tension and density of melts in the systems Al_2O_3-SiO_2 and Al_2O_3-Cr_2O_3, *Inorg. Mater.* (Eng. transl.) 13:1168 (1977).
200. V. Danek and T. Locko, Apparatus for the measurement of physicochemical properties of oxide melts, *Silikaty* 25:153 (1981).
201. I. Dragomir, and E. Rusu, Experimental installation for determining surface tension and density of melts and slags, *Metalurgi*a (Bucharest) 35:168 (1983).
202. T. Fujisawa, T. Utigard, and J. M. Toguri, Surface tension and density of molten $PbCl_2$-KCl-NaCl ternary system, *Can. J. Chem*. 63:1132 (1985).
203. V. G. Kosenko, P. I. Buler, A. V. Loshagin, and T. N. Klepikova, *Rasplavy* 1:109 (1987).
204. Z. Yuan, M. Sun, and X. Chen, Study of the surface tension and density of synthetic slags in system SiO_2-FeO-MgO-(CaO), Yu Se Chin Shu/*Nonferrous Metals* 40:58 (1988).
205. S. Hara, and K. Ogino, Density and surface tension of melts in the systems CaF_2-MO(M:Mg, Ca,Ba), *Nippon Kinzoku Gakkaishi* (J. Jpn. Inst. Metals) 52:1098 (1988).
206. P. I. Buler, E. V. Spiridonova, and A. A. Frolov, Study of the stable phase separation fo lead monoxide-boron oxide-tellurium dioxide melts by surface tension measurement, *Fiz. Khim. Stekla* 15:854 (1989).
207. N. Ikemiya, J. Umemoto, S. Hara, and K. Ogino, Surface tensions and densities of molten Al_2O_3, Ti_2O_3, V_2O_5, and Nb_2O_5, ISIJ Int. 33:156 (1993).
208. N. Ikemiya, J. Yoshitomi, S. Hara, and K. Ogino, Surface tensions and densities of melts in TiO_2-BaO and TiO_2-Na_2O systems, *Nippon Kinzuko Gakkaishi*. (J. Jpn. Inst. Metals) 57:527 (1993).
209. V. J. Fratello and C. D. Brandle, Physical properties of $Y_3Al_5O_{12}$, *J. Cryst. Growth* 128:1006 (1993).
210. T. Kojima, M. Yanagida, K. Tanimoto, Y. Tamiya, T. Asai and Y. Miyazaki, Physical properties of molten carbonate electrolyte, 1996 Fuel Cell Seminar Proc., Orlando, FL, Nov. 17-20, 1996, pp. 382-385.
211. P. Vadasz and M. Havlik, Density and surface tension of Fe_2O_3-FeO-CaO-ZnO oxidic melts, *Chemicke Listy* 90 (11):899(1996).
212. N. V. Belousova, E. A. Pastukhov, E. M. Gil'debrandt, and E. M. Istomin, Properties of Bi_2O_3 - Ga_2O_3 and Bi_2O_3 - La_2O_3 melts, *Rasplavy* (1):47(1997).
213. S. Vaisburd and D. G. Brandon, A combined unit for viscosity, surface tension and density measurements in oxide melts, *Meas. Sci. Technol*. 8:822(1997).
214. S. N. Shin and R. I. Gulyaeva, Density and surface tension of melts of the FeO_x - Al_2O_3 - CaO - SiO_2 system, *Rasplavy* (4):33 (1998).

215. P. Vadasz, M. Havlik and V. Danek, Density and surface tension of calcium ferritic slags I. The systems CaO-FeO-Fe_2O_3-SiO_2 and CaO-FeO-Fe_2O_3-Al_2O_3, *Can. Met. Quart*. 39:(2):142 (2000).
216. F. Bashforth and J. C. Adams, *An Attempt to Test the Theories of Capillary Action*, Cambridge University Press, London, 1883.
217. R. M. Prokop, O. I. Del Rio, N. Niyakan, and A. W. Neumann, Interfacial tension from the height and diameter of sessile drops and captive bubbles with an arbitrary contact angle, *Can. J. Chem. Eng*. 74:534 (1996).
218. M. V. Glazov, D. J. Lege, D. A. Weirauch, Jr. and A. S. Krylov, Computer simulation and analysis of wetting experiments, Alcoa Technical Center Report No. 98-123, (1998).
219. W. D. Kingery and M. Humenick, Jr., Surface tension at elevated temperatures. I. Furnace and method for use of the sessile drop method; surface tension of silicon, iron, and nickel, *J. Phys. Chem.* 57: 359 (1953).
220. N. E. Dorsey, A new equation for the determination of surface tension from the form of a sessile drop or bubble, *J. Wash. Acad. Sci*. 18:505 (1928).
221. R. Sangiorgi, G. Caracciolo, A. Passerone, Factors limiting the accuracy of measurements of surface tension by the sessile drop method, *J. Mat. Sci.* 17: 2895 (1982).
222. J. F. Padday, Surface tension. Part II. The measurement of surface tension, in: *Surface and Colloid Science Vol. 1,* (E. Matijevic, Ed.), Wiley-Interscience, New York, 1969, p. 101.
223. W. Bonfield, Surface tension of mercury on glass, molybdenum and tungsten substrates, *J. Mat. Sci*. 7: 148 (1972).
224. Y. Kojima, Measurements of surface tension of CaO-SiO_2 and CaO-SiO_2-Al_2O_3 slag containing sulfur, *Trans. ISIJ* 11: 349 (1971).
225. A. Passerone, R. Sangiorgi, and G. Valbusa, Surface tension and density of molten glasses in the system La_2O_3-$Na_2Si_2O_5$, *Ceramurgia Int*. 5:18 (1979).
226. B. Van Muu, H. W. Frenzke, and S. Kraus, Experimental determination of the surface tension of iron and slag, *Neue Huette* 29:113 (1984).
227. R. Bochnak, Surface tension of sodium oxide-calcia-magnesia-alumina-silica-system melts, *Hutn. Listy* 44:18 (1989).
228. D. A. Weirauch, Jr. and D. P. Ziegler, An improved method for the determination of the surface tension of silicate melts, 12th Annual Conf. on Glass Science, Alfred, NY, 1993.
229. A. Kucuk, A. G. Clare and L. E. Jones, Differences between the surface and bulk of glass melts. Part 2. Influence of the redox ratio on the surface properties of silicate melts, *Phys. Chem. Glasses* 41(2):75 (2000).
230. J. L. Bates, C. E. McNeilly, and J. J. Rasmussen, Properties of molten ceramics, in: *Ceramics in Severe Environments* (W. W. Kreiegel and H. Palmour, Eds.), Plenum Press, NY, 1971, p. 11.
231. T. Dan, K. Halada, and Y. Muramatsu, Characteristics of image data processing techniques for sessile drop method, *J. Japan Inst. Metals* 59:846 (1995).
232. Y. Chung and T. Iseki, Numerical method for determining the surface tension of a sessile drop, *J. Korean Ceram. Soc*. 33(12):1325 (1996).
233. S. V. Mikhailikov, E. K. Borodulin, S. V. Shtengelmeier, V. V. Tantsyrev, and E. A. Popova, *Tr. Inst. Metall. Sverdlovsk* 21:98 (1970).
234. J. Krusina, Surface tension in the Al_2O_3-CaO-SiO_2 system, *Hutnicke Listy* 26:625 (1971).
235. J. Krusina, Surface tension in the quaternary Al_2O_3-CaO-SiO_2-CaF_2 system, *Hutnicke Listy* 26:783 (1971).

236. J. Krusina, Surface tension of TiO_2-containing oxide systems, *Hutnicke Listy* 29:41 (1974).
237. Yu. F. Kargin, V. P. Zhereb, V. M. Skorikov, A. V. Kosov, V. A. Kutvitskii, and E. I. Nuriev, Properties of melts in the systems Bi_2O_3-SiO_2 and Bi_2O_3-GeO_2, *Neorg. Mater.* 13:135 (1977), *Inorg. Mat.*13:114 (1977).
238. T. Utigard, J. M. Toguri, and T. Nakamura, Interfacial tension and flotation characteristics of liquid metal-sodium flux systems, *Met. Trans*. B 17B:339 (1986).
239. M. Askari, A. M. Cameron, and J. Oakley, The determination of surface tension at elevated temperatures by drop image analysis, *High Temp. Tech*. 8:201 (1990).
240. K. Ghanbari-Ahari, M. Askari, and A. M. Cameron, The surface tension of some sodium borosilicate glasses, *Phys. Chem. Glasses* 32:72 (1991).
241. A. S. Krylov, A. V. Vvedensky, A. M. Katsnelson, and A. E. Tugovikov, Software package for determination of surface tension of liquid metals, *J. Non Cryst. Solids* 156-158:845 (1993).
242. S. W. Ip and J. M. Toguri, Surface and interfacial tension of the nickel-iron-sulfur, nickel-copper-sulfur, and fayalite slag systems, *Metall. Trans*. B 24B:657 (1993).
243. J. W. Nowok, J. A. Bieber, S. A. Benson and M. L. Jones, Physicochemical effects influencing the surface tension of coal ashes, *Fuel* 70:951 (1991).
244. H. Kaplan-Diedrich, A. Eckebracht, and G. Frischat, Viscosity and surface tension of oxynitride glass melts, *J. Am. Ceram. Soc*.78(4):1123 (1995).
245. D. A. Weirauch, Jr. and D. P. Ziegler, Surface tension of calcium aluminosilicate glass using computerized drop shape analysis, *J. Am. Ceram. Soc*. 79:920 (1996).
246. H. Fukuyama, J. R. Donald, and J. M. Toguri, Wetting behavior between fayalite-type slags and solid magnesia, *J. Am. Ceram. Soc*. 80:2229 (1997).
247. T. Sakai, S. W. Ip, and J. M. Toguri,, Interfacial phenomena in the liquid copper-calcium ferrite slag system, *Met. And Matls. Trans*. B 28B:401 (1997).
248. J. P. van den Brink, Thermal expansion coefficient measurements of molten glasses using the sessile drop technique, *J. Non-Cryst. Solids* 253:163 (1999).
249. J. F. Padday, Surface tension. Part III. Tables relating the size and shape of liquid drops to the surface tension, in: *Surface and Colloid Science Vol. 1*, (E. Matijevic, Ed.), Wiley-Interscience, New York, 1969, p. 151.
250. J. K. Davis and F. E. Bartell, Determination of surface tension of molten materials-adaptation of pendant drop method, *Anal. Chem*. 20:1182, (1948).
251. S. Lin, W. Wang, L. Lin, and L. Chen, Systematic effects of bubble volume on the surface tension measured by pendant bubble profiles, *Col. and Surf. A: Phys. Eng. Aspects* 114:31(1996); see also, Measurement of dynamic advancing/receding contact angle by video-enhanced sessile drop tensiometry, *Rev. Sci. Inst*. 67 (8):2852 (1996).
252. B. H. Song and J. Springer, Determination of interfacial tension from the profile of a pendant drop using computer-aided image processing 1. Theoretical, *J. Coll. Interface Sci*. 184 (1):64 (1996).
253. J. J. Rasmussen and R. P. Nelson, Surface tension and density of molten Al_2O_3, *J. Amer. Ceram. Soc*. 54:8 (1971).
254. N. P. Bansal and R. H. Doremus, Surface tension of ZrF_4-BaF_2-LaF_3 glass, *J. Amer. Ceram. Soc*. 67:C197 (1984).
255. J. M. Lihrmann and J. S. Haggerty, Surface tension of alumina-containing liquids, *J. Amer. Ceram. Soc*. 68:81 (1985).
256. Y. Rotenberg, L. Boruvka, and A. W. Neumann, Determination of surface tension and contact angle from the shapes of axisymmetric fluid interfaces, *J. Coll. Int. Sci*. 93:169 (1983).

257. C. Maze and G. Burnet, A non-linear regression method for calculating surface tension and contact angle from the shape of a sessile drop, *Surf. Sci.* 13:451 (1969).
258. B. Wang and Y. Mao, Computer approach to surface tension measurements by the sessile drop method, *J. Beijing Univ. Iron Steel Technol*. 3:76 (1986).
259. T. Dan, K. Halada, and Y. Muramatsu, Data processing for the sessile drop technique and application to copper-20% nickel/alumina system, *Nippon Kinzoku Gakkaishi* 55:1123 (1991).
260. J. C. Labbe, A. Lachau-Durand, A. Laimeche, V. Paulyou, and D. Tetard, Use of image analysis in determination of the surface tension of a drop of molten metal, *J. High Temp. Chem. Processes* 1:151 (1992).
261. Y. V. Naidich, and N. F. Grigorenko, Capillary characteristics of high temperature melts measured by sessile drop method using computer-aided TV system, *J. Mat. Sci.* 27:3092 (1992).
262. D. Homentcovschi, J. Geer, and T. Singler, Uniform asymptotic solutions for small and large sessile drops, *Acta Mech*. 128:141 (1998).
263. L. I. Muravsky, R. S. Batchevsky, and A. I. Stefansky, Evaluation of substances surface properties measuring errors with optical-digital diagnostic system, *S.P.I.E*. 2648:645 (1995).
264. D. B. Thiessen, D. J. Chione, C. B. McCreary, and W. B. Krantz, Robust digital image analysis of pendant drop shapes, *J. Coll. Interface Sci*. 177 (2):658(1996).
265. O. I. Del Rio, and A. W. Neumann, Axisymmetric drop shape analysis: computational methods for the measurement of interfacial properties from the shape and dimensions of pendant sessile drops, *J. Col. and Int. Sci.* 196:136 (1997).
266. J. Graham-Eagle and S. Pennell, Contact angle calculations from the contact/maximum diameter of sessile drops, *Int. J. Numer. Meth. Fluids* 32:851 (2000).
267. H. H. J. Girault, D. J. Schriffrin, and B. D. V. Smith, The measurement of interfacial tension of pendant drops using a video image profile digitizer, *J. Coll. Int. Sci*. 101:257 (1984).
268. L. Liggieri and A. Passerone, An automatic technique for measuring the surface tension of liquid metals, *High Temp. Tech.* 7:82 (1989).
269. L. E. Murr, Interfacial free energy, in: *Interfacial Phenomena in Metals and Alloys*, Addison-Wesley Publishing Co., Reading, MA, 1975, p. 91.
270. D. W. G. White, The surface tension of liquid metals and alloys, *Metall. Rev.* 124: 73 (1968).
271. G. J. Janz, J. Wong, and G. R. Lakshminarayanan, Surface tension techniques for molten salts, *Chem. Instrum*. 1:261 (1969).
272. G. W. Morey, The Properties of Glass, Reinhold Publishing Co., NY, 1954, p. 191.
273. J. J. Duga, Surface Energy of Ceramic Materials, Defense Ceramic Information Center Rep. 69-2, Battelle Mem. Inst., Columbus, OH, 1969, p. 60.
274. E. T. Turkdogan, *Physical Chemistry of High Temperature Technology*, Academic Press, NY, 1980, p. 193.
275. N. P. Bansal and R. H. Doremus, *Handbook of Glass Properties*, Academic Press, NY, 1986, p.101.
276. O. V. Mazurin, M. V. Streltsina, and T. P. Shavaiko-Shvaikovskaya, *Handbook of Glass Data, Part A. Silica Glass and Binary Silicate Glasses*, Elsevier, Amsterdam, pp. 126, 339, 504, 570, 1983.
277. O. V. Mazurin, M. V. Streltsina, and T. P. Shavaiko-Shvaikovskaya, *Handbook of Glass Data, Part B. Single Component and Binary Non-Silicate Oxide Glasses*, Elsevier, Amsterdam, pp. 56-58, 152, 153, 267-270, 311, 339, 340, 449, 503-506, 555-557, 716, 728, 1985.

278. O. V. Mazurin, M. V. Streltsina, and T. P. Shavaiko-Shvaikovskaya, *Handbook of Glass Data, Part C. Ternary Silicate Glasses*, Elsevier, Amsterdam, pp. 56, 57, 226-233, 465-469, 611, 612, 649, 659, 660, 701-703, 807-813, 1987.
279. O. V. Mazurin, M. V. Streltsina, and T. P. Shavaiko-Shvaikovskaya, *Handbook of Glass Data, Part D. Ternary Non-Silicate Glasses*, Elsevier, Amsterdam, pp. 58-61, 183, 184, 245, 246, 563, 564, 1991.
280. O. V. Mazurin, M. V. Streltsina, and T. P. Shavaiko-Shvaikovskaya, *Handbook of Glass Data, Part E. Single Component, Binary, and Ternary Oxide Glasses*, Supplements to Parts A, B, C, and D, Elsevier, Amsterdam, pp. 84, 122, 236, 488, 547, 1993.
281. G. J. Janz, *Molten Salts Handbook*, Academic Press, New York, 1967, p. 80.
282. G. J. Janz, C. B. Allen, N. P. Bansal, R. M. Murphy, and R. P.T. Tomkins, Physical Properties Data Compilations Relevant to Energy Storage II. Molten Salts: Data on Single and Multicomponent Salt Systems, NSRDS-NBS 61, Part II, U.S. Dept. Commerce, N.B.S., Washington, D.C., 1979.
283. K. C. Mills and B. J. Keene, Physicochemical properties of molten CaF_2-based slags, *Int. Met. Rev.* 26:21 (1981).
284. E. A. Brandes and G. B. Brook (Eds.), *Smithells Metals Reference Book*, 7th ed., Butterworth-Heinemann Ltd., Oxford, 1992.
285. V. Danek and T. Ostvold, Surface tension of binary MF.ALF (M=Li, Rb, Cs) melts, *Acta. Chem. Scand*. 49:411 (1995).
286. Y. Suzuki, A glass database system for compact disk, *Amer. Ceram. Soc. Bull*. 70:219 (1991).
287. H. von Wartenberg, G. Wehner, and E. Saran, Surface tension of molten aluminum and lanthanum oxides, Nachr. Ges. Wiss. Gottingen, Jahresber. Geschaftsjahr, Math.-physik. *Kl. Fachgruppen II*, 2:65 (1936).
288. O. K. Sokolov, *On the Surface Tension of Molten Salts and Oxides*, Russ. Metall. Mining 4:37, (1963).
289. R. W. Bartlett and J. K. Hall, Wetting of several solids by Al_2O_3 and BeO liquids, *Ceram. Bull.* 44:444 (1965).
290. R. H. Bruce, Aspects of the surface energy of ceramics, in: *Science of Ceramics* (G. H. Stewart, Ed.), Academic Press, London, 1965, p. 359.
291. C. C. Addison and J. M. Coldrey, Surface tensions of some molten metal nitrates and nitrites, *J. Chem. So*c., p. 468 (1961).
292. V. I. Ezikov and S. K. Chuchmarev, Density and surface tension in Na_2O-SiO_2 and Na_2O-B_2O_3 systems at 1100˚C, *VINITI*, 4357-72 Dep., 7 pp.
293. A. G. Shalimov, O. S. Bobkova, V. G. Kuklev, M. L. Sazonov, and V. S. Petukhov, Some properties of synthetic lime-alumina slags, in: *Fiziko-khimicheskie Osnovy Proizvodstva Stali*, Moskva, 1964, p. 176.
294. S. I. Popel, A. A. Deryabin, L. N. Saburov, and M. V. Tarkhanov, Surface properties of high-alumina slags, Tr. *Uralsk. Nauchno-Issl. Inst. Chern. Metall.* 12: 92 (1971).
295. V. I. Kostikov, M. A. Maurakh, and B. S. Mitin, Some physical properties of liquid refractory metals and oxides, in: *Vysokotemperaturnye Materialy, Metallugiya*, Moskow 49:108 (1968).
296. H. F. Shermer, Surface tension of molten glasses in the system barium oxide-boric oxide-silica, *J. Res. Natl. Bur. Stand*. 56:155 (1956).
297. R. Tupy' and M. Skrivan, Study of barium oxide-boron oxide-silica system glasses, *Sklar Keram.* 38:156 (1988).
298. A. I. Sotnikov, V. V. Petrov, and O. N. Bulatova, Temperature dependence of the surface tension for supercooled high-alkaline melts of sodium borates and silicates, *Rasplavy* 2:110 (1988).

299. J. H. Swisher and C. I. McCabe, Cr_2O_3 as a foaming agent in CaO-SiO_2 slags, *Trans. Met. Soc. AIME* 230: 1669 (1964).
300. N. I. Min'ko and V. A. Nevedomskii, Properties of molten silicon-manganese slags, Melts (Eng. trans. of *Rasplavy*) 3:359 (1991).
301. C. F. Callis, J. R. van Wazer, and J. S. Metcalf, Structure and properties of the condensed phosphates. VIII. Density and surface tension of molten sodium phosphates, *J. Amer. Chem. Soc*. 77:1468 (1955).
302. V. V. Owens and S. W. Mayer, Molar volume and surface tension of fused metaphosphate-sulfate systems, *J. Amer. Ceram. Soc*. 47:347 (1964).
303. S. A. Lyamkin, and S. A. Krasikov, in: *Struktura i Svoistva Shlakovykh Rasplovov, Kurgan*, 1984, p. 52.
304. A. S. Kim, A. A. Akberdin, and I. S. Kulikov, Density and surface tension of melts of the calcium oxide-silicon dioxide-aluminum oxide-calcium fluoride system, *Isv. Vyssh. Uchebn. Zaved. Chern. Metall*. 3:147 (1982).
305. S. V. Nesterenko and V. M. Khomenko, Study of the effects of alkalis on the surface tension and the electrical conductivity of slags of the CaO-MgO-SiO_2 system containing 5% Al_2O_3, *Izvestia Akademii Nauk SSSR. Metally* 2:44 (1985).
306. T. Izumitani and Y. Moriya, Devitrification of optical glasses, *J. Ceram. Assn. Jpn*. 70:131(1962).
307. J. B. Cronin, B. J. J. Zelinski, M. Denesuk, N. Kreidl, and D. R. Uhlmann, Wetting behavior of PbO-SiO_2 and PbO-B_2O_3-SiO_2 liquids, in: *Wettability* (J.C. Berg, Ed.) Marcel-Dekker, Inc., NY, 1993, p. 471.
308. A. Lecrenier and P. Gillard, The surface tension of molten glass, *Bull. Soc. Chem. Belg.* 34:27 (1925).
309. G. Keppeler and A. Albrecht, *Glastech. Ber.* 18: 275 (1940).
310. G. W. Morey, *The Properties of Glass*, American Chemical Monograph Series. Reinhold Publishing Corp., New York, 1938, pp. 197-211.
311. C. R. Amberg, Surface tension of glasses: effect of minor additions, Ph.D. thesis, The Pennsylvania State University, 1948, p. 107.
312. J. Gotz, Proc. 10th Int. Cong. Glass, The effect of Fluorides on Melting and Properties of Glass Melts, *Kyoto*, 2:132, 1974.
313. N. K. Boardman, A. R. Palmer, and E. Heymann, Constitution of ionic liquids. III. Surface tensions of molten salts and their mixtures, *Trans. Faraday Soc*. 51: 277 (1955).
314. R. B. Ellis, J. E. Smith, and E. B. Baker, Surface tension of fused alkaline earth metal halides, *J. Phys. Chem*. 62: 766 (1958).
315. J. S. Peake and M. R. Bothwell, Surface tensions and their temperature coefficients of molten mixtures of potassium chloride and barium chloride, *J. Am. Chem. Soc*. 76:2656 (1954).
316. F. M. Jaeger, *Optical Activity and High-Temperature Measurements*, McGraw-Hill Publishing Co., Ltd., London, 1930.
317. H. Bloom, F. G. Davis, and D. W. James, Molten salt mixtures. IV. Surface tension and surface heat content of molten salts and their mixtures, *Trans. Faraday Soc*. 56: 1179 (1960).
318. N. N. Greenwood and I. J. Worrall, Electrical conductance in fused gallium dichloride and gallium dibromide, *J. Chem. Soc*., p. 1680 (1958).
319. E. Ryshkewitch, *Oxide Ceramics: Physical Chemistry and Technology*, Academic Press, NY, 1960, p.169.

320. R. Fricke, Struktur und Verteilungsart Realer Festkorper und Katalysatoren sowie deren Untersuchungsmethoden, in: *Handbuch der Katalyse Vol. IV* (G. M. Schwab, Ed.), Springer Verlag, Vienna, 1943, p. 1.
321. G. J. Janz and M. R. Lorenz, Molten carbonate electrolytes: physical properties, structure, and mechanism of electrical conductance, *J. Electrochem. Soc*. 108:1052 (1961).
322. V. Y. Zaitsev, A. V. Vanyukov, and V. S. Kolosova, Interaction of Ni_3S_2-FeS and Cu_2S-FeS sulfide systems with iron-silicate melts, I*zv. Akad. Nauk SSSR Met.*, Engl. Trans. 5:29 (1968).
323. J. F. Elliott and M. Mounier, Surface and interfacial tensions in copper matte-slag systems, 1200˚C, *Can. Met. Quart.* 21:415 (1982).
324. S. D. Gromakov and A. I. Kostromin, Surface Tension and Liquidus Curves of the Ternary System $NaNO_3$-KNO_3-$RbNO_3$, *Univ. im V. I. Ul'Yanova-Lenina Khim*. 115:93 (1955).
325. J. L. Dahl and F. R. Duke, Surface tension of the $AgNO_3$-$NaNO_3$ and $AgNO_3$-KNO_3 systems, *J. Phys. Chem*. 62:1142 (1958).
326. K. B. Morris, N. McNair, and G. Koops, Electrical conductance, surface tension, and density in the molten system $PbMoO_4$ -$Bi_2(MoO_4)_3$, *J. Chem. Eng. Data* 7:224 (1962).
327. X. Hong and K. Lu, Physical properties of Li_2O-$4B_2O_3$ melt, *J. Cryst. Growth* 200(1-2):172 (1999).
328. S. E. Darienko, S. S. Zobnin, B. V. Kokarev, S. P. Raspopin, and Yu. F. Chervinskij, Physical properties of $Na_2B_4O_7$ -V_2O_5 system, *Rasplavy* (3):37 (1995).
329. K. Kubota, Properties of PbO-B_2O_3-SiO_2 glasses for hybrid IC, Master's Thesis, Kyushu University, Kasuga, Fukuoka, Japan, 1994.
330. U. Din-Fen, Surface tension of iron and calcium bearing slags, *Izv. Vyssh. Ucheb. Zaved. Chern. Met.* 1:27 (1963).
331. S. S. Kayalova, G. V. Baikova, and V. N. Filipovich, Effect of the amount of cobalt oxide on the surface tension and wettability of sodium silicate melt, *Rus. J. Appl. Chem.* 71(5):891 (1998).
332. E. Elchardus, Surface tension of molten mixtures containing cryolite, *Compte. Rendu*. 206:1460 (1938).
333. V. A. Izmajlov, L. M. Orlova, M. S. Mel'nikova, and I. F. Lopushinskij, Design of flux compositions for remelting of nickel and their physical and chemical properties, *Izvestiya AN SSSR: Metally* (1):5 (1994).
334. A. Kucuk, A. G. Clare and L. E. Jones, Differences between surface and bulk properties of glass melts, *J. Non Cryst,. Solids* 261:28 (2000).
335. A. Kucuk, A. G. Clare and L. E. Jones, Influence of various atmospheres on the surface properties of silicate melts, *Glastech. Ber. Glass Sci. Technol.* 73:123 (2000).
336. M. Yamashita, M. Suzuki, H. Yamanaka and K. Takahashi, Surface tension measurement of glass melts by the maximum bubble pressure method, *Glastech. Ber. Glass Sci. Technol.* 73:227 (2000).
337. D. Skupien and D. R. Gaskell, The surface tensions and foaming behavior of melts in the system CaO-FeO-SiO_2, *Met. and Matls. Trans. B* 31B:921(2000).
338. T. P. Seward, Aspects of the glass melt properties database investigations at Alfred University, *Ceram. Eng. Sci. Proc*. 22:149 (2001).
339. Z. Qiao, L. Yan, Z. Cao and Y. Xie, Surface tension prediction of high-temperature melts, *J. Alloys and Compounds* 325:180 (2001).
340. P. Vadasz, K. Tomasek and M. Havlik, Physical properties of FeO-Fe_2O_3-SiO_2 –CaO Melt systems, *Arch. Metall*. 46:279 (2001).

341. P. N. Quested and B. J. Monaghan, The measurement of thermophysical properties of molten slags and fluxes, *High Temp. Mat. Processes* 20:219 (2001).
342. J. Zhang, Q. Shu and S. Wei, Prediction of surface tension in molten ionic systems, *High Temp. Mat. Processes* 20:235 (2001).
343. M. Yamashita, M. Suzuki and H. Yamanaka, Surface tension measurement in several glasses, Inter. Cong. Glass, 19th, Edinburgh, UK, July 1–6, 1046 (2001).
344. D. R. Wing, L. E. Jones, A. G. Clare, K. Kahl and R. Beerkens, The effect of redox state on the surface tension of iron-containing soda lime silicate glasses, Inter. Cong. Glass, 19th, Edinburgh, UK, July 1-6, 948 (2001).
345. A. G. Clare, Using sessile and pendant drop methods to measure density and surface tension, *Glass Researcher* 10-11:20 (2001).
346. J. Y. Choi and H. G. Lee, Thermodynamic evaluation of the surface tension of molten CaO-SiO_2-Al_2O_3 ternary slag, *ISIJ Int*. 42:221 (2002).
347. F. Millot, J. C. Rifflet, G. Wille, V. Sarou-Kanian and B. Glorieux, Analysis of surface tension from aerodynamic levitation of liquids, *J. Am. Ceram. Soc*. 85:187 (2002).
348. R. E. Aune, M. Hayashi, K. Nakajima and S. Seetharaman, Thermophysical properties of silicate slags, *J. Metals* 54:62 (2002).
349. T. Takasu, H. Itou and T. Nakamura, Density and surface tension of CuxO bearing slags, *High Temp. Mat. Processes* 22:203 (2003).
350. A. G. Clare, D. Wing, L. E. Jones and A. Kucuk, Density and surface tension of borate containing silicate glass melts, *Glass Technol*. 44:59 (2003).
351. M. Paganelli, Measuring surface tension of glass, Am. Ceram. Soc. Bul. 82:4 (2003).
352. V. I. Nizhenko and Y. I. Smirnov, Surface phenomena and interfacial interaction at the glass-liquid tin-gas phase interface, *Powd. Metall. Met. Ceram*. (Ukraine) 42:171 (2003).
353. S. Fujino, C. Hwang and K. Morinaga, Density, surface tension and viscosity of BaO-ZnO--P_2O_5 glass melts, *Shigen to Sozai* 119:423 (2003).
354. S. Fujino, C. Hwang and K. Morinaga, Density, surface tension and viscosity of PbO-B_2O_3-SiO_2 glass melts, *J. Am. Ceram. Soc*. 87:10 (2004).
355. K. Grjotheim, C. Kron, M. Malinovsky, K. Matiasovsky, and J. Thonstad, *Aluminum electrolysis: Fundamentals of the Hall-Heroult Process* (2nd ed.), Aluminium-Verlag, Düsseldorf, Germany, 1982, pp. 141–143.
356. J. Thonstad, P. Fellner, G. M. Haarberg, J. Hives, H. Kvande, and A. Sterten, *Aluminum electrolysis: Fundamentals of the Hall-Heroult Process* (3rd ed.), Aluminium-Verlag GmbH, Düsseldorf, Germany, 2001, pp. 98–105.

7 Density of Glass Melts

Oleg V. Mazurin

CONTENTS

7.1 INTRODUCTION

Density d of a substance is the mass of a unit of the volume of this substance. In SI system, the density is expressed in kg/m^3 and in cgs system it is expressed in g/cm^3 (1 g/cm^3 = 1000 kg/m^3). Until now, the unit g/cm^3 has been broadly used in scientific literature. It is not only more habitual but also more convenient for writing and reading, so, in this chapter, this unit will also be used for presentation of numerical information. The value reciprocal to density, i.e., the volume of 1 g of a substance, is called a specific volume v. Sometimes in the scientific literature values of molar volume are presented, i.e., of volume of gram-mole (or kg-mole) of a substance.

The temperature coefficient of density is usually described by the so-called thermal expansion coefficients (TEC). The mean or average volume TEC β_m is expressed by the following formulas:

$$\beta_m = \frac{V_2 - V_1}{V_1(T_2 - T_1)} \tag{1}$$

where V_1 and V_2 are the volumes of a studied body at temperatures T_1 and T_2. Taking into account that $d = 1/v$, one can write:

$$\beta_m = \frac{\frac{1}{d_2} - \frac{1}{d_1}}{\frac{1}{d_1}(T_2 - T_1)} = \frac{\frac{d_1}{d_2} - 1}{(T_2 - T_1)} \tag{2}$$

The true or instantaneous volume expansion coefficient β is expressed as follows:

$$\beta = \frac{1}{V}\left(\frac{\partial V}{\partial T}\right)_p = \frac{d}{\left(\frac{\partial d}{\partial T}\right)_p} \tag{3}$$

For description of the expansion of solids as well as highly viscous melts (for example, in the glass transition regions) linear thermal expansion coefficients α are used. In this case, in equations (1) and (2), values V are replaced by values L, which describe any linear dimension of the studied body. For small expansion coefficients $\beta \approx 3\alpha$.

In the SI system, all expansion coefficients are expressed in K^{-1}, in cgs system, in $^oC^{-1}$.

7.2 METHODS OF MEASUREMENTS

A considerable number of methods could be used for the determination of the values of melt densities. However, their levels of popularity are quite different. About two thirds of all studies of the property in question were performed by using only one method, namely the counterbalanced sphere method. From 1917, when the first results of melt density studies were published [39] and until the end of the last century, this method remained the most frequently used. The maximum bubble pressure method was also used quite often. All other methods were used by limited numbers of scientists.

The counterbalanced method is also called the Archimedes method. Density is determined by the decrease of the weight of the spherical body after its suspension into the melt. In most cases, the sphere was made from platinum or platinum-rhodium alloy. Clearly, in special cases, one could use other materials as well. For weighing a sphere, an analytical balance is used. The sphere is suspended by a thin platinum wire, and the studied melt is put into a crucible (made as a rule also from platinum or platinum–rhodium alloy) positioned in a furnace. The scheme of the apparatus is presented in Figure 7.2.1.

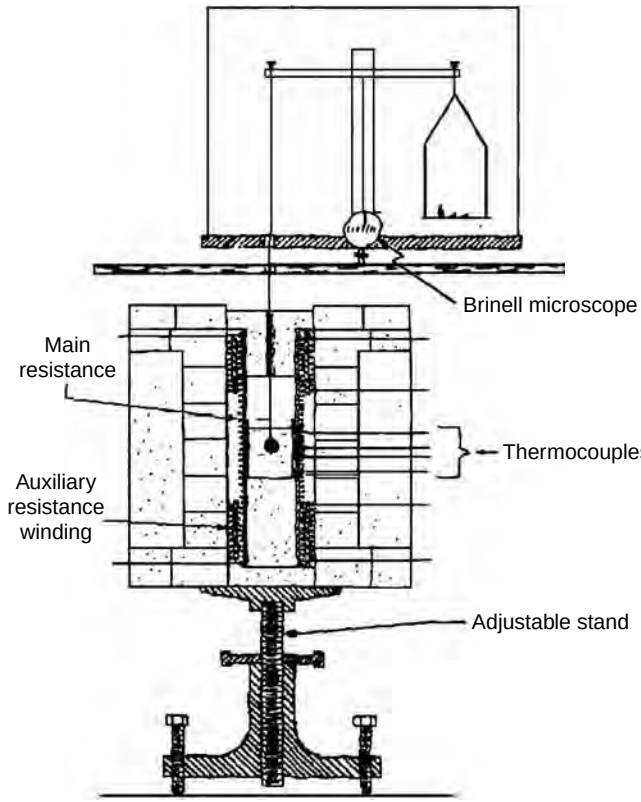

FIGURE 7.2.1 Scheme of one of the versions of apparatus for counterbalanced method of measurements of melt density (From Shartsis, L., Spinner, S. (1951). Viscosity and density of molten optical glasses. *J. Res. Nat. Bur. Stand.* 46(3)).

Upward or downward motion of the ball in the liquid is produced by changing the weights on the right-hand pan of the balance. The velocity of the ball is indicated by the motion of the balance pointer, which is observed through a Brinell microscope. The density is calculated by determining the difference of weights of the sphere in air and in the studied liquid. Due to high enough viscosity of glass-forming melts, it is difficult to determine precisely the weight of the balance corresponding to an absolute equilibrium (absence of the motion of the sphere in the liquid). Thus, usually the weights on the right-hand pan of the balance are changed to ensure either upward or downward motions of the sphere with appreciable velocities. Resulting dependencies permit the establishment of an equilibrium weight (corresponding to zero velocity) with quite reasonable accuracy. This is illustrated by Figure 7.2.2.

It should be noted that the same method could be used for measurements of viscosity, which determines the velocity of sphere motion for a given condition of measurements. Thus, the results of one series of measurements permit the data for two important properties of glass-forming melts to be obtained.

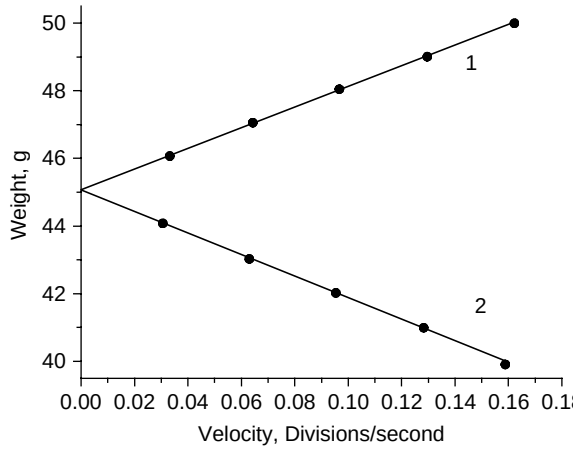

FIGURE 7.2.2 Dependence of upward or downward velocities on the weight of the balance in the course of using the counterbalanced method (From Shartsis, L., Spinner, S. (1951). Viscosity and density of molten optical glasses. *J. Res. Nat. Bur. Stand.* 46(3)). 1: Rising sphere, slope = 32.05; 2: Descending sphere, slope = 30.86.

For correct measurements of the density one should allow for the influence of surface tension of a melt around the wire. One can use a special formula for that (see for example Ref. [1]). However, there is a simple and dependable way to take this factor into account without the knowledge of the value of surface tension (see for example Ref. [2]). If two spheres of different diameters are weighed in sequence in the studied melt by using the wire of the same diameter for suspension, one result can be subtracted from the other, determining the difference between weights of two spheres in the melt. This difference can then be compared with the difference in weights of the two spheres in air.

Density measurements by the counterbalanced sphere method can be very precise. The highest precision reached by this method was reported by Napolitano et al. [3], namely ± 0.002 g/cm^3.

The main shortcoming of this excellent method is the fact that it can be used only for liquids with comparatively low viscosity. According to Ref. [1], for melts with viscosity higher than 5,000 poises the density results become unreliable.

The next most frequently used method is maximum bubble pressure, which is used rather broadly for the measurements of surface tension (a detailed description of the basic principles of the method and necessary apparatus can be found in Ref. [4]). It is known that surface tension is related to the maximum pressure attained in a bubble of gas formed at the tip of a capillary tube dipped in the liquid. Among other factors, the value of maximum bubble pressure depends on the depth of immersion of the tip of capillary tube into the liquid, and the density of this liquid. To exclude the necessity of knowing the value of surface tension of the melt, one usually determines the maximum bubble pressure at two depths, which could be done by measurements of maximum bubble pressure in two similar tubes immersed consecutively to different depths [5].

For obtaining precise results, two conditions must be met: the gas bubble should be semispherical (i.e., the quality of the capillary should be good) and the effect of viscosity should be eliminated by arranging for the rate of pressure increase to tend to zero at the maximum pressure. The use of the described method is also limited by the need to perform measurements at temperatures where viscosity of the studied melt is not too high.

As mentioned above, all other methods are rarely used. The main reason for the development and use of most of such methods is scientists' desire to measure the density of highly viscous melts. In this chapter it is not reasonable to describe these methods in detail. Only short characteristics of the specific features of the methods will be presented here.

Several methods can cover a rather broad range of temperatures. The Indirect Archimedes method used by Coenen [6] belongs to this group of methods. The idea of the method is the weighing of a crucible with the studied glass in a molten salt. Coenen used NaCl. The temperature range of such measurements in the case of the mentioned salt is between 800°C (crystallization temperature) and 1465°C (evaporation temperature). This method is used quite rarely.

The sessile drop method [7] is used somewhat more often. Sessile drop of the studied melt is positioned on a plate put into a furnace. By using an optical system the dimensions of the drop are controlled. If the weight of the drop is known, it is easy to calculate the density of the melt at any given temperature. One of the main requirements is that the drop should be symmetric about the vertical axes. Unfortunately, it is rather difficult to be sure that this requirement is met in the course of high-temperature experiments.

It is possible to determine the density of a melt by absorption of gamma rays [8, 9].

When one is interested in the density of highly viscous melts, the easiest way is to measure the density of the glass at room temperature (by one of many well known simple and precise methods) and then to obtain thermal expansion curve from room temperature to the high-temperature limit of the glass transition region. The only condition is the use of a dilatometer with low external pressure (see, for example, Ref. [10]) to ensure that the influence of viscous deformation in the high-temperature part of the measurements will be negligible.

The high-temperature limit of the use of the dilatometer for the above-described purposes corresponds to a viscosity of 10^{10} poises. However, Klyuev [10] has developed a special silica dilatometer permitted to extend the dilatometric curve up to temperatures corresponding to viscosity of 10^5 poises. He proposed to put a glass sample into a silica tube and cover the upper end of the sample by a silica disc. Thus, the density can be measured at room temperature and a traditional silica dilatometer (with low external pressure) and special dilatometer by Klyuev can be used to measure the density at room temperature as a base, and then the change in density can be followed up to the necessary temperatures. Klyuev [10] compared the results of his measurements with those reported by Coenen [6] and found quite good agreement between two sets of the data. See Figure 7.4.5.

An original method of studying melt density was used by Richards and Bergeron [11]. They kept each sample at the selected temperature for 15 minutes (in temper-

ature ranges where this time was enough for droplets of the studied melt to reach an equilibrium), then quenched it in CCl_4. Droplet densities were measured by the flotation method. Two subsequent measurements were performed: (1) for an initial droplet and (2) for the droplet after removing its surface layer by etching. Thus the density of the surface layer of the glass droplet was determined. Because the cooling rate of surface layers in the course of quenching are especially high, the structure of these layers had to be particularly close to the structure of the initial melts.

7.3 ABOUT THE INFORMATION SYSTEM SciGlass

As a great part of this chapter is based on the broad use of the information contained in the electronic Glass Property Information System SciGlass (SG)[12], we give here a short description of this system.

The version of the system used in this chapter (SciGlass-5) contains property data for more than 200,000 glasses. These data were extracted from many thousands of papers published all over the world between 1878 and 2001, as well as from theses, reports, patents, etc.

An important (and so far unique) feature of the SciGlass database is that it includes the data presented in the original publications not only in the form of tables, but also in graphic form. Using a program especially developed for SciGlass, all information from graphs was transferred into numerical form without the loss of precision. Thus, all the existing data could be presented on the screen either in numerical or graphical forms, each being fully compatible with the other.

SciGlass Information System contains two databases. The main database presents the data from original publications without any changes (with the exception of the above-mentioned transformation of graph data into the numerical form). The auxiliary database presents the data for certain standard rounded temperatures. These data were obtained by the mean square root approximation of original data on the basis of the appropriate equations. This database permits all existing data for the selected property and glass system, regardless of the specific form of the data presentation in the original publication, to be combined into one figure. This feature is used broadly in the next sections of this chapter.

One more feature of SciGlass that is used in this chapter is the so-called calculator, which permits the use of nearly all existing methods of calculations of glass and melt properties. Among them is the recently developed method Priven2000, which covers a unique number of properties and a unique area of glass compositions (properties of glass and melt compositions including any of 64 various oxides can be calculated).

7.4 INFLUENCE OF TEMPERATURE

7.4.1 Introduction

Although this chapter deals mainly with the densities of melts, it is necessary to describe the main features of the influence of temperature on the densities of glass-

forming substances from room temperature to the highest temperatures at which the melt densities were measured. One of the obvious reasons for this is the fact that, as mentioned in Section 7.2, some methods of measurements of density of highly viscous melts are based on the measurements of density of glasses at room temperature and then on determination of thermal expansion of the glass from room temperature to temperature ranges corresponding to the molten state of the studied glass-forming substance. Another reason is that knowledge of the specific changes of density of glass-forming substances in a very broad temperature range should help to better understand some features of the influence of temperature on the composition dependencies of melt density.

It is well known (see, for example, Refs. [13, 14]) that there is a clear distinction between temperature dependencies of properties of glass-forming melts and those of glasses. The reason for this is as follows.

In glass-forming melts (the same is characteristic for any melts) there are two kinds of influence of temperature on practically any property of the substance. First is the purely thermal factor: an increase in temperature leads to an increase in the intensity of thermal oscillations of atoms and accordingly to an increase in the distance between them. We will call this the oscillation factor. This factor leads directly to a decrease in density with increasing temperature. The second is the so-called structural factor. Temperature changes lead to changes in the average mutual positions of atoms in a liquid, average coordination numbers, average angles between certain bonds, etc. As a rule, such structural changes lead to an additional (and usually quite considerable) decrease in density with increasing temperature.

At the same time, in solid glass, the change in temperature does not lead to any structural changes. Thus, the thermal expansion of glass is determined solely by the oscillation factor.

When the glass-forming melt is cooled, the changes in its temperature lead to changes in its structure. The rate of structural changes is connected with the values of viscosity. At high temperatures, the viscosities of most melts are low and rates of structural changes are high. With decreasing temperature, viscosity increases and the rates of structural changes decrease. At usual cooling rates (from 1 to 10 K/min) structural changes begin to be arrested within the viscosity range 10^{11}–10^{14} poises. The corresponding temperature range is called the glass transition region. For most silicate glasses, the glass transition regions are positioned between 400 and 650°C.

Thus, below a glass transition region, the temperature changes in the density of a glass-forming substance (thermal expansion coefficients) are determined solely by oscillation factor; above this region — by both oscillation and structural factors, and inside the region in question — by oscillation factor and partially by structural factor.

7.4.2 Experimental Data

For the overwhelming number of the compositions of glass-forming substances, the structural factor plays the major role in the determination of the influence of temperature on the melt density. Because structural changes in most melts lead to a decrease of density with increasing temperature, thermal expansion of melts is usually much higher than that of glasses. See Figure 7.4.1.

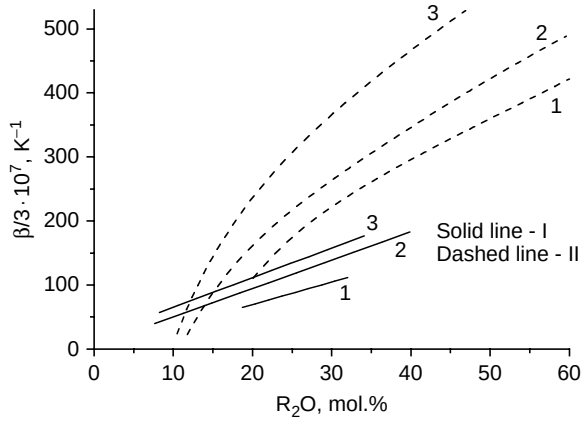

FIGURE 7.4.1 Thermal expansion of binary alkali silicate glasses (I) and melts (II) [17]. R: 1– Li; 2–Na; 3–K. Approximations were done by using the data from the following: Solid lines: Turner and Winks [18]; Gooding and Turner [19]; Shmidt and Alekseeva [20]. Dashed lines: Bockris et al. [21]; Shartsis et al. [22].

According to some general considerations [13], there are reasons to suppose that the intensity of the influence of temperature on structural changes of melts should decrease with increasing temperature. This assumption is supported by most of those experiments that cover broad enough temperature ranges. Examples of these experiments are presented in Figure 7.4.2, Figure 7.4.3, and Figure 7.4.4. It should be noted that the number of such experiments is rather limited because most studies of melt densities were performed by methods that could not be used for highly viscous liquids.

Figure 7.4.3 requires special comment. It is the result of the superposition of two sets of measurements. One was performed by Johnson et al. [15], who used the measurements of room-temperature density and the dilatometric measurements for a study of density of glasses (up to the center of glass transition region) and the

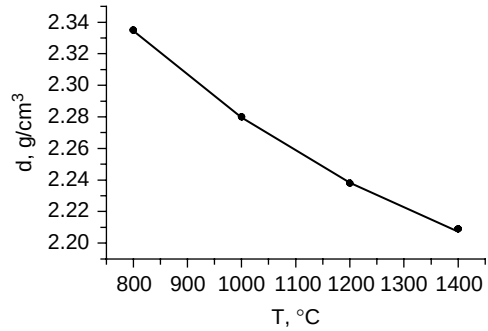

FIGURE 7.4.2 Temperature dependence of density of binary sodium silicate melt containing 32 mol.% Na_2O (data taken from Coenen, M. (1966). Dichte von "Schlierengläsern" bei hohen Temperaturen. *Glastech. Ber.* 39(3)).

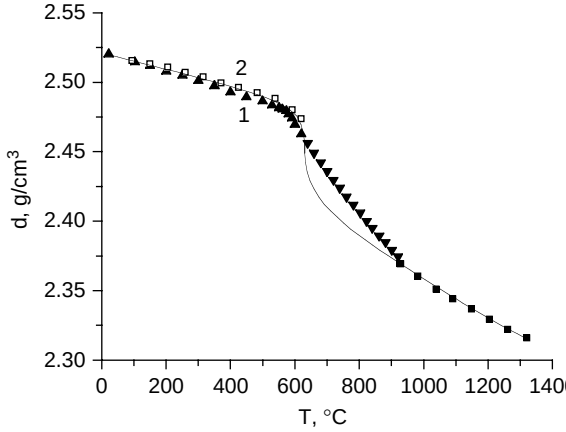

FIGURE 7.4.3 Temperature dependence of density for composition, mol.%: 68 SiO_2, 14.8 Na_2O, 10.9 CaO, 4.4 B_2O_3, 1.8 Al_2O_3. ▲, ▼: measurements by Klyuev [16] by two different methods; □, ■: measurements by and solid line interpolation of data by Johnson et al.(1950). Volume expansion of glass at high temperatures. *J. Am. Ceram. Soc*. 33(4).

counterbalanced method for the study of densities of high-temperature melts. The data of these authors were always considered especially important because they described the density changes in a glass having composition that was near enough to the compositions of many common commercial glasses. However, there was a very broad gap between the two areas of measurements. It could be filled by interpolating curve (see a solid line in a figure), but the actual temperature dependence of melt density remained unknown. Klyuev [16] performed the measurements of density changes in the glass and melts of the same composition by the methods described in Ref. [10]. It is seen from the figure that the results by Klyuev correspond

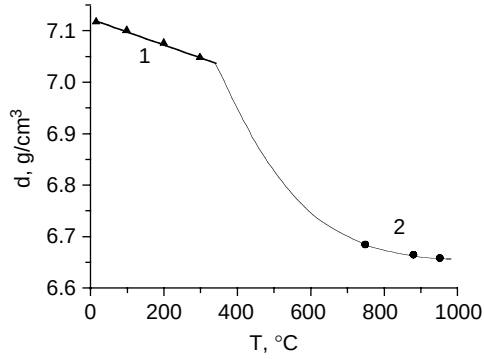

FIGURE 7.4.4 Temperature dependence of density of binary lead silicate containing 66.7 mol. % PbO in molten and glassy states (From Merker, L. (1959). Eine einfache Methode zur Dichtebestimmung von Glasschmelzen bei hohen Temperaturen. *Glastech. Ber.* 32(12)). ▲: Dilatometric measurements; ●: measurements by the method of maximum bubble pressure.

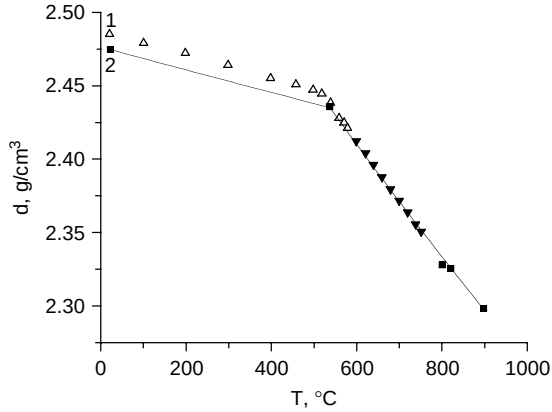

FIGURE 7.4.5 Temperature dependence of density for composition, mol.%: 64 SiO_2, 24 Na_2O, 8 B_2O_3, 4 Al_2O_3. □, ▼: measurements by Klyuev, V.P. (1997). Dilatometric method of thermal expansion measurements of softened glass in the range 10^{10}–10^5 Poise (in Russian). *Fiz. Khim. Stekla*, 23(1) by two different methods; ■: measurements by Coenen M. (1966). Dichte von "Schlierengläsern" bei hohen Temperaturen. *Glastech. Ber.* 39(3).

to results by Johnson et al. quite reasonably, providing a full dependence of glass and melt densities for such a commercial glass.

At the same time, results of experiments demonstrating linear dependence of melt density on temperature in a rather broad temperature range can be found in the literature. An example is given in Figure 7.4.5. One can suppose that at temperatures above the studied range of measurements the expansion coefficient for such kinds of glasses begins to decrease. At present, however, it is not possible to be sure of that.

There are indications that there could be various deviations from the general tendencies of temperature dependencies of melt densities. One such deviation was found by Shartsis et al. [24] and is shown in Figure 7.4.6.

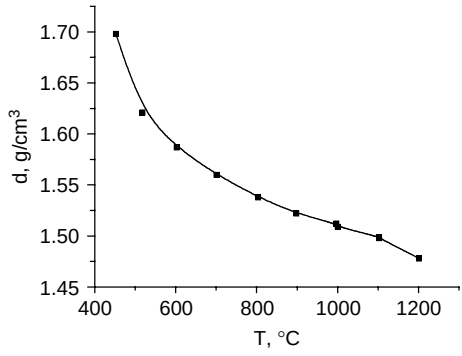

FIGURE 7.4.6 Temperature dependence of density of molten B_2O_3 (Data taken from Shartsis, L., Spinner, S., Capps, W. (1952). Density, expansivity, and viscosity of molten alkali silicates. *J. Am. Ceram. Soc.* 35(6))

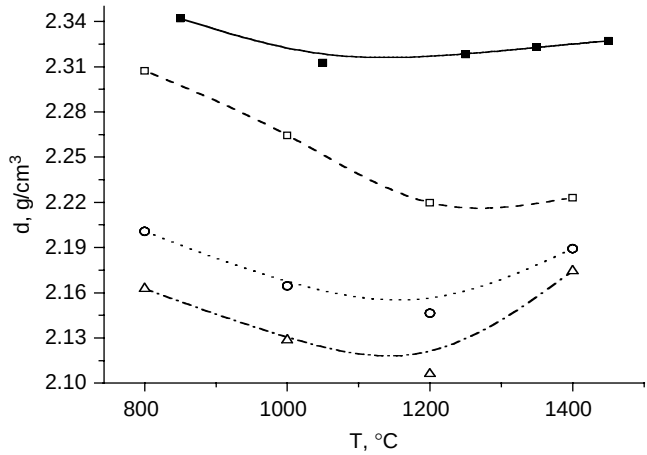

FIGURE 7.4.7 Temperature dependencies of density for some silicate melts containing considerable amounts of Al2O3 (data were taken from Coenen M. (1966). Dichte von "Schlierengläsern" bei hohen Temperaturen. *Glastech. Ber.* 39(3)). ■–12.8Na_2O • 8CaO • 20Al_2O_3 • 59.2SiO_2.; □–20Na_2O • 12B_2O_3 • 8Al_2O_3 • 60SiO_2.; o–12Na_2O • 20B_2O_3 • 8Al_2O_3 • 60SiO_2.; Δ–8Na_2O • 24B_2O_3 • 8Al_2O_3 • 60SiO_2.

As shown in the figure, in the temperature range from 1200 to 1400°C, an expansion coefficient began to increase with increasing temperature. There was no confirmation of this phenomenon by other scientists. However, Shartsis and his colleagues belonged to one of the best teams of investigators of glass and melt properties and thus their results should be considered absolutely dependable.

The other kind of deviation from the usual temperature dependencies of melt densities was reported by Coenen [6]. He found that there is a group of glass melts that at high enough temperatures showed an increase in density with increasing temperature (i.e., expansion coefficients of these melts become negative ones). An example of such results is demonstrated in Figure 7.4.7.

Quite complicated temperature dependencies of melt density were found by Bruekner [25] for some types of silica glass. Indirect but convincing enough results by this author show that, at least for some of the types of silica glasses in the molten state between 1300 and 1800°C, thermal expansion coefficients are negative (density increases with increasing temperature), and only at higher temperatures does the density begin to decrease with temperature. It should be noted that all effects of these changes are very small.

7.5 INFLUENCE OF COMPOSITION

7.5.1 Introduction

SciGlass Information System 5.0 [12] contains data on the densities of about 1800 glass-forming melts (it can be noted that the same system contains information about the densities of 39,000 glasses at room temperature). It is quite a considerable amount

of information. However, it is not an easy task to use the existing data for a detailed enough survey of the influence of composition on melt densities for at least three reasons. First, in most cases, the studies cover comparatively narrow temperature ranges, which usually resulted from the limited viscosity ranges (and hence the temperature ones) where the selected method of density measurements could be effectively used (cf. Section 7.2 of this chapter). Therefore, it is not always possible to compare results published by different authors. Second, very often the authors did not present data for systematically changing compositions. Even for ternary melts, in some cases the compositions for the studies were taken in random, which eliminated the possibility of forming a clear notion about the influence of a certain component of the studied property. Third, for a considerable number of the studies of melt densities, the precision of measurements is far from adequate.

In this section, much of all the data that could be used for a dependable description of the influence of composition on glass-forming melt densities are compiled. The reader will see that many areas of compositions of interest are not included in this description. The only way to fill some of the gaps is the broad use of the existing methods of calculations of melt densities. Some results of such calculations will be presented in Section 7.6 of this chapter.

7.5.2 Density of Silicate Melts

7.5.2.1 Density of Binary Sodium Silicate Melts

For a demonstration of some specific features of the results of melt density measurements and the influence of temperature on composition dependencies of silicate melts, it is reasonable to begin with the analysis of data on densities of binary sodium silicate melts that were studied especially actively during the 20th century.

We begin this analysis with the presentation of data on densities of sodium silicate glasses at room temperature. (See Figure 7.5.1.)

Figure 7.5.1 is created by using the SG system [12]. The SG database contains data for about 450 experimental points taken from more than 150 different publications. In original SG graphs, various points have different colors. Even this is not enough for an individual description of the set of data taken from each of the used publications, and in the SG there are additional ways for identification of points taken from every particular publication. In this chapter, it is impossible. Thus, we give here no references to the presented data. These references can be found in the SG Information System [12]. The solid curve is the result of approximation by the method of least squares (using polynomial of degree 2) of all the points presented in the graph.

It is to be noted also that from the presented set of points three points that deviated from the approximating curve for more than 0.2 g/cm^3 were deleted. It may seem rather strange, but from time to time in the scientific literature, data are published that obviously have no bearing on the real values of the studied properties of corresponding glass or melt compositions. The percentage of such blunders increased sufficiently during the last decades and usually such absolutely erroneous results were published in the most popular material science journals. Among remain-

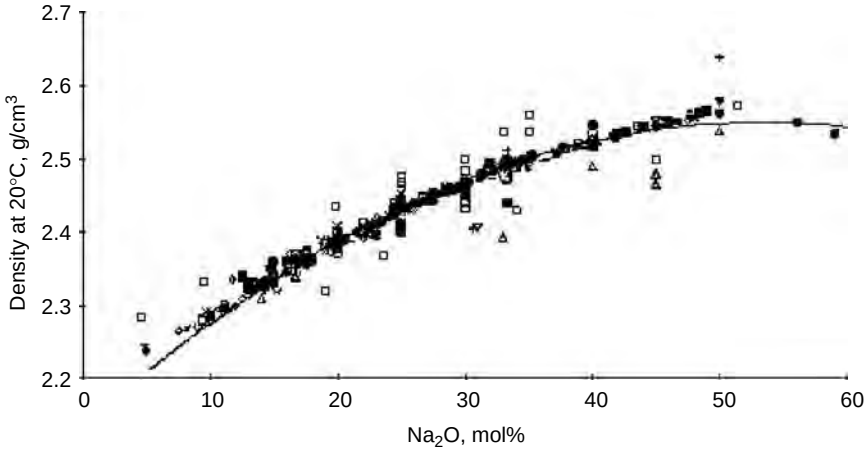

FIGURE 7.5.1 Density at 20°C of binary sodium silicate glasses (the graph was formed by the use of Ref. [12], where the references to particular publications can be found).

ing points there were several dozens that were also obviously erroneous because their deviations from the mean values of densities measured for the same compositions by many other scientists greatly exceed the usual standard error of room temperature density measurements (even for very simple methods of measurements this error is below 0.01 g/cm^3).

When there are many various sources of information, it is easy to determine the most probable values of the studied property of the glass (or binary glass system) of interest. It is clear that, despite all deviations, the area that is most densely populated by experimental points is positioned in the close vicinity of the approximation curve. Thus, this curve can be considered to describe the most probable values and the most probable composition dependence of the studied property. It is worth mentioning that the standard deviation of all points presented in the graph from this curve is equal to 0.00207 g/cm^3. It can be considered an excellent result, proving that most of the reported studies so far were performed on quite a high experimental level.

All the above information is important for better understanding of the data presented below. When the data describing a certain dependence are numerous and taken from different sources, it is easy to find the most probable composition dependence of property. When the data are scarce, the possible error in estimation of such dependence increases greatly. Especially difficult or even impossible is to find the desired dependence by using property values for different compositions taken from different sources.

For understanding the tendencies of the changes of composition dependencies of density with temperature one should take into account the influence of composition on thermal expansion. It is well known that the dependence of thermal expansion of silicate glasses on concentration of silica is very strong (see, for example, Figure 7.4.1). In a solid state, the TEC of silica glass above room temperature equals to (5–6)*10^{-7} K^{-1} [12]. Near the glass transition region (~1200°C) it decreases even

TABLE 7.5.1
Temperature Dependence of Density of Amersil Silica Glass at High Temperatures (Bacon et al. [26])

T, °C	1935	2048	2114	2165	2322
d, g/cm^3	2.094	2.072	2.057	2.045	1.929

Source: Bacon, J. F., Hasapis, A. A., Wholley, J. W. (1960). Viscosity and density of molten silica and high silica content glasses. *Phys. Chem. Glasses* 1(3).

more and, above this region in some cases, can even become negative, although at higher temperatures, it again becomes a positive one (cf. Section 7.4 of this chapter). At present, one can find in the literature only one set of direct measurements of density of silica glass in molten state [26]. These data are presented in Table 7.5.1. These results show that even in the molten state the density of silica glass decreases slowly. At the same time, a decrease in the density of alkali silicate melts in relation to temperature is considerable, and this effect increases with an increase in concentration of alkali oxides (cf. Figure 7.4.1). The results of the influence of these factors are shown in Figures 7.5.2–5.6.

After the above-presented considerations one needs only several additional comments to these graphs. In Figure 7.5.2 and Figure 7.5.3, all existing points are presented, and all are positioned precisely on the approximating curve. The compatibility of the results taken from various publications for the next three figures is considerably less. In addition, few points with especially great deviations from the approximating curves were deleted from the graphs. At the same time, the general trend of temperature changes in composition dependencies is absolutely clear and corresponds very well with the above-mentioned characteristics of the influence of composition on the thermal expansion of the system in question.

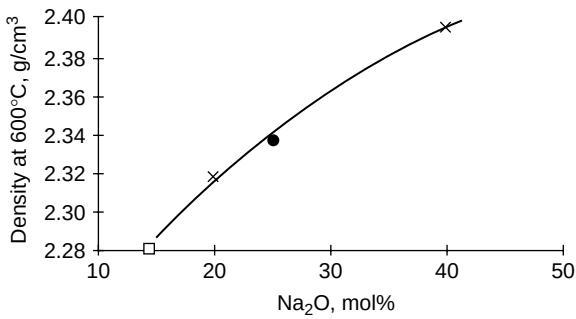

FIGURE 7.5.2 Density at 600°C of binary sodium silicate melts (the graph was formed by the use of Ref. [12]). x–Sasek and Lisy [27]; –Heidtkamp and Endell [28]; *–Sasek and Kasa [29]; ■–Scarfe et al. [30].

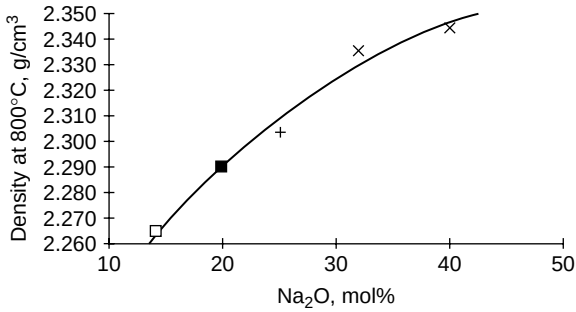

FIGURE 7.5.3 Density at 800°C of binary sodium silicate melts (the graph was formed by the use of Ref. [12]). x,- Sasek and Lisy [27]; +–Sasek and Lisy [31]; ■–Sasek and Kasa [29]; □–Din [32]; *–Coenen [6].

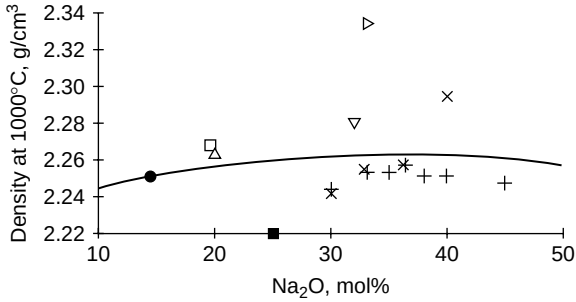

FIGURE 7.5.4 Density at 1000 °C of binary sodium silicate melts (the graph was formed by the use of Ref. [12]). x–Sasek and Lisy [27]; □–Sasek and Lisy. [31]; Δ–Sasek and Kasa [29]; +–Heidtkamp and Endell [28]; *–Shartsis et al. [22]; ■–Frischat and Beier [33]; ●Din et al. [34]; ∇–Coenen [6]; ◊–Coenen [35].

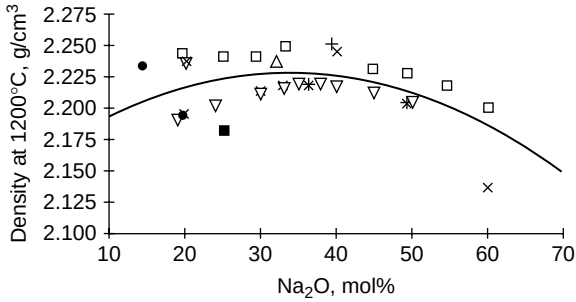

FIGURE 7.5.5 Density at 1200°C of binary sodium silicate melts (the graph was formed by the use of Ref. [12]). ∇–Sasek and Lisy [27]; □–Heidtkamp [28]; *–Shartsis [22]; ■–Frischat and Beier [33]; +–Stein et al. [2]; Δ–Coenen [6]; o–Passerone et al. [7]; ●–Din [32]; ◊–Nikonov et al. [36].

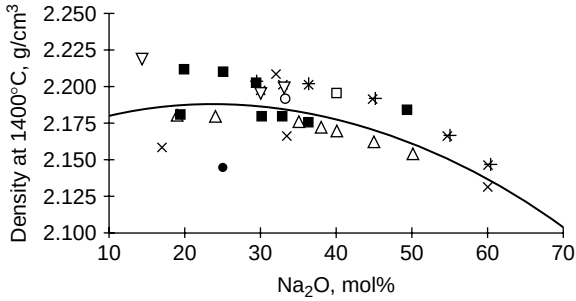

FIGURE 7.5.6 Density at 1400°C of binary sodium silicate melts (the graph was formed by the use of Ref. [12]). x–Washburn et al. [37]; □–Sasek and Lisy [27]; *–Heidtkamp and Endell [28]; ■–Shartsis et al. [22]; ●–Frischat and Beier [33]; ∇–Din [32]; –Coenen [6]; ◊–Golovin and Akhlestin [38]; o–Dertev and Golovin [39].

The same kind of temperature influences on the composition dependencies of melt densities is characteristic for all binary alkali silicate systems. In accordance with data presented in Figure 7.4.1, the effect increases with increasing radius of alkali ions. It is demonstrated by the comparison of Figure 7.5.7 with Figure 7.5.6.

As to lithium silicate melts, the only temperature for which there is a considerable number of experimental points is 1200°C. The results of the compilation of these data are shown in Figure 7.5.8. The comparison of this figure with Figure 7.5.5 shows a certain deviation from the discussed trends. It is connected with the fact that for binary silicate glasses at room temperature an increase in density with an increase in concentration of R_2O for lithium glasses is much smaller than that for sodium or potassium glasses.

Table 7.5.2. shows the results of the only study where the comparison of densities of binary silicate melts with all five alkali oxides is given [27]. It is seen that, for the studied temperature range and alkali concentration, the densities of lithium, sodium, and potassium melts are near enough to each other. At the same time, the

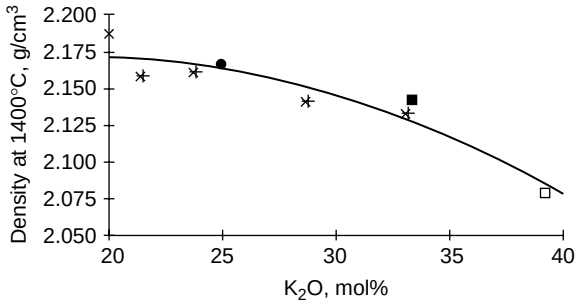

FIGURE 7.5.7 Density at 1400°C of binary potassium silicate melts (the graph was formed by the use of Ref. [12]). □–Sasek and Lisy [27]; ●–Sasek and Lisy [31]; *–Shartsis et al. [22]; ■–Golovin and Akhlestin [38].

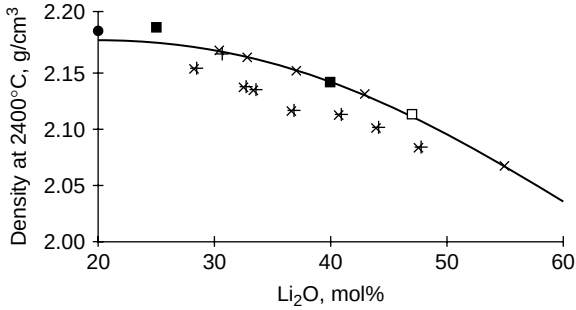

FIGURE 7.5.8 Density at 1200°C of binary lithium silicate melts (the graph was formed by the use of Ref. [12]). x–Bloom and Bockris [40]; □–Sasek and Lisy [27]; ■–Sasek and Lisy [31]; *–Shartsis et al. [22];●–Sasek et al. [41].

TABLE 7.5.2
Comparison of Melt Densities for all Binary Alkali Silicate Melts

Mol.% by batch						d, g/cm³ at T, °C			
SiO_2	Li_2O	Na_2O	K_2O	Rb_2O	Cs_2O	1100	1200	1300	1400
75	25	—	—	—	—	2.178	2.267	2.156	2.144
75	—	25	—	—	—	2.256	2.24	2.225	2.21
75	—	—	25	—	—	2.228	2.207	2.186	2.166
75	—	—	—	25	—	2.806	2.782	2.758	2.735
75	—	—	—	—	25	3.145	3.117	3.09	3.063
80		20		—	—	2.25	2.238	2.225	2.213
80		—		20	—	2.765	2.726	2.688	2.65
80		—		—	20	3.119	3.069	3.019	2.97

Source: Data from Sasek, L., Lisy, A., (1972). Structura a vlastnosti kremicitych tavenin. II. Merna hmotnost binarnich alkalicko–kremicitych sklovin. *Sb. Vys. Sk. Chem. Technol. Praze, Chem. Technol. Silik.* L2.

densities of rubidium and especially cesium melts are much higher than those of the first three melts.

7.5.2.2 Density of Mixed Alkali Silicate Melts

One can wonder what could be the influence of equimolecular substitution of one alkali ion for another one (the so-called mixed-alkali effect). Figure 7.5.9 shows that, for melt densities, such dependencies are practically linear: the deviations from linearity are well within the errors of measurements. The same kind of dependence was found by Frischat and Beier [33] for substitution of Na_2O for Rb_2O in alkali silicate system with 75% of SiO_2 at temperatures 1000, 1200, and 1400°C.

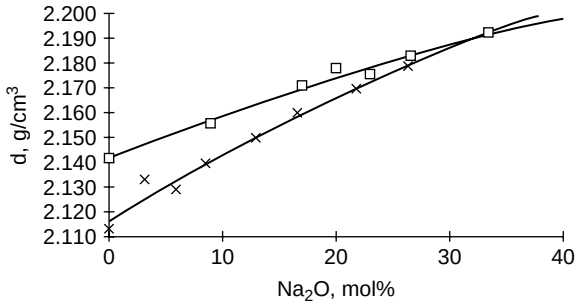

FIGURE 7.5.9 Change in densities of alkali silicate melts at 1400°C as a result of equimolecular substitution of Li_2O (x) or K_2O (□) for Na_2O. (Dertev, N. K., Golovin, E. P., Akhlestin, E. S. (1971). Thermal-EMF as function of the volume thermal expansion of R'$_2$O-R"$_2$O-SiO_2 melts (in Russian). In: *Stekloobraznoe Sostoyanie*. Leningrad: Nauka).

7.5.2.3 Influence of Bivalent Oxides on Density of Alkali Silicate Melts

Systematic investigations of the influence of most of the bivalent oxides on melt densities are quite scarce. The compilers of SG were able to find only two kinds of such studies. First is the study by Din and Hennicke [43], which is shown in Table 7.5.3. Analysis of their original work leads to the conclusion that the precision of the studies was not high. However, the comparison of the value for binary melt with data presented in Figure 7.5.6 shows that results by Din and Hennicke could be considered reasonably dependable. It is seen from the presented data that the substitution of SiO_2 for any of the studied bivalent oxides leads to an increase in melt density; the greater the concentration of the binary oxide the greater the mentioned increase. An increase in the radius of bivalent ion increases the effect.

The other series of results are shown in Table 7.5.4, which is a compilation of results presented in a series of publications by Sasek and Lisy [27]. In these publications there were no data on the densities of the corresponding binary melts containing the same concentrations of alkali oxides. However, in other publications, one can find values of densities of the melts in question for 25 and 20% R_2O (see Table 7.5.2). Because the procedure of measurements for all values presented in Tables 7.5.2 and 7.5.4 was the same, the use of all these data together is quite reasonable. From the comparison of the data in these two tables, one can conclude that the influence of the substitution of SiO_2 for RO on the melt densities of all the studied melts is practically the same as was found by Din and Hennicke for sodium silicate melts.

A very strong increase in melt density is characteristic for addition of lead oxide. This is demonstrated in Figure 7.5.10.

7.5.2.4 Influence of Other Oxides on Density of Alkali Silicate Melts

Tables 75.5–75.7 demonstrate some data on the influence of Al_2O_3, B_2O_3, and La_2O_3 on the densities of alkali silicate melts. It is clear from the presented data that the

TABLE 7.5.3
Influence of the Substitution of SiO_2 for Different Bivalent Oxides in Binary Sodium Silicate Melt at 1400°C

Mol.% by batch						
SiO_2	Na_2O	CaO	MgO	SrO	BaO	d, g/cm³ at 1400 °C
85.7	14.3	—	—	—	—	2.22
82.1	14.3	3.6	—	—	—	2.25
78.6	14.3	7.1	—	—	—	2.27
75	14.3	10.7	—	—	—	2.31
71.4	14.3	14.3	—	—	—	2.34
67.84	14.3	17.86	—	—	—	2.37
78.56	14.3	—	7.14	—	—	2.26
74.99	14.3	—	10.71	—	—	2.28
71.42	14.3	—	14.28	—	—	2.3
67.84	14.3	—	17.86	—	—	2.32
64.27	14.3	—	21.43	—	—	2.34
78.56	14.3	—	—	7.14	—	2.38
74.99	14.3	—	—	10.71	—	2.46
71.42	14.3	—	—	14.28	—	2.54
67.84	14.3	—	—	17.86	—	2.62
78.56	14.3	—	—	—	7.14	2.48
74.99	14.3	—	—	—	10.71	2.61
71.42	14.3	—	—	—	14.28	2.74
67.84	14.3	—	—	—	17.86	2.88

Source: From Din, A., Hennicke, H. W. (1974). Zum Verhalten der Magnesiumionen in Silicatgläsern. *Glastech. Ber.* 47(1)

influence of substitution of SiO_2 for aluminum and boron oxides is far not strong. On the other hand, an increase in density resulting from substitution of SiO_2 for La_2O_3 is fairly strong. Note also an increase in density with temperature rising from 1200 to 1400°C for some of the melts described in Tables 7.5.5 and 7.5.6. Temperature dependencies of densities of melts of such kind are shown and discussed in Section 7.4 of this chapter (cf. Figure 7.4.7).

7.5.2.5 Densities of Alkali-Free Silicate Melts

Table 7.5.8 shows that in the most important ternary system of alkali-free silicate melts, namely the CaO-Al_2O_3-SiO_2 system, the substitution of SiO_2 for Al_2O_3 leads to a very slight increase of melt density (actually within the error limits of the most of studies of melt densities). The substitution of SiO_2 for CaO resulted from somewhat greater but still a moderate effect.

7.5.3 Density of Borate Melts

As in the case of silicate melts it is reasonable to begin with the analysis of the densities of binary sodium borate melts. Figure 7.5.11 shows the density of sodium

TABLE 7.5.4
Influence of Bivalent Oxides on Melt Densities of Binary Alkali Silicate Melts

Mol.% by batch										d, g/cm³ at T, °C	
SiO_2	K_2O	Li_2O	Cs_2O	Rb_2O	MgO	CaO	SrO	BaO	ZnO	1300	1400
72.22	18.06				9.72	—	—	—	—	2.258	2.24
72.22	18.06				—	9.72	—	—	—	2.28	—
72.22	18.06				—	—	9.72	—	—	2.403	—
72.22	18.06				—	—	—	9.72	—	2.517	—
72.22	18.06				—	—	—	—	9.72	2.399	—
72.22		18.06			9.72	—	—	—	—	2.2225	2.207
72.22		18.06			—	9.72	—	—	—	2.277	2.247
72.22		18.06			—	—	9.72	—	—	2.431	2.405
72.22		18.06			—	—	—	9.72	—	2.578	—
72.22		18.06			—	—	—	—	9.72	2.36	—
72.22			18.06			9.72	—	—	—	—	2.993
72.22			18.06			—	9.72	—	—	3.133	3.089
72.22			18.06			—	—	9.72	—	3.235	3.194
72.22			18.06			—	—	—	9.72	3.177	3.115
72.22				18.06	9.72	—	—	—	—	2.706	2.668
72.22				18.06	—	9.72	—	—	—	2.757	—
72.22				18.06	—	—	9.72	—	—	2.836	2.803
72.22				18.06	—	—	—	9.72	—	2.953	2.912
72.22				18.06	—	—	—	—	9.72	2.837	2.803

Source: Data from Sasek, L., Lisy, A., (1972). Structura a vlastnosti kremicitych tavenin. II. Merna hmotnost binarnich alkalicko– kremicitych sklovin. *Sb. Vys. Sk. Chem. Technol. Praze, Chem. Technol. Silik.* L2

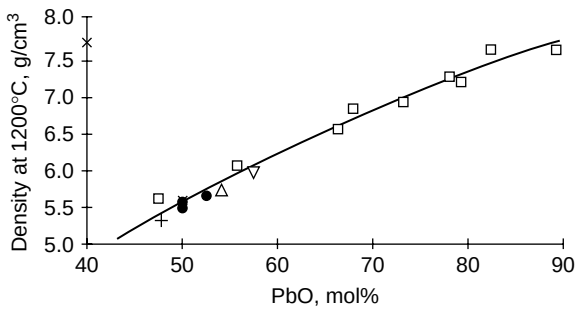

FIGURE 7.5.10 Density at 1200°C of binary lead silicate melts (the graph was formed by the use of Ref. [12]). □–Hino et al. [44]; ■–Hino et al. [45]; *–Hino et al. [46]. +–Suginohara, [47]; –Suginohara et al. [48]; ∇, ●- Suginohara [49].

TABLE 7.5.5
Influence of Composition on Melt Densities of the System Na_2O–CaO–Al_2O_3–SiO_2

Wt.% by batch				d, g/cm³ at T, °C			
SiO_2	Al_2O_3	Na_2O	CaO	850	1050	1250	1450
76.6	—	14.4	9	2.418	2.382	2.350	2.317
73.6	3	14.4	9	2.418	2.380	2.352	2.299
70.6	6	14.4	9	2.404	2.367	2.341	2.276
67.6	9	14.4	9	2.403	2.366	2.336	2.267
81.8	—	11.2	7	2.437	2.393	2.367	2.330
78.8	3	11.2	7	2.428	2.382	2.357	2.308
75.8	6	11.2	7	2.410	2.365	2.334	2.286
72.8	9	11.2	7	2.380	2.34	2.312	
69.8	12	11.2	7	2.371	2.316	2.295	2.274
66.8	15	11.2	7	2.357	2.304	2.288	2.284
63.8	18	11.2	7	2.333	2.300	2.296	
60.8	21	11.2	7	2.347	2.322	2.317	2.325
57.8	24	11.2	7	2.365	2.344	2.340	2.344
54.8	27	11.2	7	2.385	2.373	2.366	2.362
51.8	30	11.2	7	2.409	2.398	2.385	2.378

Source: Coenen, M. (1966). Dichte von "Schlierengläsern" bei hohen Temperaturen. *Glastech. Ber.* 39(3)

borate glasses at room temperature. It follows from the figure that there is an intensive increase in density with concentration of Na_2O until 35% of Na_2O. After that, the density appears practically independent of Na_2O concentration.

Nearly all data on densities of alkali borate melts correspond to concentrations of alkali oxides not higher than 40 mol.%. Unlike silicate glasses, thermal expansion coefficients of alkali-containing glasses and melts and those of the glass-former, namely B_2O_3, are of the same order of magnitude [12]. Therefore, the concentration dependence of densities of sodium borate melts (see Figures 7.5.12–7.5.14) is similar enough to that for glasses at room temperature. At the same time, one can see a certain tendency of decreasing density at concentrations of Na_2O higher than 35–40 mol.%. It is clearly connected with a great increase in thermal expansion of sodium borate melts with increasing concentration of sodium oxide.

For potassium borate melts, this effect is much more pronounced, which is demonstrated by Figure 7.5.15. For lithium borate melts, according to data by Shartsis et al. [51] (it is the only study of melt densities in this system), the concentration dependencies are similar enough to those for sodium borate melts.

As to RO-B_2O_3 systems, only two were studied in rather broad concentration intervals. These results are shown in Figures 7.5.16 and 7.5.17. Both dependencies are simple enough, and no comments for them are needed.

TABLE 7.5.6
Influence of Composition on Melt Densities of the System Na_2O–Al_2O_3–B_2O_3–SiO_2

Mol.% by batch				d, g /cm³ at T, °C			
SiO_2	Al_2O_3	Na_2O	B_2O_3	800	1000	1200	1400
68	—	32	—	2.335	2.279	2.238	2.209
68	—	24	8	2.314	2.261	2.230	2.209
68	—	20	12	2.341	2.282	2.228	2.192
68	—	12	20	2.276	2.216	2.157	2.110
68	—	7	25	2.178	2.135	2.095	2.054
64	4	32	—	2.326	2.266	2.216	2.180
64	4	24	8	2.328	2.266	2.217	2.193
64	4	20	12	2.315	2.25	2.198	2.173
64	4	12	20	2.253	2.2	2.147	2.104
64	4	8	24	2.167	2.129	2.099	2.065
60	8	32	—	2.321	2.269	2.227	2.186
60	8	24	8	2.339	2.282	2.245	2.234
60	8	20	12	2.307	2.264	2.220	2.223
60	8	12	20	2.201	2.165	2.146	2.189
60	8	8	24	2.163	2.129	2.106	2.174

Source: Coenen, M. (1966). Dichte von "Schlierenglasern" bei hohen Temperaturen. *Glastech. Ber.* 39(3)

TABLE 7.5.7
Influence of La_2O_3 on Densities of Sodium Silicate Melts

Mol.% by batch			d, g/cm³ at T, °C			
SiO_2	Na_2O	La_2O_3	900	1100	1300	1500
66.67	33.33	—	2.379	2.292	2.208	2.127
66.44	33.22	0.34	2.497	2.441	2.379	2.300
65.52	32.76	1.72	2.891	2.807	2.714	2.619
64.29	32.14	3.57	3.318	3.184	3.055	2.923

Source: Passerone, A., Sangiorgi, R., Valbusa, G. (1979), Surface tension and density of molten glasses in the system La_2O_3–$Na_2Si_2O_5$. *Ceram. Intern.* 5(1)

TABLE 7.5.8
Influence of Composition on Melt Densities of the System $CaO–Al_2O_3–SiO_2$

Mol.% by batch			d, g/cm³ at T, °C		
SiO_2	CaO	Al_2O_3	1350	1450	1550
60	35	5	2.531	2.520	2.507
55	35	10	2.545	2.530	2.517
50	35	15	2.554	2.539	2.525
50	45	5	2.609	2.594	2.58
45	35	20	2.563	2.549	2.537
45	45	10	2.615	2.602	2.587
40	45	15	2.624	2.608	2.594
35	45	20	2.628	2.614	2.600

Source: Kammel, R., Winterhager, H. (1965). Struktur und Eigenschaften von Schlacken der Metallhuttenprozesse. V. Dichtebestimmungen und elektrische Leitfähigkeitsmessungen an Schmelzen des Systems Kalk–Tonerde–Kieselsäure. *Erzmetall*, 18(1)

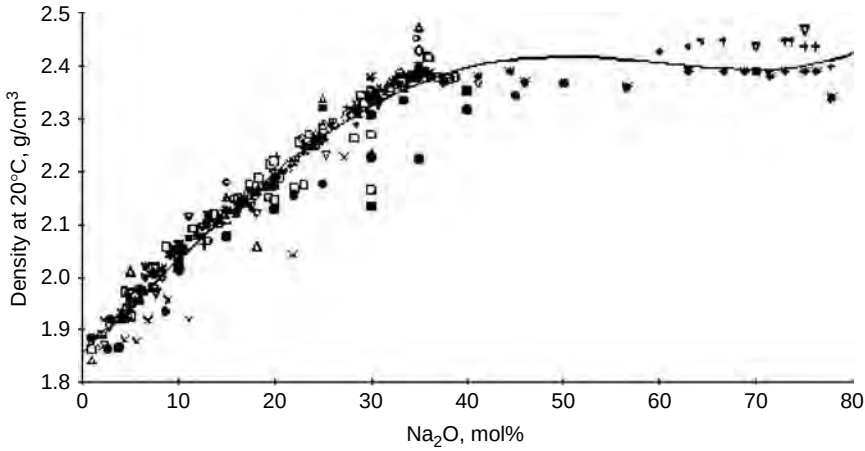

FIGURE 7.5.11 Density at 20°C of binary sodium borate glasses (the graph was formed by the use of Ref. [12], where the references to particular publications can be found).

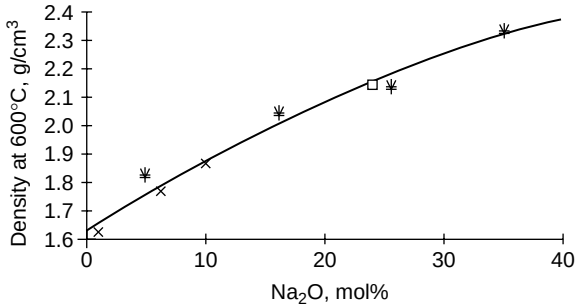

FIGURE 7.5.12 Density at 600°C of binary sodium borate melts (the graph was formed by the use of Ref. [12]). x–Shartsis et al. [24]; □–Takeuchi et al. [51]; *–Inoguchi et al. [52].

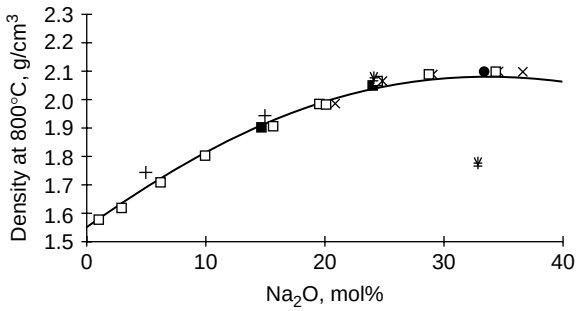

FIGURE 7.5.13 Density at 800°C of binary sodium borate melts (the graph was formed by the use of Ref. [12]). x–Nagel [53]; □–Shartsis. et al. [24]; *–Takeuchi et al. [51]; ■–Leedecke and Bergeron, [54]; ●–Kostanyan et al. [55]; +–Inoguchi et al. [52]; ∇–Sotnikov et al. [56].

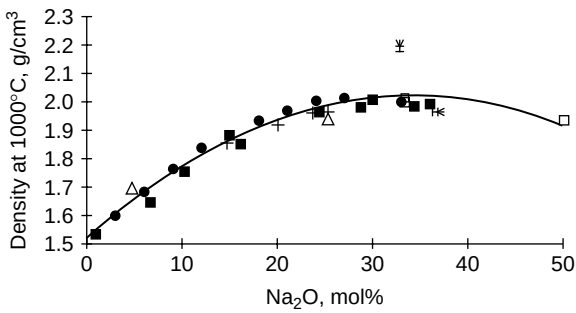

FIGURE 7.5.14 Density at 1000°C of binary sodium borate melts (the graph was formed by the use of Ref. [12]). □–Dalle Donne et al. [57]; *–Nagel [53]; ■–Shartsis et al. [24]; ●–Kunugi et al. [58]; +–Leedecke and Bergeron [54]; ∇–Kostanyan et al. [55]; Δ–Inoguchi et al. [52].

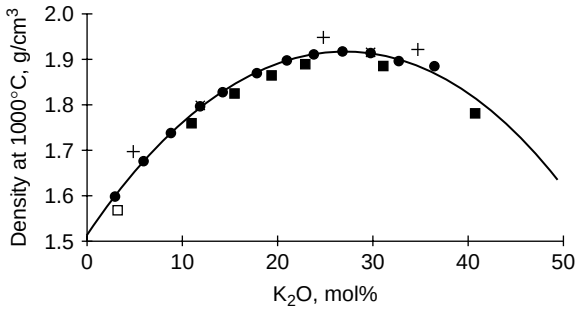

FIGURE 7.5.15 Density at 1000°C of binary potassium borate melts (the graph was formed by the use of Ref. [12]). x–Takeuchi et al. [51]; □–Coughanour et al. [59]; ■–Shartsis et al. [24]; +–Inoguchi. et al. [52]; ●–Kunugi. et al. [58].

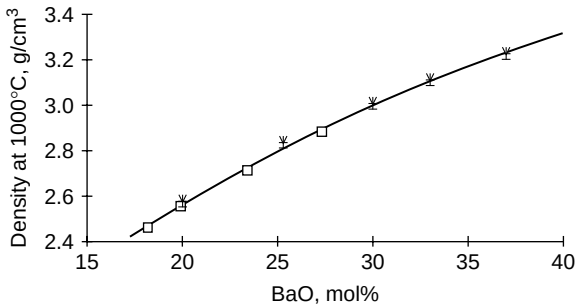

FIGURE 7.5.16 Density at 1000°C of binary barium borate melts (the graph was formed by the use of Ref. [12]). □–Leedecke and Bergeron [60]; *–Takeuchi et al. [51].

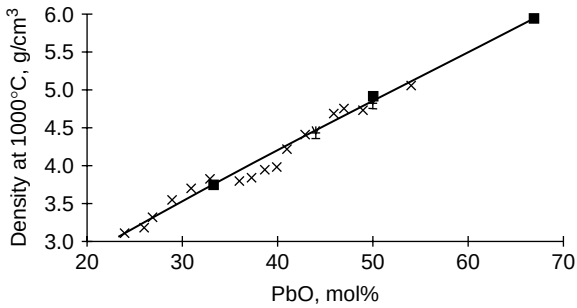

FIGURE 7.5.17 Density at 1000°C of binary lead borate melts (the graph was formed by the use of Ref. [12]). x–Ejima and Kameda [9]; ■–Hirashima and Yoshida [61].

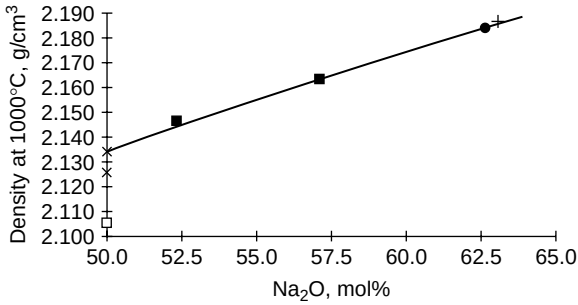

FIGURE 7.5.18 Density at 1000°C of binary sodium phosphate melts (the graph was formed by the use of Ref. [12]). +–Boyer et al. [62]; ●–Callis et al. [63]; x, ■–Williams et al. [64]; □–Krivovyazov and Voskresenskaya [65].

7.5.4 Density of Various Types of Melts

Figure 7.5.18 shows the linear increase in melt density of sodium phosphate melt with increase in sodium oxide content. Comparison of this figure with Figures 7.5.4 and 7.5.14 shows that, at 50 mol% of Na_2O, the difference in densities of binary silicate, borate, and phosphate melts is quite small. It is to be noted, however, that for silicate and borate melts, one can see a clear tendency to decreasing density with an increase in alkali content (although the measurements of melts containing more than 50% Na_2O for these two systems are absent, the tendency is clear). At the same time, the direction of corresponding dependency for phosphate melts is the opposite.

For the system K_2O-P_2O_5, the dependence is practically the same, but the absolute values of density are about 0.1 g/cm^3 lower than those for sodium phosphate melts [66]. Some other systematic data found for the systems of interest are presented in Figures 7.5.19 and 7.5.20. Probably no comments are needed here.

7.6 CALCULATION OF MELT DENSITIES

There are several methods of calculations of melt densities. One was developed by Stebbins [68], three somewhat different methods by Bottinga et al. [60, 70, 71], and one by Priven [72]. All three of Bottinga's methods give more or less similar results of calculations, but cover different areas of compositions. In this chapter, only one of these methods is used, namely the method [70] including the greatest number of oxides (18).

An idea about the dependability of these methods can be obtained on the base of data presented in Table 7.6.1, where results of calculations by all three methods are compared with the experimental data taken for a broad variety of melt compositions from various sources. For two binary melts, experimental data were taken from the approximation curves presented in corresponding figures. When comparing the experimental and calculated data, it is necessary to take into account the fact that sometimes the errors of experimental data could be quite considerable. An example of the influence of such errors on the result of comparison is presented in Table 7.6.1 for two binary lead borate melts. If only one experimental datum were

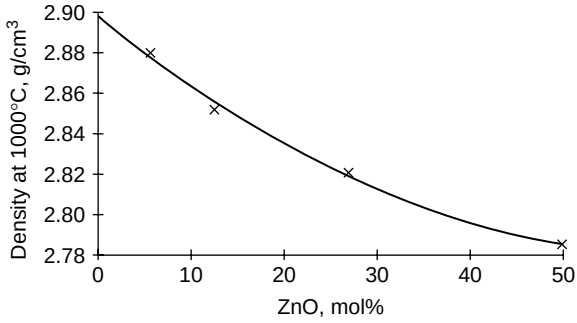

FIGURE 7.5.19 Density at 1000°C of melts in the system Cs_2O-ZnO-P_2O_5 with constant concentration of P_2O_5 equal to 50 mol.% [66].

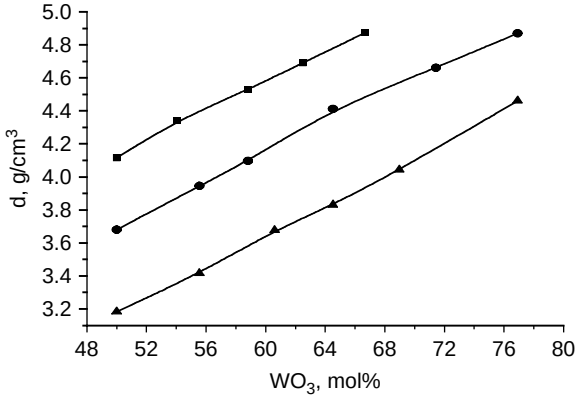

FIGURE 7.5.20 Densities at 1000°C of melts in systems R_2O-WO_3 (data from Gossink, R. G., Stein, H. N., Stevels, J. M. (1970), Propriétés des molybdates et tungstates vitreux et fondus. *Silic. Ind.* 35(10)). R_2O: ■–Li_2O; ●–Na_2O; ▲–K_2O.

to be taken, the definite conclusion would be that calculations of densities of borate lead melts by Priven's method are totally incorrect. However, the comparison of both of the presented experimental results with calculations by Priven shows that, for this particular system, calculations by Priven probably give more dependable results than the data of any of these authors. Nevertheless, the author of this paper in collaboration with A. Priven, performing the analysis of a great number of data, found that, in general, methods by Bottinga and Stebbins give somewhat more precise results than Priven's method (additional examples can also be seen in Table 7.6.1). Quite logically, the narrower the composition area covered by a certain method of calculation the easier it is to find ways for making more correct calculations. Thus, when it is possible to use all three methods, it is better to consider the data by Bottinga's or Stebbins's methods. However, there is are great areas of melt compositions where these methods are not valid. In this case, the only possibility is to use the method by Priven. Generally, it gives quite reasonable results, as is also demonstrated by Table 7.6.1.

TABLE 7.6.1
Comparison of Experimental Data on Melt Densities of Various Melts with Data Calculated by Several Methods

Composition, mol.%	Melt density, g/cm³				Sources
	Calculations				
	Bottinga	Stebbins	Priven	Experiment	
75 SiO_2, 25 K_2O	2.17	2.16	2.16	2.16	Approximation (see Figure 7.5.7)
70 B_2O_3, 30 Na_2O (T = 800°C)	—	—	2.09	2.08	Approximation (see Figure 7.5.13)
68.3 B_2O_3, 31.7 PbO (T = 800°C)	—	—	3.92	3.44	Thompson [73]
70 B_2O_3, 30 PbO (T = 800°C)	—	—	3.79	4.48	Kubota et al. [74]
75.1 SiO_2, 12.62 MgO, 0.15 CaO, 12.13 K_2O	2.26	2.26	2.25	2.35	Nelson and Carmichael [75]
42.95 SiO_2, 12.78 MgO, 32.25 CaO, 12.03 Al_2O_3	2.60	2.67	2.58	2.64	Winterhager et al. [76]
56.53 SiO_2, 0.24TiO_2 12.31 MgO, 13.15 CaO, 2.39 FeO, 2.71 Fe_2O_3, 9.79Al_2O_3, 2.46 Na_2O, 0.42 K_2O	2.53	2.58	2.50	2.58	Lange and Carmichael [77]
42.95 SiO_2, 11.23 B_2O_3, 1.26 Al_2O_3, 3.68 Na_2O, 0.72 K_2O	—	—	2.16	2.14	Volf [78]
30 SiO_2, 32.5 MgO, 17.5 BaO, 20 B_2O_3	—	—	3.02	2.91	Goleus et al. [79]
41.52 SiO_2, 23.38 MnO, 22.24 CaO, 12.24 Al_2O_3, 0.23 Ta_2O_5, 0.39 Nb_2O_5	—	—	2.90	3.02	Chuchmarev et al. [80]
61.92 SiO_2, 35.02 PbO, 0.18 As_2O_3, 2.88 K_2O (T = 1200°C)	4.44	—	4.49	4.44	Shartsis and Spinner [1]
74.69 SiO_2, 4.48 B_2O_3, 0.26 Sb_2O_3, 2.45 CaO, 14.8 Na_2O, 3.31 K_2O (T=1200°C)	—	—	2.30	2.24	Shartsis and Spinner [1]

Note: Temperature of melts 1400°C unless indicated otherwise.

TABLE 7.6.2
Influence of the Substitution of SiO_2 for Different Oxides in a Sodium Silicate Melt on Melt Densities at 1400°C According to Calculations by Various Methods

Composition, mol.%			Calculated density, g/cm³		
SiO_2	Na_2O	R_mO_n	Bottinga	Stebbins	Priven
80	20	—	2.22	2.22	2.2
70	20	10 Ag_2O	—	—	3.85
70	20	10 Al_2O_3	2.25	2.28	2.25
70	20	10 B_2O_3	—	—	2.30
70	20	10 BeO	—	—	2.21
70	20	10 Bi_2O_3	—	—	3.25
70	20	10 CaO	2.29	2.29	2.29
70	20	10 CdO	—	—	2.53
70	20	10 CeO_2	—	—	2.63
70	20	10 Fe_2O_3	2.43	2.44	2.39
70	20	10 FeO	2.38	2.38	2.37
70	20	10 Ga_2O_3	—	—	2.58
70	20	10 GeO_2	—	—	2.35
70	20	10 La_2O_3	—	—	2.87
70	20	10 MgO	2.27	2.27	2.26
70	20	10 P_2O_5	—	—	2.21
70	20	10 SnO_2	—	—	2.52
70	20	10 PbO	2.83	—	2.85
70	20	10 TiO_2	2.33	2.33	2.25
70	20	10 Tl_2O	—	—	3.26
70	20	10 V_2O_5	—	—	2.32
70	20	10 WO_3	—	—	2.69
70	20	10 ZrO_2	—	—	2.50

Source: see Refs 68, 70, 72.

In conclusion, it is possible to use the existing methods of calculations of melt density for comparison of the influence of various oxides on the density of alkali silicate melts. The results of corresponding calculations are presented in Table 7.6.2.

REFERENCES

1. Shartsis, L., Spinner, S. (1951). Viscosity and density of molten optical glasses. *J. Res. Nat. Bur. Stand.* 46(3):176–194.
2. Stein, D. J., Stebbins, J. F., Carmichael, I. S. E., (1986). Density of molten sodium aluminosilicates. *J. Am. Ceram. Soc.* 69(5):396–399.
3. Napolitano, A., Macedo, P. B., Hawkins, E. G. (1965). Viscosity and density of boron trioxide. *J. Am. Ceram. Soc*. 48(12):613–616.

4. Greenaway, H. T., (1947). The surface tension and density of lead–antimony and cadmium–antimony alloys. *J. Inst. Met*. 74(3):133–148.
5. Barrett, L. R., Thomas, A. G. (1959). Surface tension and density measurements on molten glasses in the CaO-Al_2O_3 SiO_2 system. *J. Soc. Glass Technol*. 43(211):179–190**.**
6. Coenen, M. (1966). Dichte von "Schlierengläsern" bei hohen Temperaturen. *Glastech. Ber.* 39(3): 81–89.
7. Passerone, A., Sangiorgi, R., Valbusa, G. (1979), Surface tension and density of molten glasses in the system La_2O_3-$Na_2Si_2O_5$. *Ceram. Intern.* 5(1):18–22.
8. Basin, A. S., Baginskii, A. V., Provodnikov, V. L. (1974). Temperature dependence of boron oxide density in the range of glass transition (in Russian). In: *Issledovanie Teplofizicheskikh Svoistv Rasvorov i Rasplavov*: Novosibirsk, pp. 122–135.
9. Ejima, T., Kameda, M. (1967). Viscosity of liquid lead silicate and lead borate. *J. Jpn Inst. Metals.* 31(2):120–125.
10. Klyuev, V. P. (1997). Dilatometric method of thermal expansion measurements of softened glass in the range 10^{10}–10^5 Poise (in Russian). *Fiz. Khim. Stekla*, 23(1):137–143.
11. Richards, E. A., Bergeron, C. G., (1985). Changes in volume accompanying the transition from melt to crystal in binary borate melts. *Phys. Chem. Glasses*, 26(5):177–181.
12. MDL-SciGlass™ 5.0 (2002). MDL Information Systems, San Leandro, CA.
13. Mazurin, O. V. (1985) *Glass Transition* (in Russian: Steklovanie). Leningrad: Nauka,
14. Scherer, G. W. (1986). *Relaxation in Glass and Composites*. N.Y.: John Wiley & Sons.
15. Johnson, A. G., Scholes, S. R., Simpson, H. E. (1950). Volume expansion of glass at high temperatures. *J. Am. Ceram. Soc*. 33(4): 144–147.
16. V. P. Klyuev, personal communication, 1999.
17. Mazurin, O. V., Totesh, A. S., Streltsina, M. V., Shvaiko-Shvaikovskaya, T. P. (1969). *Thermal Expansion of Glass* (in Russian: Teplovoe Rasshrenie Stekla). Leningrad: Nauka,
18. Turner, W. E. S., Winks, F. (1930). The thermal expansion of glass. Part II. Glasses of the series sodium metasilicate — silica. *J. Soc. Glass Techn.* 14(53):110–126.
19. Gooding, E. I., Turner, W. E. S. (1934). A study of the series of glasses containing sodium oxide, boric oxide and silica. *J. Soc. Glass. Techn*. 18(69):32–66.
20. Shmidt, Yu. A., Alekseeva, Z. D. (1964). Glass-like silicates of potassium, rubidium, and caesium (in Russian). *Zh. Prikl. Khim.* 37(10):2299–2303.
21. Bockris, J. O'M., Tomlinson, J. W., White, J. L. (1956). The structure of the liquid silicates: partial molar volumes and expansivities. *Trans. Farad. Soc*. 52(3):299–310.
22. Shartsis, L., Spinner, S., Capps, W. (1952). Density, expansivity, and viscosity of molten alkali silicates. *J. Am. Ceram. Soc.* 35(6):155–160.
23. Merker, L. (1959). Eine einfache Methode zur Dichtebestimmung von Glasschmelzen bei hohen Temperaturen. *Glastech. Ber.* 32(12):501–503.
24. Shartsis, L., Capps, W., Spinner, S. (1953). Density and expansivity of alkali borates and density characteristics of some other binary glasses. *J. Am. Ceram. Soc.* 36(2):35–43.
25. Bruekner, R. (1970–1971). Properties and structure of vitreous silica. *J. Non-Cryst. Solids*. 5(2): 123, (3): 177-216.
26. Bacon, J. F., Hasapis, A. A., Wholley, J. W. (1960). Viscosity and density of molten silica and high silica content glasses. *Phys. Chem. Glasses* 1(3):90–98.
27. Sasek, L., Lisy, A., (1972). Struktura a vlastnosti kremicitych tavenin. I. Vliv velikosti iontu na mernou hmotnost sklovin za vysokych teplot. *Sb. Vys. Sk. Chem. Technol. Praze, Chem. Technol. Silik.*, L2:165–215.

28. Heidtkamp, G., Endell, K. (1936). Ueber die Abhangigkeit der Dichte und der Zähigkeit von der Temperatur im System Na_2O-SiO_2. *Glastech. Ber.* 14(3):89–103.
29. Sasek, L., Kasa, S. (1970). Metodika mereni povrchoveno napeti sklovin. *Silikaty*, 14(1):75–84.
30. Scarfe, C. M., Mysen, B. O., Virgo, D. (1979). Changes in viscosity and density of melts of sodium disilicate, sodium metasilicate, and diopside composition with pressure. *Carnegie Inst. Washington, Year Book.* 78:547–551.
31. Sasek, L., Lisy, A., (1972). Structura a vlastnosti kremicitych tavenin. II. Merna hmotnost binarnich alkalicko- kremicitych sklovin. *Sb. Vys. Sk. Chem. Technol. Praze, Chem. Technol. Silik*. L2:217–254.
32. Din, A. (1968). Untersuchungen zum strukturellen Aufbau der Gläaser $Na_2O{\cdot}xMe_nO{\cdot}(6\text{-}x)SiO_2$ aus der Temperaturabhandigkeit der Dichte, der Viskosität und davon abgeleiteter Grossen. Thesis. Clausthal,
33. Frischat, G. H., Beier, W. (1979). Oberflachenspannung von Na_2O-Rb_2O-SiO_2-Glasschmelzen. *Glastech. Ber.* 52(5):116–120.
34. Din, A., Sheikh, M. R., Qureshi, A. H. (1972). Volume-composition study of silicate glasses. *Pakistan J. Sci. Ind. Res.* 15(4-5): 326–329.
35. Coenen, M. (1964). Kolloide und natärliche Makromolekäle. Kristallisationskinetik von Natriumdisilikat. *Kolloid Z., Z. Polymere* 194(2): 136–142.
36. Nikonov, A. M., Bogdanov, V. N., Mikhailov, I. G., Shono, A. A. (1980), Ultrazvukovye Issledovaniya Binarnykh Shchelochnosilikatnykh Rasplavov. Deposited in VINITI, Moscow, No.5004-80 Dep.
37. Washburn, E. W., Shelton, G. R., Libman, E. E. (1924). The viscosities and surface tensions of the soda-lime-silica glasses at high temperatures. *Univ. Ill. Bull.* 21(S140):33–48.
38. Golovin, E. P., Akhlestin, E. S. (1967). Density and thermal diffusion in silicate melts (in Russian). *Tr. Gork. Politekhn. Inst.* 23(4):33–37.
39. Dertev, N. K., Golovin, E. P. (1973). Analytical method of calculations of density of ternary silicate melts (in Russian). *Tr. Gork. Politekhn. Inst.* 29(3):27–30.
40. Bloom, H., Bockris, J. O`M. (1957). The Compressibilities of the silicates: the Li_2O-SiO_2 system. *J. Phys. Chem*. 61(5): 515–518.
41. Sasek, L., Meissnerova, H., Persin, J., (1973). Structura a vlastnosti kremicitych sklovin. IV. Vliv MgO a BaO na elektrickou vodivost ternalnich kremicitych sklovin. *Sb. Vys. Sk. Chem. Technol. Praze, Chem. Technol. Silik*. L4:87–138.
42. Dertev, N. K., Golovin, E. P., Akhlestin, E. S. (1971). Thermal-EMF as function of the volume thermal expansion of R'_2O-R''_2O-SiO_2 melts (in Russian). In: *Stekloobraznoe Sostoyanie*. Leningrad: Nauka, pp. 331–333.
43. Din, A., Hennicke, H. W. (1974). Zum Verhalten der Magnesiumionen in Silicatgläsern. *Glastech. Ber.* 47(1):14–16.
44. Hino, M., Ejima, T., Kameda, M. (1967). Surface tension and density of liquid lead silicate. *J. Jpn Inst. Metals*. 31(2):113–119.
45. Hino, M., Ejima, T., Kameda, M. (1969). Surface tension, density and viscosity of PbO-K_2O-SiO_2 ternary melts. *J. Jpn Inst. Metals*. 33(5):617–622.
46. Hino, M., Ejima, T., Kameda, M. (1968). Surface tension, density and viscosity of PbO-Na_2O-SiO_2 ternary melt. *J. Jpn Inst. Metals*. 32(9):809–814.
47. Suginohara, Y. (1962). On the surface tension (part 2) and density of molten lead silicate — effect of various oxides. *Technol. Rep. Kyushu Univ.* 35(1):24-31.
48. Suginohara, Y., Yanagase, T., Ito, H. (1962). The effect of oxide additions upon the structure sensitive properties of lead silicate melts. *Trans.Jpn Inst.Metals*. 3(4):227–233.

49. Suginohara, Y. (1963). The effects of additional oxide on the electrical conductivity of lead silicate melts. *J. Mining Inst. Kyushu.* 31(4):156–159.
50. Kammel, R., Winterhager, H. (1965). Struktur und Eigenschaften von Schlacken der Metallhuttenprozesse. V. Dichtebestimmungen und elektrische Leitfahigkeitsmessungen an Schmelzen des Systems Kalk-Tonerde-Kieselsaure. *Erzmetall*, 18(1):9–17.
51. Takeuchi, S., Yamate, T., Kunugi, M. (1965). Density of borate glass melts *J. Soc. Mater. Sci. Jpn.* 14(138): 225–232.
52. Inoguchi, K., Okamoto, K., Koide, M., Matusita, K., Michimata, T. (1998). Density measurement of glass melt at high temperture. Proc. XVIIIth Intern. Congr. on Glass CD-ROM, San Francisco, p. D5,104–109.
53. Nagel, S.R. (1973). Crystallization Kinetics of Binary Borate Glass Melts. PhD Thesis. University of Illinois.
54. Leedecke, C. J., Bergeron, C. G. (1976). The growth of $K_2B_8O_{13}$ in its stoichiometric melt. *J. Cryst. Growth*, 32(3):327–331.
55. Kostanyan, K. A., Kamalyan, S. A., Bezhanyan, S. A. (1961). Density of sodium borosilicate glasses in molten state (in Russian). *Izv. Akad. Nauk Arm. SSR, Khim. Nauki*. 14(4):319–327.
56. Sotnikov, A. I., Petrov, V. V., Kosenko, V. G. (1985). Dependence of the surface tension of sodium tetraborate on temperature (in Russian). *Fizika i Khimiya Stekla*. 11(3):382–384.
57. Dalle Donne, M., Dorner, S., Roth, A. (1983). Thermal expansion coefficient and viscosity of sodium tetraborate (brax)-UO_2 and of sodium metaborate-UO_2 solutions at high temperatures. *J. Nucl. Mater.* 18(2):195–205.
58. Kunugi, M., Konishi, A., Takeuchi, S., Yamate, T. (1972). Density of alkali borate glasses. *J. Soc. Mater. Sci. Jpn.* 21(230):978–980.
59. Coughanour, L. W., Shartsis, L., Shermer, H. F. (1958). Viscosity, density, and electrical resistivity of molten alkaline-earth borate glasses with 3 mole of potassium oxide. *J. Am. Ceram. Soc.* 41(8): 324–329.
60. Leedecke, C. J., Bergeron, C. G. (1978). Viscous flow in binary borate melts. In: Pye, L. D., Frechette, V.D., Kreidl, N.J., Eds. *Materials Science Research,v.12, Borate Glasses.* N.Y.: Plenum Press, pp. 413–426.
61. Hirashima, H., Yoshida, T. (1971). The electric conductance and structure of the molten oxide system PbO-B_2O_3-Fe_2O_3. *J. Ceram. Soc. Jpn*, 79(9):316–323.
62. Boyer, A. J. G., Fray, D. J., Meadowcroft, T. R. (1967). The surface tensions and molar volumes of the binary phosphates of sodium, lithium, calcium, and zinc. *J. Phys. Chem.* 71(5): 1442–1449.
63. Callis, C. F., Van Wazer, J. R., Metcalf, J. S. (1955). Structure and properties of the condensed phosphates. VIII. Density and surface tension of molten sodium phosphates. *J. Am. Chem. Soc.* 77(6): 1468–1470.
64. Williams, D. J., Bradbury, B. T., Maddocks, W. R. (1959). Studies of phosphate melts and glasses. Part 1. Fluoride additions to sodium phosphates. *J. Soc. Glass Technol.* 43(213):308–324.
65. Krivovyazov, E. L., Voskresenskaya, N. K. (1969). Surface tension and specific volumes of melts in systems $Zn(PO_3)_2$ – $NaPo_3$ and $Zn(PO_3)_2$ –KPO_3 (in Russian). *Neorg. Mater.* 5(4):773–776.
66. Krivovyazov, E. L., Dzhurinskii, B. F., Rakhimbekova, Kh. M., Voskresenskaya, N. K. (1972). Properties of glasses and melts of systems Zn $(PO_3)_2$ –MPO_3 (in Russian). *Neorg. Mater.* 8(9):1646–1649.
67. Gossink, R. G., Stein, H. N., Stevels, J. M. (1970), Propriétés des molybdates et tungstates vitreux et fondus. *Silic. Ind.* 35(10):245–252.

68. Stebbins, J. F., Carmichael, I. S. E., Moret, L. K. (1984). Heat capacities and entropies of silicate liquids and glasses. *Contributions to Mineralogy and Petrology*, pp. 131–148.
69. Bottinga, Y., Weill, D. F. (1970). Densities of liquid silicate systems calculated from partial molar volumes of oxide components. *Amer. J. Sci.* 269:169–182.
70. Bottinga, Y., Richet, P., Weill, D. F. (1983). Calculation of the density and thermal expansion coeffcient of silicate liquids. *Bulletin de Mineralogie*. 106: 129–138
71. Bottinga, Y., Weill, D. F., Richet, P. (1982). Density calculations I. Revised method for aluminosilicate compositions. *Geochim. Cosmochim. Acta.* 46:909–919.
72. Priven, A. I. (1998). Viscosity calculation in multicomponent oxide systems. In: Proc. XVIII Congress on Glass. San Francisco. p. 128.
73. Thompson, A. W. (1965). Structure and Viscosity of Molten Borates and Phosphates. MS Thesis. Washington.
74. Kubota, K., Masuda, H., Fujino, S., Morinaga, K. (1998), Density, surface tension and viscosity of the molten PbO-B2O_3-SiO_2 System. *J. Ceram. Soc. Jpn*, 106(9):909–913.
75. Nelson, S. A., Carmichael, I. S. E. (1979). Partial molar volumes of oxide components in silicate liquids. *Contrib. Mineral. Petrol.* 71(2):117–124.
76. Winterhager, H., Greiner, L., Kammel, R. (1966). Untersuchungen uber die Dichte und die elektrische Leitfahigkeit von Schmelzen der Systeme CaO-Al_2O_3-SiO_2 und CaO-MgO-Al_2O_3-SiO_2. *Forschungsberichte des Landes Nordrheine Westfallen.* pp. 1630–1641.
77. Lange, R. A., Carmichael, I. S. E. (1987). Densities of Na_2O-K_2O-CaO-MgO-FeO-Fe_2O_3-Al_2O_3-TiO_2-SiO_2 liquids: New measurements and derived partial molar properties. *Geochim. Cosmochim. Acta*. 51:2931–2946.
78. Volf, M. B. (1990). *Technical Approach to Glass.* Amsterdam: Elsevier.
79. Goleus, V., Belyj, J., Sasek, L. (1985). Sledovani hustoty a elektricke vodivosti sklovin MgO-BaO-B_2O_3-SiO_2. *Sb. Vys. Sk. Chem. Technol. Praze, Chem. Technol. Silik.* 13:127–143.
80. Chuchmarev, V. M., Sholokhov, V. M., Okunev, A. I. (1978). Surface tension and density of slugs containing Tantalum and Niobium (in Russian). In: Tezisy III Vses.Konf.po Stroeniyu i Svoistvam Metallicheskikh i Shlakovykh Rasplavov, Sverdlovsk, No. 3, p. 45–47.

8 Heat Capacity of Glass Melts

Alexander I. Priven and Oleg V. Mazurin

CONTENTS

8.1 INTRODUCTION

Heat capacity C of a substance is the amount of heat (in calories or joules) needed for heating of a certain amount of this substance (1 g, 1 kg, 1 mole, or 1 g-atom) by one temperature unit (mostly 1 K). Accordingly, in the SI system, the heat capacity is expressed in J/(kg·K) or in J/(mol·K), and in the cgs system it is expressed in cal/(g·K) or cal/(mol.K). The term "specific heat" is also frequently used. According to Varshneya [1],because the latter term refers to the ratio of the heat capacity of a substance to that of an equal mass of water at 15°C, it is therefore unitless. On the other hand, Banzal and Doremus [2] see no difference between the meanings of the two terms.

It should be noted that different authors (not only glass scientists, but specialists in thermodynamics, geochemistry, etc.) use the term "mole" in different meanings:

mole of oxides, mole of complex compounds (e.g., Na_2SiO_3 or $K_2Si_4O_9$), or even gram-atom. Below, when we use the term "mole" we mean mole of oxides.

Values of heat capacity depend on not only the composition and temperature of substances, but also conditions of measurements. Usually this property is measured either at constant pressure (C_p) or at constant volume (C_v). In most cases, the heat capacity of glass-forming melts is measured at constant pressure. Usually the data, which could be used for calculation of heat capacity of a melt at constant pressure, are reported in the form of the temperature dependence of enthalpy H of the melt:

$$H_{T_2} - H_{T_1} = \int_{T_1}^{T_2} C_p dT \tag{1}$$

If the approximate temperature dependence of enthalpy is known, it is possible to determine a true value of heat capacity corresponding to any selected temperature within the temperature range where the mentioned dependence is valid. However, quite often the mean values of C_p for a certain temperature interval are calculated:

$$C_{p(T_1-T_2)} = \frac{H_{T_2} - H_{T_1}}{T_2 - T_1} \tag{2}$$

It is clear that the diversity of presentation of data describing heat capacity of melts can considerable, which makes the comparison of data reported by various authors a somewhat difficult task. To simplify this comparison for readers of the present survey, measures were taken to present all data in a format that would make them as compatible with each other as possible. Processing the data was performed using SciGlass Information System [3].

First, all data expressed in the original publications in the form of temperature dependencies of enthalpy were recalculated in the form of heat capacity data. If necessary, temperature dependencies of enthalpy were approximated by polynomials of the second order. Second, all the data on heat capacity are presented in the same units, namely J/(kg·K), independently of the units used in the original publications. Third, all compositions of the melts are presented in mol.% independently of percentage used in the original publications.

8.2 TEMPERATURE DEPENDENCIES OF HEAT CAPACITY OF GLASS-FORMING SUBSTANCES

In principle, two factors should be taken into account in the course of analysis of temperature dependence of melt heat capacity:

1. Temperature dependence of heat capacity of solids (i.e., substances whose structure does not change appreciably with temperature)

2. Specific changes in heat capacity values connected with transition of a solid glass into a viscous melt and resulting from structural changes of the substance with changing temperature, which is characteristic for a liquid.

The values of heat capacity of glasses are very small at temperatures near absolute zero. They increase with temperature, becoming the largest in immediate proximity to the glass transition range, where they approach the Dulong and Petit limit for solids (3R/g-atom, where R is a gas constant). For most silicate glasses used in actual practice, the difference between the measured values of C_p and limiting values mentioned above is equal to 10–20% of the limiting values. Within the temperature range 300–500°C (i.e., just below the glass transition region for these glasses) the values of the heat capacity of glasses are slightly less than near the glass transition range.

It is well known (see, for example, Ref. [4]) that the change in temperature of any liquids, including obviously glass-forming melts, leads to change in structure of these liquids and melts. Structural changes lead inevitably to changes in practically all properties of corresponding substances. When the temperature of a melt increases, the resulting structural changes lead to an increase in the enthalpy of this melt. Thus, in melts, there is an additional factor influencing the total value of the heat capacity of the substance, namely the so-called configurational heat capacity ΔC_p. When a glass-forming substance is initially in the glassy state and, in the course of heating, goes through the glass transition region and transforms into the melt, its total heat capacity increases by ΔC_p.

Generally speaking, the value of ΔC_p greatly depends on chemical composition of the glass-forming substance. It varies from ~0.01 R/g-atom for silica glass [5] to ~2 R/g-atom [6] and even more for some special glasses. However, for most industrial glasses, this value varies not very much. It is close to 0.5 R/g-atom, i.e., 15–25% of the value of heat capacity of a substance below its glass transition region.

It is believed that raising the temperature of liquids and melts leads generally to a decrease in the intensity of structural changes with temperature. This supposition is confirmed by a decrease in configurational coefficients of viscosity, electrical conductivity, density and some other properties of glass-forming melts with increase in their temperatures.

In the case of heat capacity, two factors influence the change of its value with increasing temperature in the opposite way. For isostructural conditions, further increase in C_p connecting with an approach to the Dulong and Petit's limiting value should take place even above the glass transition region. At the same time, there is a definite probability of a certain decrease of the configurational heat capacity with temperature (see [7]). Having in mind that both changes should be rather small and that the precision of C_p measurements is usually not very high, it is not surprising that in most studies (see Section 8.5) the temperature dependence of C_p was either rather small or did not register at all. It is quite convenient for practical reasons. It is known that the simplest and most precise (at least for melts) method of heat capacity measurements is by scanning calorimeter. However, this method is seldom used at temperatures higher than 800–1000°C. In cases when it is possible to neglect the influence of temperature on heat capacity of melts, it is enough to use a scanning

calorimeter for measurements of this value at comparatively low temperatures and then to apply the measured value to various calculations for considerably higher temperatures.

8.3 GENERAL CHARACTERISTICS OF EXISTING EXPERIMENTAL DATA ON HEAT CAPACITY OF GLASS MELTS

In Section 8.5, a considerable amount of data taken from the literature is presented. As stated above, all the data are presented in the same format for easier comparison with each other. In most cases, processing of the original data was required.

In Tables 8.1–8.5, data of various authors on the heat capacity of silica glass are shown. It is to be noted that Table 8.1 contains the results of an approximation of numerous data that appeared in the literature before 1927, when Sosman [5] compiled and evaluated them.

Table 8.2 demonstrates results of measurements of several different kinds of silica glasses. There is no reason to expect that different concentrations of impurities and of redox states of these impurities, which are characteristic for different types of silica glasses, could have an appreciable effect on the heat capacity of these glasses. Thus, the results presented in Table 8.2 can be considered an illustration of the scatter of data obtained in different experiments. Obviously, deviations of various experimental data from mean values can be considered as a reasonable enough.

One can conclude that nearly all the data (the only exception are the data by Wietzel given in Table 8.3) presented in Tables 8.1–8.5 are in good agreement with each other. It is also seen that, according to all the tables, an increase in temperature leads to an appreciable increase in heat capacity of silica melts. At the same time, as mentioned above, for other glass melts the temperature dependences of heat capacity are, on the whole, fairly slight (see Tables 8.6–8.9 and others).

8.4 COMPOSITION DEPENDENCES OF HEAT CAPACITY OF GLASS MELTS

8.4.1 The Relativity of the Influence of Chemical Composition on Heat Capacity

Judging from the tables given in Section 8.5, the chemical composition of glass melts significantly affects their heat capacity. Based on these data, certain conclusions about the regularities of this influence can be drawn.

However, when considering such conclusions, a researcher should realize that the form and often even the direction of concentration dependences of heat capacity strongly depend on the units in which this property is expressed; more exactly, on the amount of a substance (gram, mole, gram-atom, etc.) to which heat capacity is referred.

Table 8.14 is remarkable in this respect. As we can see from the table, heat capacity of sodium-silicate melt 66.7 $SiO_2 \cdot 33.3\ Na_2O$ (mol.%) expressed in J/(g·K)

is significantly higher than for lead-silicate melt 62.5 SiO_2 · 37.5 PbO (1.3096 vs. 0.7868 J/(g·K)). However, if we express the heat capacity of the same melts in J/(g-atom·K), we obtain the opposite results: 26.5 vs. 36.3 J/(g-atom·K). In other words, depending on the choice of units, we could come to opposite conclusions regarding the effect of composition changes on heat capacity of melts.

That is why any reasoning such as "oxide A diminishes heat capacity whereas oxide B increases it," or "silicate melts have higher (or lower) heat capacity than borate (germanate, phosphate, etc.) ones," should *not* be considered as absolute: it depends on the unit of measurement.

8.4.2 Prediction of Heat Capacity of Glass Melts from Chemical Composition

The above statement *does not* mean that concentration of dependences of heat capacity cannot be predicted. It can be done, after choosing a certain unit of measurement. Prediction of heat capacity of a melt from its chemical composition is an important practical task, especially if the difficulties of measurement of this property (see above) are taken into account.

Several methods of calculation of heat capacity of glass melts from chemical composition have been developed. Below, some of these methods are described.

8.4.2.1 Method by Stebbins et al. [8]

According to this method, heat capacity of silicate melts can be calculated by the additive equation:

$$C_{p,i} = \sum X_i C_{p,i} \quad (3)$$

where X_i is the mole fraction of the corresponding component. Values of $C_{p,i}$ (in J/mol·K) are presented in Table 8.31.

Unfortunately, the authors of the method did not specify the concentration range of applicability of their calculations.

8.4.2.2 Method by Gudovich and Primenko [9]

This method uses the similar equation, but the authors consider X values as weight fractions and, correspondingly, express heat capacity in J/(g·K). Fit parameters and concentration ranges of applicability of the method are presented in Table 8.32.

8.4.2.3 Method by Priven [10]

This method is less accurate (see Section 8.4.2.4) but much more general than the methods mentioned above. It covers silicate, borate, phosphate, germanate, and many other types of glass systems; actually, the method allows the calculation of heat capacity for almost any composition of oxide glass melt.

The method is based on the known ([11–13]) correlation between temperature jump of the heat capacity, ΔC_p (see Section 8.2), and the value of fragility. The latter

is proportional to the temperature coefficient of the viscosity logarithm of a melt near the glass transition temperature,

$$\varphi_{13} \equiv \frac{1}{T_{13}} \frac{\partial \ln \eta}{\partial (1/T)} \bigg|_{T=T_{13}} = \frac{\partial \lg \eta}{\partial \lg T} \bigg|_{T=T_{13}}$$

where η is the viscosity, and T_{13} corresponds to the temperature at which viscosity is equal to 10^{13} dPa s; for most glass-forming melts, T_{13} is close to T_g.

Thus, to apply the algorithm one should know viscosity–temperature curve within the glass transition range. The corresponding algorithm for viscosity calculation has been proposed by Priven (see [14], where references to its description are given). However, it is very complicated, and we will not consider it here. Nevertheless, in many (probably even almost all) practical cases, when a researcher is interested in heat capacity of a glass melt, the viscosity–temperature curve for this melt *is already known*. Therefore, taking into account the generality of the method, we consider it reasonable to describe it without the details of viscosity prediction.

Most often, the temperature dependence of viscosity can be described by the well-known Vogel–Fulcher–Tamman equation

$$\log \eta(T) = A + B/(T - T_0), \quad (4)$$

where A, B and T_0 are empirical parameters. Let us suppose that these parameters are known. If so, the order of calculation of heat capacity of a melt is as follows (below heat capacity is expressed in J/(g-atom·K)):

Step 1. Calculation of heat capacity of solid glass at 20°C, $C_{p,20}$ by the formula proposed by S.A. Khalimovskaya-Churkina [15]. After simplification, this formula may be written as

$$C_{p\,20} = \frac{69\sum x_{R_2O} + 42\sum x_{RO} + 65\sum x_{R_2O_3} + 45\sum x_{RO_2} + 119\sum x_{R_2O_5}}{3\sum x_{R_2O} + 2\sum x_{RO} + 5\sum x_{R_2O_3} + 3\sum x_{RO_2} + 7\sum x_{R_2O_5}} \quad (5)$$

where *x* is the molar fraction of the corresponding oxide.

Step 2. Estimation of heat capacity of solid glass near the glass transition temperature, $C_p(T_g)$, by the formula [15]

$$C_p(T_g) \cong C_p(T_{13}) = C_{p,20}\left(1 + 0.52 \ln \frac{T_{13}}{293}\right) \quad (6)$$

where T_{13} value is expressed in K.

Step 3. Estimation of heat capacity jump in glass transition range, ΔC_p, by the formula

$$\Delta C_p = 0.022 A_O R(\varphi_{13} - 38) \tag{7}$$

where R is the gas constant (8310 J/mol), and A_O is the atomic fraction of oxygen in glass.

Temperature coefficient of viscosity, φ_{13}, can be calculated as

$$\varphi_{13} = 2.303(13 - A)\left[1 + T_0 \frac{13 - A}{B}\right] \tag{8}$$

where A, B, and T_0 are the parameters of Eq. (4).

The value of A_O in (7) is expressed by the formula

$$A_O = \frac{\sum x_{R_2O} + \sum x_{RO} + 3\sum x_{R_2O_3} + 2\sum x_{RO_2} + 5\sum x_{R_2O_5}}{3\sum x_{R_2O} + 2\sum x_{RO} + 5\sum x_{R_2O_3} + 3\sum x_{RO_2} + 7\sum x_{R_2O_5}} \tag{9}$$

Substituting the results of calculation by formulas (8) and (9) into (7), one can calculate the desired value of ΔC_p.

Step 4. Calculation of heat capacity of melt, $C_{p,m}$, by the formula

$$C_{p,m} = C_{p,g} + \Delta C_p. \tag{10}$$

8.4.2.4 Practical Recommendations for Using the Methods

The following recommendations are based on comparison of typical errors of calculation of heat capacity of melts by the methods described above. Typical errors of calculation of heat capacity by additive methods considered above (Refs [9] and [17]) for silicate glass melts are several percent. The typical error of Priven's method (Ref. [10]) is something greater, about 8–10%. Using these values, we recommend:

(a) If the composition of the studied glass is covered by the methods of Gudovich and Primenko (see Section 4.2.2), this method should be used for calculations.
(b) Otherwise, if a melt belongs to silicate systems and its composition is covered by the method by Stebbins et al. (see Section 4.2.1), this method is preferable.
(c) In the other cases, the method by Priven (see Section 4.2.3) should be used.

8.5 NUMERICAL DATA

TABLE 8.1
Heat Capacity of SiO_2 Melts

	C_p. J/(g·K) in temp. range, °C					
SiO_2	1200	1300	1400	1500	1600	1700
100	1.268	1.322	1.372	1.418	1.448	1.473

Source: Data from Sosman, R. B. (1927). *The Properties of Silica.* New York: Chem. Catalog Co.

TABLE 8.2
Heat Capacity of SiO_2 Melts

			C_p. J/(g·K) in temp. range, °C								
SiO_2, %	Trademark	Glass type	1200–1300	1300–1400	1400–1500	1500–1600	1600–1700	1700–1800	1800–1900	1900–2000	2000–2100
100	KI	I*	1.299	1.322	1.345	1.367	1.390	1.413	1.435		
100	KI	I**	1.255	1.279	1.304	1.329	1.354	1.379	1.403	1.428	1.453
100	KV	II	1.278	1.307	1.337	1.366	1.396	1.425	1.454	1.484	

Notes: *Glass was melted from synthetic SiO_2; **glass was melted from natural quartz.

Source: Data from Tarasov, V. D., Chekhovskoi, V. Ya., Puchkova, G. A. (1973). Enthalpy of some trademarks of silica glasses in the range 1300–2400 K (in Russian). *Inzh. Fiz. Zh.* 25(2).

TABLE 8.3
Heat Capacity of SiO_2 Melts

	C_p. J/(g·K) in temp. range, °C			
SiO_2	1200	1400	1600	1700
100	1.096	1.125	1.161	1.175

Source: Data from Wietzel, R. (1921). Die Stabilitäts-verhältnisse der Glas- und Kristallphase des Siliziumdioxides. *Z. anorg. allgem. Chem*. 116(1/2).

TABLE 8.4
Heat Capacity of SiO_2 Melts

	C_p. J/(g·K) in temp. range, ˚C		
SiO_2	1200–1300	1300–1400	1400–1500
100	1.263	1.287	1.318

Source: Data from Richet, P., Bottinga, Y., Denielou, L., Petitet, J.P., Tequi, C. (1982). Thermodynamic properties of quartz, cristobalite and amorphous SiO_2: drop calorimetry measurements between 1000 and 1800 K and a review from 0 to 2000 K. *Geochim. Cosmochim. Acta,* 46(12).

TABLE 8.5
Heat Capacity of SiO_2 Melts

	C_p. J/(g·K) in temp. range, ˚C						
SiO_2	1800–1900	1900–2000	2000–2100	2100–2200	2200–2300	2300–2400	2400–2500
100	1.268	1.282	1.297	1.311	1.326	1.341	1.355

Source: Data from Stout, N. D., Piwinskii, A. J. (1982). Enthalpy of silicate melts from 1520 to 2600 K under ambient pressure. *High Temp. Sci.*, 15(4).

TABLE 8.6
Heat Capacity of SiO_2–Na_2O Melts

Mol.% by batch		C_p. J/(g·K) in temp. range, ˚C							
SiO_2	Na_2O	700–800	800–900	900–1000	1000–1100	1100–1200	1200–1300	1300–1400	1400–1500
50	50	1.346	1.339	1.556	1.608	1.522	1.476	1.469	1.501
66.67	33.33	1.597	1.536	1.488	1.456	1.438	1.434	1.445	1.471
75	25	1.417	1.416	1.417	1.418	1.421	1.424	1.429	1.435
85.71	14.29	1.338	1.362	1.381	1.395	1.404	1.407	1.405	1.397

Source: Data from Richet, P., Bottinga, Y., Tequi, C. (1984). Heat capacity of sodium silicate liquids. *J. Am. Ceram. Soc.* 67(1).

TABLE 8.7
Heat Capacity of SiO_2–Na_2O Melts

Mol.% by batch		C_p. J/(g·K) in temp. range, ˚C								
SiO_2	Na_2O	600–700	700–800	800–900	900–1000	1000–1100	1100–1200	1200–1300	1300–1400	1400–1500
85	15	1.431	1.430	1.428	1.427	1.425	1.424	1.422	1.420	1.419
79.9	20.1	1.434	1.433	1.431	1.430	1.429	1.428	1.427	1.426	1.425
75	25	1.421	1.425	1.429	1.433	1.437	1.441	1.446	1.450	1.454
72.4	27.6	1.460	1.458	1.456	1.455	1.453	1.451	1.449	1.448	1.446
69.8	30.2	1.450	1.452	1.455	1.457	1.460	1.462	1.465	1.467	1.469
67.4	32.6	1.397	1.416	1.435	1.454	1.473	1.491	1.510	1.529	1.548

Source: Data from Yageman, V. D., Matveev, G. M. (1980). Experimental values of enthalpy and heat capacity of melts of the system SiO_2 – $Na_2Si_2O_5$ (in Russian). *Fizika i Khimiya Stekla*. 6(5)

TABLE 8.8
Heat Capacity of SiO_2–Na_2O Melts

Mol.% by batch		C_p. J/(g·K) in temp. range, ˚C			
SiO_2	Na_2O	600–700	700–800	800–900	900–1000
76.74	23.26	1.386	1.435	1.447	1.488

Source: Data from Schwiete, H. E., Ziegler, G. (1955). Beitrag zur spezifischen Waerme der Glaeser. *Glastech. Ber.* 28(4}.

TABLE 8.9
Heat Capacity of SiO_2–Na_2O Melts

Mol.% by batch		C_p. J/(g·K) in temp. range, ˚C								
SiO_2	Na_2O	600–700	700–800	800–900	900–1000	1000–1100	1100–1200	1200–1300	1300–1400	1400–1500
66.7	33.3	1.509	1.496	1.484	1.471	1.459	1.447	1.434	1.422	1.409

Source: Data from Naylor, B. F. (1945). High–temperature heat contents of sodium metasilicate and sodium disilicate. *J. Am. Chem. Soc.* 67(3).

TABLE 8.10
Heat Capacity of SiO_2–K_2O Melts

Mol.% by batch		C_p. J/(g·K) in temp. range, ˚C					
SiO_2	K_2O	600–700	700–800	800–900	900–1000	1000–1100	1100–1200
80	20	1.203	1.223	1.242	1.262	1.281	1.300

Source: Data from Richet, P., Bottinga, Y. (1980). Heat capacity of liquid silicates: New measurements on $NaAlSi_3O_8$ and $K_2Si_4O_9$. *Geochim. Cosmochim. Acta*. 44(10).

TABLE 8.11
Heat Capacity of SiO_2–K_2O Melts

Mol.% by batch		C_p. J/(g·K) in temp. range, ˚C			
SiO_2	K_2O	500–700	700–900	900–1100	1100–1300
71.43	28.57	1.217	1.240	1.177	1.203

Source: Data from Schwiete, H. E., Ziegler, G. (1955). Beitrag zur spezifischen Waerme der Glaeser. *Glastech. Ber.* 28(4}.

TABLE 8.12
Heat Capacity of SiO_2–Li_2O Melts

Mol.% by batch		C_p. J/(g·K) in temp. range, ˚C			
SiO_2	Li_2O	1400–1500	1500–1600	1600–1700	1700–1800
50	50	2.142	2.095	2.049	2.002
75	25	1.784	1.731	1.678	1.625

Source: Data from Tequi, C., Grinspan, P., Richet, P. (1992). Thermodynamic properties of alkali silicates: Heat capacity of Li2SiO3 and lithium–bearing melts. *J. Am. Ceram. Soc.* 75(9).

TABLE 8.13
Heat Capacity of SiO_2–R_2O–RO Melts

Mol.% by analysis					C_p. J/(g·K) in temp. range, ˚C						
SiO_2	Na_2O	K_2O	BeO	SrO	800–900	900–1000	1000–1100	1100–1200	1200–1300	1300–1400	1400–1500
61.93	12.8	—	25.27	—	1.469	1.457	1.473	1.457	1.483	1.449	1.457
64.01	17.39	—	18.6	—	1.438	1.443	1.458	1.442	1.441	1.433	1.450
62.12	27.12	—	—	10.76	1.326	1.326	1.337	1.342	1.341	1.333	1.349
80.04	—	14.61	—	5.35	—	1.180	1.191	1.196	1.194	1.186	1.203
79.57	—	7.4	—	13.03	—	1.089	1.241	1.167	1.164	1.157	1.174

Source: Data from Primenko, V. I., Gudovich, O. D.(1982). Temperature dependence of heat capacity of silicate glasses containing beryllium, strontium, and zirconium oxides (in Russian). *Fizika i Khimiya Stekla*. 8(4).

TABLE 8.14
Heat Capacity of SiO_2–Na_2O–PbO Melts

Mol.% by batch				
SiO_2	Na_2O	PbO	T.range. ˚C	C_p. J/(g·K)
66.7	33.3	—	1210–1420	1.3096
65.5	24.5	10.0	1050–1270	1.1651
64.8	17.6	17.6	970–1270	0.9296
64.5	15.5	20.0	920–1270	0.9359
63.6	14.0	22.4	1070–1270	0.8724
63.6	10.2	26.2	1020–1270	0.7474
63.2	8.3	28.5	1070–1280	0.7175
62.5	—	37.5	1220–1420	0.7868

Source: Toporishchev, G. A., Esin, O. A., Bratchikov, S. G. (1961). Thermo–chemical characteristics of PbO–SiO_2–Na_2O melts (in Russian). *Izv. Vyssh. Uchebn. Zaved., Tsvetn. Metall*. No.3.

TABLE 8.15
Heat Capacity of SiO_2–K_2O–MgO Melts

Mol.% by analysis			C_p. J/(g·K) in temp. range, ˚C		
SiO_2	K_2O	MgO	600–700	700–800	800–900
66.68	16.88	16.44	1.176	1.219	1.262

Source: Data from Carmichael, I. S. E., Nicholls, J., Spera, F. J., Wood, B. J., Nelson, S. A. (1977). High-temperature properties of silicate liquids: Applications to the equilibration and ascent of basic magma. *Philos. Trans. R. Soc. London*. 286A.

TABLE 8.16
Heat Capacity of SiO_2–K_2O–Al_2O_3 Melts

Mol.% by batch			C_p. J/(g·K) in temp. range, °C	
SiO_2	K_2O	Al_2O_3	700–900	900–1100
75.0	12.5	12.5	1.176	1.243

Source: Data from White, W. P. (1919). Silicate specific heats. Second series. *Am. J. Sci., Ser.4*. 47(277).

TABLE 8.17
Heat Capacity of SiO_2–R_2O–Al_2O_3 Melts

Mol.% by batch				C_p. J/(g·K) in temp. range, °C							
SiO_2	Na_2O	K_2O	Al_2O_3	700–800	800–900	900–1000	1000–1100	1100–1200	1200–1300	1300–1400	1400–1500
75.0	12.5	—	12.5	—	1.483	1.628	1.772	1.917	—	—	—
66.67	16.67	—	16.67	1.550	1.530	1.509	1.489	—	—	1.429	1.409
50	25	—	25	1.414	1.416	1.418	1.420	—	—	—	1.429
75.0	—	12.5	12.5	1.356	1.367	1.379	1.390	1.401	1.413	1.424	1.436

Source: Data from Richet, P. and Bottinga, Y. (1984). Anorthite, andesine, wollastonite, diopside, cordierite, and pyrope: Thermodynamics of melting, glass transitions, and properties of the amorphous phases. *Earth Planetary Sci. Lett.*, 67(3).

TABLE 8.18
Heat Capacity of SiO_2–Na_2O–R_2O_3 Melts

Mol.% by analysis				C_p. J/(g·K) in temp. range, °C						
SiO_2	Na_2O	Sb_2O_3	Bi_2O_3	600–700	700–800	800–900	900–1000	1000–1100	1100–1200	1200–1300
79.1	18.03	2.87	—	1.345	—	—	—	1.316	1.300	1.325
78.91	16.95	4.14	—	1.317	—	—	—	—	1.285	1.288
75.57	18.98	5.45	—	1.286	—	—	—	—	1.258	1.261
80.14	17.59	—	2.27	1.280	1.332	1.274	1.267	1.264	1.273	1.275
78.64	18.21	—	3.15	1.279	1.307	1.230	1.219	1.234	1.219	1.244
76.39	19.43	—	4.18	1.213	1.281	1.227	1.204	1.201	1.210	1.212

Source: Data from Primenko, V. I., Gudovich, O. D. (1981). Enthalpy and heat capacity of silicate glasses containing oxides of III and V groups (in Russian). *Fizika i Khimiya Stekla*. 7(2).

TABLE 8.19
Heat Capacity of SiO_2–Na_2O–R_2O_3 Melts

Mol.% by analysis				C_p. J/(g·K) in temp. range, °C						
SiO_2	Na_2O	La_2O_3	Y_2O_3	600–700	700–800	800–900	900–1000	1000–1100	1100–1200	1200–1300
76.62	20.54	—	2.84	1.335	1.448	1.512	1.400	1.405	1.398	1.410
74.98	20.82	—	4.21	1.306	1.418	1.482	1.411	1.357	1.370	1.350
72.49	21.55	—	5.96	1.222	1.383	1.465	1.418	1.328	1.316	1.318
76.74	21.28	1.99	—	1.347	1.432	1.400	1.344	1.341	1.350	1.353
75.05	22.22	2.73	—	1.326	1.411	1.379	1.323	1.320	1.329	1.332
72.95	23.25	3.8	—	1.291	1.375	1.380	1.312	1.313	1.302	1.204

Source: Data from Primenko, V. I., Gudovich, O. D. (1981). Enthalpy and heat capacity of silicate glasses containing oxides of III and V groups (in Russian). *Fizika i Khimiya Stekla*. 7(2).

TABLE 8.20
Heat Capacity of SiO_2–K_2O–CeO_2 Melts.

Mol.% by analysis			C_p. J/(g·K) in temp. range, °C						
SiO_2	K_2O	CeO_2	800–900	900–1000	1000–1100	1100–1200	1200–1300	1300–1400	1400–1500
78.4	15.33	6.27	1.182	1.195	1.196	1.184	1.161	1.182	1.202
76.87	19.02	4.11	1.185	1.206	1.205	1.204	1.178	1.192	1.216
75.75	22.21	2.04	1.232	1.215	1.216	1.225	1.19	1.202	1.234

Source: Data from Primenko, V. I., Galyant, V. I., Gudovich, O.D. (1986). Temperature dependence of heat capacity of silicate glasses containing cadmium and cerium oxides (in Russian). *Fizika i Khimiya Stekla*. 12(4).

TABLE 8.21A
Compositions of SiO_2–R_2O–RO–R_2O_3 Melts

	Mol.% by analysis										
No.	SiO_2	K_2O	Na_2O	CaO	MgO	PbO	BaO	Fe_2O_3	B_2O_3	Al_2O_3	SO_3
1	71.15	–	14.24	10.15	3.74	—	—	0.048	—	0.27	0.34
2	72.69	0.58	12.3	11.41	0.47	—	—	0.2	—	2.21	—
3	75.7	0.39	13.91	9.03	—	—	—	0.017	—	0.95	—
4	78.99	10.2	1.59	—	—	6.46	1.86	0.009	0.36	0.52	—

Note: For heat capacity data see Table 8.21B

Source: Data from Hartmann, H., Brand, H. (1953). Zur Kenntnis der mittleren spezifischen Waerme einiger technisch wichtiger Glassorten. *Glastech. Ber.* 26(2).

TABLE 8.21B
Heat Capacity of SiO_2–R_2O–RO–R_2O_3 Melts

	C_p. J/(g·K) in temp. range, ˚C						
No.	**600–700**	**700–800**	**800–900**	**900–1000**	**1000–1100**	**1100–1200**	**1200–1300**
1	1.280	1.310	1.312	1.182	1.207	1.766	1.410
2	1.235	1.307	1.329	1.324	1.192	1.316	1.633
3	1.274	1.454	1.304	1.182	1.407	1.435	1.444
4	1.080	1.115	1.147	1.108	1.222	1.595	1.394

Note: For compositions see Table 8.21A.

Source: Data from Hartmann, H., Brand, H. (1953). Zur Kenntnis der mittleren spezifischen Waerme einiger technisch wichtiger Glassorten. *Glastech. Ber.* 26(2).

TABLE 8.22A
Compositions of SiO_2–R_2O–RO–R_2O_3 Melts

	Mol.% by batch													
No.	**SiO_2**	**Li_2O**	**Na_2O**	**K_2O**	**MgO**	**CaO**	**BaO**	**CoO**	**NiO**	**CuO**	**Fe_2O_3**	**Al_2O_3**	**Sb_2O_3**	**SO_3**
1	69.9	—	19.7	—	—	10.2	—	—	—	—	—	—	—	—
2	72.0	—	13.2	—	4.47	8.89	—	—	—	—	0.09	1.18	—	0.08
3	71.1	—	14.5	—	5.28	8.64	—	—	—	—	0.03	0.41	—	—
4	75.2	1.15	9.21	5.4	—	—	5.16	0.00	0.0	0.08	0.1	3.31	0.31	—
5	76.3	1.37	9.12	4.5	—	—	5.46	—	—	—	0.03	3.14	—	—
6	71.8	—	12.4	0.3	5.6	8.9	—	—	—	—	0.04	0.76	—	0.08

Note: For heat capacity data see Table 8.22B.

Source: Data from Tydlitat, V., Blazek, A., Endrys, J., Stanek, J. (1972). Messung der Enthalpie und Berechnung der spezifischen Waerme von Glas. *Glastech. Ber.* 45(8).

TABLE 8.22.B
Heat Capacity of SiO_2–R_2O–RO–R_2O_3 Melts

	C_p. J/(g·K) in temp. range, ˚C						
No.	**600–700**	**700–800**	**800–900**	**900–1000**	**1000–1100**	**1100–1200**	**1200–1300**
1	1.456	1.450	1.444	1.438	1.432	1.426	1.420
2	1.319	1.321	1.323	1.324	1.326	1.328	1.329
3	—	1.254	1.339	1.424	1.509	1.595	—
4	1.078	1.113	1.148	1.183	1.218	—	—
5	1.265	1.242	1.219	1.196	1.173	1.150	1.127
6	1.386	1.403	1.420	1.437	1.454	1.471	1.488

Note: For compositions see Table 8.22A.

Source: Data from Tydlitat, V., Blazek, A., Endrys, J., Stanek, J. (1972). Messung der Enthalpie und Berechnung der spezifischen Waerme von Glas. *Glastech. Ber.* 45(8).

TABLE 8.23
Heat Capacity of SiO_2–R_2O–RO–R_2O_3 Melts

Mol.% by analysis										C_p. J/(g·K) in temp. range, ˚C			
SiO_2	Na_2O	K_2O	FeO	MnO	MgO	CaO	Al_2O_3	Fe_2O_3	TiO_2	1000–1100	1100–1200	1200–1300	1300–1400
44.7	—	—	39.3	0.03	—	7.29	7.9	0.69	—	—	1.175	1.250	1.324
57.6	26.29	—	—	—	—	—	—	—	16.0	1.439	1.455	1.470	1.486
59.4	20.9	—	—	—	19.66	—	—	—	—	1.522	1.556	1.591	1.625
66.6	—	16.8	—	—	16.44	—	—	—	—	1.236	1.279	1.292	—
80.8	4.31	2.99	—	0.02	0.52	1.46	8.81	0.79	0.25	1.488	1.409	1.331	—
64.8	4.35	0.92	—	0.17	5.86	8.32	10.27	4.22	0.79	—	1.517	1.469	1.420
79.3	7.51	2.98	—	0.23	0.05	0.42	5.15	3.87	0.27	1.480	1.468	1.457	1.445

Source: Data from Carmichael, I. S. E., Nicholls, J., Spera, F. J., Wood, B. J., Nelson, S. A. (1977). High-temperature properties of silicate liquids: Applications to the equilibration and ascent of basic magma. *Philos. Trans. R. Soc. London*. 286A.

TABLE 8.24
Heat Capacity of SiO_2–R_2O–RO–R_2O_3 Melts

Mol.% by analysis									C_p. J/(g·K) in temp. range, ˚C			
SiO_2	Na_2O	K_2O	MgO	CaO	Al_2O_3	Fe_2O_3	TiO_2	SO_3	800–900	1000–1100	1200–1300	1400–1500
75.00	—	13.74	—	11.26	—	—	—	—	—	1.212	1.215	1.224
74.47	15.21	—	0.24	9.47	0.07	0.015	0.015	0.51	1.35	1.345	1.349	1.357

Source: Data from Carmichael, I. S. E., Nicholls, J., Spera, F. J., Wood, B. J., Nelson, S. A. (1977). High–temperature properties of silicate liquids: Applications to the equilibration and ascent of basic magma. *Philos. Trans. R. Soc. London*. 286A.

TABLE 8.25
Heat Capacity of SiO_2–TiO_2–Na_2O–RO–Al_2O_3 Melts

Mol.% by analysis							C_p. J/(g·K) in temp. range, ˚C						
SiO_2	TiO_2	Na_2O	MgO	CaO	ZnO	Al_2O_3	600–700	700–800	800–900	900–1000	1000–1100	1100–1200	1200–1300
72.63	—	16.35	—	—	8.74	2.29	1.310	1.532	1.475	1.375	1.376	1.365	1.367
52.04	—	17.83	—	—	30.13	—	1.384	—	—	—	—	1.322	1.303
63.98	9.85	24.54	—	—	—	1.64	1.477	1.702	1.522	1.474	1.436	1.419	1.445
58.54	10.64	18.92	.94	8.58	—	2.38	1.485	1.639	1.452	1.416	1.419	1.406	1.409

Source: Data from Primenko, V. I., Gudovich, O. D. (1979). Heat capacity of silicate glasses containing zinc and titanium oxides (in Russian). *Fizika i Khimiya Stekla*. 5(2).

TABLE 8.26
Heat Capacity of SiO_2–RO Melts

Mol.% by batch			C_p. J/(g·K) in temp. range, °C						
SiO_2	CaO	MgO	1600–1700	1700–1800	1800–1900	1900–2000	2000–2100	2100–2200	2200–2300
50	25	25	1.595	1.548	1.502	1.645	1.616	1.587	1.558

Source: Stout, N. D., Piwinskii, A. J. (1982). Enthalpy of silicate melts from 1520 to 2600 K under ambient pressure. *High Temp. Sci.*, 15(4).

TABLE 8.27
Heat Capacity of SiO_2–R_2O–RO–R_2O_3 Melts

Mol.% by analysis					C_p. J/(g·K) in temp. range, °C			
SiO_2	Na_2O	MgO	CaO	Al_2O_3	700–800	800–900	900–1000	1400–1500
50.26	0.03	24.26	25.45	0.005	1.370	1.414	1.458	1.678

Source: Data from Richet, P., Bottinga, Y., Tequi, C. (1984). Heat capacity of sodium silicate liquids. *J. Am. Ceram. Soc.* 67(1).

TABLE 8.28
Heat Capacity of SiO_2–CaO Melts

Mol.% by batch		C_p. J/(g·K) in temp. range, °K						
SiO_2	CaO	1800–1900	1900–2000	2000–2100	2100–2200	2200–2300	2300–2400	2400–2500
50	50	1.438	1.472	1.484	1.474	1.441	1.387	1.310

Source: Stout, N. D., Piwinskii, A. J. (1982). Enthalpy of silicate melts from 1520 to 2600 K under ambient pressure. *High Temp. Sci.*, 15(4).

TABLE 8.29
Heat Capacity of B_2O_3–R_2O Melts

Mol.% by batch				C_p. J/(g·K) in temp. range, °C				
B_2O_3	Li_2O	Na_2O	K_2O	600–700	700–800	800–900	900–1000	1000–1100
66.7	33.3	—	—	2.770	2.736	2.665	2.770	2.879
80	—	20	—	2.171	2.184	2.243	2.255	2.448
66.7	—	33.3	—	2.226	2.209	2.080	2.318	2.343
80	—	—	20	1.736	1.774	1.782	1.958	2.000

Source: Data from Smith, G. S., Rindone, G.E. (1961). High-temperature energy relations in the alkali borates: binary alkali borate compounds and their glasses. *J. Am. Ceram. Soc*. 44(2).

TABLE 8.30
Heat Capacity of B_2O_3–CaO Melts

Mol.% by batch		C_p. J/(g·K) in temp. range, °C							
B_2O_3	CaO	700–800	800–900	900–1000	1000–1100	1100–1200	1200–1300	1300–1400	1400–1500
66.7	33.3	1.654	1.879	1.917	1.708	1.708	1.708	1.709	1.708

Source: Data from King, E. G., Torgeson, D. R., Cook, O.A. (1948). High–temperature heat contents of $3CaO.B_2O_3$, $2CaO.B_2O_3$, $CaO.B_2O_3$, and $CaO.2B_2O_3$. *J. Am. Chem. Soc*. 70(6).

TABLE 8.31
Fit Parameters for Silicate Liquid Heat Capacities Calculated from Weighted Linear Regression from 58 Compositions (1200–1850 K)

	$C_{p,i}$ J/(mol·K)
SiO_2	80.0 ± 0.9
TiO_2	111.8 ± 5.1
Al_2O_3	157.6 ± 3.4
Fe_2O_3	229.0 ± 18.4
FeO	78.9 ± 4.9
MgO	99.7 ± 7.3
CaO	99.9 ± 7.2
BaO	83.4 ± 6.0
Li_2O	104.8 ± 3.2
Na_2O	102.3 ± 1.9
K_2O	97.0 ± 5.1
Rb_2O	97.9 ± 3.6

Note: Second column for each parameter is the weighted standard error of the regression

Source: Data from Stebbins, J. F., Carmichael, I. S. E., Moret, L. K. (1984). Heat capacities and entropies of silicate liquids and glasses. *Contrib. Mineral. Petrol*. 86.

ACKNOWLEDGMENT

All tables containing published data were selected, transformed in the standard format, and printed using the program SciGlass [3].

TABLE 8.32
Fit Parameters for Silicate Liquid Heat Capacities (800–1500°C)

	Concentration range, wt %	$C_{p,i}$ J/(g·K)
Al_2O_3	0–30	1.297
B_2O_3	0–30	1.876
BaO	0–50	0.502
BeO	0–15	2.029
Bi_2O_3	0–25	0.544
CaO	0–30	1.05
K_2O	0–41	1.113
La_2O_3	0–20	0.665
Li_2O	0–16	4.197
MgO	0–30	1.464
Na_2O	0–36	1.879
PbO	0–50	0.289
Sb_2O_3	0–25	0.733
SiO_2	20–85	1.286
SrO	0–20	0.797
TiO_2	0–20	1.253
Y_2O_3	0–20	0.757
ZnO	0–36	1.038
ZrO_2	0–20	0.443

Source: Data from Gudovich, O. D., Primenko, V. I. (1985). Calculation of heat capacity of silicate glasses and melts (in Russian). *Fizika i Khimiya Stekla*. 11(3).

REFERENCES

1. Varshneya, A. K. (1994). *Fundamentals of Inorganic Glasses.* Boston, New York, London: Academic Press, Inc.
2. Bansal, N. P. and Doremus, R. H. (1986). *Handbook of Glass Properties.* New York, London: Academic Press, Inc.
3. SciGlass 3.5 (1998). *Glass Property Information System*. Lexington: SciVision.
4. Scherer, G. W. (1986). *Relaxation in Glass and Composites*. New York: John Wiley & Sons.
5. Sosman, R. B. (1927). *The Properties of Silica.* New York: Chem. Catalog Co.
6. Stewart, D. R., Rindone, G. E. (1963). High-temperature energy relations in borates: Alkaline-earth and lead borate compounds and their glasses. *J. Amer. Ceram. Soc*. 46(12):593–596.
7. Nemilov, S.V. (1995). *Thermodynamic and kinetic aspects of the vitreous state*. Boca Raton: CRC Press.
8. Stebbins, J. F., Carmichael, I. S. E., Moret, L. K. (1984). Heat capacities and entropies of silicate liquids and glasses. *Contrib. Mineral. Petrol*. 86:131–148.

9. Gudovich, O. D., Primenko, V. I. (1985). Calculation of heat capacity of silicate glasses and melts (in Russian). *Fizika i Khimiya Stekla*. 11(3):349–355.
10. Priven, A.I., (2001). Calculation of the heat capacity of oxide glass-forming melts and evaluation of the heat capacity jump in the glass transition range from chemical composition. *Rus. J. Glass Phys. Chem. (Engl. Transl.)*, 27(5):435–444.
11. Martin, S. W., Angell, C. A. (1986). On the glass transition and viscosity of P_2O_5. *J. Phys. Chem*. 90(25):6736–6740.
12. Lee, S.-K., Tatsumisago, M., Minami, T. Relation between local structure and fragility of sodium germanate glasses. *Phys. Chem. Glasses*. 36(5):225–227.
13. Chryssikos, G. D., Duffy, J. A., Hutchinson, J. M., Ingram, M. D., Kamitsos, E. I., Pappin, A. J. (1994). Lithium borate glasses: A quantitative study of strength and fragility. *J. Non-Cryst. Solids*. 172–174:378–383.
14. Priven, A. I. (2004). General method for calculating the properties of oxide glasses and glass-forming melts from their composition and temperature. *Glass Technol.* (in press).
15. Khalimovskaya-Churkina, S.A., Priven, A.I. (2000). Calculation of the heat capacity of oxide glasses at temperatures from 100 K to the lower boundary of glass transition range. *Rus. J. Glass Phys. Chem. (Engl. Transl.)*, 26 (6): 531–540.
16. Tarasov, V. D., Chekhovskoi, V. Ya., Puchkova, G. A. (1973). Enthalpy of some trademarks of silica glasses in the range 1300–2400 K (in Russian). *Inzh. Fiz. Zh.* 25(2):341–344.
17. Wietzel, R. (1921). Die Stabilitäts-verhältnisse der Glas- und Kristallphase des Siliziumdioxides. *Z. anorg. allgem. Chem*. 116(1/2):71–95.
18. Richet, P., Bottinga, Y., Denielou, L., Petitet, J.P., Tequi, C. (1982). Thermodynamic properties of quartz, cristobalite and amorphous SiO_2: drop calorimetry measurements between 1000 and 1800 K and a review from 0 to 2000 K. *Geochim. Cosmochim. Acta*, 46(12):2639–2658.
19. Stout, N. D., Piwinskii, A. J. (1982). Enthalpy of silicate melts from 1520 to 2600 K under ambient pressure. *High Temp. Sci.*, 15(4):275–292.
20. Richet, P., Bottinga, Y., Tequi, C. (1984). Heat capacity of sodium silicate liquids. *J. Am. Ceram. Soc.* 67(1):C6-C8.
21. Yageman, V. D., Matveev, G. M. (1980). Experimental values of enthalpy and heat capacity of melts of the system $SiO_2 – Na_2Si_2O_5$ (in Russian). *Fizika i Khimiya Stekla*. 6(5):602–608.
22. Schwiete, H. E., Ziegler, G. (1955). Beitrag zur spezifischen Waerme der Glaeser. *Glastech. Ber.* 28(4}:137–146.
23. Naylor, B. F. (1945). High-temperature heat contents of sodium metasilicate and sodium disilicate. *J. Am. Chem. Soc.* 67(3):466–467.
24. Richet, P., Bottinga, Y. (1980). Heat capacity of liquid silicates: New measurements on $NaAlSi_3O_8$ and $K_2Si_4O_9$. *Geochim. Cosmochim. Acta*. 44(10):1535–1541.
25. Tequi, C., Grinspan, P., Richet, P. (1992). Thermodynamic properties of alkali silicates: Heat capacity of Li2SiO3 and lithium-bearing melts. *J. Am. Ceram. Soc.* 75(9):2601–2604..
26. Primenko, V. I., Gudovich, O. D.(1982). Temperature dependence of heat capacity of silicate glasses containing beryllium, strontium, and zirconium oxides (in Russian). *Fizika i Khimiya Stekla*. 8(4):494–497.
27. Toporishchev, G. A., Esin, O. A., Bratchikov, S. G. (1961). Thermo-chemical characteristics of $PbO-SiO_2-Na_2O$ melts (in Russian). *Izv. Vyssh. Uchebn. Zaved., Tsvetn. Metall.* No.3:37–43.

28. Carmichael, I. S. E., Nicholls, J., Spera, F. J., Wood, B. J., Nelson, S. A. (1977). High-temperature properties of silicate liquids: Applications to the equilibration and ascent of basic magma. *Philos. Trans. R. Soc. London*. 286A:373–431.
29. White, W. P. (1919). Silicate specific heats. Second series. *Am. J. Sci., Ser.4*. 47(277):1–43.
30. Richet, P., Bottinga, Y. (1984). Glass transitions and thermodynamic properties of amorphous SiO_2, $NaAlSi_nO_{2n+2}$ and $KAlSi_3O_8$. *Geochim. Cosmochim. Acta*. 48(3):453–470.
31. Primenko, V. I., Gudovich, O. D. (1981). Enthalpy and heat capacity of silicate glasses containing oxides of III and V groups (in Russian). *Fizika i Khimiya Stekla*. 7(2):245–248.
32. Primenko, V. I., Galyant, V. I., Gudovich, O.D. (1986). Temperature dependence of heat capacity of silicate glasses containing cadmium and cerium oxides (in Russian). *Fizika i Khimiya Stekla*. 12(4):496–499.
33. Hartmann, H., Brand, H. (1953). Zur Kenntnis der mittleren spezifischen Waerme einiger technisch wichtiger Glassorten. *Glastech. Ber.* 26(2):29–33.
34. Tydlitat, V., Blazek, A., Endrys, J.,Stanek, J. (1972). Messung der Enthalpie und Berechnung der spezifischen Waerme von Glas. *Glastech. Ber.* 45(8):352–359.
35. Primenko, V. I., Gudovich, O. D. (1979). Heat capacity of silicate glasses containing zinc and titanium oxides (in Russian). *Fizika i Khimiya Stekla.* 5(2):249–251.
36. Richet, P. and Bottinga, Y. (1984). Anorthite, andesine, wollastonite, diopside, cordierite, and pyrope: Thermodynamics of melting, glass transitions, and properties of the amorphous phases. *Earth Planetary Sci. Lett.*, 67(3):415–432.
37. Smith, G.S., Rindone, G.E. (1961). High-temperature energy relations in the alkali borates: binary alkali borate compounds and their glasses. *J. Am. Ceram. Soc*. 44(2):72–78.
37. King, E. G., Torgeson, D. R., Cook, O.A. (1948). High-temperature heat contents of $3CaO.B_2O_3$, $2CaO.B_2O_3$, $CaO.B_2O_3$, and $CaO.2B_2O_3$. *J. Am. Chem. Soc*. 70(6):2160–2163.

9 Heat Transfer in Glass-Forming Melts

M.K. Choudhary and R.M. Potter

CONTENTS

9.1 INTRODUCTION

The objectives of this chapter are to (a) present a phenomenological treatment of heat transfer in glass melts, and (b) review published data on properties relevant to heat transfer in glass melts. Thus, the chapter is divided into two parts.

The first part begins with the transport equation for heat transfer (i.e., the differential thermal energy balance equation) in a glass melt and briefly discusses the conductive and convective heat transfer terms. The discussion on conduction is basically in the nature of summarizing what constitutes the thermal conductivity (or, to use the term to be introduced later, the "true" or "phonon" thermal conductivity). The convective heat transfer in a melt is, of course, intimately tied to fluid dynamics phenomena in the melt. Since fluid dynamics in glass melts is discussed in a separate chapter, our treatment of convective heat transfer in this chapter is rather cursory. Only in the case of thermal radiation have we gone beyond just a preliminary description. There are numerous books and articles on radiation in participating media (i.e., media that absorb, emit, and scatter radiation). Interested readers should consult suitable references (several are mentioned in the text) for an exhaustive treatment of this subject. Here, we have attempted to treat this subject in a manner that is succinct, provides physical insight into radiation in glass melts, and yet has enough mathematical rigor to provide a "quantitative" appreciation for the phenomena involved. Since glass melt is a semitransparent material in which heat transfer by radiation plays a prominent role, we feel that a more than just a cursory treatment for radiation is called for.

The properties that influence heat transfer in the bulk of glass melts are as follows:

- "True" or "phonon" thermal conductivity (conduction)
- Density, viscosity, specific heat (convection)
- Absorption spectra (radiation)

Density and specific heat also affect the thermal time constant in transient heat transfer phenomena (in case of transient conduction they are combined with thermal conductivity to define a thermal diffusivity). Of the properties listed above, thermal conductivity and absorption spectra are of direct interest to us. The other properties are treated elsewhere in this book. In many cases (e.g., mathematical modeling of flow and heat transfer phenomena in glass melting and processing), the item of practical interest to glass technologists is not the absorption spectrum but a "*radiation"* or *"photon" thermal conductivity.* This parameter may, of course, be derived from the absorption spectra for the melt. In the following, we will adopt the terms phonon and photon thermal conductivity to denote true and radiation conductivity of glass respectively.

In the second part of this chapter, we have focused our attention on data published on the phonon thermal conductivity and the absorption spectra for glass. We have used the published information on the absorption spectra to calculate the photon thermal conductivity. Since the measurement techniques and the data on thermal conductivity covering a period up to the late 1970s have been extensively reviewed

in a monograph published by the International Commission on Glass [3], our attempt here is to build on this earlier compilation and to go beyond it.

Thus, in the case of phonon thermal conductivity, we have not only reviewed more recent experimental data, but also calculated coefficients for the evaluation of low-temperature phonon thermal conductivity from glass composition. These coefficients fit the data to within 10% for all but four of the 186 measurements available from references cited in this chapter.

In the case of thermal radiation, we have reviewed published absorption spectra for different glass compositions with a focus on the absorption characteristics of several transition metal ions and hydroxyl ion. We have also illustrated how photon thermal conductivity can be calculated, albeit within the accuracy limits of the data and the calculation technique, directly from glass composition by using the high-temperature spectra.

It should be clear from the remarks made above that the scope of this chapter goes beyond a simple review article. In addition to reviewing the published information on some important thermal properties of glass melts, we have also provided pertinent theoretical background on heat transfer in glass melts, as well as data and techniques that can be used to calculate phonon and photon thermal conductivities of glass melts.

9.2 FORMULATION OF HEAT TRANSFER PROBLEM IN GLASS MELTS

9.2.1 Differential Thermal Energy Balance

The starting point for analyzing heat transfer in a fluid is the differential thermal energy balance equation, which for an absorbing–emitting medium such as a glass melt, may be written as follows:

$$\underset{\text{(Accumulation)}}{\rho C_p \frac{\partial T}{\partial t}} = \underset{\text{(Convection)}}{-\rho C_p V \cdot \nabla T} \underset{\text{(Conduction)}}{-\nabla \cdot q_c} \underset{\text{(Radiation)}}{-\nabla \cdot q_r} \tag{1}$$

where ρ is density, C_p is specific heat, T is temperature, t is time, V is velocity vector, q_c is the conductive heat flux vector, and q_r is the radiative heat flux vector.

Equation (1) is applicable in the absence of viscous dissipation or other sources of heat in the fluid. It relates the rate of change of thermal energy per unit volume of a fluid to a balance among the volumetric rates of convective, conductive, and radiative transfers of thermal energy.

9.2.2 Heat Transfer by Conduction

The conductive heat flux is expressed by the well-known Fourier conduction law given below:

$$q_c = -k_c \nabla T \tag{2}$$

where k_c is the thermal conductivity and T is temperature of the fluid. In literature on heat transfer in glass, k_c is referred to as the "true" or "phonon" thermal conductivity to distinguish it from the "radiation" or "photon" thermal conductivity to be discussed later. As mentioned in the introduction, we will refer to these two parameters as the phonon and photon thermal conductivities. Another quantity that is often used in the heat transfer literature is the thermal diffusivity, α_c, defined as:

$$\alpha_c = k_c / (\rho C_p) \tag{3}$$

Thermal conduction in solids can be explained by the propagation of lattice waves through a continuum or by the interaction between quanta of vibrational thermal energy (i.e., phonons). Thus, analogous to the kinetic theory of gases, one may use the concept of the mean free path of the phonon and the following expression for the phonon thermal conductivity [1–4]:

$$k_c = \frac{1}{3} C u_s l \tag{4}$$

where C is the volumetric specific heat, u_s is the velocity of sound (i.e., of the lattice waves) in the solid, and l is the mean free path of the phonons.

The above expression is valid for both crystalline and non-crystalline solids. However, as pointed out by Kittel [1] and Kingery [2], in glasses the mean free path for phonons is limited by geometrical effects associated with the disordered nature of the structure. In glasses, the random structure will limit the mean free path to a distance that is of the same order of magnitude as the dimensions of a single-structure element. Since this distance is fixed by the structure, the phonon thermal conductivity is expected to change with temperature in the same proportion as the specific heat. This has been found to be the case [1–3, 5].

Although the above discussion pertained to the mechanism of heat conduction in solid glass, it is also applicable to "true" thermal conduction in liquids. That is because, in liquids, the phonon free paths are of molecular dimensions and the lattice structure is in some respects similar to that of a disordered solid. Indeed, near the glass transition temperature, the lattice structures of solid glass and the melt are identical.

The commonly used units for thermal conductivity and diffusivity are given below.

Thermal conductivity:

$$1 \text{ W/m} \cdot \text{K} = 0.8604 \text{ kcal/m} \cdot \text{hr} \cdot ^\circ\text{C}$$

$$= 0.5778 \text{ Btu/ft} \cdot \text{hr} \cdot ^\circ\text{F}$$

$$= 2.390 \times 10^{-3} \text{ cal/cm} \cdot \text{s} \cdot ^\circ\text{C}$$

Thermal diffusivity:

$$1\ m^2/s = 38750\ ft^2/hr$$
$$= 3600\ m^2/hr$$
$$= 10.764\ ft^2/s$$

9.2.3 Heat Transfer by Convection

The calculation of heat transfer by convection (the convective heat flux vector, $q_{conv} = \rho\ C_p\ T\ V$) requires the knowledge of velocity and temperature fields in the fluid. The flow of a fluid is described by differential mass balance (i.e., equation of continuity) and differential momentum balance (i.e., Navier-Stokes equation). For the steady laminar flow of an incompressible fluid (i.e., of constant density), these equations are given as:

$$\nabla \cdot V = 0 \qquad \text{(continuity)}$$
$$\rho(V \cdot \nabla)V = -\nabla P - \nabla \cdot \tau_{ij} + \rho g \qquad \text{(momentum)} \qquad (5a,b)$$
$$\text{(Inertial)}\ \ \text{(Pr essure)}\ \ \text{(Viscous)}\ \ \text{(Gravity)}$$

where P is the pressure, τ_{ij} is the viscous stress tensor and g is the acceleration due to gravity. For an incompressible Newtonian fluid (a reasonable assumption for glass melts in most circumstances), the viscous stress tensor is given as follows:

$$\tau_{ij} = -\eta\left(\frac{\partial V_i}{\partial x_j} + \frac{\partial V_j}{\partial x_i}\right) \qquad (6)$$

where η is the viscosity and x_i and x_j denote the spatial coordinates.

The viscosity of glass-forming melts depends strongly on temperature and is usually expressed by the following equation:

$$\log \eta = A + \frac{B}{T - C} \qquad (7)$$

where A, B, C are empirically determined constants.

For the steady state situation, the differential thermal energy balance Equation (1) can be written as:

$$\rho C_p V \cdot \nabla T = -\nabla \cdot q_c - \nabla \cdot q_r \qquad (8)$$

The focus of this chapter is on heat transfer, and therefore details on flow field and viscosity will not be included here. We note, however, that in the calculation of flow field in a glass melt, one often uses the Boussinesq approximation [7, p. 524] [77]. This implies that the glass melt is treated as an incompressible liquid with a mean density, and the variation of density due to temperature gradients produces a buoyancy driving force.

Using the Boussinesq approximation, Equation (5b) can be written as:

$$\rho(V \cdot \nabla)V = -\nabla P - \nabla \cdot \tau_{ij} - \rho\beta(T - T_o)g \tag{9}$$

where ρ now stands for the mean density evaluated at the reference temperature T_o, and β is the coefficient of volumetric expansion of the glass melt.

It can be seen from Equations (7), (8) and (9) that, because of the thermal buoyancy effect and the strong dependence of glass viscosity on temperature, equations of energy and motion are coupled and have to be solved simultaneously.

9.2.4 Heat Transfer by Radiation

It is clear from the equation for energy, i.e., Equation (1), that calculation of heat transfer in a glass melt will require a formulation for the radiation heat flux vector q_r in terms of temperature, and radiation properties of the melt (and the boundaries in which the melt is confined). The problem of analyzing heat transfer in a radiation-participating medium has received considerable attention [e.g., references 6–11]. The general treatment of this problem is quite involved and will not be given here. In the following subsection we present, in an outline form, the formulation for the radiation heat flux vector. The emphasis here is on providing physical insights into the thermal radiation phenomena and on giving minimal but necessary mathematical description of these phenomena. The following analysis closely follows the treatment given in Reference 6. In analyzing heat transfer in glass melts, scattering of radiation is usually neglected and will be ignored here.

Before discussing the formulation for radiation heat flux in an absorbing, emitting medium, let us review some background information on thermal radiation.

9.2.4.1 Planck's Law

The monochromatic emissive power of a black body, $E_{b\lambda}$ is given by Planck's Law [11] written as:

$$E_{b\lambda} = \frac{n^2 C_1}{\lambda^5 (e^{c_2/\lambda T} - 1)} \tag{10}$$

where C_1 and C_2 are constants, n is the refractive index of the medium surrounding the black body, λ is the wavelength in *vacuum**, and T is the absolute temperature.

* Sometimes, Planck's law is written in terms of wavelength in the medium, λ_s; where $\lambda_s = \lambda/n$.

TABLE 9.1
Radiation Constants

Constant	Value
Boltzmann's constant, k	1.38×10^{-23} J/K
Planck's constant, h	6.625×10^{-34} Js
Speed of light, C_o	2.998×10^{8} m/s
Stefan-Boltzmann constant, σ	5.668×10^{-8} J/s – m^2 K^4
$C_1 = 2\pi hc_o^2$	3.74×10^{-16} J m^2 /s
$C_2 = hc_o/k$	1.4387×10^{-2} mK

It is noted that $E_{b\lambda}d\lambda$ is the radiation emitted per unit time per unit area by a black body in the wavelength range $d\lambda$. The values of physical constants used in the analysis of black-body radiation are given in Table 9.1.

9.2.4.2 Stefan-Boltzmann Law

The total emissive power of a black body, E_b is the total energy emitted per unit area per unit time over the entire wavelength domain. It is given as:

$$E_b(T) = \int_0^\infty E_{b\lambda}(T)d\lambda \tag{11}$$

The integration yields:

$$E_b = n^2\sigma T^4 \tag{12}$$

where, σ (Stefan-Boltzmann constant) is defined by:

$$\sigma = \frac{2\pi^5 k^4}{15c_o^2 h^3} \tag{13}$$

The value of σ was given previously in Table 9.1.

9.2.4.3 Intensity of Radiation

Intensity of radiation is a measure of amount of energy passing in a given direction. In defining intensity, it is useful to distinguish between radiation from a surface and radiation through an absorbing-emitting medium.

For a surface, referring to Figure 9.1, the intensity of radiation is the rate of radiant energy leaving the surface per unit area normal to the pencil of rays, per unit solid angle. If dQ is the rate of radiant energy leaving the surface in the direction θ and contained within a solid angle $d\omega$, then the intensity, 'i' is given by:

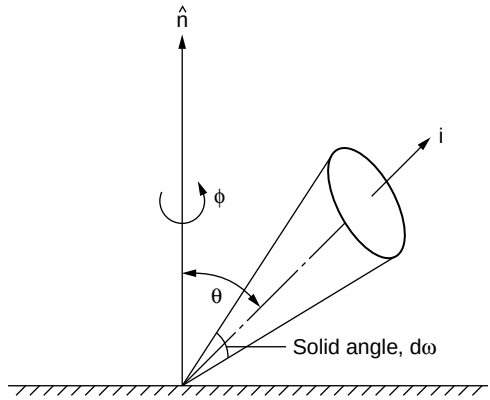

FIGURE 9.1 Radiant energy through a solid angle dω. (From *Radiation Heat Transfer*, E. M. Sparrow and R. D. Cess, Hemisphere Publishing/CRC Press).

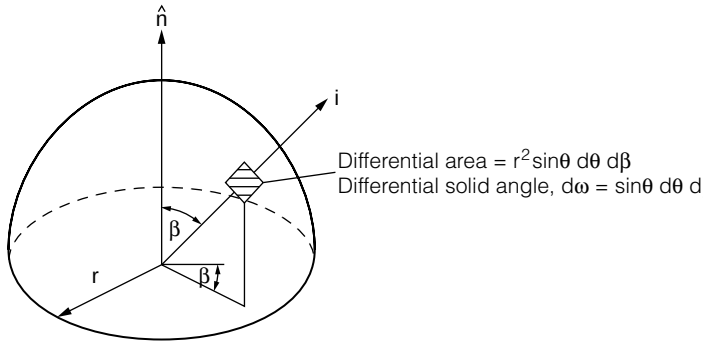

FIGURE 9.2 Radiant energy entering a hemispherical enclosure. (From *Radiation Heat Transfer*, E. M. Sparrow and R. D. Cess, Hemisphere Publishing/CRC Press).

$$i = \frac{dQ}{d\omega \cos\theta} \tag{14}$$

The radiant energy flux leaving the surface and entering a hemispherical enclosure, Q, can be obtained by the following integration (see Figure 9.2):

$$Q = \int_0^{2\pi} \int_0^{\pi/2} i \cos\theta \sin\theta d\theta d\beta \tag{15}$$

If the intensity of radiation is independent of direction (i.e., radiation is isotropic), Equation (15) yields:

$$Q = \pi i \tag{15a}$$

The intensity of radiation at any location *in an absorbing, emitting medium* (denoted by symbol I) is defined as the net rate of transfer of radiant energy per unit area normal to the pencil of rays, per unit solid angle.

The monochromatic (or spectral) and total intensities are related as follows:

$$i = \int_0^\infty i_\lambda d\lambda \qquad I = \int_0^\infty I_\lambda d\lambda \tag{16}$$

9.2.4.4 Surface Radiation

The definition of a black body provides a convenient frame of reference for characterizing the radiation properties of actual surfaces. Thus, the monochromatic emissive power of a non-black surface, E_λ is expressed as:

$$E_\lambda = \varepsilon_\lambda E_{b\lambda} \tag{17}$$

where ε_λ is called the monochromatic emissivity. $E_{b\lambda}$ was previously defined as the emissive power of a black body.

The monochromatic absorptivity of a surface, α_λ is defined as the fraction of the monochromatic incident radiation flux that is absorbed by the surface. Thus, if H_λ is the incident radiation flux, then the amount absorbed is $\alpha_\lambda H_\lambda$.

Kirchoff's law provides the following relationship between monochromatic emissivity and absorptivity:

$$\alpha_\lambda = \varepsilon_\lambda \tag{18}$$

For a black body, it is obvious that $\alpha_\lambda = \varepsilon_\lambda = 1$. We further note that blackbody radiation is isotropic. It then follows from Equation (15a) that:

$$E_{b\lambda} = \pi i_{b\lambda} \tag{19}$$

9.2.4.5 Radiation in an Absorbing, Emitting Medium

Having presented preliminary background information on thermal radiation, we now turn to a brief phenomenological discussion of radiation in an absorbing, emitting medium. For details on the absorption of radiation by glasses, including information on absorption spectra of different glasses, see [21, 22].

9.2.4.5.1 Absorption

Let I_λ be the monochromatic intensity of radiation of a beam shown in Figure 9.3. As the beam traverses distance ds, its attenuation due to absorption, $-dI_\lambda$ is given by:

$$-dI_\lambda = \kappa_\lambda I_\lambda ds \tag{20}$$

where κ_λ is the monochromatic absorption coefficient.

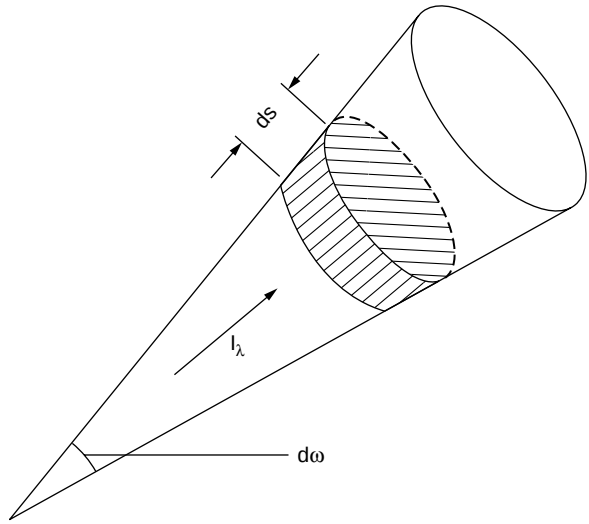

FIGURE 9.3 Absorption of radiation over a path length ds. (From *Radiation Heat Transfer*, E. M. Sparrow and R. D. Cess, Hemisphere Publishing/CRC Press).

Recalling the definition of intensity, I_λ, from the previous section and noting that ds equals volume per unit area of the differential element in Figure 9.3, the rate of monochromatic absorption per unit volume and per unit solid angle is $\kappa_\lambda I_\lambda$.

From Equation (20) we can write:

$$I_\lambda = I_{o\lambda} e^{-\kappa_\lambda s} \tag{21}$$

where $I_{o\lambda}$ is the intensity at s = 0. The term $e^{-\kappa_\lambda s}$ represents the fraction of photons whose free path exceeds a given length, s.

Thus, analogous to molecular motion, we can define a *mean free path*, λ_m for photons of wavelength λ as:

$$\lambda_m = 1/\kappa_\lambda \tag{22}$$

9.2.4.5.2 Emission

Let us now formulate an expression for the monochromatic emission of radiation energy in an absorbing, emitting medium. First we note from Kirchoff's law (see previous section) that the rate of emission per unit volume and per unit solid angle, J_λ can be expressed as:

$$J_\lambda = \frac{\kappa_\lambda}{\pi} E_{b\lambda} \tag{23}$$

For an isotropic medium, the emission is independent of direction, and therefore the rate of monochromatic emission per unit volume is given by $4\kappa_\lambda E_{b\lambda}$.

A quantity that is of considerable interest is the total emission per unit time and per unit volume. It can be obtained by integrating the above expression over the whole spectrum and expressed as $4\kappa_p E_b$, where:

$$\kappa_p = \frac{\int_0^\infty \kappa_\lambda E_{b\lambda} d\lambda}{E_b} \tag{24}$$

κ_p is called the *Planck mean absorption coefficient*

9.2.4.5.3 Radiation Regimes

The optical thickness of an absorbing medium is defined as:

$$\tau_{o\lambda} = \kappa_\lambda L \tag{25}$$

where L is a characteristic length scale. Using Equation (22) we can write:

$$\tau_{o\lambda} = \frac{L}{\lambda_m} = \frac{\text{Characteristic length}}{\text{photon mean free path}} \tag{26}$$

We can now define the following radiation regimes.

i. Optically Thick ($\tau_{o\lambda} >> 1$): In this regime, the photon mean free path is much smaller than the characteristic length scale of the system, and the radiation process approaches a diffusion process. In other words, radiation flux q_r can be described by an equation similar to Fourier equation, Equation (2), with the "phonon thermal conductivity" replaced by a "photon thermal conductivity." We will consider this case in much more detail subsequently. In a physical sense, optically thick case implies that the attenuation of radiation is so rapid that every element of radiation is directly affected by its neighbors only. This is the regime commonly assumed in mathematical modeling of heat transfer phenomena in glass melting furnaces [77].
ii. Optically Thin ($\tau_{o\lambda} << 1$): In this case, the photon mean free path is much larger than the characteristic length scale. This implies that the absorption of photons by the fluid is negligible and radiation emitted by a fluid element will tend to go directly to the surfaces bounding the medium. Its analogue in the molecular transfer process is found in the free molecule flow, where molecules travel from surface to surface without intervening collisions.
iii. Intermediate Regime: This is the general case, and occurs in the majority of radiation problems (e.g., combustion). In this case, radiation exchange takes place among all fluid elements and consequently one has to use integral expressions for the radiation flux vector, q_r.

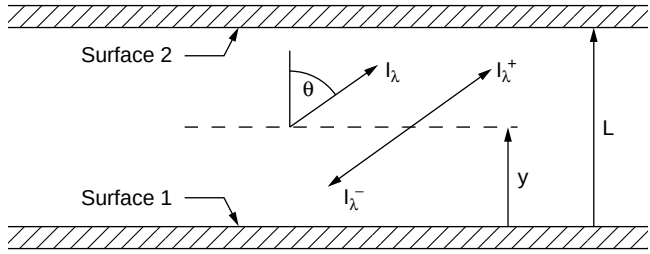

FIGURE 9.4 Schematic details of one-dimensional radiative heat transfer. (From *Radiation Heat Transfer*, E. M. Sparrow and R. D. Cess, Hemisphere Publishing/CRC Press).

9.2.4.5.4 Equations for Radiation Transfer in an Absorbing, Emitting Medium

Following are expressions governing radiation transfer in an absorbing, emitting medium. Our objective is to present physical insight with a "flavor" for mathematical treatment of radiation phenomena in glass melts. Therefore, we will consider *one-dimensional thermal radiation in an absorbing, emitting medium bounded by two infinite, parallel, opaque, and diffuse surfaces*. While the assumption of diffuse surfaces (i.e., emission and reflection from the surfaces are uniform in all angular directions) is not necessary, it will considerably simplify the writing of the expressions.

The system considered here is shown in Figure 9.4.

Denote the monochromatic intensity of radiation in the positive and negative y directions by $I_{+\lambda}$ and $I_{-\lambda}$ respectively. Let us consider radiation balance for $I_{+\lambda}$. In passing through an element of thickness dy, the intensity changes by $dI_{+\lambda}$ due to:

a. emission from the differential volume, $de_{+\lambda}$ and
b. absorption by the differential volume, $da_{+\lambda}$.

The two contributions can be written as:

$$de_{+\lambda} = \frac{\kappa_\lambda E_{b\lambda} dy}{\pi \cos\theta}$$
$$da_{+\lambda} = -\frac{\kappa_\lambda I_{+\lambda} dy}{\cos\theta} \tag{27}$$

Now we get the following differential balance equation for $I_{+\lambda}$:

$$\cos\theta \frac{dI_{+\lambda}}{dy} = \frac{\kappa_\lambda}{\pi} E_{b\lambda} - \kappa_\lambda I_{+\lambda} \tag{28}$$

A similar equation can be written for $I_{-\lambda}$.

Let us introduce the following parameters:

$$\tau_\lambda = \int_0^y \kappa_\lambda dy, \quad \tau_{o\lambda} = \int_0^L dy, \quad \mu = \cos\theta \tag{29}$$

Equation (28), and its counterpart for $I_{-\lambda}$ can now be written in terms of the optical coordinate, τ_λ:

$$\mu \frac{dI_{+\lambda}}{d\tau_\lambda} = \frac{E_{b\lambda}}{\pi} - I_{+\lambda}$$
$$\mu \frac{dI_{-\lambda}}{d\tau_\lambda} = \frac{E_{b\lambda}}{\pi} - I_{-\lambda} \tag{30a,b}$$

The boundary conditions for the above equations are given as:

$$I_{+\lambda}(0) = \frac{R_{1\lambda}}{\pi}$$
$$I_{-\lambda}(\tau_{o\lambda}) = \frac{R_{2\lambda}}{\pi} \tag{31a,b}$$

where $R_{1\lambda}$ and $R_{2\lambda}$ are the monochromatic radiosities of surfaces 1 and 2.

The radiosity is defined as the sum of energy flux leaving a surface due to emission and reflection:

$$R_\lambda = \varepsilon_\lambda E_{b\lambda} + (1 - \varepsilon_\lambda) H_\lambda \tag{31c}$$

where H_λ is the incident radiative flux.

It should be noted that from Kirchoff's law, Equation (18), it follows that $1 - \varepsilon_\lambda$ is the monochromatic reflectivity.

By integrating Equations (30a,b) we get:

$$I_{+\lambda} = \frac{R_{1\lambda}}{\pi} e^{-\tau_\lambda/\mu} + \frac{1}{\pi}\int_0^{\tau_\lambda} E_{b\lambda}(t) e^{-(\tau_\lambda - t)/\mu} \frac{dt}{\mu}$$
$$I_{-\lambda} = \frac{R_{2\lambda}}{\pi} e^{(\tau_{o\lambda} - \tau_\lambda)/\mu} - \frac{1}{\pi}\int_{\tau_\lambda}^{\tau_{o\lambda}} E_{b\lambda}(t) e^{-(\tau_\lambda - t)/\mu} \frac{dt}{\mu} \tag{32a,b}$$

The first term on the right hand side of Equation (32) represents attenuation due to absorption of energy originating at the surfaces. The integral term represents augmentation of energy due to emission over a finite path length.

Now that we have the expressions for the radiation intensities, the monochromatic radiation flux can be obtained by integrating them over the solid angle, $d\omega = 2\pi \sin\theta \, d\theta$. This gives:

$$q_{r\lambda} = 2\pi\int_0^{\pi} I_\lambda \cos\theta \sin\theta d\theta$$

$$q_{r\lambda} = 2\pi\int_0^{1} I_{+\lambda}\mu d\mu - 2\pi\int_0^{-1} I_{-\lambda}\mu d\mu \qquad (33a,b)$$

On substituting Equations (31a,b) into Equation (33b) we get:

$$q_{r\lambda} = 2R_{1\lambda}E_3(\tau_\lambda) - 2R_{2\lambda}E_3(\tau_{o\lambda} - \tau_\lambda) + 2\int_0^{\tau_\lambda} E_{b\lambda}(t)E_2(\tau_\lambda - t)dt - 2\int_{\tau_\lambda}^{\tau_{o\lambda}} E_{b\lambda}(t)E_2(t - \tau_\lambda)dt \qquad (34)$$

where $E_n(t)$ are the integral functions defined as:

$$E_n(t) = \int_0^1 \mu^{n-2} e^{-t/\mu} d\mu \qquad (35)$$

The values of these functions are tabulated in Appendix B of Reference 6.

The total radiative heat flux, q_r may be calculated by integrating the monochromatic heat flux, $q_{r\lambda}$ over all the wavelengths, or:

$$q_r(y) = \int_0^{\infty} q_{r\lambda}(\tau_\lambda) d\lambda \qquad (36)$$

We saw previously that it is the divergence of q_r (i.e., $-\nabla.q_r$) that had appeared in the energy transport equation [Equation (1)]. For the one-dimensional case:

$$\nabla \cdot q_r = \int_0^{\infty} \kappa_\lambda \frac{dq_{r\lambda}}{d\tau_\lambda} d\lambda$$

$$-\frac{dq_{r\lambda}}{d\tau_\lambda} = 2R_{1\lambda}E_2(\tau_\lambda) + 2R_{2\lambda}E_2(\tau_{o\lambda} - \tau_\lambda) \qquad (37a,b)$$

$$+ 2\int_0^{\tau_{o\lambda}} E_{b\lambda}(t)E_1(\tau_\lambda - t)dt - 4E_{b\lambda}(\tau_\lambda)$$

To calculate the surface radiosities $R_{1\lambda}$ and $R_{2\lambda}$, note from Equation (34) that the net radiant flux leaving surface 1 is given by:

$$q_{r\lambda}(0) = R_{1\lambda} - 2R_{2\lambda}E_3(\tau_{o\lambda}) - 2\int_0^{\tau_{o\lambda}} E_{b\lambda}(t)E_2(dt) \qquad (38)$$

The first term on the right-hand side of Equation (38) represents flux leaving the surface, therefore the other terms should denote radiative flux incident on surface 1, $H_{1\lambda}$:

$$H_{1\lambda} = 2R_{2\lambda}E_3(\tau_{o\lambda}) + 2\int_0^{\tau_{o\lambda}} E_{b\lambda}(t)E_2(t)dt \tag{39}$$

From the defining equation of radiosity, Equation (31c), we have:

$$R_{1\lambda} = \varepsilon_{1\lambda}E_{b2\lambda} + (1-\varepsilon_{1\lambda})H_{1\lambda} \tag{40}$$

where $\varepsilon_{1\lambda}$ is the monochromatic emissivity of surface 1.

The expression for radiosity can now be written as:

$$\begin{aligned} R_{1\lambda} &= \varepsilon_{1\lambda}E_{b1\lambda} + 2(1-\varepsilon_{1\lambda})\left[R_{2\lambda}E_3(\tau_{o\lambda}) + \int_0^{\tau_{o\lambda}} E_{b\lambda}(t)E_2(t)dt\right] \\ R_{2\lambda} &= \varepsilon_{2\lambda}E_{b2\lambda} + 2(1-\varepsilon_{2\lambda})\left[R_{1\lambda}E_3(\tau_{o\lambda}) + \int_0^{\tau_{o\lambda}} E_{b\lambda}(t)E_2(\tau_{o\lambda}-t)dt\right] \end{aligned} \tag{41}$$

9.2.4.5.5 Equations for Optically Thin Limit

As discussed earlier (Section 9.2.4.5.3), for this case, $\tau_{o\lambda} << 1$. Under these conditions, the exponential integral functions E_2 and E_3 can be approximated as $E_2(t) = 1$; $E_3(t) = 1/2$.

Using these approximations and the condition $\tau_{o\lambda} << 1$, we can derive:

$$q_{r\lambda} = R_{1\lambda} - R_{2\lambda} = \frac{E_{b1\lambda} - E_{b2\lambda}}{1/\varepsilon_{1\lambda} + 1/\varepsilon_{2\lambda} - 1} \tag{42}$$

The above equation is the same as the equation for radiation between two plates separated by a nonparticipating medium. The divergence of radiation flux, i.e., Equation (37b) can now be simplified as:

$$-\frac{dq_{r\lambda}}{dy} = 2\kappa_\lambda[R_{1\lambda} + R_{2\lambda} - 2E_{b\lambda}] \tag{43}$$

Equation (43) represents a balance between the absorption of energy originating at the two surfaces and local emission. The elimination of the integral term has resulted in considerable simplification because instead of dealing with an integro-differential equation, one now has to deal with only a differential equation.

To get the divergence of the total radiation flux, Equation (43) has to be integrated over all wavelengths. That results in:

$$-\frac{dq_r}{dy} = 2[\kappa_{1m}R_1 + \kappa_{2m}R_2 - 2\kappa_p\sigma T^4] \tag{44}$$

where κ_{1m} and κ_{2m} are modified mean absorption coefficients defined as:

$$\kappa_{1m} = \frac{\int_0^\infty \kappa_\lambda(T)R_{1\lambda}d\lambda}{R_1}$$
$$\kappa_{2m} = \frac{\int_0^\infty \kappa_\lambda(t)R_{2\lambda}d\lambda}{R_2} \tag{45a,b}$$

and κ_p is the Planck mean absorption coefficient defined earlier in Equation (24).

Considerable simplifications result if the surfaces are assumed to be black or the medium is assumed to be gray (i.e., absorption coefficient is assumed independent of wavelength).

9.2.4.5.6 Equations for Optically Thick Limit

This is the case of greatest interest in mathematical modeling of heat transfer phenomena in glass furnaces. As noted earlier, for this case, $\tau_{o\lambda} >> 1$. This condition allows us to simplify the expression for the monochromatic heat flux, i.e., Equation (34).

Let us expand $E_{b\lambda}$ using Taylor series about τ_λ.

$$E_{b\lambda}(t) = E_{b\lambda}(\tau_\lambda) + \frac{dE_{b\lambda}}{d\tau_\lambda}(t - \tau_\lambda) + \ldots \tag{46}$$

Equation (34) can now be written as:

$$q_{R\lambda} = 2R_{1\lambda}E_3(\tau_\lambda) - 2R_{2\lambda}E_3(\tau_{o\lambda} - \tau_\lambda) +$$
$$2E_{b\lambda}(\tau_\lambda)\left[\int_0^{\tau_\lambda} E_2(z)dz - \int_0^{\tau_{o\lambda}-\tau_\lambda} E_2(z')dz'\right] - \tag{47}$$
$$2\frac{dE_{b\lambda}}{d\tau_\lambda}\left[\int_0^{\tau_\lambda} zE_2(z)dz + \int_0^{\tau_{o\lambda}-\tau_\lambda} z'E_2(z')dz'\right] +$$

where $z = \tau_\lambda - t$, and $z' = t - \tau_\lambda$.

Let us now consider a region far removed from boundaries (i.e., $\tau_\lambda \to \infty$; and $\tau_{o\lambda} - \tau_\lambda \to \infty$). Using $E_3(\infty) \to 0$; Equation (47) reduces to:

$$q_{R\lambda} = -4\frac{dE_{b\lambda}}{d\tau_\lambda}\int_0^\infty zE_2(z)dz \tag{48}$$

Furthermore,

$$\int_0^\infty zE_2(z)dz = \frac{1}{3} \tag{49}$$

Equation (48) can now be written as:

$$q_{R\lambda} = -\frac{4}{3}\frac{dE_{b\lambda}}{d\tau_\lambda} = -\frac{4}{3\kappa_\lambda}\frac{dE_{b\lambda}}{dy} \tag{50}$$

The total radiative flux can be obtained by integrating $q_{r\lambda}$ over all the wavelengths [please refer to Equation. (36)]. This gives:

$$q_r = -\int_0^\infty \frac{4}{3\kappa_\lambda}\frac{dE_{b\lambda}}{dy}d\lambda$$

$$q_r = -\frac{4}{3\kappa_R}\frac{dE_b}{dy} \tag{51a,b,c}$$

where

$$\frac{1}{\kappa_R} = \int_0^\infty \frac{1}{\kappa_\lambda}\frac{dE_{b\lambda}}{dE_b}d\lambda$$

The term κ_R is called the Rosseland mean absorption coefficient. On noting that $E_b = \sigma n^2 T^4$, the expression for the total radiative flux can be written as:

$$q_r = -\left[\frac{16n^2\sigma T^3}{3\kappa_R}\right]\frac{dT}{dy} \tag{52}$$

On using the analogy with the Fourier heat conduction law, i.e., Equation (2), it is apparent that the bracketed term on the right-hand side of Equation (52) may be interpreted as a *radiation or photon thermal conductivity,* k_r. Thus:

$$k_r = \frac{16n^2\sigma T^3}{3\kappa_R} \tag{53}$$

For multidimensional heat transfer by radiation, Equation (52) may generalized to give:

$$q_r = -k_r \nabla T \tag{54}$$

When the optically thick approximation is valid, it is a common practice to lump the phonon and photon thermal conductivities together as an effective thermal conductivity, $k_{eff} = k_c + k_r$.

9.2.4.5.7 Calculation of Photon thermal conductivity

The relationships given above ("the photon diffusion equations") have been used extensively for the calculation of radiative transfer in glass melts [11–21]. Thus, the evaluation of κ_R is of considerable significance to glass melting and processing.

To evaluate κ_R let us introduce a function, f^*, defined below [11]:

$$f^* = \int_0^{\lambda} \frac{dE_{b\lambda}}{dE_b} d\lambda \tag{55}$$

Combining Equations (51c) and (55) we get:

$$\frac{1}{\kappa_R} = \int_0^1 \frac{1}{\kappa_\lambda} df^* \tag{56}$$

Tabulated values of f^* as a function of λT [16,11] can be used to evaluate above integral and calculate photon thermal conductivity.

In general, for glasses (as for many other radiating media), the absorption and emission take place in distinct wavelength bands. Thus, if κ_i represents the absorption coefficient in the wave length range from λ_{i-1} to λ_i, then:

$$\frac{1}{\kappa_R} = \sum_i \frac{(f_i^* - f_{i-1}^*)}{\kappa_i} \tag{57}$$

If, for example, the absorption coefficient of a glass can be expressed by a two-step function, with $\kappa = \kappa_1$ for $0 \le \lambda \le \lambda_1$ and $\kappa = \kappa_2$ for $\lambda \ge \lambda_1$, then Genzel [15] used an equivalent expression to calculate the radiation conductivity of a number of glasses:

$$k_r = \frac{16n^2\sigma T^3}{3}\left[\frac{f_{\lambda 1}^*}{\kappa_1} + \frac{1 - f_{\lambda 1}^*}{\kappa_2}\right] \tag{58}$$

In the discussion given above we outlined the calculation procedure for the photon thermal conductivity, k_r in terms of the Rosseland mean absorption coefficient, κ_R. We can also calculate k_r by noting from Equation (51a) that:

$$k_r = \frac{4}{3}\int_0^{\infty} \frac{1}{\kappa_\lambda}\frac{dE_{b\lambda}}{dT} d\lambda \tag{59}$$

On substituting the expression for $dE_{b\lambda}/dT$, obtained from Equation (10); we get the following expression:

$$k_r = \frac{8\pi C_o^3 h^2}{3kT^2} \int_0^\infty \frac{1}{\kappa_\lambda} \frac{n^2}{\lambda^6} \frac{e^{hc_o/\lambda kT}}{(e^{hc_o/\lambda kT} - 1)^2} d\lambda \tag{60}$$

In the above equation we have kept the refractive index n inside the integral to allow for its dependence on the wavelength.

9.2.4.5.8 Effect of Boundaries

In the derivation leading to Equation (48), we had considered a region far removed from the boundaries — i.e., we had considered the bulk region of a glass melt. Thus, the use of photon thermal conductivity can result in significant error in calculating temperature distribution and heat flux in the vicinity of boundaries, particularly for glasses with low absorptivity (e.g., white, flint, float glasses).

The effect of boundaries is usually handled through the use of a "jump" or "discontinuity" in emissive power. See, for example, [6, 10, 11]. This approach, in essence, allows one to relate the emissive powers of the boundary and the medium through the surface emissivity. Another approximation, described in [20], involves modifying Equation (51a) as shown below:

$$q_r = -\int_0^\infty \frac{4}{3\kappa_\lambda} F \frac{dE_{b\lambda}}{dy} d\lambda \tag{61}$$

The factor, F, is given by the following relationship:

$$F = 1 - (1 - \varepsilon_{w\lambda})E_3(\tau_\lambda) - (1 - \varepsilon_{w\lambda})E_3(\tau_{o\lambda} - \tau_\lambda) \tag{62}$$

where, $\varepsilon_{w\lambda}$ is the spectral emissivity of the surface.

9.3 THERMAL CONDUCTIVITY OF GLASS

9.3.1 Phonon Thermal Conductivity

9.3.1.1 Introduction

In silicate glasses, phonon thermal conductivity is the dominant mode of heat transfer at temperatures below about 500–600°C; at temperatures greater than about 1000°C photon thermal conductivity generally dominates [3]. Given the difficulty and uncertainty of measuring the phonon thermal conductivity in the presence of a strong component of photon conduction, it is not surprising that only a few estimates of phonon thermal conductivity have been made at temperatures near 600°C or above [3]. Some data exist for temperatures near 100°C [23, 24], but more recent work has been limited to near room temperature or below [25–42]. Much of the data have

been compiled in references 43 and 78. Reference 78 contains data on phonon thermal conductivity of 424 glasses taken from 64 sources published in the period 1894–2000. Careful evaluation of the data together with theoretical analyses suggests that, in the range of temperature of interest to us (above about 300°C) phonon thermal conductivity increases only slightly with temperature [3].

The experimental methods used to measure phonon thermal conductivity prior to the early 1970s have been reviewed in detail elsewhere [3]. Most of the work since that time has used a technique that measures temperature differences for linear heat flow under steady state conditions on glass discs [26]. In one instance [27], a non-steady state laser flash method was used. With a few exceptions, recent work has been designed to determine the dependence of phonon thermal conductivity on chemical composition within various silicate glass systems. Here, we will summarize this work to provide the means to calculate phonon thermal conductivity directly from glass composition.

9.3.1.2 Calculation of Room Temperature Phonon Thermal Conductivity

Two purely empirical fits to the data have been used to calculate the phonon thermal conductivity. The first uses the fact that phonon thermal conductivity tends to increase as glass density decreases. The following relation between phonon thermal conductivity (k_c) and density (ρ) is assumed, and the constants A and B are determined by a least-squares fit to the data:

$$k_c = A/\rho + B \tag{63}$$

This technique appears to have satisfactory predictive ability for regular changes within a single compositional system. It is not suitable for predictions over a broad compositional range. The optimum values of A and B vary considerably from system to system [23,38–40] reflecting changes in the dependence of phonon thermal conductivity on density. Such changes are shown clearly in plots of k_c vs. ρ for several glass systems [40].

The second type of empirical fit has been remarkably successful in predicting phonon thermal conductivity from glass chemical composition. This technique assumes that the conductivity is a linear function of glass composition as follows:

$$k_c = \Sigma\, A_i C_i \tag{64}$$

where A_i is the phonon thermal conductivity coefficient for component i and C_i is the concentration of component i in the glass. The coefficients are determined by a linear least-squares fit to the data. In the literature on phonon thermal conductivity of silicate glasses, oxide components have generally been used and the concentrations have been expressed in weight percent.

Coefficients for calculation of phonon thermal conductivity have been published for a number of glass systems [26, 28, 31, 33, 37–39] or groups of glasses of varying composition [23]. In general, the results from different research groups on different

TABLE 9.2
Coefficients for Calculation of Phonon Thermal Conductivity in W/mK from Oxide Weight Percent

	This chapter	Ref. 23[a]	Ref. 24[b]	Ref. 28[c]	Ref. 35	Ref. 37	Ref. 38	Ref. 39	Ref. 40
SiO_2	0.0133	0.0136	0.0109	0.0140			0.0133		
TiO_2	–0.0327			0.0138	–0.0314	–0.0314			
Al_2O_3	0.0139	0.0399	0.0178	0.0115	0.0136				0.0129
MgO	0.0173	0.0064		0.0217	0.0217				
CaO	0.0123	0.0078		0.0114	0.0131				0.0124
SrO	0.0084				0.0086				
BaO	0.0024	0.0034	0.0019	0.0024	0.0029			0.0022	
MnO	–0.0223					0.0263			
CoO	0.0312					0.0363			
NiO	0.0166					0.0163			
CuO	0.0333					0.0376			
ZnO	0.0078	0.0001		0.0070	0.0080				
PbO	0.0035	0.0031	0.0038	0.0031	0.0027				
Li_2O	–0.0088				–0.0093		–0.0093		
Na_2O	–0.0047	–0.0033		–0.0042	–0.0048				
K_2O	0.0027	0.0039		0.0026					
Cs_2O	–0.0006								
B_2O_3	0.0082	0.0010		0.0117	0.0082				
Fe_2O_3	0.0085	0.0076				0.0077	0.0077		
Sb_2O_3	–0.0108	–0.0124							
Bi_2O_3	0.0053		0.0056						
F_2	–0.0508	–0.0394							

[a] Recalculated from Ratcliff's data interpolated to 30°C
[b] Converted to units of W/m°C
[c] At 50°C

glass systems have given consistent values for the coefficients. This suggests that all the data can be used to develop a single set of coefficients that will give accurate predictions for a broad range of glass compositions. The results from doing this for the data from one research group have been published [35], but no one has fit the entire data set. We have analyzed all the phonon thermal conductivity data referenced in this chapter and from them developed a single set of coefficients that fit the data remarkably well. The coefficients are generally close to those developed from the individual data sets (Table 9.2) and fit the data to within 10% for all but four of the 186 measurements (Figure 9.5).

The following comments relate to development of these coefficients:

a. For many glass properties, a better fit may be obtained using a mole-based unit such as mole percent rather than weight percent. For these phonon

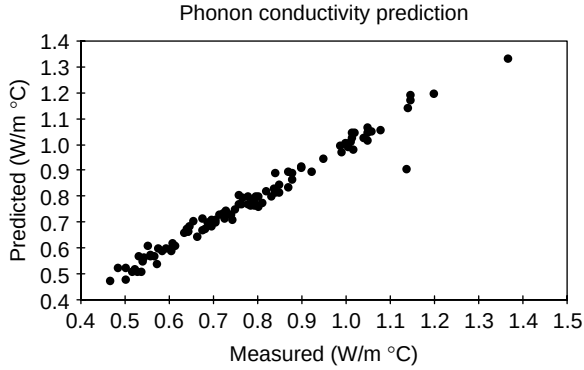

FIGURE 9.5 Comparison of predicted and measured values of photon thermal conductivity.

thermal conductivity data, however, weight percent gave a significantly better fit.

b. The data from reference 20 on glasses containing 35–45% TiO_2 were excluded from the analysis when we found that, in combination with other data, they forced the TiO_2 coefficient to be positive. This is clearly inconsistent with the effect of changing the TiO_2 concentration within the separate systems. The phonon thermal conductivity values of the glasses in reference 20 are unusually high for silicate glasses.
c. With the exception of reference 20 there appears to be no systematic offset or other difference among the data sets of different publications. Nor does the goodness-of-fit relate to composition in any obvious way except for the F_2 dependence, which is based on only one measurement. Error in the F_2 coefficient is responsible for the one anomalously low predicted value in Figure 9.5.

As opposed to the purely empirical methods just discussed, other, more fundamental approaches have been developed [11] based on the phonon scattering ability of the disordered glass network and of the individual network-modifying ions. This may lead to some improvement in the accuracy of the prediction but at the expense of a considerably more involved analysis of the data.

As pointed out previously (Section 9.I.2.) the phonon thermal conductivity changes with temperature in about the same proportion as the specific heat. Using the information on the temperature dependence of the specific heat from reference 3, it is possible to calculate the high temperature phonon thermal conductivity from the low temperature data or from values calculated using the coefficients in Table 9.2.

9.3.2 Photon Thermal Conductivity

9.3.2.1 Introduction

Above a few hundred degrees Celsius, photon conduction is generally a significant component of heat transfer in silicate glasses. Unlike phonon conduction, photon

conduction is, in general, a function of the geometry of the system as well as of the glass composition. Measurements of thermal conductivity at temperatures above a few hundred degrees Celsius must therefore be concerned with both phonon and photon conduction and with the geometry of the system. Considerable work has been done on high-temperature thermal conductivity of glass, and both the experimental methods and the data through the late 1970s have been reviewed elsewhere [3]. Since that time, there has been continued interest in direct measurement of thermal conductivity [44] and in thermal diffusivity by radial heat-flow methods, from which the thermal conductivity can be derived [45–49].

Calculation of photon thermal conductivity directly from glass spectral data has received considerable attention in part because of the flexibility it offers in application to different geometries. If the glass absorption spectrum is known in the appropriate spectral region, the photon thermal conductivity can be calculated from the pertinent theoretical equations. In this section, we will develop means to calculate the photon thermal conductivity directly from glass composition based on the available high-temperature spectral data. We will be restricted to the optically thick limit, in which edge effects are negligible. The glass thickness for which edge effects become significant is typically of the order of centimeters, but may be somewhat greater or considerably smaller depending on the glass composition.

9.3.2.2 Calculation of Photon Thermal Conductivity from Spectral Data

The equation for photon thermal conductivity in the optically thick case was derived in the first part and is reproduced below (Section 9.2.4.5.7; Equation 60):

$$k_r = \frac{8\pi C_o^3 h^2}{3kT^2} \int_0^\infty \frac{1}{\kappa_\lambda} \frac{n^2}{\lambda^6} \frac{e^{hc_o/\lambda kT}}{(e^{hc_c/\lambda kT} - 1)^2} d\lambda \tag{65}$$

All the parameters in this equation are known except for κ_λ, the glass absorption coefficient and n, the glass refractive index. These parameters eliminate the possibility of an analytical solution to Equation (65), since they are not explicit functions of wavelength. Even if they were approximated by explicit functions for a given glass, this approximation would be valid for only a small subset of glass compositions. We therefore integrate Equation (65) numerically by breaking the wavelength range into discrete regions in each of which the integrand can be considered constant:

$$k_r = \frac{8\pi C_o^3 h^2}{3kT^2} \sum_{\lambda=0}^{\infty} \frac{1}{\kappa_\lambda} \frac{n^2}{\lambda^6} \frac{e^{hc_o/\lambda kT}}{(e^{hc_o/\lambda kT} - 1)^2} \Delta\lambda \tag{66}$$

We must make a further simplification since it is not feasible to integrate numerically from zero to infinity even if we know the absorption coefficient and refractive index of the glass throughout this entire range. Fortunately, it is possible to reduce the integration limits without sacrifice in accuracy by a simple examination of the

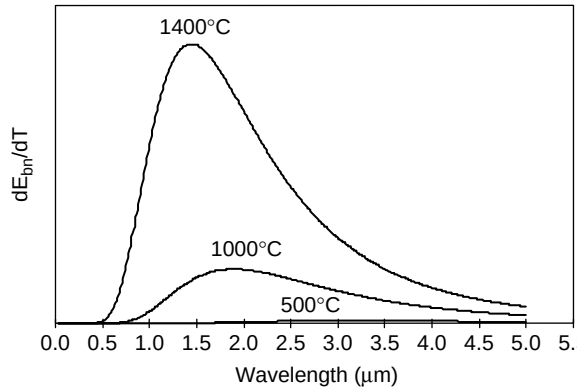

FIGURE 9.6 .Temperature derivative of the Plank function.

two factors of the integrand in Equation 66, $1/\kappa_\lambda$ and the rest of the integrand, which is $dE_{b\lambda}/dT$ (see Section 9.2.4.5.7). Any wavelength region in which either factor of the integrand approaches zero will make a negligibly small contribution to the radiation conductivity, provided the other factor does not approach infinity at the same time.

First, look at the effect of $dE_{b\lambda}/dT$. Figure 9.6 shows $dE_{b\lambda}/dT$ as a function of wavelength for several temperatures. It is seen that for typical glass-melting temperatures, at wavelengths shorter than about 0.5 μm, $dE_{b\lambda}/dT$ is negligible. The figure also indicates that the most important energy transfer region is in the 1–3 μm wavelength range, and that beyond about 3 μm wavelength, the value of $dE_{b\lambda}/dT$ falls off slowly with increasing wavelength.

Now let us see how glass absorption modifies these conclusions. Figure 9.7 shows the absorption coefficient, κ_λ, as a function of wavelength for a soda-lime glass [50, Figure lc]. This spectrum shows features common to many glass spectra. There is strong absorption at short wavelengths due to an electron transfer process between atoms. The absorption edge occurring near 0.5 μm shifts position somewhat with composition. Typically, the edge is between 0.3 and 0.4 μm. In Figure 9.7, the edge is at a larger wavelength because of the high iron content of the glass. In any case, at wavelengths less than about 0.5 μm, both $dE_{b\lambda}/dT$ and $1/\kappa_\lambda$ in Equation (66) are small. Together, they indicate that contribution to the radiative heat transfer at wavelengths less than about 0.5 μm is negligibly small and can be ignored in the radiative heat transfer calculation. There is also strong absorption at wavelengths above about 2.5 μm. The absorption in the 2.5–4.0 μm region results from vibration of the hydroxyl ion, which is present to some degree in all silicate glasses unless care is taken to exclude it. Since the radiative heat transfer has only a very slight dependence on absorption in this wavelength range because of the small value of $dE_{b\lambda}/dT$, little error is introduced by using a single typical absorption spectrum in this region for all silicate glass compositions, particularly since the hydroxyl contents of glasses of interest are seldom known. At wavelengths greater than about 4 μm,

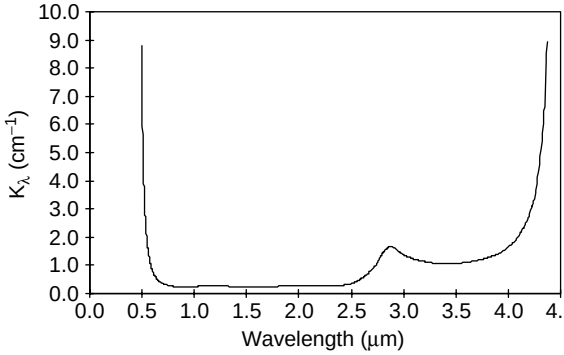

FIGURE 9.7 Soda-lime glass spectrum at 1400°C.

silicate glasses are opaque due to vibration of their basic silica framework, and there is no contribution to the radiative heat transfer.

The refractive index does not modify these conclusions. In the 0.5–4.0 μm region it is a smooth function that depends only weakly on wavelength.

We can therefore replace Equation (66) by a summation over reasonable experimental limits:

$$k_r = \frac{8\pi C_o^3 h^2}{3kT^2} \sum_{\lambda_1}^{\lambda_2} \frac{1}{\kappa_\lambda} \frac{n^2}{\lambda^6} \frac{e^{hc_o/\lambda kT}}{(e^{hc_o/\lambda kT} - 1)^2} \Delta\lambda \tag{67}$$

where: λ_1 = some wavelength less than about 0.5 μm and λ_2 = some wavelength greater than about 4.0 μm.

Calculation of the radiative conductivity therefore reduces to determination of the absorption spectrum in the 0.5–2.5 μm region for any given glass and to the choice of a suitable typical absorption spectrum in the 2.5–4.0 μm region to represent all silicate glasses. The 0.5–2.5 μm region is the minimum necessary. Inclusion of spectral data outside this range, especially above 2.5 μm, may lead to some improvement in the accuracy of the calculation.

9.3.2.3 Glass Absorption Coefficients

The absorption of glass in the 0.5–2.5 μm region is a function of the glass composition and the temperature. Although the most common major components of silicate glasses do not absorb in this region, various minor or tramp materials, in particular the first row transition metal ions, may cause significant absorption. The intensity and wavelength of an ion's absorption depends on its oxidation state and coordination. Both these are influenced by temperature and basic glass composition. This dependence cannot yet be predicted directly from theory with accuracy sufficient for our purpose here. We must rely on measured data. There is a voluminous literature on the absorption spectra of the various coloring ions in glass. Most of this work was done at room temperature and has been well summarized [51–54]. Of those

papers providing high-temperature data [50, 51, 55–63, 64–67], only three present data for silicate glasses over the entire 0.5–2.5 μm range, at several temperatures, and in a form that can be extracted from the report [50, 56, 60]. All three are limited to selected first row transition metals in soda-lime glass.

In published studies the usual experimental arrangement has been to pass light through a glass sample contained in a fused silica crucible with polished bottom or in a precious-metal cell with fused silica windows. The source light beam is chopped prior to passing through the sample, and the intermittent signal analyzed at the detector. More recently, a technique has been developed to calculate the absorption coefficient from high-temperature emission data [62–64, 66, 67]. This technique eliminates the two major difficulties with previous techniques: containment of the glass in an optically transparent medium and detection of the transmitted light in the presence of intense blackbody emission.

Nearly all the results published thus far on high-temperature spectra suffer from a serious shortcoming related to reaction of melt surface with the atmosphere. The effect of melt surface reaction on the spectra has been demonstrated by measuring the spectra at a comparatively lower temperature both before and after high-temperature measurements were conducted [78–80]. The results show that in some cases (e.g., iron containing glasses melted in a reducing atmosphere, glasses with a high concentration of water), the spectra at the lower temperature measured before and after heating the glass differed appreciably. In studies where such comparisons were not performed, the influence of the melt surface reaction may introduce significant errors. The only way to prevent this error is to use techniques that exclude the possibility of interaction between the melt and the atmosphere [82, 83].

In the following sections we review what is known of the absorption of first row transition metal ions in silicate glass at high temperature prior to using this information to construct spectra based on the glass composition. It is necessary to first review briefly concepts related to the absorption coefficient and its measurement. The absorption coefficient is defined by:

$$\kappa_\lambda = -\ln(I_\lambda/I_{o\lambda})/d \tag{68}$$

where: I_λ = intensity of light of wavelength λ transmitted through the sample, $I_{o\lambda}$ = intensity of light of wavelength λ incident on the sample, and d = sample thickness in cm.

An absorption spectrum is typically measured as the base ten logarithm of the ratio of transmitted to incident light intensity for some given sample thickness. The measured quantity is the absorbance, A_λ, given by:

$$A_\lambda = -\log(I_\lambda/I_{o\lambda}) \tag{69}$$

The absorption coefficient can then be calculated from the absorbance as follows:

$$\kappa_\lambda = 2.303A_\lambda/d \tag{70}$$

For a single absorbing species present in low concentration in a non-absorbing medium, the absorbance has a Beer's law dependence on the concentration of the absorbing species and the sample thickness:

$$A_\lambda = \xi_\lambda cd \tag{71}$$

where: ξ_λ = the molar absorptivity of the species in the medium in liter/mole cm and c = the concentration of the absorbing species in moles/liter

If there are several non-interacting absorbing species present, the effects of the various species are additive and Equation (71) becomes:

$$A_\lambda = d \Sigma \xi_{\lambda i} c_i \tag{72}$$

where: $\xi_{\lambda i}$ = the molar absorptivity of species i in the medium in liter/mole cm and c_i = the concentration of species i in the medium in moles/liter.

It should be noted that ξ_λ and c might be stated in other consistent units [e.g., 1/(wt% cm) and wt%]. Combining Equations (70) and (72):

$$\kappa_\lambda = 2.303 \Sigma \xi_{\lambda i} c_i \tag{73}$$

Equation (73) is inconvenient to use in practical applications since we generally know the weight percent of the various absorbing species rather than their molar concentrations. In addition, weight percent is invariant with temperature change, while molar concentration is not. We therefore replace Equation (73) by an equivalent expression in terms of weight percent:

$$\kappa_\lambda = 2.303 \Sigma \xi_{w\lambda i} c_{wi} \tag{74}$$

where: $\xi_{w\lambda i}$ = the absorptivity per weight percent of species i in the medium in weight %/cm and c_{wi} = the concentration of species i in the medium in weight%.

Equation (74) is not strictly correct at higher concentrations, where the absorbance is not a linear function of the concentration expressed as weight percent, but it is a good approximation at most concentrations of practical interest.

If $\xi_{w\lambda}$ and c_w are known for all absorbing species in a non-absorbing medium, it is possible to calculate the absorption coefficient. In the following sections we will review measurements of $\xi_{w\lambda}$ for the most common absorbing species. In general, $\xi_{w\lambda}$ is a function of the base glass composition. Since high-temperature data are available for soda-lime glasses only, application of these data to other compositional systems involves the assumption that $\xi_{w\lambda}$ is only a weak function of composition. This assumption and those inherent in the derivation of Equation (73) are discussed further in Section 9.2.2.7.

9.3.2.4 First Row Transition Metal Ion Absorption in Silicate Glass

We have altered the spectra in the following sections slightly from how they have been presented in the literature. This is because individual spectra will be added at the appropriate concentrations to characterize glasses containing several transition metals. The spectra should thus contain no absorption from other components of the glass. Otherwise, these absorptions would be anomalously high in the composite spectrum. Absorption from other glass components is significant only below about 0.5 μm and above about 2.5 μm. Since these regions make only a small contribution to the total radiative heat transfer, the approximations we make to the spectrum in these regions in order to remove absorptions not due to the metal ions need not be very accurate. At the short wavelength end of the spectrum we have chosen to extend the spectra to 0.3 μm by setting the absorption coefficient equal to its last measured value in the unmeasured range. This is a somewhat arbitrary, very rough approximation in this region, but some spectra have been measured at wavelengths shorter than 0.5 μm, and this procedure allows more accurate use of all the data. In the long wavelength end, we have again somewhat arbitrarily set the absorption coefficient to the measured value at 2.5 μm throughout the region 2.5–4.0 μm.

Molar absorptivity data from various references for selected first-row transition metal ions in soda-lime silicate glasses at room temperature are compiled in Table 9.3. The base glass compositions used in these references are given in Table 9.4.

9.3.2.4.1 Scandium

Scandium does not absorb in the 0.5-2.5 μm region in glass.

9.3.24.2 Titanium

Titanium alone absorbs in the 0.5-2.5 μm region in glass only in highly reducing conditions in which it is present in the +3 state. Titanium will interact with any Fe^{+2} in the glass, causing increased absorption in the ultraviolet and short wavelength region of the visible, but no high-temperature absorption spectra for titanium in glass have been published.

9.3.2.4.3 Vanadium

Johnston [68] studied the oxidation state of vanadium in glass. Vanadium is typically present in glass as a mixture of its +3, +4, and +5 oxidation states. Glasses melted in an air atmosphere contained only the +5 state. Both the +3 and the +4 ions absorb in the 0.5–2.5 μm region. The +5 state absorbs only below about 0.4 μm. Franz [56] measured the high-temperature spectrum for vanadium in soda-lime glass. He did not analyze the glass for the various vanadium species, but we can make estimates based on Franz's spectra for the iron-containing glasses and the relations between vanadium and iron oxidation states and oxygen partial pressure of the melt (pO_2) given by Johnston [68]. These data suggest that Franz's reducing conditions are at a pO_2 in the range –8 to –10. Within this range, vanadium is present as a mixture of V^{+4} and V^{+5}, with negligible V^{+3}. Since V^{+5} does not absorb significantly at wavelengths greater than about 0.4 μm, the reduced glass spectral features published by Franz are due to V^{+4}. Calculations using Coenen's molar absorptivity value (Table

TABLE 9.3
Absorption Band Position (in μm) and Molar Absorptivity (in liter/mole cm) for Selected First-Row Transition Metal Ions in Soda-Lime-Silicate Glass at Room Temperature

	Coenen Table		Coenen Data		Franz Data		Other References		
	Band	x	Band	x	Band	x	Band	x	Ref. No.
V^{+4}	0.41	11							
	0.60	6			0.63		0.61	6	62
	1.09	15			1.05		1.09	19	62
Cr^{+3}	0.45	19	0.46	15					
	0.63	16							
	0.65	17	0.66	11	0.66		0.65	18	64
	0.69	15							
Cr^{+6}	0.36	~10^3					0.37	4200	64
Mn^{+2}	0.42	0.05							
Mn^{+3}	0.49	7.8			0.59		0.50	10	66
Fe^{+2}	1.10	23	1.14	23	1.19		1.06	54	62b
Fe^{+3}	0.39	2.1	0.39	2.3			0.38	5	62b
	0.43	0.8	0.43	1.3			0.41		62b
	0.45	0.8					0.44		62b
	0.53	0.2					0.57		62b
Co^{+2}	0.54	190	0.56	200			0.54	130	67
	0.61	230	0.62	220			0.59	190	67
	0.66	230	0.67	220	640	9	0.64	180	67
	1.33	66	1.33	73	1.32	2	1.28	33	67
	1.50	70	1.54	4	1.59	2	1.49	37	67
	1.80	68	1.81	83	1.81	2	1.79	32	67
Cu^{+2}	0.79	16			0.84				

TABLE 9.4
Base Glass Compositions (Weight%) Used in References Cited in Table 9.3

	SiO_2	CaO	Na_2O
Coenen 50	74	9	17
Franz 56	74	9	17
Reference 58		Soda-lime glass	
Reference 62a		Soda-lime glass	
Reference 62	66		34
Reference 64	69		31
Reference 66	80		20
Reference 67	74		26

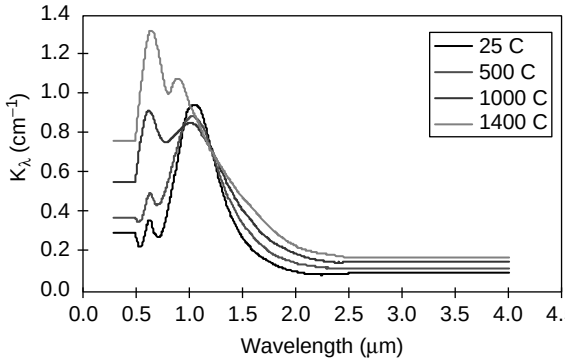

FIGURE 9.8 V^{+4} in soda-lime glass: 0.1% as V_2O_5.

9.3) suggest that about 45% of the vanadium is present as V^{+4}. This allows the calculation of the spectrum in Figure 9.8, which shows the absorption coefficient for V^{+4} as a function of wavelength at various temperatures. Spectra of V^{+3} at high temperature have not been published.

9.3.2.4.4 Chromium

Chromium is typically present in glass in its +3 and +6 oxidation states. Even for highly oxidized glasses, Cr^{+3} is the dominant species. It has been well established that Cr^{+6} and Fe^{+2} cannot both be present in glass simultaneously [69, 70]. Thus, the presence of Fe^{+2} is proof of the absence of Cr^{+6}. Coenen [50] and Franz [56] both present high-temperature spectral data for chromium in glass at two oxidation states. Coenen presents his spectral data in a form that can be extracted more accurately, and he also reports analyses for Cr^{+3} and Cr^{+6}. We will therefore rely on his data rather than that of Franz. All the spectra that Coenen presents for his chromium-containing glasses have Cr^{+3} and Cr^{+6}, but since there is a pair of spectra at different oxidation states for each temperature and we know the amount of each chromium species at each oxidation state, it is possible to solve for the spectra of the pure chromium species. Figures 9.9 and 9.10 are the result of this analysis. The Cr^{+6} spectra (Figure 9.10) contain much noise due to the calculation procedure, but they do indicate that Cr^{+6} does not absorb in the 0.5–2.5 μm region for all spectra except at 1400°C. At 1400°C there is significant absorption in much of the region of interest. It is unclear whether Cr^{+6} does indeed absorb significantly in this region or whether this absorption is an artifact attributable to the calculation.

9.3.2.4.5 Manganese

Manganese is typically present in glass in its +2 and +3 oxidation states. Even for highly oxidized glasses, Mn^{+2} is the dominant species. It has been established that Mn^{+3} and Fe^{+2} cannot both be present in glass simultaneously [70]. Thus, the presence of Fe^{+2} is proof of the absence of Mn^{+3}. The high-temperature spectrum of manganese in glass has been measured in three studies [50, 56, 60] but only Franz [56] published the data. He measured the spectrum at two different oxidation states. In the more reduced case, only Mn^{+2} is present and there is no significant absorption due to

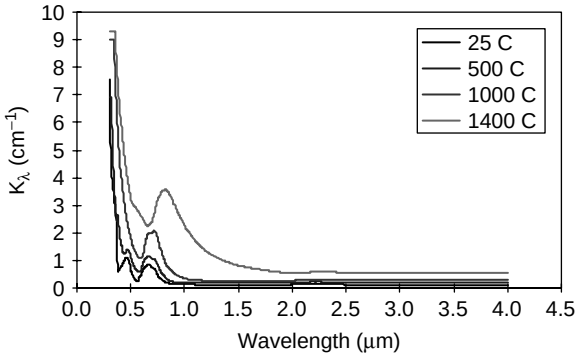

FIGURE 9.9 Cr^{+3} in soda-lime glass: 0.1% as Cr_2O_3.

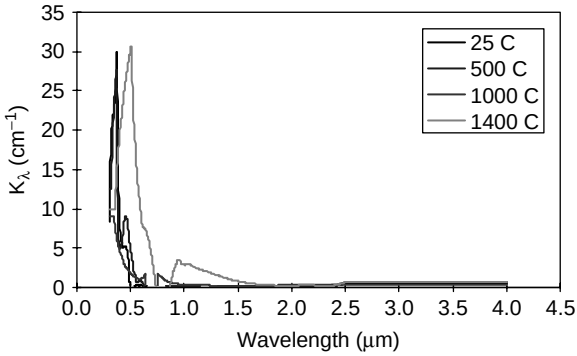

FIGURE 9.10 Cr^{+6} in soda-lime glass: 0.1% as Cr_2O_3.

manganese in the range of measurement. In the more oxidized case there is a single strong absorption band due to Mn^{+3}. At 25°C this occurs near 0.59 μm, a slightly larger wavelength than reported in other references [49, 70; Table 9.3]. Calculations using Coenen's molar absorptivity value suggest that about 60% of the manganese is present as Mn^{+3}. Figure 9.11 shows the absorption coefficient for Mn^{+3} based on these data. We calculated the spectrum at 500°C by linear interpolation from the 25°C and 600°C data at each wavelength.

9.3.2.4.6 Iron

Iron is typically present in glass in its +2 and +3 oxidation states. Under typical melting conditions both species are present in significant amounts. Coenen [50], Franz [56], and Ades et al. [60] and Ades et al. [65] have all measured the high-temperature spectra of glasses containing iron, the first three at several different oxidation states. Since Coenen presents his spectral data in a form that can be extracted more accurately we will rely on his data rather than that of the other three. The absorption of Fe^{+2} and Fe^{+3} can be separated in the same way as those for chromium. Figures 9.12 and 9.13 are the result. Fe^{+3} does not absorb in the 0.5–2.5 μm region, but it does cause an intense absorption in the ultraviolet, making the

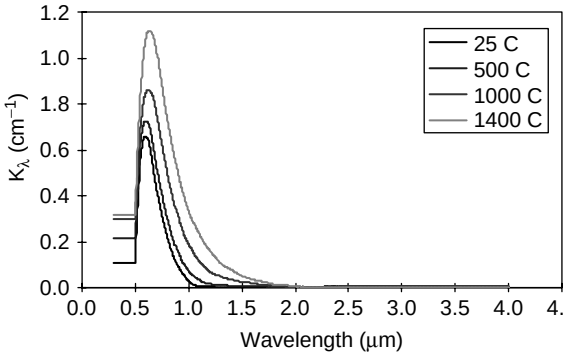

FIGURE 9.11 Mn^{+3} in soda-lime glass: 0.1% as MnO.

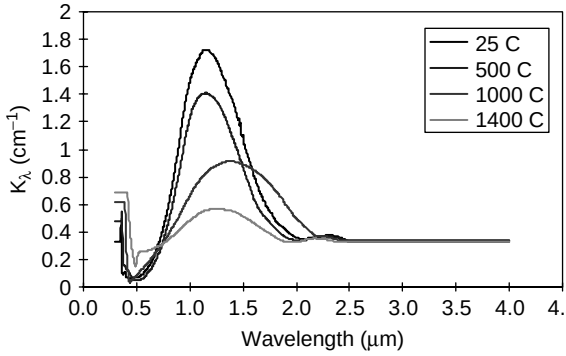

FIGURE 9.12 Fe^{+2} in soda-lime glass: 0.1% as Fe_2O_3.

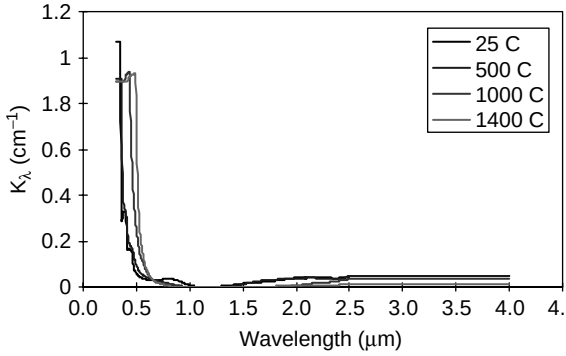

FIGURE 9.13 Fe^{+3} in soda-lime glass: 0.1% as Fe_2O_3.

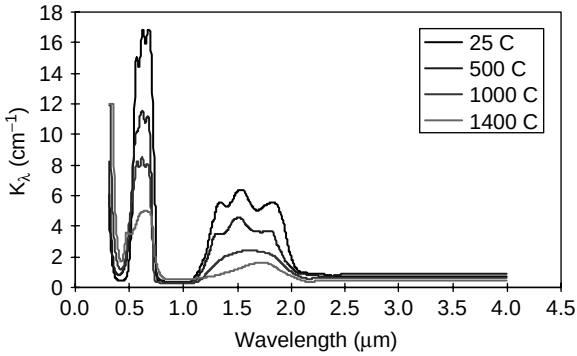

FIGURE 9.14 Co^{+2} in soda-lime glass: 0.1% as CoO.

glass opaque at wavelengths slightly less than 0.5 μm. It also has several weak absorption bands in this region.

9.3.2.4.7 Cobalt

Cobalt is typically present in glass only in the +2 oxidation state. Coenen [50] has suggested that it is present in two coordination states, fourfold (tetrahedral) and sixfold (octahedral). He indicates that Co^{+2} absorbs at about the same wavelengths in the two coordination states but that the intensity of its absorptions is considerably lower in sixfold coordination. He interprets a decrease in absorption intensity with temperature as a result of a shift to sixfold coordination. Other workers [54, 72] have found no evidence for sixfold coordination of Co^{+2} in a wide range of glass compositions at room temperature. Given this disagreement and the difficulty of determining coordination state, we will not attempt to separate the effects of cobalt in two coordination states. Coenen [50] and Franz [56] have measured the high-temperature spectra of glasses containing cobalt. The absorption coefficients reported by Franz are over an order of magnitude lower than those of Coenen and other workers [54, 72], suggesting an error in the data presentation. We will therefore rely on Coenen's data, which appears in Figure 9.14.

9.3.2.4.8 Nickel

Nickel absorbs strongly in the 0.2–2.5 μm region [50, 54]. Coenen [50] has shown that it can have a significant effect on heat transfer and has developed means to calculate the effect as a function of nickel content and temperature in the absence of other absorbing metal ions. No one has published high-temperature spectra of glasses containing nickel, and without these data it is impossible to calculate the effect of nickel in combination with other absorbing metal ions.

9.3.2.4.9 Copper

Copper is typically present in glass in its +1 and +2 oxidation states. Under typical melting conditions, both species may be present in significant amounts. Franz [56] has measured the high-temperature spectra of glasses containing copper at two different oxidation states. In the more reduced case, only Cu^{+1} is present, and there is no absorption due to copper in the range of measurement. In the more oxidized

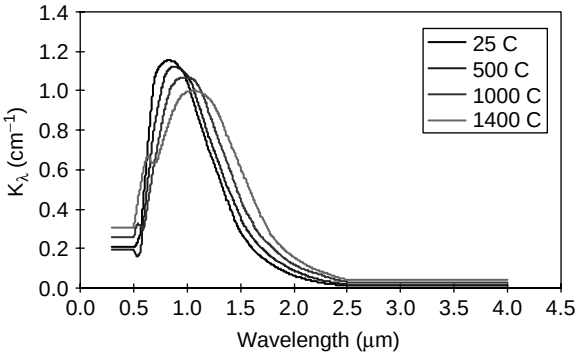

FIGURE 9.15 $Cu^{+}2$ in soda-lime glass: 0.1% as CuO.

case, there is a strong absorption band near 0.84 μm due to Cu^{+2}. Calculations using Coenen's molar absorptivity value suggest that about 93% of the copper is present as Cu^{+2}. Figure 9.15 shows the absorption coefficient for Cu^{+2} based on these data. We calculated the spectrum at 500°C by linear interpolation from the 25°C and 600°C data at each wavelength.

9.3.2.4.10 Zinc

Zinc does not absorb in the 0.5–2.5 μm region in glass.

9.3.2.5 Hydroxyl Ion Absorption in Silicate Glass

Absorption of silicate glasses in the 2.5–4.0 μm region is due primarily to the hydroxyl ion. A number of studies include spectral data in this wavelength range for silicate glasses at high temperature [50, 55, 56, 58-60, 66, 67] or are focused on hydroxyl absorption in silicate glasses [57, 73, 74]. The absorption coefficients have been measured for hydroxyl ion in a variety of silicate glasses [73], and it would be possible to treat this ion in the same way as for the transition metal ions. But the situation is somewhat different here for three reasons:

1. The magnitude of the hydroxyl absorption has only a small effect on the total radiative heat transfer due to the wavelength region in which it occurs.
2. The absorption of certain transition metal ions including Fe^{+2}, which is a common trace constituent of silicate glasses, extend into the region of hydroxyl absorption. The approximations we have made to quantify the absorptions of these ions in this region have already introduced considerable approximation in the magnitude of the absorption.
3. The hydroxyl absorption depends on both the content and structure of the hydroxyl ion in glass. We seldom have these data, which are necessary to calculate the absorption.

We have chosen to use a typical set of glass spectra (Figure 9.16) to represent the absorption of all silicate glasses in the range 2.5–4.0 μm. These spectra are of

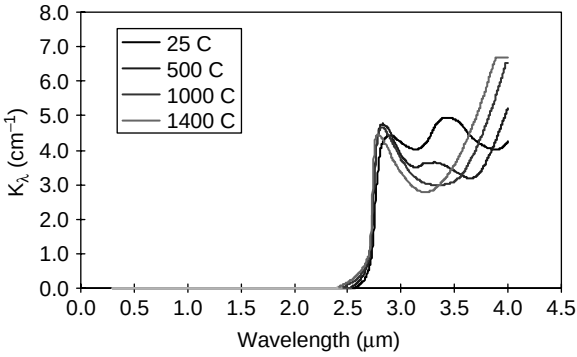

FIGURE 9.16 OH- in soda-lime glass: typical level.

the soda-lime glass measured by Franz [56]. Its composition is shown in Table 9.3. Its hydroxyl content has not been measured, but the absorption intensity suggests that it is about 0.03%, based on a room temperature molar absorptivity near 50 l/mole cm at 2.90 μm [74].

9.3.2.6 Calculation of Photon Thermal Conductivity

We are now in a position to return to Equation (67) for the calculation of photon thermal conductivity. This equation has only two unknown independent variables: the absorption coefficient and the refractive index. Both are dependent on wavelength, temperature, and glass composition.

Provided the glass does not contain an absorbing species for which we have no data (such as Ni^{+2}), we can approximate the absorption coefficient at various temperatures by combining the appropriate spectra from Figures 9.8–9.16. This is an approximation because it assumes that the transition metal ion absorptions are independent of each other, the base glass composition, and the presence of other minor constituents. This assumption is forced upon us by the paucity of data. We will discuss the error this introduces into the calculation in a later section.

The refractive index is only a weak function of wavelength and temperature. Measurements on modifications of soda-lime glasses indicate that the refractive index decreases by about 0.07 across the 0.5–4.0 μm range (T. G. Laskowski, personal communication, 1989). The refractive index also decreases with temperature due to glass expansion. It is possible to approximate the temperature-related decrease using the relationship between density and refractive index for the silica polymorphs [75], and the measured glass density change with temperature [76]. Based on this, the refractive index at 1400°C, the highest temperature for which we have spectral data, is about 0.04 lower than the value at room temperature. These estimates are probably fairly accurate for most silicate glasses of interest and allow us to calculate the refractive index, a function of temperature and wavelength, from a given point. A convenient choice for our purposes is its value at room temperature for sodium D light (0.59 μm).

We are now in a position to calculate the photon thermal conductivity as a function of temperature for a given glass based on its transition metal oxide con-

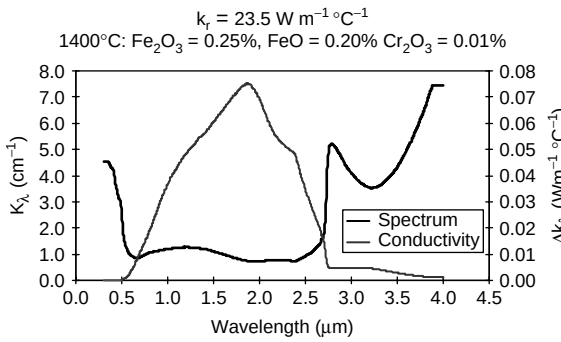

FIGURE 9.17 Calculated high temperature spectrum and corresponding differential photo thermal conductivity.

centration and its refractive index. The absorption coefficient can be calculated in the range 0.5–4.0 μm at four temperatures using Equation (74) and Figures 9.8–9.16. The corresponding refractive index values can be calculated from one measured value (for instance, room temperature and 0.59 μm) and the relations described in the preceding paragraph. These values can then be used with Equation (67) to calculate the photon thermal conductivity at these temperatures. For intermediate temperatures (for which little if any published data exists), a reasonable approximation can be obtained by interpolating the spectral data in Figures 9.8–9.16.

As an example of the application of the photon thermal conductivity calculations, let us examine the effect of varying Fe^{+2} and Cr^{+3} concentrations in the range typical of commercial glasses for a soda-lime glass at 1400°C. We will assume the glasses all have a sodium D line refractive index of 1.5 and a hydroxyl content equal to that of the glass in Figure 9.16. For various amounts of Fe^{+2} and Cr^{+3} at a constant level of Fe^{+3}, we construct high-temperature spectra using Equation (74) and the 1400°C data from Figures 9.9, 9.12, 9.13 and 9.16. We then calculate the refractive index as a function of wavelength at 1400°C as described previously. The resulting data are then used with Equation (67) to calculate the photon thermal conductivity for each compositional variation. The spectrum and differential photon thermal conductivity in Figure 9.17 are an example of the calculated results.

In Figure 9.18 the results of a 2-dimensional least-squares fit to the calculated photon conductivities of all the compositional variations show the dependence of the photon thermal conductivity on Fe^{+2} and Cr^{+3}.

The data summarized in Figure 9.18 indicate the following:

a. The effects of Fe^{+2} and Cr^{+3} on photon thermal conductivity are nonlinear. When they are present in glass in low concentration, changes in their concentrations have a larger effect than when they are present in high concentration. This is a direct effect of the inverse dependence of photon thermal conductivity on the absorption coefficient.
b. On a weight % basis, Cr^{+3} (as Cr_2O_3) has about twice the effect of Fe^{+2} (as Fe_2O_3) on photon thermal conductivity.

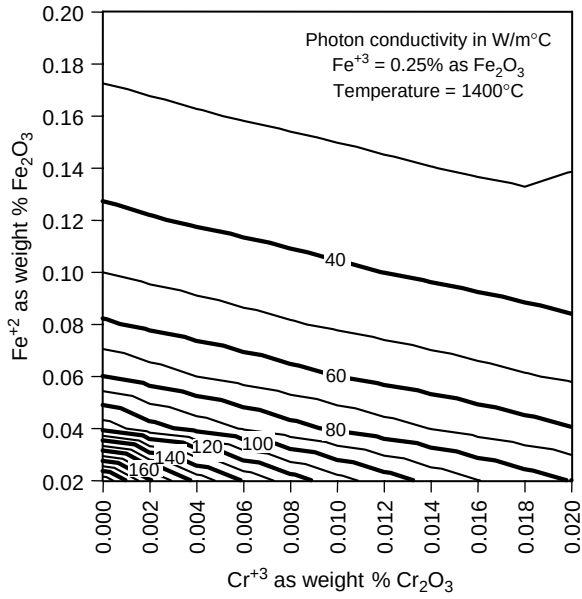

FIGURE 9.18 The effect of $Fe^{+}2$ and Cr^{+3} on high temperature photon thermal conductivity.

As a second example, let us look at the relative effects of the various ions on the photon thermal conductivity of a typical soda-lime glass at 1400°C. Because of the nonlinear relation between spectral absorption and conductivity, the effects of the various ions on the phonon thermal conductivity will depend on the base glass composition. We will choose the base glass to have 0.05% Fe^{+2} as Fe_2O_3 and 0.25% Fe^{+3} as Fe_2O_3 since iron is a common contaminant of commercial glasses. Figure 9.19 shows the effects of various ions for additions up to 0.1% of the oxides. The ions fall roughly into four groups relative to their effect on phonon thermal conductivity for this base glass:

1. Fe^{+3}: This has little effect, partly because it has strong absorption only below about 0.7 μm and partly because there is already 0.25% of it in the base glass.
2. Mn^{+3}: This has a small effect because it has strong absorption only below about 1.0–1.5 μm.
3. Cu^{+2}, V^{+4}, and Fe^{+2}: These have moderate effects due to moderate absorption throughout much of the important 0.5–2.5 μm region. Fe^{+2} would have a significantly greater effect if there were not already 0.05% in the base glass.
4. Co^{+2} and Cr^{+3}: These have a strong effect due to strong absorption in much of the important 0.5–2.5 μm region.

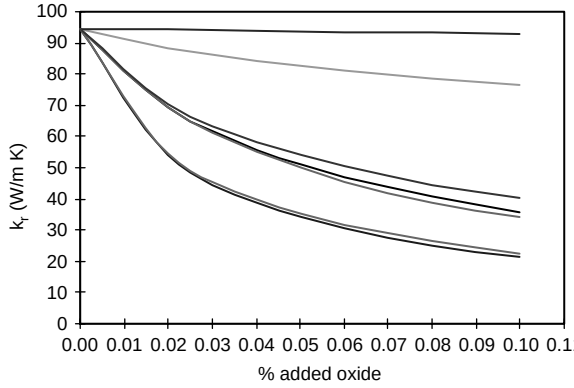

FIGURE 9.19 Effect of various ions on photon conductivity of a soda-lime glass at 1400°C. Base glass contains 0.05% Fe^{+2} as Fe_2O_3 and 0.25% Fe^{+3} as Fe_2O_3. Curves from highest to lowest k_r are: Fe^{+3} as Fe_2O_3, Mn^{+3} as MnO, Cu^{+2} as CuO, V^{+4} as V_2O_5, Fe^{+2} as Fe_2O_3, Co^{+2} as CoO, Cr^{+3} as Cr_2O_3.

9.3.2.7 Errors Associated with the Calculation

Errors associated with the photon thermal conductivity calculation method derived here are summarized below:

a. There are a number of approximations in the derivation of Equation (67), which relates photon thermal conductivity to absorption coefficient.
   i. *Optically thick conditions:* The optically thick condition must apply for the concept of photon thermal conductivity to have any meaning.
   ii. *Elimination of boundaries:* The derivation is not applicable for those regions of the glass body that are near boundaries. How close to a boundary the equations apply depends on the glass — the more strongly absorbing the glass, the closer to the boundary the equations apply. Typical boundary layers, in which the equations do not apply, are of the order of several centimeters.
   iii. *Moderate temperature gradients:* We must assume that the temperature gradient is small enough that the higher-order derivatives of the Planck function ($E_{b\lambda}$ in Equation (46), Section 9.I.4.5.6.) are negligible compared with the first derivative. For steady state conditions, this is a reasonable assumption but has not been evaluated explicitly.
   iv. *Integration limits:* The wavelength and temperature dependence of the Plank function, together with the nature of a typical glass absorption spectrum, allow us to limit the integration to a region in which spectral data are available without introducing significant errors. This is true for all silicate glasses. Doubling or halving the absorption intensity in the 2.5–4.0 μm region changes the calculated photon thermal conductivity by 2–3% for typical glass compositions.
b. Refractive index: We have chosen to calculate the refractive index as a function of temperature and wavelength from a single value (room tem-

perature and 0.59 μm) as discussed above. If a constant refractive index (at room temperature and 0.59 μm) is used in the heat transfer calculation at 1400°C, the result is about 4% greater than that using the variable refractive index. At room temperature, the results are the same (the errors in temperature and wavelength cancel). Since our approximation is certainly much better than that of a constant refractive index, the error introduced by this approximation is probably less than 1%.

c. Glass absorption coefficient: This is probably the major source of error in the calculation. This error arises from several sources:
   i. *Accuracy of the measured data:* Measurement of high-temperature absorption spectra is experimentally difficult. In the light-transmission techniques that generated the data that we use here, dissolution of the container by the glass and interference by the high-intensity black body radiation emitted by the glass could significantly alter the glass spectrum. Information provided in the literature is insufficient to allow an estimate of probable error.
   ii. *Uncertainty in glass oxidation state:* Many of the constituents that strongly affect the glass absorption coefficient can be present in the glass in two or more oxidation states, each affecting the absorption coefficient differently. To relate the concentration of such multivalent constituents to the glass absorption spectrum, it is essential to know in what valence states the constituent is present in the glass and how much of each valence state is present. Further, since the oxidation state of a glass can be changed during heating, chemical analysis should be performed after the high-temperature spectrum is measured. This still leaves some uncertainty due to possible changes during the quenching of the glass.
   iii. *Extraction of data from the literature:* Published spectral data is in the form of spectral curves. We have digitized these from copies of the curves that have been enlarged on a photostatic copier. This involves error that is particularly significant when the absorption coefficient is near zero. In calculation of the photon thermal conductivity (Equation 67), the absorption coefficient enters in the denominator. Thus, in wavelength regions in which the absorption coefficient tends to zero, the photon thermal conductivity can become very large. Coenen [50] plots his data in log form, which reduces this error considerably. But Franz [56] plots the absorption coefficient directly and in poor resolution. The error in the radiative conductivity arising from this source will be highly variable, depending on which transition metals are present in the glass and in what concentration. The worst cases would be for small concentrations of Mn^{+3} or Fe^{+3}, which have very low absorption throughout the 0.5–4.0 μm region. For Mn^{+3}, increasing the absorption coefficient throughout the spectrum by the line width of the published spectrum decreases the calculated phonon thermal conductivity by a factor of about 2 for 0.1% Mn^{+3} as MnO at 1400°C. For Fe^{+3} alone, the absorption spectrum calculated from Coenen's data on iron in mixed valence states is zero or negative at some wavelengths,

and the photon thermal conductivity cannot be calculated. For more typical glass compositions, the error is much less. There is also a large uncertainty associated with the spectra for Cr^{+6} due to the difference method we used to calculate them from the literature data.

iv. *Interaction of different metal ions:* Calculation of spectra from the published data assumes that there is no interaction between the different transition metal oxides that significantly affects the absorption coefficient. In some cases, different transition metal ions, or transition metal ions in different oxidation states, can interact by exchanging electrons. Such exchanges can lead to strong absorption bands in the region of the spectrum important for heat transfer. We are forced into ignoring these interactions because of the lack of data.

v. *Effect of glass composition:* All published high-temperature spectra are of soda-lime glass with the exception of those of Goldman and Berg [59, 62] and Fabris and Huclin [66]. These references contain spectra on iron-containing glasses that differ significantly in composition from soda-lime glass, but the absence of data below about 1 μm makes it difficult to assess any effect of the different compositions. Nelson and White [72] have published room temperature spectra showing that the maximum absorption intensity of Co^{+2} can vary by as much as a factor of 6 depending on the composition of the silicate-based glass in which it is found. It therefore seems likely that base glass composition can have a large effect on the high-temperature absorption coefficient of transition metal ions, although this has not yet been demonstrated directly.

9.4 SUMMARY

Our principal concern in this chapter was with thermal radiation in glass-forming melts and the radiative properties of these melts. Glass-forming melts are semitransparent — i.e., they attenuate electromagnetic waves passing through them. In the first part, we presented a phenomenological treatment of thermal radiation in a semitransparent medium. Our objective in doing so was to provide enough detail for a reader to gain physical insights into radiation in glass-forming melts and develop an understanding of when and how approximations such as optically thick limit can be applied. Heat transfer in semitransparent media has been discussed in considerable depth in several excellent texts. Our treatment of this subject is relatively simple (e.g., we ignored scattering of radiation by inhomogeneities in glass melts) and intended for glass scientists and engineers. In keeping with the theme of this book, namely properties of glass-forming melts, we focused on the concept of radiation or photon thermal conductivity and described how this parameter could be calculated from spectral data.

In the second part of this chapter, we provided an extensive review of published data on absorption spectra for glasses and glass-forming melts. We built upon an earlier comprehensive review of thermal conductivity data in glass published by the International Commission on Glass [3]. In our review, we focused on the absorption

characteristics of several transition metal ions and the hydroxyl ion. Finally, we illustrated how photon thermal conductivity can be calculated from the high-temperature spectra and discussed sources of error in this calculation.

As noted above, our main concern in this chapter was with thermal radiation and photon thermal conductivity. However, glass scientists and technologists are often also interested in an effective thermal conductivity that is the sum of the atomic or phonon thermal conductivity and the photon thermal conductivity. Therefore, in part 2 of this chapter, we also reviewed experimental data on phonon thermal conductivity and calculated coefficients for the evaluation of this property from glass composition.

We hope that this chapter will prove to be a valuable resource for those concerned with heat transfer in glass-forming melts.

ACKNOWLEDGMENTS

The authors thank Dr. Oleg V. Mazurin of THERMEX, St. Petersburg, Russia for a thorough review of the manuscript and for many valuable suggestions. His comments were most helpful in improving the quality of this manuscript. We also thank Ms. Stefanie Nielsen and Ms. Sue Tossmann for help with the preparation of the manuscript, and Owens Corning management for allowing the publication of this work.

REFERENCES

1. Kittel, C. (1949). Interpretation of thermal conductivity of glasses. *Physical Rev.*, 75(6):972–974.
2. Kingery, W. D. (1961). Heat-conductivity processes in glass. *J. Am. Ceram. Soc*. 44(7):302–304..
3. Blazek, A. (1983). Review of thermal conductivity data in glass. International Commission on Glass, Belgium.
4. Mann, D., Field, R. E., and Viskanta, R. (1992). Determination of specific heat and true thermal conductivity of glass from dynamic temperature data, *Wärme-und Stoffübertragung*, v 27, 225—231.
5. Sato, S., Furuya, H., Nishino, Y., and Sugisaki, M. (1985). Thermal conductivity of simulated radioactive waste glass. *Nucl. Technol*. v 70, 235—242.
6. Sparrow, E. M. and Cess R. D. (1978). *Radiation Heat Transfer.* Washington D.C.: Hemisphere Publishing, pp. 3–20, 203–234.
7. Eckert, E. R. G. and Drake, R. M. (1972). *Analysis of Heat and Mass Transfer.* New York: McGraw-Hill, p. 524 for Boussinesq approximation for natural convection, 596–642.
8. Chandrasekhar, S. (1960). *Radiative Transfer*, New York: Dover Publications; New York.
9. Viskanta, R. and Anderson, E. E. (1975). *Heat Transfer in Semitransparent Solids.* Advances in Heat Transfer, Eds. T. F. Irvine, Jr. and J. P. Harnett, v 11, New York: Academic Press, pp. 317–441.
10. Siegel, R. and Howell J. R. (1981). *Thermal Radiation Heat Transfer.* New York, McGraw-Hill. Pp. 80–117.
11. Hottel, H. C. and Sarofim, A. F. (1967). *Radiative Transfer.* New York, McGraw-Hill. pp. 4–20, 326–335.

12. Czerny, M. and L. Genzel, L. (1952). Energy flux and temperature distribution in glass baths of melting tanks resulting from conduction and radiation. *Glastech. Ber.*, 25(12): 387–392.
13. Geffcken, W. (1956). Transmission of heat in glass at high temperatures. *Glastech. Ber,* 25(12):392–396, (1952), 29(2):42–49.
14. Genzel, L. (1953). Role of radiation in heat transfer processes. *Z. Physik* 135(2):177–195.
15. Genzel, L. (1953). Calculation of radiation conductivity of glasses, *Glastech. Ber.* 26(3):69–71.
16. Czerny, M., Genzel, L. and Heilmann, G. (1955). Radiation flux inside glass tanks. *Glastech. Ber.* 28(5):185–190.
17. Gordon, R. (1961). A review of radiant heat transfer in glass. *J. Am. Cer. Soc.* 44(7):305–312.
18. Condon, E. U. (1968). Radiative transport in hot glass. *J. Quant. Spectrosc. Radiat. Transfer.* 8:369–385.
19. Chui, G. K. and Gardon, R. (1969). Interaction of radiation and conduction in glass. *J. Am. Cer. Soc*. 52(10):548–553.
20. Viskanta, R. and Song, T. H. (1985). On the diffusion approximation for radiation transfer in glass. *Glastech. Ber.* 58(4):80–86.
21. Grove, F. J., Charnock, H., and Beattie, J. R. (1960). The Spectral Transmission of Glass at High Temperatures and its Application to Heat-Transfer Problems and Techniques of Temperature Measurement. In: Symposium on Heat Transfer Phenomena in Glass, Glass Division of American Ceramic Society. Philadelphia, April 24–28, 1960.
22. Rawson, H. (1980). *Properties and Applications of Glass.* New York: Elsevier, pp. 193–229.
23. Ratcliffe, E.H. (1963). A survey of the most probable values for the thermal conductivities of glasses between about –150 and 100°C, including new data on twenty-two glasses and a working formula for the calculation of conductivity from composition. *Glass Technol.*, 4:113–128.
24. van Velden, P.F. (1965). Thermal conductivities of some lead and bismuth glasses. *Glass Technol.*, 6:166–169.
25. Krüger, J. (1972). Thermal properties of sodium silicate glasses at low temperatures. *Phys. Chem. Glasses*. 13:9–13.
26. Ammar, M. M., El-Badry, K. H., Moussa, M. R., Gharib, S, and Halawa, M. (1975). Thermal conductivity of some titania and lithia glasses. *Glass and Ceram. Bull.* 22:10–13.
27. Terai, R., Hori, M, and Yamanaka, H. (1979). Thermal conductivity of mixed-alkali glasses. *Am. Ceram. Soc. Bull.* 58:1125.
28. Primenko, V.I. (1980). Theoretical method of determining the temperature dependence of the thermal conductivity of glasses. *Glass and Ceram.* 37:240–242.
29. Muratov, A. B., and Chernyshov, A.V. (1979). Thermal conduction of silicate glasses in the low temperature region. *Sov. J. Phys. Chem.* 5:100–102.
30. Ghoneim, N. A. (1980). Thermal conductivity of some glass–ceramics. *Sprechsaal* 113:610-611.
31. Ammar, M. M., Gharib, S., El Badry, K. M., Ghoneim, N. A., El Batal, H. A., (1982). Thermal conductivity of some sodium aluminosilicate glasses. *Sprechsaal*. 115:692–693.
32. Varilov, Y. V., Komarov, V. E., and Tabunova, N. A. (1982). Calculation of thermal conductivity of glasses. *Sov. J. Glass Phys. Chem*., 8, 326-330.

33. Nassar, A. M. A., Ghoneim, N. A., Abbas, A. F. (1982). Thermal conductivity of some lead silicate glasses. *Sprechsaal* 115:429–430.
34. Ammar, M. M., Gharib, S., Halawa, M. M., El Badry, K., Ghoneim, N. A., and El Batal, H. A., (1982). Thermal conductivity of some silicate glasses in relation to composition and structure. *J. Non-Cryst. Solids* 53:165–172.
35. Ammar, M. M., Gharib, S. A., and Halawa, M. M. (1983). Thermal conductivity of some silicate and borate glasses. *J. Am. Ceram. Soc.* C76-C77.
36. Ghoneim, N. A., ElBatal, H. A., and El Badry, K. (1983). Thermal conductivity of some ternary silicate glasses containing Fe_2O_3 in relation to composition and structure. *Glastech. Ber.* 56:934–938.
37. Ghoniem, N. A., and Ahmed, A. A. (1983). Effect of transition metal oxides on the thermal conductivity of glass. *Thermochim. Acta.* 71:43–51.
38. Salman, S. M., Ghoneim, N. A., and Gharib, S. (1984). Thermal conductivity of lithium iron silicate glasses. *Thermochim. Acta.* 72:269–276.
39. Salman, S. M., and Garib, S. (1984). Some physical properties concerning the thermal conductivity data in BaO-containing silicate glasses in relation to structure. *Thermochim. Acta.* 82:345–355.
40. Salman, S. M., and Garib, S. (1984). Thermal conductivity of some multicomponent silicate glasses. *Thermochim. Acta.* 77:227–239.
41. Ghoneim, N. A., and Halawa, M. M. (1985). Effect of boron oxide on the thermal conductivity of some sodium silicate glasses. *Thermochim. Acta.* 83:341–345.
42. Salama, S. N., Salman, S. M., Gharib, S. (1987). Thermal conductivity of some silicate glasses and their respective crystalline products. *J. Noncryst. Solids.* 93:203–214.
43. Bansal, N. P., and Doremus, R. H. (1986). *Handbook of Glass Properties*, London: Academic Press, Inc. 207–219.
44. Endrys, J., Blazek, A., Ederova, J. (1993). Experimental determination of the effective thermal conductivity of glass by the steady-state method. *Glastech. Ber.* 66:151–157.
45. Derby, J. U. (1982). The Measurement of Thermal Diffusivity of Simulated Glass Forming Nuclear Waste Melts. M.S. Thesis, Alfred University, Alfred, NY.
46. Derby, J. U., Pye, D. L., and Plodinec, M. J. (1983). The measurement of thermal diffusivity of simulated glass forming nuclear waste melts. In: *Advances in Materials Characterization, Vol. 15*, Rossington, D.R., Condrate, R. A., and Snyder, R. L. Eds., Plenum Press, New York.
47. Liem, M. Y. (1984). The Thermal Diffusivity of Simulated Nuclear Waste Glass Below the Glass Transition Range. M.S. Thesis, Alfred University, Alfred, NY.
48. Jain, A. (1987). Automated Thermal Diffusivity Measurement of Glasses and Their Melts. M.S. Thesis, Alfred University, Alfred, NY.
49. Jain, J., and Pye, L. D. (1988). Automated Thermal Diffusivity Measurements of Glasses and Their Melts. In: *Advances in the Fusion of Glass*, American Ceramic Society, Westerville, OH, 40.1–40.13.
50. Coenen, M. (1968). Durchstrahlung des Glasbades bei Farbgläsern. *Glastech. Ber.* 41:1–10.
51. Yoon, I. (1977). Absorption spectra of transition metal ions in glasses as functions of oxygen pressure, temperature, and composition. Ph.D. Thesis, Iowa State University, Ames, IA.
52. Smith, H. L., and Cohen, A. J. (1963). Absorption spectra of cations in alkali-silicate glasses of high ultra-violet transmission. *Phys. Chem. Glasses.* 4:173–187.

53. Bates, T. (1962). Ligand field theory and absorption spectra of transition metal ions in glass. In: Mackenzie, J.D., Ed., *Modern Aspects of the Vitreous State II.* 195–254 London: Butterworths.
54. Bamford, C. R. (1962). The application of the ligand field theory to colored glasses. *Phys. Chem. Glasses.* 3:189–202.
55. Grove, F. J. (1961). Spectral transmission of glass at high temperatures and its application to heat-transfer problems. *J. Am. Ceram. Soc.* 44:317–320.
56. Franz, H. (1971). Infrared absorption of molten soda-lime-silica glasses containing transition metal oxides. *Proceedings of Ninth International Congress on Glass*, Versailles.
57. Wedding, B. (1975). Measurements of high-temperature absorption coefficients of glasses. *J. Am. Ceram. Soc.* 58:102–105.
58. Blazek, A., Endrys, H., Kada, J., and Stanek, J. (1976). Strahlungswärmeleitfähigkeit von Glas Einfluss der Glaszusammensetzung auf seine Wärmedurchlässigkeit. *Glastechn. Ber.* 49:75–81.
59. Goldman, D. S., and Berg, J. I. (1980). Spectral study of ferrous iron in Ca-Al-borosilicate glass at room and melt temperatures. *J. Non-Cryst. Solids* 38 & 39:183–188.
60. Ades, C., Traverse, J. P., and Naudin, F. (1983). Spectres d'absorption des oxydes de fer, de chrome et de manganese dans des verres silico-sodocalciques à temperature et elevée jusqu'à 1450°C. *Thirteenth International Congress on Glass.* pp. 530–535.
61. Blazek, A., Endrys, J., Tydlitat, V., Kada, J., and Stanek, J. (1971). Messung der Stärhlungsleitfähigkeit von Glas bei Temperaturen bis 1400°C. *Ninth International Congress on Glass*. pp. 735–755.
62. Berg, J. I. (1981). Near infrared absorption coefficient of molten glass by emission spectroscopy, *Int. J. Thermophys.* 2:381–394.
63. Banner, D., and Klarsfeld, S. (1992). High temperature infrared spectra of silicate melts. *Phys. Non-cryst. Solids.* pp. 371–375.
64. Shiraishi, Y., and Kusabiraki, K. (1990). Infrared spectrum oh high temperature melts by means of emission spectroscopy. *High Temp. Sci.* 28:67–77.
65. Ades, C., Toganidis, T., and Traverse, J. P. (1990). High temperature optical spectra of soda-lime-silica glasses and modelization in view of energetic applications. *J. Non-Cryst. Solids*. 125:272–279.
66. Fabris, R., and Huclin, J.C. (1994). Identification method for infrared adsorption spectra of semitransparent meedia by their emission data: Application to lime-aluminosilicate glasses at high temperatures. *Glastech Ber.* 67:81–86.
67. Sakami, M., and Lallemand, M. (1994). Spectres infrarouges de verres à haute temperature par inversion de l'émission thermique de couches anisothermes. *J. Phys. III France*. 4:953–965.
68. Johnston, W. D. (1965). Optical spectra of the various valence states of vanadium in $Na_2O.2SiO_2$ glass, *J. Am. Ceram. Soc.* 48:608–611.
69. Paul, A.; and Douglas, R.W. (1966). Mutual interaction of different redox pairs in glass. *Phys. Chem. Glass.* 7:1–13.
70. Close, W.P., and Tillman, J.F.; Chemical analysis of some elements in oxidation-reduction equilibria in silicate glasses. *Glass Technol*., 10, 134–146 (1969).
71. Nelson, C., and White, W.B. (1980). Transition metal ions in silicate melts–I. Manganese in sodium silicate melts. *Geochim. et Cosmochim. Acta*. 44:887–893.
72. Nelson, C., and White; W.B. (1986). Transition metal ions in silicate melts–IV. Cobalt in sodium silicate and related glasses. *J. Mater. Res.* 1:130–138.

73. Scholze, H. (1959). Der Einbau des Wassers in Gläsern I. Der Einfluss des in Glas gelösten Wassers auf das Ultrarot-Spektrum und die qualitative ultrarotspektroskopische Bestimmung des Wassers in Gläsern. *Glastech. Ber.* 32:81–88.
74. Scholze, H. (1959). Der Einbau des Wassers in Gläsern IV. Der Einfluss der Temperatur. *Glastech. Ber.* 32:314–320.
75. Deer, W. A., Howie, R. A., and Zussman, J. (1971). *Rock-Forming Minerals.* Vol. 4. London: Longmans.
76. Berg, J. I. (1977). unpublished data.
77. Choudhary, M. (1985). Three-dimensional mathematical model for flow and heat transfer in electric glass furnaces. *Heat Transfer Engineering*. 6(4) pp. 55–65.
78. Mazurin, O. V., Ed., (2002). MDL-SciGlass ™ 5.0, MDL Information Systems, San Leandro, CA.
79. Neuroth N. (1952) Der Einfluß der Temperatur auf spectrale Absorption von Gläsern im Ultraroten. *Glastechn. Ber.* 25, 242–249.
80. Endrys, J., Geotti-Bianchini, F., and De Riu, L. (1997). Study of the high-temperature spectral behavoir of container glass. *Glastechn. Ber. Glass Sci.Technol.* 70, 126–136.
81. Grove F.J., and Jellyman M.A. (1955). The infrared transmission of glass in the range room temperature to 1400ºC. *J. Soc. Glass Technol*. 39, 3-15T.
82. Prokhorenko O.A. (1998). Experimental cell for measurement of temperature dependence of absorption spectra of molten glass at temperatures up to 1550°C. *Proc. Colloquium on Modeling of Glass Forming Processes,* University of Valenciennes, France. 35–41.
83. Mazurin, O. V., and Prokhorenko, O. A. (2001). Thermal conductivity of glass-forming melts. *Glass Res. Bull. Glass Sci. Eng*., 10/11, 36–38.

10 Electrical Conductivity of Glass Melts

Oleg V. Mazurin and Oleg A. Prokhorenko

CONTENTS

10.1 INTRODUCTION

The ability of a substance to conduct an electrical current is called the electrical conduction. If a certain conducting body is placed between two electrodes to which the difference of electrical potentials V is applied, the current A which is going through the body is described by the following equation:

$$A = V \cdot \sigma \cdot S/d \tag{1}$$

where S is the area of electrodes, d is the distance between electrodes, and σ is a constant characterizing the ability of the substance to conduct electricity. This constant is called the electrical conductivity and is equal to the conduction of the sample of the corresponding substance in the form of a cube. In the SI system of units this value is expressed in $S \cdot m^{-1}$ where S stands for Simens which is equal to Ω^{-1}. However until now in most cases specialists still use more old unit, namely $\Omega^{-1} \bullet cm^{-1}$.

Because the values of electrical conductivity are considerably less than 1 for most glass-forming melts within the whole temperature range of measurements, quite often values of electrical resistivity are used for a description of the ability of

these melts to conduct electricity. Electrical resistivity ρ is a value reciprocal to electrical conductivity, and correspondingly is expressed in Ω·m or Ω·cm. In this chapter, the ability of melts to conduct electricity will be mainly presented in terms of electrical resistivity.

An overwhelming majority of known oxide glasses and melts belong to ionic conductors. Only these kinds of melts will be considered in this chapter.

From the simplest but most effective kinetic theory of liquids by Frenkel [1] and theory of rate processes by Glesston, Laidler, and Eiring [2], when the temperature changes do not influence the heights of potential barriers between possible positions of current carriers, the temperature dependence of the specific resistivity of ionic liquids and glasses could be described by the following equation:

$$\rho = \rho_0 \exp(E/RT) \tag{2}$$

where ρ_0 is a constant corresponding to the expected value of electrical resistivity at temperature tending to infinity, T the absolute temperature, R a gas constant, and E the activation energy describing the height of potential barriers between two adjacent possible positions of current carriers in a liquid or glass. For practical purposes, it is convenient to use Eq.(2) in the decimal logarithmic form:

$$\log\rho = \log\rho_0 + 0.4343 \cdot E/RT \tag{3}$$

Quite often this equation is used in the following manner:

$$\log\rho = A + B/T \tag{4}$$

where A and B are constants.

Eq. (4) is called the Rasch-Hinriksen relationship. It accurately describes the temperature dependencies of electrical resistivity for glass-forming substances in the glassy state, i.e., for substances with frozen structure, which ensures the independence of activation energy on temperature. However, the same equation can be successfully used for description of temperature dependence of electrical resistivity of melts at high enough temperatures (usually at temperatures higher than 1200–1400°C).

According to both above-mentioned theories of electrical conductance of liquids [1,2] the values of $\log\rho_0$ for all liquids should be approximately the same and equal to -2 ± 0.5. It is easy to show (see, for example, [3]) that for temperature dependencies of electrical resistivity of all glasses (i.e., for glass-forming substances below glass transition regions) containing only one kind of alkali ions, the values of $\log\rho_0$ are very near to those calculated from the above-mentioned theories, which seemed natural enough. More unexpected was the finding by Kobeko [4], who showed that the extrapolation of the high-temperature segments of temperature dependencies of melt resistivity to infinite temperature led to values that were practically the same for all melts studied at that time. A new version of the same dependence including more recent experimental data [5] demonstrated the same kind of relationship.

However, most interesting was the fact that these values were again very near to those predicted by both theories.

High-temperature extrapolations were carried out by using Eq.(3), which could lead to the theoretically correct results only if the activation energy in this temperature region were independent of temperature. One can assume that it means the independence of structure of melt on temperature. At the same time, studies of temperature dependencies of density, heat capacity, and some other properties show that it is not so. Melt structure changes with temperature up to very high temperatures, probably to temperatures of total evaporation of melts. Thus, one can suppose that at high temperatures the free volume of melts becomes great enough to diminish the influence of purely geometrical difficulties, resulting in an additional increase of the heights of potential barriers. Thus, at high enough temperatures, we can expect that temperature dependencies of resistivity of practically all glass-forming melts could be described by Eq.(4). At lower temperatures, these dependencies are somewhat more complicated. One can find in the literature quite different ideas about the character of such dependencies.

However, the analysis of many experimental data of various authors that was carried out by the authors of this paper showed that there is at least one equation that could be used successfully for the description of most of the existing data for electrical resistivity of melts in very broad ranges of temperatures. The highest of this temperature range correspond to about 10^2 Pa•s, the lowest ones correspond to viscosity at which it is still possible to measure properties of melts in equilibrium conditions (namely 10^{12}–10^{13} Pa•s). It is an equation similar to the famous Vogel-Fulcher-Tammann equation used for the description of temperature dependencies of melt viscosity:

$$\log\rho = A + B/(T - T_0) \tag{5}$$

where A, B, and T_0 are constants.

The above-discussed feature of the temperature dependencies of melt resistivity at very high temperatures have another consequence that is important from the point of view of the analysis of the influence of composition on melt resistivity. The fact that all kinds of melts have a tendency to approach nearly the same values of specific resistivity with an increase in temperature leads to a fan-shape character of a considerable part of composition-temperature dependencies. Many effects of the influence of composition on electrical resistivity are the same for glasses and melts. However, the higher the temperature, the less pronounced are these effects.

10.2 METHODS OF MEASUREMENTS

Any comparison of different published data on electrical resistivity shows that the difference between data of various authors who have measured the resistivity of melts of the same composition could be considerable. Table 10.1 demonstrates a rather typical example of such comparison. When melt compositions are measured by many authors it is sometimes possible to determine the most reliable data by using the

TABLE 10.1
Electrical Resistivity of Sodium Silicate Melts Containing ~25% Na_2O at 1000°C According to Various Authors

Authors	log(ρ, Ω·cm)
Babcock [7]	0.47
Boricheva [8]	0.44
Botvinkin and Okhotin [9]	0.65
Kostanyan and Saakyan [10]	0.50
Kroger and Weisgerber [11]	0.43
Lotto and Lazzari [12]	0.20
Piechurowski [13]	0.36
Stanek, Sasek, and Meissnerova [14]	0.60
Tickle [15]	0.38

mean values of all existing data. As experience shows, more often than not, such mean values turn out to be the most precise. However, for most studied glass-forming melts, we have only one or two authors presenting data on certain systems. In such cases, it is reasonable to pay special attention to the measurement technique.

It is well known that when the resistivity of a body is high (for example higher than 10^7 Ω·cm) the resistivity is usually measured at direct current. When a constant voltage is applied to electrodes, the temperature of a sample is constant and there are no structural changes in it, so one can usually observe the steady state current, which remains constant for a rather long time. The value of this current can be used for calculation of true electrical resistivity of the sample. However, quite often, an experimenter meets a situation where the current through the sample changes with time. When the temperature and structure of the sample do not change with time, two main factors can lead to such changes in the current, namely the so-called thermal ionic polarization and electrode polarization.

The first factor is connected with whether the distribution of the heights of potential barriers around the ions that are the carriers of electricity is broad enough. At the first period of voltage application to the electrodes, the ions can easily surmount the lowest of the barriers, which are on the way of the direction to the corresponding electrode. After surmounting some low barriers, the ions appear near higher barriers and the rate of their further movement to the corresponding electrode decreases. After a while, most ions reach positions near higher barriers, and an additional current connected with the above-mentioned distribution of potential barriers comes exponentially to a zero. Thus, at the beginning, there is always an additional electrical current that quite often is much higher than the final steady state current. It seems self evident that the higher the specific resistivity of the substance, the longer the process of thermal ionic polarization. If this kind of polarization is not completed, the values of the measured electrical resistivity are lower than the values of true (steady state) electrical resistivity.

The second factor is the electrode polarization. It is connected with the fact that the electrodes are usually (in the case of measurements of ionic glass-forming substance in solid state) or always (when ionic substances in liquid state are measured) irreversible ones. That is, they do not supply the substance with additional conducting ions when they are used as anodes and do not absorb the corresponding ions while being used as cathodes. Therefore, near anodes, layers depleted of the electric carriers (the anode layers) are formed. These layers can have very high electrical resistivity. Thus, the formation of even very thin layers could decrease the current going between two electrodes quite considerably. Clearly, at the very beginning of the process, the concentration of conducting ions near the anode does not change appreciably and the current going through the sample does not differ from the steady state one within the error limits. However, after a certain time, the influence of the formation of the cathode layer begins to show itself. The longer the time of measurements, the higher the resistance of the anode layer should be. It is evident that the time of formation of the anode layer depends on a number of factors (among them the concentration of ions, the resistivity of the layer fully depleted of the most mobile ions, etc.), but the most important factor is the value of the steady state-specific resistivity of the studied substance. The higher this resistivity, the greater the time of formation of the anode layer of a certain thickness. Contrary to the influence of thermal ionic polarization, the influence of electrode polarization always increases the apparent specific resistivity of the measured substance.

The above-described kinds of polarization lead to the following dependence of the apparent specific resistivity of any ionic-conducting substance on the frequency of measurements and temperature (see Figure 10.1). At low frequencies, the time of half a cycle of alternating current may appear long enough for formation of the anode layer, leading to an increase in resistivity. With an increase in frequency, this effect diminishes and finally disappears.When the frequency is too high, the effect of thermal ionic polarization begins to show up. The higher the frequency, the greater the influence of this effect. It is obvious that each of two kinds of polarization has its own mechanism and it is pure luck for glass scientists that in all cases studied so far no overlaps of the influence of these two mechanisms have been detected. Therefore, scientists are always able to find a frequency range where the measured resistivity of the sample does not depend on frequency, which indicates that they measure the true electrical resistivity. Both borders of this range shift to lower frequencies with an increase in electrical resistivity. The last value is the function of composition and temperature.

The next step in the evaluation of the results of measurements is the calculation of electrical resistivity on the basis of the measured value of the electrical resistance of a sample. In the case of a solid glass, it is not difficult to prepare samples whose geometry permits these calculations with the necessary precision. The best solution is to use a sample in the form of a plate having two opposite surfaces covered by electrodes, and to supply one of the electrodes with a guard ring. Then all the lines of force between the electrode encircled by the guard ring and the opposite electrode are perpendicular to the plate surfaces. The guard ring also prevents the influence of a surface conductivity on the obtained results. In this case, Eq.(1) can be used with a very high degree of precision.

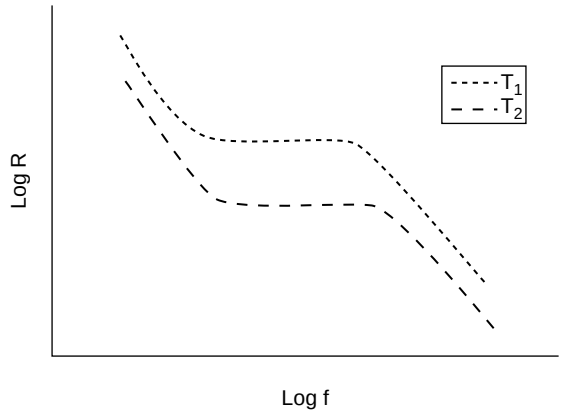

FIGURE 10.1 Schematic representation of the general dependence of apparent Electrical Resistivity on the frequency of resistivity measurements. $T_1 < T_2$.

At temperatures above 100°C (where, in most cases, the influence of the surface conductivity can be neglected) one can select the geometry of a sample and electrodes that should allow use of Eq.(1) with high enough accuracy even without the application of a guard ring.

The problem of electrical resistivity calculations on the basis of the measured resistance of a sample appears to be much more difficult to solve for measurements of glass-forming melts. The reason is that, in the overwhelming majority of cases, the form of a cell and positions of electrodes used for such measurements lead to a quite complicated form of lines of force that practically excludes calculations based on the geometry of the cell and electrodes. Therefore, one should determine a cell constant C by special experiments:

$$\rho = CR \tag{6}$$

where R is the electrical resistance of the cell filled by the studied melt.

This is a common procedure in electrochemistry. In this case, one uses a standard liquid with very well known electrical resistivity and puts it into a vessel with fixed positions of electrodes. The levels of the standard liquid and that of the studied one should be the same. Measurements of the resistance of the vessel (cell) with the standard liquid permits one to find the cell constant C and then to use it for determination of electrical resistivity of any other liquid.

For some time, this approach was broadly used by specialists measuring electrical resistivity of glass-forming melts. As standard liquids, the dilute solutions of various acids were usually used. It was found that cell constants obtained by this method depended on the electrical resistivity of the standard solutions used. Therefore, instead of determination of a certain constant, a special function $\rho = f(R)$ was determined for each new cell, which was used later for evaluation of specific resistivity of melts by the measured values of the cell resistance. It was assumed that the above-mentioned dependence is the same for all types of liquids and at any temper-

atures. Therefore, the dependencies of electrical resistivity on cell resistance determined by the use of standard acid solutions were applied for calculations of electrical resistivity of any kinds of melts.

It appeared recently that these assumptions were wrong. According to the paper by Boulos, Smith, and Moynihan [16] and from our studies (a detailed description of experiments will be published elsewhere), at similar values of resistivity the electrode polarization effects for aqueous solutions at room temperature are much stronger than those for glass-forming melts at high temperatures. In principle, it is possible to use standard aqueous solutions for determination of a cell constant [16]. One should, however, use them in conditions that prevent the influence of electrode polarization, i.e., in conditions where the measurements of steady state resistivity can be ensured. This can be attained either by an increase in resistivity of a standard solution (using more dilute solutions), or by an increase in frequency of the current used for measurements, or both. If one determines the cell constant at conditions ensuring the measurements of a steady state current by using standard solutions, this constant for calculation of resistivity of a melt in any conditions excluding the influence of any kind of polarization can be used. As it was stated above, the absence of polarization can be checked by the independence of the measured value on the frequency of the applied voltage within a broad enough frequency range.

Another possibility for determining the cell constant is by using for the calibration of a cell the same glass whose melt is measured in this particular cell. The corresponding method was proposed by Mach [17] and used later by Mazurina [18] and ourselves. In this method, the cell is in the form of a platinum crucible filled with glass melt where two platinum wire electrodes are immersed. Measurements are performed in the broad range of temperatures down to temperatures of the lower border of the glass transition region or even several hundred degrees lower. Thus, in many cases, one can measure electrical resistance of the cell with solid glass. By measurements of samples in the form of plates (made from the same glass) by the usual procedure for measurements of electrical resistivity of solid glasses, one can determine the electrical resistivity of the glass at temperatures where the resistance of the cell is measured and thus calculate the cell constant. We have developed a method that permits the extension of measurements of electric resistivity of glass plates up to temperatures corresponding to the high-temperature border of the transition regions of any glass. Therefore, the method by Mach could be used now even for glass compositions in which the thermal expansion coefficient (TEC) differs from the TEC of platinum wire so much that it leads to cracking of glass near the glass–platinum interface below the glass transition region.

10.3 THE INFLUENCE OF COMPOSITION ON ELECTRICAL RESISTIVITY OF GLASS-FORMING MELTS

It should be noted that, for some reason, after the end of World War II, systematic studies of electrical conductivity of melts were especially intensive in the Soviet Union. Probably it was connected with the great interest in this property by Prof. K.S. Evstropiev, one of the Soviet's leading glass specialists. Most of such studies

were carried out by scientists who began their scientific careers as post-graduate students of Prof. Evstropiev. Thus, the authors of a quite a considerable part of all data given in the present survey were Soviet scientists.

In this section, a short description of the main dependencies of electrical resistivity on composition of oxide glass-forming melts is presented. For illustration of these dependencies, references to tables with experimental data are given. For most of these tables, published data were used (see [19–46]). These data were compiled in the Glass Property Information System SciGlass [47] and processed in such a way as to permit the easiest comparison of these data with each other. Thus, all the presented tables are shown in a standard format, which, in most cases, differs considerably from the format of their original presentation. Thus, all compositions are presented in mol. percent and the results of measurements in $\log(\rho, \Omega\ \text{cm})$ independently of the forms used in the original papers. For greater convenience of the analysis of all tables and their comparison with each other, all tables are compiled in a special section (10.5) of the chapter.

As was mentioned in Section 10.1, in some aspects the influence of composition on electrical resistivity of glass-forming melts is similar to that of solid glasses (especially at comparatively low temperatures), but it demonstrates some specific features as well.

Monovalent ions have high mobility in glasses and melts. Accordingly, an increase in concentration of alkali oxides leads to an intensive decrease in electrical resistivity. This is illustrated by Tables 10.2–10.7. Comparison of Tables 10.2–10.5 shows the level of scatter of data describing resistivity of the melts of the same system reported by various authors. In most cases, this scatter can be considered reasonable. At the same time, it is clear that the analysis of the influence of composition changes on melt resistivity is more dependable if it is based on data obtained by a definite group of authors.

From Tables 10.5–10.7 it is clear that, in general, the lower the radius of an alkali ion, the lower the resistivity of the melt containing the corresponding oxide. However, this dependence is far from being a linear one. The resistivity of potassium silicate melts is much higher than that of sodium silicate ones. At the same time, the difference between resistivity of sodium and lithium silicate melts is much smaller and, in some cases (for example at the low-temperature part of the studied temperature range for melts with ~24% R_2O), one can even see a reverse effect.

The role of alkali ions in the conductance of melts can also be demonstrated by comparison of resistivity of alkali silicate melts with that of silica melt. It should be noted that the resistivity of silica melts is mainly determined by impurities — first of all by impurities of alkali oxides and probably water. It is clear, therefore, that the electrical resistivity of various kinds of silica melts can be quite different. Some examples of it are presented by Tables 10.8 and 10.9.

From Tables 10.9 and 10.10, a partial replacement of silica for boron oxide leads to a certain increase in resistivity, and that for alumina to a marked decrease in resistivity. However, for all melts up to very high temperatures, the level of resistivity for melts that do not contain mono- or bivalent ions is comparatively very high. The same is correct for ternary melts containing both boron and aluminum oxides (see Table 10.11).

It is well known that in alkali silicate glasses (i.e., at temperatures below glass-transition regions) the replacement of SiO_2 for RO leads to an increase in resistivity (see, for example, [3]). The greater the radius of bivalent ion, the higher the mentioned effect. Table 10.12 demonstrates the effect of the same kind of composition changes on electrical resistivity of sodium silicate melts. It is seen that, at comparatively low temperatures, the general dependencies are the same as they were found to be for glasses. However, at high enough temperatures, there is a tendency to decrease the resistivity with the increase in concentration of bivalent ions. It seems obvious that it is connected with the high enough mobility of bivalent ions at high temperatures.

From data presented in Tables 10.13 and 10.14, one can deduce that in potassium silicate melts most of the bivalent ions are less mobile than in sodium silicate ones. On the other hand, an increase of content of PbO in potassium silicate glasses leads to a pronounced decrease in resistivity of these glasses as it follows from the data in Table 10.15. In lithium silicate melts, the pattern of the influence of bivalent ions on resistivity is not clear (Table 10.16). Probably it is connected, at least partially, with considerably higher concentrations of alkali ions in the last series of melts — in this case, the mobility of these ions can be much higher than the mobility of bivalent ions and accordingly, the influence of the last ones can be close to the scatter of experimental data.

Table 10.17 demonstrates the so-called mixed alkali effect in silicate melts. In glassy state, this effect is probably the strongest of all known effects of compositional changes on the electrical resistivity. The mixed alkali effect is a very great increase in glass resistivity in the course of partial replacement of one alkali oxide for another. This increase can amount to several orders of magnitude. It increases with the increase in concentration of the sum of alkali oxides, with the increase in difference between radii of two alkali ions, and with the decrease in temperature. It is seen from the presented data that there are some indications of the existence of this effect in melts. At the same time, the effect is quite small, even at 1000°C and it decreases with further increase in temperature. According to data presented in Table 10.18, the addition of bivalent ions has no appreciable influence on the mixed alkali effect. On the other hand, results presented in Table 10.19 can lead to a quite different conclusion. It is possible that the difference is connected with the difference in pairs of alkali ions used in these two studies. It is clear that these dependencies should be investigated in future in more details.

Table 10.20 shows the influence of composition changes on the resistivity of melts, the compositions of which are similar to commercial soda-lime-silica glasses (that is why in this case we retained the weight percentage given in the original paper).

Now consider the data for alkali-free silicate melts containing bivalent ions.

The only example of the influence of the concentration of bivalent ions on the electrical resistivity of a binary RO-SiO_2 system is the data for lead silicate melts (Table 10.21). These data correlate reasonably well with several figures presented in Table 10.15. If one adds the first line of Table 10.9 to the data of Table 10.21, the influence of PbO on melt resistivity even in a broader range of compositions should be apparent. It is obvious that in all the binary melts in question, ions Pb^{++} are the carriers of electricity and their mobility is high enough.

Table 10.22 permits the formation of an idea about the resistivity of silicate melts with another two bivalent ions — Ca^{++} and Mg^{++}. Although the temperature ranges for data presented in Tables 10.21 and 10.22 are quite different, by comparing these sets of data one can make a definite enough conclusion that at high temperatures lead ions are considerably more mobile than calcium ones. It also follows from Table 10.22 that the mobility of Mg^{++} is considerably higher than that of Ca^{++}.

In Tables 10.23 and 10.24, a considerable amount of data on resistivity of alkali-free melts containing Al_2O_3 is compiled. In can be concluded that the influence of aluminum oxide on resistivity of these melts is practically negligible. Note that it means that the general level of melt resistivity for melts of similar compositions in Table 10.23 is considerably higher than in Table 10.22, which is just another indication of the possibility of an appreciable difference between the values of resistivity of the same melts reported by different authors (cf. Section 10.2). In any case, the data of Table 10.23 are another confirmation of the conclusion that the mobility of Ca^{++} ions is considerably lower than that of Pb^{++} ions. Table 10.23 (as well as comparison of some data taken from Tables 10.22 and 10.23) confirms the earlier-drawn conclusion about the higher mobility of Mg^{++} ions in comparison with Ca^{++} ions.

From Table 10.25, a comparatively small addition of CaF_2 to calcium silicate glasses leads to a considerable decrease in melt resistivity, which seems definite evidence of high enough mobility of F^- ions in these particular melts. Thus, we have here melts with essentially anionic conductivity.

In Table 10.26, some data on resistivity of SiO_2–CaO–MnO melts are presented. Unfortunately, based on these results, it is difficult to come to any definite conclusion about the influence of substitution of Ca^{++} for Mn^{++} on melt resistivity. The same is true in the case of data for iron-containing melts (Table 10.27).

Tables 10.28 and 10.29 contain data on resistivity of SiO_2–P_2O_5–CaO melts. It seems that the substitution of a comparatively small percentage of SiO_2 by P_2O_5 appreciably increases the resistivity of melts. On the other hand, the resistivity of calcium phosphate melts with or without a small addition of SiO_2 is appreciably lower than that of the silica melts with approximately the same concentration of CaO. Again, in the course of comparison of the data taken from Tables 10.28 and 10.29, one should remember the possibility of experimental errors introduced into their data by any of the authors.

Now we will analyze some results describing electrical resistivity of borate glasses.

According to data presented in Table 10.30, first percentages of substitution of SiO_2 for B_2O_3 in sodium silicate melts leads to an appreciable increase in electrical resistivity. The resistivity reaches the maximum values at about 25% of B_2O_3 and, in the course of further additions of B_2O_3, a considerable decrease of resistivity takes place.

Table 10.31 demonstrates the resistivity of alkali borate melts. It is seen that the difference among values for melts of three alkali-borate systems is small. There is also no great difference between resistivity of alkali borate melts and alkali silicate melts (see Tables 10.5–10.7) for similar concentrations of alkali oxides expressed in mol.%.

Existing information about the influence of bivalent metal oxides on the resistivity of alkali borate glasses is rather scarce. We have found only one work containing

such data (see Table 10.32). Nevertheless, one can draw some conclusions from these data. It is clear that even 3% of K_2O is enough to block the influence of the mobility of bivalent ions on melt resistivity up to 10–15% of RO. At the first percentage of the addition of RO there is even a tendency to increase the resistivity. Only when concentration of RO becomes quite considerable does the tendency of decreasing resistivity with an increase of RO concentration become quite clear. Note that the mobility of bivalent ions in borate melts increases with an increase in ionic radii.

Tables 10.33–10.34 present the results of rather systematic studies of the mixed alkali effect in alkali borate glasses. It is seen that there is a tendency to a slight increase in resistivity of mixed alkali melts in comparison with the binary ones (the higher the total concentration of alkali oxides the clearer is this tendency). However, as a whole, this effect is very weak here.

According to Table 10.35, at comparatively low temperatures the substitution of B_2O_3 for Al_2O_3 at the beginning increases resistivity of all sodium borate melts, but after the concentration of Al_2O_3 surpasses 5–10%, one can see a pronounced decrease in resistivity with further substitution of the same kind. An increase in the temperature of the melts leads to an interesting effect: in the course of the substitution, the initial increase in resistivity remains, but there is no decrease in resistivity with further increase in Al_2O_3 concentration.

Table 10.36 shows the results of the substitution of GeO_2 for B_2O_3. At comparatively low temperatures, this substitution leads to an increase in resistivity that is greatest for lithium germanate melts and least for potassium germanate melts. It is clear that, in alkali germanate melts, the difference between resistivity of melts containing different alkali ions is considerably greater than in alkali borate or alkali silicate melts. At higher temperatures, this difference decreases quite considerably. The influence of substitution of GeO_2 for B_2O_3 on melt resistivity also becomes much less pronounced at high temperatures.

Table 10.37 demonstrates the influence of substitution of B_2O_3 for SiO_2 in alkali-free melts containing constant concentration of BaO. Contrary to the influence of the similar substitution in alkali-containing melts (see Table 10.29) an increase in concentration of SiO_2 in barium-containing melts leads to a steady, strong increase in resistivity. Accordingly, one can conclude that the mobility of such a big ion as Ba^{++} is much higher in borate melts than in silicate ones. Having this in mind, it is especially interesting to compare resistivity of binary lead borate (Table 10.38) and lead silicate (Table 10.21) melts. At comparatively low temperatures, borate melts with a low concentration of PbO have considerably lower resistivity than silicate melts. At higher concentrations of PbO, this effect appears to be considerably less pronounced. At the same time, temperature dependencies of resistivity in silicate melts are much steeper than in borate ones. Accordingly, all the differences in resistivity between borate and silicate melts become considerably smaller.

Table 10.39 permits the comparison of resistivity of some binary borate melts containing various bivalent ions. For melts with similar concentrations of R_2O, the difference in resistivity is not great. The most definite conclusion can be that the mobility of Ba^{++} is substantially higher than that of Ca^{++}. At the same time, comparison of the data given in Tables 10.39 and 10.38 (note that all data were obtained by the same group of authors, so they should be compatible with each other) shows

that the mobility of Pb^{++} in binary borate melts is much higher than the mobility of any other bivalent ion studied so far.

10.4 METHOD OF CALCULATION OF ELECTRICAL RESISTIVITY OF GLASS-FORMING MELTS

As far as we know, the only methods of melt resistivity calculations proposed in the literature that have been published so far were extremely simple [40, 47, 48]. All were proposed for calculations of alkali-containing melts, and in all of them, it was assumed that the resistivity of a melt depends only on the concentration of alkali oxide, and all other components do not appreciably influence the resistivity. It is easy to see from the tables presented in this chapter that such an assumption is generally incorrect. We intended to develop a more precise method of calculation — one for melts with compositions that cover the compositions of most soda-lime-silica-based commercial glasses and the other one for sodium borosilicate melts. To accomplish this, we studied the electrical resistivity of a number of melts with systematically changing compositions. For measurements, the method described in the final part of Section 10.2 was used. Results of these measurements are presented in Tables 10.40–10.43. A description of our methods of melt resistivity calculations is presented in Section 10.4.1.

10.4.1 Calculation of Electrical Resistivity of Commercial Soda-Lime-Silica Melts

Temperature range: from 600 to 1400°C;

Composition ranges (in mol.%): 12–20 R_2O (Na_2O or partial replacement of Na_2O by K_2O, up to 7% K_2O); 4-15 RO (CaO or partial replacement of CaO by MgO, up to 5% MgO); 0–4.5

Al_2O_3; 69–81 SiO_2.

Calculations are performed in three subsequent steps.

1. Common logarithms of electrical resistivity at three reference temperatures for the given composition are calculated:

   For 1300°C:

$$R_{13} = 2.984 - 0.226 \cdot C_{NK} + 0.0255 \cdot C_{CM} + 0.00429 \cdot (C_{NK})^2 + 0.000535 \cdot C_{NK} \cdot C_{CM} - 0.00300 \cdot (C_{CM})^2 + 0.0289 \cdot C_{Al} - 0.000307 \cdot (C_{Al})^2 + 0.00439 \cdot C_{Mg} - 0.00226 \cdot (C_{Mg})^2 + 0.0685 \cdot C_K - 0.00177 \cdot C_K$$

   For 900°C:

$$R_9 = 3.984 - 0.285 \cdot C_{NK} + 0.0578 \cdot C_{CM} + 0.00646 \cdot (C_{NK})^2 - 0.00144 \cdot C_{NK} \cdot C_{CM} - 0.00189 \cdot (C_{CM})^2 + 0.0312 \cdot C_{Al} - 0.00135 \cdot (C_{Al})^2 - 0.000275 \cdot C_{Mg} - 0.0038 \cdot (C_{Mg})^2 + 0.1686 \cdot C_K - 0.0126 \cdot C_K$$

For 600°C:

$$R_6 = 5.09 - 0.313 \cdot C_{NK} + 0.154 \cdot C_{CM} + 0.00776 \cdot (C_{NK})^2 - 0.00478 \cdot C_{NK} \cdot C_{CM} - 0.00194 \cdot (C_{CM})^2 + 0.0334 \cdot C_{Al} - 0.00234 \cdot (C_{Al})^2 - 0.0211 \cdot C_{Mg} - 0.00179 \cdot (C_{Mg})^2 + 0.212 \cdot C_K - 0.0104 \cdot (C_K)^2$$

where C_{NK} is the sum of concentrations of Na_2O and K_2O, C_{CM} is the sum of concentrations of CaO and MgO, C_{Mg}, C_{A1}, and C_K are correspondingly concentrations of MgO, Al_2O_3, and K_2O (all in mol.%).

2. Constants of the Vogel-Fulcher-Tammann equation (Eq.(5)) are calculated by the following formulas:

$$M = (R_6 - R_{13}) \cdot 400$$
$$N = (R_9 - R_{13}) \cdot 700$$
$$T_0 = (M \cdot 873 - N \cdot 1173)/(M - N)$$
$$B = (R_9 - R_{13}) \cdot (1573 - T_0) \cdot (1173 - T_0)/400$$
$$A = R_6 - B/(873 - T_0)$$

3. Common logarithm of electric resistivity at any given temperature T (between 1400 and 600°C) for the given melt composition is calculated:

$$\log\rho = A + B/(T - T_0)$$

10.4.2 Glasses of Sodium Borosilicate System

Temperature range: from 600 to 1400 °C;
Composition ranges (in mol.%): 5–18 % Na_2O, 10–30 % B_2O_3, 65–78 % SiO_2.

1. Common logarithms of electrical resistivity at three reference temperatures for the given composition are calculated:

For 1300°C:

$$R_{13} = 3.598 - .2181 \cdot C_{Na} - .0853 \cdot C_B + .001682 \cdot (C_{Na})^2 + .003441 \cdot C_{Na} \cdot C_B + .001079 \cdot (C_B)^2$$

For 900°C:

$$R_9 = 4.454 - .2339 \cdot C_{Na} - .0779 \cdot C_B + .002310 \cdot (C_{Na})^2 + .003084 \cdot C_{Na} \cdot C_B + .001233 \cdot (C_B)^2$$

For 600°C:

$$R_6 = 4.979 - .2004 . C_{Na} - .0171 \cdot C_B + .003022 \cdot (C_{Na})^2 + .000820 \cdot C_{Na} \cdot C_B - .000507 \cdot (C_B)^2$$

where C_{Na} and C_B are correspondingly concentrations of Na_2O and B_2O_3 (in mol.%).

The second and third steps of calculations are the same as those described in Section 10.4.1.

Quite a few checks of the validity of this method were performed that gave satisfactory results. Here only one example of these checks is demonstrated. Two multi-component glasses with compositions near those that are characteristic for commercial soda-lime-silica glasses were melted. The glasses were analyzed, after which the electrical resistivity of their melts was measured and compared with data obtained by calculations based on the above-described method. Results are presented in Table 10.44.

There are reasons to believe that the proposed method can be used for calculations of electrical conductivity of melts of various commercial glass compositions with an acceptable accuracy. It is to be stressed here however, that all these calculations could give correct enough results only when the applied frequency of the electric current used for heating the glass-forming melts ensures the steady state current in the furnace within the whole temperature range of interest. According to our very approximate estimations for $\log(\rho, \Omega\cdot cm) = 0.0$, the results of the calculations could be used without any corrections for frequencies between 1 kHz and 1 MHz. In the case of considerably lower frequencies, one can expect a decrease of the current in real furnaces in comparison with the calculated one due to the electrode polarization. In the case of higher frequencies, the current should be higher than the calculated one due to the thermal ionic polarization (see Section 10.2). At $\log(\rho, \Omega\cdot cm) = 5.0$, this range of correct calculations is shifted to lower frequencies and is positioned between 10 Hz and 10 kHz. For determination of the corresponding borders of the mentioned frequency range for intermediate values of electrical resistivity, one can use linear approximations.

10.5 ELECTRICAL RESISTIVITY DATA

TABLE 10.2
Electrical Resistivity of SiO_2–Na_2O Melts

Mol.% by batch		log (ρ, Ω·cm) at T,°C								
SiO_2	Na_2O	700	750	800	850	900	950	1000	1050	1100
50	50			0.11	0.16	0.20	0.24	0.27	0.30	
57	43	0.24	0.12	0.01	0.07	0.13	0.18	0.23		
62,5	37,5	0.60	0.42	0.28	0.15	0.06	0.03	0.10	0.18	
66,6	33,4	0.70	0.51	0.35	0.24	0.15	0.08	0.03	0.03	0.06
70	30	0.82	0.60	0.43	0.31	0.21	0.13	0.06	0.00	0.05
73	27	1,14	0.94	0.80	0.60	0.47	0.37	0.28	0.22	0.15

Source: Data from Evstropiev, K. S. (1949). Electrical conductivity of glasses of system Na_2SiO_3–$PbSiO_3$–SiO_2 at high temperatures (in Russian). In: Fiziko–Khimicheskie Svoistva Troinoi Sistemy Na_2O–PbO–SiO_2, Moskva

TABLE 10.3
Electrical Resistivity of SiO_2–Na_2O Melts

Mol.% by analysis		log (ρ, Ω·cm) at T, ˚C					
SiO_2	Na_2O	700	900	1100	1300	1500	1600
90*	10*		—	—	—	1,03	0.92
85*	15*	—	—	—	—	0.56	—
80.1	19,9	1,34	0.76	0.48	0.30	—	—
75,2	24,8	—	0.52	0.26	—	—	—
70.3	29,7	0.78	0.34	0.08	–0.10	—	—
65,3	34,7	—	0.12	–0.11	–0.27	—	—
60.5	39,5	0.33	0.00	–0.24	–0.39	—	—
55,5	44,5	—	—	–0.38	–0.52	—	—
50.7	49,3	—	—	–0.47	–0.61	—	—
42,5	57,5	—	—	–0.52	–0.67	—	—

Source: Data from Tickle, R.E. (1967). The electrical conductance of molten alcali silicates. Pt. 1. Experiments and results. *Phys. Chem. Glasses*. 8(3).*By batch.

TABLE 10.4
Electrical Resistivity of SiO_2–Na_2O Melts

Mol.% by analysis		log (ρ, Ω·cm) at T, ˚C							
SiO_2	Na_2O	950	1000	1100	1150	1200	1250	1300	1350
90.2	19.8	0.70	0.62	0.51	0.45	0.40	0.35	0.31	0.27
75.6	24.4	0.44	0.37	0.25	0.19	0.14	0.10	0.07	0.02
71.4	28.6	0.11	0.08	–0.06	–0.11	–0.14	–0.18	–0.21	–0.24

Source: Data from Piechurowski, A. (1972). Method of measuring glass resistance at high temperatures. 4e Conference sur la fusion electrique du verre, Tchecoslovaque. 2

TABLE 10.5
Electrical Resistivity of SiO_2–Na_2O Melts

Mol.% by analysis		log (ρ, Ω·cm) at T, ˚C				
SiO_2	Na_2O	1000	1100	1200	1300	1400
85,2	14,8	—	—	0.81	0.65	—
83,4	16,6	0.86	0.75	0.64	0.53	0.45
79,7	20.3	0.62	0.49	0.40	0.28	0.18
74,1	25,9	0.50	0.35	0.26	0.16	0.08
70.2	29,8	0.27	0.15	0.10	0.02	—
67,9	32,1	0.08	—	–0.05	–0.12	—
63,7	36,3	—	–0.04	–0.10	—	—
60.5	39,5	0.02	–0.05	–0.12	—	—
55,8	44,2	–0.10	–0.18	—	—	—

Source: Data from Kostanyan, K. A., Saakyan, K. S. (1961). Electrical conductivity of glasses of Na_2SiO_3–SiO_2 system in molten state (in Russian). *Izv. Akad. Nauk Arm. SSR, Khim. Nauki*. 14(5)

TABLE 10.6
Electrical Resistivity of SiO_2–Li_2O Melts

Mol.% by batch		log (ρ, Ω·cm) at T, ˚C					
SiO_2	Li_2O	900	1000	1100	1200	1300	1400
76.1	23.9	—	0.73	0.51	0.16	0.11	0.10
73.8	26.2	0.68	0.40	0.20	0.08	0.00	–0.05
69.4	30.6	0.32	0.18	0.02	–0.05	–0.10	–0.22
66.6	33.4	0.28	0.11	0.00	–0.07	–0.15	–0.22
63.8	36.2	0.04	–0.05	–0.10	–0.19	–0.26	–0.30
62.5	37.5	—	–0.12	–0.19	–0.26	–0.30	–0.40
59.9	40.1	0.18	0.00	–0.10	–0.15	–0.30	–0.35
58.6	41.4	—	–0.12	–0.22	–0.30	–0.40	–0.40

Source: Data from Kostanyan, K. A., Erznkyan, E. A. (1967). Electrical conductivity of glasses of system Li_2O–SiO_2 in molten state (in Russian). *Arm. Khim. Zh.* 20(5)

TABLE 10.7
Electrical Resistivity of SiO_2–K_2O Melts

Mol.% by batch		log (ρ, Ω·cm) at T, ˚C					
SiO_2	K_2O	600	800	1000	1200	1300	1400
87.7	12.3	3.35	2.04	1.54	1.21	1.08	0.98
85.5	14.5	—	—	1.30	1.01	0.90	0.84
83.2	16.8	2.45	1.48	1.16	0.86	0.74	0.65
80.9	19.1	2.16	1.22	0.96	0.68	0.58	0.48
78.5	21.5	1.98	1.14	0.81	0.53	0.45	0.38
75.3	24.7	1.74	0.96	0.60	0.34	0.26	0.20
74.0	26.0	—	—	0.57	0.34	0.26	0.20
72.7	27.3	1.63	1.09	0.49	0.26	0.20	0.15
71.0	29.0	—	—	0.40	0.20	0.15	0.08

Source: Data from Kostanyan, K. A., Erznkyan, E. A. (1964). Study of electrical conductivity of glasses of system K_2O–SiO_2 in a broad temperature range (in Russian). *Izv. Akad. Nauk Arm. SSR, Khim. Nauki.* 17(6)

TABLE 10.8
Electrical Resistivity of SiO_2 Melts

Wt.% by batch SiO_2	T, ˚C	log (ρ, Ω·cm)
100	1460	4.56
100	1516	4.50
100	1658	4.26
100	1727	3.84
100	1789	3.50
100	1878	3.05
100	1915	2.85
100	1939	2.68
100	1989	2.36
100	2047	2.30
100	2137	2.19

Source: Data from Lapin, V. A., Polonskii, Yu. A. (1975). Electrical resistivity of silica glass in temperature range 400–2200 C (in Russian). *Tr. Gos. Inst. Ogneuporov.* 4(47)

TABLE 10.9
Electrical Resistivity of SiO_2–B_2O_3 Melts

Mol.% by analysis		log (ρ, Ω·cm) at T, ˚C						
SiO_2	B_2O_3	700	900	1100	1300	1500	1700	1900
100	—	6.32	5.26	4.59	4.06	3.83	3.57	3.37
97.62	2.38	—	5.30	4.72	4.40	4.02	3.76	3.56
95.2	4.8	—	5.64	5.16	4.56	4.30	4.10	3.94
90.53	9.47	—	5.74	5.08	4.69	4.40	4.16	3.98
82.72	17.28	—	5.65	4.82	4.48	4.22	4.00	3.84

Source: Data from Loryan, S. G., Saringyulyan, R. S., Kostanyan, K. A. (1977). Electrical conductivity of high–silica glasses of system Al2O3–B2O3–SiO2 in a broad temperature range (in Russian). *Fizika i Khimiya Stekla.* 3(6)

TABLE 10.10
Electrical Resistivity of SiO_2–Al_2O_3 Melts

Mol.% by analysis		log (ρ, Ω·cm) at T, ˚C						
SiO_2	Al_2O_3	700	900	1100	1300	1500	1700	1900
98.31	1.69	5.74	4.82	4.29	3.94	3.67	3.46	3.28
96.66	3.34	5.34	4.65	4.15	3.76	3.56	3.36	3.20
93.27	6.73	5.38	4.54	4.02	3.74	3.52	3.34	3.20

Source: Data from Loryan, S. G., Saringyulyan, R. S., Kostanyan, K. A. (1977). Electrical conductivity of high–silica glasses of system Al2O3–B2O3–SiO2 in a broad temperature range (in Russian). *Fizika i Khimiya Stekla.* 3(6)

TABLE 10.11
Electrical Resistivity of SiO_2–B_2O_3–Al_2O_3

Wt.% by analysis			log (ρ, Ω·cm) at T, ˚C						
SiO_2	B_2O_3	Al_2O_3	700	900	1100	1300	1500	1700	1900
79.91	14.21	5.47	5.36	4.60	4.02	3.80	3.64	3.52	3.42
79.98	10.80	8.87	5.26	4.52	4.12	3.84	3.62	3.45	3.30
79.82	9.03	10.81	5.16	4.46	4.09	3.82	3.60	3.43	3.28
80.04	5.36	14.22	5.18	4.48	4.12	3.80	3.54	3.34	3.18
82.28	11.82	5.51	5.14	4.50	3.90	3.74	3.61	3.52	3.42
82.93	5.46	11.43	5.20	4.54	4.20	3.84	3.67	3.54	3.42
88.75	5.44	5.45	5.10	4.52	4.10	3.68	3.54	3.46	3.32
94.04	2.75	2.78	5.53	4.69	4.29	4.00	3.68	3.54	3.45

Source: Data from Loryan, S. G., Saringyulyan, R. S., Kostanyan, K. A. (1977). Electrical conductivity of high–silica glasses of system Al2O3–B2O3–SiO2 in a broad temperature range (in Russian). *Fizika i Khimiya Stekla.* 3(6)

TABLE 10.12
Electrical Resistivity of SiO_2–Na_2O–RO Melts

Mol.% by batch							log (ρ, Ω·cm) at T, °C			
SiO_2	Na_2O	BeO	MgO	CaO	ZnO	SrO	800	1000	1200	1400
75	15	10	—	—	—	—	1.59	0.98	0.63	0.42
70	15	15	—	—	—	—	1.63	0.99	0.63	0.42
65	15	20	—	—	—	—	1.72	1.06	0.70	0.48
60	15	25	—	—	—	—	1.68	0.97	0.61	0.37
55	15	30	—	—	—	—	1.73	0.98	0.60	0.37
80	15	—	5	—	—	—	—	1.05	0.77	0.56
75	15	—	10	—	—	—	1.43	0.93	0.62	0.41
70	15	—	15	—	—	—	1.41	0.87	0.55	0.32
65	15	—	20	—	—	—	1.40	0.83	0.51	0.29
60	15	—	25	—	—	—	1.52	0.87	0.48	0.23
80	15	—	—	5	—	—	—	1.02	0.70	0.52
75	15	—	—	10	—	—	1.56	0.97	0.65	0.43
70	15	—	—	15	—	—	1.63	0.98	0.61	0.36
65	15	—	—	20	—	—	1.80	1.15	0.70	0.42
60	15	—	—	25	—	—	1.96	1.25	0.66	0.34
75	15	—	—	—	10	—	1.35	0.77	0.44	0.24
70	15	—	—	—	15	—	1.37	0.77	0.44	0.24
65	15	—	—	—	20	—	1.44	0.83	0.50	0.28
60	15	—	—	—	25	—	1.49	0.82	0.40	0.18
75	15	—	—	—	—	10	1.88	1.22	0.85	0.59
70	15	—	—	—	—	15	1.86	1.19	0.78	0.48
65	15	—	—	—	—	20	2.08	1.32	0.76	0.42

Source: Data from Mazurina, E. K. (1967). Influence of oxides of bivalent metals on electrical conductivity of sodium–silicate glasses in a broad temperature range (in Russian). *Steklo*. 1

TABLE 10.13
Electrical Resistivity of SiO_2–K_2O–MgO Melts

Mol.% by batch			log (ρ, Ω·cm) at T, °C		
SiO_2	K_2O	MgO	1000	1200	1400
85	15	—	1.18	0.83	0.58
80	15	5	1.31	0.93	0.67
75	15	10	1.59	1.16	0.87
70	15	15	1.43	0.99	0.69
65	15	20	1.57	1.11	0.80
60	15	25	1.58	1.09	0.79
55	15	30	1.60	1.11	0.78

Source: Data from Mazurina, E. K., Evstropiev, K. S. (1970). On certain patterns of the influence of bivalent ions on electrical conductivity of molten alkali–silicate glasses (in Russian). In: Stekloobraznoe Sostoyanie. Erevan: Izd. Akademii Nauk Arm. SSR.

TABLE 10.14
Electrical Resistivity of SiO_2–CaO–K_2O Melts

Mol.% by batch			log(ρ, Ω·cm) at T, ˚C				
K_2O	CaO	SiO_2	600	800	1000	1200	1400
15	5	80	3.46	2.07	1.37	0.94	0.68
15	10	75	4.06	2.52	1.66	1.23	0.91
15	15	70	4.41	2.80	1.86	1.34	0.97
15	20	65	4.46	2.79	1.80	1.23	0.83
15	25	60	4.78	3.02	1.96	1.32	0.91
15	30	55	5.03	3.25	2.10	1.39	0.89
15	35	50	5.25	—	—	—	—

Source: Data from Mazurina, E. K. (1967). Influence of two–valence metal oxides on electrical conductivity of alkali silicate glasses in the temperature range 200–1400°C (in Russian). Thesis. Leningrad: Lensoviet Technological Institute

TABLE 10.15
Electrical Resistivity of SiO_2–PbO–K_2O Melts

Mol.% by batch			log(ρ, Ω·cm) at T, ˚C				
SiO_2	PbO	K_2O	600	800	1000	1200	1400
80	—	20	2.29	1.36	0.82	0.48	0.23
70	10	20	2.43	1.43	0.90	0.49	0.20
60	20	20	2.39	1.32	0.77	0.36	0.06
50	30	20	2.31	1.16	0.59	0.19	—
80	10	10	4.34	2.92	2.17	1.63	1.22
70	20	10	4.26	2.74	1.94	1.38	0.95
60	30	10	4.19	2.42	1.51	0.97	0.58
50	40	10	3.40	1.70	0.96	0.49	—
70	—	30	1.69	0.84	0.43	0.13	–0.11
60	10	30	1.60	0.77	0.34	0.02	—
70	30	–	5.23	3.13	2.12	1.49	1.02
60	40	–	5.46	3.00	1.76	1.16	0.72
50	50	–	4.04	2.02	1.07	0.55	—

Source: Data from Saringyulyan, R. S., Kostanyan, K. A. (1971). Role of viscosity in a study of electrical conductivity of glasses of system K_2O–PbO–SiO_2 (in Russian). In: Stekloobraznoe Sostoyanie, Moskva

TABLE 10.16
Electrical Resistivity of SiO_2–R_2O–RO Melts

Mol.% by batch								log (ρ, Ω·cm) at T, °C			
SiO_2	Li_2O	BeO	MgO	CaO	ZnO	CdO	BaO	1000	1100	1200	1300
72	25	3	—	—	—	—	—	0.32	0.16	0.08	–0.02
69	25	6	—	—	—	—	—	0.32	0.18	0.08	0.00
66	25	9	—	—	—	—	—	0.30	0.15	0.08	0.00
63	25	12	—	—	—	—	—	0.20	0.11	0.00	–0.05
60	25	15	—	—	—	—	—	0.28	0.15	0.04	0.00
57	25	18	—	—	—	—	—	0.20	0.08	–0.02	–0.10
59	35	6	—	—	—	—	—	–0.10	–0.22	–0.30	–0.40
69	25	—	6	—	—	—	—	0.37	0.20	0.08	0.04
63	25	—	12	—	—	—	—	0.31	0.20	0.15	0.04
57	25	—	18	—	—	—	—	0.23	0.10	0.00	–0.05
59	35	—	6	—	—	—	—	–0.05	–0.22	–0.30	–0.40
69	25	—	—	6	—	—	—	0.38	0.23	0.11	0.04
63	25	—	—	12	—	—	—	0.31	0.16	0.08	–0.02
57	25	—	—	18	—	—	—	0.34	0.20	0.10	0.00
59	35	—	—	6	—	—	—	–0.05	–0.15	–0.22	–0.30
69	25	—	—	—	6	—	—	0.31	0.15	0.02	–0.02
63	25	—	—	—	12	—	—	0.24	0.11	0.00	–0.02
57	25	—	—	—	18	—	—	0.28	0.08	–0.05	—
59	35	—	—	—	6	—	—	–0.15	–0.22	–0.30	–0.40
69	25	—	—	—	—	6	—	0.28	0.15	0.04	0.00
63	25	—	—	—	—	12	—	0.18	0.08	–0.05	–0.07
57	25	—	—	—	—	18	—	0.15	0.04	–0.02	–0.10
59	35	—	—	—	—	6	—	–0.10	–0.22	–0.30	–0.40
72	25	—	—	—	—	—	3	0.43	0.26	0.11	0.04
69	25	—	—	—	—	—	6	0.45	0.32	0.20	0.11
66	25	—	—	—	—	—	9	0.38	0.24	0.13	0.06
63	25	—	—	—	—	—	12	0.40	0.28	0.18	0.08
60	25	—	—	—	—	—	15	0.59	0.44	0.31	0.23
57	25	—	—	—	—	—	18	0.54	0.40	0.30	0.24
59	35	—	—	—	—	—	6	–0.05	–0.15	–0.19	–0.26

Source: Data from Erznkyan, E. A., Kostanyan, K. A. (1968). Electrical conductivity of glasses Li_2O–RO–SiO_2 in molten state (in Russian). *Arm. Khim. Zh*. 21(9)

TABLE 10.17
Electrical Resistivity of SiO_2–Li_2O–Na_2O–K_2O Melts

Mol.% by batch				log (ρ, Ω·cm) at T, ˚C				
SiO_2	Li_2O	Na_2O	K_2O	1000	1100	1200	1300	1400
75.0	17.5	7.5	—	0.54	0.37	0.28	0.18	0.10
75.0	12.5	12.5	—	0.63	0.47	0.34	0.27	0.19
75.0	7.5	17.5	—	0.55	0.41	0.29	0.20	0.15
75.0	17.5	—	7.5	1.01	0.83	0.69	0.57	0.48
75.0	12.5	—	12.5	1.20	1.00	0.84	0.70	0.61
75.0	7.5	—	17.5	1.10	0.92	0.76	0.63	0.57
75.3	—	—	24.7	0.60	—	0.34	0.26	0.20
74.1		25.9		0.50	—	0.26	0.16	0.08
76.1	23.9			0.73	0.51	0.16	0.11	0.10

Source: Data from Kostanyan, K. A., Erznkyan, E. A. (1967).Mixed alkali effect in molten glasses II (in Russian). *Arm. Khim. Zh.* 20(9)

TABLE 10.18
Electrical Resistivity of SiO_2–MgO–BaO–K_2O–Li_2O Melts

Mol.% by batch					log (ρ, Ω·cm) at T, ˚C					
SiO_2	MgO	BaO	K_2O	Li_2O	1440	1400	1320	1200	1120	1000
70	10	—	5	15	0.36	0.40	0.49	0.67	0.78	—
70	10	—	10	10	0.56	0.63	0.75	0.96	1.14	1,46
70	10	—	15	5	0.52	0.57	0.68	0.87	1.00	—
70	—	10	5	15	0.43	0.48	0.60	0.80	0.97	—
70	—	10	10	10	0.52	0.58	0.92	0.92	1.12	—
70	—	10	15	5	0.46	0.51	0.62	0.82	0.99	—

Source: Data from Sasek, L., Meissnerova, H., Persin J. (1973). Structura a vlastnosti kremictych sklovin. IV. Vliv MgO a BaO na elektrickou vodivost ternalnich kremicitych sklovin *Sb. Vys. Sk. Chem. Technol. Praze, Chem. Technol. Silik*. L4

TABLE 10.19
Electrical Resistivity of SiO_2–CaO–K_2O–Na_2O Melts

Mol.% by batch				log(ρ, Ω·cm) at T, ˚C				
SiO_2	CaO	K_2O	Na_2O	1100	1200	1300	1400	1450
70.0	5.0	25.0	—	1.12	0.96	0.81	0.67	0.62
70.0	5.0	17.5	7.5	1.01	0.84	0.68	0.56	0.51
70.0	5.0	12.5	12.5	0.86	0.70	0.56	0.45	0.40
70.0	5.0	7.5	17.5	0.69	0.54	0.41	0.30	0.28
70.0	5.0	—	25.0	0.38	0.30	0.23	0.15	0.11
75.0	10.0	15.0	—	2.11	1.83	1.60	1.38	1.30
75.0	10.0	10.0	5.0	1.67	1.45	1.27	1.13	—
75.0	10.0	7.5	7.5	1.62	1.36	1.18	1.00	0.98
75.0	10.0	5.0	10.0	1.42	1.22	1.02	0.85	0.81
75.0	10.0	—	15.0	0.88	0.74	0.62	0.51	0.46
76.0	11.0	13.0	—	2.32	2.05	1.80	1.55	1.51
76.0	11.0	6.5	6.5	1.81	1.56	1.35	1.15	—
76.0	11.0	—	13.0	1.11	0.93	0.79	0.65	—

Source: Data from Kostanyan, K. A., Erznkyan, E. A., Avetisyan, E. M. (1967). Mixed alkali effect in molten glasses I (in Russian). *Arm. Khim. Zh.* 20(8)

TABLE 10.20
Electrical Resistivity of SiO_2–Na_2O–CaO–Al_2O_3–MgO Melts

Wt.% by batch					log(ρ, Ω·cm) at T, °C				
SiO_2	Al_2O_3	Na_2O	CaO	MgO	600	800	900	1000	1100
76	—	13	11	—	3.23	2.15	1.66	1.28	1.15
74	—	16	10	—	2.85	1.75	1.40	1.06	0.82
76	—	19	5	—	2.35	1.35	1.10	0.80	0.60
72	4	13	11	—	3.30	2.18	1.60	1.25	1.13
70	6	13	11	—	3.20	2.06	1.55	1.28	1.15
76	6	13	5	—	2.77	1.82	1.45	1.29	1.12
76	—	13	9	2	3.12	2.00	1.51	1.25	1.10
76	—	13	5	6	2.89	1.92	1.48	1.29	1.10
72	2	16	10	—	2.80	1.63	1.21	1.02	0.82
70	4	16	10	—	2.76	1.65	1.25	1.08	0.82
68	6	16	10	—	2.78	1.98	1.28	1.10	0.82
74	2	16	8	—	2.78	1.64	1.20	1.02	0.81
74	4	16	6	—	2.60	1.62	1.20	1.04	0.80
74	6	16	4	—	2.34	1.53	1.27	1.03	0.84
74	—	16	6	4	2.65	1.62	1.25	1.02	0.81
74	—	16	4	6	2.60	1.44	1.18	0.99	0.81
74	—	13	11	2	3.28	2.12	1.72	1.30	1.17
71	—	13	11	5	3.35	2.14	1.75	1.34	1.18
72	—	16	10	2	2.90	1.82	1.28	1.00	0.81
69	—	16	10	5	2.95	1.76	1.25	1.00	0.81
72	2	13	11	2	3.30	1.90	1.50	1.30	1.10
74	2	13	9	2	3.00	1.90	1.55	1.26	1.10
74	2	13	6	5	—	—	1.55	1.30	1.10
77	2	13	6	2	2.93	1.75	1.45	1.26	1.05
74	2	11	11	2	3.43	2.12	1.82	1.44	1.18
69	2	17	7	5	2.65	1.50	1.20	0.94	0.64
74	2	17	2	5	2.34	1.43	1.18	0.94	0.65
69	2	17	10	2	2.65	1.46	1.18	0.92	0.64
74	2	15	7	2	2.65	1.62	1.15	1.05	0.84
74	2	12	7	5	2.98	2.03	1.65	1.33	1.14
76	2	13	7	2	2.80	1.80	1.44	1.23	1.02
74	2	17	7	—	2.37	1.36	1.12	0.88	0.65
76	—	17	7	—	2.45	1.45	1.20	0.93	0.70
74	5	13	6	2	2.70	1.84	1.50	1.27	1.12
74	—	17	7	2	—	—	1.12	0.85	0.68
74	4	17	3	2	—	—	1.09	0.85	0.68
72	2	14	10	2	3.05	1.88	1.43	1.24	0.95
72	2	15	9	2	2.98	1.82	1.34	1.10	0.81

Source: Data from Kostanyan, K.A. (1952). Issledovanie Elektroprovodnosti Natrii–Kaltsii–Magnii–Alyumosilikatnykh Stekol v Rasplavlennom Sostoyanii. Thesis. Leningrad: Lensoviet Technological Institute

TABLE 10.21
Electrical Resistivity of SiO_2–PbO Melts

Mol.% by analysis		log (ρ, Ω·cm) at T, ˚C				
SiO_2	PbO	800	900	1000	1100	1200
63.5	36.5	3.48	2.52	1.90	1.47	1.11
58.7	41.3	2.88	2.15	1.59	1.20	0.89
53.7	46.3	2.21	1.58	1.11	0.75	0.43
51.4	48.6	1.99	1.37	0.90	0.49	0.17
49.5	50.5	1.69	1.14	0.74	0.37	0.00
48.4	51.6	1.85	1.30	0.89	0.48	0.08
45.4	54.6	1.62	1.09	0.63	0.26	0.32
44.5	55.5	1.41	0.93	0.55	0.21	0.23
41.3	58.7	1.14	0.64	0.21	0.41	—
39.1	60.9	0.91	0.41	0.08	—	—
35.4	64.6	0.84	0.31	0.20	—	—
32.6	67.4	0.62	0.24	0.20	—	—
30.5	69.5	0.47	0.14	0.38	—	—

Source: Data from Ejima, T., Watanabe, Y., Kameda, M. (1968). Electric conductance in the liquid PbO–SiO2 binary system (Electric conductance in liquid lead silicates (I)) *J. Jpn. Inst. Metals*. 32(12)

TABLE 10.22
Electrical Resistivity of SiO_2–CaO–MgO Melts

Mol.% by batch			log(ρ, Ω·cm) at T, ˚C				
SiO_2	CaO	MgO	1400	1450	1500	1550	1600
42.68	57.32	—	—	0.46	0.36	0.27	0.19
39.56	52.69	7.74	—	0.44	0.29	0.19	0.12
38.04	50.82	11.15	—	0.77	0.47	0.20	0.08
48.26	51.74	—	0.74	0.62	0.49	0.39	0.31
43.53	46.63	9.84	0.51	0.41	0.30	0.22	0.15
53.50	46.50	—	0.82	0.70	0.60	0.49	0.40
52.36	45.61	2.03	0.82	0.68	0.59	0.47	0.39

Source: Data from Kalyadina, S. A. (1977). Issledovanie Vyazkosti i Udelnoi Elektroprovodnosti Fosfatno–Kremnistykh Rasplavov. Thesis. Leningrad

TABLE 10.23
Electrical Resistivity of SiO_2–CaO–Al_2O_3 Melts

Mol.% by batch			log (ρ, Ω·cm) at T, ˚C				
SiO_2	CaO	Al_2O_3	1350	1400	1450	1500	1550
59.74	2.93	37.33	1.46	1.29	1.15	1.02	0.92
55.9	5.99	38.11	1.49	1.33	1.18	1.05	0.94
51.9	9.18	38.92	1.47	1.31	1.15	1.03	0.93
49.42	11.15	39.43	1.48	1.32	1.16	1.03	0.93
48.58	11.82	39.6	1.44	1.28	1.14	1.01	0.91
47.73	12.5	39.77	1.51	1.34	1.19	1.07	0.97
54.56	2.92	42.51	1.28	1.12	0.97	0.84	0.73
50.63	5.97	43.4	1.31	1.14	1.00	0.86	0.75
48.2	7.86	43.95	1.32	1.15	1.00	0.87	0.76
47.37	8.5	44.13	1.26	1.11	0.96	0.84	0.73
46.54	9.14	44.32	1.28	1.12	0.98	0.84	0.73
42.27	12.45	45.28	1.33	1.18	1.05	0.89	0.77
49.43	2.91	47.66	1.09	0.78	0.80	0.68	0.59
48.64	3.51	47.85	1.09	0.94	0.80	0.69	0.59
47.04	4.72	48.25	1.11	0.95	0.81	0.69	0.60
46.22	5.33	48.45	1.07	0.93	0.79	0.67	0.57
45.41	5.95	48.65	1.12	0.95	0.82	0.70	0.60
41.22	9.11	49.68	1.09	0.95	0.81	0.69	0.60
36.84	12.41	50.75	1.17	1.00	0.85	0.72	0.62
44.33	2.9	52.77	1.05	0.89	0.73	0.60	0.46
40.21	5.93	53.85	1.19	0.91	0.74	0.61	0.46
35.93	9.08	54.99	1.05	0.90	0.73	0.60	0.46
31.46	12.36	56.18	—	—	0.90	0.62	0.49
45.72	6.83	47.45	1.20	1.05	0.89	0.78	0.67
46.77	6.83	46.4	1.12	1.03	0.86	0.74	0.64
47.82	6.84	45.34	1.18	1.04	0.88	0.76	0.65

Source: Data from Kammel, R., Winterhager, H. (1965). Struktur und Eigenschaften von Schlacken der Metallhuttenprozesse. V. Dichtebestimmungen und elektrische Leitfähigkeitsmessungen an Schmelzen des Systems Kalk–Tonerde–Kieselsäure. Erzmetall. 18(1)

TABLE 10.24
Electrical Resistivity of SiO_2–Al_2O_3–MgO–CaO Melts

Mol.% by batch				log(ρ, Ω·cm) at T, °C				
SiO_2	Al_2O_3	MgO	CaO	1350	1400	1450	1500	1550
39.6	18.9	5.7	35.8	1.32	1.15	0.99	0.83	0.69
37.5	17.9	10.7	33.9	1.22	1.01	0.85	0.70	0.56
50.0	5.0	10.0	35.0	1.08	0.94	0.80	0.67	0.54
54.8	4.5	9.0	31.7	1.28	1.12	0.97	0.83	0.70
59.6	4.0	8.1	28.3	1.47	1.30	1.14	1.00	0.86
64.1	3.5	7.4	25.0	1.66	1.49	1.34	1.19	1.04
47.4	4.7	9.5	38.4	1.04	0.87	0.73	0.60	0.47
44.9	4.5	9.0	41.6	0.96	0.80	0.67	0.53	0.41
41.7	4.2	8.3	45.8	0.71	0.58	0.45	0.34	—
48.1	4.8	13.4	33.7	1.01	0.85	0.72	0.59	0.47
46.2	4.6	16.9	32.3	0.91	0.80	0.65	0.52	0.41
43.8	4.4	21.1	30.7	1.12	0.72	0.58	0.45	0.34
47.1	10.4	9.5	33.0	1.22	1.04	0.89	0.76	0.63
44.8	15.0	8.9	31.3	1.28	1.10	0.96	0.82	0.98
42.1	20.0	8.4	29.5	1.37	1.17	1.04	0.86	0.55

Source: Data from Winterhager, H., Greiner, L., Kammel, R. (1966). Untersuchungen über die Dichte und die elektrische Leitfähigkeit von Schmelzen der Systeme CaO–Al2O3–SiO2 und CaO–MgO–Al2O3–SiO2. *Forschungsberichte des Landes Nordrhein Westfahlen*.

TABLE 10.25
Electrical Resistivity of SiO_2–CaO–CaF_2 Melts

Mol.% by batch			log(ρ, Ω·cm) at T, °C				
CaO	SiO_2	CaF_2	1400	1450	1500	1550	1600
57.25	42.74	—	0.60	0.47	0.35	0.27	0.18
55.58	41.50	2.92	0.19	0.09	0.00	0.06	0.12
51.76	48.24	—	0.72	0.60	0.48	0.39	0.31
49.77	46.54	3.69	0.41	0.31	0.21	0.14	0.07
45.18	54.82	—	0.85	0.74	0.62	0.52	0.42

Source: Data from Kalyadina, S. A. (1977). Issledovanie Vyazkosti i Udelnoi Elektroprovodnosti Fosfatno–Kremnistykh Rasplavov. Thesis. Leningrad

TABLE 10.26
Electrical Resistivity of SiO_2–CaO–MnO Melts

Mol.% by batch			log (ρ, Ω·cm)
SiO_2	CaO	MnO	T, ˚C – 1500
50	33	17	0.55
50	14	36	0.27
50	9.1	40.9	0.20
45	46.6	8.4	0.40
45	37.9	17.1	0.43
45	28.8	26.2	0.27
45	19.4	35.6	0.24
45	—	55	0.04
40	47.3	12.7	0.22
40	38.4	21.6	0.13
40	34.0	26.0	0.09
40	24.5	35.5	0.00
40	14.5	45.5	0.09
40	—	60	0.26
35	34.4	30.6	0.03
35	19.6	45.4	0.13
35	9.4	55.6	0.27

Source: Data from Segers, L., Fontana, A., Winand, R. (1979). Viscosité de mélanges de silicates fondus du système CaO–SiO_2–MnO. *Electrochemical Acta.* 24(2)

TABLE 10.27
Electrical Resistivity of SiO_2–MgO–FeO–Fe_2O_3–Fe Melts

Wt.% by batch					log (ρ, Ω·cm) at T, ˚C				
SiO_2	MgO	FeO	Fe_2O_3	Fe	1200	1300	1350	1400	1450
54.73	24.81	19.49	0.39	0.58	1.40	0.89	0.75	0.68	0.55
54.61	19.92	24.08	0.60	0.89	1.30	0.85	0.72	0.62	0.49
54.6	14.90	29.74	—	0.76	1.05	0.73	0.64	0.55	0.45
54.62	10.07	34.61	—	0.70	0.82	0.64	0.56	0.49	0.40
54.56	5.08	39.45	—	0.91	0.73	0.59	0.52	0.43	0.35
49.63	24.96	24.37	0.41	0.63	0.77	0.62	0.51	0.39	0.28
49.58	20.00	29.01	0.63	0.78	0.77	0.55	0.44	0.34	0.27
49.91	14.42	34.89	—	0.78	0.72	0.49	0.37	0.28	0.21
49.67	10.02	39.73	—	0.58	0.70	0.44	0.34	0.26	0.18
44.34	24.75	29.14	1.02	0.75	0.86	0.35	0.27	0.21	0.15
44.73	19.74	33.47	1.18	0.88	0.80	0.32	0.21	0.15	0.08
44.58	15.14	39.11	0.61	0.56	0.68	0.22	0.15	0.10	0.04
39.46	25.01	32.81	1.88	0.84	0.69	0.28	0.11	0.05	0.17
39.66	19.70	37.87	2.13	0.64	0.52	0.17	0.00	0.14	0.22
34.69	24.78	36.94	2.61	0.98	0.86	0.34	0.19	0.02	0.16

Source: Data from Toropov, N. A., Bryantsev, B. A. (1965). Physical–Chemical properties and crystallization of melts of system MnO–FeO–SiO_2 (in Russian). In: Strukturnye Prevrashcheniya v Steklakh pri Povyshennykh Temperaturakh, Moskva,

TABLE 10.28
Electrical Resistivity of SiO_2–CaO–P_2O_5 Melts

Mol.% by batch			log (ρ, Ω·cm) at T, ˚C					
CaO	SiO_2	P_2O_5	1600	1550	1500	1450	1400	1350
54.27	45.08	0.64	0.28	0.36	0.46	0.57	0.70	0.82
53.74	44.64	1.62	0.33	0.41	0.49	0.62	0.72	0.85
52.68	44.76	3.56	0.39	0.47	0.57	0.70	0.82	0.96
51.45	42.75	5.80	0.47	0.55	0.66	0.77	0.89	1.05
49.32	40.97	9.71	0.59	0.68	0.80	0.89	1.05	1.15
50.99	47.59	1.42	0.47	0.54	0.64	0.74	0.89	1.05
49.72	47.43	3.85	0.59	0.66	0.74	0.85	0.96	1.10
48.60	45.46	5.94	0.68	0.74	0.85	0.96	1.10	1.22
47.84	44.65	7.50	0.74	0.82	0.89	1.00	1.15	1.22
46.13	43.06	10.83	0.82	0.92	1.05	1.10	1.22	1.30
43.74	55.52	0.75	0.60	0.68	0.77	0.89	1.05	1.15
43.38	55.08	1.55	0.68	0.77	0.85	0.96	1.10	1.22
43.04	54.63	2.32	0.74	0.82	0.92	1.05	1.15	1.30
42.40	53.83	3.78	0.82	0.92	1.00	1.15	1.22	1.40
41.16	52.25	6.59	0.96	1.05	1.15	1.30	1.40	—

Source: Data from Kalyadina, S. A. (1977). Issledovanie Vyazkosti i Udelnoi Elektroprovodnosti Fosfatno–Kremnistykh Rasplavov. Thesis. Leningrad

TABLE 10.29
Electrical Resistivity of SiO_2–CaO–P_2O_5 Melts

Mol.% by batch			log (ρ, Ω·cm) at T, ˚C			
SiO_2	CaO	P_2O_5	1350	1400	1450	1500
—	64.3	35.7	0.23	0.20	0.19	0.16
5.0	61.1	33.9	0.25	0.22	0.20	0.17
10.0	57.9	32.1	0.26	0.23	0.21	0.18
15.0	54.6	30.4	0.28	0.25	0.22	0.19
20.0	51.4	28.6	0.29	0.26	0.23	0.20
25.0	48.2	26.8	0.31	0.28	0.24	0.21
30.0	45.0	25.0	0.34	0.30	0.26	0.22

Source: Data from Zhunusov, S. M., Menlibaev, A., Esbolaeva, S. A., Serazetdinov, D. Z. (1989). Fizicheskie i Khimicheskie Svoistva Rasplavov i Stekol v Sisteme $CaO–P_2O_5–SiO_2$. Deposited in VINITI, Moscow, No.6573–V89 Dep.

TABLE 10.30
Electrical Resistivity of SiO_2–Na_2O–B_2O_3 Melts

Mol.% by batch			log (ρ, Ω·cm) at T, ˚C	
SiO_2	B_2O_3	Na_2O	1000	1300
70	10	20	0.430	0.170
65	15	20	0.703	0.205
60	20	20	0.820	0.330
55	25	20	0.912	0.424
50	30	20	0.816	0.289
45	35	20	0.620	0.223
40	40	20	0.520	0.104

Source: Data from Sasek, L., Rada, M. (1985). Vodivost alkalicko–boritych a borito–kremicitych sklovin. *Sb. Vys. Sk. Chem. Technol. Praze, Chem. Technol. Silik.* L13.

TABLE 10.31
Electrical Resistivity of B_2O_3–R_2O Melts

Wt.% by analysis				log (ρ, Ω·cm) at T, ˚C					
B_2O_3	Li_2O	Na_2O	K_2O	700	800	850	900	950	1000
98.53	1.47	—	—		2.93	2.72	2.54	2.39	2.27
96.95	3.05	—	—		2.26	2.09	1.88	1.71	1.59
95.75	4.25	—	—	2.51	2.04	1.81	1.63	1.46	1.34
94.45	5.55	—	—	2.28	1.78	1.56	1.38	1.24	1.13
92.93*	7.07*	—	—	2.22	1.60	1.38	1.21	1.07	0.95
90.43	9.57	—	—		1.27	1.09	0.89	0.76	0.63
87.45*	12.55*	—	—		0.98	0.83	0.69	0.59	0.48
96.76	—	3.24	—		2.70	2.51	2.30	2.15	2.00
95*	—	5*	—			2.06	1.87	1.71	1.57
89.09	—	10.91	—	2.43	1.89	1.67	1.48		
87.50	—	12.50	—				1.29	1.12	0.99
84.30	—	15.70	—			1.39	1.18	1.03	0.89
82.70	—	17.30	—		1.47	1.29	1.12	0.94	
80.03	—	19.97	—		1.29	1.12	0.94	0.79	0.65
77.57	—	22.43	—		1.13	0.93	0.79	0.64	
74.80	—	25.20	—		1.00	0.85	0.70	0.58	
72.39	—	27.61	—	1.16	0.83	0.67	0.54	0.46	
69.74	—	30.26	—	1.02	0.60	0.49	0.40	0.27	
94.48	—	—	5.52		2.65	2.43	2.23	2.06	1.91
89.53	—	—	10.47		2.26	1.99	1.77	1.63	1.50
84.68	—	—	15.32		2.00	1.76	1.57	1.40	1.26
79.64	—	—	20.36			1.62	1.39	1.24	1.13
75.02	—	—	24.98		1.49	1.29	1.12	0.99	
74.5*	—	—	25.5*		1.47	1.27	1.12	0.97	0.85
72.97	—	—	27.03		1.40	1.20	1.02	0.91	0.80
65.03	—	—	24.97	1.36	0.95	0.83	0.69	0.56	
61.12	—	—	38.88	1.08	0.81	0.70	0.59	0.49	0.41

Source: Data from Kostanyan, K. A. (1958). Study of electrical conductivity of molten alkali borates of systems Li_2O–B_2O_3, Na_2O–B_2O_3 K_2O–B_2O_3 (in Russian). *Izv. Akad. Nauk Arm. SSR, Khim. Nauki.* 11(2). *By batch.

TABLE 10.32
Electrical Resistivity of B_2O_3–K_2O–RO– Melts

Mol.% by analysis					log (ρ, Ω·cm) at T, ˚C			
B_2O_3	K_2O	CaO	SrO	BaO	800	900	1000	1100
93.4	3.0	3.6	—	—	3.00	2.51	2.18	1.91
92.5	3.3	4.2	—	—	3.11	2.58	—	1.92
87.6	3.1	9.3	—	—	3.36	2.65	2.14	1.78
87.4	3.2	9.4	—	—	3.22	2.59	2.11	1.75
84.9	3.1	12.0	—	—	3.43	2.63	2.07	1.68
81.8	3.0	15.2	—	—	3.62	2.69	2.05	1.62
81.7	3.0	15.3	—	—	3.60	2.68	2.14	1.8
78.0	3.2	18.8	—	—	3.79	2.66	1.99	1.52
75.7	3.0	21.3	—	—	3.97	2.74	1.97	1.50
72.5	2.7	24.8	—	—	4.11	2.78	1.94	1.40
69.4	3.2	27.4	—	—	—	—	1.85	1.33
94.9	3.1	—	2.0	—	2.95	2.50	2.13	1.92
92.6	3.2	—	4.2	—	3.00	2.52	2.17	1.87
90.5	3.2	—	6.3	—	3.09	2.53	2.11	1.85
87.5	3.1	—	9.4	—	3.31	2.59	2.10	1.72
84.3	3.2	—	12.5	—	3.55	2.67	2.09	1.68
81.2	3.2	—	15.6	—	3.72	2.74	2.07	1.60
79.2	1.7	—	19.1	—	4.15	2.92	2.08	1.61
75.0	3.2	—	21.8	—	3.89	2.70	1.97	1.47
71.8	3.2	—	25.0	—	—	2.72	1.93	1.40
68.8	3.1	—	28.1	—	—	2.61	1.89	1.31
94.9	3.1	—	—	2.0	2.98	2.55	2.17	1.76
93.0	3.1	—	—	3.9	2.95	2.52	2.15	1.84
90.9	3.1	—	—	6.0	3.07	2.52	2.10	1.80
87.7	3.2	—	—	9.1	3.17	2.52	2.02	1.70
82.9	3.1	—	—	14.0	3.48	2.63	2.00	1.55
81.7	2.9	—	—	15.4	3.53	2.59	1.97	—
78.3	3.2	—	—	18.5	3.57	2.59	1.90	1.47
76.4	3.2	—	—	20.4	3.55	2.53	1.88	1.40
72.2	3.2	—	—	24.6	3.48	2.44	1.74	1.30
69.1	3.2	—	—	27.7	3.26	2.25	1.62	1.23
60.9	3,0	—	—	36,1	—	—	1,33	1,06

Source: Data from Coughanour, L. W., Shartsis, L., Shermer, H. F. (1958). Viscosity, density, and electrical resistivity of molten alkaline–earth borate glasses with 3 Mole % of potassium oxide. *J. Am. Ceram. Soc.* 41(8)

TABLE 10.33
Electrical Resistivity of B_2O_3–Li_2O–Na_2O Melts

Mol.% by batch			log (ρ, Ω·cm) at T, ˚C				
B_2O_3	Li_2O	Na_2O	800	850	900	950	1000
88	12	—	—	1.53	1.37	1.24	1.13
88	9	3	—	1.58	1.41	1.26	1.15
88	6	6	—	1.62	1.43	1.29	1.15
88	3	9	—	1.63	1.45	1.30	1.15
88	—	12	1.89	1.67	1.48	1.33	1.18
82	18	—	1.39	1.20	1.00	0.88	0.76
82	14	4	1.57	1.33	1.12	0.96	0.85
82	9	9	1.62	1.37	1.17	1.01	0.89
82	4	14	1.54	1.33	1.12	0.97	0.84
82	—	18	1.49	1.33	1.13	0.99	0.87
75	25	—	0.98	0.83	0.65	0.58	0.48
75	20	5	1.10	0.88	0.73	0.69	0.49
75	15	10	1.18	0.97	0.79	0.65	0.53
75	10	15	1.22	1.00	0.82	0.70	0.58
75	5	20	1.08	0.93	0.81	0.65	0.56
75	—	25	1.10	0.96	0.78	0.62	0.52

Source: Data from Kostanyan, K. A. (1960). Study of mixed alkali effect for electrical conductivity in molten borate glasses (in Russian). In: Stekloobraznoe Sostoyanie, Moskva

TABLE 10.34
Electrical Resistivity of B_2O_3–K_2O–Na_2O–Li_2O Melts

Mol.% by batch				log (ρ, Ω·cm) at T, °C				
B_2O_3	Li_2O	Na_2O	K_2O	800	850	900	950	1000
88		12	—	1.89	1.67	1.48	1.33	1.18
88		9	3	1.91	1.70	1.49	1.33	1.20
88		6	6	1.97	1.73	1.53	1.36	1.26
88		3	9	1.90	1.72	1.53	1.38	1.24
88		—	12	2.00	1.76	1.57	1.40	1.27
80		20	—	1.42	1.22	1.04	0.87	0.79
80		16	4	1.52	1.30	1.11	0.96	
80		10	10	1.63	1.32	1.13	0.95	0.79
80		4	16	1.53	1.33	1.15	1.00	0.88
80		—	20	1.47	1.27	1.12	0.97	0.85
72		28	—	0.96	0.81	0.65	0.51	0.40
72		21	7	1.15	0.90	0.71	0.53	0.48
72		14	14	1.28	1.00	0.74	0.60	0.48
72		7	21	1.20	0.95	0.75	0.62	0.52
72		—	28	0.98	0.85	0.70	0.59	0.51
88	12		—	—	1.53	1.37	1.24	1.13
88	8		4	—	1.74	1.56	1.33	1.26
88	6		6	—	1.73	1.59	1.36	1.22
88	4		8	—	1.77	1.57	1.40	1.28
88	—		12	2.00	1.76	1.57	1.40	1.27
82	18		—	1.39	1.20	1.00	0.88	0.76
82	12		6	1.81	1.53	1.29	1.11	0.95
82	9		9	—	1.62	1.40	1.21	1.06
82	6		12	1.85	1.59	1.37	1.18	1.01
82	—		18	1.59	1.42	1.26	1.10	0.99
75	25		—	0.98	0.83	0.65	0.58	0.48
75	20		5	1.31	1.07	0.90	0.76	0.62
75	15		10	1.55	1.26	1.06	0.88	0.72
75	10		15	1.54	1.28	1.06	0.89	0.76
75	5		20	1.45	1.18	1.00	0.86	0.72
75	—		25	1.18	1.00	0.85	0.73	0.65

Source: Data from Kostanyan, K. A. (1960). Study of mixed alkali effect for electrical conductivity in molten borate glasses (in Russian). In: Stekloobraznoe Sostoyanie, Moskva

TABLE 10.35
Electrical Resistivity of B_2O_3–Na_2O–Al_2O_3 Melts

Mol.% by batch			log (ρ, Ω·cm) at T, ˚C			
B_2O_3	Na_2O	Al_2O_3	600	800	1000	1200
90	10	—	3.51	1.97	1.24	0.88
87	10	3	3.68	2.13	1.46	1.08
85	10	5	3.63	2.10	1.45	1.09
82	10	8	3.41	1.96	1.44	1.10
80	10	10	3.20	1.86	1.40	1.10
78	10	12	3.07	1.80	1.41	1.10
75	10	15	2.85	1.72	1.37	1.08
80	20	—	2.53	1.42	0.74	0.41
74	20	6	2.59	1.47	0.85	0.59
70	20	10	2.42	1.35	0.85	0.59
64	20	16	2.28	1.28	0.86	0.60
60	20	20	2.22	1.27	0.85	0.60
56	20	24	2.18	1.25	0.85	0.61
70	30	—	1.86	0.75	0.38	0.18
61	30	9	1.96	0.97	0.54	0.26
55	30	15	1.92	0.93	0.53	0.26
46	30	24	1.86	0.90	0.50	0.25
40	30	30	1.83	0.89	0.50	0.26

Source: Data from Kirakosyan, S. Sh. (1974). Electrical conductivity of sodium aluminoborate glasses in a broad temperature range (in Russian). In: Stekloobraznoe Sostoyanie, Erevan: Izd. Akademii Nauk Arm. SSR

TABLE 10.36
Electrical Resistivity of B_2O_3–Na_2O–Li_2O–K_2O–GeO_2 Melts

Mol.% by batch					log (ρ, Ω·cm) at T, °C			
B_2O_3	Li_2O	Na_2O	K_2O	GeO_2	600	800	1000	1200
5	20	—	—	75	1.95	0.80	0.40	0.02
10	20	—	—	70	2.05	0.83	0.35	0.05
15	20	—	—	65	2.10	0.83	0.40	0.03
20	20	—	—	60	2.13	0.85	0.41	–0.04
30	20	—	—	50	2.10	0.85	0.38	–0.03
40	20	—	—	40	2.23	0.95	0.43	0.05
50	20	—	—	30	2.40	1.10	0.50	0.10
60	20	—	—	20	2.50	1.17	0.55	0.15
70	20	—	—	10	2.65	1.26	0.60	0.20
5	—	10	—	85	3.75	2.00	1.20	0.80
10	—	10	—	80	3.65	1.78	1.05	0.63
20	—	10	—	70	3.95	2.25	1.43	0.98
30	—	10	—	60	4.02	2.35	1.54	1.05
40	—	10	—	50	4.20	2.30	1.45	1.04
50	—	10	—	40	4.27	2.40	1.52	0.98
60	—	10	—	30	4.29	2.38	1.50	1.03
70	—	10	—	20	4.18	2.42	1.53	1.05
80	—	10	—	10	4.05	2.30	1.50	1.10
5	—	20	—	75	2.65	1.20	0.65	0.35
10	—	20	—	70	2.70	1.25	0.75	0.30
15	—	20	—	65	2.58	1.30	0.73	0.30
20	—	20	—	60	2.69	1.30	0.68	0.40
30	—	20	—	50	2.88	1.40	0.75	0.35
40	—	20	—	40	2.90	1.45	0.75	0.40
50	—	20	—	30	3.00	1.55	0.84	0.40
60	—	20	—	20	2.95	1.46	0.80	0.45
70	—	20	—	10	3.00	1.50	0.90	0.45
5	—	30	—	65	1.25	0.31	–0.05	–0.25
10	—	30	—	60	1.33	0.40	0.02	–0.20
15	—	30	—	55	1.47	0.50	0.08	–0.20
20	—	30	—	50	1.55	0.42	–0.05	–0.25
30	—	30	—	40	1.73	0.50	0.02	–0.02
40	—	30	—	30	1.74	0.56	0.05	–0.19
50	—	30	—	20	1.72	0.56	0.08	–0.20
5	—	—	20	75	3.35	1.50	0.75	0.35
10	—	—	20	70	3.45	1.62	0.91	0.44
15	—	—	20	65	3.50	1.71	0.96	0.53
20	—	—	20	60	3.47	1.67	0.95	0.50
30	—	—	20	50	3.50	1.75	1.02	0.51
40	—	—	20	40	3.48	1.70	1.00	0.50
50	—	—	20	30	3.45	1.76	0.96	0.47
60	—	—	20	20	3.45	1.74	1.00	0.50
70	—	—	20	10	3.25	1.55	0.90	0.46

Source: Data from Krupkin, Yu. S., Evstropiev, K. S. (1971). Properties and structure of high–alkali borogermanate glasses (in Russian). *Neorg. Mater.* 7(9)

TABLE 10.37
Electrical Resistivity of SiO_2–BaO–B_2O_3 Melts

Mol.% by batch			log (ρ, Ω·cm) at T, ˚C				
SiO_2	B_2O_3	BaO	900	1000	1100	1200	1300
—	70	30	2.26	1.62	—	—	—
10	60	30	2.60	1.89	1.40	—	—
20	50	30	2.76	2.00	1.51	—	—
30	40	30	3.00	2.26	1.69	1.28	—
40	30	30	3.26	2.56	1.98	1.55	1.21
45	25	30	—	2.80	2.06	1.60	1.26
50	20	30	—	3.10	2.18	1.74	1.37
52	18	30	—	3.30	2.26	1.79	1.40
55	15	30	—	3.45	2.48	1.97	1.55
58	12	30	—	—	2.64	2.09	1.65
65	5	30	—	—	3.11	2.35	1.77

Source: Data from Kharyuzov, V. A., Mazurin, O. V., Zubkova, N. M. (1960). Electrical conductivity of glasses of system BaO–Al_2O_3–B_2O_3–SiO_2 (in Russian). In: Stekloobraznoe Sostoyanie, Moskva

TABLE 10.38
Electrical Resistivity of B_2O_3–PbO Melts

Mol.% by batch		log (ρ, Ω·cm) at T, ˚C					
B_2O_3	PbO	700	800	900	1000	1100	1200
92.8	7.2	4.36	3.36	2.90	2.59	2.34	2.13
84.6	15.4	3.22	2.50	2.03	1.70	1.60	1.52
82.8	17.2	3.18	2.37	1.94	1.67	1.48	1.31
75.8	24.2	2.86	2.00	1.54	1.27	1.06	0.90
68.1	31.9	2.36	1.65	1.24	0.92	0.72	0.59
67.4	32.6	2.12	1.53	1.14	0.83	0.60	0.46
55.5	44.5	1.94	1.36	1.00	0.74	0.56	0.45
54.0	46.0	1.72	1.14	0.80	0.63	0.50	0.40
52.4	47.6	—	1.00	0.64	0.50	0.40	0.32
44.7	55.3	—	0.68	0.48	0.33	0.18	0.06
42.6	57.4	1.30	0.93	0.62	0.38	0.18	—

Source: Data from Kostanyan, K. A., Geokchyan, O. K. (1968). Electrical conductivity of molten lead–silicate and lead–borate glasses (in Russian). *Arm. Khim. Zh.* 21(3)

TABLE 10.39
Electrical Resistivity of B_2O_3–RO Melts Data by Kostanyan and Geokchyan [46]

Mol.% by batch					log (ρ, Ω·cm) at T, °C					
B_2O_3	CaO	ZnO	CdO	BaO	700	800	900	1000	1200	1300
66.7	33.3	—	—	—	—	—	2.65	1.80	0.98	0.79
60	40	—	—	—	—	—	2.48	1.70	0.82	0.69
50	50	—	—	—	—	—	—	—	0.68	—
50	—	50	—	—	3.80	2.34	1.53	1.10	0.62	—
47.5	—	52.5	—	—	—	2.14	1.42	1.03	0.60	0.50
45	—	55	—	—	2.90	1.98	1.39	0.98	0.56	—
40	—	60	—	—	—	—	1.33	0.92	0.50	—
50	—	—	50	—	2.70	1.86	1.34	0.95	0.58	—
45	—	—	55	—	2.46	1.75	1.25	0.88	0.44	—
80	—	—	—	20	—	—	2.81	2.07	1.27	—
66.7	—	—	—	33.3	3.92	2.65	1.82	1.43	0.78	—
60	—	—	—	40	—	—	—	1.36	0.65	—
50	—	—	—	50	—	—	1.30	1.00	0.52	—
45	—	—	—	55	—	—	—	0.87	0.45	—

Source: Data from Kostanyan, K. A., Geokchyan, O. K. (1968). Electrical conductivity of molten lead–silicate and lead–borate glasses (in Russian). *Arm. Khim. Zh.* 21(3)

TABLE 10.40
Compositions of Experimental Melts in mol. % by Analysis

No	Na_2O	K_2O	CaO	MgO	Al_2O_3	SiO_2
A1	12.31	—	9.61	—	—	78.08
A2	14.76	—	9.89	—	—	75.36
A3	16.73	—	9.76	—	—	73.5
A4	13.93	—	5.00	—	—	81.08
A5	14.08	—	7.32	—	—	78.6
A6	14.45	—	12.28	—	—	73.25
A7	11.88	—	7.12	—	—	81.0
A8	15.52	—	12.03	—	—	72.45
A9	15.59	—	5.03	—	—	79.38
A10	13.70	—	9.74	—	2.12	74.45
A11	13.64	—	9.51	—	4.35	72.5
A12	13.46	—	8.69	1.51	—	76.34
A13	13.91	—	6.10	3.22	—	76.77
A14	12.08	2.02	9.36	—	—	76.54
A15	9.95	3.71	10.21	—	—	76.13
A16	8.48	5.73	9.82	—	—	75.97
A17	6.52	6.90	9.86	—	—	76.71
A18	13.29	—	15.02	—	—	71.68
A19	21.50	—	4.31	—	—	73.09
A20	19.80	—	8.93	—	—	70.44
A21	20.11	—	13.48	—	—	65.32
A22	19.78	—	3.25	4.80	—	72.03
A23	11.88	2.98	9.85	—	3.83	71.46
A24	9.08	6.05	10.00	—	3.88	70.99
A25	11.97	2.94	6.32	3.10	—	75.68
A26	9.01	5.78	6.21	3.08	—	75.92
A26/2	8.90	5.78	6.18	3.06	—	76.08
A27	14.37	—	5.53	2.21	3.75	68.66
A28	16.26	—	5.54	2.19	3.83	66.69
A29	18.88	—	5.59	2.29	3.54	63.63

TABLE 10.41
Electrical Resistivity of Experimental Melts

	log (ρ, Ω·cm) at T, °C								
No	**600**	**700**	**800**	**900**	**1000**	**1100**	**1200**	**1300**	**1400**
A1	3.22	2.53	2.06	1.7	1.43	1.21	1.04	0.89	0.77
A2	2.76	2.1	1.65	1.33	1.09	0.9	0.75	0.63	0.52
A3	2.56	1.91	1.47	1.15	0.9	0.71	0.55	0.42	0.31
A4	2.59	2.05	1.68	1.4	1.19	1.02	0.88	0.77	0.67
A5	2.73	2.13	1.72	1.41	1.17	0.99	0.84	0.71	0.6
A6	2.99	2.3	1.8	1.44	1.16	0.93	0.75	0.6	0.47
A7	3.03	2.41	1.99	1.68	1.44	1.25	1.1	0.97	0.87
A8	2.8	2.1	1.62	1.28	1.02	0.81	0.65	0.51	0.40
A9	2.5	1.95	1.55	1.26	1.03	0.85	0.71	0.59	0.48
A10	2.99	2.33	1.87	1.54	1.29	1.09	0.93	0.80	0.69
A11	3.03	2.37	1.92	1.59	1.34	1.14	0.98	0.85	0.74
A12	2.97	2.29	1.83	1.49	1.23	1.03	0.87	0.73	0.62
A13	2.8	2.16	1.73	1.41	1.17	0.99	0.83	0.70	0.59
A14	3.24	2.58	2.09	1.72	1.43	1.19	0.99	0.83	0.68
A15	3.61	2.88	2.35	1.94	1.61	1.35	1.13	0.95	0.79
A16	3.74	2.95	2.39	1.97	1.65	1.39	1.18	1.01	0.86
A17	3.95	3.08	2.5	2.08	1.76	1.51	1.31	1.14	1.01
A18	3.17	2.4	1.85	1.45	1.14	0.89	0.69	0.52	0.38
A19	2.15	1.62	1.23	0.93	0.7	0.51	0.35	0.22	0.13
A20	2.24	1.66	1.25	0.95	0.72	0.53	0.38	0.25	0.14
A21	2.39	1.73	1.27	0.92	0.65	0.44	0.26	0.12	0
A22	2.15	1.57	1.18	0.89	0.68	0.51	0.37	0.25	0.16
A23	3.37	2.66	2.14	1.76	1.46	1.22	1.02	0.85	0.71
A24	3.76	3	2.44	2.02	1.69	1.42	1.2	1.02	0.86
A25	3.27	2.62	2.14	1.77	1.47	1.23	1.03	0.86	0.71
A26	3.63	2.85	2.3	1.89	1.57	1.32	1.12	0.95	0.81
A26/2	3.65	2.82	2.26	1.85	1.54	1.29	1.09	0.93	0.79
A27	2.7	2.13	1.74	1.45	1.23	1.06	0.92	0.81	0.72
A28	2.61	1.96	1.53	1.22	0.99	0.82	0.68	0.56	0.46
A29	2.35	1.76	1.35	1.05	0.82	0.64	0.5	0.38	0.28

TABLE 10.42
Compositions of Experimental Alkali–Borosilicate Melts in mol. % by Analysis

No.	Na_2O	K_2O	B_2O_3	SiO_2
B1	13.19	—	13.7	73.11
B2	8.65	—	13.57	77.78
B3	4.69	—	14.42	80.89
B4	8.66	—	18.87	72.47
B5	4.75	—	19.45	75.8
B6	4.32	—	23.45	72.23
B7	4.79	4.76	14.41	76.04
B8	—	9.02	13.44	77.55
B9	4.74	—	29.18	66.07
B10	13.15	—	28.91	57.94
B11	13.61	—	19.67	66.73
B12	13.41	—	9.77	76.82
B13	18.78	—	14.29	66.93

TABLE 10.43
Electrical Resistivity of Experimental Sodium–Borosilicate Melts

	log (ρ, Ω·cm) at T, °C								
No.	**600**	**700**	**800**	**900**	**1000**	**1100**	**1200**	**1300**	**1400**
B1	3.1	2.34	1.82	1.45	1.17	0.95	0.77	0.63	0.51
B2	3.65	2.97	2.47	2.1	1.81	1.57	1.38	1.22	1.08
B3	4.3	3.62	3.13	2.75	2.45	2.21	2.01	1.84	1.7
B4	3.82	3.09	2.55	2.14	1.82	1.56	1.34	1.16	1.01
B5	4.38	3.6	3.06	2.65	2.34	2.09	1.89	1.72	1.58
B6	4.3	3.57	3.04	2.62	2.29	2.02	1.8	1.61	1.45
B7	4.75	3.99	3.43	2.99	2.65	2.36	2.13	1.93	1.76
B8	5.16	4.11	3.32	2.7	2.21	1.8	1.47	1.18	0.93
B9	4.29	3.58	3.03	2.6	2.25	1.96	1.72	1.5	1.33
B10	3.25	2.61	2.12	1.73	1.42	1.16	0.94	0.76	0.6
B11	3.16	2.35	1.82	1.45	1.17	0.96	0.79	0.65	0.53
B12	3.1	2.36	1.87	1.52	1.26	1.05	0.88	0.75	0.64
B13	2.65	1.8	1.24	0.85	0.56	0.33	0.15	0	–0.12

TABLE 10.44
Comparison of Experimental and Calculated Resistivity Values for Two Commercial Glasses

	Mol.% by analysis						log (ρ, Ω·cm) at T, ˚C			
No.	Na_2O	K_2O	CaO	MgO	Al_2O_3	SiO_2	600	900	1300	Note
1	13.03	0.25	9.10	5.01	0.75	71.86	3.12	1.50	0.68	(experiment)
							3.13	1.47	0.61	(calculation)
							0.01	0.03–	0.07	(difference)
2	14.23	0.59	6.90	5.41	1.87	71.00	2.93	1.39	0.61	(experiment)
							2.89	1.37	0.58	(calculation)
							0.04	0.02	0.03	(difference)

Source:

ACKNOWLEDGMENTS

With pleasure and gratitude we acknowledge that all our own measurements, the results of which are included in this chapter, as well as the development of the method of calculations of melt resistivity were performed due to the financial support of the Center for Glass Research (New York State College of Ceramics, Alfred, New York). We also acknowledge that all tables containing published data were selected, transformed into the standard format, and printed by using the program SciGlass (SciVision Company, Lexington, MA).

REFERENCES

1. Frenkel, Ya. I. (1945). *Kineticheskaya Teoriya Zhidkostei*. Moskva: Izd. AN SSSR.
2. Glasstone, S., Laidler, K. I., Eyring, H. (1941). *The Theory of Rate Processes*. New York, London.
3. Mazurin, O. V. (1962). *Elektricheskiye Svoistva Stekla*. Leningrad: Khimizdat.
4. Kobeko, P. P. (1952). *Amorfnyje Veshchestva*. Moskva: Izd.AN SSSR.
5. Mazurin, O. V. (1988). Properties of glass–forming melts In: *Advances in the Fusion of Glass*. Westerville, Ohio: The American Ceramic Soc. pp.32.1–32–20.
6. Mazurin, O. V. (1977). Thermal ionic relaxation in inorganic glasses (in Russian). In: *Svoistva i Razrabotka Novykh Opticheskikh Stekol*. Leningrad: Mashinostroenie, p. 101.
7. Babcock, C. L. (1934). Viscosity and electrical conductivity of molten glasses. *J. Am. Ceram. Soc*. 17(11):329–342.
8. Boricheva, V. N. (1956). Issledovanie Elektroprovodnosti Nekotorykh Prostykh Silikatnykh Stekol v Shirokom Intervale Temperatur. Thesis. Leningrad: Lensoviet Technological Institute.
9. Botvinkin, O. K., Okhotin, M. V. (1936). Electrical conductivity of molten glass (in Russian). In: *Noveishie Raboty po Fizicheskoi Khimii Stekla*, Moskva: Stroiizdat, pp. 72–81.

10. Kostanyan, K. A., Saakyan, K. S. (1961). Electrical conductivity of glasses of Na_2SiO_3–SiO_2 system in molten state (in Russian). *Izv. Akad. Nauk Arm. SSR, Khim. Nauki*. 14(5):409–416.
11. Kroger, C., Weisgerber, P. (1958). Zur Bestimmung der elektrischen Leitfähigkeit von Natrium–Silikatschmelzer. *Z. Phys. Chem.* 18(1/2):90–109.
12. Lotto, B., Lazzari, S. (1965). Mizura della resistivita elettrica del vetro “allo stato fuso” *Vetro e Silicati*. 9(50):5–10.
13. Piechurowski, A. (1972). Method of measuring glass resistance at high temperatures. 4e Conference sur la fusion electrique du verre, Tchecoslovaque. 2:16–27.
14. Stanek, J., Sasek, L., Meissnerova, H. (1966). Elektrisches glasschmelzen. *Sprechsaal Keram., Glas, Email, Silik.* No. 5, pp. 151–156.
15. Tickle, R. E. (1967). The electrical conductance of molten alcali silicates. Part 1. Experiments and results. *Phys. Chem. Glasses*. 8(3):101–112.
16. Boulos, E. N., Smith, J. W., Moynihan, C. T. (1983). Rapid and accurate measurements of electrical resistivity on glass melts. *Glastechn. Ber.* 56K(1):509–514.
17. O’Mach. (1960). Mereny teplotni zavislosti elektrickeho odporu skla za vysokych teplot. *Silikaty.* 4:357–366.
18. Mazurina, E. K. (1967). Influence of two-valence metal oxides on electrical conductivity of alkali silicate glasses in the temperature range 200–1400°C (in Russian). Thesis. Leningrad: Lensoviet Technological Institute.
19. Evstropiev, K. S. (1949). Electrical conductivity of glasses of system Na_2SiO_3–$PbSiO_3$–SiO_2 at high temperatures (in Russian). In: Fiziko–Khimicheskie Svoistva Troinoi Sistemy Na_2O–PbO–SiO_2, Moskva, p. 83–109.
20. Kostanyan, K. A., Erznkyan, E. A. (1967). Electrical conductivity of glasses of system Li_2O–SiO_2 in molten state (in Russian). *Arm. Khim. Zh.* 20(5):358–365.
21. Kostanyan, K. A., Erznkyan, E. A. (1964). Study of electrical conductivity of glasses of system K_2O–SiO_2 in a broad temperature range (in Russian). *Izv. Akad. Nauk Arm. SSR, Khim. Nauki.* 17(6):613–622.
22. Lapin, V. A., Polonskii, Yu. A. (1975). Electrical resistivity of silica glass in temperature range 400–2200 C (in Russian). *Tr. Gos. Inst. Ogneuporov.* 4(47):79–91.
23. Loryan, S. G., Saringyulyan, R. S., Kostanyan, K. A. (1977). Electrical conductivity of high-silica glasses of system Al2O3–B2O3–SiO2 in a broad temperature range (in Russian). *Fizika i Khimiya Stekla.* 3(6):612–616.
24. Mazurina, E. K. (1967). Influence of oxides of bivalent metals on electrical conductivity of sodium-silicate glasses in a broad temperature range (in Russian). *Steklo*. 1:129–135.
25. Mazurina, E. K., Evstropiev, K. S. (1970). On certain patterns of the influence of bivalent ions on electrical conductivity of molten alkali-silicate glasses (in Russian). In: Stekloobraznoe Sostoyanie. Erevan: Izd. Akademii Nauk Arm. SSR. pp. 195–199.
26. Saringyulyan, R. S., Kostanyan, K. A. (1971). Role of viscosity in a study of electrical conductivity of glasses of system K_2O–PbO–SiO_2 (in Russian). In: Stekloobraznoe Sostoyanie, Moskva,, p. 289–291.
27. Erznkyan, E. A., Kostanyan, K. A. (1968). Electrical conductivity of glasses Li_2O–RO–SiO_2 in molten state (in Russian). *Arm. Khim. Zh*. 21(9):759–765.
28. Kostanyan, K. A., Erznkyan, E. A. (1967). Mixed alkali effect in molten glasses II (in Russian). *Arm. Khim. Zh.* 20(9):686–691.
29. Sasek, L., Meissnerova, H., Persin J. (1973). Structura a vlastnosti kremictych sklovin. IV. Vliv MgO a BaO na elektrickou vodivost ternalnich kremicitych sklovin *Sb. Vys. Sk. Chem. Technol. Praze, Chem. Technol. Silik.* L4:87–138.

30. Kostanyan, K. A., Erznkyan, E. A., Avetisyan, E. M. (1967). Mixed alkali effect in molten glasses I (in Russian). *Arm. Khim. Zh.* 20(8):592–600.
31. Kostanyan, K.A. (1952). Issledovanie Elektroprovodnosti Natrii–Kaltsii–Magnii–Alyumosilikatnykh Stekol v Rasplavlennom Sostoyanii. Thesis. Leningrad: Lensoviet Technological Institute.
32. Ejima, T., Watanabe, Y., Kameda, M. (1968). Electric conductance in the liquid PbO–SiO2 binary system (Electric conductance in liquid lead silicates (I)) *J. Jpn. Inst. Metals*. 32(12): 1250–1262.
33. Kalyadina, S. A. (1977). Issledovanie Vyazkosti i Udelnoi Elektroprovodnosti Fosfatno–Kremnistykh Rasplavov. Thesis. Leningrad,.
34. Kammel, R., Winterhager, H. (1965). Struktur und Eigenschaften von Schlacken der Metallhuttenprozesse. V. Dichtebestimmungen und elektrische Leitfähigkeitsmessungen an Schmelzen des Systems Kalk–Tonerde–Kieselsaure. Erzmetall. 18(1):9–17.
35. Winterhager, H., Greiner, L., Kammel, R. (1966). Untersuchungen über die Dichte und die elektrische Leitfähigkeit von Schmelzen der Systeme CaO–Al2O3–SiO2 und CaO–MgO–Al2O3–SiO2. *Forschungsberichte des Landes Nordrhein Westfahlen.* p. 1630–1639.
36. Segers, L., Fontana, A., Winand, R. (1979). Viscosité de mélanges de silicates fondus du système CaO–SiO_2–MnO. *Electrochemical Acta.* 24(2):213–218.
37. Toropov, N. A., Bryantsev, B. A. (1965). Physical–Chemical properties and crystallization of melts of system MnO–FeO–SiO_2 (in Russian). In: Strukturnye Prevrashcheniya v Steklakh pri Povyshennykh Temperaturakh, Moskva, pp. 205–232.
38. Zhunusov, S. M., Menlibaev, A., Esbolaeva, S. A., Serazetdinov, D. Z. (1989). Fizicheskie i Khimicheskie Svoistva Rasplavov i Stekol v Sisteme CaO–P_2O_5–SiO_2. Deposited in VINITI, Moscow, No.6573–V89 Dep.
39. Sasek, L., Rada, M. (1985). vodivost alkalicko–boritych a borito-kremicitych sklovin. *Sb. Vys. Sk. Chem. Technol. Praze, Chem. Technol. Silik.* L13:165–177.
40. Kostanyan, K. A. (1958). Study of electrical conductivity of molten alkali borates of systems Li_2O–B_2O_3, Na_2O–B_2O_3 K_2O–B_2O_3 (in Russian). *Izv. Akad. Nauk Arm. SSR, Khim. Nauki.* 11(2):65–73.
41. Coughanour, L. W., Shartsis, L., Shermer, H. F. (1958). Viscosity, density, and electrical resistivity of molten alkaline-earth borate glasses with 3 mol % of potassium oxide. *J. Am. Ceram. Soc.* 41(8): 324–329.
42. Kostanyan, K. A. (1960). Study of mixed alkali effect for electrical conductivity in molten borate glasses (in Russian). In: Stekloobraznoe Sostoyanie, Moskva,. pp. 266–270.
43. Kirakosyan, S. Sh. (1974). Electrical conductivity of sodium aluminoborate glasses in a broad temperature range (in Russian). In: Stekloobraznoe Sostoyanie, Erevan: Izd. Akademii Nauk Arm. SSR. pp. 78–81.
44. Krupkin, Yu. S., Evstropiev, K. S. (1971). Properties and structure of high-alkali borogermanate glasses (in Russian). *Neorg. Mater.* 7(9):1591–1595.
45. Kharyuzov, V. A., Mazurin, O. V., Zubkova, N. M. (1960). Electrical conductivity of glasses of system BaO–Al_2O_3–B_2O_3–SiO_2 (in Russian). In: *Stekloobraznoe Sostoyanie*, Moskva, pp. 264–266.
46. Kostanyan, K. A., Geokchyan, O. K. (1968). Electrical conductivity of molten lead-silicate and lead-borate glasses (in Russian). *Arm. Khim. Zh.* 21(3):230–240.
47. Peyches, I. (1948). The principles underlying the electric melting of glass. *J. Soc. Glass Techn.* 32(149):399–424.
48. Sheludyakov, N.A. (1959). Investigations in the Field of Electromelting (in Russian). D. Sci.Thesis. Leningrad.

11 How the Properties of Glass Melts Influence the Dissolution of Refractory Materials

George A. Pecoraro

CONTENTS

11.1 INTRODUCTION

The high-wear areas of glass contact refractory materials that influence the service life of glass furnaces are usually the melter basin walls, the roof and walls of the throat, and areas of the bottom adjacent to stirrers, bubblers and booster electrodes. The metal line region in the batch melting area of the furnace wears very rapidly, even with the use of block cooling air, and usually requires the addition of water cooler pads or overcoat blocks to extend furnace life. High wear at throats, electrodes and bubblers can result in premature furnace repairs

and glass leaks. Dissolution rates of refractory materials that make up the throat of the furnace are high because of the higher velocities and shear of glass melt passing through the restricted cross-sectional area and because of upward drilling corrosion. Examples of basin wall and throat wear profiles are shown in Figure 11.l. In electrically heated furnaces, hotter glass near electrodes can cause higher dissolution rates of refractories below the glass surface. Refractory dissolution rates can be accelerated by the extensive corrosion of refractory metal electrodes, since more energy is dispersed closer to the refractory wall. Therefore, corrosion mechanisms of refractories and electrodes need to be understood, and their design and operation optimized as well. Because of the important economic and technical consequences of glass furnace refractory dissolution and metal electrode corrosion, there has been considerable effort in recent years to measure corrosion rates of furnace construction materials in glass melts, to formulate

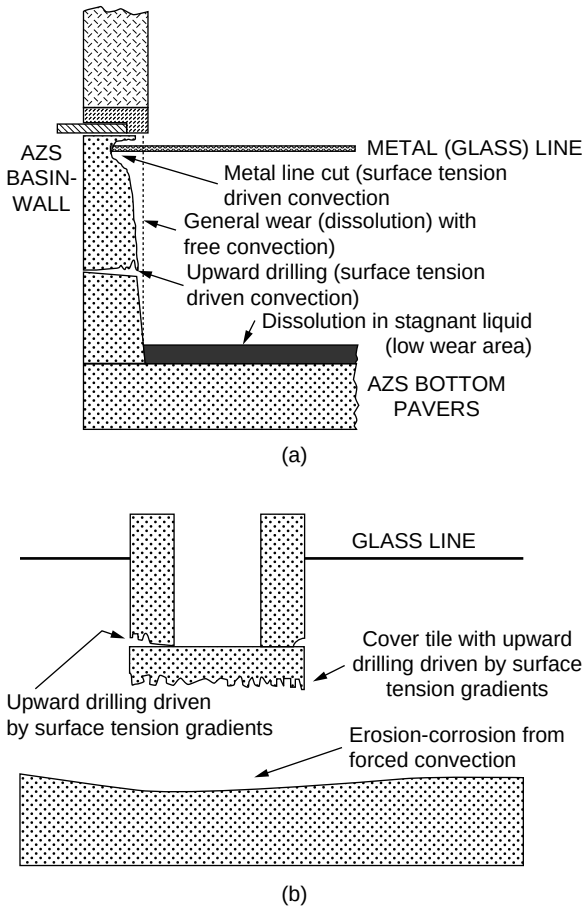

FIGURE 11.1 Schematic cross sections of glass furnaces showing regions of high and low refractory dissolution rates.

predictive equations for the kinetics of corrosion, and to better understand the principles involved.

The principles of corrosion of furnace glass contact refractories and refractory metal electrodes are found in the theories of heterogeneous systems, mass-transport kinetics, and phase equilibria thermodynamics. Mass transport equations have been developed for dissolution kinetics of various types of applications.

Inputting the physicochemical properties of glass melts into these equations has led to the calculation of dissolution rates for systems consisting of various combinations of refractories and glass melts at various temperatures, and to the selections of glass contact furnace materials and associated design configurations, which result in improved furnace life and overall process yields and throughput.

The goals of this chapter are to:

1. Identify and discuss the implications of the glass melt properties included in the dissolution kinetic equations
2. Review some of the hardware and experimental designs used for experimentally determining the dissolution rates of refractories and refractory metals by glass melts
3. Offer some suggestions for designing longer-lasting and better-performing refractory material systems based on dissolution kinetics and other industrial experiences

11.1.1 Thermodynamics of Glass Melt Corrosivity Toward Refractories

The driving force for dissolution of a solute in a solvent is the reduction of free energy of the system. The driving force for dissolution of a refractory (solute) in a glass melt (solvent) can be thought of simply as the difference between the refractory concentration of the saturated and the unaltered glass melt. The liquidus curve of the binary equilibrium phase diagram of the solute and the solvent represent the saturation composition at which the free energy of the solute equals its free energy in solution. The liquidus determines the amount of a solid that can be dissolved into the liquid (saturation composition) at any given temperature. The simplest model for dissolution of a pure refractory A dissolving in glass melt A–B at temperature T_l is shown in the phase diagram in Figure 11.2. The free energy difference is depicted by points B and L. As the temperature increases, the free energy difference increases. Hence, the thermodynamic driving force increases.

11.1.2 Refractory Dissolution: General Considerations

For most common systems, the dissolution rates of oxide solids in glass melts depend on three phenomena [2]:

1. The solubility of the refractory oxide in the melt
2. The mobility of the reacting species in the glass melt
3. The mobility of the dissolved refractory in the glass melt

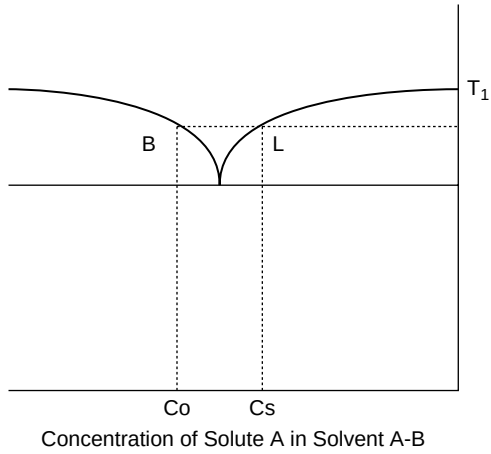

FIGURE 11.2 Binary phase diagram of glass A–B where the refractory is component A (A. R. Cooper, Jr., Dissolution Kinetics in Glass Making, *Advances in Glass Technology,* Plenum, New York (1962).

The greater the mobility or diffusivity of the reacting species in the melt, the greater the solubility of the refractory in the glass melt, and the greater the removal rate of the solute from the interface, the greater the dissolution rate.

Any natural or forced convection process that removes saturated liquid from the solid–liquid interface accelerates the dissolution rate [2–4]. The convection disturbs the chemical equilibrium of the region in the glass melt adjacent to the solid that is saturated with refractory.

A heterogeneous corrosion process is said to be "diffusion-controlled" if its slow step is either the introduction of reacting species in the glass melt to the phase boundary or the removal of the products from the interface. In either of these cases, the dissolution process is said to be controlled by the laws of diffusion kinetics. The process is said to be reaction controlled if the rate of the reaction at the phase boundary is the slow step in the process. The temperature and time characteristics of the overall corrosion process can be determined by the slowest of these steps. For example, if the diffusion of reaction products away from the surface is the rate-limiting step, then the reaction order is zero or reciprocal first order [5]. On the other hand, if a chemical or physical transformation constitutes the slowest step, the overall dissolution process will be identified by the kinetics of that transformation. To be able to calculate refractory dissolution rates, the diffusion and fluid-flow properties of the system must be known for each type of identifiable dissolution system.

11.1.2.1 Dissolution Kinetics Equations

The kinetics of four distinct types of solute/solvent transport-controlled systems will be considered in this section. They include many of the dissolution mechanisms believed to be operative in glass furnaces:

1. Stagnant liquid or molecular diffusion (furnace paving)
2. Natural or free convection (furnace side wall)
3. Forced convection (throat erosion)
4. Surface tension gradient driven (metal line, upward drilling)

The mass transport kinetic equations for these four mechanisms are presented below. For a more detailed study of their derivation, statements of assumptions, etc., and for consideration of phase boundary rate-controlled processes, the indicated references should be consulted. All of the common refractory-glass melt dissolution systems reviewed in this discussion are in the transport-controlled category.

11.1.2.2 Kinetics of Solute Dissolution in Stagnant Liquid

The general chemical and physical laws that govern diffusion-controlled dissolution of a solute by a solvent in the absence of natural or forced convection were described for aqueous systems around the turn of the century by Nernst [6,7]. However, as will be shown in the following discussion, they apply to refractory-glass melt interface systems as well. The principal postulate of the Nernst theory is that chemical reactions occur rapidly at the surface of a solid–liquid system, thereby causing the liquid to become saturated with reaction products and to subsequently hinder further reaction. Fresh molecules of reactant can, however, diffuse through this saturated layer with a velocity that is relatively small compared with the reaction velocity. The Nernst theory is described as follows: Consider a solution having a volume V cc containing n molecules of solute per cc. Between the solution and the solid of area S sq cm, there is a layer of thickness S formed by the accumulation of reaction products during the initial stages of solute–solvent contact. The number of molecules that diffuse through the stagnant layer is dN. The Nernst equation is:

$$dN/dT = -DS/V * dN/dx \tag{1}$$

The Noyes-Nernst equation has recently been presented in the following form and applied to refractory dissolution by glass melts [8]:

$$j/A = (C_s - C_o)D/\delta_{eff} \tag{2}$$

This expression is the product of two terms: a thermodynamic term $(C_s - C_o)$, and a mobility term, $D/\delta_{eff.}$ The δ_{eff} term is defined as the tangent to the concentration profile at the interface. Diffusion in multicomponent glass melts is often formulated in terms of the effective binary diffusivity that describes the diffusion process as a binary exchange of a given species with all other species grouped together as the second component. The mass transport coefficient, k_m is defined by the ratio of the mass diffusivity, D, and the boundary layer thickness δ. The mass transport of solute per unit area is therefore proportional to the product of concentration gradient $(C_S - C_o)/\delta_e$ff and D. Dissolution of melter bottom refractories in stagnant glass flow areas as shown in Figure 11.1a is described by equation

(2). Molecular diffusion is the transport of a substance in a stagnant medium, or diffusion in the absence of fluid flow produced by hydrostatic instabilities.

As reviewed in Section 11.1.1, the solute concentration difference is the driving force. An example of dissolution in a stagnant liquid is the furnace bottom near the side walls away from bubblers and electrodes where there is very little flow, if any, of molten glass. Over time, a thick, viscous layer of refractory laden glass builds up on the furnace bottom refractory. This layer tends to protect the refractory from dissolution because the distance of diffusion of the reacting species becomes increasingly larger with time. The velocity of propagation of a species from an infinite media is proportional to $t^{1/2}$ [9]. As will be shown below in several examples, it has been verified empirically that dissolution of a refractory in a stagnant glass melt has a parabolic time dependency. This parabolic time dependency is the reason that furnace bottoms can last for at least 20 years.

11.1.2.3 Temperature Dependency of Dissolution Kinetics

In most refractory dissolution processes, the concern is with heterogeneous reactions involving an interface between two reacting phases, e.g., solid–liquid. Arrhenius showed that for some processes, for example, diffusion of ions in glass melts, the rate may be related to temperature by the relation:

$$D = D_o \exp^{-E/RT} \tag{3}$$

The activation energy "E" is defined as the height of the potential barrier that must be overcome by an atom or ion taking part in a diffusion process. Generally, there is an "E" for each step of a rate process. Transport of reactants toward the refractory chemical reaction at the surface, and diffusion of the product of dissolution away from the refractory are usually activated processes.

For the effect of temperature on the viscosity of polymeric liquids such as glass melts, equation (3) should not be applied. For glass melts, as temperature increases, the size of the anion network decreases, resulting in a decrease in the E for viscous flow with increasing temperature. For some glass melts, the variation of viscosity with temperature may be represented by the equation proposed by Fulcher:

$$\eta = \eta_o e^{E/R(T-T)} \tag{4}$$

For commercial soda-lime-silica glass at 800 and 1400˚C, E = 81 and 45 Kcalories per mole, respectively.

Ionic diffusion usually occurs at a faster rate, as the viscosity is decreased since bonds between atoms are more easily broken as the diffusing species move through the solvent. The diffusion boundary layer thickness S_D is not constant as temperature varies. It is related to diffusion and viscosity. The δ_D for forced laminar flow is defined by the following equation [10,11]:

$$\delta_D = \delta_V (D/\eta)^{1/3} \tag{5}$$

The temperature dependency of mobility term (D/δ_{eff}) of the dissolution kinetics equation of refractory oxides in glass melts is usually influenced by the process that constitutes the rate limiting step in the series of processes that make up the overall process. For example, if diffusion is the rate limiting step, then the temperature dependency of the diffusion coefficient may approximate the temperature dependency of mobility term [12]. However, recall that the dissolution kinetics equation has a second term, ($C_s - C_o$). The temperature dependency of the thermodynamic term ($C_s - C_o$) is not exponential, as can be seen from a phase diagram.

For example, if increasing temperature *increases* the viscosity of the glass melt by virtue of increased solubility of a refractory, such as silica, the temperature dependency of the concentration difference term may become significant. However, if the addition of the refractory to the glass melt by dissolution does not greatly influence the diffusivity of the reacting species, for example, then the temperature dependency of the process may be similar to diffusivity.

11.1.2.4 Refractory Dissolution Kinetics under Natural Convection Conditions

Natural convection is the transport of a substance in a naturally occurring sinking or rising fluid medium. As the refractory dissolves in the glass melt and the boundary layer becomes thicker with time, the system becomes fluid dynamically unstable. If the saturated melt becomes more dense, it begins to sink. If it becomes less dense, for example in the case of silica dissolution in a soda-lime-silica glass, it begins to rise. The boundary layer becomes constant with time at constant temperature. This situation describes dissolution kinetics with free or natural convection. An example of refractory dissolution in a free convection system is depicted in Figure 11.la for the side wall block of a float glass melter. The wall is thinner near the top of the wall (excluding the metal line, which will be discussed below) and gradually gets thicker near the base of the wall. Since this wear pattern is observed in isothermal laboratory refractory dissolution tests, it is not thought to be caused by vertical thermal gradients, although they could accentuate this pattern.

The occurrence of molecular and free convection in a wide variety of refractory-glass melts has been demonstrated by many investigators [10–19]. The following equation is for that of free convection at a vertical plate, such as a furnace side wall subjected to a vertically density-driven convection current:

$$J = 1.8(\Delta C) * \{(g\Delta\rho D^3)/\nu x]^{1/4} \quad (6)$$

The (ΔC) term is the thermodynamic term described above, and the remaining expression is the mobility term. The mass transport per unit area is influenced by the refractory concentration difference of the glass melt, the change in density as the glass nears the wall picks up refractory, the kinematic viscosity of the refractory enriched melt, and the vertical downward distance from the glass line. The typical basin wall profile shows less dissolution of refractory as the distance from the glass surface increases (See Figures 11.la and 11.3a). This profile is found in most fuel-fired glass furnaces. In electrically heated furnaces, the wear profile from top to

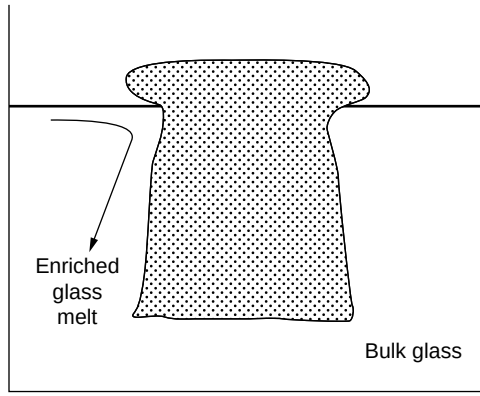

Density of refractory enriched
glass melt greater than bulk glass

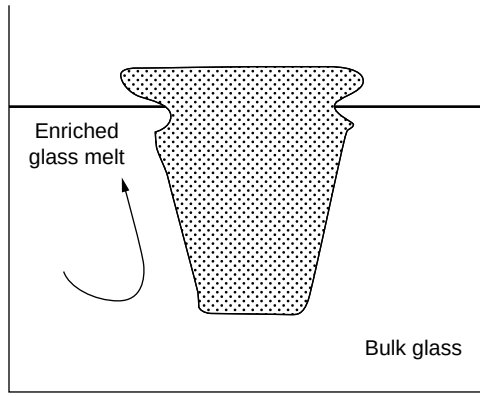

Density of refractory enriched glass melt less
than bulk glass (lead glass with alumina or soda
lime glass with silica of some fireclays)

FIGURE 11.3 Dissolution profiles of refractories that increase and decrease the density of the glass melts in which they are dissolving (From W. Trier (translation by K. L. Loewenstein) *Glass Furnaces Design, Construction and Operation (*Society of Glass Technology), Charlesworth and Co., Huddersfield, England (1987).

bottom tends to be more uniform because of upward currents of hot glass caused by the relatively hot glass produced by the electrodes. The upward currents counteract the natural downward currents caused by the sinking of the denser glass melt. However, in some high-density lead glasses, the dissolution of alumina or alumina-silica refractory in the melt actually lowers its density. This results in an upward movement of glass, as described previously, and a profile that is thicker at a higher elevation than at a lower elevation. This type of profile also occurs if a silica refractory or quartz glass solid dissolves in conventional soda-lime or fiberglass composition (See Figure 11.3b). The higher the kinematic viscosity, the lower the dissolution rate, because a more viscous glass would sink more slowly along the

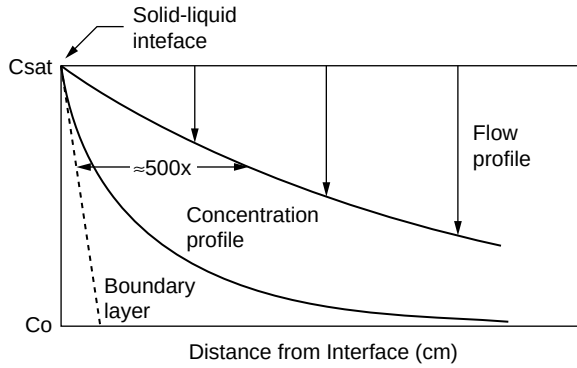

FIGURE 11.4 Schematic diagram of the refractory–glass melt interface showing the boundary layer, the dissolved refractory concentration profile, and the density-driven convection flow. (From W. Trier (translation by K. L. Loewenstein) *Glass Furnaces Design, Construction and Operation (*Society of Glass Technology), Charlesworth and Co., Huddersfield, England (1987).

wall, thus removing refractory-enriched glass from the boundary at a slower rate. The corrosion rate of the wall decreases with the one-fourth power distance from the glass line because the boundary layer thickness increases with distance.

For typical glass melts at about 1400˚C, D/δ = approximately 10^{-7} to 10^{-9} [10]. The diffusion boundary layer thickness for free convection past a vertical cylinder divided by the velocity boundary layer thickness is of the order of 1/100 [19]. The consequence of these very small ratios is that the glass flow can perturb the diffusion boundary layer thickness only to a very limited degree. This is why typical glass furnace refractories dissolve relatively slowly under free convection conditions. A schematic diagram of the basin wall–glass interface depicting the boundary layer, the dissolved refractory concentration profile of the glass melt, and the density-driven free convection flow is shown in Figure 11.4.

11.1.2.5 Kinetics of Refractory Dissolution Driven by Surface Tension Conditions

Surface tension gradients at the glass melt–refractory interface, like melt density differences, can generate motion at the interface because of the Marangoni effect. The elucidation of interfacial dynamics in boundary surface tensions developed by Marangoni have been well documented [20–22].

Metal line cut has been explained in terms of surface tension forces by several authors [10, 23, 24]. Refractory dissolution controlled by surface-free convection occurs in the meniscus of the glass melt under two conditions where:

1. The surface tension of the melt increases with the concentration of the dissolved refractory, (i.e., $A1_2O_3$ and ZrO_2)
2. This change in surface tension is large in proportion to the increase in density. Examples of surface tension-driven convection at the “metal” line

are shown in Figures 11.la and 11.3b, where there are relatively rapid dissolution processes occurring at the refractory–glass–atmosphere interface. Even though the melt is usually the hottest at the surface and coldest at the bottom of a fossil-fuel-fired glass furnace, temperature gradient is not the cause of metal line cut, since it is also seen in *isothermal* laboratory refractory dissolution tests.

Nor is the presence of alkali-rich partially melted melt on the glass surface the cause of the metal line cut. The mathematics of the mechanism by which accelerated corrosion occurs at the glass surface–refractory–atmosphere junction point is not included in equation (6). Surface tension-driven glass melt flaws are the cause of the metal line cut. Surface tension phenomena not only explain metal line corrosion, but also upward drilling by bubbles and downward drilling by tramp metal on the furnace bottom. (Upward and downward drilling will be discussed in the next section.)

If a fluid II is placed over another fluid I having a different surface tension, the interaction between the two produces a positive or negative spreading pressure shown by the equation:

$$p = \sigma_1^{-} (\sigma_2 + \Psi_{1,2}) \tag{7}$$

If $\sigma_1 > [\sigma 2 + \Psi_{1,2}]$, then fluid I spreads until an equilibrium condition is reached for immiscible melts. However, if the two melts are miscible, as is typically the case for glass melts common to the commercial glass industry, then eddy currents result. The turbulence in the flow system accelerates the dissolution process because it removes refractory enriched glass melt from the glass–refractory interface. At the metal line of a glass furnace wall, the fresh molten glass and the refractory enriched glass melt constitute the two surface active miscible substances described above. With the passage of time, a new basin wall develops a metal line cut as shown in Figure 11.5. The temperature dependency of surface tension-driven corrosion is manifested in the surface tension and viscosity properties of glass melts. A relationship from which the dissolution rate at the metal line can be calculated is shown in the next equation [25]:

$$J = B(Ci - Co)^{*}[D_o^2 \Delta \sigma g/\nu]^{l3} \tag{8}$$

11.1.2.6 Kinetics of Dissolution of Refractories by Upward and Downward Drilling Conditions

The phenomenon of upward drilling of horizontal facing downward refractories has been studied extensively [24–30]. There is fairly high correlation between metal line cut dissolution rate and upward drilling kinetics for the same refractories and glass melt chemistry [24]. Downward facing horizontal surfaces and horizontal joints between two blocks are the most susceptible to upward drilling. Perhaps the best example is the underside of the lid of a container furnace throat. As shown in Figures 11.1a and 11.1b, horizontal upward facing blocks are susceptible to downward

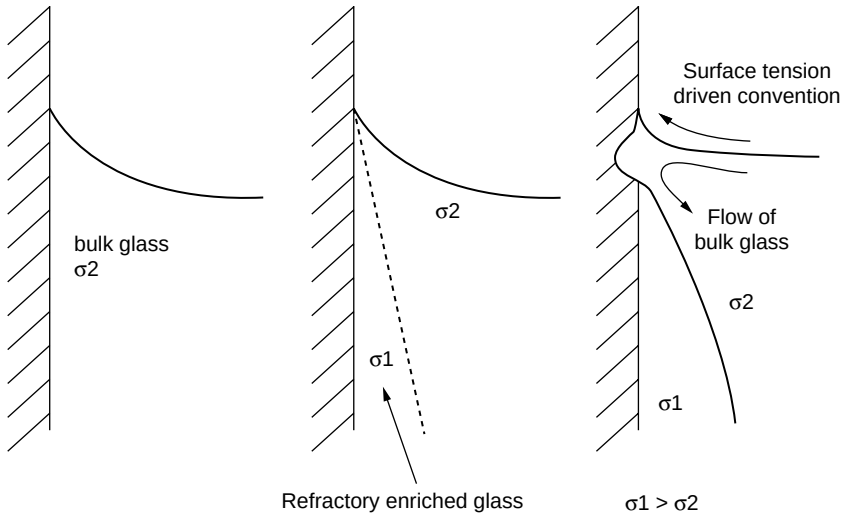

FIGURE 11.5 Sequence of events leading to metal line dissolution (From W. Trier (translation by K. L. Loewenstein) *Glass Furnaces Design, Construction and Operation (*Society of Glass Technology), Charlesworth and Co., Huddersfield, England (1987).

drilling. Many investigators have concluded that upward drilling is due to the presence of bubbles, and that downward drilling is due to the presence of heavy metal particles on the bottom of a furnace [31–33]. Laboratory studies of upward drilling of glass melt/refractory systems with cold model fluids lead to an insight into the mechanisms of refractory dissolution by glass melts caused by the presence of bubbles at the interface [34]. Upward drilling dissolution of refractories by molten glass is influenced by changes in glass density and surface tension. It is hypothesized that the mass transport of the refractory is through a boundary layer of refractory-saturated solvent, and that the thickness of the boundary layer may be modified either by natural or forced convection processes occurring in the solvent. However, with bubble-induced upward drilling, the boundary layer thickness varies with the velocities of the local flows of solvent occurring in the region of the bubble contacting the surface. The layer of solvent next to the surface that is being dissolved is in a mobile chemical equilibrium with the solid. The surface layer of the solvent will be saturated with solute. The solute moves through the boundary layer thickness, δ, into the unaltered solvent. A schematic of the upward drilling system is shown in Figure 11.6.

In a glass melt-refractory system, as the dissolution of the refractory into the glass results in a change of the density of the solution, the flow may develop. For lead glass, the solution of alumina will lower melt density, which stifles transport of solute-rich glass melt from the interface. However, for glasses such as soda-lime, TV or “E” glass, alumina will increase the density and cause the transport of solute-rich melt from the interface. For upward drilling to occur, the refractory-laden glass must be transported from the reaction zone. The viscosity of the solvent influences the flow velocity in an upward drilling system. Since high viscosity tends to hinder

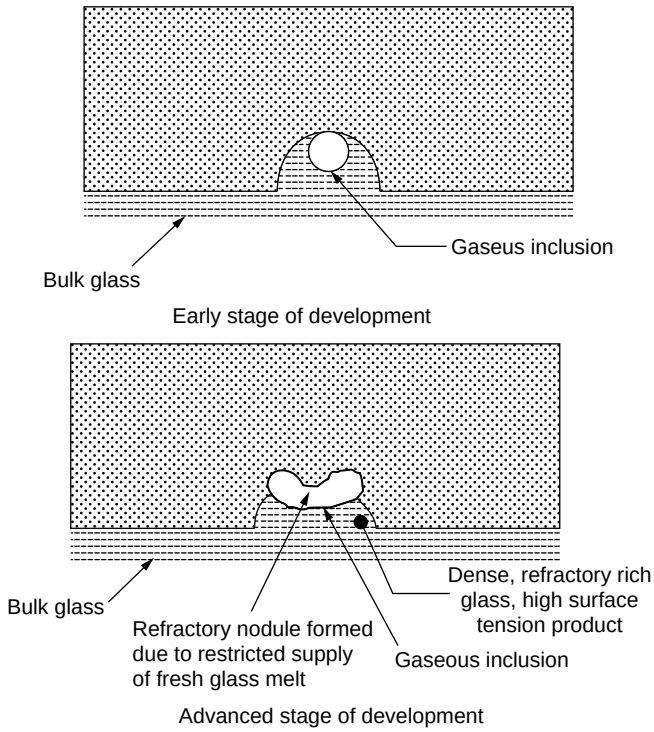

FIGURE 11.6 Schematics of gas inclusion-driven upward drilling of a refractory surface (From W. Trier (translation by K. L. Loewenstein) *Glass Furnaces Design, Construction and Operation (*Society of Glass Technology), Charlesworth and Co., Huddersfield, England (1987).

the action of surface tension forces, a temperature rise increases refractory transport rates because surface tension is relatively insensitive to temperature, whereas viscosity decreases according to the Fulcher's equation:

In summary, the properties of glass melts that influence upward drilling are:

1. Surface tension gradients caused by chemical alteration of the glass melt by refractory dissolution
2. Solubility of the refractory in the glass melt
3. Viscosity
4. Density increase caused by refractory dissolution
5. Temperature

11.1.2.7 Kinetics of Refractories Dissolution Driven by Forced Convection Conditions

The influence of forced convection of refractories by glass melts has been studied by many investigators [19,35,36]. Glass furnace refractory dissolution is enhanced

by forced convection in areas near mechanical stirring and bubblers, and where a geometric restriction such as a throat occurs. An example is shown in Figure 11.lb for the throat bottom. It was shown by equation (2) that the dissolution rate of refractories in glass melts is in general proportional to the concentration gradient $(C_i - C_o)/\delta$ of the dissolving material at the refractory–glass interface. Forced convection decreases the dimension of the boundary layer and thereby increases the dissolution rate of the refractory.

The velocity boundary layer thickness "$\delta\nu$" is given by [10]:

$$\delta\nu = -3y/(\nu * y_s/n)^{1/2} \tag{9}$$

where "n" is the zero coordinate starting point of the flow (where y = 0) and increases as the distance from the starting point increases. The mass flow density of the material dissolved away becomes:

$$m_k = 1/3(C_1 - C_o)^*(\nu/y)^{1/2}\ (D^2 n^{-1/2})^{1/3} \tag{10}$$

11.1.2.8 Kinetics of Dissolution of a Rotating Refractory Disc

Cold modeling and dissolution studies of refractories at 1400°C using a rotating disc or the bottom surface of a rotating rod were conducted to:

1. Empirically distinguish between natural and forced convection
2. Increase the understanding of metal line and subsurface corrosion
3. Obtain test results in a shorter time [34]

The conditions of flow adjacent to a rotating cylinder or rotating disc under laminar flow conditions are well understood. The expression for the hydrodynamic boundary layer thickness for a rotating disc is [37]:

$$\delta = 3.6\ (\nu/\Omega)^{1/2} \tag{11}$$

Because the hydrodynamic boundary layer is much larger than the diffusion boundary layer thickness, the interaction of the flow pattern with the crucible can usually be neglected. An equation for calculating the mass flux from disc surfaces of refractory-glass melt systems is given by the following equation [10]:

$$j = 0.62(Ci - Co)^*D^{2/3\ -\ 1/6}\Omega^{1/2} \tag{12}$$

Equation (12) is of the same general form as other mass transport equations presented above, in that there is a thermodynamic and a mobility term. Using the rotating disc method allows a distinction to be made between the dissolution rate of different refractories. At rpms of 10 to 40, the flux line dissolution virtually disappears.

11.1.2.9 Summary of the Influence of Glass Melt Properties on Their Corrosivity toward Refractories

In a convection-free glass melt, the dissolution rate of a refractory surface can depend on the rate at which the reacting ionic species, such as Na^+ or K^+, diffuse toward the surface or the rate at which the refractory component ions, such as Si^{+4} or $A1^{+3}$, diffuse away from the melt–refractory boundary. It also depends on the solubility of the refractory components in the glass near the interface, and on the boundary layer thickness for diffusion. In a glass melt where convection currents are present at vertical refractories walls, excluding the metal line, the properties of glass that influence the dissolution rate of a refractory surface are the effective binary diffusion coefficient, the viscosity, the solute concentration difference, the density difference, and the distance from the glass line. In a glass melt at the "metal" line of furnace walls, the properties of glass melts that influence the dissolution rate of refractories are the change of surface tension due to refractory enrichment, the refractory concentration difference, the diffusion coefficient, and the kinematic viscosity.

In a glass melt contacting the underside of a horizontally oriented refractory where bubbles are present, and where the refractory-rich melt is denser than the bulk melt, the glass melt properties that influence the dissolution of refractory via the upward drilling mechanism are the relative surface tensions of the refractory-rich versus the fresh-unaltered melt, the viscosity, and the solubility of the refractory in the glass melt. In a glass melt whose motion is driven by mechanical forces, the glass melt properties that influence the dissolution rate of refractories are the effective binary diffusion coefficient, the viscosity, and the concentration difference.

Table 11.1 summarizes the influence of the properties of glass melts cited in the equations in this section. Notice that a similar pattern exists for most properties. Concentration differences are to the first power, whereas the diffusivities, with only one exception, have exponents to the two-thirds to three-quarters power; kinematic

TABLE 11.1
Glass Melt Properties That Influence Corrosivitv of Refractories

Glass Melt Property	Stagnant Melt Convection	Free Convection	Metal Line Corrosion	Forced Convection	Rotating Disc
Solubility	Ci-Co	Ci-Co	Ci-Co	Ci-Co	Ci-Co
Effect Binary Diffusion Coefficient	D	$D^{3/4}$	$D^{2/3}$	$D^{2/3}$	$D^{2/3}$
Density Difference		$\Delta\rho^{1/4}$			
Kinematic Viscosity		$\upsilon^{-1/4}$	$\upsilon^{-1/3}$	$\upsilon^{-1/6}$	$\upsilon^{-1/6}$
Surface Tension			$\Delta\sigma^{1/3}$		

viscosities have an exponential range from minus one sixth to minus one third. These small fractional exponents may at first appear to render viscosity almost inconsequential on its influence toward dissolution. However, as seen from equation (4), the temperature dependency of viscosity is exponential. Therefore, the effect of viscosity can be significant.

11.1.3 Definition of Symbols

A compilation of definition of symbols for the properties of glass melts that influence their corrosivity toward refractories is presented in Table 11.2.

11.1.4 Deviations of Commercial Refractory Materials from Idealized Solute Materials

The phenomenology of dissolution of most commercial refractory materials in actual glass furnaces can be quite complex. Some examples of phenomena that can add to the complexity are:

1. Multiple dissolution mechanisms possibly occurring simultaneously
2. Lateral and vertical flows and thermal gradients in the furnace
3. Undissolved or partially melted batch on the glass surface
4. Volatility-induced chemical alteration of the melt
5. Heterogeneity of fusion-cast refractory blocks
6. Porosity and grain boundaries of the refractory structure
7. Non-smooth surface and microcracks of the blocks
8. Glassy phase exudation of the fusion-cast AZS blocks

The dissolution kinetic equations reviewed in this section are most accurately applied to simple geometric systems (plates and cylinders) consisting of idealized materials such as homogeneous porosity-free single crystals of quartz or sapphire or silica glass; the equations may not account for some aspects of commercial refractories whose contact with the glass melt lead to less than ideal behavior. The last four items on the above list involve the intrinsic characteristics of the refractory material. These are prime examples of deviations from ideal solutes.

For example, fusion-cast AZS (alumina-zirconia-silica) and fusion-cast chrome alumina are physically and chemically heterogeneous; they consist of both relatively chemically inert phases such as ZrO_2, AI_2O_3 and Cr_2O_3 and easily fluxed glassy phases. This glassy phase may exude from the AZS refractory surface into the molten glass at a fairly rapid rate initially because of diffusion of and reaction with alkali and alkaline earth fluxes from the glass. Chemically inert particles of nodular zirconia particles may be drawn into the glass melt during the corrosion process. This loss of mass is not included in the dissolution kinetic equations.

Other examples of deviations from ideality include bonded chrome refractories. They are used in E fiberglass and in small quantities in some soda-lime-silica glass producing furnaces. Chrome refractories have a relatively high percentage of fine porosity. Porosity allows penetration into the refractory along with diffusion. Fusion-

TABLE 11.2
Description of Symbols

	English Symbols
A	area of solute
B	a parameter dependent on the flux line dimension
C_s	the saturated concentration of the solute in the solvent
C_o	the concentration of solute in unaltered solvent
$C_s–C_o$	difference in solute concentration
C_i	solute concentration at the interface
dN	no. of molecules that diffuse through the stagnant layer at the interface
D	effective binary diffusion coefficient
E	the activation energy
g	gravity constant
j	dN/dt = mass of solute corroded per unit time
k	the first order rate constant for the heterogeneous reaction at the interface and reaction constant
k_m	mass transport coefficient D/δ
p	spreading pressure due to surface tension forces
R	the gas constant
T	absolute temperature. °K
S	area of solid surface in the Nernst equation
t	time
v	velocity
V	volume of solute in the Nernst equation
x	distance from leading edge of solute sample
y	coordinate in a forced convection system
	Greek Symbols
δ_{eff}	effective boundary layer thickness for diffusion
δ_V	the velocity boundary layer
δ_D	the diffusion boundary layer
h	viscosity
n	the kinematic viscosity of the flowing glass
e	a parameter dependent on the density gradient at the refractory/melt interface
W	the angular velocity of the rotating disc or rod
σ_1	surface tension of fluid 1
σ_2	surface tension of fluid 2
Ds	$\sigma_1–\sigma_2$
$\psi_{1,2}$	interfacial tension
r	density
Dr	difference in density

cast alumina products can also have several percent open porosity. Unfortunately, the dissolution kinetic equations reviewed above do not include a provision for penetration of the glass melt into the refractory apart from diffusion.

Furthermore, gases can be generated at the refractory-melt interface of some systems. This further complicates the application of the mass-transport equations

real systems. The presence of bubbles prevents the contact of solute and solvent, and in the case of horizontal surfaces, can lead to the added mechanism of upward drilling corrosion.

Other examples include non-smooth surfaces and cracked refractory blocks having larger surface areas than theoretical and the potential for non-uniform dissolution because of melt penetration into the cracks. These deviations from ideal could result in dissolution rates significantly different from those calculated by kinetic equations.

In recognition of these deviations from ideal materials, the complexity of the systems, and in keeping with the theme of this book, one focus of this chapter is on how the properties of glass melts influence their corrosivity toward refractories. Another focus will be on temperature dependencies toward refractory oxide dissolution and refractory metal corrosion. The examples of corrosion studies of materials by glass melts discussed in Section 11.3, with a few exceptions use ideal solute materials to validate the equations, to identify mechanisms or rate-limiting steps and to calculate diffusion coefficients. However, the deviation of most commercially used refractories from ideal solutes need not limit the usefulness of this discussion, but rather it will identify relative measures of how changes in bulk glass melt chemistry and temperature generally influence the dissolution rate of refractories, the corrosion rate of metals and lead to suggestions of improved materials selection, design and application.

11.2 REFRACTORY DISSOLUTION EXPERIMENTAL PROCEDURES

Various types of refractory dissolution test procedures have been devised to measure refractory corrosion in various glass melts. Some are very simple in that the glass melt motion is not forced; it is limited to what is naturally generated by the densification of the glass melt by dissolved refractory, surface tension gradients, thermally induced convection currents, etc.

Other dissolution test procedures have been developed that are more complex. They involve forced rotational motion at or entirely below the glass line that alters the various boundary layer thicknesses. These experimental procedures can separate metal line from sub metal line mechanisms, can validate theoretical expressions, can test assumptions, or attempt to simulate the velocities believed to occur in commercial processes.

11.2.1 Static Finger or Pencil Tests

The simpler refractory corrosion tests are static arrangements whereby a preheated "pencil" refractory specimen having a circular or rectangular cross-section is tested in molten glass in a small crucible. ASTM has a standard corrosion test C-621-68 (1978) Static Test for Corrosion Resistance of Refractories to Molten Glass. However, non-standard tests are also conducted throughout the industry. Depending on the length of the sample and the depth of the glass melt, the refractory sample may

extend through the melt surface or may be totally immersed. The metal line cut mechanism on pencil test-type specimens may be eliminated by wrapping the refractory cylinder with platinum foil in this region [38].

After the sample has been subjected to corrosion by the glass melt for the required time at the test temperature, it can be removed from the melt before it is cooled to room temperature when a non-expendable platinum crucible is used. However, if an expendable ceramic crucible is used, its contents can be cooled to room temperature and then sliced vertically into at least two pieces in such a way that the refractory sample is bisected. Or, altematively, the sample and the ceramic crucible can be cut horizontally into a number of cross-sectional pieces. The change in profile or length of the sample is then accurately measured with the aid of a microscope.

An alternative to physically measuring the dimensional loss of refractory due to dissolution is to measure its mass loss during corrosion. *In-situ* weight loss measurements caused by corrosion by linking the refractory specimen to an analytical balance have also been used. The concentration of the dissolved refractory in the glass can be determined, and crystalline particles identified, as additional assessments of the extent of corrosion and for calculating

$$(C_S - C_O)$$

11.2.1 Static "T" Tests

In a "T" test, the refractory sample is cut into the shape of the letter T. The length of the horizontal component of the "T" is made longer than the diameter of the crucible. The sample is suspended into the melt by supporting the underside of the horizontal member on the top edge of the crucible. The advantage of this type of arrangement over some types of tests is that the bottom horizontal surface of the sample is usually exposed to the glass melt, and an additional mode of motion of the glass melt can occur. Upward drilling can be studied with this type of test. The upper part of the vertical member of the "T" sample can be wrapped with platinum foil if desired to eliminate the effect of surface tension at the metal line.

11.2.2 Small Refractory Basin Tests

Small molten glass-containing basins built from the refractories being evaluated for dissolution potential in a given glass have also been used successfully. The larger size of a basin versus a small crucible allows the generation of some thermal and density convection currents. The potential for upward drilling and vertical joint erosion can also be studied, since the walls of the basin can contain vertical and horizontal joints of predesigned gaps. The effects of forced air cooling and insulation also have been studied by refractory suppliers and glass manufacturers using the small basin apparatus. Forced motion between the glass melt and the refractory surfaces can be induced by using a stirring mechanism. Multiple refractory products can be evaluated simultaneously and relative corrosion resistance compared in a basin corrosion tester.

11.2.3 Dynamic Rotating Cylinder or Disc Tests

Most static refractory corrosion tests evaluate the relative corrosivity of a glass melt toward one product or product class versus others. However, actual service life predictions cannot be accurately made from static tests, except perhaps for a bottom paver application where the glass is relatively static. The rotating cylinder or disc test procedure has been developed to try to match the velocities of the glass melt against a refractory, such as in the region near bubblers or electrodes, and to overcome the limitations of a small crucible. When the diameter of the cylinder is large compared with the boundary layer, the glass melt can be considered semi-infinite. This means that the physical attributes of the crucible itself do not enter into the flow equations. The glass flows around the rotating disc can vary, depending upon whether the disc is fully immersed or is located at the metal line [l9]. The rotating refractory sample test is well suited to:

1. Studying refractory dissolution under forced convection conditions
2. Making the effects of natural convection small or negligible compared with those of forced convection, or to negate the effects of the crucible on the dissolution results
3. Shortening the corrosion test time
4. Matching the surface velocity of an actual commercial application in a glass furnace
5. Studying stoning tendencies of refractories resulting from dissolution

Several investigators developed an apparatus for the boundary layer thickness variation due to rotating corrosion testing of refractories and derived the following expression for the boundary layer thickness for mass transfer from rotating discs [35,38]:

$$\delta = 1.61(n/\upsilon)^{1/3}(\upsilon/\Omega)^{1/2} \tag{13}$$

By varying the revolutions per second of the test sample, the boundary layer thickness can be altered, which gives considerable control of the experimental conditions as the experimenters attempt to simulate actual furnace conditions. The points corresponding to 5, 10 and 20 rpm lie on a line whose slope is approximately one half. Hence, the sample area loss results at these revolulional speeds may be predicted by an equation in which the corrosion rate is proportional to the square root of rotation. A similar plot having a slope of one half was presented by Cooper and Kingery [58] for the change in the length of a rotating cylinder. They also developed a theoretical relationship for dissolution rate that approximates the square root relationship and gives some credibility to their test apparatus and procedure.

This test procedure can distinguish between the relative corrosion resistance of different refractories such as sillimanite versus fusion-cast AZS. Above approximately 10 rpm for fusion-cast alpha-beta alumina, there was no sign of flux line corrosion, since the corrosion caused by the rotation predominated. Below 10 rpm, the metal line cut could still be seen [35].

11.3 LABORATORY STUDIES OF DISSOLUTION OF REFRACTORY MATERIALS IN GLASS MELTS

Many studies have dealt with the dissolution of refractory materials such as silica, alumino-silicate and alumina in glass melts. However, those linked to dissolution kinetic equations such as those reviewed in Section 11.1 are not abundant because of the complexity of the phenomena, the difficulty of the experiments, and the need for precision measurements. In most cases, accurate calculation of dissolution rate is not possible because the diffusion coefficients are not known. In the selected examples of experimental corrosion determinations reviewed in this section, the experimental designs, procedures, and equipment used allow the more theoretical aspects of dissolution or corrosion phenomena to be validated or the interdiffusion coefficients to be calculated. Once the empirical diffusivity constant is determined, then estimates of the influence of glass compositional change on dissolution rate, for example, can be attempted.

11.3.1 Studies of Refractory Dissolution in One-Component Glass Melts

Clear fused quartz (CFQ) or quartz glass and rebonded quartz glass (fused silica) are used commercially as forming end refractory material in the float glass industry because they do not usually impart defects to the glass. A silica refractory is usually the last solid material the molten glass touches before it is formed into a ribbon in the float process. At temperatures in the 1000˚C range, these products perform well in this application. CFQ is one of several commercially used refractories that are ideal in terms of being applicable to the kinetic equations presented in the previous section. This is probably one reason that it was used for dissolution studies by the following investigators. Sapphire and both fusion-cast and dense bonded alumina, alumino-silicate and AZS have also been used for dissolution studies.

The following experimental data from a number of investigators quantifies the dissolution rate of refractory materials and their temperature sensitivity in one-, two- and three-component glass melts. The investigators attempt to categorize the type of dissolution kinetics of each case.

11.3.1.1 Quartz Glass Dissolution B_2O_3

The dissolution of quartz glass plates in fused boric oxide in the temperature range 1130 to 1380°C. was determined using a stationary vertical plate placed in the melt [15]. The quartz plates were cut and polished so that the major plane surfaces were within 5° perpendicular to the C axis. Thirty-three grams of the B_20_3 glass were placed in a 28.7 mm diameter, 57.4 turn deep platinum crucible. The quartz sample was attached to a platinum chain, then to an analytical balance. The furnace containing the crucible and glass melt was raised to the point where the quartz plate became immersed in the melt. Weight loss was monitored during the duration of the test. The dissolution kinetics of this system initially demonstrated molecular diffusion as expressed by equation (2). The parabolic time behavior was deduced by the

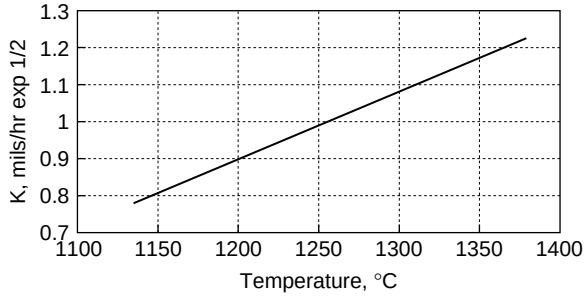

FIGURE 11.7 Transient dissolution rates versus temperature for dissolution of quartz glass in B_2O_3 (From J. R. Hutchins, III, *Glass Technology 7:*42(1966).

straight line plot of dissolution versus $t^{1/2}$ as shown in Figure 11.7. The dissolution rate for transient kinetics approximately doubled as the temperature was increased from approximately 1100 to 1370˚C. Results from profile measurements for tests at 1281˚C gave a dissolution rate ranging from 1.1 to 1.2 mils/$hr^{1/2}$. A general equation for molecular dissolution of silica in B_2O_3 glass melt according to the investigator is as follows:

$$k(mil/hr^{1/2}) = -23.39 - 40.23 \times 10^{-3}T + 17.55 \times 10 - 6T^2$$

After a longer time, the transient kinetics changed to steady state kinetics as expressed by equation (6).

The temperature dependency of the steady-state dissolution of quartz glass in molten B_2O_3 is shown in Figure 11.8. The density-driven convection was inferred from the near linear time behavior of the dissolution rate. The steady-state dissolution rate more than tripled from approximately 0.3 to 1.2 mg per hr per cm^2 as the temperature was increased from approximately 1100 to 1370˚C. The temperature dependency of viscosity of B_2O_3 as shown in Figure 11.9 is quite similar to that of the dissolution of silica glass in B_2O_3 as shown in Figure 11.8 [16].

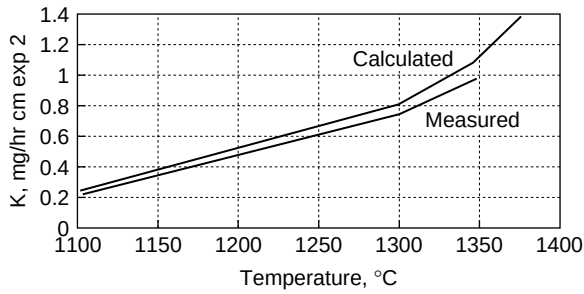

FIGURE 11.8 Steady state dissolution rates versus temperature for dissolution of quartz glass in B_2O (From J. R. Hutchins, III, *Glass Technology 7:*42(1966).

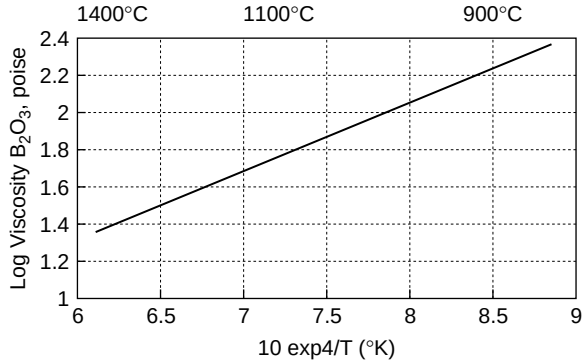

FIGURE 11.9 Arrhenius plot of viscosity of B_2O_3 (From A. Napolitano, P. B. Macedo and E.G. Hawkins, *J. Am. Ceram. Soc. 48:* 613).

The investigator opined that for some kinetic studies it is logical to represent the temperature dependence by an Arrhenius plot from which activation energies can be determined. If the data from this study were plotted in this manner, a very good linear relation would result and one might be tempted to calculate an E for this dissolution process. However, as discussed previously, this would be valid only if the concentration and density terms of equation (6) were independent of temperature. Equilibrium solubility values used to calculate E are temperature dependent as indicated by phase diagrams such as shown on Figure 11.2. Density is probably only relatively temperature-independent glass property.

11.3.1.2 Tungsten Metal Corrosion in B_2O_3

Tungsten and molybdenum are refractory metals that can be used for electrodes, stirrers, and refractory wall cladding below the glass melt surface. The corrosion rate of tungsten metal in anhydrous B_2O_3 that had previously been equilibrated with gases of varying partial pressure of oxygen from temperatures of 1000 to 1300˚C in a static system have been determined [18]. The equilibration was accomplished through bubbling of the gas in the boric oxide melt. Oxygen diffusion from the melt to the tungsten surface reacted with tungsten to form tungsten oxide at the metal–melt interface.

Figure 11.10 presents the corrosion results and time dependency for the entire oxygen and temperature range covered, virtually 100% argon to virtually 100% oxygen and 1000 to 1300˚C. Note that the corrosion rate is approximately proportional to the partial pressure of the equilibrating gas. The partial pressure of oxygen gas equilibrated in the melt is proportional to the number of oxygen atoms reaching the surface of the metal in unit time. The weight loss of tungsten is given by the following expression:

$$\Delta \text{ wt/cm}^2 = kt^n \tag{14}$$

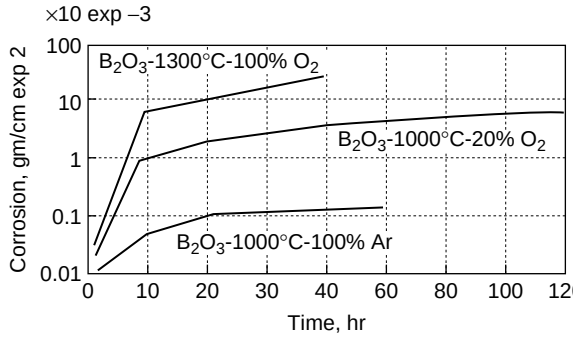

FIGURE 11.10 Corrosion rate of tungsten metal in 8203 at 1000˚C and 1300˚C equilibrated with gases of varying oxygen partial pressure (From G.A. Pecoraro, *The Corrosion of Tungsten in Boric Oxide and Sodium Borate Melts*, Ph.D. Thesis, Rensselaer Polytechnic Institute, Troy, New York (1969).

Taking the logarithm of both sides, the equation becomes:

$$\text{Log } \Delta \text{ wt per cm}^2 = \log k + n \log \text{time} \tag{15}$$

When the data from Figure 11.10 are plotted on a log–log plot, "n" is the slope and "log k" is the intercept. Such a plot is presented in Figure 11.11. The slopes of the 100% Ar-1000˚C and 20%O_2 – 80%Ar-1000˚C curves are very close to one half. It is therefore established that the corrosion of tungsten in molten B_2O_3 follows near-parabolic behavior throughout most of the entire range of conditions evaluated. It is inferred that the chemical reaction of oxygen dissolved in a B_2O_3 melt with tungsten metal to form tungsten oxide into the melt is not thought to be the rate-

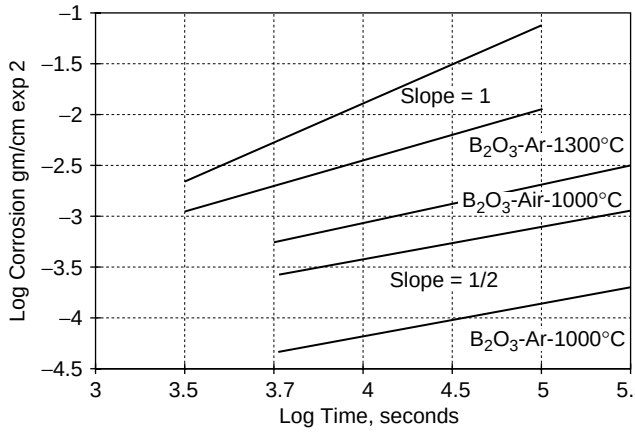

FIGURE 11.11 Log corrosion-log time plot of tungsten metal in B_2O_3 (From G. A. Pecoraro, *The Corrosion of Tungsten in Boric Oxide and Sodium Borate Melts*, Ph.D. Thesis, Rensselaer Polytechnic Institute, Troy, New York (1969).

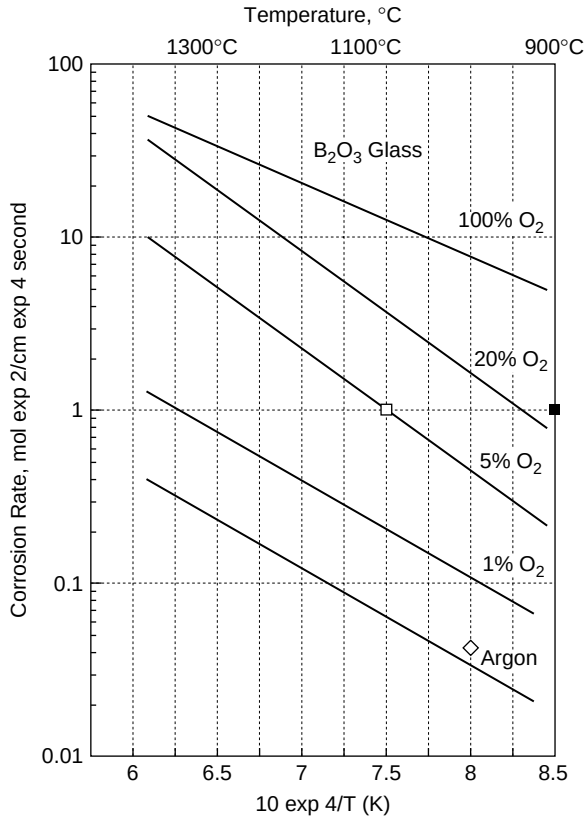

FIGURE 11.12 Arrhenius plots of parabolic corrosion rates of tungsten metal in B203 versus partial pressure of equilibrated gas (From G. A. Pecoraro, *The Corrosion of Tungsten in Boric Oxide and Sodium Borate Melts,* Ph.D. Thesis, Rensselaer Polytechnic Institute, Troy, New York (1969).

limiting step, since the kinetics follow near-parabolic behavior. The slope of the O_2 – 1300˚C plot is between one half and one. This case may represent a transition between molecular diffusion and density-driven convection, because the more fluid melt flows more easily.

That tungsten oxide was observed on the metal samples corroded by the 100% oxygen-equilibrated melt indicates that the transport of solute away from the interface is probably the rate-limiting step. The W_2O_5 is forming more rapidly than it is being removed. In contrast, the tungsten metal was bright and shiny for the 100% argon-equilibrated melt. This probably indicates that transport of oxygen to the interface versus the rate-limiting step m the corrosion process. It is being removed faster than it is being formed. Figure 11.12 is an Arrhenius plot of the parabolic corrosion rates of tungsten in molten boric oxide as a function of the partial pressure of oxygen dissolved in the melts. For the exceptional case (100% oxygen), the E was about 17 Kcalories per mole, which is close to the activation energy of B_2O_3 for viscosity of 19 Kcalories per mole [39]. As reviewed previously, the agreement

between the two may be fortuitous. The diffusion coefficient for W^{+6} in B_2O_3 calculated from this study is 1.5×10^{-8} cm^2 per second.

11.3.1.3 Al_2O_3 Dissolution in V_2O_5

The rotating pencil slag test has been used to study the dissolution of refractories under forced convection conditions. Equation (12) is a typical dissolution kinetics equation for this type of test procedure. The rotation of the sample increases the rate of dissolution because fresh melt is brought into contact with the refractory at a faster rate. A rotating pencil test was used to study the dissolution of Al_2O_3 in a V_2O_5 melt at temperatures between 720 and 1100˚C. Of course, V_2O_5 is not a glass-forming oxide. However, this study is included here because of its use of the rotating pencil test and the conclusion that reactions are the rate-limiting step. The rods were 4 mm in diameter and were rotated at various speeds exceeding 1400 rpm [40,41].

The results showed that, for slow-speed tests at lower temperatures, the dissolution followed a $t^{l/2}$ behavior. However, at higher temperatures, the dissolution rate followed linear time behavior for shorter times. After a longer time, the dissolution rate decreased. The investigators attributed this to a reduced thermodynamic driving force caused by an $A1_2O_3$ build-up in the melt (reduction in $C_i - C_O$), resulting from either the corrosion of the refractory or volatilization of the V_2O_5.

The mechanisms of corrosion of polycrystalline specimens were also studied to determine whether their dissolution behavior departs from ideal behavior [41]. The investigators concluded that grain boundaries were preferentially corroded, since aluminum oxide grains were found in the melt, and that surface chemical reaction, not diffusion in the melt, was the rate-controlling step at temperatures exceeding 850˚C.

11.3.2 Studies of Refractory Dissolution in Two-Component Glass Melts

An advantage of a two-component system in studying dissolution kinetics when one of the components is silica or $A1_2O_3$ is that the effect of concentration difference of silica can be studied by changing the S_iO_2 or AI_2O_3 content of the glass. This allows a systematically designed test of the thermodynamic term of the dissolution kinetics equations presented in Section 11.1.

11.3.2.1 Crystalline and Glass Quartz Dissolution in Na_2O-B_2O_3

The dissolution rates of crystalline quartz and quartz glass in Na_2O-B_2O_3 melts under forced convection conditions were determined from 900 to 1200˚C [42]. Time and temperature dependencies are presented in Figures 11.13 and 11.14, respectively. The authors attributed the initial non-linear region for the 900˚C system shown in Figure 11.13 to the period required for the formation of the diffusion boundary layer exemplary of molecular diffusion kinetics. For the higher-temperature systems (1000˚ and 1100˚C) and for longer times, they deduced that linear time kinetics implied that steady-state conditions were operative. The experimental E of 28 Kcal-

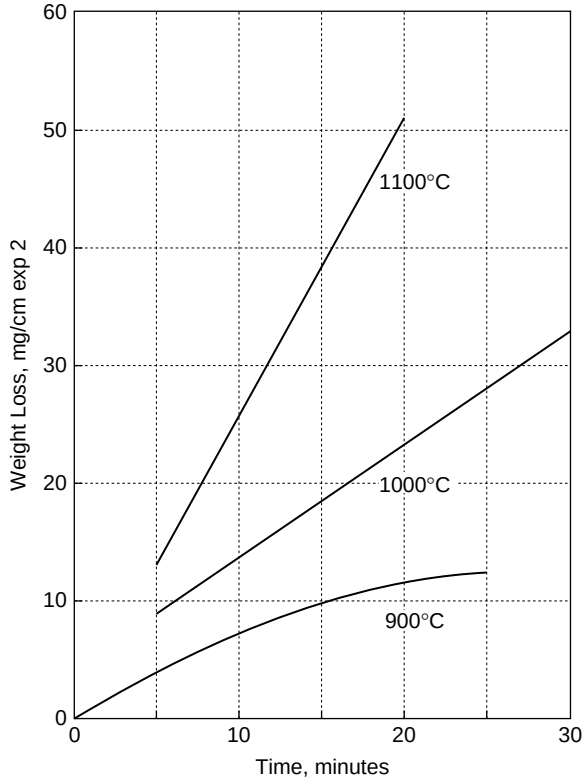

FIGURE 11.13 Transient and steady-state dissolution rates versus temperature for dissolution of quartz glass in molten sodium borate (From J. Hlavac and P. Strnad, *Silikaty* 5, (1961).

ories per mole for both forms of silica led the authors to conclude that the rate-controlling step may be diffusion through the boundary layer. The E for viscous flow of sodium borate melts for 10 and 20 mole% Na_2O are 29 and 35 Kcalories per mole, respectively [42]. The crystalline quartz was found to be slightly more corrosion resistant than the quartz glass.

11.3.2.2 Quartz Glass Dissolution in Na_2O-SiO_2

The dissolution rate of quartz glass under density-driven convection conditions in six binary glass compositions ranging from 22.5 to 50.8 wt.%Na_2O to 49.2 to 77.5 wt.%SiO_2 has been measured [43]. The quartz glass solute specimen was approximately 50 mm long and 6 mm in diameter. The procedure used was to lower the sample vertically into the glass melt after it was heated to a temperature in a vertical tube furnace heated with a platinum-rhodium winding. The sample bottom rested on the base of the crucible. The extent of dissolution was determined by measuring the decrease in the bisected diameter of the sample to +0.02 mm at a point half the distance from the metal line to the end of the sample.

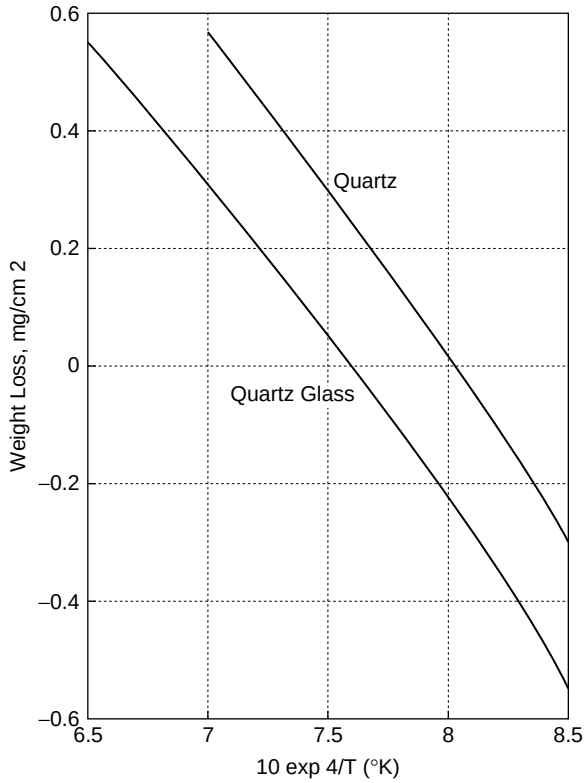

FIGURE 11.14 Arrhenius plots of steady-state corrosion rates of quartz and quartz glass in sodium borate melts (From J. Hlavac and P. Strnad, *Silikaty* 5, (1961).

An equation of the form of equation (6) was used to calculate D since data for all of the other terms of the equation were available. The saturation concentration was read off the liquidus lines of the phase diagrams; the density and viscosity data were obtained from the literature. It was necessary to multiply an additional term to the kinetic equation because of the cylindrical shape of the sample. [19]

The dissolution rate of the quartz glass in the 34.1% Na_2O melt ranged from about 0.1 to 1 cm per second at a temperature range of 1000 to 1300˚C.

Arrhenius plots of the dissolution rates and the calculations of D are presented in Figures 11.15 and 11.16, respectively. They ranged from about 6.6 to 7.5×10^{-8} cm^2/sec for a 34.1% Na_2O glass composition over the temperature range studied. As shown by the slope in Figure 11.16, the measured diffusion coefficients of Si^{+4} in sodium silicate melts are in this range [35–37] which is consistent with the investigators' hypothesis that the diffusion of Si^{+4} may be the rate-limiting step in the dissolution process.

The E for the diffusion coefficient of the slowest-moving species in the dissolution process was calculated from Figure 11.15 to be 28.9 Kcal per mole, according to the investigators. They concluded that the silica ion diffusion is the rate-limiting step in the process, and that quartz glass corrosion also increases with soda concen-

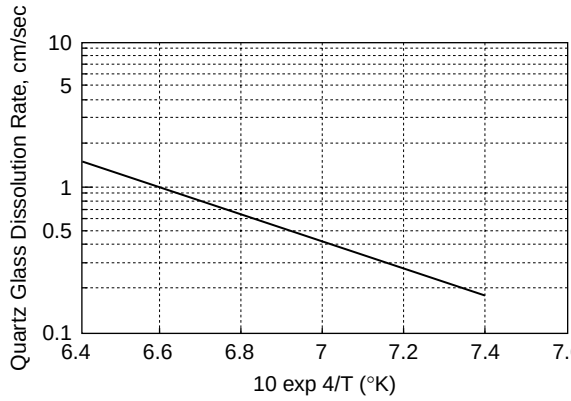

FIGURE 11.15 Arrhenius plot of steady state-corrosion rates of quartz glass in a sodium silicate melt (From M. Truhlarova and O. Veprek, *Silikaty* 14: (1970).

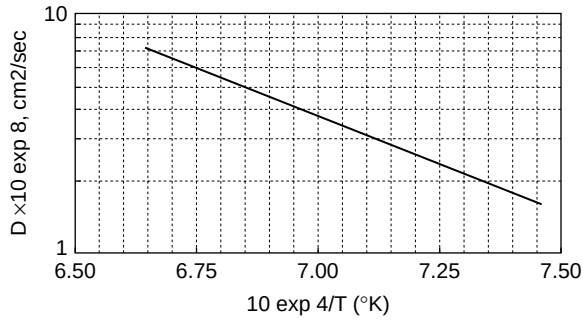

FIGURE 11.16 Arrhenius plot of effective binary diffusion coefficients of SiO_2 in molten alkali silicate glass melts (From M. Truhlarova and O. Veprek, *Silikaty* 14: (1970).

tration of the melt under the conditions of the experiment. The dissolution rate increased by almost an order of magnitude as the soda concentration was doubled.

The glass melt property data used for this study, and the calculated diffusion coefficients that resulted from them are presented in Table 11.3. The diffusion coefficients increased with temperature. At constant temperature, they increased with Na_20 concentration and $(C_i - C_O)$.

11.3.2.3 Quartz Glass Dissolution in Sodium and Potassium Silicate Melts

The rates of dissolution of solid silica in static sodium and potassium silicate melts were determined, and D's for Si^{+4} were calculated in the temperature ranges 1000–1400˚ and 1000–1200˚C. The rates of dissolution of solid silica in sodium silicate melts stirred by a rotating silica disc at 1400˚C were also measured and were calculated [44]. For static melt conditions, molecular diffusion kinetics were sug-

TABLE 11.3
Measured and Calculated Values in the Na_20-SiO_2 System

Temp.	(10exp^{-4})/ T(°K)	Ci	Co	Na_2O	SiO_2	Kinematic Visc., Exp^{-8}	Dd	j	D × 10 exp–8
1050	7.56	0.79	0.66	34.1	65.9	17.2	0.017	0.14	1.6
1100	7.28	0.79	0.66	34.1	65.9	9.83	0.016	0.28	2.6
1150	7.03	0.80	0.66	34.1	65.9	6.59	0.014	0.45	3.8
1200	6.79	0.81	0.66	22.5	77.7	4.56	0.012	0.60	4.6
1250	6.57	0.82	0.66	34.1	65.9	3.08	0.008	1.05	7.6
1200	6.79	0.81	0.77	26.4	73.6	4.56	0.002	0.05	1.9
1200	6.79	0.81	0.73	34.1	65.9	4.56	0.005	0.16	2.5
1200	6.79	0.81	0.62	38.0	62.0	4.56	0.012	3.05	26.1
1200	6.79	0.81	0.49	50.8	49.2	9.83	0.004	8.85	64.5

Source: M. Truhlarova and O. Veprek, *Silikaty* 14: (1970)

TABLE 11.4
Dissolution of Silica in Static Sodium Silicate Melts

Temp.	Ci	Co	Ci–Co	Y*t exp$^{-1/2}$ × 10 exp^{-4}	Log D
1000	0.72	0.60	0.12	1.4	–7.3
1000	0.72	0.70	0.02	0.6	–7.4
1200	0.80	0.50	0.30	6.4	–6.3
1200	0.80	0.60	0.20	3.5	–6.6
1200	0.80	0.70	0.10	1.3	–7.0
1400	0.87	0.50	0.37	8.1	–6.4
1400	0.87	0.60	0.27	5.2	6.6
1400	0.87	0.70	0.17	2.6	–7.0
1000	0.72	0.60	0.12	1.4	–7.3

Note: Y = slab thickness; Y*t exp$^{-1/2}$ – slope of dissolution plot Y vs. t exp$^{1/2}$.

Source: K.Schwerdtfeger, *J. Phys. Chem.* 70: (1966)

gested, according to the author. Dissolution results and calculated log D's are presented in Table 11.4. For each temperature, the corrosion rate decreased as the (C_i – C_o) decreased. The D's increased with increasing temperature. According to the investigator, for the static melt case, the $t^{1/2}$ behavior suggested molecular behavior diffusion kinetics. The slope of the change of diameter versus $t^{1/2}$ plot increased about 1.2% per ˚C. Effective D's increased approximately an order of magnitude from an average of 5×10^{-8} at 1000˚C to 50×10^{-g} at 1400˚C.

TABLE 11.5
Dissolution of Silica in Static Potassium Silicate Melts

Temp.	Ci	Co	Ci–Co	Y*t $exp^{-1/2}$ × 10 exp^{-4}	Log D
1000	0.77	0.65	0.12	4.5	–8.8
1000	0.77	0.73	0.04	1.0	–8.4
1200	0.81	0.57	0.24	12.5	–7.7
1200	0.81	0.65	0.16	7.5	–7.7
1200	0.81	0.73	0.08	3.7	–8.0
1000	0.77	0.65	0.12	4.5	–8.8

Source: K.Schwerdtfeger, *J. Phys. Chem.* 70: (1966)

TABLE 11.6
The Dissolution of Silica in Sodium Silicate Melt Stirred by a Rotating Disc

Temp.	Ci	Co	Ci–Co	dv/dt/Ang. Vel. $exp.^{1/2}$ × 10 exp^{-5}	Kinematic Viscosity × 10 $exp^{1/6}$	Log D
1400	0.9	0.51	0.36	1.17	0.43	–6.7
Data below from Shurygin, Barmin and Esin; Izv Vysshikh Uchebn. Zavedenii Met 5 (1962), 5						
1360	0.8	0.49	0.35	7.7	0.43	–5.4
1250	0.8	0.49	0.32	4.8	0.43	–5.6
1170	0.8	0.49	0.30	2.1	0.40	–6.0

Source: From K.Schwerdtfeger, *J. Phys. Chem.* 70: (1966).

Similar $t^{1/2}$ behavior was obtained for static melt silica dissolution in potassium silicate. Dissolution results, calculated diffusivities, and silica concentration differences at the interface for sodium silicate are presented in Table 11.5 for this case. The slope of the change of diameter versus $t^{1/2}$ plot increased about 1.4% per °C. Experimental effective binary diffusion coefficients increased approximately an order of magnitude from an average of 0.7×10^{-8} at 1000°C to 1.3×10^{-8} at 1200°C. Dissolution rates decreased as the $(C_i - C_o)$ decreased.

Linear time behavior was observed for dissolution of rotating silica discs, as expected from equation (12). The investigator verified that the dissolution rate of silica varied in direct proportion to the $\Omega^{1/2}$. Dissolution rates, calculated D's, and silica concentration differences at the interface are presented in Table 11.6 for the rotating disc case. Rates ranged from $l0^{-4}$ cm per second at 25 radians to 1.4×10^{-4} cm per second at 156 radians per second. The calculated D was $1.9 \times 10^{-}$' at 1400˚C.

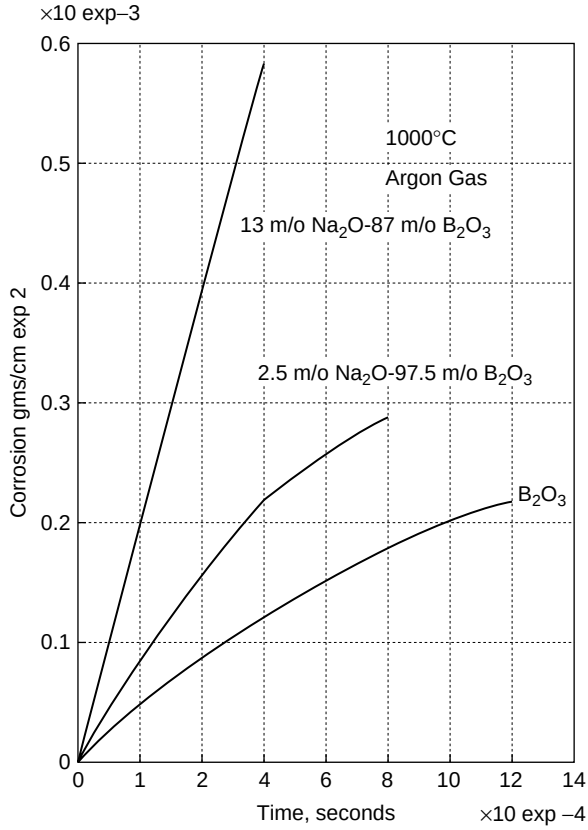

FIGURE 11.17 Corrosion versus time of tungsten metal in sodium borate melts at 1000°C equilibrated with argon gas (From R. Terai and R. Hayami, *J. Non-Crystalline Solids* 18 (1975).

This value is comparable to values for SiO_2 diffusion in sodium silicate as presented in Figure 11.16.

11.3.2.4 Tungsten Metal Corrosion in Na_2O-B_2O_3

In Section 11.3.1.2, it was shown that tungsten corrodes in molten B_2O_3 according to molecular diffusion kinetics in most cases. This same behavior was found for sodium borate melts that were equilibrated with argon gas prior to be used for the corrosion test. Figure 11.17 gives the specific tungsten metal weight loss versus time curves for several compositions [18]. The time exponent for the 2.5 mole% Na_2O3 97.5 mole% B_2O_3 system was determined to be 0.56.

When the partial pressure of the gas bubbled in the glass melt prior to its being used for the corrosion test equaled or exceeded 0.01, the slope of the log weight loss of tungsten metal versus log time approximated unity. Figure 11.18 shows the linear time behavior for four combinations of glass melt compositions and oxygen

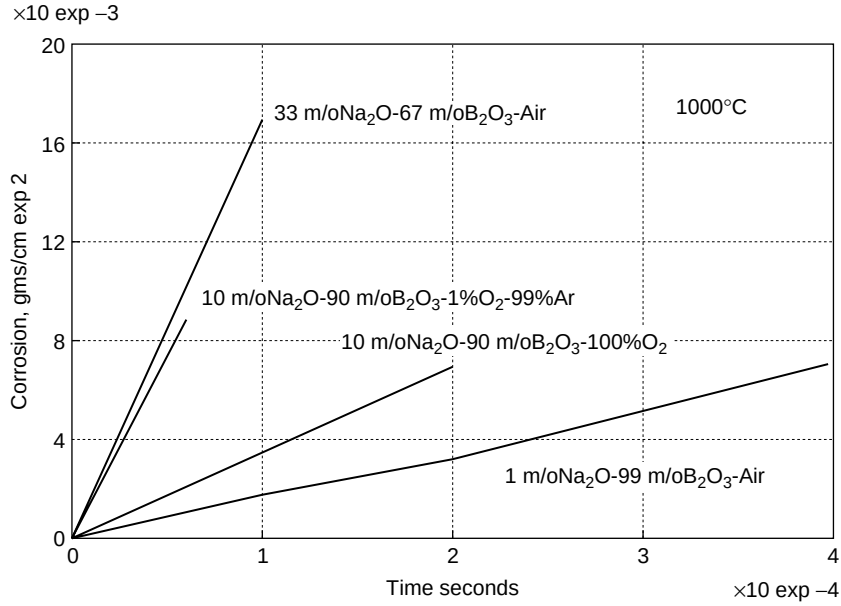

FIGURE 11.18 Corrosion versus time of tungsten metal in sodium borate melts at 1000˚C equilibrated with argon gas (From R. Terai and R. Hayami, *J. Non-Crystalline Solids* 18 (1975).

concentrations. Log–log plots of the data from Figures 11.17 and 11.18 are presented in Figure 11.19. Notice the slope change from about one half to approximately one.

The influence of the partial pressure of the gas bubbled in 1 mole% and 10 mole% Na_2O sodium borate melts on the corrosion rate of tungsten are shown in Figure 11.20. The influence of mole% Na_2O concentration of sodium borate equilibrated with air on the corrosion rate of tungsten metal is shown in Figure 11.21. The corrosion rate initially increases in a linear manner. However, at about 15 mole% it begins to increase at a lesser rate.

The E of the corrosion rate of tungsten by sodium borate glasses was also determined. An Arrhenius plots of parabolic corrosion rates of tungsten metal in argon equilibrated 2.5 mole% Na^2O and 30 mole% Na_2O melts are compared in Figure 11.22. The rate expressions are $8 \times 10^{-15}\, e^{-1100/RT}$ and $4 \times 10\, e^{-14}\, e^{-6800/RT}$ mole^2 per cm^4 second, respectively. The rate expression for the corrosion of tungsten in an air-equilibrated 33 mole% Na_2O sodium borate is $3 \times 10\, e^{-31000/RT}$ mole per cm^2 second.

Under normal conditions of corrosion, no oxide layer was detected on the surface of the tungsten since presumably tungsten oxide has an appreciable solubility in the melt. In an effort to force the oxide to remain on the surface so that it could be studied, the glass melt was saturated with WO_3 before the corrosion test. After the corrosion test was completed, a blue, strongly adherent coating was found on the metal surface. It was determined by conventional x-ray diffraction procedure to be of the general composition W_4O_{11}.

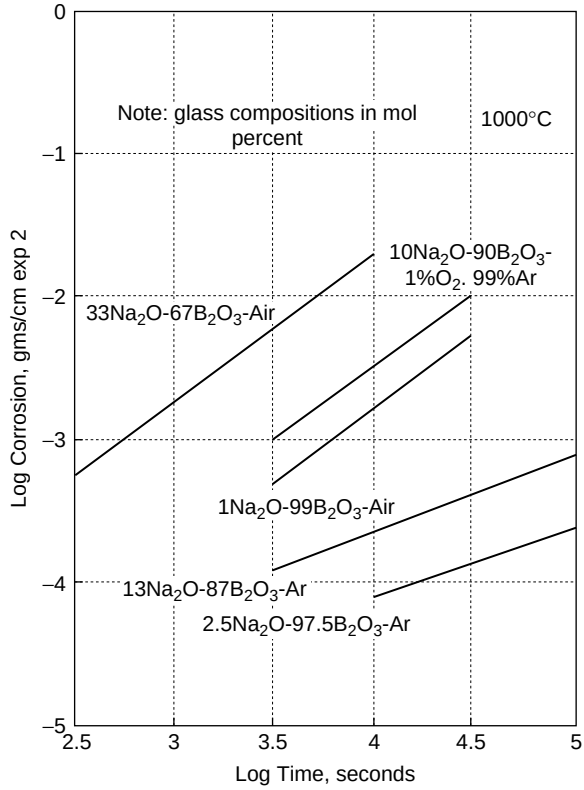

FIGURE 11.19 Log corrosion rate versus log time of tungsten metal in sodium borate melts equilibrated with various gases (From R. Terai and R. Hayami, *J. Non-Crystalline Solids* 18 (1975).

That the corrosion of tungsten metal in sodium borate melts is linear with time in most cases implies that the boundary layer for diffusion of the slow step of the process is constant with time. Therefore, steady-state conditions appeared to be in operation. This is in contrast to tungsten's corrosion in molten boric oxide, where the boundary layer for diffusion was postulated as increasing with $t^{t/2}$ time for one of the two proposed slow steps:

1. Diffusion of oxygen toward the tungsten
2. Diffusion of tungsten oxide away from the saturated region adjacent to the tungsten metal

Even though most of the results show linear time behavior, it is not surprising that parabolic time behavior was observed for corrosion of tungsten metal in sodium borate melts that had been pre-equilibrated with argon gas dissolved in them. Steady-state conditions are always preceded by unsteady state or transient conditions identified by parabolic time behavior. It is reasonable to suspect that a transient condition

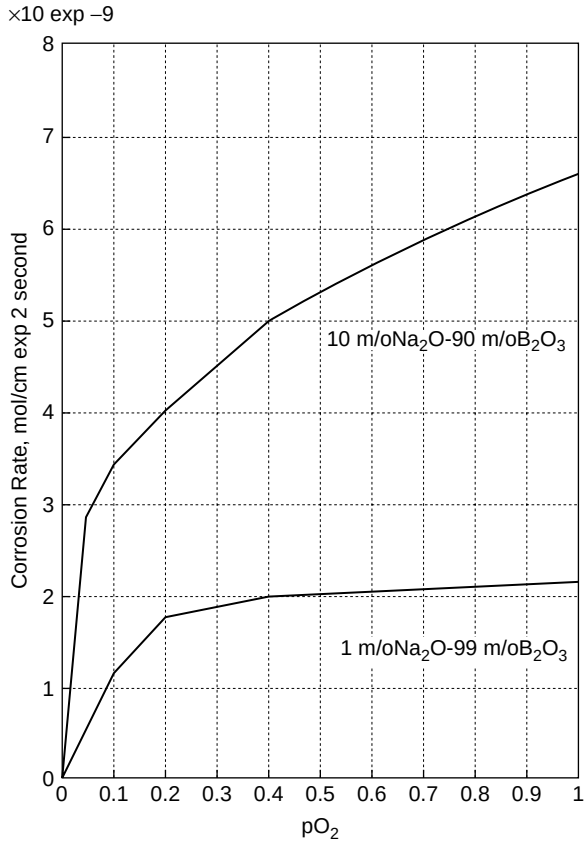

FIGURE 11.20 Corrosion rate of tungsten metal in sodium borate melts at 1000°C versus partial pressure of equilibrated gas (From R. Terai and R. Hayami, *J. Non-Crystalline Solids* 18 (1975).

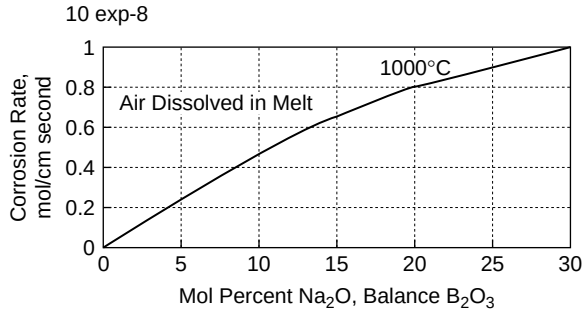

FIGURE 11.21 Corrosion rate of tungsten metal in sodium borate melts at 1000°C versus glass melt composition (From R. Terai and R. Hayami, *J. Non-Crystalline Solids* 18 (1975).

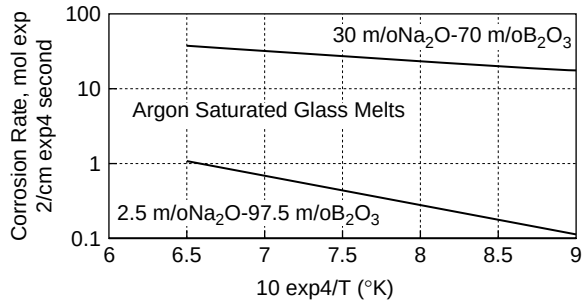

FIGURE 11.22 Arrhenius plot of transient corrosion rates of argon equilibrated sodium borate melts (From R. Terai and R. Hayami, *J. Non-Crystalline Solids* 18 (1975).

occurred for all the systems showing linear behavior, but that it was not resolvable for all but the slowest corroding systems. The investigator concluded the following regarding the corrosion of tungsten in sodium borate glass melts:

1. Tungsten corrodes in sodium borate glass melts containing dissolved oxygen. The corrosion rate increases approximately in a linear fashion with oxygen concentration of the melt, temperature, and time. Since the glass melt does not contain any multivalent ions, the dissolved oxygen must be the primary corrodant.
2. The characteristics of the corrosion process indicate that mass transport in the melt controls the rate. Either diffusion of oxygen toward the tungsten surface, or diffusion of the tungsten oxide away from the saturated melt next to the tungsten specimen can be the slow step in the process, depending on the concentration of oxygen in the melt. The former is believed to be the slow step when partial pressure of the gas, bubbled through the melt before the corrosion test, is less than 0.05 for 10 mole% Na_2O sodium borate glass melts. However, when partial pressure is one, the oxygen arrives at the reaction interface faster than it can be utilized. The undissolved W_4O_{11} on the surface inhibits further chemisorption of oxygen and subsequent corrosion. Under this condition, diffusion of dissolved reaction product away from the saturated melt controls the corrosion rate.
3. The experimental D of W^{+6} in a 10 mole% Na_2O sodium borate was calculated to be 2×10^{-7} cm^2 per second at 1000˚C. This number compares favorably with the diffusion coefficient of W^{+6} in 20 CaO-40 $A1_2O_3$-40 SiO_2 at 1432˚C, which is $5 \times 10 - 7$ cm^2/sec. This comparison was attempted because the kinematic viscosities of the two melts at their respective temperatures are similar, 3.3 and 5 stokes, respectively.

11.3.3 Studies of Refractory Dissolution in Three Component Glass Melts

Three component glass melts are typically the commercial glasses. Their corrosivity toward refractories is therefore of great interest to glass manufacturers. There is a

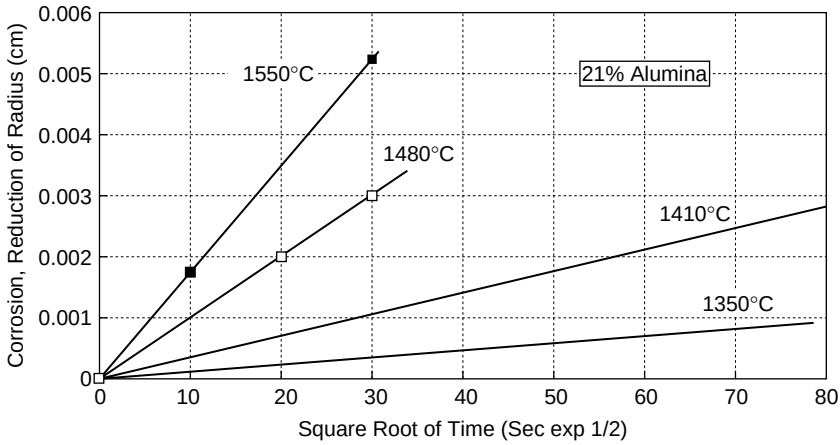

FIGURE 11.23 Dissolution of sapphire cylinders in $CaO\text{-}A1_2O_3\text{-}SiO_2$ with 21% $A1_2O_3$ versus square root of time (From A. R. Cooper, Jr., and W. D. Kingery, *J. Am. Ceram. Soc.* 47: (1964).

considerable body of literature regarding the dissolution of refractories in ternary glasses. The examples reviewed below were chosen because of their applications of dissolution kinetic theory.

11.3.3.1 Sapphire and Alumina and Alumino-Silicate Refractories Dissolution in $CaO\text{-}Al_2O_3\text{-}SiO_2$

Cooper and Kingery's classical studies of the measurement of the rate of dissolution of single crystals of sapphire and commercial refractories in glass melts from 1340 to 1500˚C are perhaps the best example of application of theory to practice [38]. These investigators chose the $CaO\text{-}A1_2O_3\text{-}SiO_2$ glass system for several reasons. First, accurate diffusion data were available. Second, the equilibrium diagram reveals that at all temperatures above 1380˚C there are stable liquids along the $CaSiO_2\text{-}A1_2O_3$ binary at all compositions from 0.1 weight fraction of alumina to the aluminus liquidus. The investigators claimed that, from the ternary equilibrium diagram, a pseudo binary can be constructed that shows the liquidus composition, and hence the saturation concentration, as a function of temperature. They present literature data for phase equilibria, diffusion coefficients, density and kinematic viscosity.

Molecular Diffusion. The investigators verified the molecular diffusion hypothesis for stationary sapphire cylinders. As shown in Figure 11.23, the amount of dissolution depends directly on $t^{1/2}$ for a glass melt containing 21 wt% Al_2O_3. The 7 mm sapphire rod lost approximately 0.01 mm of its diameter after 8100 sec at 1350˚C and 0.06 mm after approximately 900 sec at 1550˚C. The sapphire dissolution rate increased about 1% per °C. Table 11.7 presents comparisons of directly measured diffusion coefficients to calculated effective diffusion coefficients for three $A1_2O_3$ bulk concentrations for a range of temperatures. The values compare favorably. The dissolution rate increased with temperature and, at constant temperature, increased with a concentration difference parameter.

TABLE 11.7
Summary of Molecular Diffusion Data and Calculations

Measured Data				Calculation	Diffusion Coefficients ($cm^2/sec \times 10\ exp^8$)		
Ci	Co	Temp.	Y exp 2*t $\times$ 10 exp^{-8}	(Ci – Co)/ (1 – Ci)	Interfacial D	Effective D	20 wt% Al_2O_3
0.47	0.21	1550	3.20	0.49	19	20	30
0.43	0.21	1480	1.06	0.39	8.3	9.1	14
0.40	0.21	1410	0.16	0.32	2	2.1	3.2
0.38	0.21	1345	0.02	0.27	0.24	0.26	0.45
0.47	0.15	1550	5.50	0.60	23	25	37
0.47	0.07	1550	11.00	0.75	31	33	47
0.45	0.07	1510	5.80	0.69	18	20	30

Note: Y exp^2 * t ¥ 10 exp^{-8} = slope of corrosion vs. time plot. Y = change in slab thickness.

Source: From Reference 38.

Free Convection. As the dissolution process proceeded, the investigators hypothesized that a hydrodynamic instability will develop either from density differences or from surface tension differences between the alumina-saturated slag and the bulk slag. Free convection results in a virtually time independent rate of solution, as shown by equation (6). The time-independent dissolution rate for a sapphire rod in a 2l wt% CaO-$A1_2O_3$-SiO_2 melt at 1550˚C is shown in Figure 11.24. The 7 mm rod lost approximately 0.45 mm of radius in 15,000 sec. The rate of dissolution was approximately 3×10^{-5} mm per sec.

Forced Convection. Cooper and Kingery stated that forced convection studies are especially useful for assessing the rate-controlling mechanism of dissolution. As suggested by equation (11), if the rate of dissolution of the sapphire, for example, is controlled by transport in the glass melt, the rate will vary as $\Omega^{1/2}$. They presented an equation similar to (12) that shows a relationship between the boundary layer thickness and $\Omega^{1/2}$. The investigators show a linear plot of measured dissolution rates versus $\Omega^{1/2}$ and linear-with-time plots of dissolution at 126 radians per second at four temperatures.

The investigators concluded that the dissolution of sapphire in CaO-$A1_2O_3$-SiO_2 glass melt is governed by mass transport in the glass melt because the calculated D's agree rather closely with independently measured tracer diffusion coefficient for Si at temperatures above 1450˚C.

These investigators collaborated with another investigator to measure the dissolution of fused silica (92.5% theoretical density), fused-grain mullite, (85% theoretical density anorthite), and dense polycrystalline (97.5% theoretical density) Al_2O_3 in a 20 CaO-40 $A1_2O_3$ –40 SiO_2 glass melt and compared the results with sapphire dissolved in the same composition glass melt [45]. As shown in Figure 11.25, at a temperature of 1425˚C, the sapphire and the polycrystalline $A1_2O_3$ dissolve at the same rate, and at a much lower rate than fused silica, mullite, and anorthite. However,

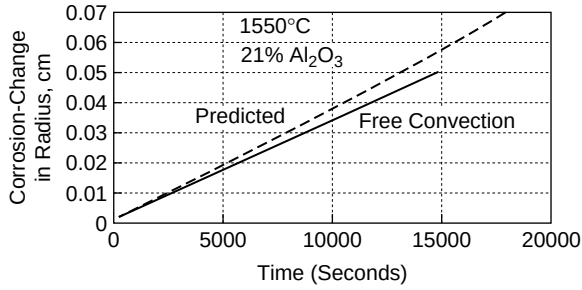

FIGURE 11.24 Dissolution at relatively long times of sapphire cylinders in CaO-$A1_2O_3$-SiO_2 with 21% $A1_2O_3$ at 1550˚C versus time (From A. R. Cooper, Jr, and W. D. Kingery, *J. Am. Ceram. Soc.* 47: (1964).

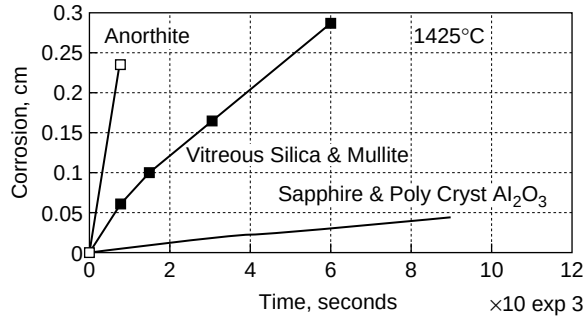

FIGURE 11.25 Dissolution versus time under forced convection conditions in the 40CaO-$20AI_20_3$-$40SiO_2$ slag of specimens of sapphire, polycrystalline alumina, mullite, vitreous silica. and anorthite at 1425˚C (From B. N. Samaddar, W. D. Kingery, and A. R. Cooper, Jr., *J. Am. Ceram. Soc.* 47 (1964).

at 1500˚C, the sapphire dissolves at a slightly slower rate than the polycrystalline Al_2O_3. Their results are presented in Table 11.8. Silica's dissolution rate increased approximately fourfold for a 150˚C temperature increase, whereas the sapphire and alumina samples' dissolution rate increased an order of magnitude from 1425 to 1500˚C. The increase in viscosity resulting from silica's dissolution may have lessened the dissolution sensitivity to temperature.

Corrosion as an Activated Process. According to these investigators, other researchers have interpreted refractory dissolution data as an activated process, and have attempted to correlate experimental activation energies with other characteristics of the materials being studied. They concluded that there is considerable difficulty in interpreting activation energies in terms of physical characteristics of the process because of several factors. First, the liquidus composition changes with temperature. Second, activity and diffusion coefficients in the silicate system depend greatly on composition. There can be large changes in the E's that are not related to any activated process. Third, the relative mobilities of the ions participating in the corrosion process determine the liquidus composition. They state

TABLE 11.8
Calculated Values of the Effective "D" for Forced Convection Dissolution of Various Refractories

		Refractory Saturated Slag			Bulk Slag			
Nature of Sample	Temp. °C	$j \times 10$ exp[5] cm/sec	Density gm/cc	Dynamic Viscosity Poise	Density gm/cc	Dynamic Viscosity Poise	Conc. Diff. gm/gm	$D \times 10$ exp[6] cm^2/sec
Silica	1500	8.9	2.17	1000	2.83	8	1	6.5
	1425	4.5	2.34	700	2.86	15	0.7	4.5
	1390	3.3	2.40	1000	2.88	21	0.64	3.2
	1350	2.1	2.43	800	2.9	35	0.58	1.8
Sapphire	1500	3.5	2.79	12	2.83	8	0.63	3.0
	1460	0.9	2.79	23	2.84	13	0.58	0.5
	1425	0.3	2.80	31	2.86	15	0.55	0.12
Polycrystalline Alumina	1500	3.6	2.79	12	2.83	8	0.64	2.9
	1460	0.9	2.79	23	2.84	13	0.59	0.49
	1425	0.3	2.80	31	2.86	15	0.56	0.12
Mullite	1500	16.5	2.68	26	2.83	8	1.65	7.8
	1425	4.3	2.76	57	2.86	15	1.56	1.3
	1390	2.9	2.81	61	2.88	21	1.52	0.8

Source: From Reference 45.

that the Arrhenius plot is suitable for reporting and interpolating data, but not for its extrapolation.

11.3.2.2 Quartz Glass Dissolution in Na_2O-CaO-SiO_2, K_2O-PbO-SiO_2 Na_2O-$B_2O_gSiO_2$ and CaO-Al_2O_3-SiO_2

The dissolution of quartz glass and devitrified (cristobalite) quartz glass thick-walled capillaries 6 mm-diameter, 50 mm-long rods have been studied under conditions of free convection in ternary glass melts at temperatures ranging from 1200 to 1500°C in small platinum crucibles [43]. The time dependency for the dissolution process of vitreous silica in all the ternary glass melts studied was identified as being linear according to the density-driven convection mechanism. The investigators concluded that the molecular diffusion mechanism preceded the natural convection mechanism because the plots of dimensional loss versus time did not pass through the origin.

Their results indicated that the dissolution of vitreous silica occurs most rapidly in the Na_2O-CaO_2-SiO_2 glass melts and most slowly in the CaO-AI_2O_3-SiO_2 glass melt at all test temperatures. Pure and silica-enriched glass melt properties, measured dissolution rates in Na_2O-CaO_2-SiO_2 glass melts and calculated diffusion rates at five temperatures are presented in Table 11.9. The dissolution rate increased by a factor of 7 as the temperature increased from 1050 to 1250˚C and as the concentration difference of silica increased from .125 to .16. In the opinion of the investigators, the D's calculated from the experimental data are probably related to the silica ion. They are within 10% of diffusion coefficients calculated from the Stokes-Einstein equation using viscosity values. The calculated E of the dissolution of vitreous silica is 39.4 Kcalories per mole.

TABLE 11.9
Measured and Calculated Values in the SiO_2/Na_2O–SiO_2 Dissolution System

Temp.	Co	Ci	Co – Ci	Kin. Visc. $\times$ 10 exp^{-2}	Density Change	j $\times$ 10 exp^{6}	D $\times$ 10 exp^{8}
1050	0.660	0.785	0.125	17.2	0.017	0.139	1.64
1100	0.658	0.789	0.131	9.83	0.016	0.28	2.58
1150	0.657	0.797	0.140	6.59	0.014	0.452	3.76
1200	0.656	0.805	0.149	4.56	0.012	0.602	4.55
1250	0.655	0.815	0.160	3.08	0.008	1.05	7.55
1200	0.771	0.805	0.034	4.56	0.002	0.046	1.86
1200	0.733	0.805	0.072	4.56	0.005	0.155	2.49
1200	0.617	0.805	0.188	4.56	0.012	3.05	26.1
1200	0.490	0.805	0.315	4.56	0.004	8.85	64.5

Source: From Reference 43.

11.3.3.3 Al_2O_3 and ZrO_2 and Fused AZS Dissolution in Alkali-Barium-Silicate

Zirconia is a very insoluble oxide in most glass melts and therefore has great corrosion resistance. However, in addition to being very expensive, zirconia has a tendency to crack during manufacture and use, and is very difficult to make in large shapes. Zirconia is therefore combined with other oxides, usually alumina and silica, to decrease the solubility of the composite refractory. Alumino-silicate refractories are fairly soluble in common glass melts. The AZS can be sintered or fused. These refractories are examples of non-ideal solutes discussed in Section 11.1.4.

The dissolution of precision-ground plates 1.0 cm × 1.0 cm, × 4.0 cm 94% sintered alumina, 95.7% sintered zirconia and fusion-cast alumina-zrconia-silica refractories (33% $Zr0_2$, 51% $A1_20_3$) in pure and solute-enriched alkali-barium-silicate glass melts were measured in a temperature range 1200 to 1500˚C for 7 days [l4]. The refractory samples were immersed halfway or 2 cm into a crucible containing 7 cm of glass. The ratio of glass-to-refractory volume was between 50 and 100 to 1. The investigators assumed that the crucible was sufficiently large to eliminate any interference by the crucible wall. The measure of dissolution, loss of dimension in the vertical direction, Δx, was measured at room temperature after the test was completed.

Data obtained from the dissolution of each of the three refractories in the base glass, when plotted as Δx versus $t^{1/2}$, were straight lines. The invesigators claimed that this strongly suggests the dissolution process at the metal line is molecular-diffusion controlled. Figure 11.26 shows the diffusion kinetics observed at the metal line for two of the three refractories in the base glass composition at 1500˚C. The fused AZS has the slowest dissolution rate and the sintered $A1_2O_3$ the fastest. The ratio from high to low is about 7 to 1.

$A1_2O_3$ and ZrO_2 were added to the base glass to alter its composition for additional dissolution tests. The D_C between the solute-enriched melt and the bulk glass were decreased by these additions. Since concentration difference is the ther -

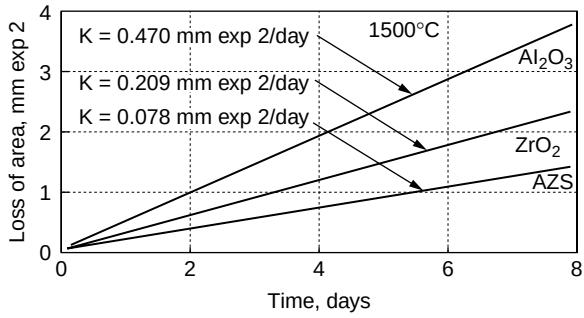

FIGURE 11.26 Dissolution versus time for three refractory-base glass systems (From L.R. Schlotzhauer and J.R. Hutchins III, *The Glass Industry,* (1966).

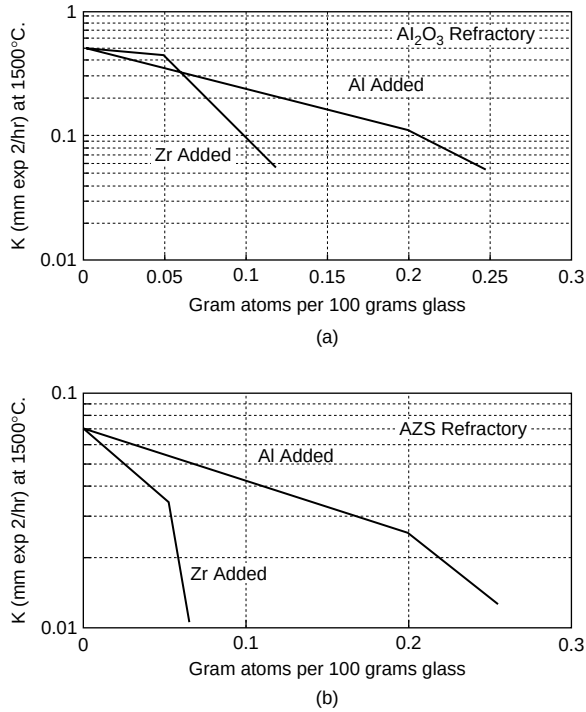

FIGURE 11.27 Dissolution rate constants at 1500˚C for two refractories as a function of glass compositions (From L. R. Schlotzhauer and J. R. Hutchins, III, *The Glass Industry,* (1966).

modynamic driving force for dissolution, lower dissolution rates would be expected. This prediction was confirmed by the investigators, as shown in Figure 11.27.

The dissolution rate constants decreased by about an order of magnitude when less than 0.2 wt% ZrO_2 and less than 0.3% alumina were each added to the base glass composition. Over most of the temperature range studied, the rate constant order is as follows: $A1_2O_3 > ZrO_2 > AZS$. Temperature coefficients, defined by the E tern in equation (3) are in the order as follows: $A1_2O_3 > AZS > ZrO_2$.

The investigators offered an explanation of the results of the dissolution in the solute-enriched glass melts. They suggested that the presence of added refractory oxide to the glass melt (in the diffusion boundary layer thickness zone for a dissolution process controlled by molecular diffusion) can influence dissolution rates at and below the metal line. The smaller difference in refractory concentration accounts for the decrease of rate constants. The investigators also offered an explanation for the greater corrosion resistance of the AZS-glass melt system. “Alumina dissolves more rapidly than zirconia. Therefore it causes the fluid at the AZS interface to become rich in $A1_2O_3$. The dissolution of the zirconia phase is slowed by an alumina-rich glass. This explains the presence of zirconia grains in the interfacial layer. These grains, however, must have a dissolution boundary layer surrounding them.”

11.3.3.4 Upward Drilling of High Al_2O_3, Corundum, SnO_2 and Fusion Cast AZS and ACZS Refractories in Soda-Alumina-Lime-Silica Glass Melts

The phenomenon of upward drilling attack (vertical honeycomb corrosion) of commercial fusion cast refractories with atypical soda-alumina-lime-silica container glass composition was thoroughly investigated in the laboratory because of very severe corrosion problems with throat payers in production furnaces. Kucheryavi et al. [46] claimed that the vertical honeycomb corrosion is caused by, or at least associated with, the presence of gas bubbles on the refractory-glass contact surface. They immersed four specimens measuring 20 mm × 20 mm × 50 mm in platinum crucibles containing the test glass melt for 40 to 96 hours, depending on the type of refractory and the test temperature. Test temperature ranged from 1300 to 1525˚C. The high-alumina and corundum refractories were tested at temperatures of 1325, 1475, 1500, and 1525˚C. The remaining refractories were tested at 1425, 1475, 1500, and 1525˚C. After the completion of a test, the refractory was removed from the crucibles, the glass was drained off, and then it was cooled to room temperature.

The extent of vertical honeycomb corrosion of each sample depended largely on temperature, as shown by Figure 11.28. The highest resistance to honeycomb corrosion was found in the chrome-alumina-zirconia and the tin oxide-based refractories. There was virtually no corrosion on the former product up to 1500˚C under the conditions of the experiments. The alumina-based refractories suffered the highest degree of honeycomb corrosion. The fusion-cast AZS products underwent less corrosion than the alumina-based refractories, but more than the chrome-alumina-zirconia and the tin oxide-based refractories.

The good performance of these refractory products seems to be partially related to their low solubility. The low vertical honeycomb corrosion of chrome-alumna-zirconia and the tin oxide-based refractories could also be due to relatively low difference in surface tension of the bulk glass to the solute-enriched glass. Tin oxide enrichment of the soda-lime-silica glass has only a very slight influence on the surface tension alteration and a slightly negative temperature coefficient [47,48]. Six to 12% SnO_2 additions to a soft ground-coat enamel resulted in only a 1.5% increase in surface tension. $A1_2O_3$ and ZrO_2 increase surface tension of soda-lime-silica glass melts [49,50]. However, Cr_2O_3 reduces surface tension of glass [49]. The opposite direction effect among the three main components of the ACZS refractory lessens the composite change in surface tension of the Cr_2O_3-containing AZS refractory compared with the AZS composition.

11.3.4 Applications of Dissolution Kinetic Principles to Refractory Systems Design-Refractory Chemistry

This review of refractory dissolution kinetic equations, experimental procedures, and refractory dissolution studies has provided a foundation for application of the principles to actual furnace refractory wall design. Some general comments regarding the more practical aspect of materials corrosion, namely refractories and electrode metals applications, can be made from what has been learned.

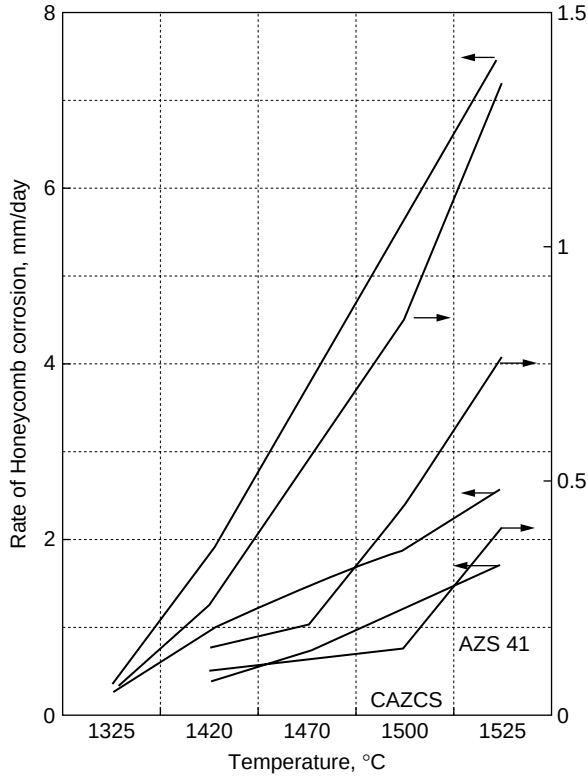

FIGURE 11.28 Temperature dependence of the rate of vertical honeycomb corrosion of six refractories in a soda-time-silica glass (From M.N. Kucheryavyi, 0.N. Popov, V.T. Selyanko and I.O. Buranov, *Glass and Ceramics*, 45 (1988).

For glass contact applications, materials should be used that have the lowest solubility in the glass melt. Concentration difference has been shown to be the thermodynamic driving force for dissolution. The best common oxides for low solubility at glass-melting temperatures are ZrO_2 and Cr_2O_3. In stabilized form, ZrO_2 is used to make small shapes such as laboratory crucibles. Fusion-cast refractories having a ZrO_2 concentration of approximately 95% have become commercially available during the last decade. They are very corrosion resistant in some glasses such as the boro-silicates. However, their corrosion resistance in soda-lime-silica glass is, at best, equivalent to fusion-cast refractories having a 33 to 41% ZrO_2 concentration. The reason for this is the manner in which $A1_2O_3$ and ZrO_2 interact at the refractory interface. Schlotzhauer and Hutchins offer a model of the AZS-glass interface that explains how the combination of $A1_2O_3$ and ZrO_2 work together to provide excellent resistance to dissolution by glass melts [14].

Unfortunately, since Cr_2O_3 imparts a green color to most commercial glasses, its application as a glass contact refractory is limited to small high-wear areas such as bonded Cr_2O_3 overcoat blocks of basin walls, entrance lintels of throats and the liner of fiberglass furnaces.

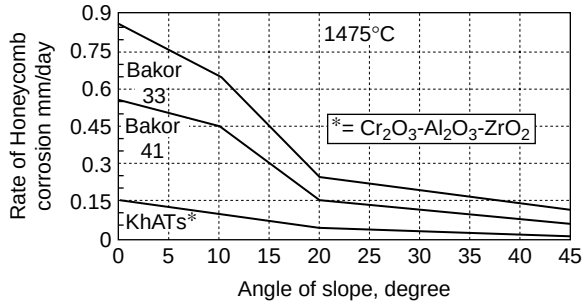

FIGURE 11.29 Dependence of the rate of vertical honeycomb corrosion of three refractories in a soda-lime-silica glass at 1475˚C versus angle of slope (From M.N. Kucheryavyi, 0.N. Popov, V.T. Selyanko and I.O. Buranov, *Glass and Ceramics*, 45 (1988).

11.3.4.1 Basin Wall Refractory Considerations

The refractories industry has circumvented some of the limitations associated with the use of these highly insoluble oxides in the pure or near-pure form by combining either ZrO_2 or Cr_2O_3 with $A1_2O_3$ and SiO_2. Fusion-cast AZS (Al_2O_3-ZrO_2-SiO_2) refractories fabricated in large blocks are the workhorse of the glass industry. For the most severe applications, such as the metal line of the melter, the recommended ZrO_2 content of the refractory is 41%. For lesser applications, ZrO_2 content of the refractory is 33% is used.

Fusion cast Cr_2O_3-$A1_2O_3$-SiO_2 refractories are also used in special applications where the highest degree of corrosion resistance is required and some color potential can be tolerated. AZS refractories are also used in the bonded form for moderately corrosion-potential applications such as furnace paving and feeder channels and canals.

For lower-temperature applications, $A1_2O_3$ and SiO_2 in their pure or near-pure forms are extensively used for glass contact applications in most types of glass furnaces. The high level of interest in these two oxides is demonstrated by their selection as solute materials in the experimental work reviewed in the previous section. They were selected not only because they are ideal or near-ideal materials, but also because of their low solubility at lower temperatures. Alumina in the fusion-cast form is used for glass contact applications in soda-lime-silica glasses at or below 2550˚F. This temperature range includes the conditioner and glass forming applications such as canals, channels, and float lips partly because of low defect potential and reasonable cost. Silica is used for glass contact refractories applications in the silica glass form and also as rebonded fused silica for tweels in the float glass industry because of low defect potential and relatively low cost. As reviewed in the previous section, a property of silica that makes it a more corrosion-resistant refractory than it would appear to be is that as it dissolves, it increases the viscosity of the glass significantly [45]. The investigators state that “both the diffusion coefficient and the viscosity change rapidly with silica content at high silica concentration. As the temperature is raised, the silica concentration at the interface is increased, with

a resultant change in the effective diffusion coefficient and viscosity opposite to that induced by temperature changes."

As mentioned above, many of the properties of glass melts that influence refractory dissolution are temperature dependent. Examples are solubility, diffussivity, density, kinematic viscosity. The strongest temperature effect is on diffusivity because it exhibits exponential behavior as shown by equation (3). Therefore, the refractory-glass melt interface is usually cooled in an effort to reduce dissolution rate. Some of the methods used for accomplishing the cooling of the interface are [46]:

1. High velocity forced air cooling perpendicular to the cold face
2. Water-cooled steel plate adjacent to the cold face
3. High-velocity forced air cooling at the glass–refractory interface (inside the furnace)
4. Water pipe installation under the melt surface just below the metal line

Popov et al. [46] claim that the glass–refractory interface temperature can be reduced as much as 400˚C by application of cooling techniques and that furnace campaign length can be increased from 5 to 15 years if the interface temperature is reduced from 1320 to 1100˚C for a 41% ZrO_2, fusion-cast AZS refractory basin wall. Air velocity was in the range 3.5 to 6.5 meters per second.

A method for enhancing the cooling effect of cooling air applied to the cold face of the block on the glass–refractory interface temperature is to design the block cross-section so that it is thinnest at the metal line, the region where the glass melt is the hottest. One way to accomplish thus is by tapering the block from top to bottom so that it is thinner at the top, near the glass line. Another method that is used by glass refractory engineers is to cast a notch in the uppermost 25 to 30 cm so that the thickness is about 15 cm at and just below the metal line where the cooling requirements are the highest. The remainder of the block, below 25 to 30 cm, is at its full thickness of about 25 to 30 cm. When the refractory at the metal line wears to less than about 10 cm, the interface temperature is greatly depressed by the cooling air. A fusion-cast AZS patch block or water-cooled steel box can be placed on the shelf formed by the notch when the remaining refractory thickness warrants. A 7.5 cm-thick patch block can last more than 1 year.

The ZrO_2 and Al_2O_3 based fusion-cast refractories increase the density of the solute-enriched glass melt. Fortunately, as shown by equation (6), the influence of density difference is to the one-fourth power. One way to reduce the influence of density change on the dissolution rate of basin wall refractories is to slope the wall outward from top to bottom. This geometry tends to slow the vertical transport of solute-enriched melt away from the interface because it increases the boundary layer thickness. This slower transport rate reduces the dissolution rate of the wall.

Avoid multi-course basin wall construction whenever possible, because bubbles can get trapped under a horizontal downward face. This condition could lead to upward drilling corrosion. The trend in the glass industry has been to avoid horizontal joints by using soldier course blocks. Their height is equal to that of the entire furnace wall. Although it is not the focus of this chapter to discuss the intrinsic properties of refractories, it should be mentioned that minimizing porosity and

maximizing the density of the refractory block used in melter basin walls are of extreme importance. The dissolution equations reviewed in Section 11.1 were developed for heterogeneous dissolution of a solute by a solvent at an interface. If the glass melt is able to penetrate into the porosity of the refractory, then the dissolution rate will occur at an accelerated rate because a greater mass is reacted upon within unit time. Fusion-cast refractories used for basin walls vary in density, grain size, and ZrO_2 content as they are cast. It is very beneficial if the low-density, low-ZrO_2 portion of the block is removed by the manufacturer because of its low corrosion resistance. The resulting void-free block will provide the best corrosion resistance possible for the composition used. The densest and highest ZrO_2 portion of the block should be placed upward for a fossil-fired furnace since the metal line suffers the greatest rate of wear. In joule-heated furnaces, the most corrosion-resistant part of the block should be placed at, or near, the electrodes.

11.3.4.2 Throats

As reviewed above, the refractories used for the leading edges of throats of container and tableware furnaces are subjected to severe temperature and velocity conditions. The acceleration of refractory solution due to motion is described for a rotating cylinder by equation (12). The dissolution rate is proportional to the square root of the angular velocity. The most corrosion-resistant refractories are used for the leading edge of throat configurations. Fusion-cast and ACZS refractories are the choice for this application because of their high corrosion resistance.

The roof of the throat is a region of very severe attack because of high velocity and temperature, and also because of upward drilling. Bubbles in the glass tend to collect on this surface or form from air entrapment from motion of the glass melt along a crack or joint. The resultant corrosion profile resembles a honeycomb structure. According to Kucheryavyi et al., there is virtually total wear of the paving blocks of the throat after only 1.5–2 years of use [46]. They stated that for fusion-cast AZS refractories, a 50°C increase in temperature results in a 2.2 to 4.3-fold increase in the corrosion rate. They claim that the chrome-alumina-zirconia refractory system does not show any upward drilling corrosion in the 1425–1500°C interval in laboratory tests. They also claimed that the SnO_2 refractory composition had high resistance to upward drilling corrosion in laboratory tests. In addition to using refractories having high corrosion resistance, the investigators also recommended that the roof refractories be installed at a slope of at least 20° to the horizontal base on laboratory tests. The elevation of the entrance end of the throat is lower than that of the exit end. The glass flows tend to sweep bubbles along the refractory surface and out into the conditioner, thereby avoiding honeycomb (upward drilling) dissolution.

11.3.4.3 Bottom Paving

Some furnace areas are not subjected to high dissolution rates. Examples are melter and conditioner bottom refractories some distance from electrodes, bubblers, and stirrers. Since glass flows are low at many regions of the furnace, and since the bottom is a horizontal-facing upward application, density-driven convection cannot

occur. The diffusion boundary layer tends to grow with time under these conditions and therefore follows the molecular diffusion behavior described by equation (2). The refractories used for a large percentage of the bottom melter and conditioner can possibly be of a lower grade, such as clay flux, bonded AZS, or fusion cast $A1_2O_3$. However, there are at least three potential high-refractory wear situations that require consideration:

1. The first is downward drilling. Particles of metal resting on the furnace bottom can drill downward through the refractories much like bubbles drill upward. Every effort should be made to prevent metal particles from getting into the furnace.
2. The second situation is for areas of the bottom where high flow rates are present. Examples of these are waist or throat bottoms, and areas at and adjacent to electrodes, stirrers and bubblers. The most corrosion-resistant refractories, such as fusion-cast AZS, should be used in these situations.
3. The third application is that of steps in multilevel furnaces. Since the glass melt is exposed to the top surface and one side, dissolution occurs from at least two sides. Furthermore, the molten glass can penetrate under the pavers and corrode their undersides via an upward drilling mechanism. Therefore, the corrosion of the pavers can occur on at least three faces. Therefore, the most resistant fusion-cast AZS or $A1_2O_3$ refractories should be used for these areas. The use of cement or a ramming material under the bottom paver can minimize its upward drilling.

11.3.4.4 Refractory Metals

Refractory metals such as molybdenum and tungsten are used for electrodes in joule heated glass furnaces. As shown in Section 11.3.2.4, the first step in the corrosion of tungsten is the oxidation of the metal. It develops a layer of oxide on it and then behaves like a refractory oxide. The oxide dissolves in the melt, and after the solute layer becomes hydrodynamically unstable, it is transported away from the interface. These metals will corrode reasonably slowly if the oxygen potential of the glass melt is not excessive and if these are not subjected to foam. Foam contains a high concentration of gases such as oxygen, water and oxides of sulfur that rapidly react with metals such as tungsten and molybdenum. The high glass melt velocities caused by the heat generated by the electrodes result in an additional condition that accelerates the transport of reactants to the surface and metal oxides from the surface.

Electrodes can also accelerate the dissolution of refractories in at least two ways:

1. Some of the electric power enters the refractory block near an electrode because its electrical resistance is only 1 to 10 times that of the glass before alkali migrates into it. The block therefore becomes elevated in temperature and, as shown above, dissolution can occur at an accelerated rate.
2. If the electrodes are allowed to dissolve to the extent that only short stubs remain, then an even higher percentage of its power can enter the refractory. Very high temperature can be generated at the refractory wall because

of the concentration of power in a relatively small volume. Under this circumstance, very rapid refractory dissolution can occur.

REFERENCES

1. A. R. Cooper, Jr., Dissolution Kinetics in Glass Making, *Advances in Glass Technology,* Plenum, New York (1962) p. 217.
2. G. V. McCauley, *Bull. Amer. Ceram. Soc. 4:* 605 (1925).
3. W. K. Brownlee, *J. Am. Ceram. Soc. 7:* 457 (1924).
4. F. C. Flint and A. R. Payee, *J. Am. Ceram. Soc. 9:* 613 (1926).
5. G. M. Schwab, H. S. Taylor, and R. Spencer, *Catalysis,* Van Nostrand Reinhold, 236 (1937).
6. A. A. Noyes and W. R. Whitney, Rate of solution of solid materials in their own solutions, *Z. Phvsik. Chem. 23:* 689 (1896).
7. W. Nernst, Theory of reaction velocities in heterogeneous systems, *Z. Physik. Chem.* 47:52 (1904).
8. W. D. Kingery, *Kinetics of High-Temperature Processes,* The Technology Press of MIT and John Wiley & Sons, Inc., New York (1959) p. l.
9. T. B. King and P. J. Koros, *Kinetics of High-Temperature Processes,* The Technology Press of MIT and John Wiley & Sons, Inc., New York (1959) p.80.
10. W. Trier (translation by K. L. Loewenstein) *Glass Furnaces Design, Construction and Operation (*Society of Glass Technology), Charlesworth and Co., Huddersfield, England (1987) p.82.
11. A. R. Cooper, Jr., Kinetics of Refractory Corrosion, *Ceramic Engineering and Science Proceedings 2:* 1053 (1981).
12. S. Glasstone, K. J. Laidler and H. Eyring, *The Theory of Rate Processes,* McGraw-Hill, New York (1941) p.477.
13. A. R. Cooper, Jr., D. Sc.Thesis, Dept of Metallurgy, M.I.T. (1960).
14. L. R. Schlotzhauer and J. R. Hutchins III, *The Glass Industry* (1966).
15. J. R. Hutchins, III, *Glass Technology 7:*42 (1966).
16. A. Napolitano, P. B. Macedo and E.G. Hawkins, *J. Am. Ceram. Soc. 48:* 613 (1965).
17. R. Terai and R. Hayami, *J. Non-Crystalline Solids 18:* 217 (1975).
18. G. A. Pecoraro, The Corrosion of Tungsten in Boric Oxide and Sodium Borate Melts, Ph.D. Thesis, Rensselaer Polytechnic Institute, Troy, New York (1969).
19. A. R. Cooper, Jr., and W. D. Kingery, The corrosion of refractories by liquid slags and glasses, in *Kinetics of High-Temperature Processes,* The Technology Press of MIT and John Wiley & Sons, Inc., New York (1959) p.85.
20. C. V. Stemling and L. E. Scriven, Interfacial turbulence: hydrodynamic instability and the Marangoni effect, *A.I.Ch.E. J. 5:* 514 (1959).
21. T. S. Bushy, *Glass* 34 (1962) 182; 44(1967) 311.
22. L. Reed, *Trans. Br. Ceram. Soc.* 53, (1954) 180.
23. M. Dunkl and R. Bruckner, *Glastech. Ber. 53:* 321 (1980)
24. P. Hrma, *Chem. Engr. Science 25:* 679 (1980).
25. T. S. Bushy, G. C. Cox, and B. E. Gillespie, *Glass Technol.* 12:94(1971).
26. T. S. Bushy and J. Barker, *J. Amer. Ceram. Soc.* 49:441 (1966).
27. E W. Preston and J. C. Turnbull, *Am. L Sci.* 234 (1941) 96.
28. H.J. Tress, *J. Soc. Glass Tech 32*: 891 (1954).
29. W. G. Cochran, *Proc Cambr. Phil. Soc.30:* 365 (1934).

30. E. Vago and C. E. Smith, *Proc. VII Int. Cong. on Glass,* Brussels, 1965, Charleroi Inst. Natl. du Verre, Paper No. 62.
31. F. W. Preston and S.C. Turnbull, *Am. J. Sci. 239:* 92 (1941).
32. D. W. Ross, *J. Am. Cer. Soc. 9:* 641 (1926).
33. H. Jebsen-Marwedel, *Glastech. Ber. 29,* (1956) 233.
34. T. A. Bushy and R. J. Turner, *Glass Technol.* 22: 15 (1981).
35. L. Reed and L. R. Barren, *Trans. Brit. Ceram.* Soc. 54: 671 (1955).
36. H. R. Moore and R. Heeley, *J. Soc. Glass Tech* 34: 274 (1950).
37. V. G. Levich, *Physicochemical Hydrodynamics,* Prentice-Hall (1962) p.62.
38. A. R. Cooper, Jr, and W. D. Kingery, *J. Am. Ceram. Soc.* 47: (1964) p. 37.
39. J. D. Mackenzie, *J. Phys. Chem.* 63: (1959) p.1875.
40. T. D. McGee, *Ceramic Engineering and Science Proceedings,* Nov.–Dec. (1981) p.41.
41. M. Sadfar, G. H. Frischat and H. W. Hennicke, *Ber. Dtsch. Keram. Ges.* 51: (1964) p.291.
42. J. Hlavac and P. Strnad, *Silikaty* 5, (1961) p.302.
43. M. Truhlarova and O. Veprek, *Silikaty* 14: (1970) p.1.
44. K. Schwerdtfeger, *J. Phys. Chem.* 70: (1966) p.2131.
45. B. N. Samaddar, W. D. Kingery, and A. R. Cooper, Jr., *J. Am. Ceram. Soc.* 47 (1964) p.249.
46. M.N. Kucheryavyi, 0.N. Popov, V.T. Selyanko and I.O. Buranov, *Glass and Ceramics,* 45 (1988) p.251.
47. C. R. Amberg, Thesis, Pennsylvania State College, 1948.
48. W. N. Harrison and D. G. Moore, *J. Res. Nat. Bur. Standards,* R. P.113321(3) (1938) p.337.
49. A. E. Badger, C. W. Parmalee, and A. E. Williams, *J. Am. Cer. Soc.* 20 (1937) p.325.
50. C. W. Parmalee and C.G. Harmon, *J. Am. Cer. Soc.* 20, (1937) p.224.
51. O. N. Popov, R. Z. Fridkin, and Z. T. Mamedov, *Steklo i Keramica 5,* (1983) p.6–8

12 Nuclear Waste Glasses

John D. Vienna

CONTENTS

12.1 INTRODUCTION

High-level nuclear wastes (HLWs) were generated as a byproduct of dissolving nuclear fuels and separating heavy elements. Most of these wastes generated in the United States are stored in 177 underground tanks (ranging in size up to 1.1 million gallons) at the Hanford Site in southeastern Washington State. Other significant nuclear waste sites in the United States include the Savannah River Site (SRS, near Aiken, South Carolina), the West Valley Demonstration Project (WVDP, near West Valley, New York), and the Idaho National Engineering and Environmental Laboratory (INEEL, near Idaho Falls, Idaho). In addition, nuclear fuels reprocessing and defense wastes are generated and stored in many other nations throughout the world.

Glasses for immobilizing nuclear and hazardous wastes have been widely studied. The processing and chemical durability of nuclear waste glasses and their melts have been investigated for over 50 years. Unfortunately, a large fraction of the results from these studies have been published in relatively obscure places, such as government reports, technical meeting proceedings, and internal corporate memorandums and letters. The purpose of this chapter is to call attention to the wealth of information, generated for the purpose of waste immobilization, that may be of use to the broader glass community. However, a complete literature review of waste-glass chemistry is well beyond the scope of this chapter.

Borosilicate glass was selected as the waste form for HLW immobilization in the United States and various nations throughout the world. The selection of the borosilicate waste form for U.S. defense wastes was based on several aspects unique to these glasses (see, for example, [1,2]):

- High solubility of waste components in the glass
- Tolerance to variation in waste composition
- Low raw materials costs

TABLE 12.1
Partial List of Industrial-Scale Nuclear Waste Vitrification Plants

Plant/Project	Site/Location	Hot Ops	Reference
Marcoule Vitrification Plant	Marcoule, France	1978	[3]
Pamela	Mol, Belgium	1985	[4]
Mayak	Russia	1987	[5]
R7/T7	Lahauge, France	1989/1992	[6]
Waste Vitrification Plant	Sellafield, UK	1990	[7]
Tokai Vitrification Facility	Tokai, Japan	1995	[8]
West Valley Demonstration Project (WVDP)	West Valley, NY	1996	[9]
Defense Waste Processing Facility (DWPF)	SRS, Aiken, SC	1996	[10]
Waste Treatment and Immobilization Plant	Hanford, Richland, WA	"2010"	[11]

- Highly durable waste form
- Continuous, high-throughput operation of glass melters
- Technology based on extensive commercial application of glass fabrication
- High resistance to damage from radiation and radioactive decay
- Well understood corrosion/release mechanisms with available rate equations

The vitrification of wastes from spent fuel reprocessing began on an industrial scale in 1978 in Marcoule, France, and continues today throughout the world. Table 12.1 lists several nuclear waste vitrification plants. Also listed are example references to obtain more information on their operation.

Table 12.2 lists a current estimate of the component concentration ranges for U.S. nuclear waste glasses by site: WVDP, DWPF, Hanford HLW, INEEL calcined HLW, Hanford low-activity waste (LAW), and INEEL sodium bearing waste (SBW). It should be noted that glass compositions evolve with improved understanding of waste-glass chemistry and variation in waste composition. These compositions are meant only as an example. The common feature of these compositions with those produced throughout the world is that they all can be classified as alkali-borosilicate glasses with 30 to 60 mass% SiO_2, 5 to 23 mass% Na_2O, 5 to 20 mass% B_2O_3, 2 to 18 mass% Al_2O_3, and 0 to 18 mass% Fe_2O_3 plus various other components. The compositions of waste glasses are determined primarily by the composition of the wastes being immobilized and by the required glass properties.

This chapter discusses the key properties of nuclear waste glasses that affect their chemical durability, their resistance to damage from radiation exposure and radioactive decay, and their mechanical strength. These properties include the viscosity–temperature relationship, conductivity, corrosivity, liquidus temperature, the stability of the melt phase, solubility, and density.

12.2 KEY NUCLEAR WASTE-GLASS PROPERTIES

The reason for vitrifying nuclear wastes is primarily to immobilize the hazardous (including radioactive) components. Therefore, the glasses must have adequate

TABLE 12.2
Component Concentration Ranges for U.S. Nuclear Waste Glasses (in mass%)

	WVDP		DWPF		Hanford HLW		INEEL Calcine		Hanford LAW		INEEL SBW	
	Lower	Upper	Lower	Upper	Lower	Upper	Lower	Upper	Lower	Upper	Lower	Upper
Al_2O_3	3.5	8.5	2.4	5.5	3	18	3.5	20	2	12	3	15
B_2O_3	8.8	16.9	6.8	7.5	3	20	5	18	5	15	5	15
CaO	0.5*	2.5*	0.7	1.3	0	8	0	12	0	8	0	6
Cr_2O_3	0	0.35			0	1						
F^-					0	2.8	0	6	0	1		
Fe_2O_3	9	15	8.5	12.4	1	18	0	8	0	15	0	5
K_2O	3.5	6.5	2.1	2.6	0.05	3	0	10	0	8	1	5
Li_2O	2.7	4.7	4.3	5	0.05	6	0	9	0	6	0	6
MgO	*	*	1.3	2.1	0.05	3			0	4.3	0	5
MnO	0.1	2	1.1	2.8	0.02	10					0	1
MoO_3					0	0.6	0	2				
Na_2O	6	10	7.8	10.6	5	20	5	20	5	23	10	20
NiO			0.1	1.2	0.1	3	0	1.5				
P_2O_5	0	4			0	3	0	3	0	3		
SO_3					0	0.5			0	1.5	0	1.5
SiO_2	37.5	44.5	49.1	55.1	33	60	35	60	36	60	35	60
SrO	*	*			0	10	0	6				
ThO_2					0	4						
TiO_2	0.1	1.5	0.2	0.4	0	2			0	5		
U_3O_8	0.1	2	0.8	5	0	12						
ZnO					0	3			0	3		
ZrO_2	0.5	2			0	10	0	14	0	6	0	5
V_2O_5											0	8

* WVDP glass has between 0.5 and 2.5 wt% of CaO+MgO+SrO, combined.

chemical durability or resistance to degradation when exposed to various chemical environments expected during long-term storage and disposal. The release of hazardous components from a waste glass in an aqueous environment occurs by two interrelated processes: diffusive ion exchange and matrix dissolution. Each of these processes has associated rate laws that depend on temperature, glass composition, and composition of the aqueous environment. For further discussion of these processes and how they relate, see [12–17]. Therefore, a detailed study and modeling for each glass composition in each environment are required to determine the useful life of a glass. However, there is a need to compare the relative durability between many waste-glass compositions. A series of standardized tests were developed for that purpose, including (but not limited to):

- Product consistency test (PCT) [18]
- Vapor hydration test (VHT) [19,20]
- Materials characterization center test number one (MCC-1) [21]
- Sodium leach index test (ANSI-16.1) [22]
- Toxicity characterization leaching procedure (TCLP) [23]
- Soxhlet test [21,24]

Each of these tests is performed under a standard set of conditions, and the response of a glass to these standard conditions can be (loosely) considered a property of the glass.

In addition to chemical durability, the usefulness of waste glasses is determined by their resistance to damage from radiation exposure and radioactive decay—see, for example, [25]—and by their mechanical strength [26,27]. These properties are generally suitable within the region of alkali-borosilicate waste-glass composition described above.

Many of the most important waste-glass properties relate to the capability of processing the waste in an economical and timely fashion. The typical waste-vitrification process includes the mixing of waste with additives such as SiO_2, H_3BO_3, Na_2CO_3, and $LiOH{\cdot}H_2O$ (often premelted and crushed into a frit). The slurried mixture is then liquid fed onto the top of the melt pool in a ceramic melter. The slurry is dried and heated from the hot glass melt. The dried material forms a hard, insulating layer called the cold-cap. As the cold-cap is heated from the hot glass melt, it reacts, liberating gasses and converting the waste-additive mix into a glass melt. The melt is heated by passing alternating current through the melt by apposing sets of electrodes. The melt is then cast into steel canisters by either air-lift or vacuum-assisted pouring. Glass is formed when the melt cools in the canister.

To successfully process waste glass in these melters, some important properties to consider are:

- Viscosity at nominal melter operating temperature (and pour-stream temperature)
- Electrical conductivity at nominal melter operating temperature
- Corrosivity to glass-contact materials (e.g., electrodes and refractories)
- Liquidus temperature (T_L) or melt-phase stability

A viscosity of 1 to 15 Pa·s is generally considered the appropriate range. At lower viscosity, the melt may be too corrosive to the glass-contact materials, the insoluble materials may settle too fast, and the risk of pressurization due to waste-slurry mixing with the melt increases. At higher viscosities, the heat transfer to the cold-cap slows, reducing the processing rate; the ability to pour and fill the canister may be hindered.

The melt is heated by passing an alternating electric current through it. Submerged electrodes supply the current, which is carried through the melt primarily through alkali ion motion. The resistance of the melt generates the heat to maintain the operating temperature. The conductivity is therefore a critical operating parameter. At high conductivity, the current density limit of the electrodes can be exceeded. At lower conductivity, the risk of thermal instability is increased. The exact range of conductivity is generally set through melter design but typically ranges between 10 and 100 S/m.

The corrosivity to the melt-contact materials is often a processing constraint. Extremely corrosive melts may limit the useful life of the glass melter. The cost of replacing melters is high because of the highly radioactive environment in which they operate.

One of the most restrictive property constraints used in waste-glass formulation relates to maintaining a single-phase melt. As waste loading increases, the sparsely soluble waste components can form a separated phase (either amorphous or crystalline). Waste loading is defined as the fraction of the waste glass that originated from waste or one minus the fraction that originated from chemical additives. The cost of waste vitrification is strongly influenced by waste loading. Some of the waste components of most concern include Cr, Ni, Mn, Zr, Ti, S, F, Mo, P, Al, and noble metals. When the concentrations of noble metals, Cr, Ni, Mn, Zr, Ti, and Al, exceed their solubility limits in glass, they precipitate as crystalline solids. These solids may settle and accumulate at the melter bottom, blocking the flow of glass and possibly disrupting the current flow (and thus heating). The highest temperature at which the melt is in equilibrium with its primary crystalline phase is the T_L. The T_L of the melt is often controlled to be below the temperature within the waste-glass melter to avoid the deleterious effects of crystal accumulation in the melter. In some cases, the fraction of crystals at equilibrium with the melt is controlled rather than T_L. When the concentrations of salts (e.g., S, F, Mo, and P) are exceeded, a molten alkali-oxyanionic/halide salt will segregate from the melt. This salt is a low-viscosity corrosive liquid that may corrode through any material that it contacts, which increases the risk of a steam explosion.

12.3 GLASS PROPERTY–COMPOSITION RELATIONSHIPS

The product-quality and processing-related properties of nuclear waste glasses have been studied extensively. Vienna et al. [28] have compiled a database of key waste-glass properties that have been correlated to glass composition to enable waste-glass producers to control glass properties through head-end composition control. The

relationships between waste-glass/melt properties and composition are derived from a fundamental understanding of the physical and chemical phenomena responsible for the effect. They are fitted to experimental data with systematic change in composition, making them (semi-) empirical models.

One of the primary advantages of vitrification as a treatment technology for nuclear waste glass is the fact that most glass and melt properties vary smoothly with changes in composition. In fact, over sufficiently narrow composition space, the variation in glass properties is well approximated by a linear function of composition. For example, models for the chemical durability are generally of the form:

$$\ln[R_\alpha] = \sum_{i=1}^{N} r_{\alpha,i} x_i \tag{1}$$

where R_α is the α^{th} measure of glass durability, and $r_{\alpha,i}$ and x_i are the i^{th} glass component coefficient and concentration, respectively. R_a is the response to a durability test, such as the normalized element release from glass exposed to the PCT or the rate of glass alteration under VHT conditions. Over sufficiently narrow composition space, this linear approximation of glass response to durability tests is reasonably accurate. However, as the glass-composition region increases, nonlinear effects become stronger, and the linear approximation becomes a poor representation of the actual composition effect. For this reason, durability models are typically fitted over relatively narrow composition regions of interest to each individual waste-vitrification project. Examples of such models are reported by Ellison et al. [29], Hrma et al. [30], Jantzen et al. [31], Feng et al. [32], Vienna et al. [28], and Kim and Vienna [34]. Other model forms have been suggested, such as Hrma et al. [35] or Gan and Pegg [36].

The viscosity–temperature relationship is generally described using the Vogel-Tamman-Fulcher (VTF) relationship:

$$\ln[\eta_T] = A + \frac{B}{T - T_0} \tag{2}$$

where η_T is the viscosity at absolute temperature T, and A, B, and T_0 are empirically fit parameters that vary with melt composition. Over sufficiently narrow temperature ranges, the effect of temperature can be approximated by the Arrhenius function:

$$\ln[\eta_T] = E + \frac{F}{T} \tag{3}$$

or, the VTF relationship is expanded in inverse temperature, with the first term being the Arrhenius function, and the second term being G/T^2. The empirical parameters (A, B, E, F, G, and T_0) were found to be linear with composition—see, for example, [37]. Some nonlinear approximations for these fit parameters were also proposed (38). In the cases where viscosity at a single nominal temperature

(e.g., 1150˚C) is of most import, then a linear expansion of E and F in composition can be condensed to:

$$\ln[\eta_{1150^\circ}] = \sum_{i=1}^{N} h_i x_i \tag{4}$$

where η_{1150° is the viscosity of the melt at 1150˚C, and h_i is the i^{th} component coefficient ($h_i = E_i + F_i/[1150+273.15]$).

As conductivity relates to temperature in the same fashion as viscosity, the same functions are used to relate composition and temperature to conductivity as viscosity. With conductivity, the effect of alkali ion concentrations far outweighs any other component effect. Examples of viscosity- and conductivity-composition relationships are reported by Jantzen et al. [38], Hrma et al. [35], Hrma et al. [37], Shah et al. [39], Vienna et al. [40], and Vienna et al. [28].

The corrosivity of melt-contact materials is enhanced by increasing the alkali concentrations in the melt and can be reduced by increased concentrations of transition elements that form spinel crystals ([Fe, Mn, Ni, Zn][Fe, Cr, Mn]$_2O_4$ type spinels commonly form in waste-glass melts). The redox of the melt often strongly influences the rate of corrosion of metal melt contact materials (such as electrodes and bubblers). A systematic study of the melt corrosivity–composition relationship was not performed. However, some useful studies include Bickford et al. [41], Hayward et al. [42], Wang et al. [43], Xing et al. [44], and Imrich and Jenkins [45].

Solubility and T_L are directly related for those components that form solids upon exceeding their solubility limit [46]. Therefore, the solubility of waste in glass is often controlled by maintaining the melt composition such that T_L is greater than the melt temperature. As with other waste-glass properties, the T_L varies smoothly with composition within primary phase fields. The T_L can change abruptly with composition changes when phase-field boundaries are crossed. T_L–composition relationships for nuclear waste glasses have been modeled using a range of different model forms within the spinel primary phase field [28,33,35,37,38,40,47–51]. T_L–composition relationships have also been developed for waste-glass melts in the zircon ($ZrSiO_4$) primary phase field [28,53–56], the parakeldeshite primary phase field [55,56], the clinopyroxine ([Ca,Na,Li][Fe,Mg,Al,Mn,Ni,Cr]Si_2O_6) primary phase field [35,51], and the nepheline ($NaAlSiO_4$) primary phase field [57,58].

The solubility of various salt components (e.g., S, P, Mo, F) in waste has also received a lot of attention in nuclear waste-glass research—see, for examples, [52, 59–71]. As the concentration of these components reaches a critical level, a molten salt phase begins to segregate. It is a mistake to call that critical concentration for salt development/accumulation a solubility limit because the salt begins to form at salt concentrations well below their equilibrium solubilities in the glass melt. The phenomenon responsible for the kinetically controlled salt segregation has been recently studied; however, it is still not well understood.

The densities of waste glasses have been studied. It was shown that the partial molar volumes of typical waste glasses are generally close to those of the oxide crystals most similar to the structure of components in the glass [28].

12.4 SUMMARY

A wealth of property data exists for nuclear waste glasses. These glasses are among the most studied glass compositions. However, the data are largely found in relatively obscure sources such as government and corporate reports and the proceedings from specialized meetings on the subject. The intent of this chapter is to point the reader toward some of this literature and act as a starting point for a more in-depth literature review. The properties of interest for waste glasses include those related to the product quality (primarily chemical durability) and to the processability of the waste glasses in electric-heated ceramic melters.

It is interesting to note that the composition effects on the complex waste glasses tend to be very simple (in relation to many commercially important glasses). In fact, most waste-glass properties can be well approximated by linear functions of composition over composition regions broad enough to meet the needs of a waste vitrification program or campaign. The simplicity in composition effects is largely a result of the large number of components in waste glasses and the narrow range that each individual component can vary.

A number of references have been supplied for the reader. Although they are relatively obscure, most technical and university libraries can access them. U.S. government reports are generally available online at the Office of Scientific and Technical Information: http://www.osti.gov/bridge/.

REFERENCES

1. U. S. Department of Energy (DOE) (1982). The Evaluation and Selection of Candidate High-Level Waste Forms. DOE/TIC-11611, Aiken, SC.
2. U. S. Department of Energy (DOE) (1990). Evaluation and Selection of Borosilicate Glass as the Waste Form for Hanford High-Level Radioactive Waste. DOE/RL-90–27, Richland, WA.
3. Bonniaud, R., Jouan, A., and Sombret, C. (1980). Large scale production of glass for high level radioactive waste. *Nucl. Chem. Waste Mgmt.* 1:3–16.
4. Weise, H., and Ewest, E. (1988). Industrial vitrification of high level liquid wastes in the PAMELA plant. In *Waste Mgmt. '88*. 2:173-179, University of Arizona, Tucson, AZ.
5. Odell, M. (1992). Vitrification: World Review. *Nucl. Eng. Internat.*, p. 52.
6. Masson, H., Desvaux, J. L., Pluche, E., and Jouan, A. (1999). Ten years of vitrification in La Hauge's R7/T7 from R&D to production. In *Proceedings of Global '99*, American Nuclear Society, LaGrange Park, IL.
7. Millington, D. (1995). Progress with highly active waste vitrification at BNFL Sellafield. *Nucl. Eng.* 36:42–45.
8. Aoshima A., Kozaka, T., and Tanaka, K. (2004). Glass Melter Replacement and Melter Technology Development in the Tokai Vitrification Facility. In *Proceedings of 12th International Conference on Nuclear Engineering*, ICONE12-49175, pp. 1–6, American Society of Mechanical Engineers, Washington, D.C.
9. Hamel, W. F., Sheridan, M. J., and Valenti, P. J. (1998). Vitrification at the West Valley Demonstration Project. *Radwaste Magazine*, March 1998.

10. Marra, S. L., Gee, J. T., and Sproull, J. F. (1999). The defense waste processing facility: Two years of radioactive operation. In *Ceram. Trans.* 93:147–154, American Ceramic Society, Westerville, OH.
11. U.S. Department of Energy (DOE) (2000). Design, Construction, and Commissioning of the Hanford Tank Waste Treatment and Immobilization Plant. Contract Number: DE-AC27-01RV14136, as amended, Office of River Protection, Richland, WA.
12. McGrail, B. P., Ebert, W. L., Bacon, D. H., and Strachan, D. M. (1998). A Strategy to Conduct an Analysis of the Long-Term Performance of Low-Activity Waste Glass in a Shallow Subsurface Disposal System at Hanford. PNNL-11834, Pacific Northwest National Laboratory, Richland, WA.
13. McGrail, B. P., Baer, D. R., Darab, J. G., Engelhard, M. H., Icenhower, J. P., Shuh, D. K., Thevusathan, S. (1999). Ion Exchange Processes and Mechanisms in Glasses. In Science to Support DOE Site Cleanup: The Pacific Northwest National Laboratory Environmental Mgmt. Science Program Awards. PNNL-12208, Pacific Northwest National Laboratory, Richland, WA.
14. McGrail, B. P., Icenhower, J. P., Bacon, D. H., Vienna, J. D., Saripalli, K. P., Schaef, H. T., Martin, P. F., Orr, R. D., Rodriguez, E. A., and Steele, J. L. (2002). Low-Activity Waste Glass Studies: FY2002 Summary Report, PNNL-14145, Pacific Northwest National Laboratory, Richland, WA.
15. Delage, F., and Dussossoy, J. L. (1991). R7T7 Glass initial dissolution rate measurements using a high-temperature Soxhlet device. In *Proceedings Scientific Basis For Nuclear Waste Management XIV,* Materials Research Society, Pittsburgh, PA.
16. Cunnane, J.C., Ed. (1994). High-level Waste Borosilicate Glass: A Compendium of Corrosion Characteristics. DOE-EM-0177, U.S. Department of Energy, Office of Waste Management, Germantown, MD.
17. Grambow, B. E. (1985). A general rate equation for nuclear waste glass corrosion. *Mat. Res. Soc. Symp. Proc.* 44:15–27.
18. American Society for Testing and Materials (ASTM) (1998). Standard test methods for determining chemical durability of nuclear, hazardous, and mixed waste glasses: the product consistency test (PCT). C 1285-97. In *1998 Annual Book of ASTM Standards,* Vol. 12.01, West Conshohocken, PA.
19. Jiricka, A., Vienna, J. D., Hrma, P., and Strachan, D. M. (2001). The effect of experimental conditions and evaluation techniques on the alteration of low-activity waste glasses by vapor hydration. *J. Non-Cryst. Sol.* 292(1–3):25–43.
20. Vienna, J. D., Hrma, P., Jiricka, A., Smith, D. E., Lorier, T. H., Reamer, I. A., and Schulz, R. L. (2001). Hanford Immobilized LAW Product Acceptance Testing: Tanks Focus Area Results. PNNL-13744, Pacific Northwest National Laboratory, Richland, WA.
21. Materials Characterization Center (MCC) (1984). *Materials Characterization Center Test Methods Submitted for the Nuclear Waste Materials Handbook.* PNL-3990, Pacific Northwest Laboratory, Richland, WA.
22. American Nuclear Society (ANS) (2003). Measurement of the Leachability of Solidified Low-Level Radioactive Wastes by a Short-Term Test Procedure. ANSI/ANS-16.1, An American National Standard, LaGrange Park, IL.
23. U. S. Environmental Protection Agency (EPA) (1997). Toxicity Characteristic Leach Procedure. SW-846 Method 1311, Washington, D.C.
24. Delage, F., and Dussossoy, J. L. (1991). R7T7 Glass Initial dissolution rate measurements using a high-temperature Soxhlet device. In *Proceedings Scientific Basis For Nuclear Waste Management. XIV,* Materials Research Society, Pittsburgh, PA.

25. Weber, W. J., Ewing, R. C., Angell, C. A., Arnold, G. W., Cormack, A. N., Delaye, J. M., Griscom, D. L., Hobbs, L. W., Navrotsky, A., Price, D. L., Stoneham, A. M., and Weinberg, W. C. (1997). Radiation effects in glasses used for immobilization of high-level waste and plutonium disposition. *J. Mat. Res.* 12(8):1946–1975.
26. Farnsworth, R. K., Chan, M. K. W., and Slate, S. C. (1985). The effect of radial temperature gradients on glass fracture in simulated high-level waste canisters. In *Mat. Res. Soc. Symp. Proc.* 44:831–838.
27. Peters, R. D., and Slate, S. C. (1981). Fracturing of simulated high-level waste canisters. *Nucl. Eng. Design* 67:425–445.
28. Vienna, J. D., Kim, D. S., and Hrma, P. (2002). Database and Interim Glass Property Models for Hanford HLW and LAW Glasses. PNNL-14060, Pacific Northwest National Laboratory, Richland, WA.
29. Ellison, A. J. G., Mazer, J. J., and Ebert, W. L. (1994). Effect of Glass Composition on Waste Form Durability: A Critical Review. ANL-94/28, Argonne National Laboratory, Argonne, IL.
30. Hrma, P., Piepel, G. F., Vienna, J. D., Redgate, P. E., Schweiger, M. J., and Smith, D. E. (1995). Prediction of nuclear waste glass dissolution as a function of composition. *Ceram. Trans.* 61:497–504.
31. Jantzen, C. M., Pickett, J. B., Brown, K. G., Edwards, T. B., and Beam, D. C. (1995). Process/Product Models for the Defense Waste Processing Facility (DWPF): Part I. Predicting Glass Durability from Composition Using a Thermodynamic Hydration Energy Reaction Model (THERMO). WSRC-TR-93-0672, Westinghouse Savannah River Company, Aiken, SC.
32. Feng X., and Metzger, T. B. (1996). A Structural bond strength model for glass durability. *Ceram. Trans.* 72:51–60.
33. Vienna, J. D., Hrma, P., Crum, J. V., and Mika, M. (2001). Liquidus temperature-composition model for multi-component glasses in the Fe, Cr, Ni, and Mn spinel primary phase field. *J. Non-Cryst. Sol.* 292(1-3):1–24.
34. Kim, D.-S., and Vienna, J. D. (2004). Glass composition-TCLP response model for waste glasses. In *Ceram. Trans.* 155:297-308, American Ceramic Society, Westerville, OH.
35. Hrma, P., Piepel, G. F., Schweiger, M. J., Smith, D. E., Kim, D.-S., Redgate, P. E., Vienna, J. D., LoPresti, C. A., Simpson, D. B., Peeler, D. K., and Langowski, M. H. (1994). Property/Composition Relationships for Hanford High-Level Waste Glasses Melting at 1150°C. PNL-10359, Vol. 1 and 2, Pacific Northwest Laboratory, Richland, WA.
36. Gan, H., and Pegg, I. L. (2002). Effect of glass composition on the leaching behavior of HLW glasses under TCLP conditions. *Ceram. Trans.* 132:335–344.
37. Hrma, P., Piepel, G. F., Redgate, P. E., Smith, D. E., Schweiger, M. J., Vienna, J. D., and Kim, D.-S. (1995). Prediction of Processing properties for nuclear waste glasses. In *Ceram. Trans.* 61:505-513, American Ceramic Society, Westerville, OH.
38. Jantzen, C. M. (1991). First principles process-product models for vitrification of nuclear waste: relationship of glass composition to glass viscosity, resistivity, liquidus temperature and durability. *Ceram. Trans.* 23:37–51.
39. Shah, R., Behrman, E. C., and Oksoy, D. (1990). Calculation of the viscosity of nuclear waste glass systems. In *Matl. Res. Soc. Proc.* 176:427–432, Materials Research Society, Pittsburgh, PA.
40. Vienna, J. D., Hrma, P., Kim, D.-S., Schweiger, M. J., and Smith, D. E. (1996). Compositional dependence of viscosity, electrical conductivity, and liquidus temperature of multicomponent borosilicate waste glasses. In *Ceram. Trans.* 72:427–436, American Ceramic Society, Westerville, OH.

41. Bickford, D. F., Ondrejcin, R. S., and Salley, L. (1986). High-temperature materials for radioactive waste incineration and vitrification. In *Advan. Ceram.* 20:65–78, American Ceramic Society, Westerville, OH.
42. Hayward, P. J., George, I. M., Woods, M. P., and Busby, T. S. (1987). An evaluation of electric melter refractories for contact with glass used for the immobilization of nuclear waste. In *Glass Tech.* 28(1):43–49.
43. Wang, E., Mohr, R. K., Buechelle, A. C., and Pegg, I. L. (1996). Current density effects on the corrosion of ceramic and metallic electrode materials in waste glass. In *Sci. Basis Nucl. Waste Mgmt. XIX*, pp173–180, Materials Research Society, Pittsburgh, PA.
44. Xing, S. B., Lin, Y., Mohr, R. K., and Pegg, I. L. (1996). Corrosion resistance of ceramic refractories to simulated waste glasses at high temperatures. In *Sci. Basis Nucl. Waste Manage. XIX*, pp. 181-189, Materials Research Society, Pittsburgh, PA.
45. Imrich, K. J., and Jenkins, C. F. (1994). Corrosion study for a DOE radioactive waste vitrification facility. In *Corrosion 94*, 115, NACE International, Houston TX.
46. Hrma, P., and Vienna, J. D. (2003). Relationship between liquidus temperature and solubility. In *Ceram. Trans.* 143:159–167, American Ceramic Society, Westerville, Ohio.
47. Hrma, P., Vienna, J. D., Mika, M., Crum, J. V., and Piepel, G. F. (1999). Liquidus Temperature Data for DWPF Glass, PNNL-11790, Rev. 1, Pacific Northwest National Laboratory, Richland, WA.
48. Mika, M., Schweiger, M. J., Vienna, J. D., and Hrma, P. (1997). Liquidus temperature of spinel precipitating high-level waste glasses. In *Sci. Basis Nucl. Waste Manage. XX*, pp. 71–78, Materials Research Society, Pittsburgh, PA.
49. Plodinec, M. J. (1999). Solubility approach for modeling waste glass liquidus. In *Sci. Basis Nucl. Waste Manage. XXII*, pp. 223-230, Materials Research Society, Warrendale, PA.
50. Gan, H., and Pegg, I. L. (2001). Development of Property-Composition Models for RPP-WTP HLW Glasses. VSL-01R3600-1, Vitreous State Laboratory, Washington, D.C.
51. Brown, K. G., Jantzen, C. M., and Ritzhaupt, G. (2001). Relating Liquidus Temperature to Composition for Defense Waste Processing Facility (DWPF) Process Control (U). WSRC-TR-2001-00520, Westinghouse Savannah River Company, Aiken, SC.
52. Vienna, J. D., Kim, D.-S., and Peeler, D. K. (2003). Glass formulation for INEEL sodium bearing waste. In *Ceram. Trans.* 143:169-176, American Ceramic Society, Westerville, OH.
53. Crum, J. V., Schweiger, M. J., Hrma, P., Vienna, J. D. (1997). liquidus temperature model for Hanford high-level waste glasses with high concentrations of zirconia. In *Sci. Basis Nucl. Waste Manage. XX*, pp. 79–86, Materials Research Society, Pittsburgh, PA.
54. Rao, Q., Piepel, G. F., Hrma, P., and Crum, J. V. (1997). Liquidus temperature of HLW glasses with zirconium-containing primary phases. *J. Non-Cryst. Sol*. 220:17–29.
55. Plaisted, T., Hrma, P., Vienna, J. D., and Jiricka, A. (2000). Liquidus temperature and primary crystallization phases in high-zirconia high-level waste borosilicate glasses. In *Sci. Basis Nucl. Waste Manage. XXIII*, pp. 709-714, Materials Research Society, Warrendale, PA.
56. Vienna, J. D., Peeler, D. K., Plaisted, R. L., Plaisted, T. J., Reamer, I. A., Tillotson, R. D., Crum, J. V., Musick, C. A., and James, T. L. (1999). Glass Formulation For Idaho National Engineering and Environmental Laboratory Zirconia Calcine High-Activity Waste. PNNL-12202, Pacific Northwest National Laboratory, Richland, WA.

57. Li, H., Jones, B., Hrma, P., and Vienna, J. D. (1998). Compositional effects on liquidus temperature of Hanford simulated high-level waste glasses precipitating nepheline ($NaAlSiO_4$). In *Ceram. Trans.* 87:279-288, American Ceramic Society, Westerville, OH.
58. Li, H., Hrma, P., Vienna, J. D., Qian, M., Su, Y., and Smith, D. E. (2003). Effects of Al_2O_3, B_2O_3, Na_2O, and SiO_2 on nepheline formation in borosilicate glasses: Chemical and physical correlations. *J. Non-Cryst. Sol.* 331(1-3):202–216.
59. Sullivan, G., Langowski, M. H., and Hrma, P. (1995). Sulfate segregation in vitrification of simulated Hanford nuclear waste glasses. In *Ceram. Trans.* 61:187–193, American Ceramic Society, Westerville, OH.
60. Li, H., Darab, J. G., Matson, D. W., Smith, P. A., Hrma, P., Chen, Y., and Liu, J. (1996). Phosphate-sulfate interaction in simulated low-level radioactive waste glasses. In *Sci. Basis Nucl. Waste Manage. XIX*, pp. 141–148, Materials Research Society, Pittsburgh, PA.
61. Fu, S. S., Matlack, K. S., Mohr, R. K., Luo, W., Wang, E., Leontiev, M., Hojaji, H., Brandys, M., Pegg, I. L., and Macedo, P. B. (1996). Minimelter runs of mixed wastes high in lead, barium, phosphorous, and sulfur. In *Ceram. Trans.* 72:27–40, American Ceramic Society, Westerville, OH.
62. Jantzen, C. M., Brown, K. G., Pickett, J. B., and Ritzhaupt, G. L. (2000). Crystalline Phase Separation in Phosphate Containing Waste Glasses: Relevancy to Vitrification of Idaho National Engineering and Environmental Laboratory (INEEL) High Activity Waste (U). WSRC-TR-2000-00339, Westinghouse Savannah River Company, Aiken, SC.
63. Pegg I. L., Gan, H., Muller, I. S., McKeown, D. A., and Matlack, K. S. (2000). Summary of Preliminary Results on Enhanced Sulfate Incorporation During Vitrification of LAW Feeds. VSL-00R3630-1, Rev. 1, Vitreous State Laboratory, The Catholic University of America, Washington, D.C.
64. Crum, J. V., Vienna, J. D., Peeler, D. K., and Reamer, I. A. (2001). Formulation Efforts for Direct Vitrification of INEEL Blend Calcine Waste Simulate: Fiscal Year 2000. PNNL-13483, Pacific Northwest National Laboratory, Richland, WA.
65. Crum, J. V., Vienna, J. D., Peeler, D. K., and Reamer, I. A. (2002). Glass formulation for direct vitrification of INEEL calcine HLW. In *Ceram. Trans.* 132:163–170, American Ceramic Society, Westerville, Ohio.
66. Li, H., Hrma, P., and Vienna, J. D. (2001). Sulfate retention and segregation in simulated radioactive waste borosilicate glass. In *Ceram. Trans.* 119:237–246, American Ceramic Society, Westerville, OH.
67. Peeler, D. K., Edwards, T. B., Reamer, I. A., Workman, R. J., Vienna, J. D., Crum, J. V., and Schweiger, M. J. (2001). Glass Formulation Development for INEEL Sodium-Bearing Waste (WM-180) (U). WSRC-TR-2001-00295, Westinghouse Savannah River Company, Aiken, SC.
68. Darab, J. G., Graham, D. D., MacIsaac, B. D., Russell, R. L., Peeler, D. K., Smith, H. D., and Vienna, J. D. (2001). Sulfur Partitioning During Vitrification of INEEL Sodium Bearing Waste: Status Report. PNNL-13588, Pacific Northwest National Laboratory, Richland, WA.
69. Hrma, P., Vienna, J. D., and Ricklefs, J. S. (2003). Mechanism of sulfate segregation during glass melting. In *Sci. Basis Nucl. Waste Manage. XXVI*, pp. 147–152, Materials Research Society, Warrendale, PA.

70. Hrma, P., Vienna, J. D., Buchmiller, W. C., and Ricklefs, J. S. (2004). Sulfate retention during waste glass melting. In *Ceram. Trans.* 155:239–248, American Ceramic Society, Westerville, OH.
71. Vienna, J. D., Hrma, P., Buchmiller, W. C., and Ricklefs, J. S. (2004). Preliminary Investigation of Sulfur Loading in Hanford LAW Glass. PNNL-14649, Pacific Northwest National Laboratory, Richland, WA.

13 Solubility of Gases in Glass Melts

Fritz W. Krämer

CONTENTS

13.1 INTRODUCTION

When batch material is heated up, a huge amount of gases are released by the decomposition of raw materials. These released gases interact with the gases in the furnace atmosphere and in the glass melt, and dissolve into the melt. The solubility of gases in glass melts, as that in normal liquids, is defined as the equilibrium concentration of dissolved gases in those liquids or melts at a given gas pressure and given temperature. The solubility of gases in glass melts depends on temperature, glass composition and on gas fugacities (function of gas partial pressures). These factors, as well as the transport of dissolved gases by diffusion, are of great importance to gas release and gas absorption mechanisms in melting, refining and conditioning. The formation, change of content, growth, shrinkage and general behavior of gas bubbles in glass can essentially be understood by understanding solubility and diffusivity of gases in melts.

Additionally, the amount and type of dissolved gases in glasses can influence the properties of these glasses. For instance, the influence of dissolved gases on density, viscosity, thermal expansion, surface tension, refractive index and electric resistance has been proven [1–6].

The solution of gases in molten silicates or borates and in aqueous solutions seems to be the result of the development of two types of processes: one of a physical nature, the other of a chemical nature.

In chemical solubility, chemical reactions occur during the process of dissolution, and the interaction between gas and melt is strong when a solution of water vapor, hydrogen, sulfur dioxide, carbon dioxide, oxygen in the presence of multivalent ions, and nitrogen at reducing conditions is present in the melt.

In the case of physical solubility, the interaction forces between gases and melts are considerably weaker due to the Van der Waals forces with a solution of inert gases or nitrogen at oxidizing conditions.

The amount of physically dissolved gases at normal pressure is only 1/1000 to 1/10000 of the quantity that can be dissolved chemically. This is why physically dissolved gases under normal pressures cannot be made responsible for the formation of bubbles in glass melts: their quantity is too small and the changes in solubility with temperature, glass composition and gas partial pressures are too small to produce a supersaturation pressure sufficient for the formation of new inner surfaces. Nevertheless, the physical solubility of gases in glass melts is of great practical importance in the refining of melts.

All chemically dissolving gases have a certain (small) physical solubility that interacts with the chemically dissolved quantity. This interaction results in a fugacity of the physically dissolved gas that can interact with the furnace atmosphere or with bubbles. As an example, the redox equation for antimony shows the reaction between chemically dissolved oxygen in antimonate oxocomplex and physically dissolved oxygen in the melt:

$$(SbO_4)^{3-}_{melt} \leftrightarrow Sb^{3+} + 3\ O^{2-} + 1/2\ O_2 \qquad (1)$$

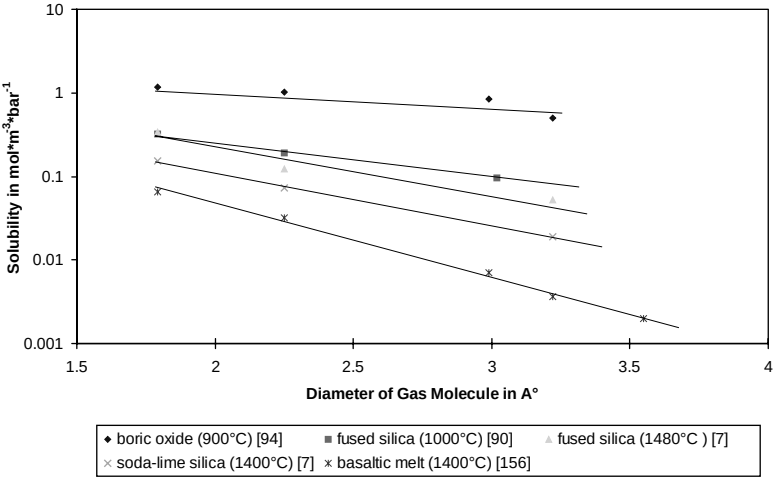

FIGURE 13.1 Physical solubility of He, Ne and N_2 vs. R_2O content of binary alkali silicate melts.

It is this interaction of gas fugacity of physically dissolved gases with gas bubbles in glass melts during the refining stage which is of practical importance, since the amount of gas fugacities decides whether the quality of the end product is bad or not. The amount of gas fugacities also determines whether the bubbles will grow, shrink or stabilize.

13.2 PHYSICAL SOLUBILITY

The process of dissolving an inert gas such as helium or neon in a molten silicate is a purely physical process. This means that the gas molecules do not react with the medium melt in which they are incorporated, but simply occupy the holes in the network structure.

According to Mulfinger, Dietzel and Navarro [7], Shelby [8] and Shackelford et al. [9], fused silica as well as binary alkali silicate glass melts that have a certain distribution of holes that determine the amount of dissolved gases. Larger molecules can only be placed in larger holes while smaller molecules, such as helium, can also occupy larger ones. This explains why Bunsen gas solubility of smaller molecules is higher than that of larger ones. Figure 13.1 shows the physical solubility for He, Ne, Ar, N_2, Kr and Xe [164], and obviously a linear relationship is given between the size of the gas molecules and the physical solubility in soda-lime-silica, fused silica and boric acid oxide melts.

Henry's Law describes the equilibrium between a gas mixture and a chemically indifferent solvent in diluted solutions:

$$C_i = S_i * p_i \tag{2}$$

where C_i is the concentration of the gas in the liquid phase (solubility), S_i is the solubility coefficient and p_i is the partial pressure or fugacity of the dissolving gas i in the gas phase (atmosphere).

The solubility coefficient [10] is often defined as either the volume of gas per unit volume of glass (cubic centimeter (STP) per cubic centimeter of glass), dissolved at standard temperature and pressure (equivalent to Bunsen solubility coefficient S_{Bu}, or as the number of atoms or molecules dissolved per unit volume of glass per unit applied pressure. It was pointed out earlier that these definitions introduce an artificial component into the temperature dependence of the solubility as a result of the temperature dependence of gas pressure. Therefore, a better definition of solubility is that of Ostwald, expressed as $C_T/C_g = S_{os}$ where C_T is the concentration of gas dissolved in the melt at temperature T, and C_g is the concentration of atoms or molecules in the gas phase, i.e., the gas molecular density. The relation between Ostwald and Bunsen solubility coefficients for p = 1 bar is:

$$S_{os} = (S_{Bu}/c_g) * T/273 \quad (3)$$

In modern literature, solubility is defined as the mass of the gas dissolved per unit volume of glass melt (kg/m^3 or mol/m^3) at given temperature and gas pressure. And consequently, the physical solubility coefficient (dependent on temperature) is solubility per unit pressure (kg/m^3*bar or mol/m^3*Pa).

As already mentioned, the concentration of a physically dissolved gas in a glass melt is determined by the outer gas pressure, by the magnitude of the gas atoms or molecules to be dissolved, by the volumes and the size of holes available in the melt and by the temperature of the melt.

13.2.1 Dependence on Glass Composition

The works of Mulfinger [11], Mulfinger and Scholze [10], Mulfinger, Dietzel and Navarro [7] and Shelby [8,12] primarily deal with the behavior of physically dissolved gases as helium, neon and nitrogen in molten binary alkali silicates or borates. An approximate linear relationship between solubility at a temperature of 1480˚C and the alkali content of silicates was established. In this relationship, the solubility of smaller gas molecules such as helium and neon decreases with increasing alkali content, while remaining roughly constant for the larger nitrogen molecules (Figure 13.2). The extrapolation of the straight lines to an alkali content of 0, meaning fused silica, produces helium and neon values that satisfactorily agree with others [13,14].

The decrease of helium and neon solubility with increasing alkali content achieves this result because the volume of holes in the structure gets increasingly occupied by the alkali ions themselves. This is why the smaller lithium ions can more easily occupy the smaller helium and neon holes, resulting in a larger decrease of gas solubility than with the larger potassium or sodium ions.

At constant alkali content, the physical solubility increases with increasing volume of alkali ions due to an additional expansion of the network.

The physical solubility of helium, neon and nitrogen is very small compared with the chemical solubility of other gases. In binary alkali silicate melts at 1480˚C,

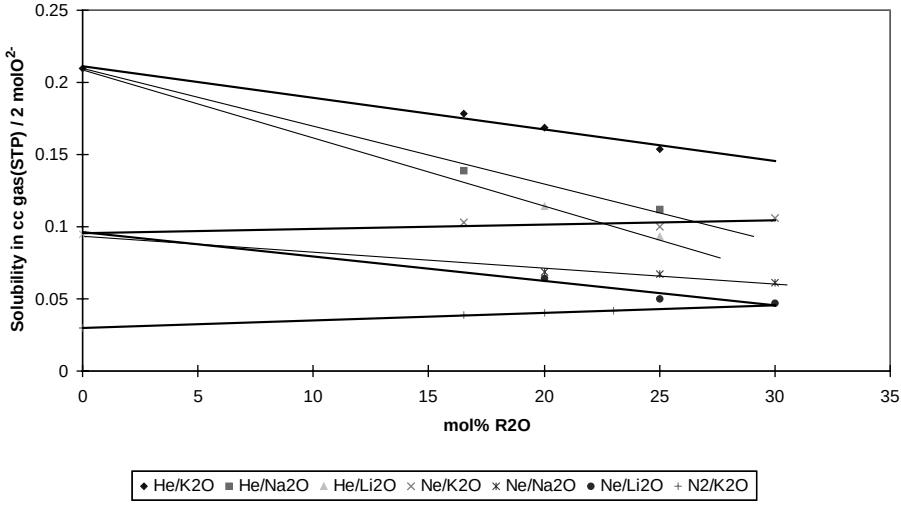

FIGURE 13.2 Physical solubility of He, Ne and N_2 vs. R_2O content of binary alkali silica melts at 1753 K according to [7].

helium solubility ranges from $3.3 * 10^{-4}$ to $5.5 * 10^{-3}$ cm^3 STP per cm^3 melt, while neon solubility ranges from $1.6 * 10^{-3}$ to $3.2 * 10^{-3}$ and nitrogen solubility from $1.2 * 10^{-4}$ to $1.4 * 10^{-4}$ cm^3 STP/cm^3 melt.

According to [7] the physical solubility of mainly chemically dissolved gases such as oxygen, carbon dioxide, water vapor and sulfur dioxide should be in the same order as nitrogen, and its dependence on alkali content should be poor.

13.2.2 Dependence on Temperature

Mulfinger, Dietzel and Navarro [7] recorded an increase in solubility for binary alkali silicate melts with increasing temperature (Figure 13.3). The increase is small for helium, stronger in the case of neon and strongest for nitrogen. The heat of solution evaluated in this experiment is 6.7 kJ/g-atom for helium, 13 kJ/g-atom for neon and 57,4 kJ/g-atom for nitrogen.

The increasing temperature dependence of solubility in the sequence helium, neon and nitrogen can be explained by the increase of volume of holes calculated in correlation to the cubic expansion coefficient. Furthermore with increasing alkali content, or at constant alkali content with increasing size of the alkali ion, increasing heats of formation are found. This increase of solubility by temperature as a measure of increasing the volume of holes is:

$3.11 * 10^{-4}$/°C for helium
$6.0 * 10^{-4}$/°C for neon
$24.5 * 10^{-4}$/°C for nitrogen

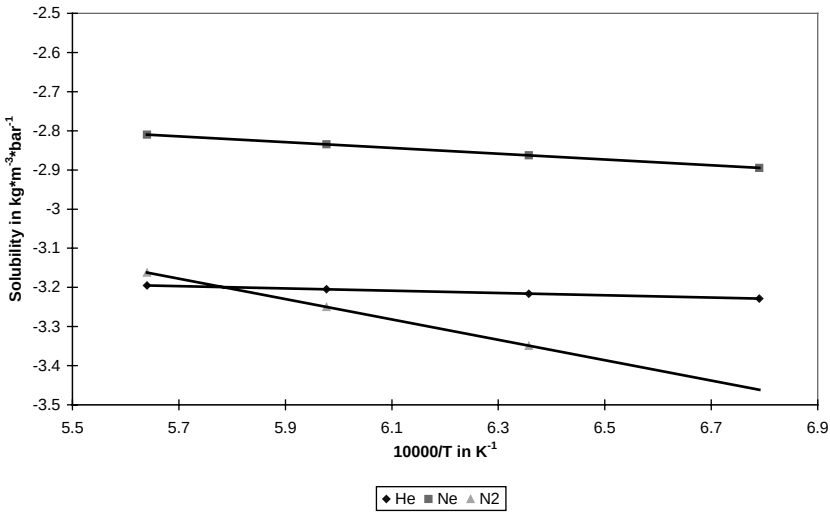

FIGURE 13.3 Physical solubility of He, Ne and N2 vs. 1/temperature for a soda-lime silica glass melt according to [7].

higher than the cubic expansion coefficient of the melt. This means that the larger holes play a considerably larger role in the temperature-dependent enlargement of the hole volume in the melt than the smaller holes do.

Obviously, the interaction forces between alkali ions and oxygen ions get smaller as the holes in which the alkali ion is situated get bigger. Holes that have no alkali ions, i.e., nitrogen holes, expand when temperature is increased.

It is worth noticing that in vitreous silica the temperature dependence of helium and neon solubility is opposite that of alkali silicate melts. In vitreous silica, the physical solubility of helium and neon decreases with increasing temperature [12,15]. But also, in binary alkali silicate glasses at temperatures below the transformation point, heats of solution are found for helium that are positive or negative depending on the alkali content [16].

13.2.3 Dependence on Pressure

According to Henry's Law, physical solubility increases linearly with the partial pressure of the gas in the atmosphere in contact with the melt. Henry's Law was proved at pressures up to 300 atmospheres by Nair, White and Roy for oxygen solubility in sodium borate, sodium silicate and sodium germanate melts[17]. For helium, argon and nitrogen Faile and Roy showed the validity of Henry's Law at pressures up to 3 kbar [18]. Results received at pressures up to 10 kbar show that an additional amount of gas was pressed into an approximately constant volume of holes in the melt. This is due to the compressibility of the gases.

At atmospheric pressure or less, only a small portion of the interstices or holes of the melt structure are occupied by gas molecules, while, under fairly high pressure, all the holes of this structure are progressively occupied. At very high pressures, the

validity of Henry's Law allows the assumption that additional holes or interstices are formed [19].

13.3 CHEMICAL SOLUBILITY

The volume of gases released by glass using high-temperature extraction methods is not compatible with the relatively low values from physical solubility of the different inert gases or nitrogen, since this volume is about 1000 to 10,000 times higher than gains due to physical solubility.

On the basis of present-day knowledge of molten silicate structures, the nature of the principal gases released, H_2O, CO_2 and SO_3, suggests that the solution of these gases is controlled by a chemical process. This process is basically an equilibrium relationship between the molecular and ionic forms of these constituents and expresses the development either of an acid–base reaction or of a redox reaction. Examples for the former are the solubilities of water, sulfur trioxide and carbon dioxide, whereas oxygen and nitrogen are dissolved by redox reactions.

13.3.1 Dependence on Glass Composition

The solution of H_2O, CO_2 and SO_3 is controlled by an acid–base relationship characterized by the exchange of an oxygen ion particle between the corresponding molecular and ionic forms of the gases:

$$H_2O + O^{2-} \rightarrow 2\ OH^- \tag{4}$$

$$CO_2 + O^{2-} \rightarrow CO_3^{\ 2-} \tag{5}$$

$$SO_3 + O^{2-} \rightarrow SO_4^{2-} \tag{6}$$

Since oxygen ion activity is a measure of basicity of the melt and is therefore strongly related to the melt composition, equations (4) to (6) state that the chemical solubility is proportional to the basicity of the melt. This implies that gas solubility increases with increasing concentration and size of the modifying ions and decreases with the electric charge of these. This is also valid with oxygen solubility when multivalent ions M^{m+} and $M^{(m+n)+}$ are present in the melt. This is represented by the equation:

$$n/4\ O_2 + (y - n/2)O^{2-} + M^{m+} \leftrightarrow MO_y^{(m+n-2y)+} \tag{7}$$

where y is the ligand number of the oxocomplexes with higher valency of the multivalent ion. Basicity models have now been developed to transfer known gas solubility data from one glass composition to another [20,21].

Silicium ion activity is decisive for the chemical solution of nitrogen. Since this is inverse to the oxygen ion activity, nitrogen solubility decreases with increasing

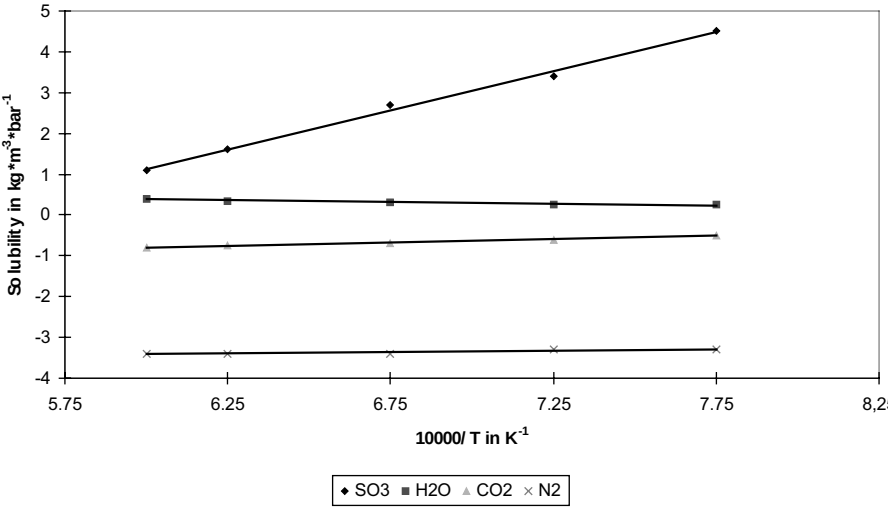

FIGURE 13.4 Solubility of various gases in soda-lime silica glass melts vs. 1/temperature according to [7,127].

basicity, which is to say that it decreases with increasing alkali content and increasing size of network modifiers.

13.3.2 Dependence on Temperature

The temperature dependence of chemical solubility of gases in melts is not uniform. While the chemical solubility of oxygen, carbon dioxide and sulfur trioxide decreases with increasing temperature, that of water and nitrogen increases (Figure 13.4). This means that the solution heats are positive for O_2, CO_2, and SO_2 and negative for H_2O and N_2. Nevertheless, for all gases, the chemical solubility C_{chem} can be given by:

$$\log C_{chem} = A/T + B \tag{8}$$

13.3.3 Dependence on Pressure

For many gases, a direct proportional relationship is given between chemical solubility C_{chem} and the partial gas pressure p in the atmosphere in contact with the melt. This means that Henry's Law can be applied here too, showing:

$$C_{chem} = S_{chem} * p \tag{9}$$

where S_{chem} is the chemical solubility coefficient of the gas in the melt. The chemical solubility of water vapor and hydrogen depends on the square root of the corresponding partial pressures (see 13.4.1), the dependence of chemical dissolved oxygen on oxygen partial pressures is more complex (see 13.4.4).

According to equations (4) to (6), an inner equilibrium between physical solubility, gases as molecules in the holes with their macroscopic fugacity and chemically

dissolved gases bonded as compounds adjusts very quickly. An equilibrium between the outer atmosphere and the gas fugacity inside the melt is never given in industrial glass melts.

13.4 SOLUBILITIES

13.4.1 Hydrogen and Water

Many detailed investigations have been made into the solubility of water vapor in glass melts [22–28]. Dissolved water is present in glasses in the form of OH-groups as shown using infrared spectroscopy. In a soda-lime-silicate glass, three bands can be determinied at 2.85 µm, 3.60 µm and 4.25 µm, indicating differently bound OH-groups according to the type of hydrogen bond established with neighboring oxygen atoms [23]. The solubility of water vapor is dependent on the partial pressure of water in the furnace atmosphere. As one water molecule or one hydrogen molecule enters the melt in form of two hydroxyl groups, the solubility of water and that of hydrogen is proportional to the square root of its partial pressure, i.e.,

$$C_{H2O} = S_{H2O} * p_{H2O}^{1/2} \tag{10}$$

The solubility of water depends on the composition of the melt, in particular on the basicity of the melt (see equation (4)).

Other water-solving mechanisms such as

$$O^{\circ} + H_2O \rightarrow 2\,(OH)^{\circ} \text{ or} \tag{11}$$

$$2O^{-} + H_2O \rightarrow 2\,(OH)^{-} + O^{\circ} \tag{11a}$$

are possible.

In binary alkali silicate melts, water solubility increases with increasing basicity [22]. The replacement of equimolar amounts of alkali by alkaline earth causes a decrease of water solubility. But in alkali borate melts Franz [24] recorded a minimum in water solubility. A decrease of water solubility with increasing alkali content up to 15 mol% alkali was shown, while higher alkali contents displayed an increase in water solubility. This is due to the intensity of cation field strength in relation to proton and hydroxyl ion activity [24].

A linear relationship exists between water solubility and temperature. Water solubility increases with increasing temperature, but the heat of solutions is not high with 42 kJ/mol for binary silicate melts and 33 kJ/mol for ternary silicate melts. A decrease of the solution heat is shown with decreasing alkali content in binary alkali silicate melts [22].

The solubility of water in melts is relatively high. In a soda-lime-silica melt at 1480°C the solubility is about 0.11 wt% or $2.8 * 10^{-3}$ g-H_2O/cm^3 – melt.

The reducing capacity of hydrogen rapidly becomes evident during the process of hydrogen solution. The solution process is governed by the following chemical equilibrium:

$$H_2 + 2\ O^{2-} + 2/n\ R^{(x+n)+} \rightarrow 2/n\ R^{x+} + 2\ OH^- \quad (12)$$

where R can be a polyvalent ion or an alkali ion (x = 0), which will be reduced to metal, or even silicium [29].

13.4.2 Carbon Dioxide

Glass batches usually contain a lot of carbonates. During the melting process, carbonates decompose and CO_2 is released into the furnace atmosphere. But smaller amounts of carbonate remain undecomposed in the melt due to its carbon dioxide solubility (see equation (5)) and lead to an oversaturation of CO_2 in the first fining stages of the melt.

The solubility of CO_2 is dependent on the basicity of the melt, meaning its alkali and alkaline earth content, as well as on the CO_2 partial pressure and on temperature.

The solubility of carbon dioxide in silicate as well as in borate melts can usually be described by equation (5). This solubility increases with increasing alkali or alkaline earth content according to Pearce [30,31] and Kröger [32,33]. The dependence on melt composition is very strong and ranges from 1 wt% CO_3^{2-} at 56% Na_2O to 10^{-4} wt% CO_3^{2-} at 25 % Na_2O and 1200˚C (Figure 13.5) [30]. Strnad [34] discovered that Henry's Law is valid for CO_2 partial pressures between 0.2 and 1 bar at 1000˚C in sodium silicate melts.

The temperature dependence of CO_2 solubility is very strong, showing a large solution heat of about 167 kJ/mol. The solubility decreases with increasing temperature, a fact that is the basis of the abovementioned melting practice using carbonates as raw materials. A temperature increase of 100˚C decreases the solubility in sodium silicate melts to 1/5.

13.4.3 Sulfur

Most glasses in the flat-glass and container-glass industries are refined with sulfate [35–38]. Since the refining mechanism is based on the behavior of sulfur solubility in glass melts, the knowledge of this solubility is of great importance. The solubility of sulfur depends on temperature and on the oxidation state of the melt and is different for oxidized and reduced melts. Therefore, changes in temperature or oxidation state that lead to sulfur saturation and to bubble formation in oxidized melts may not do so in reduced melts and vice versa.

13.4.3.1 Oxidizing Conditions

The solution of SO_2 and SO_3 in oxidized glass melts is similar to that of water and carbon dioxide in that it is principally an acid–base reaction characterized by the exchange of O^{2-} between the corresponding molecular (SO_2 or SO_3) and ionic form (SO_4^{2-}) of the gases. (See equation (6)).

The solubility of sulfur trioxide and the solution of sodium sulfate in sodium silicate melts are closely related problems. The stoichiometric reaction of sulfur trioxide with a given sodium silicate melt is equivalent to adding sodium sulfate to a more siliceous melt [39]. As molten sulfate dissociates according to reaction (6) and sulfur trioxide is almost completely dissociated above 1100˚C, one obtains

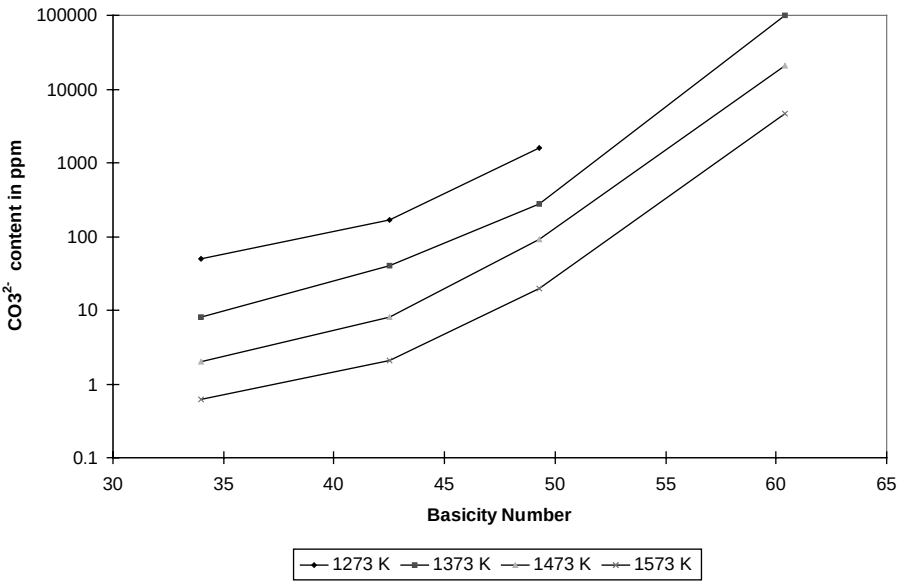

FIGURE 13.5 CO_2 solubility [30] vs. basicity numbers [21] for binary alkali silica glass melts at different temperatures.

$$SO_3 + O^{2-} \leftrightarrow SO_4^{2-} \text{ or (13) } SO_2 + 1/2\ O_2 + O^{2-} \leftrightarrow SO_4^{2-} \qquad (13)$$

Thus, sulfur solubility in silicate melts depends on oxygen ion activity (basicity) and oxygen and sulfur dioxide fugacities.

Holmquist [39] examined the SO_3 solubility in sodium silicate melts at 1150˚C, 1200˚C and 1250˚C and their dependence on the partial pressures of SO_2 and O_2. When plotting the logarithm of $p_{SO2} * p_{O2}^{1/2}$, which corresponds to p_{SO3}, versus the logarithm of the amount of sulfate, straight lines with a slope of 1 were obtained. That means that for a given glass composition and a constant temperature the sulfate content can be written as

$$\log (\%SO_3) = \log (p_{SO2} * p_{O2}^{1/2}) + \log C \qquad (14)$$

where C is a constant depending on glass composition and temperature.

According to Holmquist [39] a sodium silicate glass melt with 20 mol% Na_2O at 1200˚C has in equilibrium with 3% SO_2 and 1.6% O_2 in the furnace atmosphere an SO_3 content of 0.75 wt%. By decreasing the oxygen content to 0.6%, a decrease of SO_3 solubility to 0.48 wt% was achieved. That means that about 10 cm^3 gases (SO_2 and O_2) at 1200˚C pro cm^3 melt can be released. This shows how sensitive melts containing sulfate react as a result of only small changes in SO_2 or O_2 partial pressures.

A particularity with sulfur solubility is the miscibility gap in the Na_2O – SiO_2 – SO_3 system, which leads to a saturation solubility at SO_3 fugacities far below 1 bar. The SO_3 partial pressure at which saturation is reached depends on basicity and decreases with increasing alkali content.

Many papers [38–42] deal with the influence of melt composition on SO_3 solubility. According to equation (13), increasing basicity increases the amount of dissolved SO_3. Even an increase of 1 wt% SiO_2 in the neighborhood of a dissolving sand grain or near refractories leads to a diminishing amount of dissolved SO_3 of 0.03 wt% corresponding to a release of about 2 cm^3 of SO_2 and O_2 per cm^3 of melt [40].

The temperature dependence is the same as with CO_2. With increasing temperature at constant $p_{SO2} * p_{O2}^{1/2}$ as well as at constant p_{SO3} the SO_3 solubility decreases [39]. This decrease is larger when the basicity of the melt is lower.

13.4.3.2 Reducing Conditions

Whereas under oxidizing conditions sulfur is incorporated exclusively in the melt as the sulfate ion, under reducing conditions Fincham and Richardson [42] found out that sulfur dissolves in the melt solely as sulfide ion. The incorporation of sulfur into the melt under reducing conditions can be considered as [42]:

$$1/2\ S_2(g) + O_2(g) \rightarrow SO_2(g) \tag{15}$$

$$1/2\ S_2(g) + O^{2-}{}_{(melt)} \rightarrow 1/2\ O_2(g) + S^{2-}{}_{(melt)} \tag{16}$$

$$SO_2(g) + O^{2-}{}_{(melt)} \rightarrow 3/2\ O_2(g) + S^{2-}{}_{(melt)} \tag{17}$$

It is expected and shown [41–42] from equations (15–17) that log-log plots of % S and $(p_{S2})^{1/2}/(p_{O2})^{1/2}$ or $(p_{SO2})/\ (p_{O2})^{3/2}$ should be linear with slopes of 1. At a constant volume percentage of SO_2 a log-log plot of % S and p_{O2} should be linear with a slope of –3/2 indicating that sulfide solubility in the melt should increase as the atmosphere becomes more reducing.

13.4.3.3 General Consideration

In oxidizing melts, the solubility of sulfur as sulfate ion increases with increasing oxygen fugacity (in log-log plots with a slope of 1/2). In reducing melts, the solubility of sulfur functions conversely as the sulfide ion increases with decreasing oxygen fugacity. As a consequence of this, the typical V-shaped sulfur solubility curve with a minimum in sulfur solubility is obtained [43–44].

At a constant melt temperature and sulfur fugacity, there exists only a small range of oxygen fugacities over which sulfide ions coexist with sulfate ions. As the melt temperature increases, sulfate solubility decreases while sulfide solubility increases. Therefore, the minimum sulfur solubility moves in the oxidizing direction. This was verified by the studies of Nagashima and Katsura [45] for sodium silicate melts at 1250˚C and 1300˚C and by Schreiber et al. [46] for an alkali borosilicate glass melt (frits considered for the eventual immobilization of high level nuclear wastes) at temperatures between 850˚C and 1150 ˚C.

Similar V-shaped curves were obtained at non-equilibrium melt studies by Budd [43] who examined sulfur solubility in soda-lime-silica melts as a function of the oxidation state by adding a constant amount of sodium sulfate and carbon to the starting batch material. The oxidation state was monitored by observing the ferrous–ferric ratio in the glass. At a melting temperature of 1400˚C, a minimum of

sulfur solubility was found at log (Fe^{3+}/Fe^{2+}) = –0.4, corresponding to 72 wt% Fe^{2+}, or according to Goldmann [41] to an oxygen activity of 0.2 Pa, or according to Williams [38] to a batch redox number of –22.

It was found that carbon does not completely reduce sulfate to sulfide in the glass batch; therefore reactions such as

$$Na_2SO_4 + Na_2S + 2\ SiO_2 \rightarrow Na_2SiO_3 + SO_2 + S \tag{18}$$

are possible [44] at temperatures above 860˚C.

Swarts [47] again reports on a disproportion of SO_2 in SO_4^{2-} and elemental sulfur, which he found as deposits in bubbles from sulfate-refined melts. This reaction can be formally expressed as:

$$3\ SO_2 + Na_2O \rightarrow 2\ Na_2SO_4 + S \tag{19}$$

Both products, droplets of glassy or crystalline sulfur and patterns of crystalline sulfate, are seen in typical defects from sulfate-refined melts.

13.4.4 Oxygen

The solubility of oxygen, the oxygen partial pressure and the oxygen content are very important for the refining of glass melts and their color, the transmission of glasses and the corrosion of melts against metals as electrodes.

While the physical solubility of oxygen is very small, in the presence of multivalent ions such as iron, manganese, arsenic, antimony, cerium, chromium, titanium and so on, considerable amounts of oxygen can be dissolved chemically. The solution reaction is governed by a reduction-oxidation (redox) reaction.

The redox equilibrium of multivalent metal ions in a glass-forming melt can be represented in simplified form [48] as

$$M^{(m+n)+}{}_{melt} + n/2\ O^{2-}{}_{melt} \leftrightarrow M^{m+}{}_{melt} + n/4\ O_{2\ melt} \tag{20}$$

where M is the polyvalent ion, m+ is the lower valency state, (m+n)+ is the higher valency state, O^{2-} is the oxygen ion activity or basicity of the melt and O_2 is the physically dissolved oxygen in the holes of the network structure.

By performing redox equilibrium experiments, straight lines with a slope of –n/4 were obtained when log ($M^{m+}/M^{(m+n)+}$) was plotted against the logarithm of oxygen fugacity [48].

But redox equilibrium experiments relative to melt basicity that showed (with one exception: the redox pair Cu^+/Cu^{2+} [49]) an increasing higher valency state with increasing network former content [50–53] were not consistent with equation (20). As the different ionic forms of multivalent elements may exist within the melt structure not as isolated ions but in characteristic coordination spheres of network oxygens, the formation of complexes connected to the higher valence state of the redox ion was first proposed by Dietzel [54] and later on by others [55–56] as:

$$M^{(m+n)+} + y\ O^{2-} \rightarrow (MO_y)^{(m+n-2y)+} \quad (21)$$

or

$$M^{m+} + x\ O^{2-} \rightarrow (MO_x)^{(m-2x)+} \quad (22)$$

The redox equation in consideration of basicity and oxocomplexes for both valency states can be expressed as

$$(MO_y)^{(m+n-2y)+} \leftrightarrow (MO_x)^{(m-2x)+\prime} + (y - x - n/2)\ O^{2-} + n/4\ O_2 \quad (23)$$

where y and x are the number of oxygen atoms directly associated with the oxidized and the reduced form of the multivalent element. For y = x = 0 equation (23) changes to equation (20).

As an example, the redox equation for iron and chromium [57] can be written as:

$$(FeO_4)^{5-} \leftrightarrow Fe^{2+} + 7/2\ O^{2-} + 1/4\ O_2 \quad (24)$$

$$(CrO_4)^{2-} \leftrightarrow Cr^{3+} + 5/2\ O^{2-} + 3/4\ O_2 \quad (25)$$

The temperature-dependent equilibrium constant K1 of equation (23) can be written as

$$K1 = a^{y-x-n/2}(O^{2-}) * a^{n/4}(O_2) * a((MO_x)^{(m-2x)+})/a((MO_y)^{(m+n-2y)+}) \quad (26)$$

According to Toop and Samis [58], the activity of the free oxygen ions O^{2-} is buffered by the large reservoir of free oxygen ions of the parent melt:

$$O^{\circ} + O^{2-} \leftrightarrow 2\ O^{-} \quad (27)$$

Therefore, $a(O^{2-})$ in equation (26) is constant for a given composition.

If it is assumed that the amount of redox ions is small so that the activity ratio can be approximated by the concentration ratio, and if this ratio can be replaced by the experimentally determined redox ratio, one gets:

$$k1(T,M,glass) = \{M^{m+}/M^{(m+n)+}\}_{exper.} * a^{(y-x-n/2)}(O^{2-}) * p_{O2}{}^{n/4} \quad (28)$$

where p_{O2} is the oxygen fugacity within the melt.

As $\{M^{(m+n)+}/M^{m+}\}_{exper.} = v$ corresponds to a certain amount of dissolved oxygen, equation (28) shows that oxygen solubility depends on oxygen fugacity, basicity of the glass melt, the sort and concentration of the multivalent ion and the temperature.

For a given glass composition the equilibrium constant k1′ calculates to

$$k1'(T,M) = p_{O2}{}^{n/4}/v \quad (29)$$

The oxygen solubility (g – O_2/cm^3 – melt) due to a multivalent ion M can then be calculated [21] by

$$C_{O2} = n * d * 0.08 * c_M / G_M * v/(1+v) \quad (30)$$

where d is the density of the melt, G_M is the molecular weight and c_M is the concentration in wt% of the multivalent element and v is the experimental gained redox ratio at a certain partial pressure of oxygen.

As an example for a glass melt with 0.5 wt% Sb_2O_3 = 0.418 wt% Sb and a density of 2.5 g/cm^3, the amount of chemically dissolved oxygen C_{O2} calculates to

$$C_{O2} = 1.37 * 10^{-3} (C_{Sb\ 5+}/C_{Sb\ 3+})/(1+ C_{Sb\ 5+}/C_{Sb\ 3+}) \text{ (g – } O_2\text{/cm}^3\text{ – melt)} \quad (31)$$

To compare the oxygen solubilities of different multivalent ions and those of different authors, the solubility data are given later on (Tables 13.25–13.28, 13.39–13.41) for an oxygen partial pressure of 1 bar. That means that redox ratios in melts equilibrated with air must be divided by $(0.2095)^{n/4}$ to get the redox ratio for p_{O2} = 1 bar.

The dependence of oxygen solubility on temperature for television panel glass is given in Figure 13.6. This figure shows that by increasing temperature from 1000˚C to 1400˚C the oxygen solubility in this melt with 0.5 wt% Sb_2O_3 decreases rapidly and the melt releases about 1 cm^3 oxygen (STP) per cm^3 melt. This is one of the principles of refining with antimony.

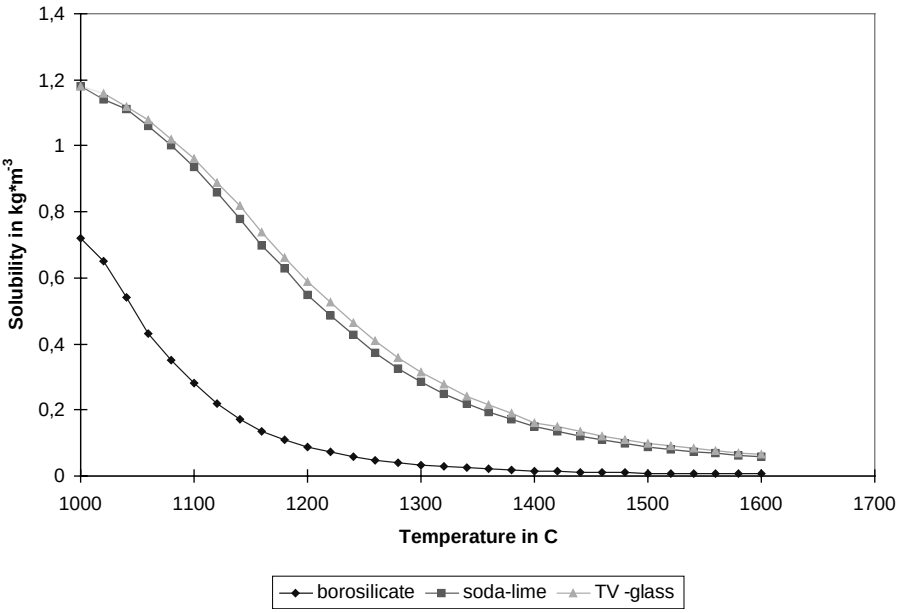

FIGURE 13.6 Chemical oxygen solubility (p_{O2} = 1 bar) vs. temperature for antimony for several glass melts [21].

Generally, those ions are suitable as refining agents whose redox ratios at melting temperatures are near 1 and that evolve a sufficient amount of oxygen during a temperature rise.

13.4.5 Nitrogen

When nitrogen is present in oxidizing melts, it is only dissolved physically in small amounts (about $2*10^{-5}$ wt% or $0.5*10^{-6}$ g/cm^3 at 1400 ˚C and 1 bar). Mulfinger and Meyer [59] found out in 1963 that large amounts of nitrogen can be chemically dissolved in melts under reducing conditions (about 0.01 g – N_2/cm^3 melt at 1 bar). Frischat [3] reported in 1980 soda-lime-silica melt saturation values of 4 wt% nitrogen.

Mulfinger and Franz [60] suggested the existence of two ways of chemical incorporation of nitrogen into molten silicates. First, in the form of nitrogen-hydrogen groupings such as $–NH_2$ and =NH in the presence of hydrogen or small amounts of water. These groups are identifiable in the infrared spectrum of the silicate, in which their absorption band is distinguished from that of the OH– groupings as much by its more pointed shape as by its greater wavelength.

Second, when the partial pressure of water vapor is nearly zero, nitrides are formed. Possible reactions are:

$$\equiv Si - O^- + NH_3 \rightarrow \equiv Si - NH^- + H_2O \quad (32)$$

$$\equiv Si - O^- + 1/2\ N_2 + 3/2\ H_2 \rightarrow \equiv Si - NH_2 + HO^- \quad (33)$$

$$\equiv Si - O^- + 1/2\ N_2 + C \rightarrow - Si \equiv N + CO \quad (34)$$

$$\equiv Si - O^- + N\equiv \rightarrow -Si \equiv N + O^- \quad (35)$$

Nitrogen solubility strongly depends on the melt atmosphere [61]. In melting conditions with reducing flames, ten times the physical solubility could be incorporated (about $2*10^{-4}$ wt% N_2). Additions of 3% coal to a soda-lime-silica melt increases the solubility to about 0.36 wt% N_2 [11]. Davis [63] found a relation between solubility and the square root of the nitrogen partial pressure in alumosilicate melts. While heating up melts saturated with nitrogen in N_2-O_2 or N_2-H_2O atmospheres, a strong decrease in chemical nitrogen solubility with a release of molecular nitrogen leading to a supersaturation of physically dissolved nitrogen was observed [11].

As the chemical solution of nitrogen depends on the silicium ion activity, the solubility decreases with increasing basicity. Borate melts can dissolve more nitrogen than silicate melts.

According to Davis [63] in silicate melts and Navarro [64] in borate melts, the chemical solubility of nitrogen increases with increasing temperature. A solution heat of about 419 kJ/g-atom N was found for alumosilicate melts at 1500˚C.

13.5 CALCULATION OF GAS SOLUBILITY

The physical solubility of the inert gases can be calculated by structural analysis of simulated systems. The configuration of silicon dioxide simulated by molecular dynamics was analyzed by Mitra and Hockney [65] to calculate the free volume or hole site distribution. They discovered that holes are randomly distributed throughout the volume and almost all the adjacent holes are connected by a small overlap. The size distribution of holes looks like a log-normal probability distribution function. Conclusions were drawn from the size distribution of holes in simulated glass concerning inert gas solubility. Assuming that holes with radius equal to or greater than 1.28 A˚ can be occupied by helium atoms only, about $3.3*10^{21}$ of such sites/cm^3 can be evaluated. This seems to be in reasonable agreement with Shelby's [8] results of $2.3*10^{21}$ sites/cm^3 in SiO_2 glass derived by the Langmuir adsorption model. Shelby's high-pressure solubility values were also confirmed. Similar calculations for neon solubility (r(Ne) = 1.38 A˚) give $2.6*10^{21}$ sites/cm^3.

Another method of predicting gas solubilities is that of Lee and Johnson [66], who applied the scaled-particle theory of Reiss et al. [67]. The reversible work required to introduce a hard-sphere solute molecule into a solvent can be used to calculate solubilities. The solubilities of argon, chlorine and carbon dioxide in various molten alkali halides were calculated, and these values corresponded closely with observed values.

Another method, based on the theory of ionic solutions with an arbitrary number of cations and anions, was successfully used in evaluating the solubility of water in oxide melts. But for the calculation of carbon dioxide solubility in glass melts, Korpachev and Novokhatskiv [68] showed that the applicability of this theory is given only when experimental data are also used.

13.6 MEASUREMENT OF GAS SOLUBILITY

Coefficients of solubility in glasses are determined either by the saturation-outgassing or by the membrane-permeation technique. The latter makes use of the relation

$$S = P/D \tag{36}$$

where P is the permeability rate of the gas concerned (obtained for the case of steady-state flow rate of a gas through a membrane), and D is the diffusion coefficient obtained by the time-lag method (case of non-stationary permeation).

The saturation-outgassing technique is normally used for glass melts. In this case, solubility measurements require the adjustment of an equilibrium by saturating the melt with gas. The measurement of gas solubility can be divided into three steps: saturation of glass melts with gas, extraction of the gases and gas analysis.

13.6.1 Saturation of Melts with Gases

To saturate a melt with gas, the melt must be subjected to the atmosphere of the gas in question. The simplest way to do this is to put the sample in a gas-tight furnace

at a certain temperature that can be purged by the gas or gas mixtures [10,27]. After a sufficiently long period, the melt is saturated by the indiffusing gas. After the run, the samples must be quenched to room temperature very quickly. A variant of this method used by Slavyanski [69], Scholze and co-workers [70] adds the advantage of considerable time savings and a thorough homogenization. In these experiments, the gas to be dissolved was bubbled through the melt. In this way, the melt is kept constantly in motion, new surfaces are continually being formed, the diffusion paths are short and considerably less time is needed to reach saturation. Care must be taken that the melt is completely free of bubbles after the experiment.

A method for the measurement of gas solubility at pressures up to 10,000 bar was described by Faile and Roy [18]. The samples used as powder were put into a pressure vessel and subjected to the pressure of the desired gas, which is pumped into the vessel through a system of valves and tubings. The samples are treated for times varying from a few minutes to several days. After the run, the sample is fast-quenched to room temperature with the full pressure maintained. Weight gains during the saturation and weight losses on heating to a preset temperature are recorded.

13.6.2 Gas Detection

13.6.2.1 Extraction and Gas Analysis

The efficiency of various glass melt degassing methods [71–76] depends on how well one succeeds in keeping the blind value small and in preventing the absorption of the extracted gases on evaporated glass components, which have been condensed in the colder parts of the extraction device.

Two methods for the extraction of gases are principally used: the vacuum hot extraction method and the carrier gas extraction method.

In vacuum hot extraction, the samples are heated in a vacuum at temperatures up to 1300˚C. The dissolved gases are released in this environment and can be carried to a gas chromatograph or to a mass spectrometer, where they can be analyzed. There is a problem with heating up the sample: if the extraction vessel is heated from outside, the method is imperfect for exact determination of very small amounts of gas, as the extraction vessel is already permeable for some gases at high temperatures. If the sample is heated inside the vessel, current lead-ins are a source of possible leakage, while the vessel itself can be cooled. An elegant and simple method consists of using an induction furnace: no lead-ins are needed, and the vessel can also be cooled. Unfortunately, the platinum crucible can be oxidized by extracted oxygen. This problem has now been solved using commercially available thermoanalysis equipment [71].

The problem of the adsorption of extracted gas on evaporated glass components, which is especially high in vacuum, has still not been solved. Dobrozemsky [72] uses a silver lining and permanently calibrates his vacuum extraction device, which is also connected to a mass spectrometer while extracting, to minimize the errors due to readsorption of gases.

In the carrier gas extraction method, the samples are disintegrated in a stream of an inert carrier gas or of oxygen. Alkali evaporation is less than in vacuum

extraction, but the reaction temperatures must be higher (about 1400˚C or more). To improve the sensitivity of the analyzing method, the extracted gases should first be collected in a cooled trap, and then after heating this trap, flushed to the analyzer. Gas analysis can then be done by gas chromatography or by mass spectrometry.

Beerkens [165] describes this method in more detail: About 7 to 30 grams of the glass to be extracted is put in a fused silica glass cuvet that is connected gas tight with a detection setup. He uses purified helium as carrier gas with which the cuvet is purged. Preheating cuvet and cullet glass pieces up to about 800˚C, the gases (CO_2 and H_2O) that are adsorbed at the surface of the cuvet and the glass pieces are removed. After 1 hour the furnace is heated up to 1450˚C. The dissolved gases are now extracted from the glass melt by bubbling the melt with helium for a period of 2 hours. (It is important to use fused silica cuvet and tubes to minimize readsorption of the extracted gases). A cooled trap (liquid nitrogen) is collecting the extracted gases and desorbs them later on when heated to 120˚C. All gas ducts are heated at about 200˚C to avoid adsorption on the duct's walls. The gases (CO_2, O_2, N_2, SO_2 and H_2O) are analyzed by a gas chromatograph or recently by a mass spectrometer [179].

13.6.2.2 Physical Measuring Methods

Besides vacuum hot extraction and carrier gas techniques there are some further substance-specific methods. The water content of glasses nowadays is measured by IR spectroscopy. One of the three absorption bands in IR (2,7–3,0 µm, 3,35–3,85 µm, 4,25 µm), most frequently that from 2,7–3,0 µm, is used. To calculate the water content, the molar absorptivity coefficient, which is dependent on composition, must be known. Therefore, the IR spectroscopic determination of water is a good relative method, but for absolute measurements it must be calibrated by an absolute method e.g., by hot extraction.

Nevertheless, in the glass industry, the transmittance at 2.8µm is often used to compare and calculate the water content of different glass samples. An extinction coefficient E [168] is calculated with the thickness d of the sample, the transmittance T_o at 2.5µm and the transmittance T at 2.8µm

$$E = 1/d * \log (T_o/T) \quad (37)$$

This formula takes into account not only reflectance losses but also absorption outside the OH-band (color of the glass). Taking Scholze's practical molar absorptivity of $\varepsilon = 41$ l/mol*cm [23] for a soda-lime-silica glass the absolute water content C is given by

$$C = E/\varepsilon \text{ mol } H_2O/l - \text{glass} \quad (38)$$

The nuclear magnetic resonance (NMR) technique (proton resonance) [77] can be used to determine the water content and, by comparing with IR measurements, to evaluate the molar absorptivity. However, discrepancies appear in older literature.

The nuclear reaction technique (NRA)

$$^{15}N + {}^{1}H \rightarrow {}^{12}C + {}^{4}He + \gamma\,(4{,}4\ MeV) \qquad (39)$$

is getting more and more interesting. Ten years ago, only water in the surface layer of the glasses could be detected [78], but nowadays the method is improved and also bulk material can be measured [166,170]. As the γ can be counted, it is an absolute method with which IR measurements of water can be calibrated. Round-robin tests within TC 14 of ICG [167] of dissolved water stated that the practical molar absorptivity coefficient of a soda-lime-silica glass (brown bottle glass) is with $\varepsilon_{2.85\,\mu m} = 41$ l/mol*cm in good agreement with Scholze's values [23]. Recently [170], the water contents were determined for a number of commercial glasses with different chemical compositions by these nuclear reaction analysis measurements. These results were used to deduce practical extinction coefficients by comparison with measured IR absorbance values at 2.8 µm. Practical extinction coefficients found are dependent on glass composition. With increasing basicity of the glasses studied, they decrease from 182 to 24 l/(mol*cm).

Chemically dissolved nitrogen can be determined by Nessler's reagent [79] or by the Kjeldahl method [80]. More recent examination methods were Fourier transform infrared spectroscopy and X-ray photoelectron spectroscopy [81], as well as other nuclear techniques [82].

Nowadays, substance-specific instruments are available and can be used [83] to detect the gases in a carrier gas stream, preferably oxygen. These instruments also have an IR cell as a substance-specific detector. Analyzers with electronic balance and data output have established themselves in industry, especially in iron and steel works and in large-scale non-ferrous metals manufacturing for control and quality-assurance of metallurgical processes. With caution and some restriction, these analyzers can also be applied to measure dissolved gases in silicates and borates.

Stahlberg et al.[84] developed a new method for measuring the dissolved oxygen content or the solubility of oxygen in antimony-containing glass melts. A cell was constructed that served three purposes: a heating unit to keep the melt at any desired temperature, an electrochemical gas concentration cell for determining oxygen fugacities with a Pt-working electrode and an yttrium-doped zirconia reference electrode [85] and an electrolytic cell (oxygen pumping cell) for varying the oxygen concentration driven by a constant current source. This cell allows the antimony redox ratio in melts to be varied, whereas the Sb^{3+}/Sb^{5+} concentration ratio could be determined by ^{121}Sb-Mössbauer spectroscopy.

The combination of both electrochemical and Mössbauer measurements allows the determination of the equilibrium constant of the redox reaction (28) and with this, the evaluation of the gas content of chemically dissolved oxygen and the oxygen solubility.

Another method to determine *in situ* redox ratios of multivalent ions is the application of voltammetry techniques [86–88,165]. A lot of redox equilibrium constants expressed as enthalpies and entropies are now available for many redox pairs in soda-lime-silica, TV-glass and E-glass melts. With these equilibrium constants, oxygen solubility can be calculated according to equations (29) and (30).

13.7 APPLICATION OF GAS SOLUBILITY

13.7.1 Glass Melt Structure

From the very beginning of glass science two models of glass structure have been developed that originally appeared to be contradictory: the "crystallite model" and the "random-network model". Today it is well recognized that glasses may possess a highly complex microstructure ranging on an order scale somewhere between complete randomness and polycrystalline configurations, which means that a glass structure can be envisaged as a deviation from crystallinity or as a pre-ordering of a statistically disordered ensemble [89]. Glass structure is generally characterized by a short-range order for silicate systems, consisting in the simplest case of SiO_4 tetrahedra, and by a certain degree of long-range order, which depends on the way in which different SiO_4 units are linked together. The introduction of network modifiers into the silicate network leads to a perturbation of short-range order that creates intrinsic vacancies and extrinsic interstitials. More network modifiers and soluble gases can be incorporated into these interstitial sites or into these vacancies or "free volume" [90–93].

It is mainly the solubility and diffusivity of rare gases in silicate melts that provide valuable insights into the structure of vitreous phases. Although the nature of a melt is very different from that of solid glass, the structure of a melt is continuous with that of the glass that forms during cooling. That means that there is no abrupt change in structure on solidification as there is with a material that crystallizes. It follows that inert gases probably dissolve in a melt in much the same manner as they do in solid glass. This contention is made and supported by the studies of Kohli and Shelby [94], which show that the solubility of helium in molten boric acid is continuous with that in solid glass. It is assumed that inert gases also dissolve in the melt in the form of isolated atoms that occupy interstices in the structure. This is particularly true at low pressures where the number of dissolved atoms/cm^3 of gases (10^{17} – 10^{18}) is only a very small fraction of the number of interstices in the structure (approximately $10^{21}/cm^3$), which means that only 1 of 10^3 – 10^4 interstices is occupied. This means that the melt is not saturated with gas in the sense that all sites are filled, but rather that an equilibrium exists between the dissolved atoms and those in the surrounding atmosphere [94].

According to Shackelford et al. [9], Shelby [15,94] and Roselieb et al. [95–96], high-pressure solubility data of inert gases in vitreous silica and in glass melts provide a unique tool for characterizing glass network geometry. As an example, the density of interstitial sites in vitreous silica — already mentioned in section 13.4 for helium and neon sites — indicates that, compared with the calculated total number of sites ($2.22*10^{22}$ sites/cm^3), about 10.4% of the interstices have an effective size greater than 2.56 A˚ and 5.86% are greater than 2.75 A˚ [9]. For albite glass melts up to 1000˚C, Roselieb et al. [96] give data for neon, argon and krypton with $5.7*10^{21}$,; $8.2*10^{20}$ and $4*10^{19}$ atoms/cm^3 respectively.

Mulfinger et al. [7] state that the solubility of gases depends on the number and size of holes in the silica network and that solubility can be interpreted by a model of holes. From physical solubility measurements of helium, neon and nitrogen in

binary silicate melts, they found out that larger holes have a larger expansion with temperature than the smaller holes, and that the expansion coefficient even of the smaller helium holes is larger than that of the melt itself.

13.7.2 Glass Melting Process

13.7.2.1 Melting

Glass batch normally consists of silica (sand) and many other chemical compounds. There are hydrates, nitrates, sulfates and, above all, carbonates. If heat is supplied to these raw materials, a huge amount of gases is released due to the vaporization of the batch water, the decomposition of the hydrates and chemical reactions. Sodium carbonate is the most reactive major component of many batches, while quartz is the least reactive. Good insight into the early stages of melting many glasses would thus be obtained by detailed knowledge of the reactions that occur between Na_2CO_3 and SiO_2 [97]. These reactions are mainly studied by the application of differential thermal and thermogravimetric analysis [98], evolved gas analysis [99] or Raman spectroscopy [100–101]. Thus, the abovementioned soda-quartz reaction occurs above 575˚C in the solid state, forming sodium metasilicate and carbon dioxide

$$Na_2CO_3 + SiO_2 \rightarrow Na_2SiO_3 + CO_2 \quad (40)$$

First, liquid phases are found at about 780˚C at Na_2SiO_3-SiO_2 eutictic, but this still leaves excess unreacted silica. At higher temperatures, the residual silica grains dissolve in the liquid melt. It is worth noticing that the addition of components that decompose to gases such as fluorides [102], sulfates [38] and nitrates [99] accelerate these first reactions.

Much of the gases are evolved by decomposition and reaction of carbonates and other compounds while solid batch particles are still present, thus, the escape of the majority of the gases occur relatively easily [97]. Some quantities of these gases form bubbles in the liquid phases. During that stage of the melting process, the melt may be opaque because of innumerable small bubbles. The gases in the bubbles can be physically and, above all, chemically dissolved in the liquid melt by the reactions already mentioned (equations 4–26, 32–35). It is assumed that the melt is saturated with these gases in the first stages of the melting process. The number of residual bubbles and the degree of saturation of the gases (because of a later reboil) cannot be accepted by the quality control management. Therefore, the melt must be fined.

13.7.2.2 Fining and Conditioning

The fining [103–107] at the glass-melting process has two tasks: eliminating the residual bubbles and decreasing the amount of dissolved gases in the melt.

Due to their buoyancy in liquids, bubbles rise to the surface in static melts. According to Stoke's Law, the velocity u of rising bubbles is given by

$$u \text{ proportional } \rho * g * r^2/\eta \quad (41)$$

where ρ, η, g and r are, respectively, the density of the melt, the viscosity of the melt, the gravitational constant on Earth and the radius of the bubble. In the case of typical melts with bubbles smaller than 0.2 mm in diameter, the velocity of rise is too small to eliminate bubbles during usual tank residence times, therefore other steps must be taken. One fining measure is to enlarge the bubble diameter, since r is decisive in equation (41). This can be done by physical fining measures such as fining by vacua, by ultrasonic or centrifugal forces, but above all by chemical fining measures that are normally used in the glass industry.

With the addition of so-called fining agents (arsenic, antimony and cerium oxides, sulfates and alkali halides), the melt will be saturated or oversaturated with some evolved gases (oxygen, sulfur dioxide, HCl) or vapors (NaCl) at the required high temperatures, because the solubility of these gases decreases with increasing temperatures. Due to this saturation, a high partial pressure of these gases will be created, while the gases diffuse via mass transport and enlarge bubbles. Thus, in specialty glasses, the redox fining agents, i.e., multivalent oxides, produce oxygen at high temperatures (equation (20)). In flat and hollow glasses, sulfates decompose to oxygen and sulfur dioxide (equation (13a)). In both cases, sulfur dioxide and oxygen enlarge the residual bubbles by diffusion. Through indiffusion of the fining gases and the bubble growth, the concentration of the original gases in the residual bubbles is decreased, which causes an intensified permeation of the gases dissolved in the melt into the bubbles. Thus, the melt will be degassed by these rising bubbles via an “elevator effect.”

After this fining process, most of the larger bubbles (> 0.2 mm in diameter) have been removed. Smaller bubbles that had no chance to get to the surface within the normal residence time can be eliminated by a second process. During conditioning, the temperatures are decreased, which increases the solubility of the chemically dissolved gas (with the exception of water). That is why bubbles with fast-diffusing gases (oxygen and carbon dioxide) then shrink and can even be dissolved.

If the melt contains more than one redox pair, an interaction during cooling the melt exists between these redox pairs so that in this quasi closed oxygen system the sum of physically and chemically dissolved oxygen remains nearly constant. Thus, the solubility of oxygen due to one redox pair will be changed at the cost of another.

As explained, gas solubility plays a very important role in fining and conditioning. Therefore, the whole fining process can only be well understood by understanding gas solubilities in glass melts.

13.7.2.3 Foaming and Reboil

Foaming and reboil are similar problems that can give rise to serious troubles in glass melting. In both cases, a sudden release of gases causes foam or reboil bubbles, which hampers the glass production process.

Foaming is the accumulation of bubbles in the surface layer that can be explained by the fact that the intensity of bubble formation is greater than the rate at which the bubbles emerge from the melt [108]. The occurrence of many gas bubbles at the surface of the melting bath is normally a problem encountered early in melting and is thus a high-temperature and melting-end problem [97]. It can be a very serious

problem in a melting tank heated by flames from above because the foam is an excellent thermal insulator. Lower bottom temperatures in the tank and a poorer melting and fining are a consequence of this. Preventing foams requires some mechanism to unstabilize thin liquid films and to help them to drain until they are so thin that they rupture sponaneously [97,109–110]. The supersaturation needed to cause foaming can be attained in two ways: by changing the temperature or by altering some chemical balance such as oxygen or other gas fugacities.

The solubility of dissolved gases may have either a positive or a negative temperature coefficient, so cooling or heating can affect bubble formation. But a change in oxygen fugacity is more likely to cause large changes in the gas fugacities needed to keep the existing dissolved gas concentration in equilibrium. It is, above all, the sulfur-containing glass melts that tend to foam, because sulfur solubility (see 13.3.4.3) strongly depends on oxygen fugacity (V-shaped-curve [42]) and its solubility varies on decades.

Experience in tank melting shows that foaming is often an individual problem, depending on the starting conditions. But laboratory and tank studies indicate that the amount of sulfates, the water content of the melt, the oxidation state of the melt, the gas atmosphere, and the humidity of the atmosphere play an important role in gas solubilities and thus in foaming behavior [111–119]. To summarize, one can say that lightly reducing melt conditions and a reducing atmosphere minimize foam problems.

The ASTM definition states that reboil is the reappearance of bubbles in molten glass after it previously appeared plain [120]. Reboil bubbles from the melting tank tend to occur at lower temperatures toward the end of fining and are thus a working-end or a forehearth problem that may lead to bubbles in the product. Reboil bubbles may also appear during reheating of the finished glass with a flame (thermic reboil). As with foaming, reboil occurs because of a supersaturation of dissolved gases or a change in temperature or the alteration of some chemical balance. Reboil can thus only be a problem if the melt is insufficiently fined. The dependence of reboil on melt parameters is nearly the same as with foaming. Gases are produced during reboil and form bubbles that have the highest gas fugacity at that condition, f.g. at thermic reboil oxygen is released. A numeral for reboil is the so-called reboil temperature at which new bubbles are formed in the melt when the melt is heated up, and that is a measure of the dissolved gases [121]. The higher the reboil temperature, the less gas is dissolved in the melt [122].

13.7.3 Bubble Defect Trouble Shooting

Gas bubbles in the end product lead to production losses and frequently represent the largest single defect glass manufacturers face. Therefore, the effective reduction of frequency and size of bubbles to acceptably low levels is one of the goals of modern glass melting. One of the best methods nowadays to discover where bubbles come from is to analyze their content. But this alone is not sufficient. As all bubble gases in glass melts interact with the gases dissolved in the melt, and consequently change their contents, a troubleshooter will be able to determine the causes of defects and the origins of these bubbles from their analyzed contents only when he has a

sufficient knowledge of the variation of bubble contents as a function of time, temperature, initial content and size of the bubbles.

Nowadays, one is inclined to use mathematical methods. Based on the diffusion equation and some initial conditions, a more or less complicated variety of mathematical solutions of bubble behavior in glass melts can be derived [123–129, 175–176]. But the solutions all have one common relation: the amount of the gases diffusing to or from the bubbles is proportional to the expression gas diffusivity D times gas solubility coefficient S times a gradient of gas fugacities Δp

$$m \text{ prop. } D * S * \Delta p \tag{42}$$

This underlines the importance of gas solubilities and gas fugacities, which determine whether a bubble will shrink or grow and how it will change its content. Therefore, to calculate the behavior of bubbles in glass melts, the explicit solubility coefficient values of the gases concerned must be known.

13.8 SOLUBILITY DATA

Gas solubility data and gas solubility coefficient data are given for melts above the transformation range. For comparison, all gas solubility coefficient data and gas solubility data are converted to $kg*m^{-3}*bar^{-a}$ or $kg*m^{-3}$ respectively (where a is 0.5 for H_2 and H_2O and 1 for the other gases). To this, the density of the melts at given temperature has to be taken into account. If the density of the melts was not explicitly given, density data were estimated from [158–16].

TABLE 13.1

Glass System	silica
Authors	Mulfinger, Dietzel, Navarro [7]
Gases	He, Ne, N_2

Temperature in K	Gas	Solubility coefficient in $kg*m^{-3}*bar^{-1}$
1753	He	0.00136
1753	Ne	0.00249
1753	N_2	0.00146

TABLE 13.2

Glass System	silica
Author	Papanikolau [130]
Gas	He

Temperature in K	Solubility coefficient in $kg*m^{-3}*bar^{-1}$
1973	0.001 ± 0.00005
2273	0.001 ± 0.00005

TABLE 13.3

Glass System	silica
Authors	Franz, Scholze [25]
Gas	H_2O

Temperature in K	Solubility coefficient in $kg*m^{-3}*bar^{-0.5}$
2023	0.74

TABLE 13.4

Glass System	silica
Author	Krämer [164]
Temperature	1753 K

Gas	Gas kinetic diameter [169] in A	Physical solubility coefficient in $kg*m^{-3}*bar^{-1}$ estimated from [7]
H_2O	2.27	0.00286
Ar	2.99	0.00256
O_2	3.02	0.00195
NO	3.09	0.00168
H_2S	3.18	0.00170
N_2	3.22	0.00134
CO	3.23	0.00132
CO_2	3.45	0.00158
SO_2	3.71	0.00166
COS	3.73	0.00150

TABLE 13.5

Glass System silica

Author Bedford [131]

Gas H_2O

Temperature in K	Solubility coefficient in $kg*m^{-3}*bar^{-0.5}$
1668	3.2

TABLE 13.6

Glass System boric oxide melt

Authors Kohli, Shelby [94]

Gases He, Ne, Ar, Kr

	Gas Solubility in $kg*m^{-3}*bar^{-1}$			
Temperature in K	He	Ne	Ar	Kr
573	0.002	0.010	0.011	0.020
673	0.003	0.014	0.017	0.030
773	0.003	0.017	0.031	0.052
873	0.004	0.020	0.036	0.055
973	0.005	0.022	0.040	0.052
1073	0.005	0.022	0.038	0.049
1173	0.005	0.021	0.035	0.044

TABLE 13.7

Glass System boric oxide melt

Authors Faile, Roy [18]

Gases H_2, Ar

Temperature in K	Gas	Solubility coefficient in $kg*m^{-3}*bar^{-1}$
623	H_2	0.0023
823	H_2	0.0025
1023	H_2	0.0026
623	Ar	0.035
1023	Ar	0.036
1173	Ar	0.035

TABLE 13.8

Glass System boric oxide melt

Authors Faile, Roy [18]

Gases H_2, Ne

Temperature in K	Gas	Pressure in kbar	Gas content in kg*m^{-3}
573	H_2	1	1.9
573	Ne	1	10.8

TABLE 13.9

Glass System boric oxide melt

Authors Faile, Roy [132]

Temperature in K	Gas	Pressure in kbar	Gas content in kg*m^{-3} at given pressure
1023	Ar	1	30.3
1023	Ar	2	53.4
1023	Ar	3	66.8
1023	Ar	4	74.8
1023	Ar	6	81.5
1023	Ar	8	89.1
1023	N_2	1	17.5
1023	N_2	2	28.7
1023	N_2	3	37.4
1023	N_2	4	43.6
1023	CO_2	1	44.1
1023	CO_2	2	70.5
1023	CO_2	3	82.3

TABLE 13.10

Glass System boric oxide melt

Author Krämer [164]

Temperature 1173 K

Gas	Gas kinetic diameter [169] in A	Physical solubility coefficient in $kg*m^{-3}*bar^{-1}$ estimated from [94]
H_2O	2.27	0.0176
Ar	2.99	0.0272
O_2	3.02	0.0214
NO	3.09	0.0195
H_2S	3.18	0.0211
N_2	3.22	0.0171
CO	3.23	0.0168
CO_2	3.45	0.0238
SO_2	3.71	0.0300
COS	3.73	0.0282

TABLE 13.11

Glass System boric oxide melt

Author Franz [24, 62]

Gas H_2O

Temperature in K	Solubility coefficient in $kg*m^{-3}*bar^{-0.5}$
973	11.4
1073	9.8
1173	8.4
1273	7.6
1373	6.9
1473	6.4

TABLE 13.12

Glass System	binary alkali silicate melts
Authors	Mulfinger, Dietzel, Navarro [7]
Gases	He, Ne, N_2 (physically dissolved)

Melt composition mol fraction alkali oxide	**Temperature in K**	**Gas solubilities in $kg*m^{-3}*bar^{-1}$**		
		He	**Ne**	**N_2**
0.165 K_2O	1673	0.00092	–	–
0.165 K_2O	1753	0.00098	0.00284	0.00150
0.20 K_2O	1673	0.00081	–	–
0.20 K_2O	1753	0.00089	–	0.00151
0.24 K_2O	1673	0.00067	–	–
0.24 K_2O	1753	0.00077	0.00248	–
0.30 K_2O	1753	–	0.00248	–
0.20 Na_2O	1673	0.00077	–	–
0.20 Na_2O	1753	0.00082	0.00203	–
0.25 Na_2O	1673	0.00058	–	–
0.25 Na_2O	1753	0.00064	0.00194	–
0.30 Na_2O	1753	–	0.00168	–
0.20 Li_2O	1673	0.00074	–	–
0.20 Li_2O	1753	0.00073	0.00209	–
0.25 Li_2O	1673	0.00057	–	–
0.25 Li_2O	1753	0.00055	0.00161	0.00146
0.30 Li_2O	1753	–	0.00147	0.00169

TABLE 13.13

Glass System	binary potassium silicate melt
Authors	Faile, Roy [132]
Melt composition	0.2 K_2O*0.8 SiO_2
Temperature in K	1073
Gases	Ar, H_2O, CO_2

Pressure in kbar	Gas	Gas content in kg*m^{-3}
2.00	Ar	26.3
9.50	Ar	90.8
0.05	H_2O	8.9
0.20	H_2O	32.6
0.28	H_2O	43.8
0.50	CO_2	14.5
2.00	CO_2	58.0
4.00	CO_2	110.0

TABLE 13.14

Glass System	binary sodium silicate melt
Authors	Nair, White, Roy [17]
Melt composition	0.33 Na_2O*0.67 SiO_2
Gas	O_2 (physically dissolved)
Temperature in K	1173

Pressure in bar	Gas content in kg*m^{-3}
165	2.6
200	5.9
280	5.2

TABLE 13.15

Glass System	binary sodium silicate melts
Authors	Franz, Scholze [25]
Gas	H_2O

Melt composition mol fraction Na_2O	**Temperature in K**	**Solubility coefficient in $kg*m^{-3}*bar^{-0.5}$**
0.026	1973	1.0
0.059	1873	1.4
0.095	1873	1.8
0.137	1753	2.2
0.180	1523	2.4
0.179	1593	2.5
0.178	1673	2.5
0.175	1753	2.6
0.260	1523	3.2
0.259	1593	3.3
0.258	1673	3.4
0.256	1753	3.5
0.279	1523	3.3
0.276	1593	3.4
0.272	1673	3.5
0.267	1753	3.6
0.378	1523	4.4
0.375	1593	4.5
0.370	1673	4.6
0.362	1753	4.7

TABLE 13.16

Glass System	binary potassium silicate melts
Authors	Franz, Scholze [25]
Gas	H_2O

Melt composition mol fraction K_2O	**Temperature in K**	**Solubility coefficient in $kg*m^{-3}*bar^{-0.5}$**
0.013	1973	0.9
0.045	1873	1.3
0.051	1753	1.5
0.075	1753	1.8
0.107	1753	2.2
0.176	1523	2.9
0.170	1593	2.9
0.160	1673	2.9
0.144	1753	2.9
0.279	1523	4.4
0.276	1593	4.5
0.273	1673	4.6
0.267	1753	4.7
0.377	1523	5.6
0.373	1593	5.7
0.367	1673	6.0
0.356	1753	6.1

TABLE 13.17

Glass System	binary lithium silicate melts
Authors	Franz, Scholze [25]
Gas	H_2O

Melt composition mol fraction Li_2O	**Temperature in K**	**Solubility coefficient in $kg*m^{-3}*bar^{-0.5}$**
0.020	1973	0.9
0.045	1973	1.0
0.096	1873	1.5
0.138	1873	1.7
0.179	1753	2.2
0.280	1523	2.8
0.279	1593	2.9
0.277	1673	2.9
0.275	1753	3.0
0.379	1523	3.6
0.378	1593	3.7
0.375	1673	3.7
0.370	1753	3.8

TABLE 13.18

Glass System	binary silicate melts
Authors	Uys, King [26]
Gas	H_2O

Melt composition in mol fractions	**Temperature in K**	**Solubility coefficient in $kg*m^{-3}*bar^{-0.5}$**
0.05 Li_2O	1680–1925	2.5
0.35 Li_2O	1680–1925	2.8
0.45 Li_2O	1680–1925	3.2
0.55 Li_2O	1680–1925	5.7
0.60 Li_2O	1680–1925	13.1
0.63 Li_2O	1680–1925	20.1
0.46 ZnO	1800–1925	2.2
0.50 ZnO	1800–1925	2.1
0.65 ZnO	1800–1925	1.8
0.70 ZnO	1800–1925	1.2
0.50 CoO	1773	1.5
0.60 CoO	1773	1.7
0.65 CoO	1773	1.2
0.74 CoO	1773	0.7

TABLE 13.19

Glass System	binary sodium silicate melts
Authors	Kröger, Goldmann [32]
Gas	CO_2

Melt composition mol fraction Na_2O	**Temperature in K**	**Solubility coefficient in $kg*m^{-3}*bar^{-1}$**
0.166	1573	0.0005
0.250	1373	0.0015
0.250	1573	0.0024
0.285	1373	0.013
0.285	1573	0.015
0.330	1373	0.044
0.330	1573	0.044

TABLE 13.20

Glass System	binary sodium silicate melts
Authors	Berjoan, Coutures [133]
Gas	CO_2

Melt composition mol fraction Na_2O	**Temperature in K**	**Solubility coefficient in $kg*m^{-3}*bar^{-1}$**
0.33	1223	0.5
0.45	1333	1.9
0.45	1353	1.3
0.45	1393	0.5
0.467	1363	16
0.497	1373	15
0.497	1383	13
0.497	1433	7
0.497	1473	4
0.545	1343	84
0.545	1373	69
0.545	1423	41
0.545	1473	19
0.594	1373	189

TABLE 13.21

Glass System	binary sodium silicate melts	
Author	Pearce [30]	
Gas	CO_2	
Melt composition mol fraction Na_2O	**Temperature in K**	**Solubility coefficient in $kg*m^{-3}*bar^{-1}$**
0.25	1223	0.21
0.25	1273	0.11
0.25	1308	0.037
0.25	1333	0.016
0.25	1473	0.004
0.35	1173	1.57
0.35	1243	0.51
0.35	1283	0.19
0.35	1373	0.08
0.35	1413	0.03
0.35	1473	0.02
0.43	1303	1.6
0.43	1333	1.1
0.43	1373	0.45
0.43	1423	0.32
0.43	1473	0.08
0.43	1533	0.06
0.56	1343	83.9
0.56	1408	76.0
0.56	1473	33.3
0.56	1533	19.0
0.56	1573	7.9

TABLE 13.22

Glass System	binary sodium silicate melts	
Author	Strnad [34]	
Gas	CO_2	
Melt composition mol fraction Na_2O	**Temperature in K**	**Solubility coefficient in $kg*m^{-3}*bar^{-1}$**
0.244	1273	0.16
0.278	1273	0.20
0.303	1273	0.23
0.344	1273	0.46

TABLE 13.23

Glass System	binary sodium silicate melts
Author	Holmquist [39]
Gas	SO_3

Melt composition mol fraction Na_2O	**Temperature in K**	**Pressure p_{SO3}*10⁶ at**	**Gas content in kg*m⁻³**
0.33	1423	13	76
0.25	1423	13	7
0.40	1473	10	200
0.364	1473	10	100
0.33	1473	10	48
0.286	1473	10	9
0.25	1473	10	2
0.33	1523	8	18

TABLE 13.24

Glass System	binary sodium silicate melts
Authors	Brow, Pantano [134]
Gas	N Chemically dissolved

Melt composition mol fraction Na_2O	**Temperature in K**	**Additions of Si_3N_4 in mol %**	**N–content in kg*m⁻³**
0.25	1873	0	0
0.255	1873	1.06	4.2
0.269	1873	2.17	4.8
0.267	1873	3.33	11.3
0.273	1873	4.55	13.3

TABLE 13.25

Glass System	binary sodium silicate melts
Authors	Baak, Hornyak [135]
Gas	O_2 chemically dissolved due to redox equilibria
Multivalent ion	Sb^{5+}/Sb^{3+}
Assumed	0.5wt% Sb_2O_3

Melt composition mol fraction Na_2O	**Temperature in K**	**Oxygen solubility for pO_2 = 1bar in $kg*m^{-3}$**
0.33	1374	0.88
0.33	1470	0.82
0.33	1588	0.58
0.33	1690	0.39

TABLE 13.26

Glass System	binary alkali silicate melts
Authors	Pyare [136], Paul, Douglas [51,52]
Gas	O_2 chemically dissolved due to redox equilibria
Multivalent elements	As^{5+}/As^{3+} Fe3+/Fe2+ Ce4+/Ce3+
Temperature	1673 K
Assumed	0.5 wt% of lower multivalent oxide

Melt composition mol fraction alkali oxide	**Oxygen solubility for p_{O2} = 1 bar in kg*m^{-3}**		
	Multivalent elements		
	As	**Fe**	**Ce**
0.20 Li_2O	0.87	0.94	–
0.25 Li_2O	1.07	1.04	–
0.30 Li_2O	1.27	1.08	0.12
0.35 Li_2O	1.49	1.12	0.15
0.40 Li_2O	1.57	1.15	0.18
0.15 Na_2O	0.83	–	–
0.20 Na_2O	1.16	–	–
0.25 Na_2O	1.39	1.11	0.15
0.30 Na_2O	1.55	1.15	0.20
0.35 Na_2O	1.62	1.19	0.27
0.40 Na_2O	1.70	1.21	0.33
0.45 Na_2O	–	1.23	0.38
0.10 K_2O	–	0.85	–
0.15 K_2O	0.97	1.00	–
0.20 K_2O	1.31	1.10	0.20
0.25 K_2O	1.53	1.19	0.25
0.30 K_2O	1.60	1.21	0.32
0.35 K_2O	1.63	–	–

TABLE 13.27

Glass System	binary sodium silicate melt
Author	Johnston [48]
Melt composition	0.33 Na_2O*0.67 SiO_2
Gas	O_2 chemically dissolved due to redox equilibria
Multivalent element	Fe^{3+}/Fe^{2+}, Mn^{3+}/Mn^{2+}, Ce^{4+}/Ce^{3+}, Sb^{5+}/Sb^{3+}
Assumed	0.5wt% of multivalent oxide, ρ=2.3*10^3 kg*m^{-3}

Temperature in K	**Oxygen solubility in kg*m^{-3} for p_{O2} = 1bar**			
	Multivalent element			
	Fe	**Mn**	**Ce**	**Sb**
1273	–	0.24	0.45	–
1358	–	0.19	0.42	1.18
1373	1.27	–	–	–
1473	1.25	0.15	0.40	0.94
1543	1.24	–	–	–
1573	1.23	0.10	0.39	0.52
1723	1.18	–	–	–

TABLE 13.28

Glass System	binary alkali silicate melts
Authors	Nath, Douglas [53]
Gas	O_2 chemically dissolved due to redox equilibria
Multivalent element	Cr^{6+}/Cr^{3+}
Assumed	0.5wt% Cr_2O_3
Temperature	1673 K

Melt composition mol fraction of alkali oxide	**Oxygen solubility for p_{O_2} = 1 bar in kg*m^{-3}**
0.216 Li_2O	1.13
0.249 Li_2O	1.34
0.296 Li_2O	1.51
0.349 Li_2O	1.75
0.393 Li_2O	2.18
0.191 Na_2O	1.51
0.239 Na_2O	2.02
0.333 Na_2O	3.11
0.390 Na_2O	3.36
0.426 Na_2O	3.47
0.140 K_2O	1.81
0.179 K_2O	2.52
0.240 K_2O	3.00
0.275 K_2O	3.39
0.307 K_2O	3.60
0.327 K_2O	3.61

TABLE 13.29

Glass System	binary lead silicate melt
Authors	Sasabe, Goto [137]
Gas	O_2 due to permeation techniques

Melt composition fraction of PbO	**Temperature in K**	**Solubility coefficient in kg*m^{-3}*bar $^{-1}$**
70 % PbO	1273	4.02
70 % PbO	1473	0.80
90 % PbO	1273	5.07
90 % PbO	1473	1.00

TABLE 13.30

Glass System	binary aluminate melt
Authors	Shimoo, Kimura, Kawai [138]
Melt composition	0.645 CaO*0.355 Al_2O_3
Gas	N_2 (chemically dissolved)
Gas atmosphere	0.92 at N_2 + 0.08 at CO

Temperature in K	**Nitrogen content in kg*m^{-3}**
1743	6.7
1773	13.4
1823	34.8
1873	66.0

TABLE 13.31

Glass System	binary sodium germanate melt
Authors	Nair, White, Roy [17]
Melt composition	0.33 Na_2O*0.67 GeO_2
Gas	O_2 (physically dissolved)
Temperature	1173 K

Pressure in bar	**Gas content in kg*m^{-3}**
50	0.98
110	1.31
140	2.30
230	4.90
300	8.80

TABLE 13.32

Glass System	binary lithium borate melts
Authors	Faile, Roy [132]
Gas	H_2, He, Ne
Temperature	573 K
Pressure	1 kbar

Melt composition mol fraction Li_2O	Gas	Gas content in $kg*m^{-3}$
0.04	H_2	1.42
0.07	H_2	1.00
0.13	H_2	0.53
0.25	H_2	0.20
0.05	He	1.70
0.13	He	0.88
0.05	Ne	5.35

TABLE 13.33

Glass System	binary sodium borate melts
Authors	Faile, Roy [132]
Gas	Ar
Temperature	1023 K

Melt composition mol fraction Na_2O	Pressure in kbar	Gas content in $kg*m^{-3}$
0.000	1	30.3
0.000	2	53.4
0.021	1	17.9
0.021	2	32.1
0.078	1	5.4
0.078	2	10.8
0.310	1	1.8
0.310	2	3.6

TABLE 13.34

Glass System	binary alkali borate melts
Authors	Faile, Roy [18]
Gas	H_2
Temperature	1073 K
Pressure	2.5 kbar

Melt compositionmol fraction alkali oxide	**Gas content in kg*m^{-3}**
0.05 Li_2O	4.05
0.05 Cs_2O	3.40
0.06 K_2O	2.62
0.06 Cs_2O	2.47
0.07 Li_2O	2.83
0.10 Cs_2O	1.82
0.32 Cs_2O	0.41
0.32 K_2O	0.41

TABLE 13.35

Glass System	binary sodium borate melt
Authors	Nair, White, Roy [17]
Melt composition	0.33 Na_2O*0.67 B_2O_3
Gas	O_2 (physically dissolved)
Temperature	1173 K

Pressure in bar	**Gas content in kg*m^{-3}**
210	1.8
250	4.0
340	6.0

TABLE 13.36

Glass System	binary alkali borate melts
Author	Franz [24]
Gas	H_2O
Temperature	1173 K

Melt composition mol fraction of alkali oxide	**Solubility coefficient in $kg*m^{-3}*bar^{-0.5}$**
0.00 Li_2O	8.53
0.08 Li_2O	8.54
0.16 Li_2O	7.64
0.24 Li_2O	5.61
0.32 Li_2O	4.45
0.40 Li_2O	3.77
0.08 Na_2O	8.88
0.16 Na_2O	7.68
0.24 Na_2O	5.91
0.32 Na_2O	5.54
0.40 Na_2O	5.49
0.08 K_2O	8.28
0.16 K_2O	7.75
0.24 K_2O	6.54
0.32 K_2O	6.44
0.40 K_2O	10.84

TABLE 13.37

Glass System	binary sodium borate melts
Author	Pearce [31]
Gas	CO_2

Melt composition mol fraction Na_2O	Temperature in K	Solubility coefficient in $kg*m^{-3}$
0.388	1173	0.26
	1273	0.12
	1273	0.08
	1373	0.07
	1373	0.04
0.454	1223	2.20
	1253	1.70
	1303	1.10
	1353	0.70
	1403	0.40
0.497	1273	6.60
	1293	5.20
	1338	3.90
	1393	2.20
	1473	1.10
0.540	1273	30
	1323	20
	1373	14
	1403	11
	1473	10

TABLE 13.38

Glass System binary lithium silicate melts

Authors Beier, Krüner, Frischat [139]

Gas N (chemically dissolved)

Melt compositon 0.33 Li_2O*0.67 B_2O_3

Melting process	Nitrogen compound	Temperature in K	Atmosphere	Nitrogen content in kg*m^{-3}
conventional	BN	1273	air	1.5
	BN	1373	air	2.5
	BN	1623	Ar	4.2
	Li_3N	1623	Ar	3.8
Sol-gel	BN	1623	Ar	6.5
	NH_3	1273	N_2	3.4
	BN	1623	Ar	5.9
	Li_3N	1623	N_2	4.6

TABLE 13.39

Glass System binary sodium borate melt

Author Lahiri [140]

Gas O_2 chemically dissolved due to redox equilibria

Melt composition 0.2 Na_2O * 0.8 B_2O_3

Multivalent elements Mn^{3+}/Mn^{2+}, As^{5+}/As^{3+}, Ce^{4+}/Ce^{3+}

Assumed 0.5 wt% of multivalent oxide

Temperature in K	Oxygen content at 1 bar in kg*m^{-3} Multivalent element		
	Mn	As	Ce
1073	0.30	–	0.26
1173	0.23	1.53	0.20
1273	0.19	1.48	0.20
1373	0.07	1.43	0.17
1473	–	1.22	–

TABLE 13.40

Glass System	binary alkali borate melts
Authors	Paul, Lahiri [141]
Gas	O_2 chemically dissolved due to redox equilibria
Multivalent element	Mn^{3+}/Mn^{2+}
Assumed	0.5wt% Mn_2O_3
Temperature	1173 K

Melt composition mol fraction of alkali oxide	Oxygen solubility for pO_2 = 1 bar in $kg*m^{-3}$
0.228 Li_2O	0.12
0.300 Li_2O	0.16
0.345 Li_2O	0.21
0.400 Li_2O	0.25
0.200 Na2O	0.11
0.250 Na2O	0.21
0.300 Na2O	0.33
0.350 Na2O	0.40
0.400 Na2O	0.55
0.150 K_2O	0.15
0.200 K_2O	0.26
0.250 K_2O	0.37
0.300 K_2O	0.63

TABLE 13.41

Glass System	binary sodium borate melts
Authors	Lee, Brückner [142]
Gas	O_2 chemically dissolved due to redox equilibria
Multivalent element	Mn^{3+}/Mn^{2+}, Fe^{3+}/Fe^{2+}, Cr^{6+}/Cr^{3+}
Assumed	0.5 wt% of multivalent oxide
Temperature	1273 K

Melt composition mol fraction Na_2O	Oxygen solubility for pO_2 = 1 bar in $kg*m^{-3}$ Multivalent elements		
	Mn	Fe	Cr
0.10	0.07	0.99	1.00
0.20	0.20	1.06	1.60
0.30	0.29	1.14	2.00

TABLE 13.42

Glass System	binary borosilicate melts
Authors	Kröger, Goldmann [32]
Gas	CO_2

Melt composition in mol fractions	**Temperature in K**	**Solubility coefficient in $kg*m^{-3}*bar^{-1}$**
0.5 B_2O_3*0.5 SiO_2	1373	0.0004
	1573	0.0004
	1773	0.0020
0.667 B_2O_3*0.333 SiO_2	1173	0.0020
	1373	0.0020
	1573	0.0030

TABLE 13.43

Glass System	ternary silicate melt
Authors	Mulfinger, Dietzel Navarro [7]
Gases	He, Ne
Melt composition	0.74 SiO_2*0.10 CaO* 0.16 Na_2O

Temperature in K	**Solubility coefficient in $kg*m^{-3}*bar^{-1}$**	
	He	**Ne**
1473	0.00059	0.00122
1573	0.00061	0.00146
1673	0.00062	0.00148
1753	0.00064	0.00150

TABLE 13.44

Glass System	ternary silicate melt
Authors	Mulfinger, Dietzel, Navarro [7]
Gas	N_2 (physically dissolved)
Melt composition	0.74 SiO_2*0.10 CaO*0.16 Na_2O

Temperature in K	Solubility coefficient in $kg*m^{-3}*bar^{-1}$
1573	0.00046
1673	0.00053
1773	0.00071

TABLE 13.45

Glass System	ternary soda-lime-silicate melt
Author	Krämer [164]
Temperature	1673 K

Gas	Gas kinetic diameter [169] in A	Physical Solubility coefficient in $kg*m^{-3}*bar^{-1}$ estimated from [7]
H_2O	2.27	0.00137
Ar	2.99	0.00104
O_2	3.02	0.00080
NO	3.09	0.00066
H_2S	3.18	0.00068
N_2	3.22	0.00053
CO	3.23	0.00050
CO_2	3.45	0.00057
SO_2	3.71	0.00058
COS	3.73	0.00054

TABLE 13.46

Glass System	ternary soda–lime–silicate melt
Author	Müller–Simon [143]
Gas	O_2 physically dissolved (estimated)

Temperature in K	Solubility coefficient in $kg*m^{-3}*bar^{-1}$
1473–1773	about 0.05

TABLE 13.47

Glass System	ternary soda-lime-silicate melt
Authors	Meyer, Frischat, Krämer [144]
Gas	N_2 physically dissolved
Melt composition	0.74 SiO_2*0.10 CaO*0.16 Na_2O

Temperature in K	Solubility coefficient in $kg*m^{-3}*bar^{-1}$
1673	0.00056

TABLE 13.48

Glass System	ternary silicate melt
Authors	Uys, King [26]
Gas	H_2O
Temperature	1673 K

Melt composition in mol fractions	Solubility coefficient in $kg*m^{-3}*bar^{-0.5}$
0.19 Li_2O*0.26 CaO*0.55 SiO_2	2.65

TABLE 13.49

Glass System	ternary soda-lime-silicate melts
Authors	Scholze, Mulfinger, Franz [22]
Gas	H_2O

	Solubility coefficient in $kg*m^{-3}*bar^{-0.5}$			
Melt composition in mol fractions	**1523 K**	**1593 K**	**1673 K**	**1753 K**
0,15 Na_2O*0,05 CaO*0,80 SiO_2	2.45	2.48	2.49	2.54
0,15 Na_2O*0,15 CaO*0,70 SiO_2	2.39	2.42	2.45	2.50
0,16 Na_2O*0,10 CaO*0,74 SiO_2	2.46	2.48	2.50	2.55
0,20 Na_2O*0,05 CaO*0,75 SiO_2	2.61	2.63	2.65	2.69
0,20 Na_2O*0,10 CaO*0,70 SiO_2	2.51	2.53	2.56	2.59
0,20 Na_2O*0,15 CaO*0,65 SiO_2	2.46	2.48	2.53	2.55
0,25 Na_2O*0,05 CaO*0,70 SiO_2	2.82	2.85	2.87	2.90
0,,25 Na_2O*0,10 CaO*0,65 SiO_2	2.72	2.74	2.74	2.75
0,25 Na_2O*0,15 CaO*0,65 SiO_2	2.56	2.61	2.65	2.67

TABLE 13.50

Glass System	ternary silicate melts
Authors	Franz, Scholze [25]
Gas	H_2O

Melt composition in mol fractions	Solubility coefficient in $kg*m^{-3}*bar^{-0.5}$			
	1523 K	1593 K	1673 K	1753 K
$0.26Na_2O*0.04Al_2O_3*0.7\ SiO_2$	2.76	2.78	2.79	2.81
$0.26Na_2O*0.08Al_2O_3*0.66\ SiO_2$	2.44	2.45	2.47	2.50

TABLE 13.51

Glass System	ternary silicate melts
Authors	Scholze, Mulfinger, Franz [22]
Gas	H_2O

Melt composition in mol fractions	Solubility coefficient in $kg\ m^{-3}*\ bar^{-0.5}$			
	1523 K	1593 K	1673 K	1753 K
$0.15Na_2O*0.10MgO*0.75SiO_2$	2.33	2.35	2.37	2.40
$0.15Na_2O*0.10SrO*0.75SiO_2$	2.46	2.49	2.53	2.58
$0.15Na_2O*0.10BaO*0.75SiO_2$	2.52	2.56	2.6	2.63

TABLE 13.52

Glass System	ternary soda-lime-silicate melt
Author	Götz [28]
Gas	H_2O
Melt composition	$0.16\ Na_2O*0.10\ CaO*SiO_2$

Temperature in K	Solubility coefficient in $kg*m^{-3}*bar^{-0.5}$
1473	2.16
1623	2.30
1773	2.51

TABLE 13.53

Glass System	ternary soda-lime-silicate melts
Authors	Kröger, Lummerzheim [33]
Gas	CO_2

Melt composition in mol fractions	Temperature in K	Solubility coefficient in $kg*m^{-3}*bar^{-1}$
0.15 Na_2O*0.15 CaO *0.7 SiO_2	1173	0.38
	1373	0.25
	1573	0.005
	1773	0.002
0.18 Na_2O*0.13 CaO*0.69 SiO_2	1173	0.21
	1373	0.056
	1573	0.010
	1773	0.006
0.15 Na_2O*0.11 CaO*0.74 SiO_2	1173	0.55
	1473	0.013
	1573	0.0025
	1773	0.0022

TABLE 13.54

Glass System	ternary silicate melts
Authors	Yamato, Goto [145]
Gas	CO_2

Melt composition in mol fractions	Temperature in K	Solubility coefficient in $kg*m^{-3}*bar^{-1}$
0.7Na_2O*0.3SiO_2	1373	360
	1423	333
	1473	310
0.686Na_2O*0.02P_2O_5*0.294 SiO_2	1373	310
	1423	286
	1473	265
0.658 Na_2O*0.06 P_2O_5*0.282 SiO_2	1373	188
	1423	173
	1473	150
0.63 Na_2O*0.10 P_2O_5*0.27 SiO_2	1373	76
	1423	66
	1473	55

TABLE 13.55

Glass System	ternary silicate melt
Authors	Kröger, Goldmann [32]
Gas	CO_2
Temperature	1573 K

Melt composition in wt %	Solubility coefficient in $kg*m^{-3}*bar^{-1}$
71,0 SiO_2; 15,2 Na_2O; 13,8 CaO	0.0013
68,7 SiO_2; 18,1 NaO_2; 12,2 CaO	0.0016
74,1 SiO_2; 15,8 NaO_2; 10,1 CaO	0.00085

TABLE 13.56

Glass System	ternary soda-lime-silicate melt
Author	Jebsen–Marwedel [40]
Gas	SO_3
Temperature	1663 K

Melt composition in wt %	SO_3 content in $kg*m^{-3}$
61 SiO_2; 25 Na_2O; 14 CaO	18.3
64 SiO_2; 22 Na_2O; 14 CaO	15.9
67 SiO_2; 19 Na_2O; 14 CaO	11.9
70 SiO_2; 16 Na_2O; 14 CaO	11.9
73 SiO_2; 13 Na_2O; 14 CaO	11.9
76 SiO_2; 10 Na_2O; 14 CaO	6.8
79 SiO_2; 7 Na_2O; 14 CaO	2.6

TABLE 13.57

Glass System	ternary soda-lime-silicate melt
Author	Papadopoulos [146]
Gas	SO_3
Melt composition	0.675 SiO_2*0.135 Na_2O*0,190 CaO
p_{SO3} = 0.01 bar	

Temperature in K	SO_3 content in kg*m^{-3}
1646	36.8
1646	34.0
1706	18.6
1726	16.1
1756	13.3

TABLE 13.58

Glass System	ternary soda-lime-silicate melts
Authors	TNO [165]
Melt composition	75 wt% SiO_2, 15wt% Na_2O, 10wt% CaO

Gas	Temperature in K	Solubility coefficient in kg*m^{-3}*bar^{-1}
CO_2	1493	0.0204
CO_2	1633	0.0099
CO_2	1633	0.0091
CO_2	1733	0.0086
SO_2	1473	0.680
SO_2	1598	0.578
SO_2	1673	0.288
SO_2	1673	0.288
SO_2	1723	0.261
N_2	1493	0.00095
N_2	1493	0.00297
N_2	1623	0.00098
N_2	1723	0.00084
O_2	1493	0.00922
O_2	1623	0.00600
O_2	1728	0.00326

TABLE 13.59

Glass System	ternary silicate melt
Authors	Paul, Lahiri [141]
Gas	O_2 chemically dissolved due to redox equilibria
Assumed	0.5 wt % As_2O_3; $\rho = 5000$ kg*m^{-3}
Melt composition in wt %	5 K_2O; 70 PbO; 25 SiO_2

Temperature in K	Solubility coefficient in kg*m^{-3}*bar$^{-0.5}$
1273	3.91
1573	3.78

TABLE 13.60

Glass System	ternary soda-lime-silicate melts arsenic+sulphate fining
Authors	Klouzek,Nemec [171]

Gas	Temperature in K	Solubility coefficient in kg*m^{-3}*bar^{-1}
H_2O	1473	2.10
H_2O	1573	2.24
H_2O	1673	2.34
H_2O	1753	2.42
O_2	1523	0.055
O_2	1623	0.062
O_2	1723	0.084
SO_2	1523–1723	0.1 estimated

TABLE 13.61

Glass System	ternary soda-lime-silicate melts
Authors	Beerkens [177]
Gas	SO_2 dissolved as sulfite

wt % as SO_3^{2-}	Solubility coefficient in kg*m^{-3}*bar^{-1}
0.02–0.06	0.4–1.2

TABLE 13.62

Glass System	ternary soda-lime-silicate melts
Authors	Brow, Pantano [134]
Gas	N chemically dissolved
Temperature	1873 K

Melt composition in mol fractions	**N content in kg*m^{-3}**
0.2264 Na_2O*0.1132 CaO* 0.6509 SiO_2*0.0094 Si_3N_4	1.0
0.2308 Na_2O*0.1154 CaO* 0.6346 SiO_2*0.0192 Si_3N_4	9.8
0.2353 Na_2O*0.1176 CaO* 0.6176 SiO_2*0.0294 Si_3N_4	12.6
0.2400 Na_2O*0.1200 CaO* 0.6000 SiO_2*0.0400 Si_3N_4	16.2

TABLE 13.63

Glass System	ternary soda-lime-silicate melts
Authors	Frischat, Schrimpf [3]
Gas	N reducing conditions
Melt composition	0.74 SiO_2*0.16 Na_2O*0.10 CaO
Temperature in K	1623

Additions of Si_3N_4 in wt %	**Nitrogen content in wt %**	**Nitrogen content in kg*m^{-3}**
1.5	0.5	11
3.4	1.0	22
4.8	1.5	33
7.0	2.2	48
9.0	2.7	59
13.0	3.8	84

TABLE 13.64

Glass System	ternary borosilicate melt
Authors	Kröger, Goldmann [32]
Gas	CO_2

Melt composition in mol fraction	Temperature in K	Solubility coefficient in $kg*m^{-3}*bar^{-1}$
0.35 SiO_2*0.51B_2O_3*0.14 Na_2O	1173	0.0013
	1373	0.0025
	1573	0.0027
0.25 SiO_2*0.50B_2O_3*0.25 Na_2O	1173	0.0015
	1373	0.0038
	1573	0.0021

TABLE 13.65

Glass System	television glass melt
Authors	Frischat, Buschmann, Meyer [147]
Gas	N_2 physically dissolved

Temperature in K	Solubility coefficient in $kg*m^{-3}*bar^{-1}$
1673	0.000375

TABLE 13.66

Glass System	television glass melt
Author	Kawachi [148, 175]
Gases	O_2, N_2, CO_2

	Gas solubilities for 1 bar in $kg*m^{-3}$		
Temperature in K	O_2	N_2	CO_2
1623	0.166	0.00025	0.00081
1673	0.078	0.00028	0.00078
1773	0.037	0.00035	0.00074
1823	0.027	0.00038	0.00072

TABLE 13.67

Glass System	television glass melt
Authors	Krämer, Mulfinger [27]
Gas	H_2O

Temperature in K	Solubility coefficient in $kg*m^{-3}*bar^{-0.5}$
1273	2.13
1473	2.64
1623	3.14
1773	3.78

TABLE 13.68

Glass System	television glass melt
Author	Krämer [150]
Gases	CO_2, O_2 chemically dissolved
Temperature in K	1273
Refining agent	0.5 wt % Sb_2O_3 + 0.15 wt%As_2O_3

	Solubility coefficient for p_{O_2} = 1bar in $kg*m^{-3}$
O_2	2.0
CO_2	0.22

TABLE 13.69

Glass System television glass melt antimony refined

Authors Krämer [172]

Gas	Temperature in K	Solubility coefficient in $kg*m^{-3}*bar^{-1}$
CO_2	1273	0.252
CO_2	1373	0.070
CO_2	1473	0.023
CO_2	1573	0.009
CO_2	1673	0.004
CO_2	1773	0.002
N_2	1273	0.00011
N_2	1373	0.00015
N_2	1473	0.00019
N_2	1573	0.00024
N_2	1673	0.00030
N_2	1773	0.00036
O_2	1273	2.0
O_2	1373	1.5
O_2	1473	1.1
O_2	1573	0.90
O_2	1673	0.74
O_2	1773	0.61
H_2O	1273	2.99
H_2O	1373	3.40
H_2O	1473	3.80
H_2O	1573	4.19
H_2O	1673	4.56
H_2O	1773	4.92

TABLE 13.70

Glass System	television glass melt
Authors	Krol, Rommers [149]
Gas	O_2 chemically dissolved due to redox equilibria
Refining agent	0.5 wt % Sb_2O_3

Temperature in K	Solubility coefficient for p_{O_2} = 1 bar in kg*m^{-3}
1173	1.24
1273	1.20
1373	1.04
1473	0.774
1573	0.515
1673	0.311
1773	0.179

TABLE 13.71

Glass System	television glass melt
Authors	TNO [165]

Gas	Temperature in K	Solubility coefficient in kg*m^{-3}*bar^{-1}
CO_2	1523	0.0283
CO_2	1533	0.0268
CO_2	1583	0.0217
CO_2	1623	0.0161
CO_2	1633	0.0175
CO_2	1708	0.0088
SO_2	1498	2.377
SO_2	1598	0.706
SO_2	1723	0.234
N_2	1578	0.00098
N_2	1633	0.00110
N_2	1723	0.00283
N_2	1738	0.00170
O_2	1523	0.01060
O_2	1578	0.00150
O_2	1633	0.00285
O_2	1723	0.00221

TABLE 13.72

Glass System	flat glass melt
Authors	Nemec, Mühlbauer [127]
	H_2O, CO_2
Gases	SO_2

Temperature in K	Gas solubilities for 1 bar in kg*m^{-3}		
	H_2O	CO_2	SO_3
1273	2.207	0.341	4309
1373	2.337	0.274	654
1473	2.457	0.226	128
1573	2.565	0.192	31
1673	2.665	0.166	8.8
1773	2.757	0.146	2.9

TABLE 13.73

Glass System	Industrial soda-lime-silica melt
Authors	Matyas, Nemec [176]
Gases	N_2, Ar

Temperature in K	Gas solubilities for 1 bar in kg*m^{-3}	
	N_2	Ar
1273	0.00054	0.00054
1373	0.00085	0.00055
1473	0.00128	0.00056
1573	0.00182	0.00057
1673	0.00248	0.00058
1773	0.00326	0.00059
1823	0.00370	0.00059

TABLE 13.74

Glass System container glass melt

Author Williams [38]

Gas SO_3

Remarks Non-equilibrium values after the melting process

Glass color	Fe^{2+}/Fe_{total}	redox number	SO_3 content in kg*m^{-3}
halfgreen	0.15	17	3.4
white	0.40	0	2.2
green	0.61	–14	0.9
light brown	0.82	–28	0.7
brown dark	0.83	–29	1.4

TABLE 13.75

Glass System E–glass

Authors TNO [165]

Gas	Temperature in K	Solubility coefficient in kg*m^{-3}*bar^{-1}
CO_2	1493	0.01050
CO_2	1563	0.00506
CO_2	1613	0.00629
CO_2	1693	0.00365
SO_2	1493	0.58900
SO_2	1573	0.40700
SO_2	1723	0.40700
N_2	1493	0.00106
N_2	1623	0.00048
N_2	1723	0.00270
O_2	1493	0.00157
O_2	1623	0.00032

TABLE 13.76

Glass System	E–glass melt
Authors	Schreiber, et al [153]
Gas	H_2O, SO_3, O_2 chemically dissolved

Temperature in K	Gas	Solubility coefficient in kg*m^{-3} for p = 1 bar
1373–1773	H_2O	4
1373	SO_3	100
1473	SO_3	16
1573	SO_3	6
1673	SO_3	1.4
1373	O_2 [0.12%Fe]	0.5
1673	O_2 [0.12% Fe]	0.5

TABLE 13.77

Glass System	E–glass melt	Wool glass melt
Authors	Mesko, Shelby [174]	
Gas	H_2O	
Absorpt (3500 cm^{-1})	ε = 46.8 l/mol*cm	ε = 51.5 l/mol*cm

Temperature in K	Solubility coefficient in kg*m^{-3} for p= 1 bar	Solubility coefficient in kg*m^{-3} for p= 1 bar
1173	2.4	
1273	2.7	
1373	2.6	
1473	2.6	
1523	2.4	
1573	2.6	
1323		2.6
1473		2.6
1523		2.5

TABLE 13.78

Glass System	Commercial borosilicate glass
Authors	Mesko, Kenyon, Shelby [173]
Gas	He

Temperature in K	Solubility coefficient in $kg*m^{-3}*atm^{-1}$
1273	0.0012
1723	0.0014

TABLE 13.79

Glass System	Commercial borosilicate glass
Authors	Seuwen, Köpsel [178]
Gas	N_2, CO_2
Temperature in K	1623

	Solubility coefficient (estimated) in $kg*m^{-3}*bar^{-1}$
N_2	0.00023
CO_2	0.00280

TABLE 13.80

Glass System	Commercial borosilicate glass alkali free
Authors	Aigner, Köpsel [179]
Gas	CO_2

Temperature in K	Solubility coefficient in $kg*m^{-3}*bar^{-1}$
1633	0.050
1733	0.023
1823	0.018

TABLE 13.81

Glass System	alkali borosilicate melt SRL–131
Authors	Schreiber, et al [151,152]
Gas	H_2O, SO_3, O_2 chemically dissolved
Melt composition (wt %)	57.9 SiO_2, 1.0 TiO_2 0.5 ZrO_2, 14.7 B_2O_3 0.5 La_2O_3, 2.0 MgO, 5.7 Li_2O, 17.7 Na_2O

Temperature in K	Gas	Solubility coefficient in kg*m^{-3} for p= 1 bar
1423–1573	H_2O	2.75
1273	SO_3	3100
1373	SO_3	310
1473	SO_3	50
1300	O_2 [10% Fe]	40
1443	O_2 [10% Fe]	25
1300	O_2 [1% Fe]	4
1443	O_2 [1% Fe]	4

TABLE 13.82

Glass System	alkali borosilicate melt SRL–131
Authors	Schreiber, et al [46]
Gas	O_2 due to redox equilibria
Melt composition (wt%)	57.9 SiO_2, 1.0 TiO_2, 0.5 ZrO_2, 14.7 B_2O_3, 0.5 La_2O_3, 2.0 MgO, 5.7 Li_2O, 17.7 Na_2O
Assumed	c = 0.5 wt%; $\rho = 2.1*10^3$ kg*m^{-3}
Temperature	1423 K

Redox element	Oxygen solubility for 1 bar in kg*m^{-3}
V^{5+}/V^{4+}	1.00
Fe^{3+}/Fe^{2+}	1.14
U^{6+}/U^{5+}	0.29
As^{5+}/As^{3+}	1.61
Cu^{2+}/Cu^{+}	1.00
Sb^{5+}/Sb^{3+}	0.74
Cr^{6+}/Cr^{3+}	2.24
Ce^{4+}/Ce^{3+}	0.28
Ag^{+}/Ag	0.10
Mn^{3+}/Mn^{2+}	0.15
Co^{3+}/Co^{2+}	0.05
Ni^{3+}/Ni^{2+}	0.04

TABLE 13.83

Glass System	metallic glass melt Pd–Ni–P
Authors	Dietrichs, Frischat [154]
Gas	He

Melt composition	Solubility coefficient in 10^{-6}*kg*m^{-3}*bar^{-1}		
	1223 K	1373 K	1523 K
$Pd_{43}Ni_{43}P_{14}$	25.9	53.1	75.1
$Pd_{41.5}Ni_{41.5}P_{17}$	24.9	38.6	59.9
$Pd_{40}Ni_{40}P_{20}$	19.6	33.2	65.5
$Pd_{38.5}Ni_{38.5}P_{23}$	16.9	31.8	44.2
$Pd_{37}Ni_{37}P_{26}$	9.9	21.3	38.3

TABLE 13.84

Glass System	Natural silicate melts
Author	Lux [155]
Gases	He, Ne, Ar, Kr, Xe
Temperature in K	1623

Melt	Solubility coefficient in 10^{-4}*kg*m^{-3}*bar^{-1}				
	He	Ne	Ar	Kr	Xe
Andesite	—	—	6.7	10.5	11.7
Leucite basanite	3.1	10.0	5.5	8.9	5.1
Tholeiite basalt	3.0	9.0	4.1	6.2	4.1
Alkali–olivine basalt	2.7	6.8	3.0	4.4	2.3
Ugandite	2.3	5.5	2.1	3.0	1.5

TABLE 13.85

Glass System	natural silicate melts
Authors	Jambon, Weber [156]
Gases	He, Ne, Ar, Kr, Xe
Temperature in K	1673

Melt	Solubility coefficient in 10^{-4} $kg*m^{-3}*bar^{-1}$				
	He	**Ne**	**Ar**	**Kr**	**Xe**
Tholeiite basalt	2.6	6.5	2.8	3.0	2.6

TABLE 13.86

Glass System	Natural silicate melt
Author	Roselieb [95, 96]
Gases	Ne, Ar, Kr
Temperature in K	1273
Melt composition	albite

Solubility coefficient in 10^{-4} $kg*m^{-3}*bar^{-1}$		
Ne	**Ar**	**Kr**
138	84	43

TABLE 13.87

Glass System	natural silicate melt
Authors	Mysen, Eggler, Seitz, Holloway [157]
Gas	CO_2
Melt Density	$2.4*10^3$ kg*m^{-3}

Melt composition	Temperature in K	Pressure in kbar	Gas content in kg*m^{-3}
Albite $NaAlSi_3O_8$	1723	10	27
	1798	10	29
	1898	10	29
	1723	20	36
	1798	20	38
	1898	20	38
	1973	20	48
	1723	30	38
	1798	30	43
	1898	30	53
	1973	30	65

TABLE 13.88

Glass System	natural silicate melts
Authors	Mysen, Eggler, Seitz, Holloway [157]
Gas	CO_2

Melt composition	Density in 10^3 kg*m^{-3}	Temperature in K	Pressure in kbar	Gas content in kg*m^{-3}
Diopside $CaMgSi_2O_6$	3.1	1763	10	41
		1853	10	52
		1898	10	59
		1853	20	74
		1898	20	102
		1973	20	140
Orthoclase $KAlSi_3O_8$	2.4	1898	20	36

REFERENCES

1. Roy, D.M., Faile, S.P. et al.; Effect of large concentrations of dissolved gas on properties of glasses. *Phys. Chem. Glasses* 5 (1964), 176–177.
2. Jewell, J.M., Shelby, J.E., Effect of water content and alumina additions on the transformation range, properties of Na_2O-3SiO_2 glasses. *J. Non-Cryst. Solids* 102 (1988), 24–29.
3. Frischat, G.H., Schrimpf, C., Preparation of nitrogen-containing Na_2O-CaO-SiO_2 glasses. *J. Am. Ceram. Soc.* 63 (1980), 715.
4. Belkhiria, N., Pye, L.D., The effect of the oxidation state of iron on the properties of Na_2O*2B_2O_3 glasses. *XIV. Intern. Congress Glass*, New Delhi (1986), Vol 1, 155–163.
5. Brückner, R., Properties and structure of vitreous silica. *J. Non-Cryst. Solids* 5 (1970), 123–175.
6. Dietrichs, J., Frischat, G.H., Properties of metallic glasses in the system Pd-Ni-P and in related systems. *J. Am. Ceram. Soc.* 67 (1984), C 233-C 235.
7. Mulfinger, H.O., Dietzel, A. et al., Physikalische Löslichkeit von Helium, Neon und Stickstoff in Glasschmelzen. *Glastech. Ber.* 45 (1972), 389–396.
8. Shelby, J.E., Pressure dependence of helium and neon solubility in vitreous silica. *J. Applied Physics*, Vol 47 (1976), 135–139.
9. Shackelford, J.F, Masaryk. J.S., The interstitial structure of vitreous silica. *J. Non-Cryst. Solids* 30 (1978), 127–139.
10. Mulfinger, H.O., Scholze, H., Löslichkeit und Diffusion von Helium in Glasschmelzen. I. Löslichkeit, *Glastech. Ber.* 35 (1962), 466–478.
11. Mulfinger, H.O., Physical and chemical solubility of nitrogen in glass melts. *J. Am. Ceram. Soc.* 49 (1966), 462.
12. Shelby, J.E., Solubility of Inert Gases in Glasses and Melts. *Proc. Advances in Fusion & Processing of Glass*, (*Ceramic Trans. v. 29*) New Orleans, The American Ceramic Society, 1992.
13. Swets, D.E., Lee, R.W. et al., *J. Chem. Phys* 34 (1961), 17 ff.
14. Frank, R.C.: Swets, D.E. et al., *J. Chem. Phys* 35 (1961), 1451 ff.
15. Shelby, J.E., Molecular solubility and diffusion. *Tr. Mat. Sci. Techn*. 17 (1979), 1–40.
16. Shelby, J.E., Helium diffusion and solubility in K_2O-SiO_2-glasses. *J. Am. Ceram. Soc.* 57 (1974), 260–263.
17. Nair, M., White, W.B. et al., Solubility of oxygen in glasses. *J. Am. Ceram. Soc*. 48 (1965), 52.
18. Faile, S.P., Roy, D.M., Gas solubility in relation to the structures of glasses and liquids. *J. Am. Ceram. Soc.* 56 (1973), 12-16.
19. Scholze, H., Einige Grundlagen zur physikalischen Löslichkeit von Gasen in Gläsern. *Tech. Comm.* I, DGG (1975).
20. Baucke, F.G.K., Duffy, J.A., The effect of basicity on redox equilibria in molten glasses. *Phys. Chem. Glasses* 32 (1991), 211–218.
21. Krämer, F.W., Contribution to basicity of technical glass melts in relation to redox equilibria and gas solubilities. *Glastech. Ber.* 64 (1991), 71–80.
22. Scholze, H., Mulfinger, H.O. et al., Measurement of the physical and chemical solubility of gases in glass melts. *Adv. In Glass Technol*. (1962), 230–248.
23. Scholze, H., Der Einbau des Wassers in Gläsern.I-IV. *Glastech. Ber.* 32 (1959), 81–88,142–152, 278–281, 314–320.
24. Franz, H., Solubility of water vapor in alkali borate melts. *J. Am. Ceram. Soc.* 49 (1966), 473–477.

25. Franz, H., Scholze, H., Die Löslichkeit von H2O-Dampf in Glasschmelzen verschiedener Basizität. *Glastech. Ber.* 36 (1963), 347–356.
26. Uys, J.M., King, T.B., The effect of basicity on the solubility of water in silicate melts. *Trans. Metallurg. Soc. Aime* 227 (1963), 492–500.
27. Krämer, F.W., Mulfinger,H.O., Solubility and diffusivity measurements of water in a television tube glass. *Rev. Staz. Sper. Vetro* 5 (1984), 39–42.
28. Götz, J., Über den Einfluß von Schmelzparametern auf den Wassergehalt des Glases. *Glastech. Ber.* 45 (1972), 14–18.
29. Hetherington, G., Jack, K.H., Water in vitreous silica. *Phys. Chem. Glasses* 3 (1962), 129–133.
30. Pearce, M.L., Solubility of carbon dioxide and variation of oxygen ion activity in soda-silica melts. *J. Am. Ceram. Soc.* 47 (1964), 342–347.
31. Pearce, M.L., Solubility of carbon dioxide and variation of oxygen ion activity in sodium borate melts. *J. Am. Ceram. Soc.* 48 (1965), 175–178.
32. Kröger, C., Goldmann, N., Kohlendioxydlöslichkeit in Gläsern. *Glastech. Ber.* 35 (1962), 459–466.
33. Kröger, C., Lummerzheim, D., Radiologische Bestimmung des Kohlendioxidgehalts von Natronkalkgläsern unterschiedlichen Schmelzzustandes. *Glastech. Ber.* 38 (1965), 229–232.
34. Strnad, Z., Determination of the solubility of carbon dioxide at various partial pressures in soda-silica melts using GC. *Phys. Chem. Glasses* 12 (1971), 152–155.
35. Chopinet, M-H., Barton, J.L., The Effect of Melting Temperature on the residual Sulfate Content of Glass. *XIV. Intern. Congress Glass*, New Delhi,(1986), Vol III, 9–15.
36. Conroy, A.R., Manring, W.H. et al., The role of sulfate in the melting and fining of glass batch. *The Glass Industry* 1966, 84–89, 110, 133–139.
37. DiBello, P.M., Controlling the oxidation state of a glass as a means of optimizing sulfate usage in melting and refining. *Glass Techn.* 30 (1989), 160–165.
38. Williams, H.P., Einfluß des Oxidationszustandes des Gemenges auf die Glasläuterung mit schwefelhaltigen Läutermitteln. *Glastech. Ber.* 53 (1980), 189–194.
39. Holmquist, S., Oxygen ion activity and the solubility of sulfur trioxide in sodium silicate melts. *J. Am. Ceram. Soc.* 49 (1966), 467–473.
40. Jebsen-Marwedel, H., Einfluß der Lösung von Kieselsäure auf den Gasgehalt von Glasschmelzen. *Glastech. Ber.* 17 (1939), 325–327.
41. Goldman, D.S., Redox and sulfur solubility in glass melts. International Commission on Glass: *Gas Bubbles in Glass* (1985), 74–91.
42. Fincham, C.J.B., Richardson, F.D., The behavior of sulfur in silicate and aluminate melts. *Proc. Roy. Soc. London*, (1954) 223A, 40–63.
43. Budd, S.M., Oxidation-reduction equilibrium in glass with especial reference to sulfur. 67th Annual Meeting American Ceramic Society (1965) Philadelphia.
44. Manring, W.H., Billings, D.D. et al., Reduced sulfur compounds. *The Glass Industry* (1967), 374–380.
45. Nagashima, S., Katsura, T., The solubility of sulfur in Na_2O*SiO_2 melts under various oxygen partial pressures at 1100, 1250 and 1300˚C. *Bull. Chem. Soc. Japan* 46 (1973), 3099–3103.
46. Schreiber, H.D., Leonhard, P.G. et al., Oxidation-Reduction Chemistry of Nonmetals in a Reference Borosilicate Melt. *Proc. Advances in the Fusion of Glass*, held at Alfred University, 1988, 29.1–29.14.
47. Swarts, E.L., Grimm, R.E., Bubble defects in flat glass from large tanks. *Am. Ceram. Soc. Bull.* 55 (1976), 705–710.

48. Johnston, W.D., Oxidation-reduction equilibria in molten Na_2O-$2SiO_2$ glass. *J. Am. Ceram. Soc.* 48 (1965), 184–190.
49. Lee, J.H., Brückner, R., Redoxgleichgewicht von Kupferoxid in Alkaliborat-,-germanat- und –silicatgläsern. *Glastech. Ber.* 55 (1982), 219–227.
50. Paul, A., Lahiri, D., Manganous-manganic equilibrium in alkali borate glasses. *J. Am. Ceram. Soc.* 49 (1966), 565–568.
51. Paul, A., Douglas, R.W., Ferrous-ferric equilibrium in binary alkali silicate glasses. *Phys. Chem. Glasses* 6 (1965), 207–211.
52. Paul, A., Douglas, R.W., Cerous-ceric equilibrium in binary alkali borate and alkali silicate glasses. *Phys. Chem. Glasses* 6 (1965), 212–215.
53. Nath, P., Douglas, R.W., Cr(III)-Cr(VI) Equilibrium in binary alkali silicate glasses. *Phys. Chem. Glasses* 6 (1965), 197–202.
54. Stegmaier, W., Dietzel, A., Die Bedeutung der Basizität von Glasschmelzen und Versuche zu deren Messung. *Glastech. Ber.* 18 (1940), 297–308, 353–362.
55. Holmquist, S.B., Ionic formulation of redox equilibria in glass melts. *J. Am. Ceram. Soc.* 49 (1966), 228–229.
56. Karlsson, K.H., Covalent oxocomplexes and electrovalent coordination in glass. *Glastech. Ber.* 62 (1989), 110–111.
57. Hirashima, H., Yoshida, T. et al., Redox equilibria and constitution of polyvalent ions in oxide melts and glasses. *Glastech. Ber.* 61 (1988), 283–292.
58. Toop, G.W., Samis, C.S., Some new ionic concepts of silicate slags. *Can. Met. Quart*. 1 (1962), 129–152.
59. Mulfinger, H.O., Meyer, H., Über die physikalische und chemische Löslichkeit von Stickstoff in Glasschmelzen. *Glastech. Ber.* 36 (1963), 481–483.
60. Mulfinger, H.O., Franz, H., Über den Einbau von chemisch gelöstem Stickstoff in oxidischen Glasschmelzen. *Glastech. Ber.* 38 (1965), 235–242.
61. Eloy-Martinez, R., Nobuo, S., Nitrogen Solubility in CaO-SiO_2, CaO-MgO-SiO_2,and BaO-MgO-SiO_2 Melts. *Met. Trans*. B, 21B, (1990), 97–104.
62. Franz, H., Untersuchungen über die Aciditäts-Basizitätsverhältnisse in oxidischen Schmelzen. *Glastech. Ber.* 38 (1965), 54–59.
63. Davis, M.W., Merhali, S.G., The equilibrium solubility of nitrogen in alumo-silicate melts. *Met. Trans*. 2 (1971), 2729–2733.
64. Navarro, J.M.F., Einführung von Stickstoff in Alkaliboratgläsern bei verschiedenen Temperaturen. *Glastech. Ber.* 45 (1972), 397–405.
65. Mitra, S.K., Hockney, R.W., Distribution of holes in simulated silicon dioxide glass. *J. Phys. G: Solid St. Phys*., 13 (1980), L737–741.
66. Lee, A.K.K., Johnson, E.F., Prediction of gas solubility in molten salts. *I & EC Fundamentals* 8 (1969), 726–729.
67. Reiss, H., Mayer, S.V. et al., *J. Chem. Phys* 31 (1959), 369.
68. Korpachev, V.G., Novokhatskii, I.A., The calculation of the solubility of carbon dioxide in glass melts. *Fizika i Khimiya Stekla*, Vol 3 (1977), 395–398.
69. Slavianski, V.T., *Zeitschrift für Chemie* 30 (1941), 9.
70. Scholze, H., Franz, H. et al., Der Einbau des Wassers in Gläsern. *Glastech. Ber.* 32 (1959), 421.
71. Stelzner, T., Heide, K., Degassing behavior of optical glasses. *Glastech. Ber.* 65 (1992), 150–156.
72. Breth, A., Dobrozemsky, R. et al., Analysis of Hot-Extracted Gases from Glasses by a Dynamic Method. *Proc. 3. Intern. Vacuum Congress*, Cannes, France (1980), 94–97.

73. Zluticky, J., Stverak, J. et al., Bestimmung der im Glas gelösten Gase über die Hochtemperatur-Vakuum-Extraktion und die gaschromatografische Analyse. *Glastech. Ber.* 45 (1972), 406–409.
74. Nagulevich, K.V., Polyakov, V.P. et al., Analysis of gases dissolved in alkali-free alumoborosilicate glass. Glass and Ceramics 5 (1968), 290–293.
75. Götz, J., Vosahlova, E., Beitrag zur quantitativen Bestimmung des Wassergehalts in Glas mit Hilfe der infraroten OH-Banden. *Glastech. Ber.* 41 (1968), 47–55.
76. Brass, I.J., Kodama, Y. et al., Measurement of the solubilities of gases in liquids at moderate pressures. *J. Phys. E: Sci. Instrum*. Vol 15 (1982), 62–70.
77. Müller-Warmuth, W., Schulz, G.W. et al., Protonen in Gläsern. *Zt. Naturforsch.* 20a (1965), 902–917.
78. March, P., Rauch, F., Soda-lime glass studied by ion-induced nuclear reactions. *Nucl. Instrum. Meth*. B15 (1986), 516–519.
79. Swarts, E.L., Relation of dissolved nitrogen to phototropy of reduced silicate glasses. *J. Am. Ceram. Soc.* 53 (1970), 472–475.
80. Kelen, T., Mulfinger, H.O., Mechanismus der chemischen Auflösung von Stickstoff in Glasschmelzen. *Glastech. Ber.* 41 (1968), 230–242.
81. Clabes, J.G., Fern, R.E. et al., Characterization of nitrogen-containing glasses by x-ray photoelectron spectroscopy. *J. Vac. Sci. Technol*. A 4 (1986), 1580–1584.
82. Debras, G., Deconninck, G., Light element analysis and application to glass industries. *Proc. Int. Conf. Modern Trends Activation Analysis*, München, Germany, 1976, 873–881.
83. Sugawara, K.E., Su, Y.-S., A study of the determination of low levels of carbon, hydrogen and nitrogen using an elemental analyzer. *Microchem. J.* 31 (1985), 173–175.
84. Stahlberg, B., Mosel, B.D. et al., Combined electrochemical and Mössbauer studies of the Sb(III)/Sb(V) equilibrium in a silicate glass-forming melt. *Glastech. Ber.* 61 (1988), 335–340.
85. Baucke, F.G.K., Electrochemical cells for on-line measurements of oxygen fugacities in glass-forming melts. *Glastech. Ber.* 61 (1988), 87–90.
86. Rüssel, Ch., Freude, E., Voltammetric studies in a soda-lime-silica glass melt containing two different polyvalent ions. *Glastech. Ber.* 63 (1990), 149–153.
87. Rüssel, C., Kohl, R. et al., Interaction between oxygen activity of Fe_2O_3 doped soda-lime-silica glass melts and physically dissolved oxygen. *Glastech. Ber.* 61 (1988), 209–213.
88. Kordon, T., Rüssel, C. et al., Voltammetric investigations in Na_2SO_4-refined soda-lime-silica glass melts. *Glastech. Ber.* 63 (1990), 213–218.
89. Schaeffer, H.A., *The Structure of Glass and Its Relation to the Solubility and Mobility of Gases*. Nato Advanced Study Institute, Canterbury (1976).
90. Doremus, R.H., Physical solubility of gases in fused silica. *J. Am. Ceram. Soc.* 49 (1966), 461–462.
91. Sanditov, D.S., Bartenev, G.M., The application of free volume theory to vitreous melts and glasses. *Fizika i Khimiya Stekla*,Vol 1 (1975), 414–420.
92. Popescu, M.A., Hole structure of computer models of non-crystalline materials. *J. Non-Cryst. Solids* 35 & 36 (1980), 549–554.
93. Franz, H., Kelen, T., Erkenntnisse über die Struktur von Alkalisilicatgläsern und -schmelzen aus dem Einbau der OH-Gruppen. *Glastech. Ber.* 40 (1967), 141–148.
94. Kohli, J.T., Shelby, J.E., The solubility of inert gases in vitreous and molten boric oxide. *Phys. Chem. Glasses* 31 (1990) 93–97.

95. Roselieb, K., Löslichkeit und Entgasungsverhalten von Edelgasen in amorphem Albit im Druckbereich bis 5 kbar. Dipl. Arbeit Mineral.-Petrolog. Institut, Göttingen, Germany (1987).
96. Roselieb, K., Rammensee, W. et al., Solubility and diffusion of rare gases in silicate melts. *Terra Cognita*, 8 (1988).
97. Cable, M., Principles of glass melting. *Glass Sci. Technol*., Vol 2 (1984).
98. Wilburn, F.W., Metcalfe, S.A. et al., Differential thermal analysis,differential thermogravimetric analysis and high temperature microscopy. *Glass Technol*. 6 (1965), 107–114.
99. Krämer, F.W., Gasprofilmessungen zur Bestimmung der Gasabgabe beim Glasschmelzprozess. *Glastech. Ber.* 53 (1980), 177–188.
100. Verweij, H., Raman study of the reactions in a glass forming mixture with molar composition. *J. Am. Ceram. Soc.* 62 (1979), 450–455.
101. Krol, D.M.,Jansen, R.K., Research on television glass. *Philips Tech. Rev.* 43 (1987) 253–259.
102. Götz, J., The Effect of Fluorides on Melting and Properties of Glass Melts. *Intern. Congress Glass* 1974, Kyoto, Vol 2, 132–140.
103. Cable, M., A study of refining, Part 2: Mechanisms of refining. *Glass Technol*. 2 (1961), 60–70.
104. Nemec,L., The refining of glass melts. *Glass Technol.* 15 (1974), 153–156.
105. Okamura, T., Uno, T. et al., Gases Contained in Glass during the Refining Process. *Proc. Symposium sur l'Affinage du Verre,* Paris (1955), 167–180.
106. Manabe, S., Kitamura, K., Effect of sodium sulfate and temperature on the fining of float glass. *J. Non-Cryst. Solids* 80 (1986), 630–636.
107. Nagulevich, K.V., Kudryavtsev, N.I. et al., Effect of fining temperature on the gas content of alumina-borosilicate glass. *Glass and Ceram*. 29 (1972), 318–320.
108. Pankova, N.A., Reasons for formation of foam in glass-melting tank furnaces. *Glass and Ceram.* 34 (1977), 417–419.
109. Cable, M., Rasul, C.G. et al., Laboratory investigation of foaming and reboil in soda-lime-silica melts, *Glass Technol*. 9 (1968), 25–31.
110. Kappel, J., Conradt, R. et al., Foaming behavior on glass melts. *Glastech. Ber.* 60 (1987) 189–201.
111. Hanke, K.P., Einfluß von polyvalenten Ionen und Sauerstoff auf die Sekundärblasenbildung sulfathaltiger Glasschmelzen. *Glastech. Ber.* 50 (1977), 144–147.
112. Hanke, K.P., Scholze, H., Durch SO_3 verursachte Blasenbildung H_2O-haltiger Gläser. Sprechsaal 107 (1975), 979–984.
113. Williams, H.P., Störungen durch Schaumbildung in einer Hohlglaswanne. Tech. Comm. III of DGG, April 20, 1983.
114. Schumacher, L., Beispiele zur Schaumbildung auf Glasschmelzen. Tech. Comm. III of DGG, April 20, 1983.
115. Goldman, D.S., Melt foaming, foam stability and redox in nuclear waste vitrification, *J. Non-Cryst. Solids* 84 (1986), 292–298.
116. Budd, S.M., Exelby, V.H. et al., The formation of gas bubbles in glass at high temperature. *Glass Technol*. 3 (1962), 124–129.
117. Cable, M., Rasul, C.G., Spontaneous bubble formation in silicate melts at high temperatures 2. *J. Am Ceram. Soc*. 50 (1967), 528–531.
118. Oldfield, L.F., Notton, M.A., Kinetics of Cristobalite Scum Formation on Borosilicate Glass. VII. Intern. Congress Glass, Bruxelles 1965, 66.1–66.8.
119. Rasul, C.G., Cable, M., Spontaneous bubble formation in silicate melts at high temperatures. *J. Am. Ceram. Soc.* 49 (1966), 568–571.

120. ASTM C: Standard Definitions of Terms Relating to Glass and Glass Products. ASTM Standards, part 5 (1958), 626–639.
121. Krämer, F.W., Methoden zur Bestimmung des Sauerstoffpartialdrucks und der Reboiltemperatur in sauerstoffgeläuterten Gläsern. Tech. Comm I of DGG, 17.4.1975.
122. Krämer, F.W., Reboil temperature: Measure of glass quality. Laboratorni Metody pro Kontrolu Vyroby Skla, Hradec Kralove, CSFR (1985) 35–54.
123. Cable, M., Frade, J.R., Theoretical Analysis of the Dissolution of Multi-Component Gas Bubbles. *Glastech. Ber.* 60 (1987), 355–362.
124. Krämer, F.W., Mathematsches Modell der Veränderung von Gasblasen in Glasschmelzen. *Glastech. Ber.* 52 (1979), 43–50.
125. Krämer, F.W., Mathematical Models of Bubble Growth and Dissolution in Glass Melts. Intern. Commission Glass: Gas Bubbles in Glass (1985).
126. Nemec, L., Mühlbauer, M., Verhalten von Gasblasen in der Glasschmelze bei konstanter Temperatur. *Glastech. Ber.* 54 (1981), 99–108.
127. Nemec, L., Mühlbauer, M., Mathematical model of bubble behavior during refining of glass melts. *J. Non-Cryst. Solids* 38 & 39 (1980), 593–598.
128. Ramos, J.I., Behavior of multicomponent gas bubbles in glass melts. *J. Am. Ceram. Soc.* 69 (1986, 149–154.
129. Weinberg, M., Subramanian, R.S., Dissolution of multicomponent bubbles. *J. Am. Ceram. Soc.* 63 (1980), 527–531.
130. Papanikolau, E., The solubility and diffusion of helium in fused silica above the transformation range. *J. Non-Cryst. Solids* 38 & 39 (1980), 563–568.
131. Bedford, R.G., The solubility of water in molten silicates. *Glass Technol*. 16 (1975), 20–24.
132. Faile, S.P., Roy, D.M., Solubilities of Ar, N_2, CO_2, and He in glasses at pressures to 10 kbars. *J. Am. Ceram. Soc.* 49 (1966), 638–643.
133. Berjoan, R., Coutures, J.-P., Solubilite de CO_2 dans les Liquids du Systeme Binaire Na_2O-SiO_2. Rev. Int. Hautes Temper. Refract. Fr.1983, 115–127.
134. Brow, R.K., Pantano, C.G., Nitrogen coordination in oxynitride glasses. *Comm. Am. Ceram. Soc*. (4/1984), C72-C74.
135. Baak, T., Hornyak, E.J., Antimony in glass. *The Glass Industry* 1966, 374–377.
136. Pyare, R., Singh, S.P. et al., The As(III)-As(V) equilibrium in borate and silicate glasses. *Phys. Chem. Glasses* 23 (1982), 158–168.
137. Sasabe, M., Goto, K.S., Permeability, diffusivity, and solubility of oxygen gas in liquid slag. *Metal. Trans*. 5 (1974), 2225-2233.
138. Shimoo, T., Kimura, H. et al., *J. Japan Inst. Metals* 35 (1971), 1103–1108.
139. Beier, W., Krüner, G. et al., Incorporation of nitrogen in Li_2O-B_2O_3 glasses by conventional melting and via different sol-gel routes. *Glastech. Ber.* 61 (1988), 91–100.
140. Lahiri, D., Mukherjee, B. et al., Mechanismus der Wechselwirkung zweier Redox-Oxide in Glas. *Glastech. Ber.* 47 (1974), 4–9.
141. Paul, A., Lahiri, D., A Note on the study of the As_2O_3-As_2O_5 equilibrium in glass. *Trans. Indian Ceram. Soc*. 22 (1963), 146–150.
142. Lee, J-H, Brückner, R., The electrochemical series of the 3d transition metal ions in alkali borate glasses. *Glastech. Ber.* 59 (1986), 233–251.
143. Müller-Simon, H., Einfluß der physikalischen Sauerstofflöslichkeit auf das Redox-Verhältnis des Eisens in kommerziellen Silicatgläsern. Tech. Comm. I of DGG, 19.03.1992.
144. Meyer, H. et al., Diffusion von Stickstoff in Glasschmelzen für den Fall physikalischer Lösung, *XI. Intern. Congress Glass 1977*, Prague, Vol 2, 317–326.

145. Yamato, N., Goto, K.S., Measurement of solubility of CO_2 in Na_2O-P_2O_5-SiO_2 ternary melt using a thermobalance. *J. Japan Inst. Metals* 48 (1984), 983–989.
146. Papadopoulos, K., The solubility of SO_3 in soda-lime-silica melts. *Phys. Chem. Glasses* 14 (1973), 60–65.
147. Frischat, G.H., Buschmann, O. et al., Diffusion von Stickstoff in Glasschmelzen. *Glastech. Ber.* 51 (1978), 321–327.
148. Kawachi, S., NEG, Comm. TC 14 of ICG.
149. Krol, D.M., Rommers, P.H., Oxidation-reduction behavior of antimony in silicate glasses prepared from raw materials and cullet. *Glass Technol*. Vol 25 (1984), 115–118.
150. Krämer, F.W., Estimation of Gas Solubilities from the Behavior of Gas Bubbles in Glass Melts. Schott internal report No 82/ 1983.
151. Schreiber, H.D., Schreiber, C.W. et al., Solubility and diffusion of gases in a reference borosilicate melt. *Diffusion and Defect Data*, Vol 53-54 (1987), 345–350.
152. Schreiber, H.D., Schreiber, C.W. et al., The interaction of water vapor with a borosilicate melt. *Diffusion and Defect Data* Vol 53–54 (1987), 145–154.
153. Schreiber, H.D., Kozak, S.J. et al., Equilibrium and transport properties of gases in e-glass melts. *J. Am. Ceram. Soc.* 72 (1989), 1680–1691.
154. Dietrichs, J., Frischat, G.H., Solubility of helium in melts of the metallic glass system Pd-Ni-P and in related systems. *J. Materials Sci* 21 (1986), 2535–2539.
155. Lux, G., The behavior of noble gases in silicate liquids: solution, diffusion, bubbles and surface effects with application to natural glasses. *Geochimica et Cosmochimica Acta* 51(1987), 1549-1560.
156. Jambon, A., Weber, H. et al., Solubility of He, Ne, Ar, Kr and Xe in a basalt melt in the range 1250–1600˚C, *Geochimica et Cosmochimica Acta* 50 (1986), 401–408.
157. Mysen, B.O., Eggler, D.H. et al., Carbon dioxide in silicate melts and crystals. I. Solubility measurements, *Am. J. Sci.* 276 (1976), 455–479.
158. Shartsis et al., Density and expansivity, and viscosity of molten alkali silicates. *J. Am. Ceram. Soc.* 35 (1952), 155–160.
159. Shartsis et al., Density and expansivity of alkali borates and density characteristics of some other binary glasses. *J. Am. Ceram. Soc.* 36 (1953), 35–43.
160. Riebling, E.F., *J. Chem. Phys* 39 (1963), 3022–3030.
161. Li, P.C., Ghose, A. C., Su, G. J., Density of molten boron oxide, rubidium and caesium borates. *Phys. Chem. Glasses* 1 (1960), 198–199.
162. Dymov, V.V., Baidov, V.V., Teoriya metallurgicheskikh protsessov (1968), 61, 78–90.
163. Coenen, M., Dichtemessungen an Bor-Aluminium-Silicatschmelzen. Schott Intern Notice 72/77.
164. Krämer, F.W., Solubility of gases in glass melts. *Ber. Bunsenges. Phys. Chem.* 100, (1996), 1512–1514.
165. Beerkens, R.G.C., van Kersbergen, M., Redox Reactions and Properties of Gases in Glass Melts. NCNG-Novem, TNO-Report HAM-RPT-9577.
166. Hammer, M.F., Beran, A., Endisch, D., Rauch, F., OH-concentrations in natural titanites determined by FTIR spectroscopy and nuclear reaction analysis. *Eur. J. Mineral*. 8 (1996), 281–288.
167. Krämer, F.W. TC 14 meeting, Istanbul, Sept. 1996 (internal report of ICG).
168. Geotti-Bianchini, F., de Riu, L., Infrared spectroscopic analysis of water incorporated in the structure of industrial soda-lime-silica glasses. *Glastech. Ber. Glass Sci. Technol*. 68 (1995), 228–240.
169. Landoldt-Börnstein, Atom- und Molekülphysik, 1. Teil: Atome und Ionen.

170. Ilievski, S., Dersch, O. et al., Practical IR extinction coefficients for water in commercial glasses determined by nuclear reaction analysis. *Glastech. Ber. Glass Sci.Technol*. 73 (2000), 39-45.
171. Klouzek, J., Nemec, L., A study of gas absorption by a glass melt using image recording and analysis. *Proc. 4th Int. Conf. Advances in the Fusion and Processing of Glass*, Würzburg, Germany 1995, *Glastech. Ber. Glass Sci. Technol*. 68 C2 (1995), 128–133.
172. Krämer, F.W., Simulation of fining in specialty glass. Advances in the fusion and processing of glass II, Toronto 1997. *Ceram. Trans*. 82, 7–17.
173. Mesko, M.G., Kenyon, B.E., Shelby, J.E., Helium solubility in commercial borosilicate glasses and melts. *Glastech. Ber. Glass Sci. Technol*. 73 C2 (2000), 33–42.
174. Mesko, M.G., Shelby, J.E., Solubility and diffusion of water in melts of E and wool glasses. *Phys. Chem. Glasses* 42 (2001), 389–396.
175. Kawachi, S., A study on the bubble removal process in high-temperature glass melting. Ph.D. Dissertation Kyoto University 2002, Kyoto, Japan.
176. Matyas, J., Nemec, L., Behavior of bubble files in glass melting space. *Glass Sci. Technol*. 76 (2003), 71–80.
177. Beerkens, R.G.C., Sulfate decomposition and sodium oxide activity in soda-lime-silica glass melts. *J. Am. Ceram. Soc.* 86 (2003) 1893–1899.
178. Seuwen, R., Köpsel, D., Methoden zur Messung der Blasenveränderung in Glasschmelzen. 77. *Glastechnische Tagung*, Mai 2003, Leipzig, 23–28.
179. Aigner, M-L., Köpsel, D., et al., Restgasanalyse in silicatischen Gläsern: Bestimmung von CO_2, O_2 und SO_2 – Restgasgehalt mittels Trägergasextraktion.78.Glastechnische Tagung, Juni 2004, Nürnberg, Poster Session.

Index

D

E

F

G

H

I

J

K

L

M

N

O

P

Q

R

S

T

U

V

W

X

Z

Materials Science

Properties of Glass-Forming Melts

This book presents state-of-the-art information concerning properties and processes involved in glass melts. Based upon contributions by renowned authors and scientists working with glass melt systems, **Properties of Glass-Forming Melts** is an excellent compilation of the current knowledge on property data, mechanisms, measurement techniques, and structure-related properties of glass-forming. The authors provide in-depth analyses of such topics as glass-melt density, thermal expansion, heat conductivity, and chemical activities.

Each chapter combines fundamental concepts with a compilation of recent and reliable data that is essential in the modeling of glass melting, fining, conditioning, and forming. The book first discusses the glass-forming melts, thermodynamics, transport properties, and redox effects of glass. This provides a sound basis to the analysis of important properties of glass melts such as viscosity, surface tension, density, and heat capacity as well as more generalized subjects of heat transfer and gas solubility. A chapter on electrical properties provides a solid foundation for understanding glass melting via direct Joule heating of the melt. The examination of the corrosive nature of molten glasses will be of great interest to tank designers and operators. This unique handbook concludes with an overview of nuclear waste vitrification, a growing discipline that relies on current data and encourages research in glass melts.

Features:

- Provides a thorough treatment of the abundant topics relating to glass melts
- Offers illuminating contributions from leading international experts working with glass melt systems
- Includes information on chemical, physical, and thermodynamic properties and mechanisms involved in glass melts
- Features a summary of the science and applications of nuclear waste vitrification
- Supports the exchange of technology and the advance of glass science and engineering

This book is an ideal starting place for future-generation glass scientists, an effective reference for scientists who require data on the behavior of viscous melts, and for glass technologists who apply mathematical models simulating the melting and forming processes. **Properties of Glass-Forming Melts** offers a one-of-a-kind and valuable source of reliable data and insight by those with firsthand knowledge and experiences in this field.

DK4087

ISBN 1-57444-662-2

90000

9 781574 446623

Taylor & Francis
Taylor & Francis Group

A CRC PRESS BOOK
www.taylorandfrancisgroup.com